Université de Paris

École doctorale Bio Sorbonne Paris Cité (BioSPC, ED562)

Institut Imagine, Laboratoire des Maladies Rénales Héréditaires

Modeling Nephrotic Syndrome using iPSC-derived Kidney Organoids

Par Giulia Menara

Thèse de doctorat de Biologie Cellulaire et Moléculaire

Dirigée par le Dr. Géraldine Mollet

Présentée et soutenue publiquement le 23 septembre 2020

Devant un jury composé de :

Pr. Adrian Woolf, Professor, University of Manchester	Rapporteur
Dr. Vasiliki Kalatzis, Directrice de Recherche, Université de Montpellier	Rapporteuse
Dr. Andreas Schedl, Directeur de Recherche, Université Nice Sophia Antipolis	Examinateur
Dr. Sophie Thomas, Chargée de Recherche, HDR, Université de Paris	Examinatrice
Dr. Géraldine Mollet, Chargée de Recherche, HDR, Université de Paris	Directrice de thèse

Except where otherwise noted, this is work licensed under
https://creativecommons.org/licenses/by-nc-nd/3.0/fr/

They told me "*Anyway, no one is going to read your Thesis*"
I dedicate it to who is going to do it instead.

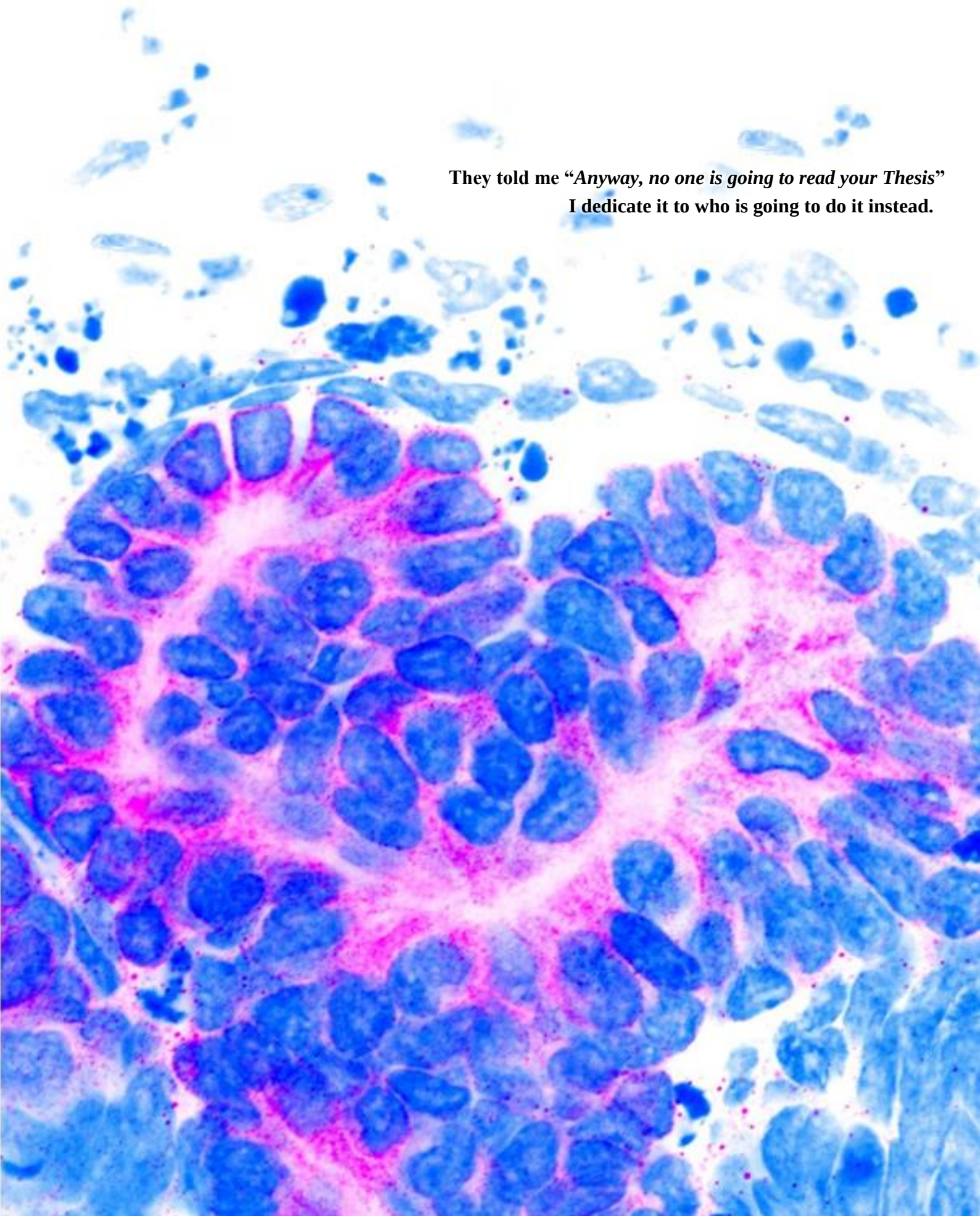

Acknowledgments

Je souhaite remercier tout d'abord le Pr. **Corinne Antignac** et le Dr. **Géraldine Mollet** : quand je vous ai rencontrées lors mon entretien, j'ai très vite réalisé que le projet que vous me proposiez avec autant d'enthousiasme allez être ma voie. Bien qu'à l'époque je n'étais qu'une timide et naïve étudiante en Master 2 qui n'avait qu'à peine une vague idée de comment changer du milieu aux cellules, vous m'avez confié ce défi monumentale. Quatre ans après le début de cette aventure je n'ai qu'un mot pour tout exprimer : merci ! Certainement, c'était ambitieux ; bien sûr, ça a été dur. Mais c'était passionnant ; c'était stimulant. J'ai eu la chance d'apprendre énormément de choses pendant ma thèse et je repars d'*Imagine* avec un bagage d'expériences unique.

Merci ***Géraldine*** pour m'avoir accompagnée et soutenue tout au long de ce parcours. Tu as su être compréhensive et à l'écoute... et aussi très souvent "à la parole", avec nos looongues réunions, pendant lesquelles le temps et les idées s'écoulaient pourtant si vite ! Avec toi j'ai toujours senti pouvoir m'exprimer librement, en me permettant de m'épanouir dans l'univers scientifique. J'admire ta positivité, que tu réussis à garder face aux nombreuses occupations dont tu es parfois submergée ; et que tu transmets à ton entourage. J'aimerais conserver ton esprit d'émerveillement, que tu manifestais en découvrant dans mes images des formes et des personnages comme on le fait avec les nuages.

Corinne, je voudrais vous remercier pour avoir été un exemple de passion et dévouement constants dans la recherche. Vous vous êtes impliquée dans les enjeux de mon projet avec une sincère curiosité scientifique et des grandes attentes envers ce nouvel horizon inexploré. Pour cela vous avez été très exigeante, ce qui m'a poussé au-delà de mes limites. Dans le laboratoire que vous avez dirigé, j'ai trouvé un terrain fertile pour construire, conjointement à l'évolution de mon projet, la personne et la scientifique que je suis aujourd'hui.

I would then like to express all my appreciation to the members of my jury committee, Pr. **Adrian Woolf**, Dr. **Vasiliki Kalatzis**, Dr. **Andreas Schedl** and Dr. **Sophie Thomas**, for having accepted to evaluate my work. Despite the sanitary situation that has developed by the end of my PhD, you all did not hesitate to confirm your availability. In those uncertain circumstances you agreed twice to assume your role, for which I am doubly grateful.

I would particularly like to thank ***Andreas***, who followed closest the progression of my PhD project during these years, as a member of my *comité de suivi individuel*. Your comments were always extremely pertinent and also attentive for an assured advancement of my PhD.

I must say I had the great pleasure to receive very positive reviews of this manuscript from my referees, Pr. Woolf and Dr. Kalatzis. Dear ***Adrian*** and ***Vasiliki***, I would like you to know how much it was important for me you that you recognized the value of the work I have done during these years. I am looking forward to present it and I am sure it will lead to a fruitful discussion.

Je suis reconnaissante envers le Dr. Thomas, de m'avoir fait le plaisir de représenter *Imagine* dans mon jury. En me confrontant aux aspects neuronaux du GAMOS dans mon projet de thèse, j'ai réalisé l'importance des programmes interdisciplinaires de collaboration tel que le cross-lab. Merci ***Sophie*** pour en être ici l'ambassadrice.

Je vais essayer de reparcourir le cheminement de ma thèse pour énoncer tous mes remerciements envers les personnes les plus importantes qui en ont fait partie.

Accueillie pendant les 6 premiers mois de ma thèse par la Plateforme iPSC, cette communauté a été pour moi comme une sorte de chaleureuse famille. Je remercie énormément le Dr. **Nathalie Lefort**. Merci ***Nathalie*** pour tout le savoir-faire que tu m'as transmis, pour ton aide et tes conseils. Ça a été un plaisir de travailler à tes côtés : ça m'a permis d'apprendre dans une ambiance amicale et détendue, où j'ai eu tous les moyens pour prendre confiance en moi. Je n'oublierai jamais les bons moments que j'ai passé avec toi dans le L2 : nos longues discussions, souvent extra-scientifiques, tes rassurants "c'est pas grave" quand je faisais des bêtises, et que dans ta tête probablement il se passait des "mais qu'est-ce qu'elle a fait, sacrebleu ?!", les feutres colorés et les ciseaux crocodile, qui mettaient tout de suite l'ambiance ! Bien évidemment, tu étais la personne la plus à mène d'être un membre exceptionnel de mon *comité de suivi individuel* : tu as toujours été à mon écoute ; tu m'as soutenue et encouragée. Tu es une des plus belles rencontres que j'ai fait à *Imagine* !

Nous t'avons parfois attribué un rôle de "maman". Littéralement ayant donné naissance à nos chères lignées iPS, tu es le point d'appui de cette sorte de famille, qui a été rejointe par **Céline Banal**, **Eddy Quelennec**, et qui réunit au sens plus large toutes les personnes qui savent ce que signifie travailler avec ces cellules à la fois merveilleuses et maudites !

En première ligne, **Ekin Ucuncu**, qui veille toujours à garder cette cohésion. ***Ekin***, tu es sans doute la personne la plus gentille que je connaisse. Nous avons franchi côte à côte les étapes de ce parcours compliqué appelé thèse (ou plutôt "esclavage" !). Bientôt ce sera à toi de devenir Docteure. Je te souhaite que la fin se passe dans les meilleures conditions, pour que tu puisses ensuite t'envoler vers les horizons qui te font rêver et que tu mérites !

Je ne peux absolument pas oublier de citer **Clémantine Dimartino**. Merci ***Clémantine*** d'avoir été une super cool "demi-stagiaire partagée" ! Ton caractère fort et ta

détermination sont ta force, et les personnes qui ne l'ont pas compris ont raté l'occasion de travailler aux côtés d'une étudiante curieuse et motivée, ce que j'ai eu au contraire le plaisir d'expérimenter. Je n'étais encore qu'une doctorante en herbe. Ça a été accompagné par toi que j'ai eu le courage d'affronter ma première redoutable manip de nucléofection pour le CRISPR, tellement stressée au point de ne pas avoir remarqué ma jupe remonté et mon c*l à l'air, un peu comme les patients à l'hôpital, avec leur blouse ouverte à l'arrière. Merci pour la magnifique œuvre d'art qu'on a réalisé. Une capture unique qui garde la place méritée sur le podium des plus belles images de ma thèse. ça a été un cadeau touchant de l'avoir converti en tableau pour m'offrir ce souvenir.

Je peux dire que ma thèse a commencé une deuxième fois le 14 septembre 2017 avec l'arrivée de **Bruno Estèbe**. Merci ***Bruno*** pour la quantité impressionnante et surtout l'incontestable qualité du travail que tu as mené. Je ne peux pas imaginer une meilleure personne que toi qui aurait pu travailler à mes côtés ! Pas seulement une "machine expérimentale de guerre", mais aussi un collaborateur sur lequel on peut toujours compter. J'ai partagé avec toi mes idées et projets ; des problèmes, des soucis, des problèmes encore… et finalement leurs solutions ! Infinies discussions scientifiques, pendant lesquelles cette lumière qui s'allumait dans tes yeux soulignait ton implication enthousiaste dans le projet. Tu a eu à faire avec mes sauts d'excitation pour les résultats positifs, mais aussi à des fleuves de larmes salées. Parce que la thèse est éprouvante, oui ; mais réalisable avec ton soutien (et que la condition optimale est sans doute celle avec un "♡" dessiné sur la boîte) !

Mis à part les perles rares avec qui j'ai partagé des moments agréables, parmi lesquelles le Dr. **Laurine Buscara**, **Gaëlle Martin** et **Charline Henry**, je tiens à remercier "l'ancienne génération" d'étudiants du labo pour une seule chose ; être partie ! Les personnes qui sont arrivées ensuite, toutes se demandant inévitablement au moins une fois "c'est quoi ce labo ?!?", ont été une bouffé d'air frais.

La première pièce en or à se retrouver coincée dans cet engrenage rouillé a été **Sonia Keddani**. Wesh, c'était grave ouf le jour où en s'en est rendu compte, t'as vu ?? Et dans la foulée, c'est **Julie Pernelle** qui a débarqué à *Imagine*, et tout a vraiment changé. ***Julie*** et ***Sonia***, vous m'avez démontré que l'on peut avoir de vrai(e)s ami(e)s parmi ses collègues ! Vous m'avez soutenue et aidée dans le moment le plus difficile de ma vie, en me prenant par la main pour me déterrer. Les soirées filles restent parmi les plus beaux souvenirs de cette période ! Votre bureau est vite devenu mon endroit préféré pour les pauses thé/café, auxquelles **Marie Michael**, **Marie Boisson** et **Mikaëlle Bocel** se sont progressivement ajoutées. Merci les filles pour avoir illuminé les journées grises de ma thèse ! #boissonmariemikaelbocel

Quelque mot en plus pour ma p'tite stagiaire ***MaRLie*** Boisson (à lire avec un "R" bien roulé, sinon ce n'est pas elle !) : ton arrivée était inattendue, mais après le petit choc initial je me suis vite faite à mon rôle de mini-chef ! Tu avais soif d'apprendre ; j'ai trouvé agréable et épanouissant de t'enseigner ce que je savais. Ce qui était bien avec toi… c'était qu'il ne manquait jamais de chocolat dans ton tiroir ! Entre un goûter, un muffin et une tasse de thé bien sucré (d'ailleurs, c'est un miracle que je n'aie pas terminé obèse ou diabétique !), nous nous sommes confrontées à la partie peut-être la plus épineuse de mon projet de thèse. Tu as bien assuré !

Je remercie l'équipe Antignac-Sonier dans sa totalité : en particulier, en plus des personnes déjà mentionnées, **Frances Tilley**, **Julie Patat**, **Francesco Miscia**, **Katy Billot**, **Eléonore Birgy**, **Daniel Pouly**, **Guillaume Dorval**, **Alexia Mahuzier**, **Yoann Martin**, **Marceau Quatredeniers**, **Alice Sérafin**, **Bastien Masson**, **Aurélien Juven**, **Christelle Arrondel**, **Olivier Gribouval**… !

I would like to particularly thank **Amandine Viau** et **Friederike Petzold**, who shared with me an office that was always too hot for Amandine, but at the right temperature for me and Friederike, and with too much light for Friederike, but nicely exposed for me and Amandine. ***Amandine***, sache que je te considère comme un exemple de bonne chercheuse ; un jour tu m'as dit que ce que tu veux c'est faire "de la bonne science". C'est tout ce que je te souhaite et qui, vu ta détermination, va surement se passer pour l'avenir ! Dear ***Friederike***, it was a great pleasure for me to meet such a sweet and friendly person as you!

Je remercie également le Dr. **Mathilda Bedin**, qui a saupoudré de piment ma thèse. Un grand sourire, une énergie positive et du jaune solaire... difficile de s'ennuyer avec toi !

Je remercie toutes les personnes qui font battre le cœur de l'association de sport. Quand je suis arrivée j'ai trouvé absolument exceptionnel d'avoir accès à ces activités sportives dans l'Institut. J'ai… détesté les sessions de CrossFit, jurant de ne plus jamais y participer après le premier essai ! Et pourtant j'y suis retournée encore et encore ; parce que c'était de la souffrance à la limite de la torture, mais finalement très agréable en si bonne compagnie ! **Lam Son Nguyen**, **Julien Fregeac**, **Daniel Medina Caño**, **Diana Dinca**, **Lucas Fares Taie**, **Vincent Abramovski**, **Olivier Alibeu**… et le board actuel avec qui je me suis investie pour l'association : **Daniel Darby**, **Stefania Musilli**, **Anna Sole Ferre**, **Francesco Miscia** et **Marion Pilorge**.

Merci ***Julien F.*** de m'avoir assistée pour cette fameuse (et terrible) première session de CrossFit. Toute petite, nouvelle dans l'Institut et avec un français hésitant, j'avoue que tu me faisais peur au début ! Et finalement nous sommes devenus (poké)amis. C'est toi qui, muni d'un grand sourire, m'a poussé à devenir coach de Yoga, selon la procédure standard de recrutement de l'association ; c'est-à-dire, en étant bien coincé(e/s) !

Je remercie **Loren Wolfe**, ***Ekin*** et **Marketa Zatloukalova**, qui ont rendu possible *our lovely Yoga sessions*. *Namaste* à tous mes chers Yogini : le partage de cette pratique avec vous a été un privilège unique. Dans le cadre spectaculaire du coucher du soleil sur une vue de Paris à couper le souffle ; il n'y avait pas de meilleur façon pour terminer en beauté la semaine !

Je remercie également le groupe de théâtre, magistralement conduit par **Anne-Marie Stikel**. Comme tu l'as dit pendant une des premières séances, "le théâtre est thérapeutique". Pour moi ça a été le cas ! Cet atelier a ouvert des parenthèses privilégiées pour s'exprimer librement dans une ambiance de confiance et complicité.

Ringrazio la mia famiglia, il mio papà **Roberto**, la mia mamma **Stefania**, i miei fratello e sorella **Andrea** e **Paola** e la mia fresca cognata **Annalisa**. Pur a 1000 km di distanza, non siete mai stati così vicini! Mi avete tirata giù dal letto quando non ero in grado di svegliarmi la mattina, fatto compagnia quando mi sentivo sola, fornito assistenza telefonica alla preparazione dei pasti ("mostrami il risotto… mmmh… ancora 2 minuti ed è pronto!")…! Il tutto tramite innumerevoli video-chiamate, chiacchierando, parlandosi sopra tutti insieme o anche senza dir niente, semplicemente stando insieme!

Et enfin, car *dulcis in fundo*, je remercie de tout mon cœur le Dr. **Julien Branchu** ♡. ***Julien***, tu es ici comme le dernier auteur d'un papier ; c'est parce que tu m'as fourni toutes les ressources nécessaires pour que je réussisse, que ce soit matérielles ou morales.

T'as su gérer le combo impressionnant $\frac{\sqrt[pandémique]{confinement \times rédaction^{thèse}}}{depression}$ grâce à ton bagage d'expérience et une infinie patience.

Et, le plus important, tu as cru en moi ! La thèse se termine, je (re)commence à vivre, en étant sûre pouvoir compter sur toi !

Résumé

Le **syndrome néphrotique cortico-résistant** (SNCR) est une maladie rénale rare caractérisée par une protéinurie massive due à des altérations structurelles de la barrière de filtration glomérulaire, dont le podocyte est un composant majeur. Plus de 50 gènes ont été impliqués dans les formes monogéniques de SNCR, tous exprimés dans le podocyte. Parmi eux, ***NPHS2***, codant pour la **podocine**, a été identifié par le groupe du Pr. Antignac comme responsable de SNCR sévère précoce ; la mutation p.**R138Q** de le **podocine** étant la plus répandue dans la population européenne.

Bien que le SRNS se présente principalement sous forme **isolée**, il peut également être associé à des **manifestations extra-rénales**. Ainsi, le groupe du Pr. Antignac a récemment décrypté les bases génétiques du **syndrome de Galloway-Mowat** (GAMOS), associant le SRNS à une **microcéphalie** et des **troubles neurologiques**, dont les mécanismes pathologiques restent encore mal compris.

Le premier objectif de ma thèse de doctorat a été de **mettre en place les techniques et outils adéquats** pour utiliser les **cellules souches pluripotentes induites** (iPSC) dans la modélisation *in vitro* de ces maladies. Deuxièmement, je me suis concentrée sur leur utilisation afin de **déchiffrer les mécanismes cellulaires et moléculaires pathologiques** impliqués dans les formes isolées et systémiques (néphro-cérébrales) des troubles glomérulaires héréditaires. Nous avons obtenu des cellules d'un patient atteint de **SRNS** portant la mutation homozygote R138Q de la podocine, ainsi que des cellules de patients atteints de **GAMOS**.

Ainsi, j'ai mis en place la différenciation des iPSC en **organoïdes rénaux**. Ceux-ci possèdent les mêmes caractéristiques que les **néphrons** *in vivo*, à savoir la succession ordonnée des segments du néphron. Au niveau du glomérule, j'ai confirmé l'expression et la localisation de marqueurs clés des **podocytes**, tels que **WT1** au noyau, la **podocalyxine** à la surface apico-latérale et au pôle basal la **néphrine**, la **podocine** et la **synaptopodine** ; de même que leur identité podocytaire par **analyse transcriptomique**. L'emploi des organoïdes rénaux représente la pierre angulaire de cette étude.

J'ai démontré que les organoïdes arborant la mutation de la podocine R138Q ont un **niveau d'expression inférieur** et une **localisation subcellulaire altérée de la podocine R138Q**. Lors de la **correction générée par CRISPR/Cas9** des iPSC de patient, nous avons **restauré la localisation et le bon niveau d'expression de la podocine**. De plus, j'ai étudié le profil transcriptomique des podocytes triés par FACS afin de mieux comprendre les mécanismes moléculaires en jeu. De manière inattendue, les données RNA-Seq suggèrent l'implication d'une activation de la **réponse de type interféron** dans les podocytes du patient R138Q. Des analyses supplémentaires sont désormais nécessaires pour statuer entre un effet de mutation ou l'influence dû au fond génétique du patient.

Grâce aux iPSC il est possible de modéliser les aspects rénaux et neuronaux du **GAMOS**. Des **organoïdes rénaux** et des **progéniteurs neuronaux** dérivés d'iPSC ont été utilisés dans ce travail. Nous avons observé une **perturbation** des processus cellulaires fondamentaux tels que la **prolifération**, la **survie** et une augmentation de **l'apoptose** dans les deux systèmes. Ceux-ci confirment nos données récemment publiées sur des lignées de podocytes. Cela serait la conséquence d'une **diminution dans l'efficacité et fidélité de traduction protéique**, due à un **défaut de synthèse de la modification** universelle **t^6A** des ARNt décodant les codons de type ANN.

Cette nouvelle approche basée sur iPSC nous a permis de **mettre en évidence des phénotypes cellulaires** liés à des maladies rénales héréditaires dans de types cellulaires pertinents et un contexte spécifique au patient. Bien que certaines limites persistent et que la technique puisse encore être améliorée, les iPSC représentent actuellement un **système complémentaire** qui est en train d'être mis en place au laboratoire pour d'autres sujets de recherche.

FOREWARD

Steroid-resistant nephrotic syndrome (SRNS) is a rare renal disease characterized by massive proteinuria due to structural alterations of the glomerular filtration barrier, of which the podocyte is a major component. Over 50 genes have been implicated in monogenic forms of SRNS, all relevantly expressed in the podocyte. Among them, the ***NPHS2*** gene, encoding **podocin**, has been identified by Pr. Antignac's group as causative of severe early-onset SRNS with the **podocin** p.**R138Q** mutation being the most prevalent mutation in the European population.

Although SRNS mostly occurs as an **isolated** glomerular disorder, it may also be **associated with extra-renal manifestations**. In particular, Pr. Antignac's group recently elucidated the genetic basis of **Galloway-Mowat syndrome** (GAMOS), associating SRNS with **microcephaly** and **neurological impairment**. While several causative genes have been linked to GAMOS, pathological mechanisms underlying this disease are still poorly understood.

Kidney organoids differentiated from **induced pluripotent stem cells** (iPSCs) have recently emerged as powerful tools for in vitro renal disease modeling. The first aim of my PhD thesis has been to **set up the suitable techniques and tools** to employ iPSCs in disease modeling. Secondly, I focused on their use to **decipher the pathological cellular and molecular mechanisms** implicated in both isolated and systemic (nephro-cerebral) forms of hereditary glomerular disorders. We obtained cells from **SRNS patient** bearing the R138Q podocin mutation in the homozygous state, as well as cells from **GAMOS patients**.

Thus, I set up the differentiation of patient-derived iPSCs into **kidney organoids** which possess the same features of in *vivo* **nephrons**, namely ordered structural development of nephron segments. Glomeruli contain polarized octopus-shaped **podocytes** extending cellular protrusions at their base. I confirmed the expression and localization of key podocyte markers, such as nuclear **WT1**, **podocalyxin** at the apico-lateral surface and basal **nephrin**, **podocin** and **synaptopodin**, as well as their podocyte identity by **transcriptomic analysis**. iPSC-derived kidney organoids represent the milestone of this study, extensively employed to compare patient- and healthy control-derived podocytes.

I demonstrated, by differentiating podocin R138Q iPSCs into organoids that these latter display **lower expression level** and **altered subcellular localization of R138Q podocin**, with diffuse perinuclear staining. Upon **CRISPR/Cas9-mediated correction** of patient iPSCs, we succeeded in rescuing the **proper podocin localization and expression level**. Moreover, I investigated the transcriptomic profile of FACS-sorted podocytes to gain

insights into the molecular mechanisms underlying the disease. Unexpectedly, RNA-Seq data suggest implication of an **interferon-like response activation** in R138Q patient podocytes, although further analyses are needed to discriminate between a mutation effect or the influence of the patient genetic background.

Since iPSCs offer the possibility to model both renal and neural aspects of **GAMOS**, iPSC-derived **kidney organoids** and **late cortical progenitor cells** have then been employed in this work. We observed a **perturbation** of fundamental cell processes such as **proliferation** and **survival**, pointing to an increase in **apoptosis** in both systems. Such defects, which confirm our recently published data on podocyte cell lines, are likely to be consequent to reduced efficiency and fidelity in protein translation due to the **deficient synthesis of the** universal **t^6A modification** of ANN-decoding tRNAs.

This new iPSC-based approach allowed us to **highlight cellular phenotypes** linked to hereditary kidney diseases on relevant cell types, podocytes and/or neural cells and in a patient-specific context. Although some limitations still persist and the technique can be further improved, iPSCs currently represent a **complementary system** that is being set up in the laboratory for other research subjects.

Abbreviations

AD: autosomal dominant

ADPKD: autosomal dominant polycystic kidney disease

AR: autosomal recessive

ARPKD: autosomal recessive polycystic kidney disease

AMP: adenosine monophosphate

ATP: adenosine triphosphate

BER: base excision repair

BDM: basic differentiation medium

BDNF: brain-derived neurotrophic factor

BFP2: blue fluorescent protein 2

BH: Benjamin-Hochberg

BMP: bone morphogenetic protein

CAKUT: congenital abnormalities of the kidney and urinary tract

CAM: (chick embryo) chorioallantoic membrane

cAMP: cyclic adenosine monophosphate

Cas: CRISPR-associated

CD: collecting duct

cDNA: complementary DNA

ChIP: chromatin immunoprecipitation

CHIR: CHIR99021

CNS: central nervous system

CPC: cortical progenitor cell

CRISPR: clustered regularly interspaced short palindromic repeats

crRNA: CRISPR RNA

DAG: diacylglycerol

DSB: double-strand break

DMS: diffuse mesangial sclerosis

D*N*: (kidney organoids) differentiation day *N* (i.e. D21=differentiation day 21)

ECM: extracellular matrix

EDTA: ethylenediaminetetraacetic acid

EGF: epidermal growth factor

EGFP: enhanced green fluorescent protein

EHS: Engelbreth-Holm-Swarm (sarcoma)

EMT: epithelial to mesenchymal transition

ER: endoplasmic reticulum

ESC: embryonic stem cell

ESRD: end-stage renal disease

E*N*: (chicken embryo) embryonic developmental day *N*
(i.e. E0=embryonic developmental day 0)

FACS: fluorescence-activated cell sorting

FBS: fetal bovine serum

FGF*N*: fibroblast growth factor *N*

FP: foot process

FSGS: focal segmental glomerulosclerosis

GAMOS: Galloway-Mowat syndrome

GBM: glomerular basement membrane

GFB: glomerular filtration barrier

GFP: green fluorescent protein

GDNF: glial-cell-derived neurotrophic factor

GO: gene ontology

gRNA: guide RNA

HBV: hepatitis B virus

HCV: hepatitis C virus

HDR: homology-directed repair

HIV: human immunodeficiency virus

ICM: inner cell mass

IF: immunofluorescence

IFN: interferon

Ig: immunoglobulin

IM: intermediate mesoderm

INS: idiopathic nephrotic syndrome

iPSC: induced pluripotent stem cell

IP_3: 1,4,5-trisphosphate

IVIS: *in vivo* imaging system

LC-MS/MS: liquid chromatography-tandem mass spectrometry

LDN: LDN193189

lncRNA: long non-coding RNA

LPM: lateral plate mesoderm

LTL: *Lotus tetragonolobus* lectin

KEOPS: Kinase, endopeptidase and other proteins of small size (complex)

MACS: magnetic-activated cell sorting

mascRNA: MALAT1-associated small cytoplasmic RNA

MCD: minimal change disease

MEF: mouse embryonic fibroblast

MM: metanephric mesenchyme

MRI: magnetic resonance imaging

mRNA: messenger RNA

mtDNA: maternal DNA

MTT: 3-(4,5-dimethylthiazol-2-yl)-2,5-diphenyltetrazolium bromide

m^6A: N6-methyladenosine

m^7G: N7-methylguanosine

NAD(P)H: nicotinamide adenine dinucleotide phosphate

NB: nuclear bodies

NEPH: nephrin-like protein

NGS: next-generation sequencing

NHEJ: non-homologous end joining

NPC: nephron progenitor cell

NS: nephrotic syndrome

OSKM: Oct4 (Pou5f1), Sox2, Klf4, c-Myc

PAM: protospacer-adjacent motif

PBMC: peripheral blood mononuclear cell

PBS: phosphate-buffered saline (buffer)

PCR: polymerase chain reaction

PHB: prohibitin (domain)

PIP_2: phosphatidylinositol 4,5-bisphosphate

PIP_3: phosphatidylinositol 3,4,5-trisphosphate

PKD: polycystic kidney disease

PSC: pluripotent stem cell

qPCR: quantitative PCR

RA: retinoic acid

RIN: RNA integrity number

RT: reverse transcription

RNA: ribonucleic acid

ROCK: Rho-associated kinase

RV: renal vesicle

sc: single-cell

SD: slit diaphragm

SEM: scanning electron microscopy

SEM: standard error of the mean

SeV: Sendai virus

snRNA: small nuclear RNA

SRNS: steroid resistant nephrotic syndrome

SSNS: steroid sensitive nephrotic syndrome

ssoDN: single-stranded oligo deoxynucleotide

TEM: transmission electron microscopy

TGF-β: transforming growth factor beta

tracrRNA: trans-activating crRNA

tRNA: transfer RNA

TSEN: tRNA-splicing endonuclease (complex)

t^6A: N6-threonylcarbamoyladenosine

UB: ureteric bud

VEGF: vascular endothelial growth factor

XD: X-linked dominant

XL: X-linked

XR: X-linked recessive

2/3D: bi/three-dimensional

Figures

Figure 1: Kidney anatomy 1
- **A)** Anatomical location of kidneys
- **B)** Kidney internal anatomy
- **C)** Renal parenchyma anatomy

Figure 2: Nephron structure 2
- **A)** Glomerulus
- **B)** Proximal tubule
- **C)** Henle's loop thin descending limb
- **D)** Henle's loop thick ascending limb
- **E)** Distal tubule

Figure 3: Mammalian early development 3

Figure 4: Mesodermal regions 4

Figure 5: Early renal specification 5
- **A)** T^+ primitive streak
- **B)** T^+/$TBX6^+$ posterior primitive streak derivatives
- **C)** Anterior and posterior intermediate mesoderm

Figure 6: Nephrogenesis 6
- **A)** Renal vesicles
- **B)** Comma-shaped and S-shaped bodies
- **C)** Nephron vascularization

Figure 7: Glomerular filtration barrier and podocyte structure 8
- **A)** Schematic representation of the glomerular filtration barrier
- **B)** Glomerular filtration barrier under transmission electron microscopy
- **C)** Podocyte under scanning electron microscopy
- **D)** Podocyte under transmission electron microscopy

Figure 8: Podocyte development 9
- **A)** Apical junctions
- **B)** Lateral junctions
- **C)** Basal junctions
- **D)** Slit diaphragm at foot processes

Figure 9: Slit diaphragm structure 11
- **A)** Glomerular filtration barrier structure
- **B)** Slit diaphragm transmission electron microscopy
- **C)** Slit diaphragm molecular components

Figure 10: Podocin protein 12
- **A)** Podocin immunohistochemistry in glomerular podocytes
- **B)** Podocin immunofluorescence at late S-shaped body stage
- **C)** Podocin immunogold labeling and transmission electron microscopy
- **D)** Podocin structure

Figure 11: Histopathology of idiopathic nephrotic syndrome 14
- **A)** Minimal change disease under light microscopy
- **B)** Focal segmental glomerulosclerosis under light microscopy
- **C)** Diffuse mesangial sclerosis under light microscopy
- **D)** Foot process effacement under transmission electron microscopy
- **E)** Foot process effacement under scanning electron microscopy

Figure 12: Podocyte genes associated with steroid-resistant nephrotic syndrome ... 15

Figure 13: Podocin p.R138Q position 20

Figure 14: Microcephaly 23
A) Representation of normal *versus* microcephalic head size
B) Normal brain MRI
C) Microcephalic brain MRI
Figure 15: tRNA structure and covalent modifications 26
A) tRNA covalent modification emplacement
B) Codon-anticodon interaction between mRNA and tRNA
Figure 16: t^6A biosynthetic pathway 28
Figure 17: KEOPS complex space-filling representation 28
Figure 18: Induced pluripotent stem cells 32
A) iPSC applications
B) Shinya Yamanaka
Figure 19: CRISPR/Cas9 system components 34
A) CRISPR/Cas9 system with crRNA and tracrRNA
B) CRISPR/Cas9 system with gRNA
Figure 20: DNA double-strand breaks repair systems 35
A) Double-strand break induction
B) Non-homologous end joining
C) Homology-directed repair
Figure 21: Embryonic epiblast and germ layers derivatives 38
Figure 22: Central nervous system development 41
A) Neurulation
B) Brain development
Figure 23: Organoid generation 42
Figure 24: Brain organoids 43
A) Cerebral organoid
B) Original cerebral organoid culture protocol
C) Unguided and guided methods to generate brain organoids
Figure 25: Forebrain organoids 45
A) Schematic representations of immature forebrain organoid cellular architecture
B) Schematic representations of mature forebrain organoid cellular architecture
C) Laminar organization of the human cortex
D) Cell type legend
Figure 26: Kidney organoids 47
Figure 27: Kidney organoid differentiation protocol comparison 51
Figure 28: Kidney organoid general workflow 52
Figure 29: Kidney organoid vascularization in the CAM 55
A) Vascularized kidney organoid on the CAM.
B) Semi-thin section of a kidney organoid vascularized on the CAM
C) Podocytes wrapping around a capillary under TEM.
D) Podocyte FPs bridged by SDs
Figure 30: Chick embryo 56
A) Amniotic egg features
B) Chick embryo development
Figure 31: Kidney organoid differentiation protocol 64

Figure 32: WT1 antibodies....65
A) Immunofluorescence staining for "WT1" at D7
B) Immunofluorescence staining for "WT1" on D21 kidney organoids
C) Immunofluorescence staining for "WT1" on conditionally immortalized podocytes
D) Immunofluorescence staining for WT1 on D21 kidney organoids
E) Immunofluorescence staining for WT1 on conditionally immortalized podocytes
Figure 33: Proximal tubular-like epithelial structures 66
Figure 34: First kidney organoids....67
Figure 35: RT-qPCR time course for differentiation markers 67
A) RT-qPCR time course for *OCT4*, *SOX2*, *T* and *TBX6* from day 0 to day 7
B) RT-qPCR time course for *HOXD11*, *WT1* and *SIX2* from day 7 to day 21
Figure 36: Crucial differentiation stages....68
A) Immunofluorescence staining for T and TBX6 on D7 late primitive streak
B) Immunofluorescence staining for SIX2 on D9 metanephric mesenchyme NPCs
C) Immunofluorescence staining for nephrin and LTL on D21 kidney organoids
Figure 37: Renal rosette morphology....69
A) Flat renal rosettes
B) Renal rosettes in a high cellular dense zone
C) Late renal vesicles
D) Late renal vesicles and pretubular aggregates
Figure 38: Characterization of renal rosette by IF....70
A and B) Immunofluorescence staining for SIX2, PAX2 and LHX1 on D9 renal rosettes
Figure 39: Characterization of induced NPCs around D9 by RT-qPCR....70
Figure 40: Cytofluorimetric analysis of ITGα8 and PDGFRα....71
A) Representative cytofluorimetric analysis of ITGα8 and PDGFRα
B) Time course quantification of $ITG\alpha8^{+}/PDGFR\alpha^{-}$ cell percentage from D8 to D10
Figure 41: Renal rosette markers 72
Figure 42: Kidney organoid obtained upon freezing and thawing of D9 NPCs 72
Figure 43: Kidney organoids....73
A) D21 kidney organoid under light microscopy
B) D21 kidney organoid compared to the structure of a nephron
Figure 44: Characterization of kidney organoid tubular compartment by IF....74
A) Immunofluorescence staining for LRP2, podocin and nephrin on D21 kidney organoids
B) Immunofluorescence for ARL13B, LTL and podocalyxin on D21 kidney organoids
Figure 45: Characterization of kidney organoid tubular compartment by TEM 74
A) Frontal section of D21 kidney organoid putative proximal tubule
B) Transversal section of D21 kidney organoid putative proximal tubule
C) Frontal section of D21 kidney organoid putative distal tubule
Figure 46: Characterization of kidney organoid glomerular podocytes by TEM....75
A) Global ultrastructure of a D21 kidney organoid glomerulus
B) Focus on podocyte basal cellular protrusions
C) Podocytes connected by a SD-like intercellular junction
D) Focus on the SD-like structure
Figure 47: Characterization of kidney organoid glomerular podocytes by IF 76
A) Schematic representation of a D21 kidney organoid glomerulus
B) Comparison of capsulated *versus* un-capsulated D21 kidney organoid glomeruli

Figure 48: Glomerular sieving 77
A) Sieved spherical aggregates
B) Cultured aggregates 1 day after sieving
C) Immunofluorescence staining for WT1, podocin and podocalyxin 1 day after sieving

Figure 49: Podocalyxin^{high} and Podocalyxin^{low} cell populations 79
A) Cytofluorimetric profile of kidney organoid dissociated cells stained for nephrin and podocalyxin
B) Confluent cultures of Podocalyxin^{high} and Podocalyxin^{low} cell populations after 1 week of culture
C) Podocalyxin^{high} and Podocalyxin^{low} immunofluorescence staining for podocalyxin and Ki-67

Figure 50: Podocalyxin^{high} and Podocalyxin^{low} cells after 1 week in culture 80

Figure 51: Gating strategy 80

Figure 52: RNA-Seq pilot analysis 82
A) Unsupervised clustering
B) Venn diagram of podocyte-related genes

Figure 53: Kidney organoid *in ovo* transplantation 86
A) E3 chick embryo
B) Deposition of a kidney organoid on the CAM at E6 on a zone delineated by a sterile plastic ring
C) Kidney organoid stuck on the plastic ring upon transplantation

Figure 54: Kidney organoid vascularized on the chick embryo CAM 87
A) Follow-up of the graft from E8 to E14
B) Kidney organoid transplant gathered from the CAM
C) Semi-thin section of the graft stained with Toluidine blue
D) Kidney organoid graft under transmission electron microscopy

Figure 55: Proteasome inhibition 91

Figure 56: RT-qPCR for IFN-stimulated genes in immortalized podocyte cell lines ..93

Figure 57: RT-qPCR for IFN-stimulated genes in immortalized podocyte cell lines overexpressing podocin constructs 94

Figure 58: RT-qPCR for IFN-stimulated genes in in iPSCs and NPCs 94

Figure 59: Functional protein association network 95

Figure 60: Nuclear bodies 96
A) Immunofluorescence staining for podocin and promyelocytic leukemia on control D21 kidney organoids
B) Immunofluorescence staining for promyelocytic leukemia on SNRS^{NPHS2} patient D21 kidney organoids

Figure 61: Characterization of GAMOS patient kidney organoids 99
A and B) Immunofluorescence staining on GAMOS^{GON7} 006#04 and GAMOS^{OSGEP} 008#04 patient D21 kidney organoid

Figure 62: Characterization of GAMOS patient kidney organoids by TEM 100

Figure 63: Apoptosis in GAMOS^{OSGEP} patient kidney organoids glomeruli 100

Figure 64: Late cortical progenitor cell differentiation protocol 101

Figure 65: Late cortical progenitor cell quality control 102
A) Cytofluorimetric profiles of CPCs stained for P75 and HNK1
B) Immunofluorescence staining for nestin and SOX2

Figure 66: Late cortical progenitor cell MTT proliferation assay 103

Figure 67: Late cortical progenitor cell IncuCyte phase contrast mask 103

Figure 68: Control late cortical progenitor cell IncuCyte proliferation assay 104
A) Growth curves of control CPC lines
B) Representative images of 009#09 and 004#17 control CPC lines stained for Annexin V 3 days after seeding
Figure 69: Late cortical progenitor cell IncuCyte proliferation assay 104
Figure 70: Slope of late cortical progenitor cell growth curves at the log phase 105
A) Mean slope of CPC growth curve ± SEM for independent CPC lines/clones
B) Mean slope of CPC growth curve ± SEM for grouped CPC lines/clones according to the respective mutation
Figure 71: Late cortical progenitor cell IncuCyte apoptosis assay 106
Figure 72: Late cortical progenitor cell t^6A quantification 107
Figure 73: Late cortical progenitor cell HPG protein synthesis assay 107

Tables

Table 1: Genes associated with steroid-resistant nephrotic syndrome 16
Table 2: iPSC lines generated at the iPSC Platform of the *Imagine Institute* 59
Table 3: Podocyte-related genes comprised in the top 50 most expressed genes 82
Table 4: Glomerular laminin and collagen IV isoforms.....83
Table 5: Candidate gene expression in Nphs2 mouse models and SRNS^{NPHS2} 007#27 podocytes.84
Table 6: Slope of late cortical progenitor cell growth curves at the log phase 105
Table A1: Podocyte-related markers expression .....Appendix
Table A2: Laminin and collagen IV isoforms expression.....Appendix
Table A3: Adult human podocyte transcription factors .....Appendix
Table A4: Nephrotic syndrome-related gene expression .....Appendix
Table A5: Most abundantly expressed genes in control kidney organoid podocytes .....Appendix

Table of contents

Introduction

Chapter 1: The Kidney From anatomo-physiology to molecular components

1. Kidney
   A) Structure and function 1
   B) Nephron, the kidney functional unit 2
2. Kidney development
   A) Early development 3
   B) Renal specification and nephrogenesis 4
3. Glomerular filtration barrier (GFB)
   A) Structure and function 7
   B) The podocyte: a crucial component of the GFB 8
      B.a) Podocyte development 9
      B.b) Slit diaphragm (SD) 10
         B.b;i) Podocin: a major SD component 11

Chapter 2: Nephrotic Syndrome Podocin mutations as a prototypical example

1. Clinical and pathological features 13
2. Genetics
   A) Genetic convergence towards to podocyte 15
   B) Steroid-resistant nephrotic syndrome due to *NPHS2* mutations 19
      B.a) p.R138Q podocin mutation 20

Chapter 3: Galloway-Mowat Syndrome A neuro-renal disorder

1. Clinical and pathological features 23
2. Genetics
   A) *WDR73* 24
   B) Transfer RNA (tRNA) modifiers 24
   C) Nucleoporins 25
3. tRNA modifications 25
   A) N6-threonylcarbamoyladenosine (t^6A) 27
      A.a) KEOPS complex 28
   B) t^6A deficiency leads to GAMOS 29

Chapter 4: Disease Modeling Induced pluripotent stem cells as a polyvalent tool

1. Induced pluripotent stem cells (iPSCs)
   A) General features 31
   B) iPSC reprogramming 32

2. CRISPR/Cas9-mediated genome editing
A) Principles of the technique 33
B) Combining CRISPR/Cas9 and kidney organoid technologies 36
B.a) Tools for kidney development investigation 36
B.b) Isogenic controls in disease modeling 37
3. iPSC differentiation 37
A) Bi-dimensional (2D) cell culture 38
A.a) iPSC-derived podocytes 38
A.b) iPSC-derived late cortical progenitor cells (CPCs) 40
B) Three-dimensional (3D) organoid culture 42
B.a) Brain organoids 43
B.a;i) Forebrain organoids 44
B.a;ii) Modelling microcephaly with brain organoids 45
B.b) Kidney organoids 47

Chapter 5: **Kidney Organoids** **Mini kidneys in a dish**

1. Mimicking embryonic kidney development with different protocols
A) Late primitive streak induction 49
B) Intermediate mesoderm induction 50
C) Nephrogenesis 50
2. Kidney organoid general features 52
3. Kidney organoid vascularization
A) Kidney organoid *in vitro* “vascularization” 54
B) Kidney organoid *in vivo* vascularization 55
B.a) Chick embryo chorioallantoic membrane (CAM) 56
4. Kidney organoids in disease modeling
A) Tubular diseases: polycystic kidney disease and nephronophthisis 57
B) Glomerular diseases: nephrotic syndrome 57

Results

Part 1: Setting-up of necessary tools

Induced Pluripotent Stem Cells

1. iPSC line reprogramming 59
2. Introduction to Article 1 60

Article 1: Generation of an induced pluripotent stem cell (iPSC) line (IMAGINi007) from a patient with steroid-resistant nephrotic syndrome carrying the homozygous p.R138Q mutation in the podocin-encoding *NPHS2* gene

3. iPSC culture conditions
A) Culture matrix 61
A.a) Geltrex 61
A.b) Vitronectin 61

A.c) Matrigel 62
A.d) Laminin-521 62
B) Culture medium 63
B.a) ReproFF2 63
B.b) mTeRS Plus 63

Kidney organoids

4. Choice of the differentiation protocol 64
5. Setting-up of the Morizane's protocol 64
A) Adjustment of late primitive streak induction 65
B) Identification of "renal rosettes" and adjustment of NPC induction 68
B.a) Characterization of renal rosettes 69
6. Characterization of kidney organoids
A) Tubular compartment 73
B) Glomerular compartment 74
7. Podocyte isolation
A) Glomerular sieving 76
B) Podocytes fluorescence-activated cell sorting (FACS) 78
B.a) Kidney organoid dissociation 78
B.b) Detection conditions 79
8. Pilot transcriptomic analysis of nephrin^{+}/podocalyxin^{+}/LTL^{-} cells
A) Podocyte identity 81
B) Maturation degree 83
C) Preliminary comparison of patient *versus* control podocytes 84
9. Vascularization Attempts 85

Part 2: Disease modeling

Early-onset SRNS **Podocin p.R138Q**

1. Introduction to Article 2 89

Article 2: CRISPR/Cas9-mediated rescue of the mutant p.R138Q podocin mislocalization in steroid-resistant nephrotic syndrome patient-derived kidney organoids

2. Complementary results
A) Proteasome inhibition 91
B) *NPHS2* expression 92
C) Validation of the interferon-like response activation 92
D) Functional protein association network analysis 95
D.a) Nuclear autoantigen Sp-100 (*SP100*) and nuclear bodies (NBs) 96
D.b) Vascular cell adhesion protein 1 (*VCAM1*) 97

D.c) Phospholipase C γ2 (*PLCG2*) and PI3K adapter protein 1 (*PIK3AP1*) 97
D.b) Actin γ1 (ACTG1) and actin-related proteins 97

Galloway-Mowat Syndrome KEOPS complex

1. Characterization of GAMOS kidney organoids 99
2. Late Cortical Progenitor Cells (CPCs) 100
A) Late CPC induction and quality control 101
B) Proliferation 102
B.a) MTT assay 102
B.b) IncuCyte 103
C) Apoptosis 106
D) t^6A measurement 106
E) Protein synthesis 107

Discussion

Setting-up of the necessary tools iPSCs and kidney organoids

1. iPSCs in disease modeling 109
2. Variability in iPSCs and their derivatives
A) Genetic variation 110
B) Epigenetic variation 112
C) Kidney organoid differentiation variability 112
C.a) Dealing with kidney organoid differentiation variability 113
D) Podocyte variability 114
D.a) Podocyte proportion 114
D.a;i) FACS strategy for podocyte isolation 115
D.a;ii) Avenues to improve podocyte isolation 116
D.b) Podocyte maturity 117
3. Kidney organoid vascularization 118
4. Kidney organoid-isolated podocyte RNA-Seq 120
A) New candidate genes for nephrotic syndrome 121
A.a) *MALAT1* 121
A.b) *FREM2* 122
A.c) *TJP1* 122
B) Additional applications 123
5. Conclusion 123

Early-onset SRNS Podocin p.R138Q

1. Endogenous podocin expression in kidney organoid podocytes
A) p.R138Q podocin decreased expression and mislocalization 125

B) p.R138Q podocin ER retention and proteasomal degradation 125
C) p.R138Q podocin impact on nephrin expression pattern 125
2. Interferon-like signature
A) Intrinsic clone or line properties possibly determining the IFN signature 127
B) Possible explanation of an eventual IFN-related pathological mechanism 129

Galloway-Mowat Syndrome KEOPS complex

1. GAMOS iPSC derivatives phenotypic characterization
A) Apoptosis increase in GAMOS pathogenesis 133
B) Investigation of other GAMOS-related phenotypes 134
2. RNA processing and the tRNA hypothesis 135
3. t^6A deficiency impact on podocytes and neurons 136
4. Perspectives 137

Materials and Methods

iPSC reprogramming 139
iPSC quality controls 139
iPSC culture 140
CRISPR/Cas9-mediated genome editing 140
Kidney organoid differentiation 141
Kidney organoid *in ovo* transplantation 142
Immunofluorescence (IF) 142
Co-localization analysis 143
Transmission electron microscopy (TEM) 143
Reverse transcription and quantitative PCR (RT-qPCR) 144
Glomerular sieving 144
Kidney organoid dissociation 144
Podocytes FACS-sorting 145
RNA sequencing (RNA-Seq) 145
RNA-Seq analysis 146
Late cortical progenitor cell (CPC) induction 146
Late CPC quality controls 147
MTT proliferation assay 147
IncuCyte proliferation assay 147
IncuCyte apoptosis assay 148
t^6A measurement 148
HPG protein synthesis assay 148

Bibliography.....149

Appendix

INTRODUCTION

Chapter 1: The Kidney
From anatomo-physiology to molecular components

1. Kidney
A) Structure and function

Kidneys are two bean-shaped organs located in the retro-peritoneal sub-diaphragm space of the abdominal cavity. They span the transition between the thoracic and lumbar vertebrae and are partially protected by the ribcage on each side of the spine (Fig. 1A). Blood supply is provided by the renal artery, entering the kidney through the hilum, while the renal vein takes blood away. Ureters come out of the hilum as well, bringing urine downward into the bladder and then out through the urethra. Surrounded by a **renal capsule** of fibrous connective tissue, the renal parenchyma is divided in two major layers: the inner renal **medulla** and the outer **renal cortex** that comprises microscopic filtering structures called **nephrons** (Fig. 1B and C). The renal corpuscle and the majority of the renal tubule reside in the cortex, whereas varying amounts of the renal tubule dip into the renal medulla.

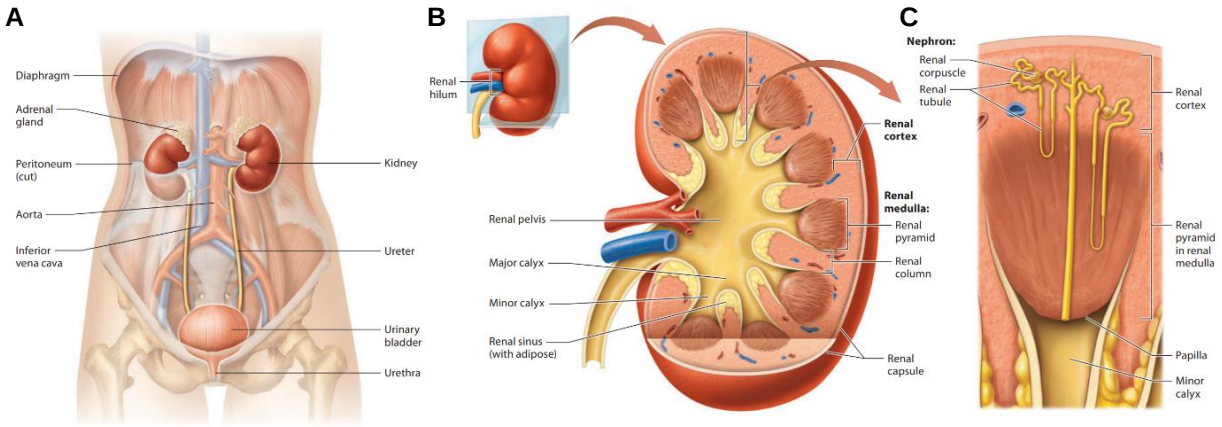

Figure 1: Kidney anatomy. **A)** Anatomical location of kidneys. **B)** Kidney internal anatomy. Frontal section of the kidney reveals its three distinct regions: the renal cortex, the medulla, and the inner renal pelvis, surrounded by the capsule. **C)** Renal parenchyma anatomy. Multiplicities of nephrons compose the renal parenchyma.
Adapted from Human Anatomy & Physiology, by Erin C. Amerman 2019 [1]

Kidneys are the primary functional organs of the **urinary system**, together with the urinary tract, made up of ureters, bladder, and the urethra. Their capital function is **excretion**, which is essentially accomplished by filtering the blood to remove metabolic waste products. The filtered fluid is modified, allowing maintaining liquid volume, electrolyte, acid-base, and blood pressure homeostasis, before to be finally excreted. This process involves reabsorption of water, glucose, and amino acids, preserving their balance body. In addition to their homeostatic function, kidneys are responsible for hormone production including calcitriol, erythropoietin, and the enzyme renin. Moreover, they play important metabolic roles, including detoxifying substances in the blood, activating vitamin D, and producing glucose through the process of gluconeogenesis.

B) Nephron, the kidney functional unit

Etymologically derived from the Greek *nephros*, "kidney", nephrons are the essential and functional units of the kidney. Each kidney count about 1 million nephrons[2], which represent >90% of the cortex volume.

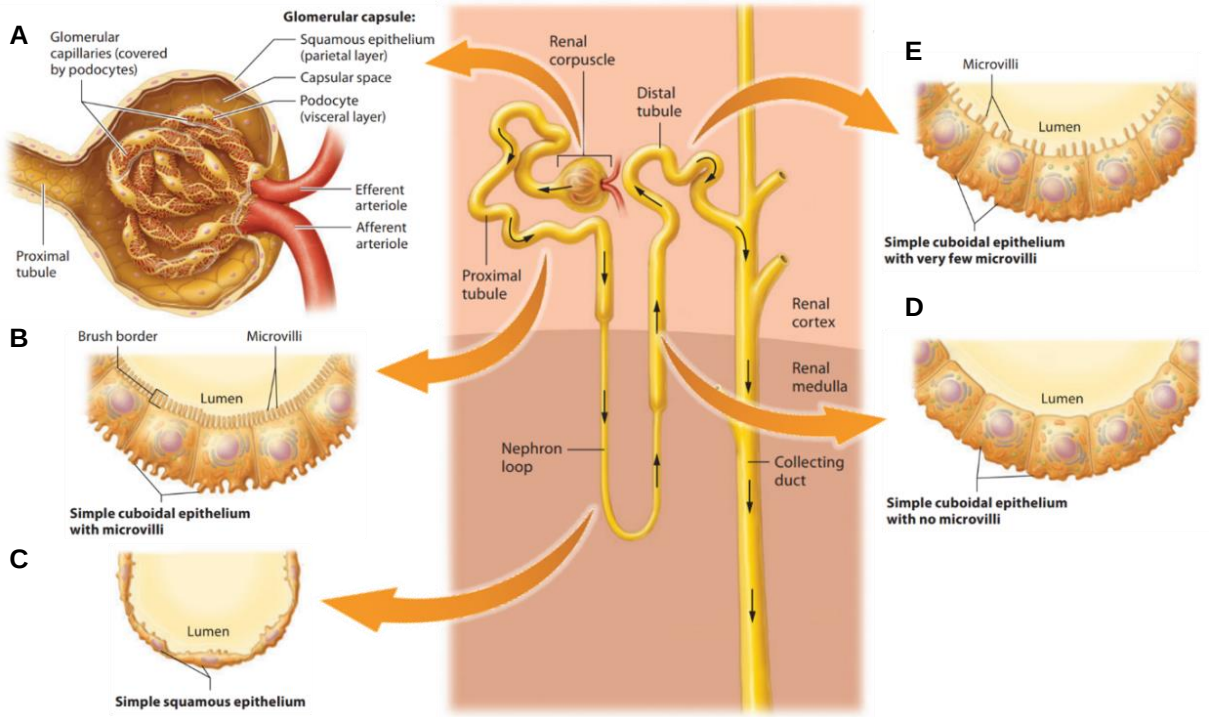

Figure 2: Nephron structure. **A)** Glomerulus. **B)** Proximal tubule. **C)** Henle's loop thin descending limb. **D)** Henle's loop thick ascending limb. **E)** Distal tubule.
Adapted from Human Anatomy & Physiology, by Erin C. Amerman 2019 [1]

The nephron is composed by two main parts:

- The renal corpuscle is the structure where blood **filtration** occurs through the glomerular filtration barrier (GFB). It refers to a **glomerulus** surrounded by the **Bowman's capsule**. About 20% of plasma volume is filtered and pass into the urinary space. The glomerulus consists of a tuft of looping fenestrated capillaries that are enwrapped by podocytes and supported by the mesangium. Parietal cells of the Bowman's capsule envelop the glomerulus while creating a capsular - also known as urinary - space between the visceral and parietal layers (Fig. 2A).

- The multi-segmented renal tubule is responsible for **filtrate modification** as it flows through. It is subdivided into different portions along the nephron, namely the **proximal tubule** (Fig. 2B), **loop of Henle** - descending (Fig. 2C) and ascending limbs (Fig. 2D) - and **distal tubule** (Fig. 2E). These structures accomplish with a different degree of specificity the processes of reabsorption of water, glucose, amino acids, and electrolytes as well as they mediate secretion of substances to be excreted, entering the filtrate from peritubular capillaries, before to reach the collecting system.

2. Kidney development

A) Early development

Development of a whole human being starts from one single cell, the zygote (Fig. 3), which is the result of a **fertilization** event of the maternal oocyte by the paternal sperm. The **zygote**, from Greek *zugōtós*, "yoked", has the unique capacity of generating each single cell of an organism, but also the chorion, which is the fetal component of the placenta. This ability to produce the ensemble of all the embryonic and extraembryonic structures necessary for the development of a new individual is termed **totipotency**, from the Latin *totus*, "whole", and *potens*, "potent".

The fertilized zygote undergoes successive coordinated cleavage events (Fig. 3), dividing into blastomers that retain totipotent capacity until the 8-cell stage. Then cells adhere tightly to each other in a compact arrangement. By the following division, the 16-cell resulting **morula** (Fig. 3) consists of a small group of internal cells surrounded by a layer of external cells[3].

The morula evolves towards the **blastocyst** by cavitation with secretion of fluid that creates an internal space called blastocoel. Cells that located internally give rise to the **inner cell mass** (ICM) of the blastocyst, while the outer cells become the **trophoblast** (Fig. 3). At this stage, the embryonic *versus* extraembryonic contribution of cells is determined by the fact they belong to the ICM or trophoblast respectively[4,5]. Reduction of the potency by restriction of trophoblast derivative fate makes the cells of the ICM of the blastocyst to be considered as pluripotent. **Pluripotency** is defined as the ability of generating the whole set of differentiated cell types of the body, with the exception of extraembryonic annexes. The ICM then organizes into a bilaminar germ disc (Fig. 3), composed by the **hypoblast**, which gives rise to the yolk sac, and the **epiblast**, origin of the amnion, allantois and embryo properly speaking.

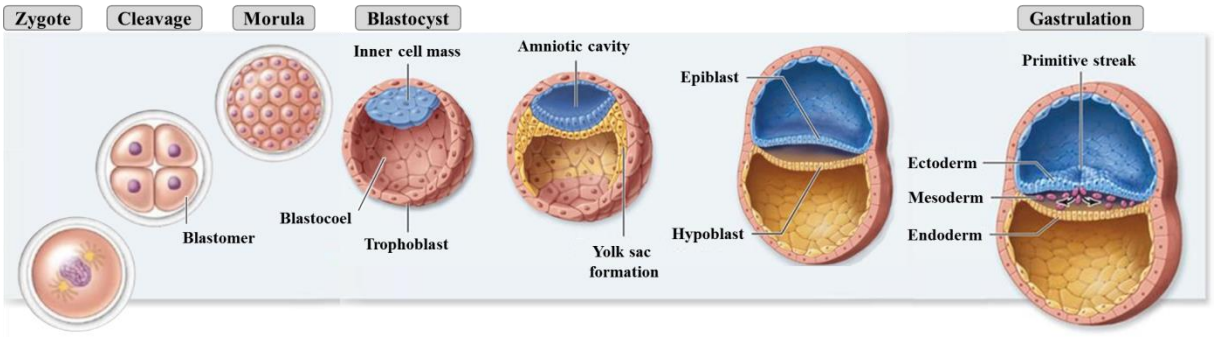

Figure 3: Mammalian early development.
Adapted from BIO 202 Human Anatomy & Physiology II [6] *and SlidePlayer.com* [7]

The early stages of embryonic development include the impressive event of **gastrulation** (Fig. 3), which reorganizes the blastocyst into a multilayered structure composed of the three germ layers. Formation of the **primitive streak**, the structure that establishes bilateral symmetry in the embryo, marks the beginning of gastrulation.

Emerging from the epiblast, endodermal and nascent mesodermal precursors expressing T and TBX6 undergo epithelial to mesenchymal transition (EMT) and migrate through the primitive streak, passing into the deep layers. The first cells entering the primitive streak migrate most anteriorly and deeply, replacing the hypoblast with definitive **endoderm**. Cells that follow populate the middle layer of **mesoderm**, sandwiched between the endoderm and the **neuroectoderm**, made of the epiblast cells remaining outside.

Mesoderm is the embryonic germ layer from which kidneys origin in development. Mesodermal regionalization is progressively defined by inductive influences during gastrulation. The earlier mesodermal precursors entering the groove populate the most rostral and mid-axial regions, while the later successively settle the more and more caudally and distal to the midline. By the end of gastrulation, the mesoderm is organized into four regions: the **axial** mesoderm (or chordamesoderm), the **paraxial** mesoderm, the **intermediate** mesoderm and the **lateral plate** mesoderm (Fig. 4).

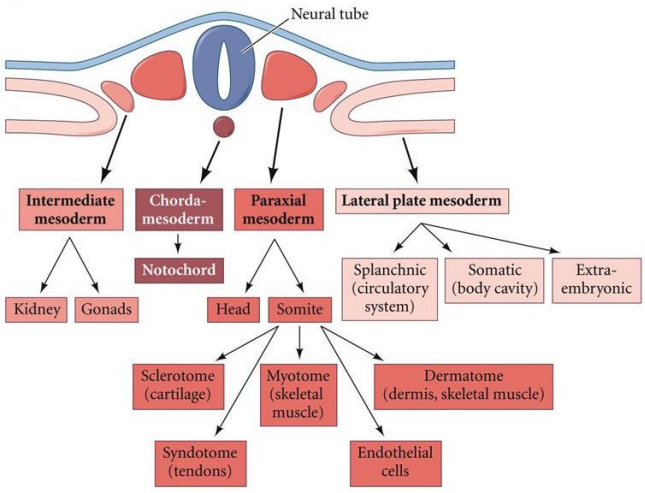

Figure 4: Mesodermal regions. Mesoderm is subdivided into distinct regions along the medio-lateral axis. The axial, or chordamesoderm, forms the notochord. Flanking the neural tube, the paraxial mesoderm gives rise to muscles, skeleton and connective tissues. The intermediate mesoderm generates kidney and gonads. The lateral plate mesoderm produces the circulatory system, somato- and splanchnopleura lining the body cavities and contributes to the extra-embryonic membrane formation.
Adapted from Developmental Biology, 10th edition [8]

B) Renal specification and nephrogenesis

Cells deriving from the late primitive streak that ingress the groove tardily, the **intermediate mesoderm** (IM), which express the transcription factors PAX2 and LHX1, will generate the **urogenital system**, namely the kidneys, gonads and their respective duct systems. At its rostral part, two transient kidney developmental stages rise: the **pronephros**, which is a rudimentary vestigial organ with no remaining function in human beings, and the **mesonephros**, in charge of blood filtration during a limited period of fetal life and source of hematopoietic stem cells. These structures almost completely rostro-caudally degenerate. HOXD11 participates in the longitudinal patterning of the IM, specifying the posterior IM towards a metanephric fate[9].

The permanent - or **metanephric - kidney** arises by reciprocal inductive interaction of two precursor structures with temporally and spatially independent developmental origin[10], the **ureteric bud** (UB) and **metanephric mesenchyme** (MM)[11,12] (Fig. 5). Their combination is required for proper kidney epithelial morphogenesis [11].

The UB is a side outgrowth of the nephric duct that derives from the anterior intermediate mesoderm and gives rise to the collecting ducts (CD) and ureter. The UB branches from the nephric duct and invades the MM in response to GDNF produced by nephron progenitor and cortical stromal cells[12]. The MM supports dichotomous branching growth of UB. In turn, induction of the MM is required by the UB for both self-renewal and commitment of the progenitor pool.

The MM forms in the posterior intermediate mesoderm. It comprises $SIX2^+$ self-renewing multipotent **nephron progenitor cells** (NPC) that produce all the epithelial cell types of the definitive kidney different nephron segments[13].

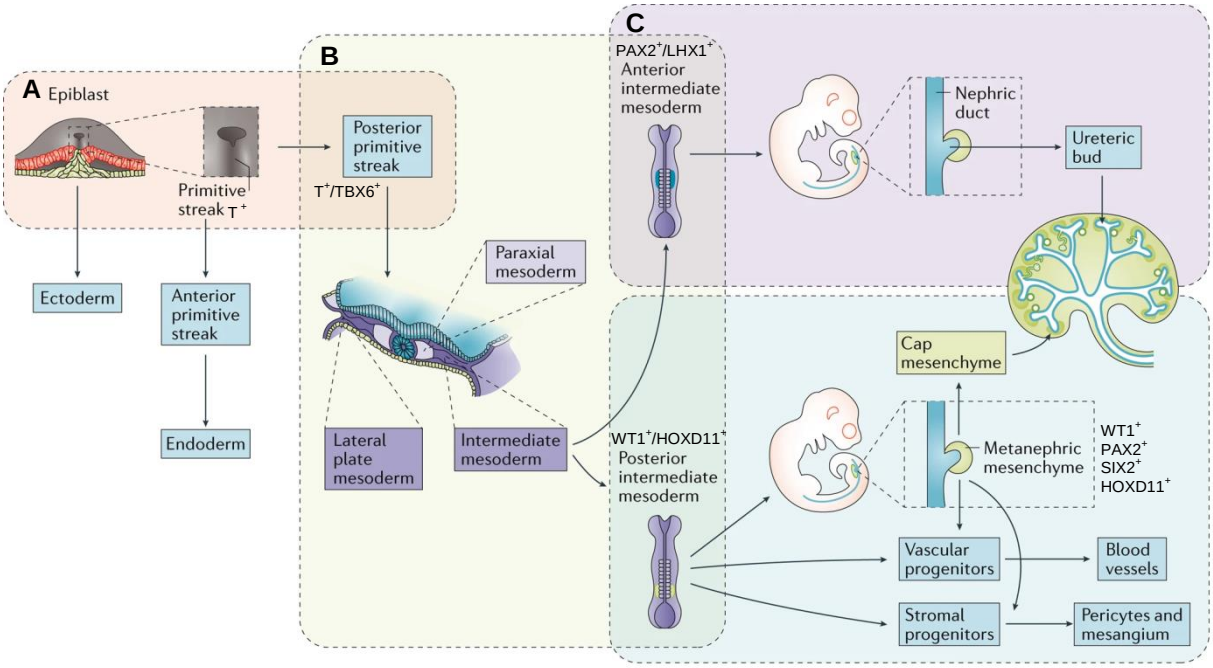

Figure 5: Early renal specification. Development of the ureteric bud and metanephric mesenchyme lineages. **A)** T^+ primitive streak rising at gastrulation. **B)** $T^+/TBX6^+$ posterior primitive streak derivatives, comprising the intermediate mesoderm. **C)** Anterior and posterior intermediate mesoderm giving raise to the ureteric bud and metanephric mesenchyme lineages, respectively.
Adapted from Little et al. 2016 [14]

The earliest response in the MM is mediated by Wnt9b expressed in the UB, through the canonical Wnt/β-catenin signaling[15]. This signal leads to condensation of local areas of MM at each UB tip to form the **pretubular aggregates**. The terminal aspects of the branched duct create thus the niche for NPCs, which organize in cellular layers of so called **cap mesenchyme** distally to tips. Each single NPC can populate several adjacent nephrons, generating all the epithelial cell types that constitute its different segments, while a single nephron is not clonally derived from a single NPC[13].

In that context, FGF9 derived from UB acts redundantly with FGF20 expressed by - and acting in a paracrine manner on - NPCs to maintain the nephrogenic zone[16]. FGF signal is essential for proliferation and survival of NPCs and to promote their stem properties of self-renewal while preserving competence to respond to permissive Wnt9 cues for differentiation.

The Wnt9b-dependent activation of Wnt4 in the MM, in a continuum of - but switching from canonical to non-canonical - Wnt signaling, is necessary to complete the inductive process. Wnt4 acts downstream to Wnt9b[15] to promote mesenchymal to epithelial transition (MET)[17,18]. MET contemplates the coordinate expression of epithelial cell adhesion molecules, among which integrin α8β1 plays a critical role in early renal morphogenesis[19] culminating in cell polarization and organization into **renal vesicles** (RV) with a basement membrane and a lumen (Fig. 6A). RVs constitute the primitive nephric epithelium, each one giving rise to a single nephron.

Following induction, the fate of NPCs becomes restricted to a single discrete nephron segment[13]. As the renal vesicle elongates, each portion on the proximo-distal axis differentiate into **committed progenitors of nephron segments**. The nephron anlage fusions with the CD by basement membrane degradation in the prospective distal segments of the late renal vesicles[20], creating a continuum between the lumens of the MM and UB-derivatives (Fig. 6B).

Progression in nephron development involves morphological changes that principally take place at the most proximal prospective glomerulus. The appearance of a cleft marks its conversion to a **comma-shaped body**, which further elongates and folds to form the **S-shaped body** (Fig. 6B). Endothelial progenitor cells subsequently infiltrate into the S-shaped body cleft (Fig. 6C).

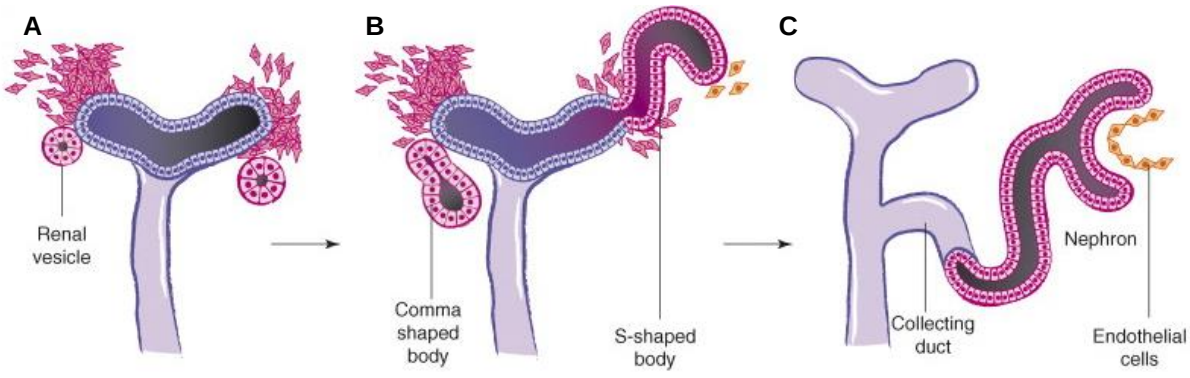

Figure 6: Nephrogenesis. **A)** Renal vesicles. MM cells organize into epithelial RVs. **B)** Comma-shaped and S-shaped bodies. Elongation of RVs progressively produces comma and S-shaped bodies. **C)** Nephron vascularization. Endothelial progenitor cells populate the vascular cleft of the late S-shaped body.
Adapted from Uhlenhaut et al. 2008 [21]

Nephrogenesis initiates around 8-9 weeks of gestation in humans[22] and it is mostly active during the third trimester[23]. It terminates at 34-36 weeks of pregnancy[22], ending up with the definitive number of nephrons in the adult. During post-natal life, new nephrons do not form in humans. When adult nephrons are damaged or lost, they are ineligible for regenerating, meaning their depletion is permanent.

3. Glomerular Filtration Barrier (GFB)

A) Structure and function

The GFB laying at the interface between circulating blood and the urinary space constitutes the filtration apparatus of the kidney. It is composed by the **fenestrated endothelium**, the **glomerular basement membrane** (GBM) and the **podocyte**[24] (Fig. 7A and B). This three-layered barrier retains blood cells, platelets, and high molecular weight proteins, while being permeable to water and small solutes that will constitute the filtrate. It acts as a sophisticated molecular mesh that filters blood plasma, performing a selection that is primarily based on **size**:

- The glomerular capillary is freely permeable to proteins and solutes due to large fenestrations that represent ~20-50% of the endothelial wall. Their amplitude, of a mean diameter of about **100-175 nm**[25], is sufficient to retain the corpuscular blood fraction, composed by erythrocytes, leucocytes and platelets, into the blood stream.

- The GBM is a layer of specialized extracellular matrix proteins that create a hydrogel meshwork with pores of an average **10 nm** diameter[26]. It is constituted of an electron-dense thick inner layer of the so called *lamina densa*, in between the two layers of thin and clear *lamina rara externa* and *interna* (Fig. 7B). Mature GBM comprises specific isoforms of critical proteins such as laminin-521 (α5β2γ1), type IV collagen (α3α4α5), nidogen and proteoglycans[27].

- The podocyte slit diaphragm (SD) constitutes the ultimate molecular size filter. The reference protein considered as a limit of size exclusion is albumin - the most prevalent plasma protein - with an effective Stock-Einstein radius of **3.5 nm**[28].

In addition to size-based selection, the GFB was proposed to display moderate **charge** selectivity by restricting anionic molecules more than neutral and cationic ones of the same size. Indeed, all its constituents are enriched in **negatively charged components** that exert a repulsive force on negatively charged proteins:

- A negatively-charged **glycocalyx** coats the luminal surface of the glomerular endothelium, contributing to GFB permeability properties[29].

- The GBM contains **collagen** and **proteoglycans**, mainly perlecan and agrin, both rich in heparan sulfate moieties[30].

- The apico-lateral surface of podocyte foot processes (FPs) is covered by a **glycocalyx** with heavily sialyated glycoconjugates - the major sialoprotein being podocalyxin[31]- and sulfated molecules.

However, recent studies have challenged the hypothesis of charge-mediated permeability[32].

B) The podocyte: a crucial component of the GFB

Podocytes are highly specialized epithelial cells lining the visceral layer of the renal glomerulus. They are terminally differentiated post-mitotic cells characterized by a complex octopus-like cytoarchitecture. Numerous cell protrusions extend from a voluminous cell body and enwrap glomerular capillaries (Fig. 7C and D). These projections are organized in **primary processes**, supported by a microtubule and intermediate filament network, which branches into α-actin and myosin rich contractile secondary processes, also called pedicels or **foot processes** (FP) (Fig. 7A and B).

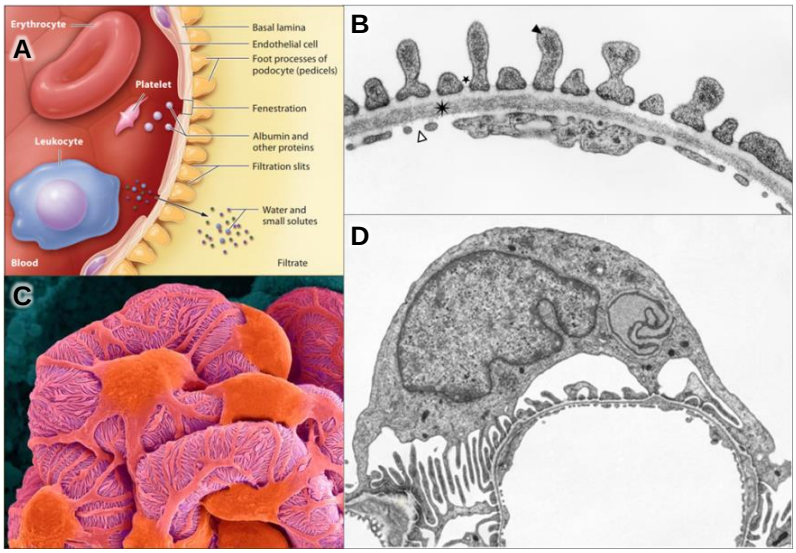

Figure 7: Glomerular filtration barrier and podocyte structure. Glomerular filtration barrier **A)** schematic representation and **B)** under transmission electron microscopy. Regularly interspaced FPs (black arrow) are connected by the SD (star) and lay on the GMB (asterisk). On the opposite side, the endothelium displays characteristic fenestrations (white arrow). Podocyte under **C)** scanning and **D)** transmission electron microscopy.
Adapted from Human Anatomy & Physiology, by Erin C. Amerman [1]*, Welsh et al. 2012* [33] *and Pavenstädt et al. 2003* [34]

Podocytes display three distinct subcellular domains:

- The **apical domain** principally involves their prominent cell body that bulges towards the urinary space. The negatively charged glycocalyx that coats the apical membrane[31] exert a repulsive force between neighboring podocytes, which maintains separated their cell bodies.

- The **junctional domain** encompasses a peculiar type of intercellular junction called **slit diaphragm** (SD). The SD bridges FPs of adjacent podocytes, which regularly interdigitate on the GBM (Fig. 7A and B). These singular structural features of the podocyte allow it to regulate selective permeability in the glomerulus, making it an essential component of the GFB.

- The **basal domain** is responsible for anchoring the podocyte to the *lamina rara externa* of the GBM through integrins and dystroglycans.

Each single podocyte covers one or two capillary loop(s), providing full coverage to the whole glomerular tuft in their ensemble.

B.a) Podocyte development

Podocyte precursors are specified around the comma-shaped body stage at the most proximal end of the prospective nephron, where they populate the inferior layer of the forming vascular cleft (Fig. 6C and 10B). Their development implies the progressive loss of lateral attachment at their apical domains, accompanied by a distinctive apico-basal shift of intercellular junctions[35]. Actually, the earliest podocyte progenitors have a classical columnar epithelial morphology, and are sealed by an apical belt of ZO-1 containing tight junctions (Fig. 8A). Expansion of the apical surface correlates with displacement of cell-cell contacts along the lateral cell side (Fig. 8B). This atypical epithelial condition is found around the S-shaped body stage, when primitive podocytes occupy the vascular cleft. *Adherens*-like junctions sequentially appear at the basal part of immature podocytes in parallel to development of **capillary loops** (Fig. 8C). Podocyte-specific proteins such as nephrin, Neph1 and podocin start to constitute pre-slit diaphragms. Podocytes wrap around in-growing capillaries and become flatter. Their cell bodies being isolated one from each other, mature podocytes finally interdigitate their FPs, bridged by proper specialized intercellular junctions called slit diaphragms (SD) (Fig. 8D and 9).

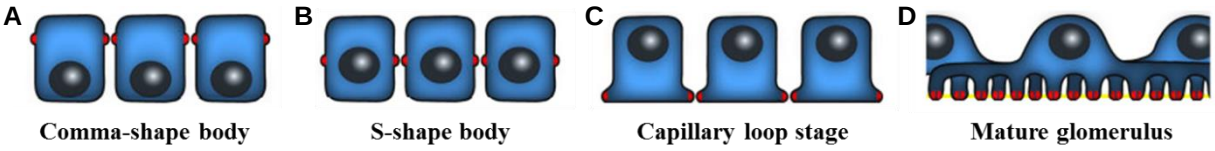

Figure 8: Podocyte development. **A)** Apical junctions. At the comma-shaped body stage, podocyte precursor junctions are located apically. **B)** Lateral junctions. Expansion of the apical membrane occurring during the S-shaped body stage shifts the junctions laterally. **C)** Basal junctions. By the capillary loop stage, junctions locate at the basal side of immature podocytes, whose apico-lateral domain is separated from each other's. **D)** Slit diaphragm at foot processes. Mature podocytes elongate basal FP, which are connected by the SD.
Adapted from Schell et al. 2014 [35]

While morphological changes shape the assembly of the glomerulus, the composition of the glomerular basement membrane (GBM) evolves by **laminin** and **collagen IV** isoform switch[36].

The earliest α1β1γ1 laminin expression accompanies nephric epithelialization[36]. As soon as the renal vesicle develops, nascent GBM contemplates the co-existence of laminin α1 and α4 chains[37]. Expression of laminin α1 chain is lost at early capillary loop stage, and α5 isoform deposition starts hereafter[38,39]. By this time, laminin β1 is replaced by the β2 isoform, that is mutually exclusive with the α1 chain[39]. The fully mature GBM is composed by α5β2γ1 laminin[36].

The immature GMB initially contains α1α2α1 trimers of type IV collagen. Collagen α1α2α1 (IV) persists instead until late capillary loop stage, when α3α4α5 (IV) collagen starts to appear discontinuously[38]. As the glomerulus maturates, α3α4α5 (IV) trimers accumulate and become the most abundant component of the GBM, albeit of type IV α1 and α2 chains are retained in the mature GBM in far less amount[40].

B.b) Slit diaphragm (SD)

The SD is a unique intercellular contact point laterally connecting adjacent FPs on the GBM (Fig. 9A), which integrates features of tight[41], *adherens*[42] and neuronal junctions[43]. Initially described as an ultrathin electron-dense **zipper-like substructure**[44] (Fig. 9B) whose orderly arranged components constitute a static **isoporous molecular sieve**[45] with rectangular pores of 4×14 nm width[44], SD dynamic and flexible nature has been evidenced by more recent investigations[46]. Repetitive cycles of strain and relaxation are indeed necessary to adapt to mechanical forces experienced by the GFB, in particular related to variable blood pressure[46].

Several specific proteins (Fig. 9C) are necessary - and because of that they are linked to glomerular pathologies when mutated (Introduction, Chapter 2, Table 1) - to develop and maintain the features of such a peculiar and complex structure:

- The first and principal SD integral component, **nephrin**[47], was identified as the protein product of the *NPHS1* gene. *NPHS1* mutations lead to congenital nephrotic syndrome of the Finnish type[48]. Nephrin is a type I transmembrane glycoprotein belonging to the immunoglobulin (Ig) superfamily. Its extracellular portion contains a fibronectin type III domain and eight C2 type Ig-like domains. Nephrin molecules span the slit and establish homophilic interactions[46]. Tyrosine residues at its intracellular domain, when phosphorylated, are docking sites for kinases and adaptor proteins that act as scaffolds and/or signal transducers.

- Together with nephrin and sharing with it a certain homology, the **nephrin-like protein 1** Neph1, encoded by *KIRREL1*, constitute the central core of the SD[46,49,50]. Neph1 possess a shorter extracellular domain with only five C2 type Ig-like domains and lacking a fibronectin-like one. Neph1 molecules establish quasiperiodic homophilic interactions in the lower part of the SD, closest to the GBM with respect to nephrin junctions[46]. As it is the case for nephrin, its C-terminal domain is an anchoring platform for structural and signal transducing proteins.

- The third main SD component is represented by **podocin**, encoded by the *NPHS2* gene. Podocin is a membrane-associated protein anchoring the SD to the intracellular adaptors of the actin cytoskeleton (Fig. 9C), thus facilitating nephrin signaling. (*NPHS2* and podocin being the focus of one part of my PhD project, please refer to the following section for more details, to the "SRNS due to *NPHS2* mutations" section (Chapter 2) for its role in pathology).

- Other actors of the SD structure comprise CD2AP[51] linking it to actin modulators, TRPC6[52] adjusting the Ca^{2+} flux, the phospholipase C epsilon 1 PLCε1[53], and different scaffold proteins such as FAT1[54] and MAGI2[55].

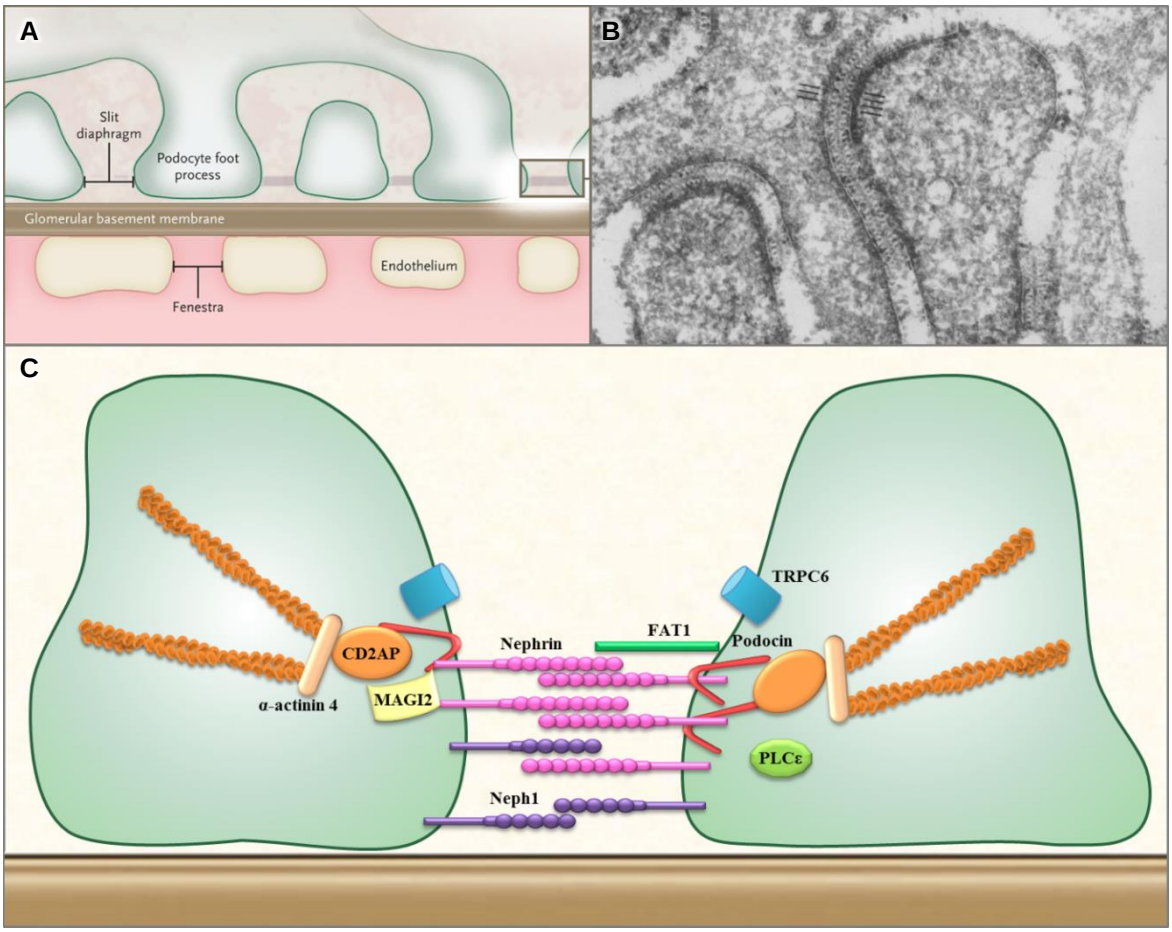

Figure 9: Slit diaphragm structure. **A)** Glomerular filtration barrier structure. The SD connects adjacent podocyte FPs with regularity of spacing. GBM is interposed between them and the fenestrated endothelium on the opposite side. **B)** Slit diaphragm transmission electron microscopy. Tangential section of the SD in a rat glomerulus reveals a zipper-like conformation. A central filament is cross bridged to the FPs on either side. The cytoplasm in close proximity to the SD displays an increased density. **C)** Slit diaphragm molecular components.
Adapted from Human Anatomy & Physiologyby Erin C. Amerman 2019 [1] *and Rodewald et al. 1974* [44]

In addition of acting as a macromolecular sieve that prevents high molecular weight protein from entering the urinary space, the SD is a **signaling** hub that integrates and transfers internal and external cues to regulate FP plasticity[56]. Nephrin is responsible for triggering signal transduction at the SD[57], thus regulating podocyte structure, cytoskeletal reorganizations, cell adhesion, cell survival/apoptosis, differentiation and cellular homeostasis[58].

B.b;i) Podocin: a major SD component

Podocin is a 383 amino acid protein of 42 kDa belonging to the band-7-stomatin protein family. It is encoded by the ***NPHS2* gene** (NM_014625) that was found to locate at the q25-q31 position on chromosome 1 by linkage analysis[59]. It was subsequently identified by positional cloning and shown to be mutated in patients with autosomal recessive **steroid-resistant nephrotic syndrome** by the Pr. C. Antignac's laboratory[60]. The *NPHS2* genes contains 8 exons and produces 2 isoforms by alternative splicing, the canonical form being considered as the longest one with exon 5 retention.

Podocin is specifically expressed in glomerular podocytes[60,61] (Fig. 10A). It is firstly detectable starting from late S-shaped body stage in the future podocytes that populate the inferior cleft, concomitantly to its vascularization[60–62] (Fig. 10B). It localizes at the basal region of podocytes along the GBM, strictly following its course. More precisely, podocin is found on FPs membrane adjacent to the slits, at the insertion site of the SD[61,63] (Fig. 10C).

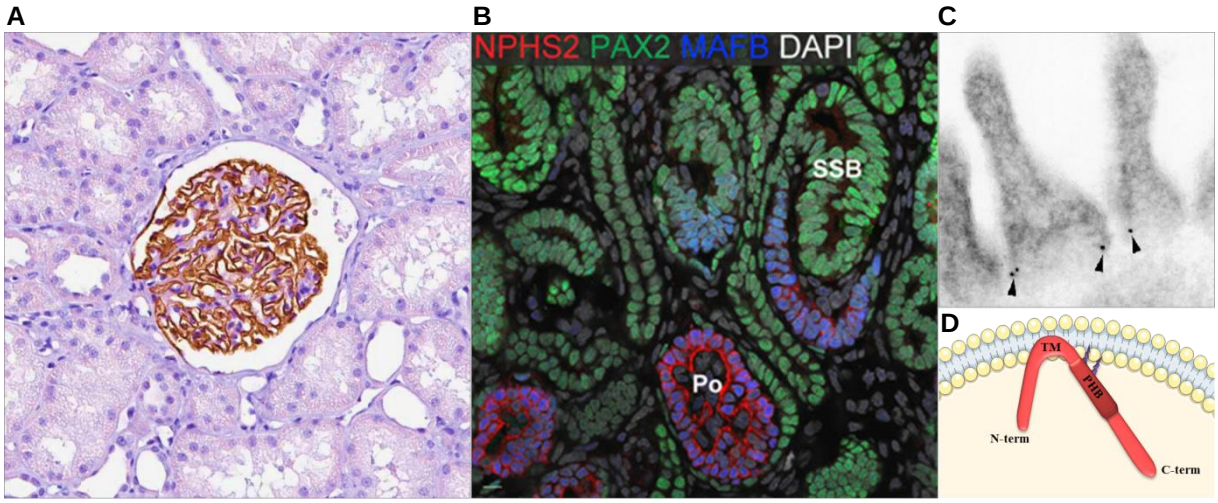

Figure 10: Podocin protein. **A)** Podocin immunohistochemistry in glomerular podocytes. **B)** Podocin immunofluorescence at late S-shaped body stage. **C)** Podocin immunogold labeling and transmission electron microscopy. Frontal section of adult rat kidney reveals podocin subcellular localization (black arrows ▶) at the cytosolic face of the FPs plasma membrane adjacent to filtration slits. **D)** Podocin structure. Podocin displays a hairpin-like structure with a short cytosolic amino-terminal tail (N-term), a transmembrane domain (TM), a PHB domain with two palmitoylation sites (violet) and an intracellular carboxyl-terminus (C-term).
Adapted from NovusBio.com [64]*, Lindström et al. 2018* [62] *and Schwarz et al. 2001* [63]

As predicted by its homology with stomatin family members, podocin is a membrane-associated protein with a hairpin-like structure consisting in a hydrophobic intramembrane domain followed by a prohibitin (PHB) domain and both the amino- and carboxyl-terminal regions facing the cytoplasmic side[61,63] (Fig. 10D). It also possesses two palmitoylation sites conserved among stomatins within the PHB domain, allowing its binding to the inner leaflet of the plasma membrane[65] (Fig. 10D). Podocin reaches the membrane through the classical pathway of exocytosis, passing via the ER and Golgi[66].

Genetic studies evidenced the pivotal role of podocin in **glomerular permeability** and made presume it was a **SD key component**, as it is the case for nephrin or CD2AP. Podocin has indeed been shown to directly interact with CD2AP and nephrin through its carboxyl-terminus, in particular thanks to its PHB domain[63,67].

As it is the case for stomatin, podocin undergo oligomeric accumulation at specialized slit membrane micro-domains named lipid rafts[63]. These are patches of the plasma membrane with a unique lipid composition which act as signaling platforms through concentration of signal transduction molecules. Podocin by forming these highly ordered complexes may act as a **scaffold protein** to trigger **SD assembly**, primarily anchoring nephrin to the membrane. In particular, it is presumed to be required for nephrin recruitment to lipid rafts[67] and thus facilitate nephrin signaling at the SD[57].

Chapter 2: Nephrotic Syndrome
Podocin mutations as a prototypical example

1. Clinical and pathological features

Nephrotic syndrome (NS) is a heterogeneous glomerular disorder characterized by massive **proteinuria**, greater than 3.5 g/1.73 m^2 body surface area/day or over 50 mg/kg/day in children. Proteinuria is accompanied by **hypoalbuminemia** (serum albumin concentration lower than 30 g/l), resulting in **edema**, **hyperlipidemia**, and various potentially life-threatening complications.

NS can be classified based on underlying pathogenic cause as **primary - idiopathic** (INS) - or **secondary** when the glomerular injury is related to systemic conditions with metabolic or immunological dysregulation, infections, hematological diseases, drug effects or some kinds of malignancies[68].

Corticosteroid treatment is the first-line therapy for INS patients. It induces remission in ~80% of pediatric cases, thus allowing to dramatically reduce NS-related mortality in children[68]. Responsiveness to treatment defines the disease as **steroid-sensitive** (SSNS) or **steroid-resistant** (SRNS). Two main forms of idiopathic INS are classically defined:

- **Hereditary podocytopathies** are caused by mutations in genes encoding essential components of the GFB. Insensitivity to corticosteroid therapy is a main feature of genetics forms of NS. Almost inevitably, hereditary SRNS progress to **end-stage renal disease** (ESRD), requiring renal replacement therapies as dialysis and/or transplantation[69]. The genetic bases of hereditary NS will be described in the following section.

- **Immune NS** is delineated based on several lines of evidence suggesting the immune system implication in the triggering and maintaining of non-genetic forms of INS[70,71]. The prognosis of patients is generally good, mainly due to responsiveness to steroids and immunosuppressors. While several studies have described the involvement of **T**[72,73] **or B**[74,75] **lymphocytes**, **cytokines release**[70] or **complement system**[76,77] in the tubular and peritubular compartment, the immune NS pathophysiology have not been elucidated yet. The presence of a hypothetical **circulating permeability factor**[72,78], although still unidentified, is considered the most probable theory. This proposition is supported by - and might be responsible for - rapid post-transplantation recurrence[79], responsiveness to plasmapheresis[80] and neonatal transient proteinuria by feto-maternal transmission[81]. In addition, resolution of recurrent FSGS has been evidenced after re-transplantation[82], and patient serum or plasma induces proteinuria in animal models[83].

At the histological level, **minimal change disease** (MCD) is most commonly observed in INS during childhood. In MCD, renal biopsies display glomeruli with a normal aspect at light microscopy (Fig. 11A), with FP effacement only detectable by electron microscopy (Fig. 11D and E). **Focal segmental glomerulosclerosis** (FSGS) lesions that manifest as scarring injury in partial regions of some glomeruli (Fig. 11B) are more frequently associated with SRNS. **Diffuse mesangial sclerosis** (DMS) may be present to a lesser extent. DMS is characterized by mesangial expansion and increased mesangial matrix (Fig. 11C). Capillary wall may undergo hypertrophy and podocytes display hyperplasia.

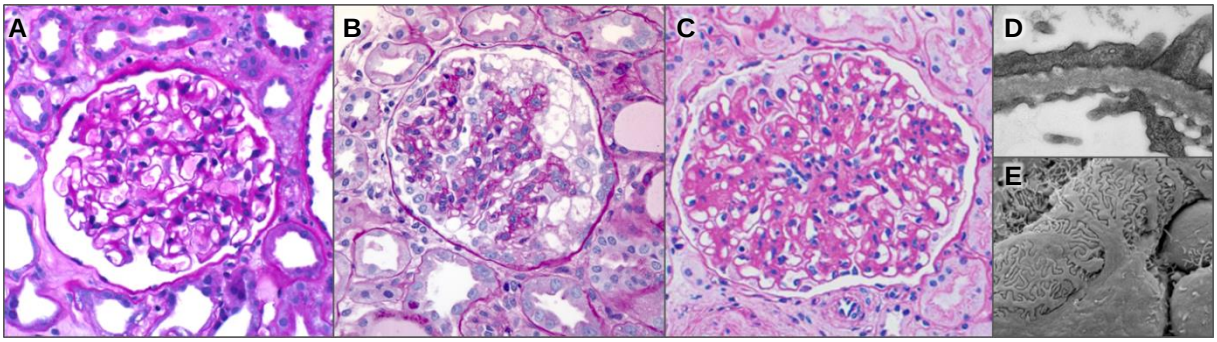

Figure 11: Histopathology of idiopathic nephrotic syndrome. **A)** Minimal change disease under light microscopy. **B)** Focal segmental glomerulosclerosis under light microscopy. **C)** Diffuse mesangial sclerosis under light microscopy. **D)** Foot process effacement under transmission electron microscopy. FPs fusion and form a single layer on the GBM, losing their individuality and regularity of interspacing. **E)** Foot process effacement under scanning electron microscopy. FPs display a disorganized melted-like appearance instead of being orderly interdigitated.
Adapted from Rastogi et al. 2018 [84]*, PathologyOutlines.com* [85]*, Said et al. 2011* [86] and *Gaelle et al. 2010* [87]

The age of presentation of clinical symptoms defines NS as **congenital** from 0 to 3 months, **infantile** from 3 to 12 months, **childhood** after 1 year, or **juvenile**/**adult**-onset[88]. The age of onset inversely correlate with the likelihood to identify a **genetic** cause for NS, which is particularly elevated in congenital and infantile forms[89].

During the last two decades, genetic and mechanistic investigations of these familial forms of NS, as well as in animal models, helped to dissect the molecular actors of glomerular permeability maintenance, and elucidated the central role of the GFB and especially of the podocyte in NS pathogenesis.

Actually, NS results from **structural alterations of the GFB**, and **podocyte damage** is considered as a hallmark event in NS pathogenesis. Indeed, any stress or insult occurring at the podocyte level over a critical threshold will lead to **FP effacement** and **alteration of the SD**[90]. Podocyte dysfunction, injury or loss may have diverse etiology, including nephrotoxic, genetic, hemodynamic, infectious, oxidative or immune causes[90]. Podocyte damage can propagate to intact podocytes, in a vicious cycle of progressive podocyte deterioration[91,92]. Whatever the origin, podocyte depletion disrupts the organization of the cellular and molecular glomerular mesh, which inevitably leads to impaired filtration capacity. Dysfunctional GFB displays increased permeability, leading to large - over albumin - size proteins leakage in the urine.

In addition to detrimental effects due to protein deprivation and perturbed homeostasis, the increased glomerular permeability also leads to **tubular uptake system overload** that has long-term detrimental consequences for the kidney: proximal tubular cells are perturbed by the abnormal exposure to proteins and protein-associated factors, such as free fatty acids bound to albumin, progressing to **chronic tubulo-interstitial fibrosis**. Global glomerular sclerosis at late stages of the disease contributes to interstitial injury through misdirected filtration into the interstitial compartment[90] and, as a final result, to **kidney failure**.

2. Genetics

A) Genetic convergence towards the podocyte

A cell type convergence pointing at the podocyte is observed in the etiology of hereditary SRNS, with all monogenic forms of NS being associated with **genes relevantly expressed in the podocyte**[93]. To date, more than 50 genes have been identified as causative factors for NS (Fig. 12. Table 1).

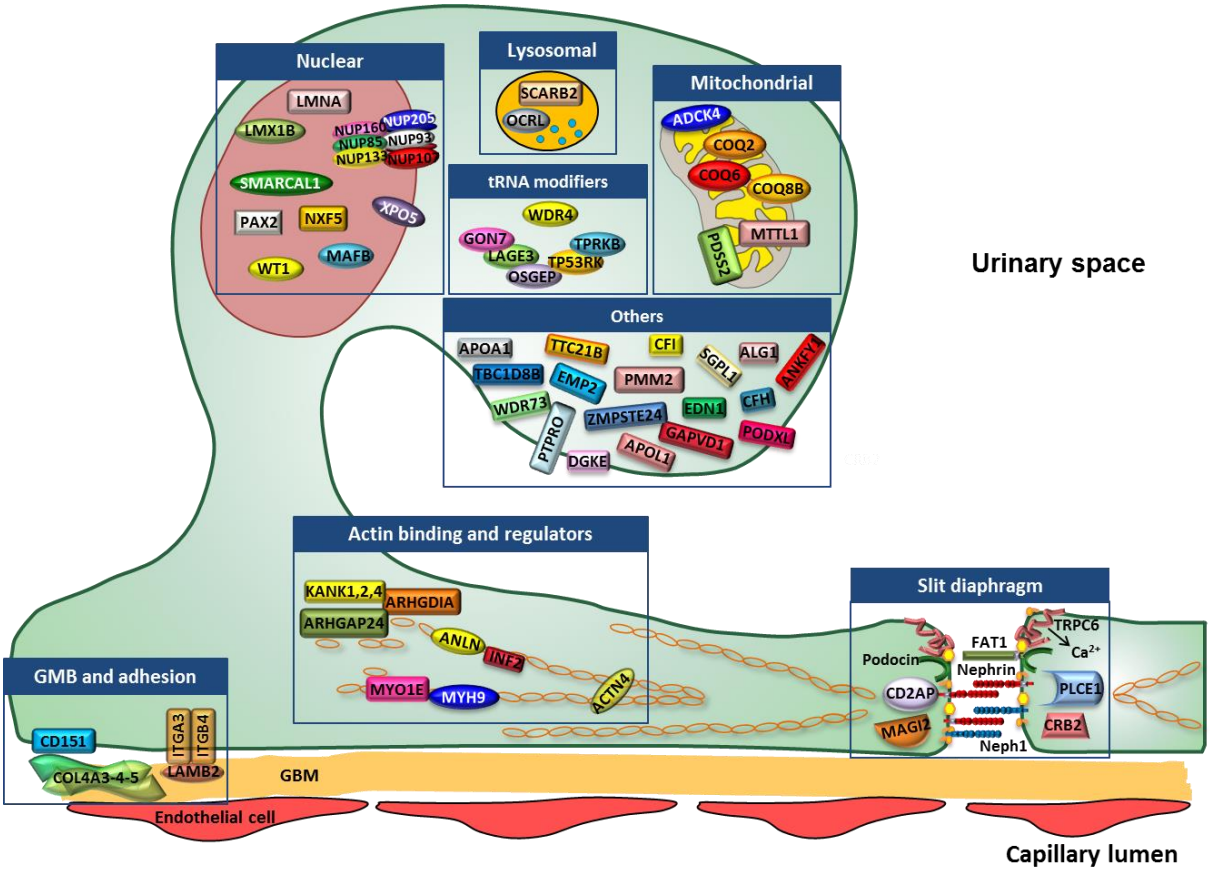

Figure 12: Podocyte genes associated with steroid-resistant nephrotic syndrome. Schematic representation of the genes associated with SRNS, coding for proteins that can be classed in various categories within the podocytes: SD and adaptors, actin cytoskeleton-related, GMB and adhesion, mitochondrial, lysosomal, nuclear and other proteins.
Kindly provided by Dr. G. Dorval

Since the initial implication of **structural component of the SD**, with the identification of mutations in *NPHS1*[48] and *NPHS2*[60] as causative of congenital and early-onset SRNS, respectively, the importance of the GFB integrity maintenance began to delineate.

In agreement with that, several constituents of the **GBM** as well as **adhesion molecules** anchoring the FPs were also found to associate with NS, given their role in preserving the cohesion of the renal filtration apparatus. In addition, FP plasticity and adaptation capacity to environmental changes are necessary to ensure regular function of the GFB, as evidenced by the involvement of proteins implicated in the **actin** and **microtubule cytoskeletal network rearrangement** in NS pathogenesis. Finally, mutations in genes coding for **nuclear**, **mitochondrial** and various **other proteins** that may perturb the podocyte biology have been found to be causative of inherited forms of NS.

Even though SRNS most commonly occurs as an isolated glomerular disorder, it may also be far less frequently associated with **extra-renal manifestations**. Their presence is often diagnostic, and increases the likelihood of identifying a genetic cause for the disease[94].

Syndromic NS forms are caused by mutations in genes not exclusively expressed in the podocyte, mainly coding for **nuclear** proteins, **basement membrane** and **adhesion** components, **actin cytoskeleton**-related proteins or even **mitochondrial** and **lysosomal** proteins. Some genes are responsible for isolated or syndromic diseases, depending on the mutation. The renal manifestation can be the predominant feature, presenting alone or with additional extra-renal phenotypes, or it may be facultative in reverse. For instance, mutations in the *LMX1B* gene usually lead to Nail-Patella syndrome with or without renal disease, but cases with FSGS only have also been reported[95]. Extra-renal manifestations are largely variable depending on the implicated gene and its underlying pathogenic mechanism. They may range from urogenital abnormalities and malignancy (*WT1*) to skeletal defects (*LMHX1B*, *SMARCAL1*), eye abnormalities (*LAMB2*) or skin affection (*ITGA3*).

Table 1: Genes associated with steroid-resistant nephrotic syndrome

Gene	Protein	Inheritance	Phenotype	Reference
Slit Diaphragm and Adaptor proteins				
NPHS1	Nephrin	AR	Congenital and infantile SRNS	Kestilä et al. 1998 [48]
NPHS2	Podocin	AR	Infantile and childhood SRNS	Boute et al. 2000 [60]
CD2AP	CD2-associated protein	AD/AR	Infantile SRNS	Kim et al. 2003 [96]
TRPC6	Transient receptor potential channel 6	AD	Juvenile and adult-onset FSGS	Winn et al. 2005 [97]
PLCE1	Phospholipase C ε1	AR	Infantile and childhood SS/SRNS	Hinkes et al. 2006 [53]
CRB2	Crumbs homolog 2	AR	Early-onset SRNS	Ebarasi et al. 2015 [98]
FAT1	Protocadherin Fat 1	AR	Childhood SRNS; multi-systemic disorder	Gee et al. 2016 [99] Lahrouchi et al. 2019 [100]
MAGI2	Membrane-associated guanylate kinase, WW and PDZ domain-containing protein 2	AR	Congenital and childhood SRNS	Bierzynska et al. 2017 [55]
KIRREL1	Kin of IRRE-like protein 1	AR	Juvenile SRNS	Solanki et al. 2019 [101]

(Continued)

Table 1 | *Continued*

GBM and Adhesion proteins				
COL4A5	Collagen (IV) α5	XD	Alport syndrome	Barker et al. 1990 [102]
COL4A4	Collagen (IV) α4	AD/AR	Alport syndrome; Hematuria	Mochizuki et al. 1994 [103] ; Jefferson et al. 1997 [104]
COL4A3	Collagen (IV) α3	AD/AR	Alport syndrome; Hematuria	Lemmink et al. 1994 [105] ; Badenas et al. 2002 [106]
ITGB4	Integrin-β4	AR	Epidermolysis bullosa	Kambham et al. 2000 [107]
CD151	Tetraspanin	AR	Nephropathy with pretibial epidermolysis bullosa and deafness	Karamatic et al. 2004 [108]
LAMB2	Laminin subunit β2	AR	Pierson syndrome; congenital SRNS	Zenker et al. 2004 [109] ; Hasselbacher et al. 2006 [110]
ITGA3	Integrin- α3	AR	Congenital interstitial lung disease, SRNS, and epidermolysis bullosa	Has et al. 2012 [111]
Actin Cytoskeleton-related proteins				
ACTN4	α-actinin-4	AD	Juvenile and adult-onset FSGS	Kaplan et al. 2000 [112]
MYH9	Non-muscle myosin heavy chain IIA	AD	Macrothrombocytopenia and granulocyte inclusions with or without nephritis or sensorineural hearing loss	Seri et al. 2000 [113]
INF2	Inverted formin-2	AD	Juvenile and adult-onset FSGS; Dominant intermediate Charcot-Marie-Tooth disease	Brown et al. 2010 [114] ; Boyer et al. 2011 [115]
MYO1E	Myosin IE	AR	FSGS	Mele et al. 2011 [116]
ARHGAP24	Rho GTPase-activating protein 24	AD	Infantile and juvenile Infantile and juvenile FSGS	Akilesh et al. 2011 [117]
ARHGDIA	Rho GDP-dissociation inhibitor α1	AR	Congenital SRNS	Gupta et al. 2013 [118] Gee et al. 2013 [119]
ANLN	Anillin	AD	Adult-onset FSGS	Gbadegesin et al. 2014 [120]
KANK2	KN motif and ankyrin repeat domain-containing protein 2	AR	Childhood SS/SRNS	Gee et al. 2015 [121]
KANK1	KN motif and ankyrin repeat domain-containing protein 1	AR	Childhood SS/SRNS	Gee et al. 2015 [121]
KANK4	KN motif and ankyrin repeat domain-containing protein 4	AR	Childhood SS/SRNS	Gee et al. 2015 [121]
Nuclear proteins				
WT1	Wilms' tumor protein	AD/AR	Denys-Drash syndrome; Frasier syndrome; isolated SRNS	Pelletier et al. 1991 [122] ; Barbaux et al. 1997 [123] ; Jeanpierre et al. 1998 [124]
LMX1B	LIM homeobox transcription factor 1-β	AD	Nail-Patella syndrome; isolated FSGS	Dreyer et al. 1998 [125] ; Boyer et al. 2013 [95]
SMARCAL1	HepA-related protein	AR	Schimke immuno-osseous dysplasia	Boerkoel et al. 2002 [126]
LMNA	Lamin A/C	XD	Familial partial lipodystrophy ; FSGS	Javor et al. 2004 [127] Thong et al. 2013 [128]
MAFB	Transcription factor MafB	AD	Multicentric carpotarsal osteolysis syndrome; FSGS with Duane retraction syndrome	Zankl et al. 2012 [129] Sato et al. 2018 [130]
NXF5	Nuclear RNA export factor 5	XR	FSGS	Esposito et al. 2013 [131]
PAX2	Paired box gene 2	AD	Renal coloboma syndrome; adult-onset FSGS	Amiel et al. 2000 [132] Barua et al. 2014 [133]
NUP93	Nuclear pore complex protein Nup93	AR	Infantile SRNS	Braun et al. 2016 [134]
NUP205	Nuclear pore complex protein Nup205	AR	Infantile SRNS	Braun et al. 2016 [134]
XPO5	Exportin-5	AR	Infantile SRNS	Braun et al. 2016 [134]
NUP107	Nucleoporin 107	AR	Galloway-Mowat syndrome	Rosti et al. 2017 [135]
NUP133	Nucleoporin 133	AR	Galloway-Mowat syndrome	Fujita et al. 2018 [136]
NUP85	Nuclear pore complex protein Nup85	AR	Childhood SRNS	Braun et al. 2018 [137]
NUP160	Nuclear pore complex protein Nup160	AR	Juvenile SRNS	Braun et al. 2018 [137]

(Continued)

Table 1 | *Continued*

Mitochondrial and Lysosomal proteins				
MT-TL1	Mitochondrially encoded tRNA leucine 1 (UUA/G)	Maternal mtDNA	MELAS syndrome	Kurogouchi et al. 1998 [138]
PDSS2	Decaprenyl-diphosphate synthase subunit 2	AR	SRNS; CoQ_{10} deficiency	López et al. 2006 [139]
COQ2	4-hydroxybenzoate polyprenyltransferase	AR	SRNS; CoQ^{10} deficiency	Quinzii et al. 2006 [140]
COQ6	Ubiquinone biosynthesis monooxygenase COQ6	AR	SRNS; CoQ^{10} deficiency	Heeringa et al. 2011 [141]
COQ8B	Atypical kinase COQ8B, mitochondrial	AR	SRNS; CoQ^{10} deficiency	Ashraf et al. 2013 [142]
SCARB2	Scavenger receptor class B, member 2	AR	Progressive myoclonic epilepsy with or without renal failure	Berkovic et al. 2008 [143]
OCRL	Inositol polyphosphate 5-phosphatase	XR	Dent disease	Hoopes et al. 2005 [144]
tRNA Modifiers				
LAGE3	L antigen family member 3	XR	Galloway-Mowat syndrome	Braun et al. 2017 [145]
OSGEP	O-sialoglycoprotein endopeptidase	AR	Galloway-Mowat syndrome	Braun et al. 2017 [145]
TP53RK	TP53 regulating kinase	AR	Galloway-Mowat syndrome	Braun et al. 2017 [145]
TPRKB	TP53RK binding protein	AR	Galloway-Mowat syndrome	Braun et al. 2017 [145]
WDR4	WD repeat domain 4	AR	Galloway-Mowat syndrome	Trimouille et al. 2018 [146]
GON7	GON7 subunit of KEOPS complex	AR	Galloway-Mowat syndrome	Arrondel et al. 2019 [147]
YRDC	yrdC N6-threonylcarbamoyltransferase domain containing	AR	Galloway-Mowat syndrome	Arrondel et al. 2019 [147]
Others				
CFH	Complement factor H	AD, AR	Complement factor H deficiency; Secondary FSGS	Vogt et al. 1995 [148]; Sethi et al. 2012 [149]
PMM2	Phosphomannomutase 2	AR	Congenital disorder of glycosylation, type Ia	Matthijs et al. 1997 [150]
CFI	Complement factor I	AR	Complement factor I deficiency	Sadallah et al. 1999 [151]
ALG1	β1,4 mannosyltransferase	AR	Congenital disorder of glycosylation, type Ik	Schwarz et al. 2004 [152]
ZMPSTE24	Zinc metallo-proteinase	AR	Mandibuloacral dysplasia with type B lipodystrophy	Agarwal et al. 2006 [153]
APOL1	Apolipoprotein L1	AR	Susceptibility to develop NS with FSGS	Genovese et al. 2010 [154]
APOA1	Apolipoprotein A	-	Variants associated with general disorder of lipid metabolism in NS	Santucci et al. 2011 [155]
PTPRO	Tyrosine phosphatase receptor-type O	AR	Childhood SRNS	Ozaltin et al. 2011 [156]
DGKE	diacylglycerol kinase-ε	AR	Atypical hemolytic uremic syndrome, membranoproliferative lesions	Lemaire et al. 2013 [157] Ozaltin et al.2013 [158]
EMP2	Epithelial membrane protein 2	AD	Childhood SS/SRNS	Gee et al. 2014 [159]
TTC21B	Tetratricopeptide repeat protein 21B	AR	Nephronophthisis; FSGS	Cong et al. 2014 [160]
EDN1	Endothelin-1	-	Polymorphisms association with the clinical NS phenotype	Yang et al. 2014 [161]
WDR73	WD repeat domain 73	AR	Galloway-Mowat syndrome	Colin et al. 2014 [162]
PODXL	Podocalyxin	AR/AD	Congenital SRNS; FSGS	Kang et al. 2017 [163] Lin et al. 2019 [164]
SGPL1	Sphingosine-1-phosphate lyase 1	AR	SRNS and facultative ichthyosis and adrenal insufficiency	Lovric et al. 2017 [165]
GAPVD1	GTPase-activating protein and VPS9 domain-containing protein 1	AR	Infantile SRNS	Hermle et al. 2018 [166]
ANKFY1	Rabankyrin-5	AR	Childhood SRNS	Hermle et al. 2018 [166]
TBC1D8B	TBC1 domain family member 8B	XL	Early-onset SRNS	Dorval et al. 2019 [167]

Table reporting the genes associated with SRNS and the corresponding phenotypic manifestations and mode of inheritance caused by mutations in these genes.

B) Steroid-resistant nephrotic syndrome due to *NPHS2* mutations

NPHS2 is the second gene that has been implicated in SRNS, after *NPHS1*. *NPHS2* mutations were recognized to be causative of a form of **early-onset autosomal recessive SRNS** presenting with FSGS that rapidly progress to ESRD[60] (NEPHROTIC SYNDROME, TYPE 2, OMIM#600995). Although only MCD is present at very early stages, FSGS lesions that progressively develop are the main histological features. DMS may be observed to a lesser extent, usually in the more severe forms.

NPHS2 mutations represent the **most frequent genetic cause of SRNS in childhood** and they are responsible for ~35-40% of familial congenital and infantile SRNS[89]. Patients with *NPHS2* mutations do not respond to steroid treatment for NS[168]; anyhow, they have been shown to have strongly reduced - 8 *versus* 33% - likelihood of post-transplant recurrence[169].

Nevertheless, the disease presents variable course and high clinical heterogeneity, which strongly correlate with the causative gene mutation(s)[169,170]. Indeed, *NPHS2*-SRNS mean age of onset is ~6 years[171], but it may manifest as severe congenital/infantile NS[60] or establish later in childhood as a milder disease[169]. Juvenile and adult onset forms have also rarely been described[172–177].

To date, ~200 *NPHS2* different mutations have been implicated in NS[178]. The type, position and combination of various mutations correlate with the severity of the pathology to some extent[169]. Frameshift and truncating mutations are generally less tolerated than missense ones, although their location with respect to functional domains and/or crucial positions may have distinctive impact on the phenotype. Homozygous or compound heterozygous states for 2 pathogenic mutations manifest earlier than heterozygous variants, which may contribute to atypical mild case of late-onset proteinuria with higher risk of post-transplant recurrence. Non-neutral polymorphisms can be associated with a second mutant *NPHS2* allele, the most commonly reported being the p.R229Q, which enhances susceptibility for disease that present with proteinuria[174].

Specific missense mutations have been shown to impair the normal targeting of podocin to the plasma membrane. Missense mutations cluster in the region of homology with the stomatin-like family[169]. Most of them are responsible for ER retention of podocin (among them, the p.R138Q, p.P118L, p.D160G, p.R168C, p.R168H and p.R168S), and correlate with earlier-onset of proteinuria and more severe manifestation of NS with respect to the mutants that manage to reach the plasma membrane (among them p.P20L, p.G92C, p.V180M and p.R238S)[66]. Others localize in late endosomes (such as the p.R291W), correlating with early-onset SRNS)[66].

NPHS2 mutations have been also shown to lead to secondary changes in the distribution of nephrin, CD2AP and α-actinin in patients[179], reinforcing the evidence for the important role of podocin as a scaffold protein in the organization of the SD structure.

B.a) p.R138Q podocin mutation

The **c.413G>A** missense mutation leading to **p.Arg138Gln** amino acid substitution - hereafter referred to as **p.R138Q** - was originally found as the Western European founder mutation in approximately one-third of the patients in the first *NPHS2*-related study[60]. This prevalence has been confirmed in larger patient cohorts[180], corroborating the fact it represent **the most frequent mutation linked to early-onset SRNS**. Patients with the homozygous p.R138Q mutation develop particularly early-onset SRNS usually before 6 years of age, which underlies the severity of this substitution[180].

The 138th amino acid of podocin is enclosed within the PHB domain, right after the transmembrane region and interposed between the palmitoylation sites (Fig. 13). The arginine residue (R) at position 138 is highly conserved among the stomatin-like protein family[60]. Substitution of this positively charged amino acid with an uncharged glutamine (Q) may interrupt intra- or inter-molecular interactions, leading to protein misfolding.

```
        10         20         30         40         50
MERRARSSSR ESRGRGGRTP HKENKRAKAE RSGGGRGRQE AGPEPSGSGR
        60         70         80         90        100
AGTPGEPRAP AATVVDVDEV RGSGEEGTEV VALLESERPE EGTKSSGLGA
       110        120        130        140        150
CEWLLVLISL LFIIMTFPFS IWFCVKVVQE YERVIIFR/QLG HLLPGRAKGP
       160        170        180        190        200
GLFFFLPCLD TYHKVDLRLQ TLEIPFHEIV TKDMFIMEID AICYYRMENA
       210        220        230        240        250
SLLLSSLAHV SKAVQFLVQT TMKRLLAHRS LTEILLERKS IAQDAKVALD
       260        270        280        290        300
SVTCIWGIKV ERIEIKDVRL PAGLQHSLAV EAEAQRQAKV RMIAAEAEKA
       310        320        330        340        350
ASESLRMAAE ILSGTPAAVQ LRYLHTLQSL STEKPSTVVL PLPFDLLNCL
       360        370        380
SSPSNRTQGS LPFPSPSKPV EPLNPKKKDS PML
```

Figure 13: Podocin p.R138Q position. Primary amino acid podocin sequence with the wild-type Arg (R, green) or the mutant Gln (Q, red) residue at position 138. Transmembrane and PHB domains are evidenced in blue and magenta respectively. Palmitoylation sites are indicated by purple arrows.

The p.R138Q substitution does not influence podocin interaction with nephrin[67,181] or its ability to engage homophilic interactions[67]. However, functional studies by overexpression of the p.R138Q (or its equivalent mouse p.R140Q) podocin in cellular systems have shown the mutated protein to be **retained in the endoplasmic reticulum** (ER)[66,67,181,182]. So, the mutant p.R138Q podocin would be unable to follow the classical secretory pathway to reach the plasma membrane[66]. This is supported by *in vivo* evidence for p.R138Q (or murine p.R140Q) podocin retention into the podocyte cell body in patient biopsies[179] and in the Nphs2$^{R140Q/R140Q}$ knock-in mouse model[183].

Indeed, direct observation of kidney tissue from a compound heterozygous patient, with the combination of p.R138Q and p.V180M mutations, showed association of a normal staining along the GBM - presumptively attributable to the p.V180M podocin that is correctly targeted to the plasma membrane[179] - together with a staining in the podocyte cell body, likely reflecting the ER retention of the p.R138Q mutant protein.

Podocin p.R138Q overexpression in cellular systems also revealed its predominant N-glycosylation, in contrast to the wild-type form, which is suggestive of a non-conventional transmembrane topology[184]. A dynamic interconversion between the transmembrane and hairpin p.R138Q podocin has been proposed, as it has been described for stomatin, the prototype for this family of related proteins[185]. The ER quality control system would massively address the hairpin form to proteasomal degradation[184], whereas p.R138Q N-glycosylated podocin with a transmembrane topology would enter the calnexin cycle, to eventually be subjected to ER-associated degradation[184].

While the wild-type podocin localizes to the lipid rafts, the targeting of the p.R138Q mutant form to these specific micro-domains is impaired. p.R138Q podocin would consequently fail to recruit nephrin to lipid rafts, losing that way the ability to enhance downstream signaling[67]. However, **nephrin presence at the plasma membrane** itself is an arguable issue in the context of p.R138Q podocin mutation. *In vivo* observations from patient[179] and mouse[183] kidney tissue suggest podocin mutations to perturb nephrin distribution. Nephrin was indeed found not only along the glomerular basement membrane, where it displayed a granular and discontinuous distribution, but also in the podocyte body[179,183]. Co-expression of p.R138Q (or murine p.140Q) podocin and nephrin in cellular systems had controversial outcomes instead, from complete absence of nephrin at the plasma membrane[181] to the opposite case in which podocin state would not influence nephrin levels at the plasma membrane[67], including intermediate conditions with some extent of ER retention (Dr. G. Mollet, personal communication).

Chapter 3: Galloway-Mowat Syndrome
A neuro-renal disorder

1. Clinical and pathological features

Galloway-Mowat syndrome (GAMOS, OMIM#251300) is an extremely rare genetic disease with autosomal - or X-linked - recessive inheritance, initially described by Galloway and Mowat in 1968[186]. It consists in a neuro-renal disorder characterized by **microcephaly** and **central nervous system** (CNS) **anomalies**, associated with **SRNS**.

Since its initial definition, a variety of case reports and studies on small series of patients revealed that it constitutes a **clinically heterogeneous** group of disorders. This matter challenged the categorization of GAMOS according to specific clinical manifestations, resulting in the lack of a standard accepted classification.

Microcephaly is the most consistent and prominent hallmark of GAMOS (Fig. 14). It consists of a reduction in brain - paralleled by a decrease also in the head - size[187]. Brain dimension correlates with the number of neurons. Microcephaly is often present at birth in GAMOS patients, referred to as **primary microcephaly** but it may also be **secondary**, with later establishment in postnatal life. Primary microcephaly is underlined by developmental causes, mainly attributable to perturbed proliferation of progenitors in the ventricular zone, which determines the final number of neurons. Secondary microcephaly may result from neurodegenerative processes or abnormal neuronal maturation.

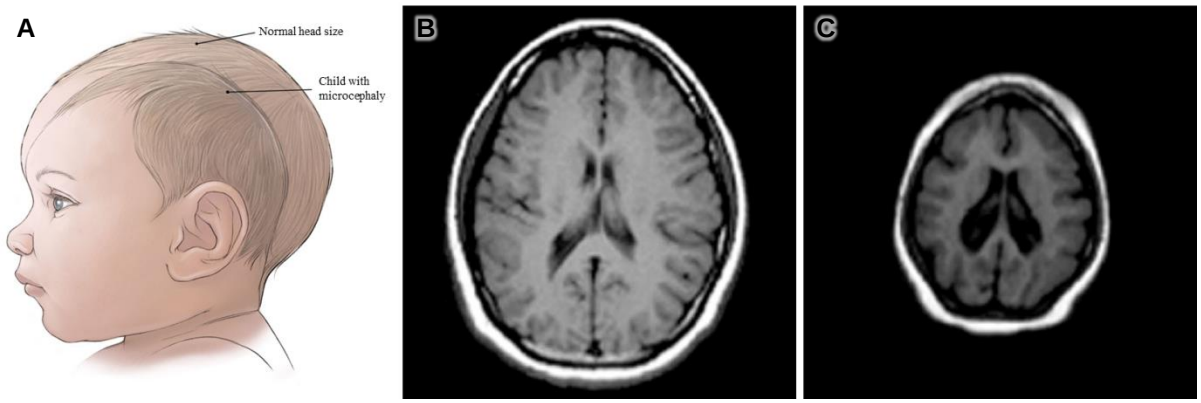

Figure 14: Microcephaly. **A)** Representation of normal *versus* microcephalic head size. **B)** Normal brain MRI. Transversal section. **C)** Microcephalic brain MRI. Transversal section.
Adapted from Prezi.com [188] *and Pang et al. 2008* [189]

Clinical manifestations of GAMOS embrace a broad spectrum of different CNS abnormalities reported in patients that include **cerebral or cerebellar atrophy**, **gyration and/or myelination defects** and **lissencephaly**. These structural anomalies are associated with **severely delayed psychomotor development**, **hypotonia**, **movement disorders** and **seizures**.

Kidney symptoms may range from isolated **proteinuria** to **SRNS** that rapidly progress to **ESRD**, even though some cases in which kidney functionality was not affected during the follow-up period have been reported[162,190]. Renal lesions observed in GAMOS patients include **MCD**, **FSGS** and **DMS** (Fig. 11).

Most patients have **dysmorphic facial features**, often presenting hypertelorism, ear abnormalities, and micrognathia. Other features, such as hiatal hernia, arachnodactyly, optic atrophy or endocrine abnormalities are more variable. The prognosis of GAMOS is poor, and most affected children die in the first years of life.

2. Genetics

The **clinical variability** of GAMOS is the reflection of the **genetics heterogeneity** underling the disease. Indeed, several genes have been identified to be implicated in this disease so far.

A) WDR73

The first causative gene implicated in GAMOS, ***WDR73***, have been identified by the Pr. C. Antignac's laboratory[162], describing 2 truncating mutations in 3 individuals from 2 unrelated families. Since then, several other articles have been published reporting new mutations in the *WDR73* gene (4 truncating mutations and 7 missense mutations) in patients with the same clinical characteristics, in particular a very severe **cerebellar atrophy**[190–195]. It seems, however, that the prevalence of renal involvement is lower in patients with missense mutations than those with truncating - loss of function - mutations, with half of the patients having no renal impairment. *WDR73* encodes a WD40-repeated-containing protein that may play a role in the regulation of microtubule organization and dynamics[162]. Recent unpublished work of our group further progressed in WDR73 characterization, suggesting a role for this protein in small nuclear RNA (snRNA) and non-polyadenylated RNA processing as a component of the integrator complex (Dr. F. Tilley, under revision).

B) Transfer RNA (tRNA) modifiers

The panel of monogenic causes for GAMOS was then expanded by implication of ***WDR4***[196], a component of the METTL1/WDR4 holoenzyme responsible for N7-methylguanosine (m^7G) modification of tRNAs, and of ***LAGE3***, ***OSGEP***, ***TP53RK*** and ***TPRKB***[145], coding for 4 of the KEOPS complex subunits, by our group in collaboration with the laboratory of Dr. F. Hildebrandt (Boston, United States). More recently, we further extended it to all the components of the N^6-threonylcarbamoyladenosine (t^6A) tRNA modification biosynthetic pathway with the involvement of **GON7**, the 5th subunit of KEOPS and the upstream-acting enzyme **YRDC**, in a collaborative study with Dr. H. van Tilbeurgh's laboratory (Paris, France) I'm a co-author of which[147] (Appendix, Article 3).

The 4 affected siblings with the *WDR4* mutation display various degrees of intellectual disability, growth retardation, endocrine anomalies and nephrotic range proteinuria[196].

The clinical manifestations of patients bearing mutations in *YRDC*, *LAGE3*, *OSGEP*, *TP53RK* or *TPRKB* are globally similar, presenting primary microcephaly, severe developmental delay, propensity for seizures and early-onset SRNS[145,147]. Of note, biallelic null mutations were never found in patients, suggesting the complete deficiency of one of these proteins to be lethal. Conversely, *GON7* mutations lead to milder neurological and renal symptoms. These patients display secondary microcephaly with no gyration defects, later onset of proteinuria and slower progression to ESRD[147]. Homozygous loss of function mutations identified in these patients lead to complete absence of GON7 protein expression.

Identification of GAMOS causative mutations in genes involved in **tRNA modification** points to an emergent role for post-transcriptional tRNA-mediated regulation of protein translation as a potential common denominator in the pathogenesis of neuro-renal disorders. A focus on tRNA modifications, with particular concentration on the t^6A biosynthesis and its molecular actors, will be carried out in the following sections.

C) Nucleoporins

Mutations in genes encoding structural constituents of the **nuclear pore complexes** have also been recently reported in patients featuring a GAMOS. Nuclear pores are large complexes that principally mediate bidirectional nucleo-cytoplasmic transport. They also participate to a wide variety of cellular processes including regulation of transcription, chromatin organization and cell division[197].

Although biallelic ***NUP107*** mutations were originally identified in isolated SRNS[198,199], a missense homozygous mutation has then been shown to lead to microcephaly with cranio-facial dimorphism and mild to moderate intellectual disability in association with childhood SRNS[135]. In addition, a homozygous mutation in the ***NUP133*** gene has been identified in patients manifesting microcephaly, neurodevelopmental delay, profound intellectual disability and childhood SRNS[136]. Both nucleoporins interact together and are part of the essential Y-complex or NUP107-160 complex, which is a key structural component forming the cytoplasmic and nuclear rings of the nuclear pore complex.

3. tRNA modifications

tRNAs are adaptor ribonucleic acid molecules mediating the translation of genetic information contained in messenger RNAs (mRNA) into a corresponding elongating polypeptide chain. They constitute 4 to 10% of total cellular RNA content, being the most abundant of all small non-coding RNA entities.

All RNA species carry **post-transcriptional modifications** that provide a finer level of regulation to the transcriptome. The entire setup of ribonucleic actors of translation - messenger, ribosomal and transfer RNAs - are heavily modified. Particularly, tRNAs are processed by 3' trailer and 5' leader sequences removal[200], addition of an essential 3'-CCA tail[201], introns removal[202] and they count over 80 distinct covalent modifications that can be present at different positions[203] (Fig. 15A). Eukaryotic tRNAs contain on average 13 modifications, whose pattern depends on several factors including grow rate, oxygen level or nutrients, metals and vitamin presence. Hence the tRNA epitranscriptome is composed by a heterogeneous population of molecules[204].

Modifications that are present in the **core** of the tRNAs mainly have a structural importance, regulating **folding and stability** of the molecule. The **anticodon stem loop** (positions from 34 to 36) - or its close vicinity - is instead a hotspot where the greatest diversity of hyper modified nucleosides is found, in particular at **wobble 34** and **dangling 37 positions**[205] (Fig. 15), where wobbling signifies interactions via non-Watson-Crick base pairing and dangling refers to the influence of bases outside the anticodon. The editing of this emplacement is crucial to ensure **proper decoding capabilities**. This is underlined by the fact that these modifications are generally conserved among eukaryotes. Modifications at the anticodon stem loop are also responsible to mediate **recognition** of tRNAs by their **cognate aminoacyl-tRNA synthetase** and thus ensure charging with the correct amino acid[203].

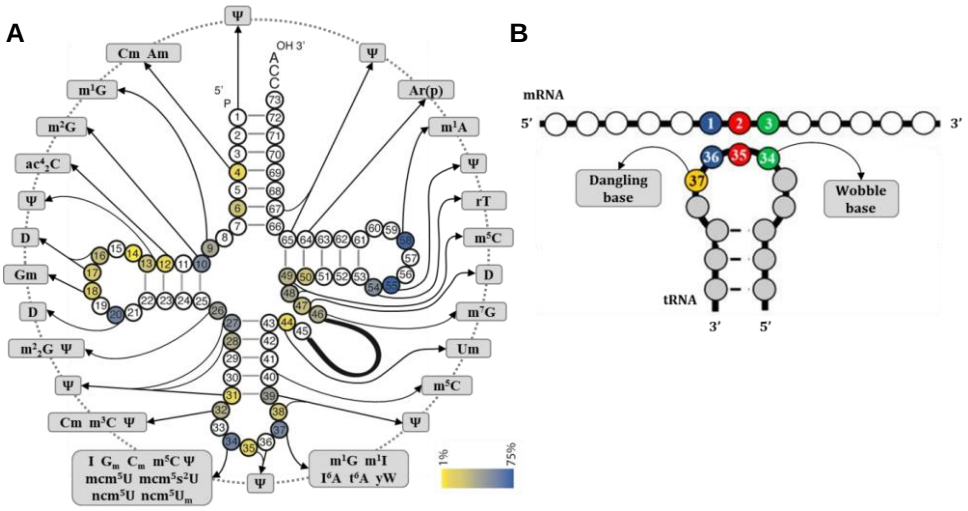

Figure 15: tRNA structure and covalent modifications. **A)** tRNA covalent modification emplacement. Over 80 distinct modifications can be present at different tRNA positions. Possible modifications that can occur at specific nucleosides are reported. Heat map on a yellow to blue scale represents the frequency of modification events occurring for each given position. **B)** Codon-anticodon interaction between mRNA and tRNA. Bases at positions 36, 35 and 34 on the tRNA anticodon stem loop interact respectively with the 1st, 2nd and 3rd base of the codon on the mRNA. The wobble base (34, green) can interact with the 3rd base of the codon through non-Watson-Crick base pairing interactions. The dangling base (37, yellow) influences the codon/anticodon interaction despite it localizes outside the anticodon.
Adapted from Lyons et al. 2018 [206]*, El Yacoubi et al. 2012* [203]*, Phizicky and Hopper* [207] *and Thiaville et al. 2016* [208]

Enzymes that catalyze tRNA modifications are often linked to **human diseases**[204,209], as it is the case of the components of the **t^6A** biosynthetic pathway, mutations of which are causative of GAMOS[145,147].

A) N6-threonylcarbamoyladenosine (t^6A)

The **t^6A modification** consists of a **threonine** amino acid linked though a **carbamoyl group** to the 6th amino group of **adenine** at **position 37** of the anticodon loop[210,211]. Together with m^1G_{37}, t^6A_{37} is a primordial modification belonging to a minimal translational machinery that have been universally conserved in evolution[203,212].

The so-called dangling base at position 37 is immediately at the 3' of the anticodon on tRNAs. This emplacement mainly stabilizes interaction between the first base of the codon with the third of the anticodon, especially for A:U and U:A pairs[203]. In particular, the t^6A modification **strengthens the A:U codon/anticodon interaction** on the ribosome when decoding the ANN-type codons[213]. It contributes that way to accurate protein translation.

Hence, defects in the t^6A biosynthesis have profound effects on translation efficiency and fidelity, severely affecting protein synthesis:

- Of note, the **translational initiator $tRNA^{Met}$** contains t^6A modification in all eukaryotes. The initiator - t^6A unmodified - tRNA responsible for bacterial and organellar translation initiation, the N-formylmethionine tRNA, recognizes AUG, GUC and UUG as initiator codon. It has thus been proposed[214] - and confirmed[215] - that the t^6A modification prevents mispairing between the first base of the codon and the third of the anticodon. Deficient t^6A production leads to **lower starting AUG codon recognition efficiency** and incorrect protein synthesis initiation.
- During **elongation**, the t^6A modification ensures accurate decoding by reducing frameshifts and regulates translational speed. t^6A decrease affects frame maintenance, causing a **higher frameshift rate**, especially in the presence of tandem ANN codons[215].

Leaky scanning bypass of start AUG codons, aberrant misinitiation at non-canonical starting codons, increased internal ribosome entry site (IRES)-dependent initiation, higher frameshift rates and read-through of stop UAG, UAA and UGA codons have been indeed observed in *Saccharomyces cerevisiae sua5*[216], *kae1*, *pcc1*, *bud32* and *pcc2* mutants[217], respectively homologs to the human components of the t^6A biosynthetic pathway *YRDC*, *OSGEP*, *LAGE3*, *TP53RK* and *GON7*. These translational defects impact protein synthesis and folding, with unfolded and misfolded proteins accumulation being evidenced by formation of insoluble protein aggregates[208].

The 16 combinations of ANN codons decode 7 out of the 20 standard amino acids, representing 35% of them. As a consequence of the genetic code degeneracy, each of these amino acids can be specified by a multiplicity of codons. While most of them (Asn, Ile, Lys, Met and Thr) are exclusively decoded by ANN-type codons - including the start AUG one as mentioned before - both Arg and Ser can be specified by 2 ANN- and 4 BNN-type codons.

The t^6A is synthetized in a two-steps reaction (Fig. 16) occurring in the cytoplasm:

- In the first step, **YRDC** catalyzes the production of the **threonyl-carbamoyl-AMP** intermediate from threonine, bicarbonate and ATP[218].
- The second step is then accomplished by mean of the **KEOPS complex**. The minimal functional core necessary and sufficient for the reaction is composed by the LAGE3, OGEP and TP53RK subunits. LAGE3 and OSGEP constitute the binding site for the tRNA, whereas TP53RK acts as an allosteric regulator. OSGEP is the genuine catalytic component, responsible for the iron-dependent transfer of the threonyl-carbamoyl-AMP moiety on the adenine at position 37 of the substrate tRNA and stimulating the ATPase activity of LAGE3 to release the **t^6A_{37} tRNA** product[219].

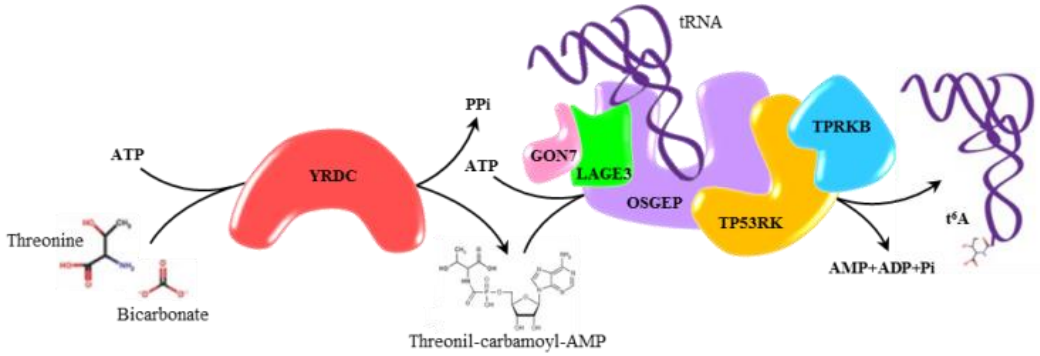

Figure 16: t^6A biosynthetic pathway.

a) KEOPS complex

The eukaryote Kinase, Endopeptidase and Other Proteins of small Size (KEOPS)[220] complex is a heteropentameric structure consisting of the **GON7**, **LAGE3**, **OSGEP**, **TP53RK** and **TPRKB** subunits, linearly arranged in that order (Fig. 17)[147,221–224].

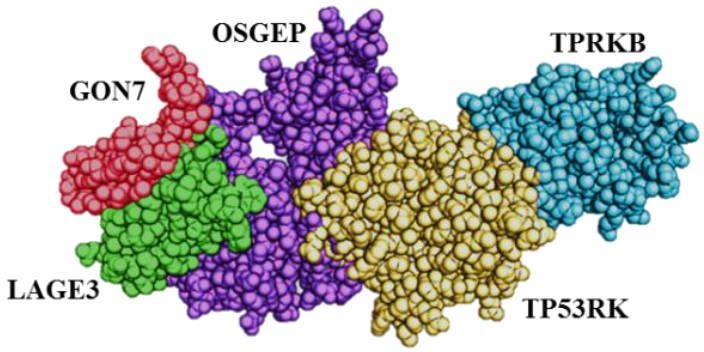

Figure 17: KEOPS complex space-filling representation. GON7 (pink), LAGE3 (green), OSGEP (violet), TP53RK (yellow) and TPRKB (blue) subunits are linearly arranged in that order to compose the KEOPS complex *Adapted from Drew et al. 2017* [224]*thanks to A. Menara*

With the only exception of Gon7 subunit, found only in yeast until recently, the whole complex, is extremely **conserved among Archaea and Eukarya**[225–227], with the OSGEP catalytic subunit having homologs also in Bacteria[228,229]. Evolutionary conservation of OSGEP among all the domains of life, together with the fact that eukaryotic genomes include a mitochondrial OSGEP paralog, OSGEPL1, strongly suggest it is part of a small core of **essential genes** for survival and growth[230,231]. In some species of Archaea, the homologs of

OSGEP and TP53RK are even fused in a polypeptide encoded by a single gene[226], further supporting their functional and reciprocal conservation in evolution. Three out of the five subunits have indeed been shown to be essential in human cells[232]. Not surprisingly, the KEOPS complex has an ubiquitous expression in most - if not all - human tissues[222].

The KEOPS complex was initially described by two independent studies performed in *Saccharomyces cerevisiae* as a critical regulator of **telomere maintenance**[220], as well as playing a direct role in **transcription**, in association with transcribed chromatin[227]. It has also been subsequently implicated in **chromosome segregation** and **genomic stability**[233]. Successive studies demonstrated that the KEOPS complex is required for the **universal t^6A modification** at position 37 on ANN-decoding tRNAs[215,217,234].

B) t^6A deficiency leads to GAMOS

As already mentioned before, the work performed in our research group greatly contributed to the implication of the t^6A deficiency in GAMOS pathogenesis by identifying mutations in all the genes encoding the proteins involved in its biosynthesis:

- In **Braun, D. A. *et al.* (2017) Nat. Genet.** we reported mutations in 4 KEOPS subunits, namely ***LAGE3***, ***OSGEP***, ***TP53RK*** and ***TPRKB***, in 37 individuals with GAMOS from 32 different families[145]. Zebrafish and mice knock-out models recapitulated the microcephaly but not the renal phenotype, and displayed early lethality. *OSGEP* knock-down in conditionally immortalized podocyte cell lines evidenced a significant reduction in t^6A levels. Silencing of the KEOPS subunits in podocytes induced impaired proliferation, translational attenuation, ER stress, DNA-damage-response signaling activation, increased apoptosis and defects in actin regulation.

- In **Arrondel, C. *et al.* (2019) Nat. Commun.** (Appendix, Article 3) we identified ***GON7*** mutations in 11 individuals affected with GAMOS from 5 unrelated families and ***YRDC*** mutations in 3 affected individuals from 2 unrelated families[147]. This work integrates genetic and functional analysis with structural crystallography data, demonstrating that, GON7 represents the functional homologue of yeast Gon7, which contributes to the stability of the KEOPS complex. Indeed, despite extremely weak sequence similarity (19% identity, 34% similarity), resolution of the GON7/LAGE3/OSGEP subcomplex crystal structure revealed their conformation is nearly identical. The t^6A content was significantly decreased in fibroblasts derived from patients with mutations in both *YRDC* and *OSGEP*, and to a lesser extent in *GON7*-mutated ones. Knock-down in immortalized podocytes evidenced a defective *de novo* protein synthesis. Cell proliferation was comparably impaired in *YRDC* and *OSGEP*, and slightly affected in *GON7* knock-down, while the apoptotic rate inversely correlated with proliferation.

Chapter 4: Disease Modeling
Induced pluripotent stem cells as a polyvalent tool

1. Induced pluripotent stem cells (iPSCs)
A) General features

Exhaustive definition of induced pluripotent stem cells (iPSCs) can be inferred from the bottom-up disassembly of their compound name that comprises - etymologically speaking - all their properties:

C: **cell**; from Medieval Latin *cellula*, "small rooms which monks inhabited", as Robert Hooke first named it in 1665, it is the smallest structural and functional unit of an organism.

S: **stem**; from Old English *stemn, stefn*, "stem of a plant, trunk of a tree", as the ancestor of ontogeny trees was named *Stammzelle* by Ernst Haeckel; it implies iPSCs' main features of **self-renewal** and **multilineage potential**.

P: **pluripotent**; from Latin *plus, plur-*, "more", and *potens, potent-*, "being able", it specifies the degree of potency, referring to the capability of generating **any cell lineage** that belongs to the **three embryonic germ layers**.

i: **induced**; from Latin *in*, "into, in, on, upon" and *ducere*, "to lead", underlying the artificial **reprogramming** process cells have been subjected to acquire the PS properties just mentioned.

iPSCs are supposed to represent a cellular entity that possess equivalent features to the pluripotent **epiblast**, arising from the **inner cellular mass of the blastocyst** during mammalian early development. Indeed, upon **reprogramming**, they acquire - or re-acquire in a certain way - the capacity to potentially give rise to any of the over 220 specialized cell types of an organism, except for extra-embryonic annexes. This **pluripotent** ability, coupled with indefinite **self-renewal** capacity, makes iPSCs the most convenient substrate for several purposes, allowing to dispose of a powerful tool almost limitless in availability and conceivable applications (Fig. 18A). These include fundamental research on stemness and pluripotency mechanisms, developmental biology studies, *in vitro* disease modeling - which will make the object of this dissertation - drug screening and cell-based therapy.

The discovery - or somehow the invention - of iPSCs earned the **2012 Nobel Prize in Physiology or Medicine** to **Shinya Yamanaka** (Fig. 18B), jointly to Sir John B. Gurdon "for the discovery that mature cells can be reprogrammed to become pluripotent" [235].

This finding allowed to produce stem cells with equivalent key features of their embryonic (ESC) counterpart[236–238], circumventing the ethical issues related of the work on human embryos. In addition, iPSCs can be easily derived from patient cells.

The possibility of disposing of a patient-specific accessible experimental system is among the great advantages provided by iPSCs. It allows exploring disease mechanisms in the patient own genetic background, and eventually testing the effects of therapeutic compounds. Moreover, they can be a source of immuno-compatible cells and tissues for autologous transplantation.

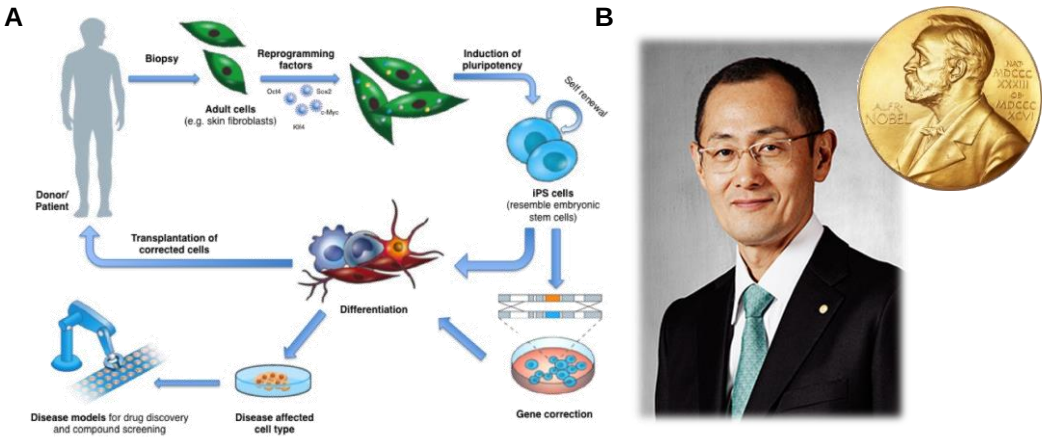

Figure 18: Induced pluripotent stem cells. **A)** iPSC applications. Somatic adult cells can be derived from healthy donors or patients and induced to iPSCs with reprogramming factors. Functional studies can be performed on iPSCs themselves or differentiation can be applied, eventually preceded by gene editing. iPSC-derivatives can be used to model development or disease or for drug screening. Alternatively, corrected cells can be transplanted to patients with therapeutic aim. **B)** Shinya Yamanaka. Yamanaka is the Japanese Nobel Prize-winning researcher considered as the "father" of iPSCs. He screened a library of pluripotency-related factors to find a combination that was both necessary and essential for reprogramming pluripotency.
Adapted from EuroStemCell.org [239] *and NobelPrize.org* [240]

B) iPSC reprogramming

Somatic reprogramming is most generally - even in the case of iPSCs used for this study - performed though ectopic expression of a core of defined pluripotency-related transcription factors, mainly the original set composed by **Oct4** (Pou5f1), **Sox2**, **Klf4**, and **c-Myc** (OSKM), also called the "Yamanaka's factors"[241,242]. Alternatively, the Thomson/Yu combination consists of Oct4, Sox2, Nanog and Lin28[243].

If fibroblasts - mouse embryonic (MEFs)[241], tail-tip[241] or adult human dermal[242] fibroblasts - were initially employed, successful reprogramming was subsequently reported starting from various cell types, such as primary keratinocytes[244], adult neural stem cells[245], cord blood cells[246], mature B[247] and T[248] lymphocytes, hepatocytes[249], gastric epithelial cells[249], pancreatic β cells[250], hematopoietic stem cells, lymphoid and myeloid progenitors[248], mature granulocytes and macrophages[248], intestinal epithelial, kidney, adrenal gland and muscle cells[251].

Even though any somatic nucleated cell can be virtually reprogrammed, **efficiency** of reprogramming may vary depending on cell type. Along with the yield and also the **ease** of the procedure, cell **availability** is another important factor to take into account when choosing the source of cells for reprogramming. In this study we opted for peripheral blood mononuclear cells (PBMCs) as cell source of choice for iPSC derivation:

- PBMCs are **easily accessible** through a **minimally invasive** blood sampling. Nucleated cells in peripheral blood comprise granulocytes, monocytes, T and B lymphocytes, but also a small fraction of ~0,01-0,1% of **hematopoietic CD34$^+$ stem/progenitor cells**[252]. CD34$^+$ cells can be expanded in favorable culture conditions[253,254] and efficiently reprogrammed to iPSCs using several approaches[252].

Reprogramming factors can be delivered in different ways. The design strategy should take into account several parameters, including the source of cells, the application iPSCs are planned to be used for and any kind of case-specific requirement.

Two broad categories of reprogramming methods exist: the **integrative systems**, with the use of retro-[241] or lentiviral[243] vectors or linear DNA transfection - eventually designed to undergo excision from the host genome through the Cre/LoxP[255] or piggyBac transposon[256] systems - and the **non-integrative** technics, employing replication-defective adenoviral vectors[257], non-replicative[258] or replicative[259] episomal vectors, F-deficient Sendai viral vectors[260], minicircle vectors[261], synthetic mRNA [262] or protein[263] delivery and even chemical reprogramming with small-molecule compounds[264]. Non-integrative methods have the main advantage of not leaving "scars" in the genome, which may be causative of insertional mutagenesis. iPSCs used in this study have been obtained using the Sendai viral strategy:

- The Sendai virus (SeV), also known as *Murine respirovirus*, is a negative sense, single-stranded RNA virus of the *Paramyxoviridae* family, non-pathogenic for humans[265]. Since it replicates in the cytoplasm without undergoing a DNA phase, there is no risk of genomic integration[266]. PBMCs can be efficiently reprogrammed using F-deficient (ΔF) SeV vectors[260], deprived of the fusion (F) protein which is required for the formation of infectious SeV particles. Viral vector is diluted out of cells ~10 passages after infection.

2. CRISPR/Cas9-mediated genome editing

A) Principles of the technique

The CRISPR/Cas9 system is based on bacterial and archaeal adaptive immune defense system against foreign nucleic acids from virus and plasmids, termed clustered regularly interspaced short palindromic repeats (CRISPR)/CRISPR-associated (Cas)[267]. It relies on **sequence-specific RNA-guided endonuclease**, which acts in a ribonucleoproteic complex to cleave a DNA target sequence.

- The **CRISPR RNA** (crRNA) is a small RNA providing sequence-specificity to drive the endonuclease. It is composed by a **protospacer** sequence, matching by base-pair complementarity with the 20 nucleotides target sequence, which must be followed by a short specific **protospacer-adjacent motif** (PAM) that is crucial for cleavage[267], and a **repeat sequence** (Fig. 19A). The systems also require a **trans-activating crRNA**

(tracrRNA), which is complementary to the repeat sequence and essential for crRNA maturation[268], target recognition and subsequent DNA cleavage by Cas9[267] (Fig. 19A). The crRNA may be fused through a linker loop to the tracrRNA, in a single chimeric crRNA:tracrRNA **guide RNA** (gRNA) equally efficient for target DNA cleavage[267] (Fig. 19B).

- The most widely used **endonuclease** is the **Cas9** from *Streptococcus pyogenes*. In this system, a **NGG** consensus PAM motif is required[267]. The protospacer sense target sequence is cleaved 3 nucleotides upstream the PAM, while the antisense strand is cleaved at one or more sites within 3 to 8 base pairs upstream the PAM[267].

- Alternatively, the CRISPR/Cas9 **double nickase** strategy contemplates the use of engineered endonucleases termed nickases, in which one catalytic domain is inactivated to cut a single DNA strand[269]. By using a pair of gRNAs targeting each strand of the region of interest it is possible to effectuate double nicking in close proximity. Single nicks produced at off-target sites are repaired through the high fidelity base excision repair (BER) mechanism, thus minimizing off-target mutagenesis.

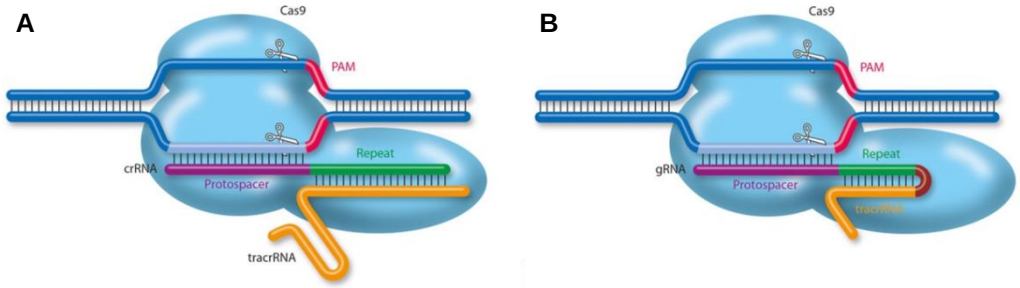

Figure 19: CRISPR/Cas9 system components. **A)** CRISPR/Cas9 system with crRNA and tracrRNA. The crRNA is composed by a protospacer sequence (purple) that pairs with a 20 nucleotides target sequence (light blue) and by a repeat sequence (green). A specific PAM motif (pink) directly downstream the target sequence is required for cleavage. The system comprises a tracrRNA (yellow) complementary to the repeat. **B)** CRISPR/Cas9 system with gRNA. The gRNA consists of the fusion of protospacer (purple) and repeat (green) with an engineered shorter tracrRNA (yellow) through a linker loop (brown).
Adapted from mpg.de [270]

The various components involved in the genome editing process can be delivered to cells in different forms and ways. The endonuclease and the gRNA can be expressed through a **DNA vector**, or they can be provided in the form of **RNA**. Alternatively, they can be directly delivered as a pre-constituted **ribonucleoprotein complex** (RNP).

Depending on the target cell, the delivery can be performed applying diverse methods. These include chemically-based methods, the most widely applied being **lipofection**, **viral transduction** or physical procedures that contemplate the creation of temporary holes in the plasma membrane by **electroporation** or **nucleofection**, in which electrical pulses make the material pass through the plasmatic or nuclear membrane respectively, or directly by **microinjection**.

The customable gRNA protospacer allows directing the endonuclease towards a 20 nucleotides target DNA sequence that immediately precedes a PAM NGG motif, thus inducing **site-specific double-strand breaks** (DSB) (Fig. 20A). DSBs can be repaired by different cellular mechanism:

- **Non-homologous end joining** (NHEJ) is an error-prone DNA repair pathway, with generation of small indels - insertions or deletions - that may modify the reading frame and result in functional knock-out of the targeted gene (Fig. 20B).
- **Homology-directed repair** (HDR) requires a homologous DNA sequence as a support to restore a genomic damage. A **donor DNA template** can be exogenously provided to induce defined modifications[271]. Homology arms must flank the desired modification to introduce[272]. The use of a single-stranded oligo deoxynucleotide (ssoDN) is preferable for the editing of single bases or small modifications, as it has done for genome editing of iPSC applied in this study. Larger rearrangements, including specific deletions or insertions and reporter line generation can be obtained by employing plasmids or adenoviral vectors (Fig. 20C).

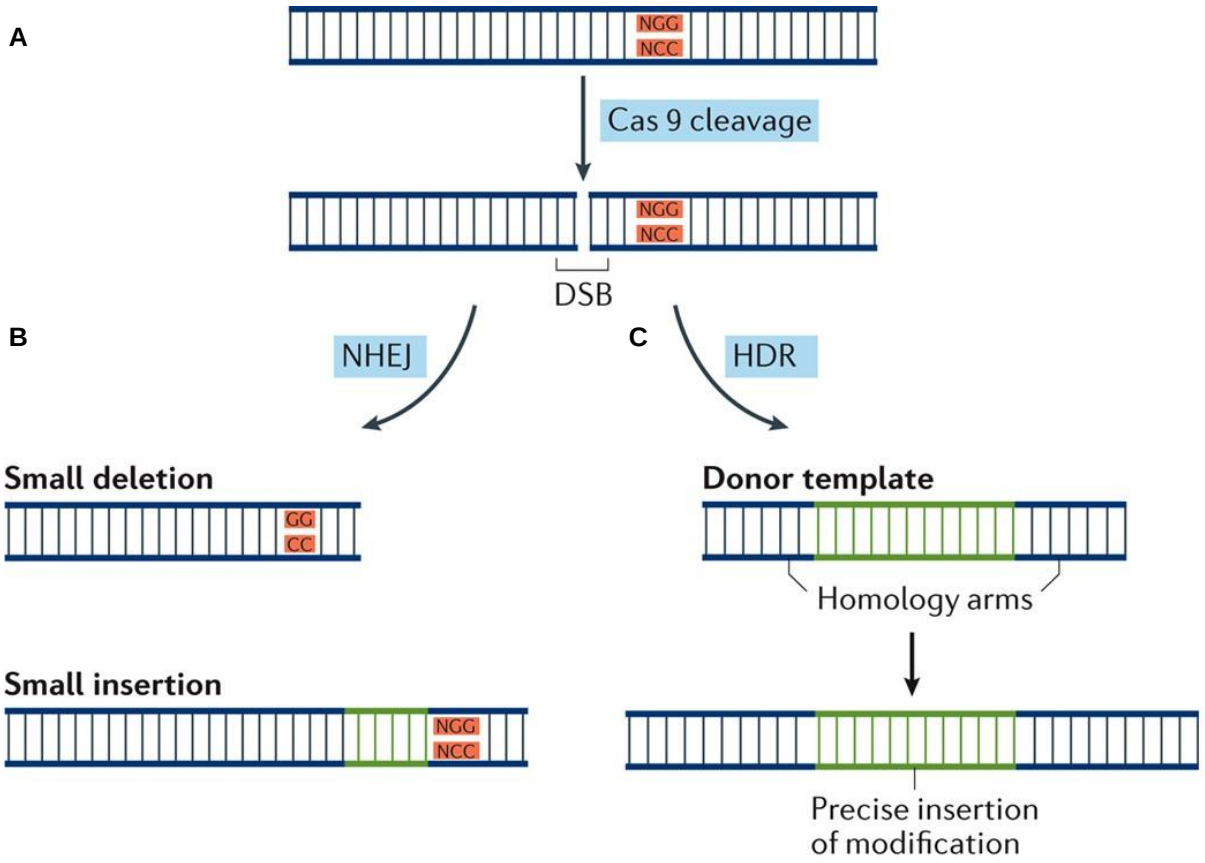

Figure 20: DNA double-strand breaks repair systems. **A)** Double-strand break induction. **B)** Non-homologous end joining. **C)** Homology-directed repair.
Adapted from Gibson et al. 2017 [273]

B) Combining CRISPR/Cas9 and kidney organoid technologies

The combination of iPSC versatility in human disease modeling with the possibility to directly perform experimental genetics on the human genome offered by the CRISPR/Cas9 technology provides an extremely powerful experimental approach, widely adopted nowadays in the stem cell research field.

Nevertheless, iPSCs are striking resilient to genomic modification, which challenges the editing process. So, optimization of conventional strategies to more adapted protocols has been necessary to increase the efficiency of genome editing on iPSCs[274].

The CRISPR/Cas9 system has already been successfully applied in the kidney organoid domain. Genome editing is generally performed on established PSC clones. As the only exception, iPSC reprogramming and genome editing are performed together in a single-step procedure in the laboratory led by Pr. M. Little[275].

B.a) Tools for kidney development investigation

Generation of various **reporter iPSC lines** for renal lineage markers supported improvement and better understanding of kidney organoid differentiation, providing at the same time useful working tools and transferable knowledge on human development.

The ***SIX2*$^{\mathbf{(E)GFP}}$** reporter iPSC lines allowed to detect the emergence, characterize and follow the evolution along differentiation of SIX2 expressing cells[276,277]. It resulted that SIX2 firstly defines the mesenchymal population of induced NPCs, as expected. Nevertheless, SIX2 expression persists in fully differentiated kidney organoids, where it marks alternative cell types[276] including renal stroma and muscle-like off-target cells[277].

Conditional ***SIX2*$^{\mathbf{Cre/Cre}}$*:GAPDH*$^{\mathbf{dual}}$** and inducible ***SIX2*$^{\mathbf{CreERT2/CreERT2}}$*:GAPDH*$^{\mathbf{dual}}$** reporter iPSC lines have also been then established, in which the Cre - or tamoxifen inducible CreERT2 - recombinase inserted into the endogenous *SIX2 locus* controls the switch from LoxP-flanked EGFP to mCherry expression. These tools allowed conducing fate-mapping analysis of kidney organoids, stating the contribution of $SIX2^+$ NPCs in nephron generation[277].

A dual ***SIX2*$^{\mathbf{GFP}}$*:NPHS1*$^{\mathbf{mKate}}$** iPSC reporter line has been shown to valuably assist consistent kidney organoid generation by facilitating direct quality controls on ongoing differentiation experiences[276]. Emergence of GFP-expressing NPCs and their maturation towards nephrons evidenced by $mKate^+$ glomerular structures could be monitored on live.

Reporter iPSC lines consenting to specifically follow developing of the podocyte lineage in live cells contemplate the knock-in of fluorescent probes into podocyte-specific gene *loci*. Over the visualization of podocytes emergence[276,278], the ***NPHS1*$^{\mathbf{GFP}}$** iPSC line was shown to be useful to efficiently isolate them by FACS[278]. Analogously, the ***MAFB*$^{\mathbf{mTagBFP2}}$**

reporter iPSC line has been used to monitor developing podocytes within kidney organoids[279], as well as to visualize glomerular structures by intravital imaging in transplanted mice[280].

B.b) Isogenic controls in disease modeling

A major concern faced when working with iPSCs is the high degree of inter- and intra-cell line variability - between different cell lines and various clones of the same line - iPSCs and their derivatives are subjected to[274].

The CRISPR/Cas9 technology offers the possibility to dispose of **isogenic controls**, meaning iPSC clones that exclusively differ for the genomic editing performed[281]. This is especially important for monogenic disease modeling, since it allows to **correct or introduce a patient mutation** and to assess its effect within the **same genetic background**.

The first example of combination of CRISPR/Cas9 and kidney organoids applied to renal disease modeling is the generation of **knock-out human ESC lines** by introduction of biallelic truncating mutations in the ***PODXL***, ***PKD1*** or ***PKD2*** genes[282].

The case of polycystic kidney disease (PKD) modeling is emblematic in demonstrating how the establishment of isogenic clones is valuable for overcoming the immanent and unpredictable variation of iPSCs. Indeed, the authors could highlight a defined phenotype, delineated by cysts formation in kidney organoids differentiated from *PKD* knock-out iPSC clones[283]. Contrariwise, PKD patient-derived iPSCs displayed a dramatic heterogeneity that confounded the analysis of PKD-specific effects[283].

Correction of the causative mutation on one of the affected alleles has otherwise been effected for ***IFT140***[284] and ***PKHD1***[285] mutated patient-derived iPSCs, restoring the respective disease-related phenotypes.

3. iPSC differentiation

Pluripotency of iPSCs is comparable to the **embryonic epiblast** state. It means they have the potential to give rise to all the derivatives of the three germ layers: **endoderm**, **mesoderm** and **ectoderm** (Fig. 21).

Specific protocols progressively developed to direct iPSC differentiation towards the destiny of interest, specifically to the **kidney** (podocytes, kidney organoids) and **neuronal** (late cortical progenitor cells, brain organoids) lineages in our case. The rationale behind iPSC differentiation essentially rest on translating our current knowledge about embryogenesis, looking at *in vivo* development as a model to reproduce. Instructive stimuli specifically applied are spatiotemporally integrated by cells, thus recapitulating the sequential stages of embryonic development.

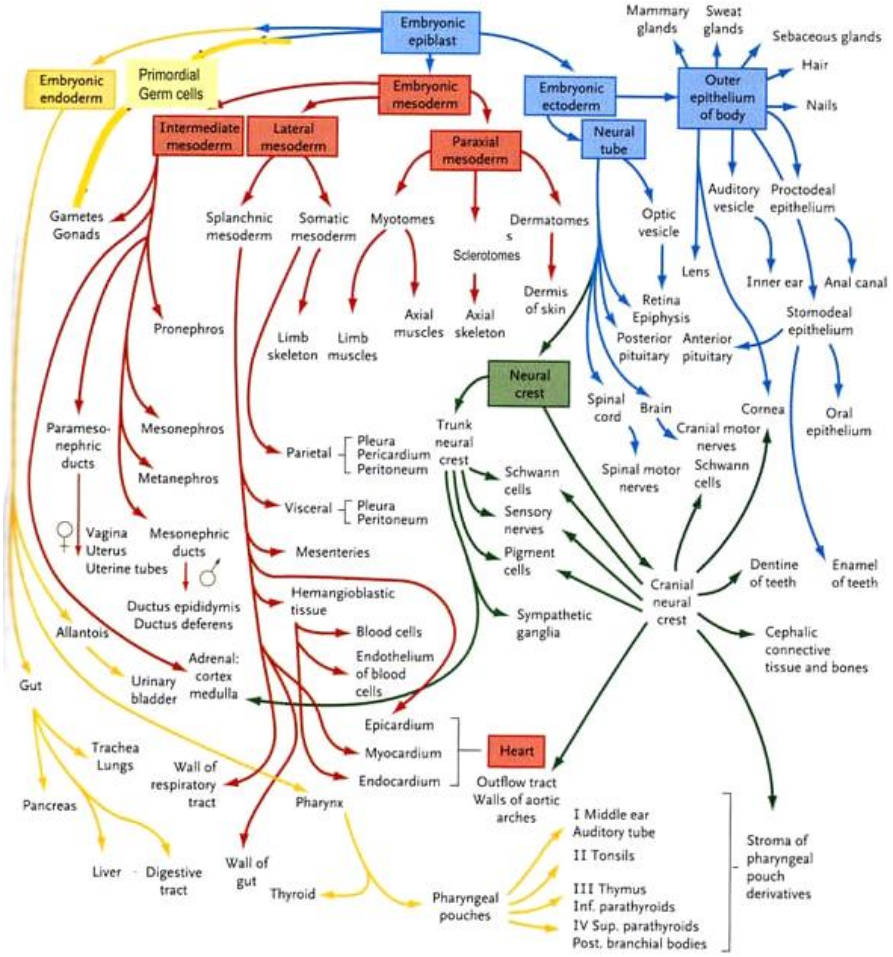

Figure 21: Embryonic epiblast and germ layers derivatives.
Adapted from Epomedicine.com 2017 [286]

A) Bi-dimensional (2D) cell culture

Since the beginning of stem cell research, considerable effort was made with the aim to obtain specific cell types of interest that could be relevant for the particular required application. A plethora of different protocols - much more numerous than the existing cell types - were established, most of them leading to obtain monolayer culture of homogeneous cell populations. From neuronal, cardiac, gastrointestinal and any other fate, almost all the possible subset of mammalian derivatives can be obtained from stem cells.

Here I will focus on 2 particular cell types that are relevant for the modeling of the diseases confronted in this study: **podocytes** and **late cortical progenitor cells**.

A.a) iPSC-derived podocytes

In vitro studies on NS have been considerably hampered by difficulties in obtaining *bona fide* podocytes.

Primary cultures of podocytes are challenging to set up because of their propensity to rapidly dedifferentiate *in vitro*. Podocytes in culture are unable to retain they identity features, namely FPs, SD and key markers expression. Furthermore, podocytes being terminally differentiated cells, they display a limited proliferation capacity that ends to quick growth arrest, making their culture even more ephemeral[287].

Limited **podocyte cell lines** have been established in an attempt to circumvent these major obstacles. Firstly, optimization of culture conditions and avoiding repeated sub-cultivation allowed to get arborized podocyte-like cells that express WT1 and synaptopodin, while undergoing irreversible growth arrest[288]. **Conditionally immortalized human podocyte cell lines** were then established using the thermosensitive SV40-T antigen tsA58[289]. Under the 33°C "permissive temperature", undifferentiated podocytes are proliferative epithelial cells displaying a cobblestone-like polygonal morphology. Differentiation is induced by transfer at a "non-permissive temperature" of 37°C. Within 14 days at 37°C, podocytes exit the cell cycle and extend cellular processes. They express podocyte-specific markers such as WT1, synaptopodin and low levels of SD-related proteins nephrin, podocin and CD2AP. However, the effective resemblance of conditionally immortalized podocytes with their *in vivo* counterpart remains controversial[290].

One reasonable strategy in modeling NS may imply the derivation of a **homogeneous podocyte population from iPSCs**. Actually, the podocyte is the first reported renal cell type that has been obtained through iPSC directed differentiation.

First attempts in that direction allowed the generation of **podocyte-like cells** that display a similar morphology compared to immortalized podocyte cell lines and express some podocyte markers, such as WT1, podocin and synaptopodin[291]. However these iPSC derivatives still display immature features, as they retain proliferative capacity and the expression of the progenitor-related marker PAX2.

A more mature state was achieved by applying differentiation protocols[292–294] leading to obtain a homogeneous cell population with morphological and molecular aspects and growth behavior consistent with human glomerular podocytes. Moreover, in an effort of simplifying the currently existing protocols, optimization of several parameters of culture conditions allowed - or at least that is what has been claimed - to achieve a one-step standardized procedure to obtain podocyte-like cells[295]. **"Mature" iPSC-derived podocytes** are multinucleated cells characterized by an arborized main large cell body[292–295]. In contrast to previous reports, they display a low proliferation rate ending in growth arrest[292,294], and express the typical mature podocyte markers WT1, nephrin[292–294], synaptopodin[292,294,295], podocin[293–295], P-cadherin[292,294], α -Actinin-4[292], CD2AP and ZO-1[294], although retention of PAX2 expression has also been evidenced[294].

The establishment of a **microfluidic device** mimicking the GFB environment further improved iPSC-derived podocytes maturation[293]. In this so called **glomerulus-on-a-chip**, podocytes are differentiated *in situ* on a porous membrane, interfacing a layer of primary endothelial cells on its opposite side[296]. Remarkably, application of fluid flow and cyclic strain was shown to enhance podocyte differentiation in monolayer culture[293].

Although some clues for iPSC-derived podocyte **functionality** are displayed in the monolayer classic culture condition, such as albumin uptake[291,292,294,295], contractile response to angiotensin II[291,292,294] or susceptibility to nephrotoxic doxorubicin[295] or TGF-β1-triggered cell death[294], podocytes exhibit more relevant functional features on the micro-engineered glomerulus-on-a-chip. Specifically, this system displays selective permeability to small molecules, which is evidenced by differential clearance between inulin and albumin, and clinically relevant drug toxicity response[293].

At the midway between direct differentiation of podocytes in two-dimensional culture and their derivation within a complex organoid system (that will be discussed later), **pseudo-three-dimensional podocyte culture** with a >90% purity was achieved by forcing proximalization of iPSC-derived renal vesicles (RV)[10] and subsequent specification of podocyte lineage[297]. These podocytes have a global gene expression signature comparable to adult human podocytes and form SD-like intercellular junctions[297]. Treatment with the PAN podocytotoxin[298] provoked decrease in SD-related protein expression, with lower nephrin translocation at the membrane[297]. In an analogous way, RVs induced from iPSCs have been reported to generate several distinct nephron cell types, which include **podocyte precursors** expressing synaptopodin and podocin capable of albumin uptake[299].

Finally, podocytes "primary" culture can be derived secondly to **kidney organoids differentiation** of iPSCs by **glomerular isolation**[279]. Podocytes with a typical "mature" morphology migrate out and spread around plated glomeruli. They express WT1, synaptopodin, nephrin, podocin, CD2AP and P-cadherin. Organoid-derived podocytes equally display functional properties such as active albumin endocytosis and membrane translocation of GLUT4 accompanied by actin cytoskeleton rearrangement upon insulin stimulation[279]. Nevertheless, similarly to what mentioned above, they had a tendency to rapidly lose their identity in a bi-dimensional environment, as underlined by lower expression level of podocyte markers compared to glomeruli and reduction in MAFB^{TagBFP} reporter gene expression[279].

A.b) iPSC-derived late cortical progenitor cells (CPCs)

Relying on the same principle of direct differentiation as a developmental mirror on a dish, the neural cellular counterpart relevant in GAMOS disease modeling can be generated from iPSCs as well.

A **dual SMAD inhibition** strategy has been shown to efficiently induce the neuroectodermal fate from pluripotent cells[300]. Combined treatment with inhibitors of the bone morphogenic protein (BMP) and transforming growth factor beta (TGF-β) pathways, which both transduce through SMADs, has indeed a synergistic action on neural conversion. Dual SMAD inhibition mediates at first the destabilization of the pluripotency network relying on Nanog, which is a direct target of the TGF-β/Nodal/Activin signaling[301,302].

Secondly, it suppresses alternative fate acquisition such as the endodermal, mesodermal[303] or trophoblast lineages[304] robustly orienting cells towards the **ectoderm**, which is the embryonic germ layer that gives rise to the neural plate, neural crest and epidermis (Fig. 22A).

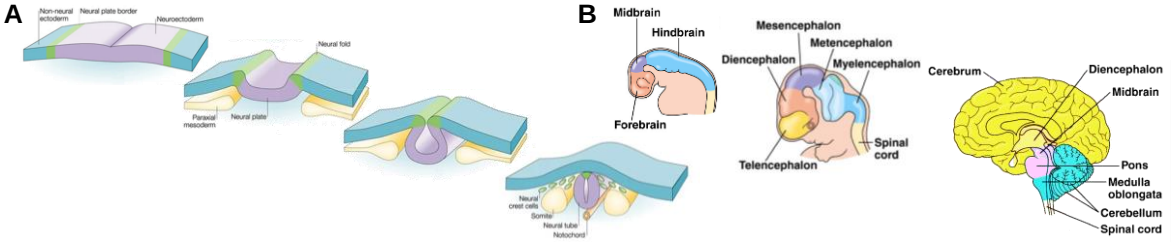

Figure 22: Central nervous system development. **A)** Neurulation. **B)** Brain development. *Adapted from Gammill et al. 2003* [305] *and StudyBlue.com* [306]

BMP signaling has also a major role in its specification, with higher levels favoring the epidermal fate, whereas intermediate levels promote the formation of neural crest cells. The **neural plate** can be instead considered as an ectodermal "default state"[307,308], emerging in low BMP conditions. The dual SMAD inhibition is accomplished by using small molecules such as SB431542 and LDN193189, respectively inhibiting the TGF-β and BMP4 signaling pathways. Combination with FGF (fibroblast growth factor) 2 might help neural stem cell specification[309,310] by promoting cell self-renewal[307].

Early neuroepithelial cells thus induced, spontaneously self-organize *in vitro* into three-dimensional epithelial structures called "**neural rosettes**" according to their characteristic morphology with radial polarized cells departing from a central lumen. This stage is reminiscent of the **neural plate**[309,311], right before the closing of the **neural tube** by raising and convergence of folds delimitating the neural groove (Fig. 22A). Neural rosettes adopt anterior **forebrain** CNS features by default[311]: they display a **dorsal telencephalic identity**, and more precisely they are engaged in **neocortical differentiation** (Fig. 22B).

Under pro-proliferative conditions, specifically when growth factors (EGF, FGF2[312,313] and BDNF) are provided in a medium supplemented with N2B27, the neurogenic competence of these cells is promoted, while preventing spontaneous neuronal differentiation at the same time. Neural rosettes spontaneously dissociate, and further enzymatic passages lead to obtain homogeneous and stable population of **late cortical progenitor cells** (CPC) growing as a monolayer[314]. These CPCs can be kept in culture for several passages.

Late CPCs principally differentiate into **glutamatergic neurons of the superficial (II-IV) layers** upon removal of the neuronal differentiation barrier[314]. The extended period of proliferation CPCs are constrained to experience is consistent with their strong differentiation bias towards late appearing neurons of the superficial cortex. Glutamatergic excitatory neurons constitute the majority of neurons in the cerebral cortex, where they mainly mediate interconnectivity between cortical regions within a hemisphere, and are responsible for the higher cognitive functions of the human brain.

B) Three-dimensional (3D) organoid culture

Organoids are defined as 3D structures formed by multiple organ-specific cell types that develop from stem cells or organ progenitors and self-organize recapitulating *in vitro* the structural arrangement and one or some function(s) of an *in vivo* organ[315].

Organoids development relies on fundamental cell intrinsic properties of autonomous organization[315]: **self-assembly**, **self-patterning**, and **self-driven morphogenesis**[316]. Actually, cells aggregate and have the tendency to segregate in clusters with homogeneous histological features by sorting out, according to cells respective selective affinity[317]. Subsequently, they undergo spatially restricted lineage commitment as cells reciprocally interact depending on their location. Their interplays also evolve in time, finally giving rise to a complex lineage hierarchy.

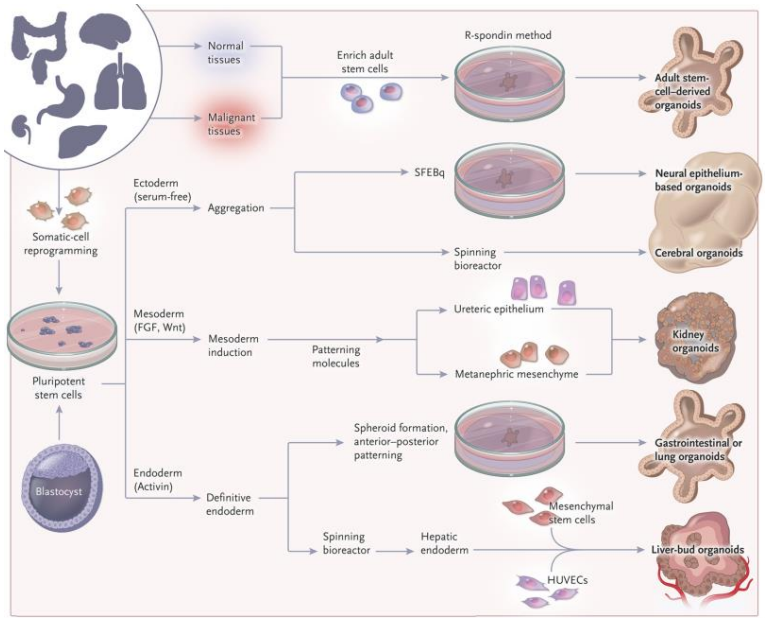

Figure 23: Organoid generation. Organoids can be obtained from normal or malignant tissue-resident adult stem cells or from PSCs, either derived from the blastocyst ICM (ESCs) or by somatic cell reprogramming (iPSCs).
Adapted from Li et al. 2019 [318]

Organoids can at present be obtained for most of - if not all - mammalian tissues. They can be both derived from **tissue resident adult stem cells**, as demonstrated for intestinal crypt[319] and colon[320], stomach[321], pancreas[322], liver[323] and lingual[324] organoids, or generated from **pluripotent stem cells** (PSC), either **embryonic** or **induced** (Fig. 23). PSC-derived organoids include intestinal[325], retinal[326], brain[327]; liver bud[328] and - among the most recent - kidney organoids[10,329,330]. A focus on brain and kidney organoids will be will be carried out in the following sections and a more detailed state of the art for kidney organoids will be treated in the following chapter.

As mentioned for iPSCs, organoid applications include but extend to a higher order of complexity recapitulation of developmental processes and disease modeling applied to genetic and/or developmental conditions but also to cancer, infectious disease or degeneration, and drug screening. Furthermore, they are promising for personalized and regenerative medicine, providing new perspectives for immunocompatible cell-based therapy up to whole-organ replacement, eventually upon gene correction.

B.a) Brain organoids

Cerebral organoids containing a variety of discrete brain regions and different neural and neuronal subtypes (Fig. 24A) were established in 2013 in the group of Dr. **J. Knoblich** in Vienna (Austria) by Dr. **M. Lancaster**[327].

The original protocol contemplates **embryoid body** (EB) formation. EBs are then induced towards **neuroectoderm** and embedded in droplets of Matrigel that are transferred and cultured into a spinning bioreactor[327] (Fig. 24B). More recent techniques imply the use of multiple-well culture with orbital shakers[331] and miniaturized spinning bioreactors[332].

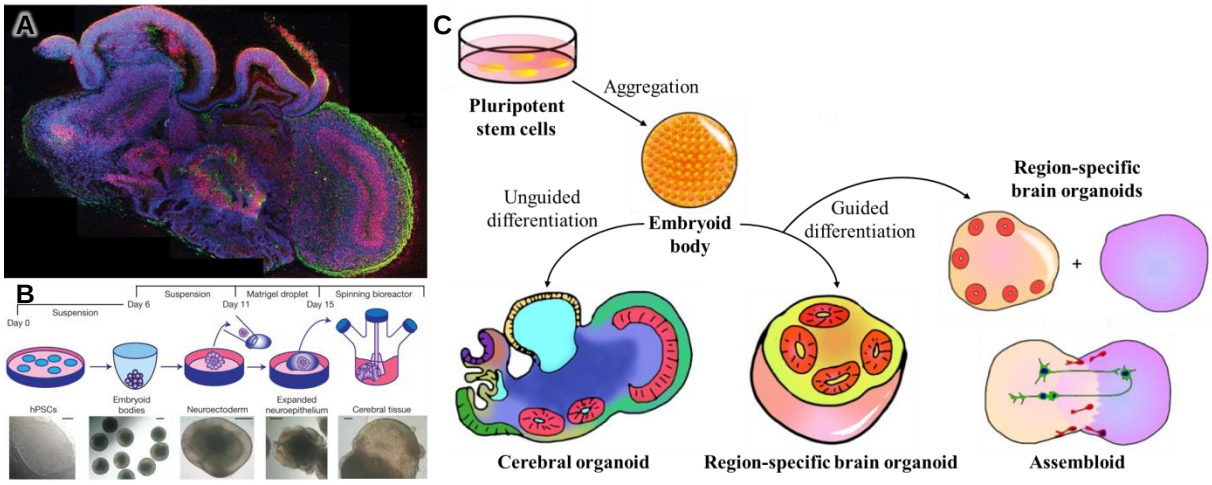

Figure 24: Brain organoids. **A)** Cerebral organoid. SOX2 (red), TUJ1 (green). **B)** Original cerebral organoid culture protocol. **C)** Unguided and guided methods to generate brain organoids.
Adapted from Lancaster et al. 2013 [327] *and Qian et al. 2019* [333]

Brain organoids recapitulate the development and general tissue architecture of the fetal human brain, being composed of progenitor, neuronal and glial cell types that coherently organize in a spatial and temporal manner. Neuronal calcium waves and action potentials have been induced by current injections[327], suggesting functional neural activity. Along with organoid maturation, spontaneous action potentials progressively establish[334].

Brain organoids can be currently generated by two principal methodologies:

- **Unguided differentiation** relies on spontaneous self-organization of neuroectodermal induced PSCs. **Cerebral organoids** (Fig. 24C) contain a variety of regional identities ranging from forebrain, midbrain and hindbrain to meninges, retina and choroid plexus[327]. Consistently with this vast lineage assortment, a diversity of cell types have been evidenced in cerebral organoids, which contain neural progenitors, excitatory and inhibitory neurons, interneurons, astrocytes, oligodendrocyte precursors and retinal photosensitive cells[327]. However, the stochastic nature of spontaneous morphogenesis culminates into unpredictable proportions and a heterogeneous arrangement of each lineage and cell type.

- **Guided differentiation** is performed by providing instructive patterning clues to PSCs to homogeneously obtain lineage-committed progenitors that organize into **region-specific brain organoids** (Fig. 24C) with reduced variation. Forebrain[332,335], midbrain[332,336,337], cerebellum[338], hippocampus[339], hypothalamus[332] and pituitary gland[340] organoids have thus been generated applying adapted protocols for each neuronal lineage. Different region-specific brain organoids separately generated can be fused together to generate an **assembloid** (Fig. 24C). In that way, it is possible to regulate the proportion of distinct cerebral regional identities and to model specific inter-regional interactions[341–343].

B.a; i) Forebrain organoids

The **neocortex**, which underwent great expansion during human evolution, is responsible of the higher cognitive, emotional, and social abilities that characterize our species[344,345]. For this reason, **forebrain organoids** with **cortical tissue** formation are of particular interest for understanding human development and disease.

Guided protocols have been established to derive forebrain organoids from ESCs[346,347] and iPSCs[332,335]. Remarkably, human cortical development and structural organization are recapitulated with considerable accuracy by these *in vitro* counterparts (Fig. 25).

Indeed, forebrain organoids present distinct layers that closely resemble the six-layered laminated architecture of the *in vivo* cortex. They contain the **progenitor** ventricular, subventricular and intermediate zones as well as the **neuronal** subplate, cortical plate, and Cajal-Retzius cell zones in the proper apico-basal order[347].

The mammalian neocortex develops though species-specific processes that may remarkably vary even in species that are genetically similar[348], exhibiting maximal extension and complexity in human beings. Forebrain organoids recapitulate human-specific features such as the expansion of the outer ventricular zone, populated by radial glia and intermediate progenitor cells[349]. Over the structural similarity, the cortical neurogenesis temporality is maintained in forebrain organoids, following the **"inside-out" rule** as *in vivo*: the deeper the layer, the earlier the neurons are born from cortical progenitors[347]. Both excitatory and inhibitory neurons are functional, even though less mature than adult neurons, displaying spontaneous synaptic transmission[332]. In addition, forebrain organoids gene expression pattern is encouraging well correlated to human fetal brain for the early-mid stages of embryonic development[350,351].

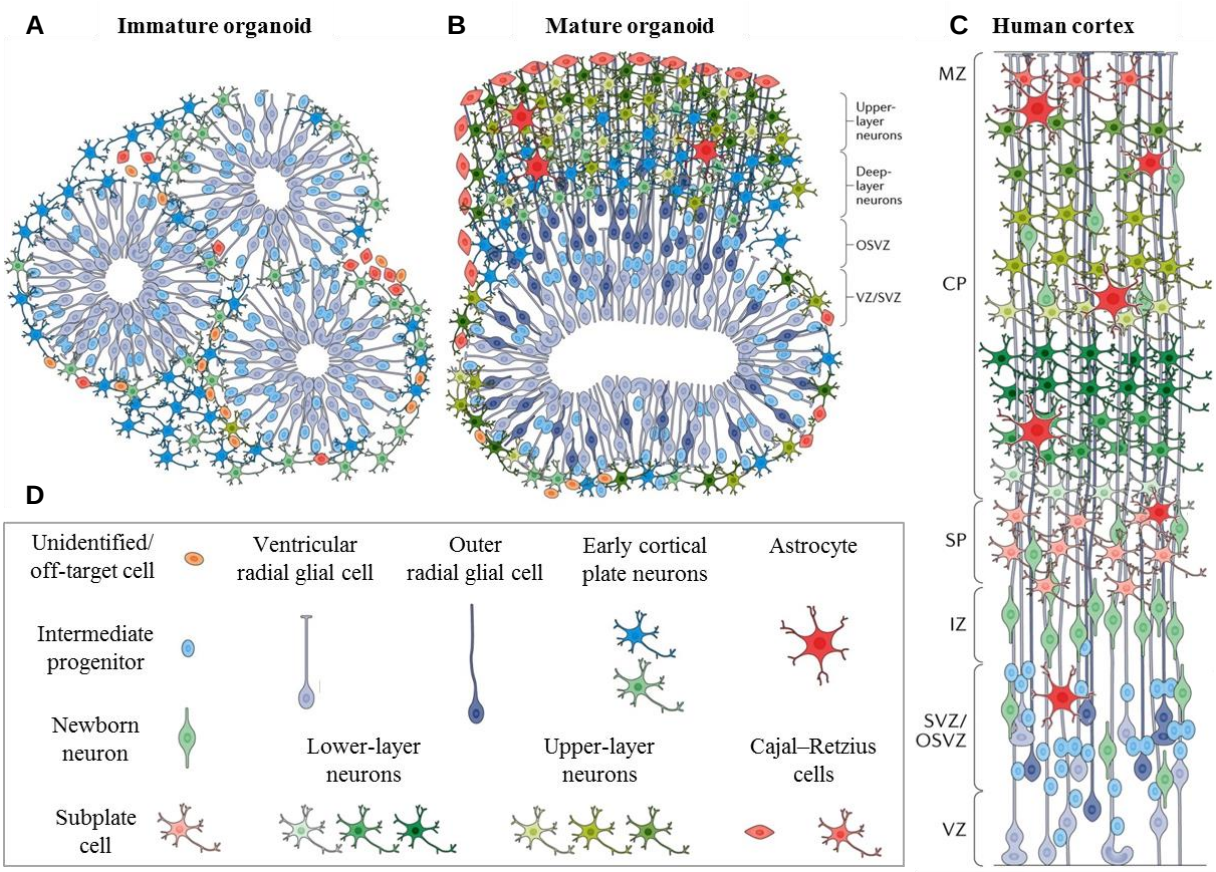

Figure 25: Forebrain organoids. Schematic representations of **A)** immature and **B)** mature forebrain organoid cellular architecture compared to **C)** the laminar organization of the human cortex. (VZ, ventricular zone; SVZ, subventricular zone; OSVZ, outer subventricular zone; IZ, intermediate zone; SP, subplate; CP, cortical plate; MZ, marginal zone). **D)** Cell type legend.
Adapted from Di Lullo et al. 2017 [352]

B.a;ii) Modeling microcephaly with brain organoids

Brain organoids, either unguided[327] or neocortex regional-specific[347], have been shown to pertinently recapitulate diseases and malformations with early embryonic origin, microcephaly being among the principal center of interest.

The pioneer work on establishment of the brain organoid system already addressed to **primary autosomal recessive microcephaly** modeling, employing patient-derived iPSCs that bear compound heterozygous mutations in the *CDK5RAP2* gene[327]. Analogously, iPSCs were afterwards obtained from a patient with compound heterozygous mutation in *ASPM*[353]. Brain organoids recapitulated patient microcephalic phenotype by invariably displaying reduced organoid size and smaller neural tissues[327,353]. Moreover, these neuronal aggregates were globally less condensed, with a large degree of scattered neuronal outgrowth[327,353]. This phenotype is mainly resulting from early exhaustion of the neural progenitor pool, which is notably reduced in mutant organoids[327,353]. This depletion relies on defective progenitor proliferation[353], leading to premature neuronal differentiation by neurogenic cell divisions[327] and a consequent reduction of mature neurons, which does not seem to be caused by neuron apoptosis[353]. Dysregulation of such cellular processes have repercussions on the organoid

architecture, in which the luminal structure organization is severely perturbed[353]. Electrophysiological analysis evidenced a reduction in the proportion of cells with calcium events and a desynchronization of their activity, confirming the presence of fewer mature neurons and denoting the dysfunctionality of the neuronal circuit in microcephalic patient-derived brain organoids[353].

Similar observations have been conducted in **Seckel syndrome** patient-derived brain organoids differentiated from iPSCs carrying a splice-site mutation in *CENPJ*[354]. Seckel syndrome manifest with severe growth retardation and microcephaly, mental impairment and dysmorphic features. The defects noticed included reduction in organoids size, neural epithelial tissues and progenitor pool, premature neuronal differentiation despite an apoptotic cell death-mediated progenitor loss and disorganization of the luminal architecture. Orientation of the apical radial glia mitotic spindle orientation has been investigated in Seckel organoids, revealing an increase in mitotic cleavage planes perpendicular to the ventricular surface. Premature switching from symmetric self-maintaining to asymmetric neurogenic cell division mechanistically supports neural progenitor depletion and anticipated neurogenesis.

iPSC lines were also derived from patients affected with the **Miller-Dieker syndrome**[355,356], presenting lissencephaly often associated with microcephaly. The disease is caused by deletion of chromosome 17p13.3 involving the *PAFAH1B1* and *YWHAE* genes. Patient iPSCs were differentiated towards forebrain-type organoids[347], which presented with significantly smaller size and structurally dysorganized[355,356]. Switch of the mitotic spindle orientation from vertical to horizontal was evidenced to reduce the neural progenitor pool in favor of fate-restricted intermediate progenitors increase[355,356]. It follows the counterintuitive overproduction of deep-layer neurons[356], a phenomenon that is restricted on the short-term, conveying to the reduction in the final number of neurons. While proliferation rate is unlikely to be altered[356], implication of apoptosis in Miller-Dieker syndrome pathogenesis is controversial, since it has been reported to be rare and invariant[355], or increased and suggested as a potential mechanism[356] by independent research groups. Defective radial migration[356], prolonged mitosis of the outer radial glia[356], alterations in microtubule network organization[355] and N-cadherin/β-Catenin-dependent disruption of cortical niche architecture have also been highlighted in mutant organoids[355]. Rescue of some of these phenotypes has been achieved by introducing a doxycycline-inducible *PAFAH1B1* or *YWHAE* into the human AAVS1 *locus* of patient iPSCs by CRISPR/Cas9-mediated genome editing[355], or trough replacement of a ring abnormal chromosome by duplication of the wild-type homologue chromosome 17[356] through compensatory uniparental isodisomy upon reprogramming[357].

B.b) Kidney organoids

Pioneers in the renal domain concerning organoids are three main laboratories lead by Dr. **R. Nishinakamura** in Kumamoto (Japan), Pr. **M. Little** in Melbourne (Australia) and Dr. **J.V. Bonventre** in Boston (USA). Within a narrow period of time, they succeeded in recreating *in vitro* appropriate conditions that lead human PSCs to undertake the renal destiny, and came out with the three protocols of reference in the field, namely the **Taguchi's 2014**[10], **Takasato's 2015**[329] and **Morizane's 2015**[330], respectively (Fig. 26).

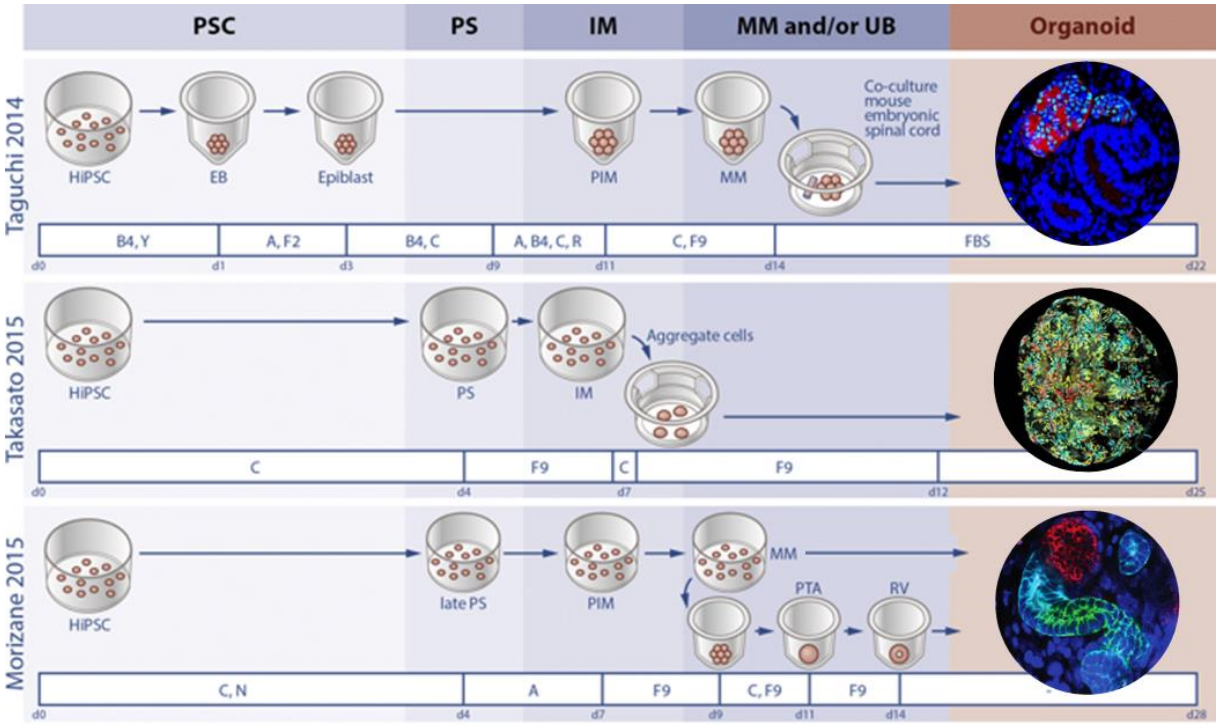

Figure 26: Kidney organoids. Main original procedures to generate kidney organoids developed by Dr. R. Nishinakamura (Taguchi 2014), Pr. M. Little (Takasato 2015) and Dr. J.V. Bonventre (Morizane 2015) research groups. (PSC, pluripotent stem cells; PS, primitive streak, IM, intermediate mesoderm, MM, metanephric mesenchyme, UB, ureteric bud).
Adapted from Koning et al. 2019 [358]*, Taguchi et al. 2014* [10]*, Takasato et al. 2015* [329] *and Morizane et al. 2015* [330]

In all these studies, as in the ones that followed in the last years, **PSCs** are induced towards the **mesoderm** and then lead to generate **nephron progenitor cells** (NPC). NPCs are multipotent progenitors that subsequently give rise to **nephron structures**. These PSC derivatives possess the same features of *in vivo* nephrons, showing ordered structural development of glomeruli, proximal tubules, Henle's loop and distal tubules[10,329,330]. Some protocols also contemplate ureteric bud (UB) generation, either simultaneously[329,359] or independently[360] from NPCs induction, to produce the collecting system.

Kidney organoids being the core of this dissertation, this part will be developed in details in the following "Kidney Organoids. Mini kidneys in a dish" dedicated chapter.

Chapter 5: **Kidney Organoids**
Mini kidneys in a dish

1. Mimicking embryonic kidney development *in vitro*

Since the initial findings of Dr. R. Nishinakamura**,** Pr. M. Little and Dr. J. Bonventre's laboratories in 2014-2015[10,329,330], adapted versions of these protocols and "new" procedures established by other groups came out in the following years (Fig. 27). The delay to obtain organoids from PSCs is of ~2.5 weeks on average, excluding the vascularization procedures that sensibly extend this duration.

A) Late primitive streak induction

The first crucial decision a pluripotent cell - either belonging to the epiblast of a blastocyst *in vivo* or epitomizing its characteristics as an iPSC *in vitro* - must undertake during development resides in its engagement in one of the three embryonic germ layer fates, namely endoderm, mesoderm or ectoderm. The key factor involved in the induction of **primitive streak**, marking the emergence of mesendodermal progenitors, has been identified in the Wnt3a, Nodal/Activin and BMP4 signaling pathways interplay[361,362]. Anterior definitive primitive streak fates are mainly prompted by high **Nodal/Activin** concentrations[363,364]. However, the kidney arises from cells that ingress later the groove during the extension of the primitive streak from posterior to anterior.

Canonical **Wnt** signaling activation was shown to induce and maintain nascent **mesoderm**[365]. Mesodermal specification of PSCs is thus most commonly achieved using the **Wnt agonist** CHIR99021 (CHIR), an inhibitor of the GSK3. If the current protocols are globally in agreement with the efficiency of CHIR in inducing the late primitive streak, the duration of the treatment may vary from 2 to 5 days[329] with CHIR concentration ranging from 3[330] up to 12 µM[282]. These changes are true not only among the different protocols, but also between each independent experiment within the context of a chosen procedure. Indeed, treatment requires adjustments to the intrinsic responsiveness of each cell line or clone.

Moreover, not only a sustained activation of the canonical Wnt/β-catenin signaling turned out to be sufficient to efficiently induce mesoderm, rather a moderate inhibition of **BMP4** may also be required[330]. Although in ostensible contradiction with the evidence for the involvement of this latter in the primitive streak rising[361], the need to downregulate the BMP4 pathway can be explained by the stimulation of its endogenous expression upon β-catenin stabilization[294,365,366]. Among the rare exceptions of CHIR use, combination of high dose BMP4 with low Activin A could replace canonical Wnt/β-catenin activation in inducing the primitive streak[359], further corroborating the reciprocal interplay between these signaling

pathways. However, Wnt/β-catenin *versus* high BMP4/low Activin A induced mesoderm is not exactly equivalent, the second option having lower nephrogenic potential[359].

B) Intermediate mesoderm induction

A judicious equilibrium of BMP4 signaling is needed in the establishment of the mesodermal regions, since it is also responsible of their patterning along the medio-lateral axis[367]. Increasing amounts of BMP4 are found to correlate with cell fate from the midline to the lateral plate mesoderm (LPM). Here, it acts as a lateralizing signal coming from the LPM and the overlying ectoderm. It specifies in that way the intermediate mesoderm (IM), which responds to lower concentrations of BMP4, from the LPM itself, promoted by high doses of BMP signaling. Activin and retinoic acid (RA) also are implicated in IM rising. Particularly **Activin A** was shown to favor expression of renal progenitor's markers[368], and combination of RA with FGF2 has been shown to induce IM markers[366]. A prolonged exposure to canonical Wnt/β-catenin signaling prompt to posteriorize the IM[329,361] and therefore selectively generate **nephron progenitor cells** (NPCs) of the permanent - or **metanephric - kidney**[10,330]. The time and intensity of Wnt3a-mediated stimulation determine the IM - and within it the metanephros - fate along the rostro-caudal axis, with shorter exposure favoring the ureteric bud (UB) production[360] and progressively moving to a mixture of epithelial nephron structures and collecting ducts with increasing doses[329].

C) Nephrogenesis

While *in vivo* the metanephric mesenchyme (MM) and UB induce and sustain one each other, their interaction requires to be artificially mimicked *in vitro* when one of these components is missing. FGF9 is most commonly exogenously provided to simulate the NPC niche conditions in the absence of UB-derived stimulation. The FGF9 signaling, which promotes maintaining and propagation of NPCs, should be balanced with the Wnt signaling, which induce NPCs and favors their nephron commitment and differentiation in turn. Similarly, induction in culture with dorsal spinal cord explant efficiently mimics the signal for MM condensation, epithelialization and subsequent tubulogenesis[18].

Once renal vesicles (RV) are formed, segmental nephron patterning along the proximo-distal axis occurs by spontaneous self-organization of NPCs, with involvement of Wnt/β-catenin, BMP - member of the TGF-β superfamily - and Notch signaling pathways[369]. Selective enrichment for proximal *versus* distal portions can be thus modulated though manipulation of these latter. Wnt stimulation correlates with medio-distal segment specification[285] in accordance with their spatial closeness to the UB in the developing kidney, while inhibition of the TGF-β/SMAD pathway supports domination of proximal RV domains[297]. Treatment of proximalized RVs with inhibitors of both TGF-β and Wnt in combination with retinoic acid synergistically push differentiation to the most proximal nephron cell type, the podocyte[297].



Figure 27: Kidney organoid differentiation protocol comparison.

2. Kidney organoid general features

Despite the variety of different approaches aimed to differentiate iPSCs into kidney organoids, most protocols adopt congruent multistep strategies (Fig. 27) that converge to the derivation of complex multicellular kidney-like tissue.

All the protocols are based on the induction of **intermediate mesodermal cells**, from which the kidney arises. Optimization of the subsequent steps shapes the IM fate, defining lineage commitment. Specific protocols generate the **ureteric bud** epithelium (Fig. 28) by inducing the early anterior mesoderm[360,370,371].

Particular attention will be provided in this dissertation to the **metanephric mesenchyme** lineage, generating "nephron organoids" - which include glomerular podocytes - that will be henceforward formally termed "kidney organoids" (Fig. 28). NPCs of the MM derive from the late posterior IM. *In vitro* as *in vivo*, NPCs have been demonstrated the capability to generate properly segmented nephrons[10,329,330]. Kidney organoids are composed by a variety of cell types, comprising podocytes, parietal cells, proximal tubular and Henle's loop/distal tubular cells. Moreover stromal, endothelial and mesenchymal cells have been evidenced (Fig. 28), as well as several types of off-target cell types unrelated to the kidney.

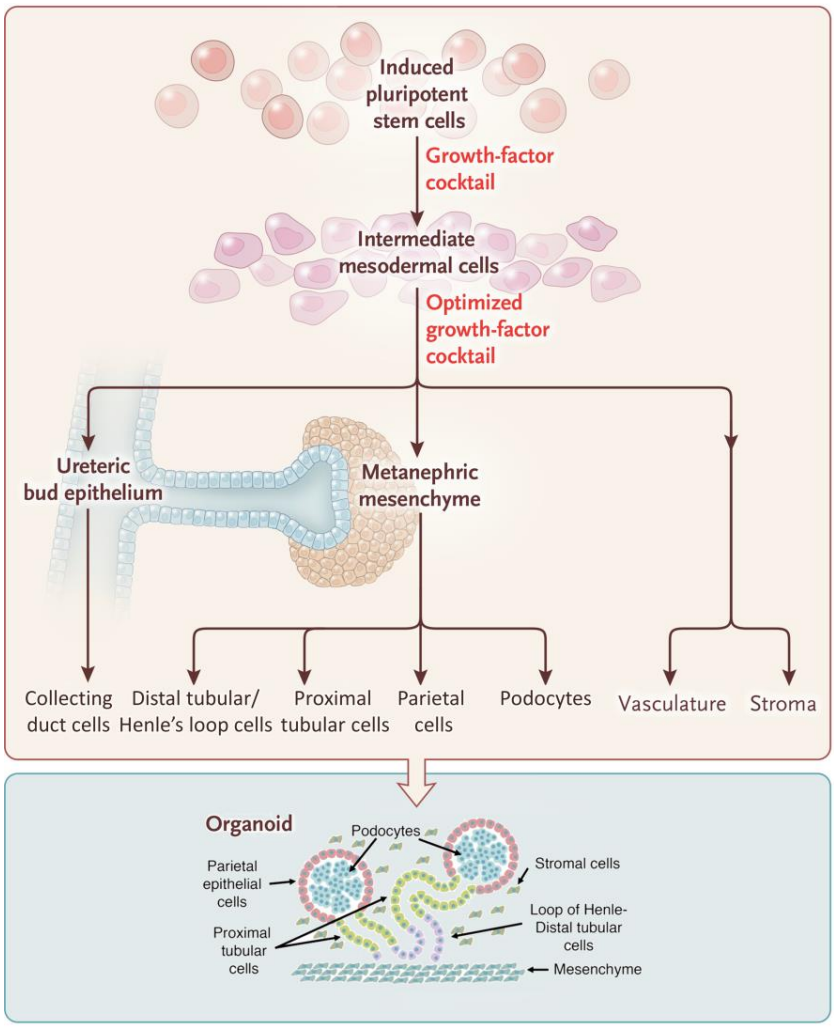

Figure 28: Kidney organoid general workflow.
Adapted from Quaggin et al. 2016 [372] *and Harder et al. 2019* [373]

Initial reports based on established renal markers suggested that kidney organoids are complex structures composed by at least 10 different cell types[374]. Actually, over 20 transcriptionally defined populations have been evidenced by single-cell RNA sequencing, belonging to 4 broad categories: podocytes, tubular epithelium, mesenchyme and off-target cells[375].

While kidney organoids recapitulate quite faithfully the cellular composition and structural architecture of the *in vivo* kidney, they display relative immaturity.

Bulk transcriptomic analysis clustered organoids with **1st trimester** human embryonic kidney[329]. Prolonged culture has not been shown to improve maturation, rather it causes extracellular matrix deposition, expansion of ectopic stromal tissue, occasional overgrowth of off-target cell populations and increased cell death[280]. Single-cell (sc) RNA-sequencing evidenced a strong correlation of the podocyte cluster with **week 16** fetal podocytes[375]. Further improvement of the techniques demonstrated iPSC-derived RVs to match with week 16 of gestation instead, while fully differentiated kidney organoids correlated with **week 22** embryonic kidney[376].

Over the transcriptomic investigation, the highly representative podocyte features revealed to be advantageous to determine the maturation degree of kidney organoids. Marker expression and rounded epithelial morphology, delineated by junctional apico-basal migration, were compatible with a **capillary loop stage**[377]. Cellular ultrastructure coherently displayed microvilli extending in the apico-lateral intercellular space and an apical prominent nucleus[377]. Glomerular isolation agreed with the proposed capillary loop stage for kidney organoids, showing high expression level of podocyte specific markers and switch of laminin and collagen IV chains with increasing culture time, suggestive of maturation[279].

De facto, kidney organoids would relate to an **early but broad nephrogenic stage** of development, contemplating a **spectrum of maturation** in which early and more mature cell types and structures coexist together[378]. Anyhow, the nephron epithelial cells of kidney organoids exhibit a significant degree similarity in gene expression compared to their respective adult human kidney counterparts[276].

Fine tuning the organoid microenvironment has been shown to enhance the generation of kidney organoids. When cultured on soft hydrogel that recapitulates tissue biophysical and mechanical properties, organoids displayed more mature features, such as an increase in late-stage nephron markers expression, podocytes with FPs bridged by SD-like structures and prominent brush border above proximal tubular cells[376].

However fundamental clues for complete maturation of renal structures are generally missing and/or tricky to reproduce *in vitro*. For instance, glomeruli normally harbor pulsating capillary tufts, and tubules are subjected the filtrate flow *in vivo*.

3. Kidney organoid vascularization

Although the presence of sparse endothelial cells[276,282,329] or of a disorganized vascular network dependent on VEGF secreted by podocytes[285] have been evidenced by different groups, one major limitation of the kidney organoids system resides in the absence of properly structured capillaries, with particular concern regarding avascular glomeruli. Fenestrated endothelium represents indeed a major component of the GFB. Its absence makes iPSC-derived podocytes to kind of "collapse" inside the glomerulus, extending protrusions that chaotically interconnect instead of displaying regular structures. In this context, the possibility to **observe FPs with mature SD** and their eventual effacement under pathological conditions perform is hampered. The system is also inaccessible to almost any kind of conceivable **functional tests**. Moreover the deprivation of reciprocal signaling between the endothelial and visceral epithelial layers, coupled with the absence of glomerular blood hydrostatic pressure - which is estimated at 55 mmHg and counterbalanced by capsular hydrostatic pressure (15 mmHg) and blood colloid osmotic pressure (30 mmHg) in kidney - may be responsible for incomplete **maturation of podocytes**.

Several approaches are available and have been adopted by the diverse research groups worldwide to overcome that problem[379].

A) Kidney organoid *in vitro* "vascularization"

Generation of a **glomerulus-on-a-chip** was first reported by cultivating iPSC-derived podocytes on a **bioengineered microfluidic device** that recapitulates the structural, functional, and mechanical properties of the GFB[293,296]. In this system, podocytes lay on a laminin-coated flexible membrane, at the interface with human primary endothelial cells. Moreover, fluid flow and cyclic mechanical strain - that improved podocyte maturation - can be applied to the cell layer to model the dynamic physiological conditions. The glomerulus-on-a-chip recapitulates functional features of the GFB, displaying differential in clearance between inulin and albumin. Treatment with clinically-relevant dose of adriamycin cause podocyte delamination, cell processes retraction and albumin leakage, which underline its relevance in glomerular toxicity modeling.

Incubation with **VEGF** during differentiation in kidney organoids was shown to augment the number of endothelial progenitor cells, but only a minor fraction of them reached a mature state[378]. With the aim of enhancing vascular network development, several conditions have been tested on kidney organoids grown a **gelatin-fibrin-coated chip**[380]. Addition of **low concentration of FBS** was favorable for both nephrogenesis and vessel formation, and application of high flow rate superfusion has been demonstrated to represent a critical environmental clue that favors vascular development *in vitro*[380].

B) Kidney organoid *in vivo* vascularization

The first attempt of *in vivo* vascularization has been performed by transplanting mouse ESC-derived EBs induced to nephrogenic mesenchyme along with spinal cord under the kidney capsule of immunodeficient mice. Successful formation of renal-like structures - particularly of glomeruli - with integrated vasculature[10] has encouraged further advancements in this direction.

Effective vascularization of human iPSC derivatives was achieved by transplanting **nephron progenitor** aggregates stimulated for 1 day with dorsal spinal cord under the **renal capsule** in PCs in immunodeficient mice in the presence of **VEGF**[278]. The same approach was applied to examine SD and FPs structural features in a patient with mutations in the *NPHS1* gene[381], with the only difference that NPCs were enriched as an ITG8α^+/PDGFRα^- fraction[10] by FACS.

Alternatively, **subcutaneous** transplantation of **NPCs** also gave rise - even though with a low efficiency - to organoids with vascularized glomeruli that display mature features[382]. Intravenously administrated fluorescence-labeled low molecular weight dextran was found in the tubular lumens, demonstrating filtration capacity of grafts.

Fully differentiated **kidney organoids** were also shown to be prone to vascularize under the renal capsule[280,285]. Glomeruli developed capillary tufts with specialized fenestrae. Podocytes with elaborate processes aligned on the GBM deposed above capillaries[280,285] and displayed apico-basal migration of junctions[280]. When injected with fluorescence-labeled dextrans, transplanted organoids displayed selective filtration and reabsorption of low in contrast to high molecular weight dextrans[285]. In addition, it was possible to follow-up the graft development by intravital imaging[280] through an implanted transabdominal imaging window[383], although this techniques is quite invasive, or by *in vivo* imaging system (IVIS) analysis[384] of firefly luciferase expressing organoids[285].

An original "old-school" approach similarly allowed to produce vascularized **kidney organoids** by transplanting them ***in ovo* on the chick embryo chorioallantoic membrane (**CAM) (Fig. 29)[376]. *In vivo* injection of fluorescent-labeled dextran permitted to observe vasculature within the implanted organoids by live imaging. Podocyte-like cells with primary and secondary processes bridged by a SD-like structure were observed (Fig. 29C and D).

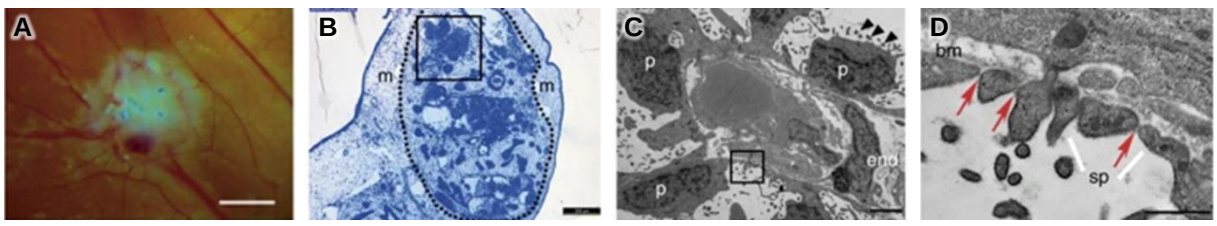

Figure 29: Kidney organoid vascularization on the CAM. **A)** Vascularized kidney organoid on the CAM. **B)** Semi-thin section of a kidney organoid (dashed line) vascularized on the CAM (m) stained with Toluidine blue. **C)** Podocytes (p) wrapping around a capillary under TEM. **D)** Podocyte FPs (sd, secondary processes) bridged by SDs (red arrows).
Adapted from Garreta et al. 2019 [376]

Transplanted kidney organoids coherently responded to nephrotoxic cisplatin treatment by upregulating KIM-1 and Caspase 3 in proximal tubules. (A brief focus on the chick embryo CAM will be developed in the following section, since vascularization attempts using this system have been performed in this study).

Interestingly, in almost all the studies performed *in vivo*, the **contribution of both human and host-derived vascular network** was evidenced[280,285,376,382], with the exception of one early experiment, in which endothelium was reported to be from exclusively mouse origin[278].

B.a) Chick embryo chorioallantoic membrane (CAM)

The CAM is a highly vascularized extraembryonic tissue derived from the fusion of the chorion with the allantois (Fig. 30A), which constitutes an interface to mediate gas and waste exchange during avian development.

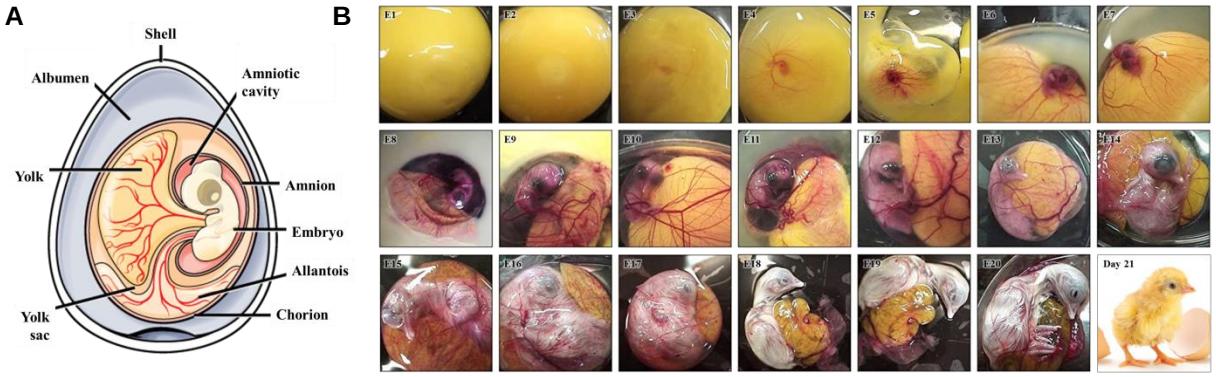

Figure 30: Chick embryo. **A)** Amniotic egg features. **B)** Chick embryo development.
Adapted from OpenStax.com [385] *and Dbios.org* [386]

Given its direct accessibility, rapid development and ease of manipulation with minimal invasive procedures, the chick embryo (*Gallus gallus domesticus*) CAM has been extensively used as a model to study angiogenesis and vascular growth, but also as an experimental platform for allo- and xeno-transplantation in developmental, cancer biology and tissue ingineering[387,388]. Chick embryonic development takes place in 21 days (Fig. 30B). Meanwhile, the CAM rapidly maturates between embryonic day 3 (E3) and 10, attaching to the shell by E4-5. So, *in ovo* transplantation procedures contemplate the opening of a "window" on the egg shell by E2-3, and subsequent intervention on a more mature CAM, around E7. The transplant is **accessible** for **real time monitoring and imaging**, allowing the **direct follow-up** of the experiments. A considerable advantage favoring transplantation rests on the slow establishment of immune system, which becomes physiologically active by E15. Thus, the CAM consists in a naturally **immunodeficient environment** that can accommodate grafts without incompatibility issues. In addition, manipulation of the embryos can be carried out until 2/3 of fetus development, in accordance with ethical recommendation for animal experimentation. Last but not least, the **time and cost-effectiveness** of the system, allows the scaling up of the procedures, permitting to increase both the number of samples - and conditions - for each experiment and their frequency.

4. Kidney organoids in disease modeling

A) Tubular diseases: polycystic kidney disease and nephronophthisis

The first efforts in kidney organoids-based renal disease modeling have focused in **autosomal dominant polycystic kidney disease** (ADPKD), which is the most common hereditary kidney disease[389], showing cysts formation in CRISPR/Cas9-generated *PKD1* and *PKD2* knock-out organoids[282]. The low initial incidence of cysts establishment could be enhanced by modification of the microenvironment. Indeed, suspension culture leaded to a substantial increase of the cystic phenotype of *PKD1*$^{-/-}$ and *PKD2*$^{-/-}$ kidney organoids[283]. However, dramatic variability hampered the authors to highlight evident PKD-related phenotypes in patient-derived iPSCs[283]. The same research group subsequently described an automated miniaturized system adapted for high-throughput screening to assess the therapeutic or toxic effect of treatments. Screening for candidate agents revealed a role for blebbistatin, a specific inhibitor of non-muscle myosin II, in increasing *PKD1*$^{-/-}$ organoids cystogenesis[378]. More recently, **autosomal recessive polycystic kidney disease** (ARPKD) patient-derived iPSCs bearing compound heterozygous mutations in the *PKHD1* gene were reported to undergo drastic cystogenesis when challenged in increased cAMP level conditions[285]. The cystic phenotype was rescued by CRISPR/Cas9-mediated correction of one allele. Cystogenesis was also decreased in a dose-dependent manner by treatment with specific chemical compounds, providing a proof of concept for the relevance of the organoid system for drug screening and personalized medicine.

The matter was then addressed to **nephronophthisis** (NPHP), a cystic kidney ciliopathy[390]. Patient-derived kidney organoids mutated for *IFT140* displayed in this context shortened club-shaped primary cilia in tubular cells[284]. Upon CRISPR/Cas9-mediated correction of one of the pathogenic mutations, this ciliary phenotype was restored[284].

B) Glomerular diseases: nephrotic syndrome

Concerning **nephrotic syndrome**, a defective translocation to the cell surface of mutant nephrin was highlighted in patient-derived organoids carrying homozygous mutation in the *NPHS1* gene, leading to impaired SD formation[381]. In glomeruli of kidney organoids obtained from another patient with combined heterozygous *NPHS1* mutations, hypertrophic podocyte were observed, and both nephrin and podocin protein levels were found to be markedly reduced[279].

Knock-out *PODXL*$^{-/-}$ kidney organoids exhibited defective assembly of microvilli at the apico-lateral surface of podocytes, revealing the crucial role of podocalyxin in podocyte development. The inadequacy of repulsive force between adjacent podocytes - normally sustained by the negative charged podocalyxin - reduced the lateral space and contributed to an increased intercellular junction organization.

RESULTS

Part 1: Setting-up of the necessary tools

In this part of my PhD thesis dissertation, I will report the most technical aspects of the work I performed. Laborious and time-consuming efforts were required in order to dispose of suitable tools for generating meaningful "renal disease in a dish" models.

These include:

- **Induced pluripotent stem cells**

Here I present the generation of the iPSC lines that have been used for this study. You can also find **Article 1**, about the "Generation of an induced pluripotent stem cell (iPSC) line (IMAGINi007) from a patient with steroid-resistant nephrotic syndrome carrying the homozygous p.R138Q mutation in the podocin-encoding *NPHS2* gene".

Next, I expose technical adaptations of culture conditions, which were fundamental to guarantee the quality of iPSCs for following applications.

- **Kidney organoids**

Here I present the establishment of the differentiation protocol to generate kidney organoids from iPSCs. I expose the characteristics of kidney organoids, with particular interest for glomerular podocytes.

Then, I detail the procedure of podocyte isolation from kidney organoids and I report the analysis of their transcriptomic profiling.

Finally, I show the attempt of vascularization I performed by transplanting kidney organoids on the chick embryo chorioallantoic membrane.

Induced Pluripotent Stem Cells

1. iPSC line reprogramming

When I joined Pr. C. Antignac's team in October 2016, the reprogramming of the first patient-derived iPSC lines was ongoing on the iPSC Platform at the *Imagine Institute*. PBMCs were obtained from:

- a patient affected with early-onset SRNS, harboring the homozygous p.R138Q substitution in the podocin-encoding *NPHS2* gene,
- two GAMOS patients, the first one bearing a homozygous stop mutation in the *GON7* gene, and the second one being a compound heterozygote for a frameshift and a missense mutation in *OSGEP*.

Reprogramming gave rise to the IMAGINE iPSC lines 007, 006 and 008 respectively (Table 2). I was trained to the iPSC culture by Dr. N. Lefort, head of the iPSC Platform, concomitantly to the reprogramming process, which allowed me to follow the picking of clones and quality controls steps.

In the following months, one other iPSC line was generated from a GAMOS patient. The 023 line was derived from a second patient with the same homozygous stop mutation in the *GON7* gene as the 006 line (Table 2). To be clearer, I will refer to patient-derived iPSCs or derivatives as **SRNS**^{NPHS2}, **GAMOS**^{GON7}and **GAMOS**^{OSGEP}.

I disposed of 1 to 2 validated clones for each reprogrammed cell line (Table 2), including common **control iPSC lines** shared between the *Imagine Institute* teams (IMAGINE iPSC lines 004, 005 and 013), as well as a healthy control, coming from the father (line 009) of the *OSGEP* mutated patient (line 008).

Table 2: iPSC lines generated at the iPSC Platform of the *Imagine Institute*

Type	Disease	Line	Clones	Mutated gene	Mutation (status)	Gender
Controls	/	004	17	/	/	Male
		005	4	/	/	Female
		009	2 and 9	(*OSGEP*)	(c.974G>A p.Arg325Gln (het))	Male
		013	19	/	/	Male
Patients	SRNS	007	27 and 34	*NPHS2*	c.413 G>A p.Arg138Gln (hom)	Female
	GAMOS	006	4 and 33	*GON7*	c.21 C>A p.Tyr7* (hom)	Female
		023	11		c.21 C>A p.Tyr7* (hom)	Male
		008	4 and 26	*OSGEP*	c.839G>A p.Arg280His (het) c.974G>A p.Arg325Gln (het)	Male

Table reporting the iPSC lines used in this study. iPSCs have been generated from healthy controls and patients affected with SRNS or GAMOS, each giving rise to a single iPSC line comprising independent clones. Corresponding genetic information relative to the mutated gene, the mutation(s) and status are reported (hom, homozygous; het, heterozygous), as well as the gender of the source individual. The 009 iPSC line is considered as a control even if carrying a heterozygous mutation in the *OSGEP* gene since it comes from a healthy individual and the disease has a recessive inheritance.

2. Introduction to Article 1

Generation of the IMAGINi007 iPSC line is the object of a publication as "Lab Resource: Single Cell Line article" in *Stem Cell Research*, which I signed in first author (**Article 1**)[391]. The article presents the derivation of our SRNS^{NPHS2} iPSC line, but it is straightly transposable to all the other GAMOS^{GON7}, GAMOS^{OSGEP} and control lines, since the same reprogramming procedure, characterization and quality controls have been applied. The SRNS^{NPHS2} 007 iPSC line represented a valuable resource to get insights into the pathological cellular and molecular mechanisms implicated in SRNS, but also a promise as novel tool for drug screening and developing new therapeutic strategies for SRNS.

The work I performed in SRNS modeling employing this line is presented in an article that is currently under preparation (**Article 2**) (Please refer to Results, Part 2). The state of advancement of the SRNS^{NPHS2} project incited us to publish the generation of the related IMAGINE 007 iPSC line, here presented. Generation of GAMOS^{GON7} and GAMOS^{OSGEP} iPSC line may be equivalently the object of future publications.

The cell source for reprogramming consisted of PBMCs obtained from a 22-year-old transplanted woman affected with **early-onset SRNS**. Patient cells harbor the homozygous **c.413G>A** missense mutation in the *NPHS2* gene, which leads to the **p.Arg138Gln** (p.R138Q) amino acid substitution in podocin.

PBMCs were reprogrammed to pluripotency by non-integrative Sendai viral transduction of OSKM Yamanaka's factors. The resulting iPSC line thus generated display **normal karyotype**, express **pluripotency hallmarks**, and are capable of **multi-lineage differentiation**.

Article 1

Generation of an induced pluripotent stem cell (iPSC) line (IMAGINi007) from a patient with steroid-resistant nephrotic syndrome carrying the homozygous p.R138Q mutation in the podocin-encoding *NPHS2* gene

Giulia Menara, Nathalie Lefort, Corinne Antignac & Géraldine Mollet

Stem Cell Research *46, (2020) 101878*

Lab resource: Stem Cell Line

Stem Cell Research 46 (2020) 101878

Contents lists available at ScienceDirect

Stem Cell Research

journal homepage: www.elsevier.com/locate/scr

Lab resource: Stem Cell Line

Generation of an induced pluripotent stem cell (iPSC) line (IMAGINi007) from a patient with steroid-resistant nephrotic syndrome carrying the homozygous p.R138Q mutation in the podocin-encoding *NPHS2* gene

Giulia Menara[a], Nathalie Lefort[b,*], Corinne Antignac[a,c], Géraldine Mollet[a,*]

[a] Université de Paris, Imagine Institute, Laboratory of Hereditary Kidney Diseases, INSERM UMR 1163, Paris, France
[b] iPS Core Facility, Université de Paris, Imagine Institute, INSERM UMR U1163, Paris, France
[c] Département de Génétique, AP-HP, Hôpital Necker-Enfants Malades, Paris, France

A B S T R A C T

Mutations in the *NPHS2* gene, encoding podocin, are responsible for the majority of familial cases of steroid-resistant nephrotic syndrome (SRNS), a rare glomerulopathy that rapidly progresses to end-stage renal disease. We obtained peripheral blood mononuclear cells (PBMCs) from a patient carrying the homozygous c.413G > A substitution (p.R138Q) in *NPHS2* gene, which is the most prevalent mutation in the European population. The PBMCs were reprogrammed by non-integrative viral transduction of the Yamanaka's factors. The resulting iPSCs display normal karyotype, express pluripotency hallmarks and are capable of multi-lineage differentiation, offering a useful tool to study pathological mechanisms of SRNS and perform drug testing.

1. Resource table

Unique stem cell line identifier	IMAGINi007
Alternative name(s) of stem cell line	IMAGINE007#27, IMAGINE007#32, IMAGINE007#34
Institution	Imagine Institute, Inserm U1163
Contact information of distributor	geraldine.mollet@inserm.fr
Type of cell line	iPSC
Origin	Human
Additional origin info	Age: 22
Sex	Female
Ethnicity if known	Caucasian
Cell Source	Peripheral blood mononuclear cells (PBMCs)
Clonality	Clonal
Method of reprogramming	Non-integrative SeV-mediated delivery of OCT4, SOX2, c-MYC and KLF4
Genetic Modification	Yes
Type of Modification	Spontaneous mutation
Associated disease	Steroid-resistant Nephrotic Syndrome
Gene/locus	*NPHS2* (NM_014625)/1q25-1q31 Homozygous c.413G > A, p.R138Q mutation
Method of modification	Not applicable
Name of transgene or resistance	Not applicable
Inducible/constitutive system	Not applicable
Date archived/stock date	January 2017
Cell line repository/bank	Not applicable
Ethical approval	hiPSC culture and storage protocols were performed with approval from French Research Ministry (DC 2015–2595, 09/05/2016)

2. Resource utility

NPHS2-mutated iPSCs can be differentiated into podocytes (Ciampi, 2016) and/or kidney organoids (Takasato, 2015; Morizane, 2015) in order to characterize and compare their phenotype to healthy controls. They will be useful to investigate the cellular and molecular pathological mechanisms leading to *NPHS2*-linked SRNS, as well as to screen drugs and develop new therapeutic strategies.

2.1. Resource details

Steroid-resistant nephrotic syndrome is a rare autosomal recessive disorder characterized by a massive leakage of protein in the urine due to structural alterations of the glomerular filtration barrier. Massive proteinuria arising at a mean age of 6 years is clinically associated with hypoalbuminemia, hyperlipidemia and edema. The disease rapidly progresses to end-stage renal disease, usually before the age of 10, requiring renal replacement therapies such as dialysis and/or transplantation.

The most frequent causative mutation in the *NPHS2* gene (NM_014625) is the c.413G > A missense substitution, which leads to an Arg to Gln amino-acid replacement at position 138 of the podocin protein (p.R138Q, hereafter referred to as R138Q) (Boute, 2000). This mutation leads to the endoplasmic reticulum (ER) retention of the R138Q podocin and its massive degradation by the proteasome

* Corresponding authors.
E-mail addresses: nathalie.lefort@institutimagine.org (N. Lefort), geraldine.mollet@inserm.fr (G. Mollet).

https://doi.org/10.1016/j.scr.2020.101878
Received 4 May 2020; Received in revised form 4 June 2020; Accepted 9 June 2020
Available online 18 June 2020
1873-5061/ © 2020 The Author(s). Published by Elsevier B.V. This is an open access article under the CC BY-NC-ND license (http://creativecommons.org/licenses/BY-NC-ND/4.0/).

Table 1
Characterization and validation.

Classification	Test	Result	Data
Morphology	Phase contrast bright field microscopy	Normal morphology	Fig. 1 panel D
Phenotype	Qualitative analysis by Immunocytochemistry	Expression of the pluripotency markers: OCT4 and SOX2	Fig. 1 panel E
	Quantitative analysis by Flow cytometry	TRA-1-81: 93% SSEA-4: 99%	Fig. 1 panel F
Genotype	SNP array (> 240000 markers)	Normal karyotype Arr(1–22,X)x2	Fig. 1 panel A
Identity	SNP array (> 240000 markers)	SNP array to compare iPSCs and the starting PBMC. Matching iPSC genotype with that of the parental PBMCs confirms the origin of iPSCs	Fig. 1 panel B
Mutation analysis (IF APPLICABLE)	Sequencing	Confirmation of patient homozygous c.413G > A p.R138Q mutation presence by Sanger sequencing	Fig. 1 panel C
	Southern Blot OR WGS	N/A	N/A
Microbiology and virology	Mycoplasma	Mycoplasma testing by luminescence. Negative	N/A
Differentiation potential	Direct differentiation into three germ layers	TaqMan® hPSC Scorecard™ analysis; negative score for self-renewal gene expression and positive score for trilineage gene expression. Positive immunostaining for β-III-tubulin, α -smooth muscle actin and α-fetoprotein	Fig. 1 panel G and H
Donor screening (OPTIONAL)	HIV 1 + 2 Hepatitis B, Hepatitis C	Negative	e.g. not shown but available from author
Genotype additional info (OPTIONAL)	Blood group genotyping	N/A	N/A
	HLA tissue typing	N/A	N/A

(Serrano-Perez, 2018). However, mechanisms involved in this ER retention still remain unclear.

In this study, we generated an iPSC line from a 22-year-old female patient carrying the *NPHS2* c.413G > A (R138Q) mutation in the homozygous state (Table 1).

Cryopreserved peripheral blood mononuclear cells (PBMCs) were reprogrammed into iPSCs using non-integrating Sendai virus vectors releasing the Yamanaka's factors. Colonies with a typical morphology of pluripotent stem cells appeared and were individually and manually selected to establish feeder-free iPSC culture.

To determine the quality of generated iPSCs, several genotypic and functional assays were performed. The characterization included analysis of genomic integrity given by comparative SNP analysis of parental PBMC and the iPSC cell line (Fig. 1A). Genome SNP array analysis of iPSCs and parental PBMCs confirmed the absence of aneuploidies, deletions or insertions. SNP arrays have a high resolution allowing the detection of sub-chromosomal defects. They can also detect copy-neutral loss of heterozygosity events. However this technique is not able to detect balanced rearrangements or low level mosaicism (15%). Matching the iPSCs genotype with that of parental PBMCs confirms the origin of iPSCs (Fig. 1B). The resequencing of the mutation-site confirms the presence of the podocin R138Q mutation (Fig. 1C).

The generated cell line displayed morphological features consistent with an iPSCs identity. Round colonies with sharp-edged defined borders were composed of small compacted cells with a high nucleus/cytoplasm ratio and large nucleoli visible at phase contrast microscopy (Fig. 1D).

Furthermore, the expression of pluripotent stem cell markers was assessed by immunofluorescence staining for OCT4 and SOX2 (Fig. 1E) and by cytofluorimetric assay of TRA-1–81 and SSEA-4 (Fig. 1F). Absence of mycoplasma contamination was verified every month using a MycoAlert™.

The ability to differentiate spontaneously into cells of the three germ layers was confirmed by embryoid body (EB) formation and subsequent molecular analyses at both transcriptional and protein levels. Trilineage differentiation potential was assessed using the TaqMan® hPSC ScorecardTM kit and immunofluorescence stainings. iPSCs expressed mRNA levels comparable to the reference standard and did not show any lineage bias (Fig. 1G). Upon EB derivation, expression of ectodermal (β-III-tubulin), mesodermal (α-smooth muscle actin, α-SMA) and endodermal proteins (α-fetoprotein, α-FP) has been observed (Fig. 1H).

3. Materials and methods

3.1. Ethics statements

The generation, use and storage of human iPSCs were performed with approval from French Research Ministry (DC 2015–2595, 09/05/2016). Formal informed consent was obtained from the patient.

3.2. Generation of iPSCs

Before reprogramming, PBMCs were cultured for 4 days in StemPro™-34 SLM medium (ThermoFisher Scientific) with FBS FLT-3 (100 ng/ml), IL-3, and IL-6 (20 ng/ml) (PeproTech) cytokines. Then, 2.5×10^5 PBMCs were transduced using the CytoTune-iPS 2.0 Sendai Reprogramming Kit (ThermoFisher Scientific) following manufacturer's instructions. After 3 days, transduced cells were plated on vitronectin-coated culture dishes (StemCell technologies) in StemPro™-34 SFM medium without cytokines. At day 7, the medium was changed by replacing half of the StemPro™-34 medium with ReproTeSR™ medium (StemCell technologies). The following day, the entire medium was replaced with ReproTeSR medium and changed daily until iPSC colonies appeared. After 2–3 weeks, colonies appeared and were manually picked and expanded at least 10 passages for further characterization. iPSC clones were cultured on vitronectin-coated culture dishes with daily renewal of mTeSR™1 medium (StemCell technologies) and manually passaged every 5–7 days. Cells were cultured at 37 °C in a humidified atmosphere containing 5% CO2.

3.3. In vitro trilineage differentiation by embryoid body (EB) formation

25 to 30 iPSCs colonies were manually cut into small clumps, collected and transferred into low attachment dishes. EBs were cultured in suspension for 7 to 9 days with DMEM/F-12 medium containing 20% pluriQ Serum Replacement (GlobalStem), 1% Non-essential amino acids, 1% Penicillin-streptomycin and 0.2% beta-mercaptoethanol (ThermoFisher Scientific). EBs were then collected for RNA analyses or transferred onto gelatin-coating dishes for 1 week and stained using antibodies specific for early differentiation for each germ layer (Table 2). EBs were cultured at 37 °C in a humidified atmosphere containing 5% CO2 with the culture medium refreshed every other day.

A

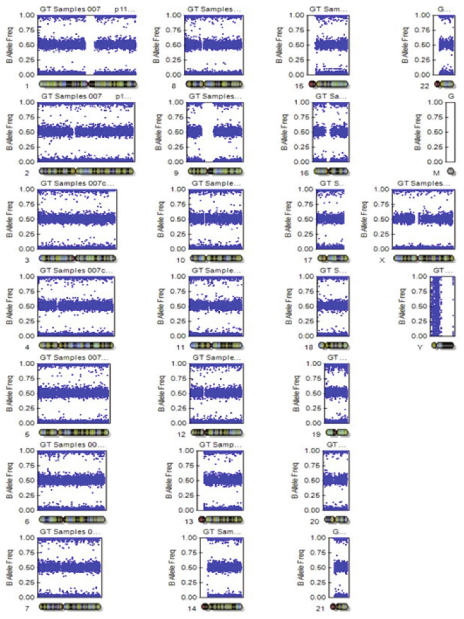

B

Name	Chromosome	Position	PBMC007	IMAGINi007
rs1083877	1	233742345	AB	AB
rs10193825	2	233510622	BB	BB
rs1006514	7	28961321	BB	BB
rs10102855	8	114676890	AA	AA
rs10839595	11	6720186	AB	AB
rs10840745	12	17710521	BB	BB
rs11087000	20	44809374	AA	AA
rs11089816	22	37370022	AA	AA
Sexe			XX	XX

C

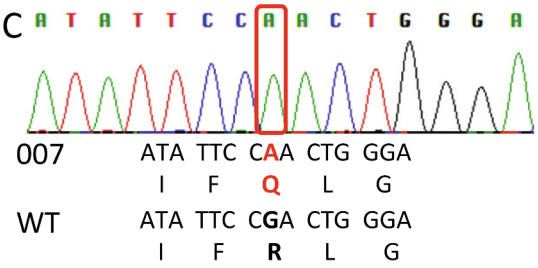

D

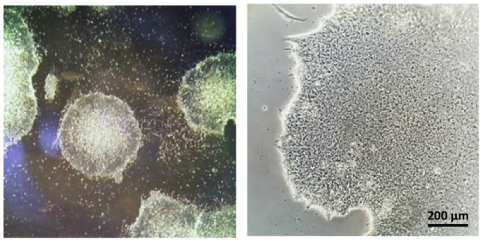

E

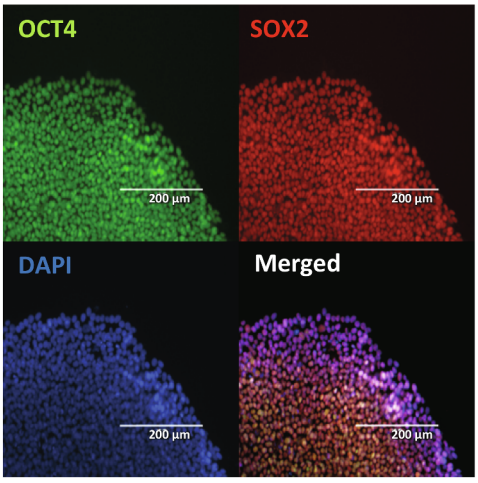

F

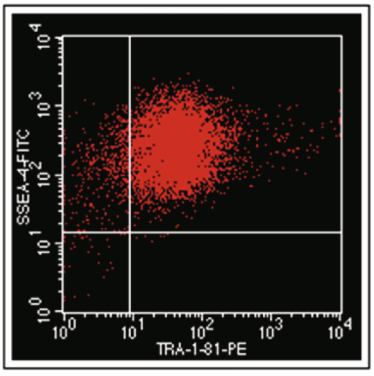

G

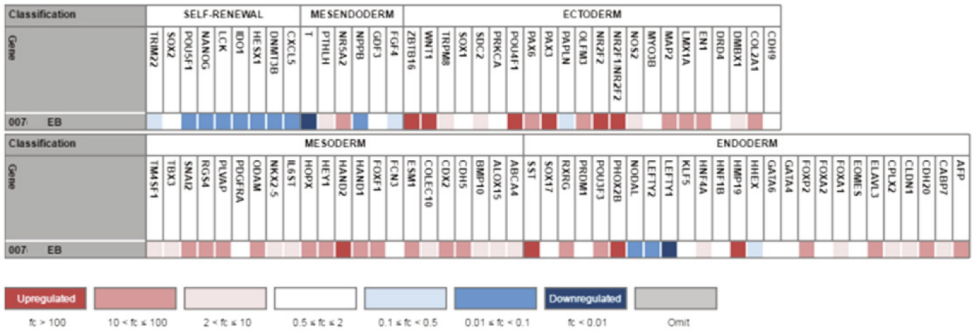

H

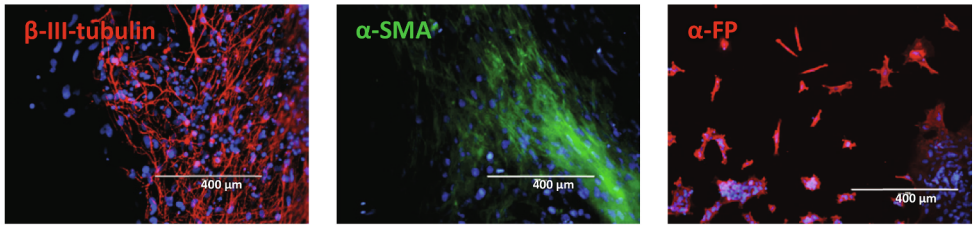

(caption on next page)

Fig. 1. A) IMAGINE007#27 P11 genomic SNP array analysis showing a normal female karyotype. Arr(1–22,X)x2. The same result has been observed for IMAGINE007#32 P11, IMAGINE007#33 P7 and IMAGINE007#34 P6. **B)** Identity match of iPSC genotype with that of the parental PBMCs confirming the origin of iPSCs. **C)** Sanger sequencing confirming the presence of patient homozygous c.413G > A p.R138Q mutation. **D)** Bright-field (left panel) and phase contrast (right panel, scale bar 200 μm) microscopy showing normal iPSC morphology. **E)** Immunofluorescent staining for the pluripotency markers OCT4 and SOX2. Scale bar 200 μm. **F)** Cytofluorimetric assay for the pluripotency markers TRA-1-81 and SSEA-4. **G)** TaqMan® hPSC Scorecard™ analysis showing negative score for self-renewal gene expression and positive score for trilineage gene expression. **H)** Immunofluorescent staining for the ectodermal β-III-tubulin (left panel), mesodermal α-smooth muscle actin (middle panel) and endodermal α-fetoprotein (right panel) markers. Scale bar 400 μm.

Table 2
Reagents details.

Antibodies used for immunocytochemistry			
	Antibody	Dilution	Company Cat # and RRID
Pluripotency Markers	Monoclonal Anti-OCT3/4 (Mouse)	1:100	Clinisciences sc-5279
	Monoclonal Anti-Sox2 (Rabbit)	1:1000	Sigmaaldrich AB5603
	SSEA-4-FITC (clone REA 101)	1:50	Miltenyi biotec 130–098-371
	TRA-1–81-PE (clone REA 246)	1:50	Miltenyi biotec 130–101-410
	REA Control (S)-PE	1:11	Miltenyi biotec 130–104-612
	REA Control (S)-FITC	1:11	Miltenyi biotec 130–104-610
Differentiation markers	Monoclonal anti-Tubulin β 3 (Mouse)	1:1000	Biolegend 801,202
	Monoclonal Anti-Actin, α-Smooth Muscle – FITC (Mouse)	1:300	Sigmaaldrich F3777
	Monoclonal Anti-alpha-Fetoprotein (Mouse)	1:60	R&D system MAB1369
Secondary antibodies	goat anti-rabbit alexa fluor plus 488	1:1000	ThermoFisher Scientific A32723
	goat anti-mouse alexa fluor plus 555	1:1000	ThermoFisher Scientific A32732
Primers			
	Target	Forward/Reverse primers	
Targeted mutation analysis	*NPHS2*	Forward 5′-TCAAAATTCTGTCTATGGGT-3′ Reverse 5′-CATTTAATCTGAGGTCCATA- 3′	

3.4. RNA extraction and RT-PCR analyses

Total RNA was extracted using RNeasy Mini Kit (Qiagen). cDNA was synthesized using high capacity cDNA RT kit (ThermoFisher Scientific) from 1 μg of total RNA. The TaqMan® hPSC Scorecard™ assay was carried out according to the manufacturer's protocol to evaluate the trilineage differentiation potential of the cells. This scorecard compares the gene expression pattern of key pluripotency and germ lineage markers relative to a reference standard that consists of 9 different human ES and iPS cell lines. Data analysis was performed using the cloud based TaqMan® hPSC ScorecardTM analysis software.

3.5. Immunofluorescence staining

Cells were fixed with 4% paraformaldehyde for 15 min at room temperature (RT). After being washed in PBS/1% BSA blocking solution for 1 h, iPSCs were incubated overnight at 4 °C with a primary antibody, washed 3 times in PBS and incubated with a secondary antibody for 2 h at RT (Table 2). Antibodies were diluted in PBS/1% BSA/0.1% triton solution. Immunofluorescence staining was analyzed using the Celena S™ Digital Imaging System (Logos Biosystems).

3.6. Flow cytometry

iPSCs were dissociated with TrypLE Express (ThermoFisher Scientific). Then, cells were suspended in PBS/2% BSA to a cell density of 2×10^5 cells per 100 μl and incubated with the specific antibodies (TRA-1–81-PE, and SSEA4-FITC, Table 2) for 30 min at RT. Cells were washed with PBS/2% BSA and analyzed using a FACSCalibur (Becton Dickinson) and CellQuest software. Unstained iPSCs and the corresponding isotype antibodies were used as negative controls to exclude data from non-specific fluorescence.

3.7. DNA isolation

DNA isolation was performed using the PureLink™ Genomic DNA Mini Kit (Invitrogen).

3.8. Mutation analysis/Sanger sequencing

DNA was analyzed through PCR (Table 2) and Sanger sequencing in order to confirm the presence of the p.R138Q (c.413 G > A) mutation in the *NPHS2* gene. Fragments were sequenced using the automated 3500xl DNA Analyzer (Applied-Biosystems).

3.9. Karyotype analysis

Molecular karyotype was performed using an Infinium Core-24 v1.2 Kit (Illumina) containing 300,000 SNPs. Data were analyzed with BeadStudio/GenomeStudio software (Illumina).

4. Mycoplasma detection

Mycoplasma contamination was checked every month using a MycoAlert™ PLUS Mycoplasma Detection Kit (Lonza) according to manufacturer's instructions. This kit enables the detection of the vast majority of the 180 different mycoplama species. The monthly mycoplasma detection tests were always found negative with a ratio lower than 1.2.

Declaration of Competing Interest

None.

Acknowledgements

This study was supported by State funding from the Agence Nationale de la Recherche under “Investissements d’avenir” program (ANR-10-IAHU-01). We acknowledge the use of the bioresources of the Necker Imagine DNA biobank (BB-033-00065). We are very grateful to the patient carrying the NPHS2 mutation.

References

Ciampi, O., et al., 2016. Generation of functional podocytes from human induced pluripotent stem cells. Stem Cell Res. https://doi.org/10.1016/j.scr.2016.06.001.

Takasato, M., et al., 2015. Kidney organoids from human iPS cells contain multiple lineages and model human nephrogenesis. Nature. https://doi.org/10.1038/nature15695.

Morizane, R., et al., 2015. Nephron organoids derived from human pluripotent stem cells model kidney development and injury. Nat. Biotechnol. https://doi.org/10.1038/nbt.3392.

Boute, N., et al., 2000. NPHS2, encoding the glomerular protein podocin, is mutated in autosomal recessive steroid-resistant nephrotic syndrome. Nat. Genet. https://doi.org/10.1038/74166.

Serrano-Perez, M.C., et al., 2018. Endoplasmic reticulum-retained podocin mutants are massively degraded by the proteasome. J. Biol. Chem. https://doi.org/10.1074/jbc.RA117.001159.

3. iPSC culture conditions

We decided to adopt the Morizane's protocol[330] for kidney organoids differentiation, starting from the closest conditions compared to what reported, namely culturing iPSCs in ReproFF2 medium on Geltrex matrix[392]. Therefore, this implied the adaptation of the iPSC culture since, at the *Imagine* iPSC Platform, iPSCs where cultured in mTeSR1 medium and mostly on feeder-free vitronectin support, even though some laminin and MEF feeder cells have been tested.

A) Culture matrix

A.a) Geltrex

Control 004#04 and 004#17 iPSC lines were at first transposed from vitronectin to Geltrex matrix. This support switch was performed as a habitual passage by manually clumps collection of iPSC colonies grown on vitronectin and transfer to a Geltrex-coated support in mTeSR1 medium in which cells were adapted. Emerging iPSC colonies displayed typical iPSC morphological features. Colonies were composed of small compacted cells with a high nucleus/cytoplasm ratio and large nucleoli visible at phase contrast microscopy. Compared to vitronectin, colonies grown on Geltrex matrix were flatter and spread to a more irregular shape, anyhow still maintaining sharp-edged defined borders. This change can be explained by the wide variety of ECM adhesion molecules derived from murine Engelbreth-Holm-Swarm (EHS) sarcoma, mainly including laminin, collagen IV, nidogen and heparin sulfate proteoglycan, which is manifestly richer compared to a single purified protein. In addition to influence colony shape, increased adhesion also had an impact on cell manipulation: clumps detachment for iPSCs passaging was harder to perform, with consequent smaller pieces formation which impacts iPSC culture kinetics and maintenance. The first kidney organoids I obtained were differentiated on Geltrex matrix.

A.b) Vitronectin

Even though I validated Geltrex as a matrix that allow iPSCs to expand while maintaining pluripotency and being then capable to give rise to kidney organoids, I afterwards decided to try differentiation starting from iPSCs cultured on vitronectin. In fact, vitronectin is a ECM adhesion glycoprotein that can be easily purified as a recombinant human protein to sustain chemically defined and xeno-free maintenance of iPSCs through integrin αVβ5-mediated adhesion[393], increasing the reproducibility of downstream applications. Moreover, vitronectin has been found to be more convenient to handle. Coating can be performed at room temperature, bypassing the risk of matrix gelling. Vitronectin is advantageous also for manual iPSC maintenance and mechanical passaging. Kidney organoid differentiation tests had positive outcome, allowing organoids generation on vitronectin, which permitted to switch to a vitronectin-based iPSC culture and differentiation support.

Next, I wondered about the step of preparation of iPSCs for differentiation. The Morizane's protocol contemplates accutase-mediated cell dissociation and seeding that allow getting 50% cell confluence after 3 days of culture to start induction[392]. I initially applied this procedure without any variation. However, iPSCs are routinely maintained by enzymatic passaging in Dr. J.V. Bonventre's laboratory, while I used to pass iPSCs manually. I reasoned that accutase dissociation could evoke a greater stress in cells that are not adapted to enzymatic passaging, that could negatively impact following kidney organoid differentiation efficiency. So, I tested the inductive protocol starting from iPSC colonies that were obtained by manually clumps passaging. Most of the kidney organoids I will present in the present study have been generated starting from iPSC colonies. The method to prepare iPSCs for differentiation - either enzymatically or on colonies - is still debated in the laboratory. Enzymatic dissociation is most tricky to perform, and it might easily end up in fail of the differentiation experience. However, if rigorously mastered, it would allow increasing standardization and homogeneity of kidney organoid generation.

A.c) Matrigel

Although the advantages mentioned above, and independent confirmation that morphology of kidney organoids was more reproducible when performed on vitronectin compared to Matrigel[280], we faced periodical problems of iPSC adhesion and organoid detachment on vitronectin. We found that the use of Matrigel matrix minimized this issue. As Geltrex, Matrigel is derived from EHS mouse sarcoma that contains a rich assortment of ECM components. iPSCs easily adapted to Matrigel-based culture, forming colonies more consistently and growing at a higher rate than on vitronectin. The increased adhesion properties of Matrigel seemed to influence colony formation efficacy and expansion speed more than their morphology, requiring small adjustments.

Kidney organoid differentiation performed on Matrigel displayed a lower extent of detachment along differentiation, so switch on Matrigel has been recently considered by other members of the laboratory. The great majority of kidney organoids I used for this study have been generated on vitronectin-coated supports instead.

A.d) Laminin-521

Laminin-521 has been exclusively used for low density iPSC culture in CRISPR/Cas9 experiments in the present study. Laminin-521 use allowed a 10 fold increase of clone emergence compared to vitronectin, which was clearly advantageous to increase the chance of obtaining clones with the desired genome editing.

B) Culture medium

B.a) ReproFF2

With the same aim of sticking to the closest conditions to the Morizane's protocol[392], control 004#04 and 004#17 iPSC lines grown on Geltrex matrix in mTeSR1 medium were switched to ReproFF2 medium. Medium was either entirely or progressively replaced. For the progressive change, I first tested $^{2}/_{3}$ mTeSR1+ $^{1}/_{3}$ ReproFF2 for 1 day, $^{1}/_{3}$ mTeSR1+ $^{2}/_{3}$ ReproFF2 for 2 days, and then complete ReproFF2 medium. iPSCs rapidly differentiated and lost their typical morphological features. I thus tested a more gradual transition, by switching from $^{2}/_{3}$ mTeSR1+ $^{1}/_{3}$ ReproFF2, then $^{1}/_{2}$ mTeSR1+ $^{1}/_{2}$ ReproFF2, next $^{1}/_{3}$ mTeSR1+ $^{2}/_{3}$ ReproFF2, and finally to complete ReproFF2 medium every 2 days. In none of these conditions iPSCs maintained their pluripotent state. Hence, I pursued iPSC culture in mTeRS1 medium.

B.b) mTeSR Plus

Since the mTeSR1 furnisher proposed an upgrade - and consequently stopped the production - of mTeSR1 medium, we had to switch to mTeSR Plus medium. Among the advantages of the latter, in particular concerning an increased stability of critical components such as of the FGF2, the greater expansion rate of iPSC cultured in mTeSR Plus medium was on one hand beneficial, and on the other it forced us to adjust the timing for passaging and differentiation experiences. Indeed, we noticed a decrease in efficiency of kidney organoids generation right after the iPSC medium change. We realized that iPSC colonies were ready in advance when cultured in these conditions compared to mTeRS1. We thus shortened the "preparatory" period of iPSC culture from ~7 days to ~4 days before to start induction.

Kidney Organoids

4. Choice of the differentiation protocol

At the time I started my PhD - in October 2016 - few recently published protocols were available to induce iPSCs differentiation into kidney organoids[10,282,329,330]. Among them, we decided to apply the Morizane's 2015 one[330] since, corresponding to our needs, it seemed to yield the **maximum number of podocytes**. We reasoned indeed that organoids obtained that way would be more enriched in proximal nephron segments - and thus in glomerular components - compared to the Takasato's ones, who reported at that time - albeit later discussed[375] - the presence of $GATA3^{+}$/$ECAD^{+}$ collecting ducts[329]. Even though at that time we did not dispose of enough data to confirm that supposition, more direct studies focused on kidney organoids cell composition afterward suggested a more important podocyte representation in Morizane's *versus* Takasato's organoids[375]. Moreover, Morizane's podocytes appeared to reflect a **more mature state**, as evidenced by their higher expression of differentiation markers (*MAFB*, *PTPRO*, *PODXL*, *NPHS2*) and their lower expression of development (*SOX4*, *EMX2*, *CCND1*, *CDH6*) and proliferation (*MKI67*, *NASP*, *CENPF*, *HIST1H4C*) markers[375]. Furthermore, practical aspects such as the **ease of the procedure** and the **cost-effectiveness** were also favorable. The major concern related to the Taguchi's protocol was the use of mouse spinal cord for induction, a procedure requiring not negligible handling skills.

5. Setting-up of the Morizane's protocol

The Morizane's 2015 protocol includes 6 major steps (Fig. 31), each one leading to a particular developmental stage that can be verified by the expression of specific markers[330]. We decided to validate the intermediate stages between iPSCs and kidney organoids by immunofluorescence (IF) and reverse transcription quantitative PCR (RT-qPCR), using the same markers reported in the publication (Fig. 31).

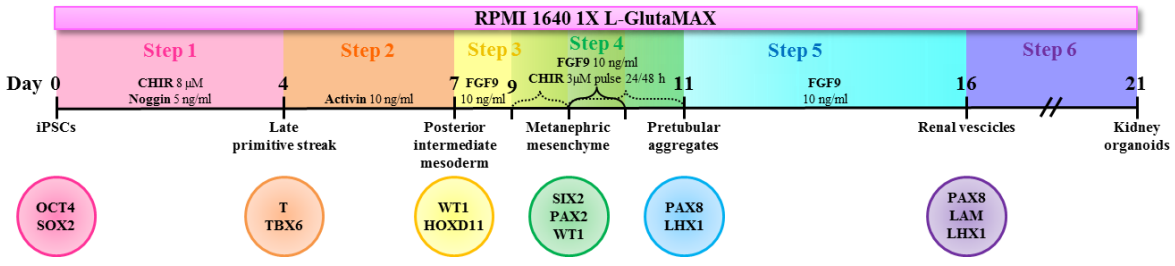

Figure 31: Kidney organoid differentiation protocol. Schematic representation of the 21 days lasting differentiation protocol applied to induce kidney organoids from iPSCs. Differentiation protocol consists of six successive steps to reproduce the sequential stages of embryonic kidney development, as described elsewhere[392]. Timing of "Step 4" is adjusted according to cell morphology, as explained later (5.B section) (dashed braces correspond to adjustments compared to the canonical protocol, reported with filled brace).

A) Adjustment of late primitive streak induction

I started to work with the control iPSC line 004#17 for the settings of these first differentiation attempts. Upon a first test of accutase dissociation, a seeding density of ~1.2×10^4 cells/cm^2 was estimated to be suitable to reach 50% confluence upon 3 days of culture on Geltrex matrix in mTeSR1 medium, before to start differentiation. The first step of differentiation protocol consists in the induction of the late primitive streak by activating the Wnt/β-catenin and inhibiting the BMP4 signaling pathways[330]. To replace Noggin in the published CHIR 10 µM/Noggin 5 ng/ml treatment, I also tested three different concentrations of another BMP4 inhibitor named LDN193189 (LDN) (LDN 50 nM, 75 nM and 100 nM). I mainly used IF validation of early steps as a readout of induction, looking for the conditions that improved the production cells positively stained for the expected markers. In particular, I verified the induction of the T^+/$TBX6^+$ **late primitive streak** markers at differentiation day 4 (D4), the $WT1^+$/$HOXD11^+$ **posterior intermediate mesoderm** markers at D7 and the $SIX2^+$/$PAX2^+$ **metanephric mesenchyme** markers at D9 (Fig. 31).

This kind of analysis provided some clues to orient differentiation. Nevertheless, most of these antibodies were not commonly used in the laboratory, and I did not dispose of proper positive controls to validate them. I proceeded by observing the expression pattern of these markers in response to inductive stimuli. A comparable behavior to what reported[330] reciprocally validated the developmental stage achieved and in turn ensured confidence in the antibodies in use. Some of the antibodies were discarded given their incoherent staining. It was the case for the ones claimed to be specific for the transcription factors T (B8436, Sigma-Aldrich), WT1 (6F-H2, Cell Marque) or HOXD11 (SAB1403944, Sigma-Aldrich), which did not give a nuclear staining. The case of anti-WT1 antibody (sc-393498, Santa Cruz Biotechnology) has been more deceitful, since it displayed a plausible nuclear staining at D7 (Fig. 32A). However, it failed *a posteriori* to exhibit a trustful glomerular staining in kidney organoids (Figure 32B).

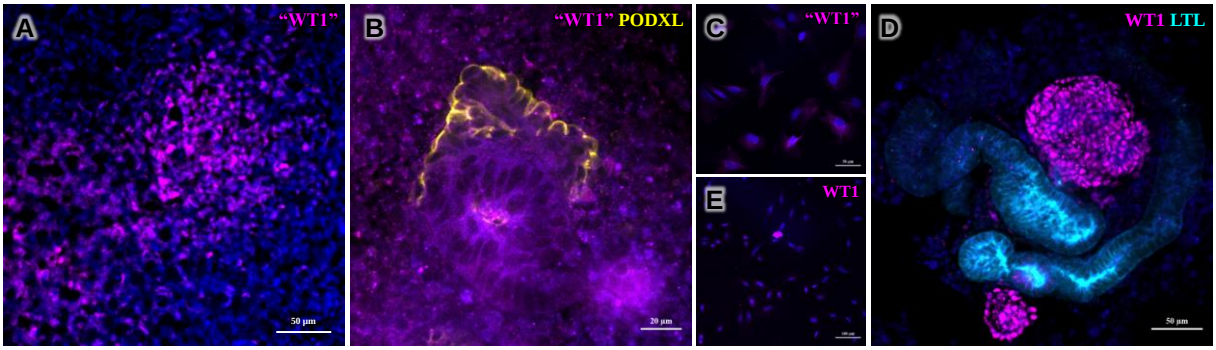

Figure 32: WT1 antibodies. Immunofluorescence staining for: **A)** "WT1" at D7. Dense packages of "$WT1"^+$ cells displayed pseudo-nuclear staining that seemed coherent for a transcription factor and with the timing of differentiation. **B)** "WT1" on D21 kidney organoids. Non-specific background noise was encountered in kidney organoids. In particular, glomerular cells, as defined by podocalyxin immunostaining (PODXL, yellow), were negative for "WT1". **C)** "WT1" on conditionally immortalized podocytes. Podocytes displayed faint non-specific "WT1" staining with fiber-like appearance in the cytoplasm. **D)** WT1 on D21 kidney organoids. Glomerular-like structures in the proximity of LTL+ tubules (cyan) were clearly evidenced by WT1 staining. **E)** WT1 on conditionally immortalized podocytes. Only rare big nuclei positively stained for WT1, perhaps indicating podocyte dedifferentiation in culture. ("WT1", sc-393498 antibody; WT1, sc-7385 antibody).

I thus tested it and another anti-WT antibody (sc-7385, Santa Cruz Biotechnology) on conditionally immortalized podocytes differentiated at 37°C and on kidney organoids. Only an exiguous fraction of podocytes displayed WT1 positive nuclear staining with the second antibody (Fig. 32E), which was not at all the case for the first one (Fig. 32C). Conversely, nuclei of glomerular cells were clearly defined by WT1 expression in kidney organoids (Fig. 32D), which lead me accredit the sc-7385 as a confident anti-WT1 antibody.

Meanwhile, Dr. R. Morizane and Dr. J.V. Bonventre published the detailed protocol for kidney organoids differentiation[392], available online by the end of December 2016. According to this version of the protocol, each PSC line requires proper adjustment of CHIR concentration in the initial step of late positive streak induction. The highest CHIR dose that is not producing cell death and/or detachment should be used, which ranges from 3 to 10 µM[392]. Requirement of a BMP4 inhibitor is also dependent on the intrinsic properties of the cell line and culture conditions[392].

Based on this information, I tested three concentrations of CHIR (3, 5 and 7 µM), alone or in combination with LDN at either 50 or 75 nM, and performed the following steps conforming to the basic protocol[330,392]. Interestingly, I observed the formation of LTL-expressing structures at D21 (Fig. 33), using the CHIR 7 µM/LDN 50 condition. LTL^+ cells were tightly associated in epithelial-like distinct architectures, sometimes lining a liquid-filled internal cavity, reminding the **proximal tubular epithelial structures** reported by the Bonventre's group in previous work[366].

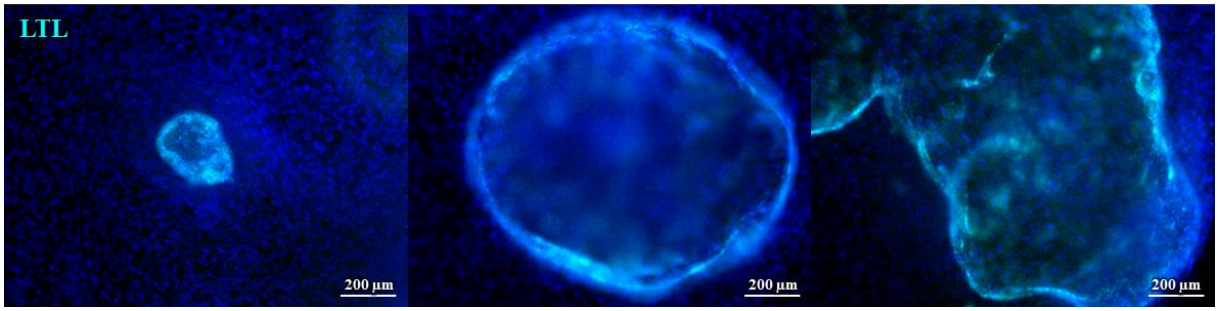

Figure 33: Proximal tubular-like epithelial structures. Immunofluorescence staining for LTL (cyan) on control 004#17 D21 epithelial structures. LTL stained epithelial-like structures with different size and shape. The bigger among them formed swollen internal cavities with a cystic appearance.

The same condition (CHIR 7 µM/LDN 50) in a subsequent experiment resulted in obtaining the first **kidney organoids** of my PhD, evidenced by IF staining of LTL in **tubular-like structures** and podocin-expressing **putative glomeruli** (Fig. 34).

Although this positive outcome was highly promising for the pursuit, it also highlighted the discontinuous efficiency of the protocol. Kidney organoids generation from the control 004#17 iPSC line was not reproducible in the following experiments using CHIR 7 µM/LDN 50 treatment.

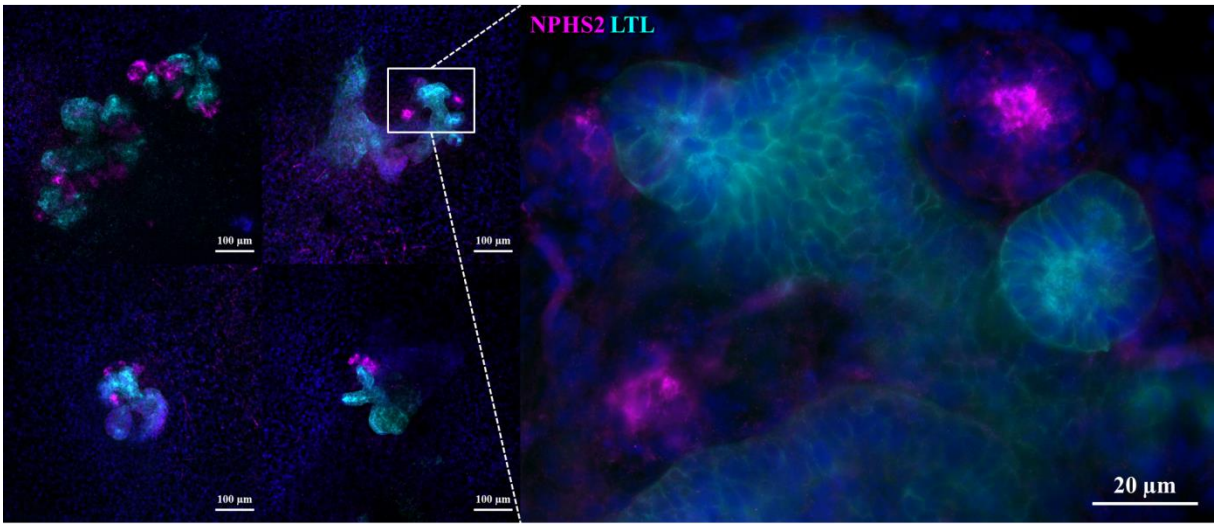

Figure 34: First kidney organoids. Immunofluorescence staining for podocin (NPHS2, magenta) and LTL (cyan) on control 004#17 D21 kidney organoids. Left panels: 10X magnification; right panel: zoom on one organoid. Several independent organoid structures emerged in the culture. Kidney organoids were characterized by a knotty arrangement of LTL^+ proximal tubules with associated glomerular-like clusters of $podocin^+$ cells.

Progressive familiarization with the iPSC culture and the kidney organoids differentiation protocol allowed me to work on more iPSC lines in parallel. Besides the 004#17, I started to use a second control, the 005#04 line, the $SRNS^{NPHS2}$ 007#27 patient line and two GAMOS patient lines ($GAMOS^{GON7}$ 006#04 and $GAMOS^{OSGEP}$ 008#04). All these iPSC cell lines displayed similar progression though the protocol steps (Fig. 35).

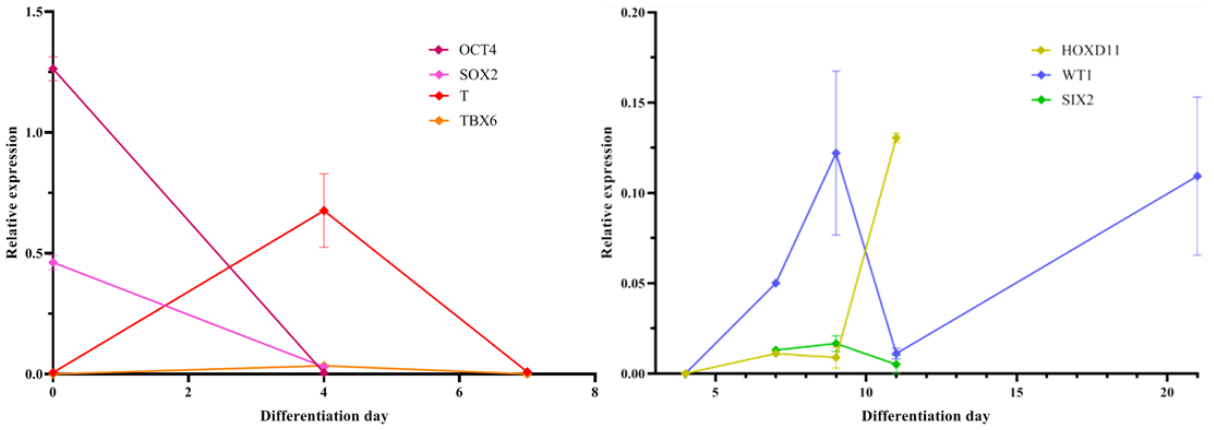

Figure 35: RT-qPCR time course for differentiation markers. RT-qPCR time course on for: **A)** *OCT4*, *SOX2*, *T* and *TBX6* from day 0 to day 7. The expression of the pluripotency markers *OCT4* and *SOX2* drastically dropped down upon iPSC induction, and it was virtually absent at D4. The expression of *T* picked at that time, accompanied by limited upregulation of *TBX6*. **B)** *HOXD11*, *WT1* and *SIX2* from day 7 to day 21. The expression of *SIX2* and *WT1* picked at D9, when NPCs are supposed to arise. After rapid extinction, *WT1* expression was detected again at D21, *videlicet* in kidney organoids. HOWD11 expression increased later than expected. The analysis include the control 004#17 and 005#04 iPSC lines, the $GAMOS^{GON7}$ 006#04 and the $GAMOS^{OSGEP}$ 008#04 iPSC lines.

Quite surprisingly, the $SRNS^{NPHS2}$ 007#27 patient iPSC line turned out to be highly responsive to the differentiation protocol. Indeed, I highlighted by IF the presence of $T^+/TBX6^+$ cells at D4 (Fig. 36A), the emergence of $SIX2^+$ putative NPCs at D9 (Fig. 36B) and I finally consistently obtained kidney organoids on D21, characterized by nephrin expression in putative glomeruli and LTL^+ tubular structures (Fig. 36C) at a very efficient rate of differentiation, producing numerous organoids in most of the experiments carried out.

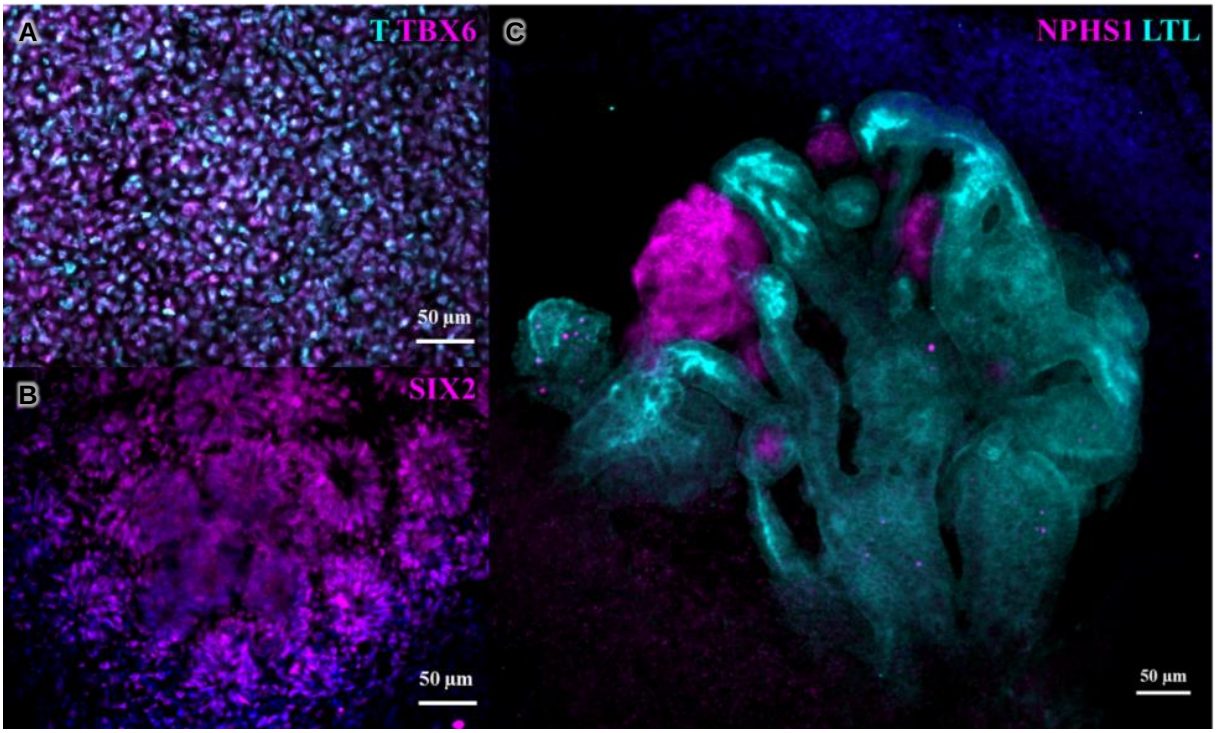

Figure 36: Crucial differentiation stages. Immunofluorescence staining for: **A)** T and TBX6 on D7 late primitive streak. Nearly 100% of cells express or co-express T and/or TBX6. **B)** SIX2 on D9 metanephric mesenchyme NPCs. SIX2^{+} cells organize in epithelial circular structures. **C)** Nephrin (NPHS1, magenta) and LTL (cyan) on D21 kidney organoids. SRNS^{NPHS2} patient kidney organoids display the same structural organization, comprising LTL^{+} tubules and nephrin^{+} glomeruli, as control kidney organoids. The analysis concerns the differentiation of the SRNS^{NPHS2} 007#27 patient iPSC line.

Taking into account all the experiments performed on these cell lines, all of them presented a higher potential for differentiation than the control 004#17 line. These cell lines globally did not well tolerate CHIR doses higher than 8 µM. Both Noggin and LDN allowed producing kidney organoids, but the latter being less proficient. Compared to Noggin, LDN-induced organoids were generally lower in number, smaller and less developed. The ensemble of these observations oriented me towards a **CHIR 8 µM/Noggin 5 ng/ml "consensus" condition** that I generally applied with few adaptations. In parallel, adjustments of the following differentiation steps - of "Step 4" in particular (Fig. 31) - have been carried out, as explained below.

B) Identification of "renal rosettes" and adjustment of NPC induction

A peculiar observation I made, concerned the ordered organization of SIX2^{+} nuclei at D9 (Fig. 36B), which seemed to be aligned in circular structures. I noticed that morphological changes were happening in the culture around D9, with clusters of epithelial structures tending to emerge. Most probably corresponding to **pretubular aggregates** or **very early renal vesicles**[392], I will hereafter refer them to as "**renal rosettes**" based on their characteristic honeycomb morphology with radial cells departing from a central lumen (Fig. 37), as they resemble to neural rosettes[311]. The fact that renal rosettes were firstly identified by SIX2 positive IF let me consider they could constitute an easy morphological read-out for **NPC** emergence.

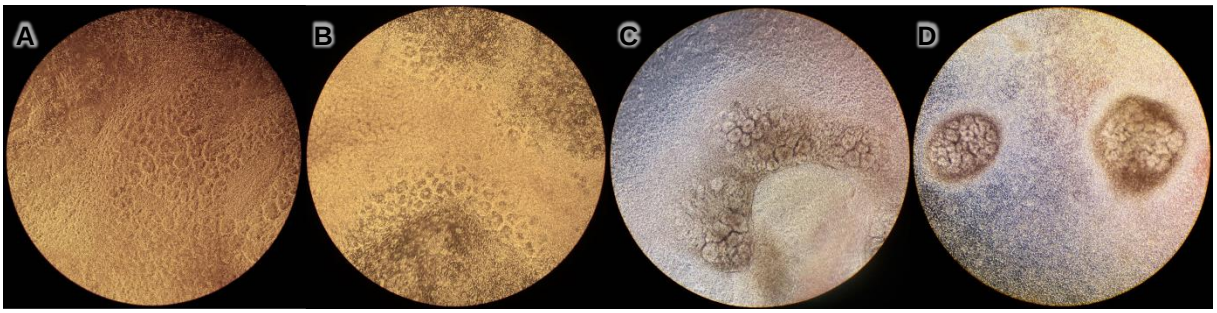

Figure 37: Renal rosette morphology. **A)** Flat renal rosettes. **B)** Renal rosettes in a high cellular dense zone. **C)** Late renal vesicles. **D)** Late renal vesicles (left) and pretubular aggregates (right) under light microscopy (10X magnification). The appearance of the differentiating cell culture undergoes noticeable modifications around D9. Cell epithelialization is marked by the formation of what we call renal rosettes. These structures sharing a common circular disposition of cells around a central lumen, actually display a wide spectrum of morphologies that are evolving in time.

We empirically noticed a general correlation between the presence of D9 renal rosettes and the D21 kidney organoids development. This was coherent with the partial information about cell morphology at this critical step reported in the published protocol[392]. Indeed, the authors suggested to "*check the morphology of cells. If many cells form round polarized structures with lumens resembling renal vesicles, you should adjust the treatment time of this step by shortening it from 2 to 1 d* " [392]. Although the distinction of the ongoing developmental phases is faint, a short window exists - between the beginning of NPC epithelialization (Fig. 37A and B) and the formation of proper renal vesicles (Fig. 37C and D) - during which it is crucial to intervene. We found that by adjusting the timing of CHIR-mediated MET regulation according to cell morphology around D9 we could increase the yield of differentiation.

Renal rosettes were usually located within or in the vicinity of denser multilayered zones of the culture (Fig. 37B). The time they appeared and their aspect was iPSC line- and clone-dependent and may slightly vary among independent experiments, even though the behavior of each clone was quite consistent. In general we observed "early" rosettes appearing at day 8 for some iPSC lines/clones, and rosettes appearing at day 9 for others. Rosettes could have very defined borders or they could be barely visible. In the practice, we advanced the "Step 4" (Fig. 31) treatment when we faced early renal rosettes and/or we shortened it from 1 to 2 days if rosettes displayed very well defined borders, a sign that they might be too "advanced".

B.a) Characterization of renal rosettes

I confirmed by IF that renal rosettes consistently express the principal NPC marker SIX2 (Fig. 36B and 38). The expression pattern of PAX2 and LHX1 was more variable, presumably depending on the maturation stage of these structures. I observed some extent of co-expression of SIX2 and PAX2, whereas $LHX1^{+}$ cells mostly surrounded (Fig. 38A) but sometimes also composed (Fig. 38B) the rosettes.

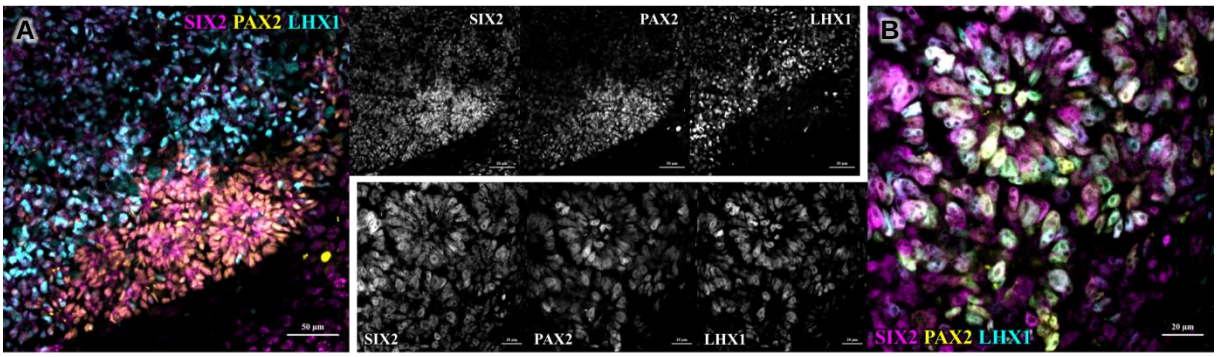

Figure 38: Characterization of renal rosette by IF. Immunofluorescence staining for SIX2 (magenta), PAX2 (yellow) and LHX1 (cyan) on D9 renal rosettes. All the nuclei having a circular disposition that defines renal rosettes express the NPC marker SIX2. Some of these cells also co-express PAX2. **A)** $LHX1^{+}$ cells have been found to be located in the close proximity of renal rosettes (20X magnification), **B)** or to be integrated within them (40X magnification). Middle panels: single stainings.

I then sought to determine the evolution in time of NPC markers expression along differentiation at the transcriptional level by RT-qPCR. I observed variable expression patterns of *SIX2* and *PAX2*, globally picking at D9 or still increasing at D10 (Fig. 39). Both genes displayed either minimal induction, or an up to 5 fold change. Interestingly, the expression of *SIX2* and *PAX2* correlated one to each other, having similar profiles for a given clone within the same experiment. The control 013#19 line represents an emblematic example, in which the first batch of differentiation displayed poor induction (Fig. 39, light green, n=1), while in the second one both *SIX2* and *PAX2* expression continues to increase from D8 to D10 (Fig. 39, light green, n=2). This correlation of marker expression supported the presence of NPCs, the *SIX2* and *PAX* expression levels reflecting their relative amount in the culture.

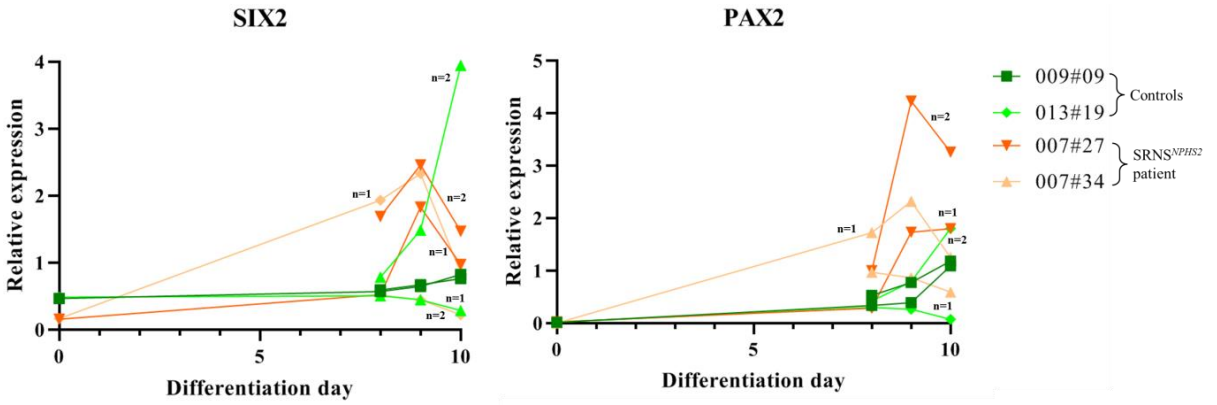

Figure 39: Characterization of induced NPCs around D9 by RT-qPCR. Time course relative expression of *SIX2* (left panel) and *PAX2* (right panel) from D8 to D10 compared to iPSCs (D0). SIX2 and PAX2 expression generally peak at D9 or it is still increasing at D10. Of note, the expression pattern of these genes strikingly correlated for each iPSC clone within the same batch of differentiation. Relative expression has been calculated using the $2^{-\Delta\Delta Ct}$ method normalizing on *GAPDH* expression. Distinct differentiation batches are indicated as n=1 or n=2.

Finally, I tried to employ a cytofluorimetric assay, using the cell surface integrin α8 (ITGα8) and platelet-derived growth factor-α receptor (PDGFRα) markers, the **ITGα8^{+}/PDGFRα^{-}** having been described do define the NPC population[10]. I measured the

fraction of ITGα8^{+}/PDGFRα^{-} cells at D8, 9 and 10, which can be used as readout of a good MM induction (personal communication of Dr. R. Nishinakamura at the 12th International Podocyte Conference 2018 in Montréal).

I conducted two independent experiments, using the control 009#02 and 013#19 lines, and the SRNS^{NPHS2} 007#27 and 007#34 patient lines. An ITGα8^{+}/PDGFRα^{-} cell population was detected (Fig. 40), even though the proportion of "NPCs" defined this way was quite low, ranging from 3 to 8% for the first batch of differentiation, and from 0.5 to 3% for the second one (please consider that one of the D9 analyses has been hampered due to cytofluorimeter breakdown). Data published from Dr. R. Nishinakamura' group reported significantly higher percentage of ITGα8^{+}/PDGFRα^{-} cells induced from mouse ESCs (~60%)[10], and a yield of ~15% from human iPSCs[394].

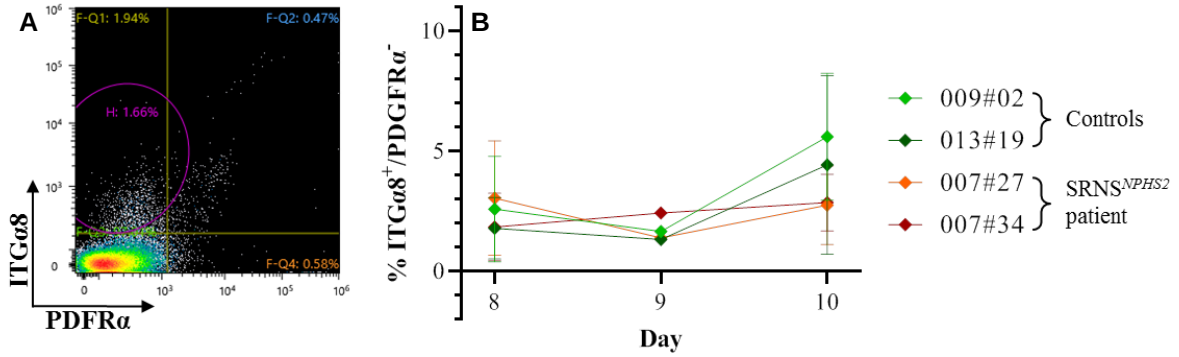

Figure 40: Cytofluorimetric analysis of ITGα8 and PDGFRα. **A)** Representative cytofluorimetric analysis of ITGα8 and PDGFRα. Yellow gating subdivides the 4 quadrants of negative, single positive for each marker and double positive cells. Purple gating defines the ITGα8^{+}/PDGFRα^{-} cell population. **B)** Time course quantification of ITGα8^{+}/PDGFRα^{-} cell percentage from D8 to D10.

By IF, I evidenced positive staining for integrin α8 surrounding renal rosettes, at the basal domain of SIX2^{+} NPCs (Fig. 41). Although the fraction of ITGα8^{+}/PDGFRα^{-} cells in the cytofluorimetric analysis was lower than expected, the relative amount of NPCs *versus* all the surrounding off-target cells must be taken into account. Indeed, renal rosettes represent dispersed clusters that emerge among a continuous and often multilayered cellular blanket. All the surrounding cells might have drowned the ITGα8^{+}/PDGFRα^{-} population, which is anyway clearly detectable. The different proportion might be imputable to the different protocol applied, if supposing the Taguchi's 2014[10] allows to have a more favorable NPCs/surrounding off-target cells ratio than the Morizane's 2015[330].

Anyway, IF showing integrin α8 that encircles renal rosettes further supports their NPC nature. Cytofluorimetry would thus not be the most suitable technique to evaluate efficiency of induction, since it largely depends on the amount of cells that are not engaged in the renal lineage. According to the ensemble of these data, I consider morphological observation as the most convenient and straightforward readout at this stage. ITGα8^{+}/PDGFRα^{-} could be preferably useful as a tool to enrich for NPCs, as it has already been reported[381].

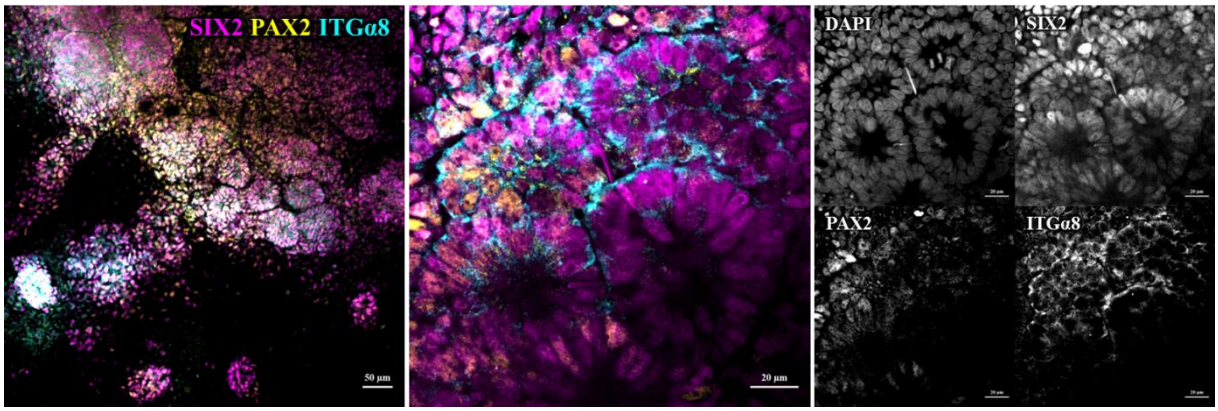

Figure 41: Renal rosette markers. Immunofluorescence staining for SIX2 (magenta), PAX2 (yellow) and integrin α8 (ITGα8, cyan) on D9 renal rosettes. Renal rosettes are clearly identifiable in the culture as $SIX2^+$ circles of nuclei, with some extent of PAX co-expression. These circular structures are surrounded by integrin α8 staining. Left panel: 10X magnification; middle panel: 40X magnification; right panels: single stainings.

Despite NPCs have a pivotal importance in nephrogenesis, these transient amplifying cells do not persist long-term *in vitro*. The presence of NPCs is an ephemeral transition during differentiation, their expansion and maintenance being extremely limited[395]. Having the possibility to freeze NPCs would allow to stock pre-induced progenitors, or eventually to exchange frozen vials between different laboratories in collaborative studies.

I thus explored the possibility to freeze D9 NPCs and evaluated their capacity to eventually recover and proceed with differentiation. Upon **freezing and thawing** of D9 vials, directly proceeding with the differentiation protocol from "Step 4", almost all the clones survived and the major part of them had an "epithelial" aspect. In one case I observed formation of a kidney organoid (Fig. 42). Even though this result is very preliminary, I consider it encouraging. While in these experiences all of D9 cells have been enzymatically collected using accutase, a promising perspective would be to manually collect renal rosettes, which would be more enriched for NPCs.



Figure 42: Kidney organoid obtained upon freezing and thawing of D9 NPCs. Day 21 kidney organoid obtained upon freezing D9 induced NPCs and thawing proceeding with the differentiation protocol from "Step 4" (10X magnification).

6. Characterization of kidney organoids

Most of the work aimed to characterize the principal features of kidney organoids has been achieved using the 005#04, 007#27, 006#04 and 008#04 cell lines. Throughout my PhD, I succeeded in differentiating the control 004#17, 005#04, 009#02, 009#09 and 013#19, and the patient SRNS^{NPHS2} 007#27 and 007#34, GAMOS^{GON7} 006#04, 006#33 and 023#11 and GAMOS^{OSGEP} 008#04 and 008#26 iPSC lines. With the only exception of podocin expression pattern in 007 kidney organoids (please refer to Results, Part 2 and Article 2), all the organoids obtained from the various cell lines shared the main characteristics of kidney organoids that are described in several publications issued from independent research groups concerning structural organization and renal marker expression[10,329,330].

Upon ~21 days of differentiation, elaborated **3D structures** emerged in culture (Fig. 43A). These iPSC-derived kidney organoids displayed the same features of *in vivo* nephrons, namely the **ordered structural development of proximal to distal segments** (Fig. 43B).

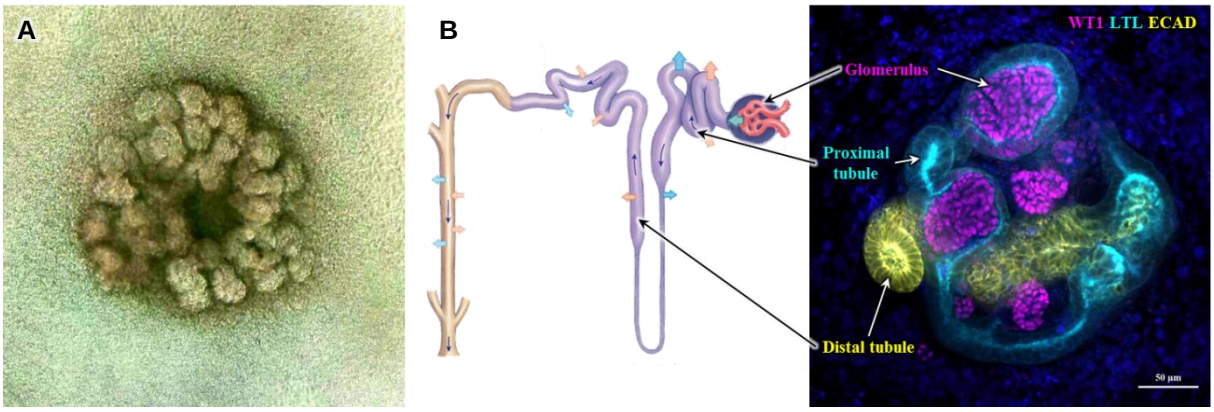

Figure 43: Kidney organoids. **A)** D21 kidney organoid under light microscopy. Elaborated 3D structures adherent to the support emerge from the differentiating culture. **B)** D21 kidney organoid compared to the structure of a nephron. The kidney organoid is stained with WT1 (magenta), evidencing the glomerulus, LTL (cyan), staining the proximal tubule, and E-cadherin (ECAD, yellow), defining the distal tubule.

A) Tubular compartment

I evaluated LTL and E-cadherin as suitable markers to define the proximal and distal tubular segments, respectively. LTL and E-cadherin were almost mutually exclusive, with limited degree of superposition at the transition zones (Fig. 43B). LRP2 expression, a proximal tubular cell transporter, also known as megalin, has been detected at the luminal side of proximal tubules, but also at the apical surface of presumptive parietal cells of the Bowman's capsule (Fig. 44A). Although unexpected, LRP2 positive staining in parietal cells of the Bowman capsule in human kidney has been already reported elsewhere[396]. Prominent primary cilia populated the lumen of proximal tubules, especially in their portion most in proximity to glomeruli, as evidenced by ARL13B IF (Fig. 44B).

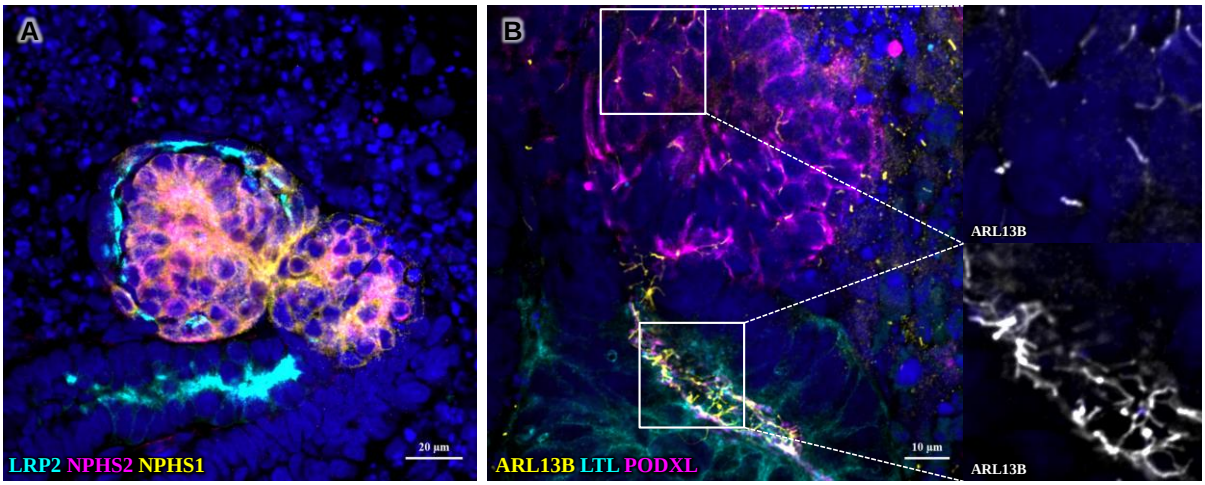

Figure 44: Characterization of kidney organoid tubular compartment by IF. **A)** Immunofluorescence staining for LRP2 (cyan), podocin (NPHS2, magenta) and nephrin (NPHS1, yellow) on D21 kidney organoids. LRP2 localizes at the apical surface of proximal tubular cells and also of parietal cells, which encapsulate podocin^{+}/nephrin^{+} glomerular podocytes. **B)** Immunofluorescence for ARL13B (yellow), LTL (cyan) and podocalyxin (PODXL, magenta) on D21 kidney organoids. ARL13B^{+} primary cilia extend towards the lumen of proximal tubules; they also stand on podocytes, suggesting their relative immature state. Right panels: zoom on primary cilia on podocytes (upper panel) and tubular cells (lower panel).

Using transmission electron microscopy (TEM), I observed that tubular cells displayed typical columnar epithelial morphology. Nuclei were basally located, while the apical cytoplasm was rich in mitochondria (Fig. 45A). Tight junctions sealed the apical domains of tubular cells (Fig. 45B). Towards the luminal side, the presence of densely packed protrusions of an immature brush border-like organization (Fig. 45B) or more sparse microvilli (Fig. 45C) could suggest a proximal or distal identity, respectively.

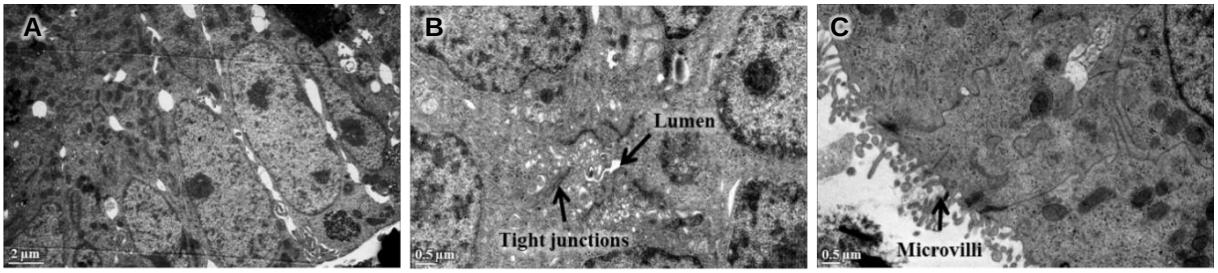

Figure 45: Characterization of kidney organoid tubular compartment by TEM. **A)** Frontal section of D21 kidney organoid putative proximal tubule. Columnar cells are nicely aligned to constitute the tubular epithelium. **B)** Transversal section of D21 kidney organoid putative proximal tubule. It is possible from this perspective to appreciate the apical projections that extend towards the lumen, and the tight junctions consolidating the apical tubular belt. **C)** Frontal section of D21 kidney organoid putative distal tubule. Cuboidal tubular cells display moderately abundant, short apical microvilli.

B) Glomerular compartment

Since my PhD project focused on NS, I dedicated most efforts in defining podocyte-related aspects in kidney organoids, which I characterized using IF and TEM, as well as by analyzing their transcriptomic profile upon isolation from organoids and RNA-Seq.

By TEM, I showed that podocytes are organized in clusters of octopus-shaped polarized cells covered by microvilli and extending cellular protrusion at their basal side (Fig. 46A). These basal extensions subdivided into primary and thinner secondary processes that laid on a basal lamina. Intercellular junctions were found to connect these basal projections

(Fig. 46B). Actually, podocytes seem to "collapse" inside the glomerulus, extending protrusions that chaotically interconnect instead of regularly interdigitating. Only occasionally - and extremely rarely - I observed intercellular junctions with a ladder appearance that may be interpreted as SD-like structures (Fig. 46C and D). Anyway, establishment of proper FPs connected by reliable SD was in fact absent in kidney organoids, which hampered the possibility to eventually observe effacement of these structures when comparing patient-derived podocytes to healthy controls. The ultrastructural organization of podocytes, displaying basally located intercellular junctions, apical prominent nuclei and microvilli covering the apico-lateral surface is consistent with a capillary loop stage of development[377].

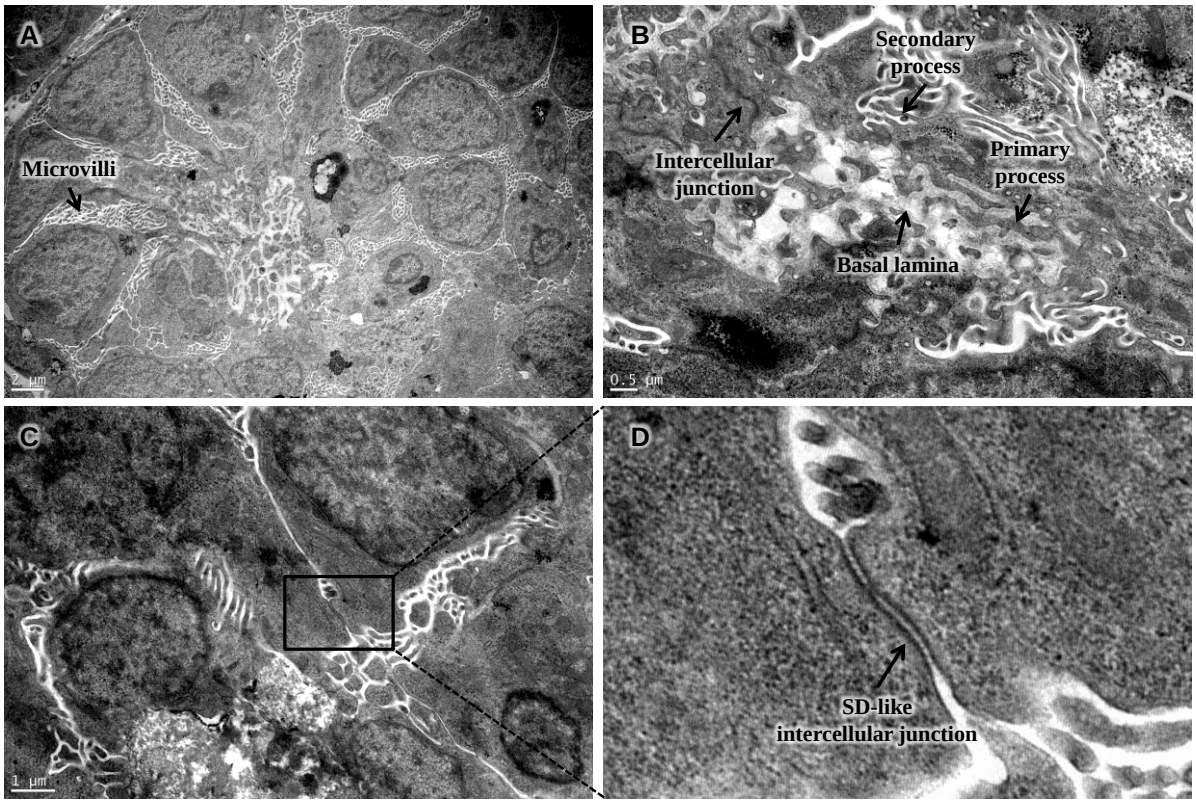

Figure 46: Characterization of kidney organoid glomerular podocytes by TEM. **A)** Global ultrastructure of a D21 kidney organoid glomerulus. Podocytes are octopus-shaped polarized cells covered by microvilli and extending cellular protrusions towards the center of the glomerulus. **B)** Focus on podocyte basal cellular protrusions. Podocyte basal protrusions are organized into primary and secondary processes, which are interconnected by intercellular junctions. **C)** Podocytes connected by a SD-like intercellular junction. **D)** Focus on the SD-like structure. Sporadically, zipper-like cellular junctions interconnecting adjacent podocyte were observed, and cautiously interpreted as SD-like structures.

I validated the expression and subcellular localization of several podocyte-specific markers by IF. The transcription factor **WT1**, a key regulator of podocyte function[397], displayed nuclear expression. Essential components of the SD such as **nephrin** and **podocin** localized at the basal side as well as **synaptopodin**, while **podocalyxin** was restricted to the apico-lateral surface of podocytes (Fig. 47A). Although I observed the presence of a layer of flat cells highly reminiscent of parietal epithelial cells of the Bowman's capsule surrounding kidney organoids glomeruli, podocyte clusters were most often un-capsulated (Fig 47B). The size of podocyte clusters turned out to be extremely variable, especially when not capsulated.

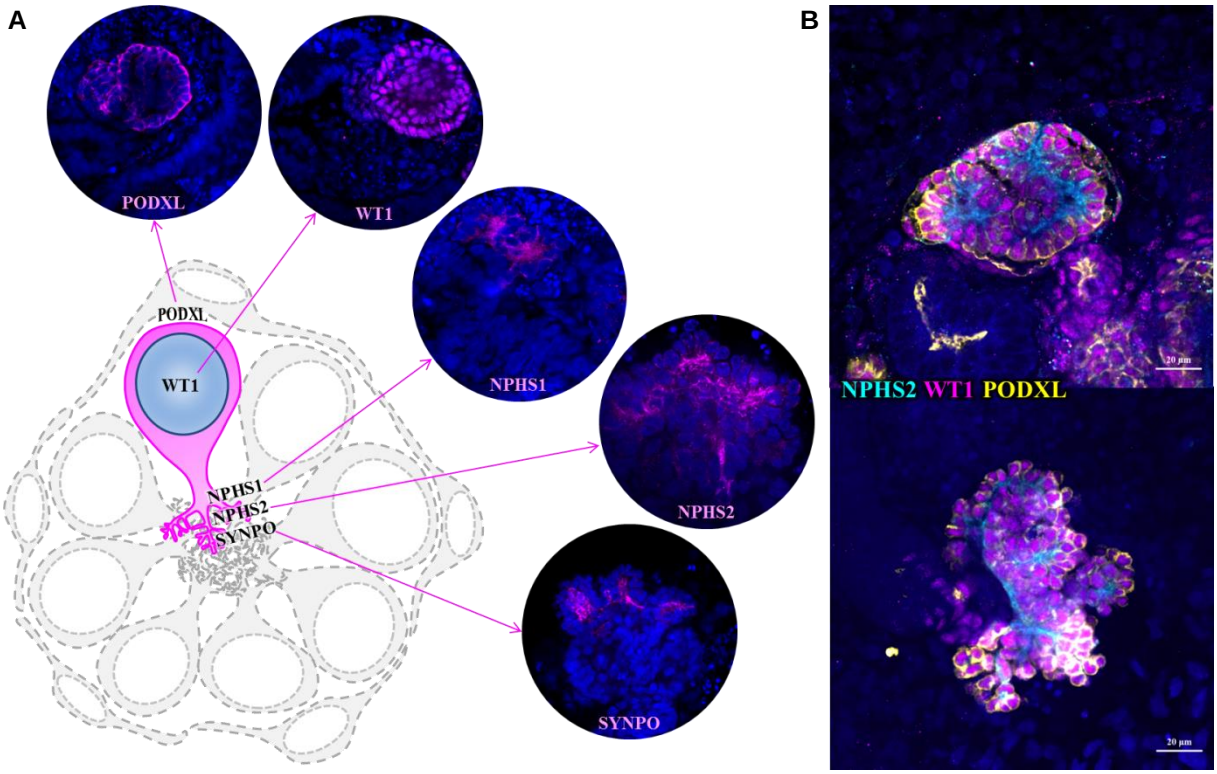

Figure 47: Characterization of kidney organoid glomerular podocytes by IF. **A)** Schematic representation of a D21 kidney organoid glomerulus. Immunofluorescence staining for podocalyxin (PODXL), WT1, nephrin (NPHS1), podocin (NPHS2) and synaptopodin (SYNPO) are reported corresponding to their relative subcellular localization within the podocyte (magenta). **B)** Comparison of capsulated (upper panel) *versus* un-capsulated (lower panel) D21 kidney organoid glomeruli. Glomeruli are stained for podocin (NPHS2, cyan), WT1 (magenta) and podocalyxin (PODXL, yellow). A layer of flat parietal cells is distinguishable around the capsulated glomerulus, while in the un-capsulated one podocytes writhe into tufts.

7. Podocyte isolation

The most problematic issue we - and others - faced is the variability in the relative proportions of nephron segments, particularly regarding the glomerulus *versus* tubules ratio. Considering that our main interest is focused on podocytes, any molecular analysis of whole kidney organoids would be biased by this ratio.

We thus considered several options to enrich - or ideally purify - the podocyte population. These included **glomerular sieving**[398] and **fluorescence-activated cell sorting** (FACS)[399]. At that exact time, B. Estèbe joined Pr. C. Antignac's group as an engineer. He initially worked with me on kidney organoid differentiation, and progressively dedicated his work to the setting up of the technical details of this procedure. The establishment of the procedure for podocyte isolation from kidney organoids lasted about a year in total, taking into account that the protocol to obtain kidney organoids was not fully effective.

A) Glomerular sieving

Glomerular isolation by differential sieving is a conventional technique applied to mouse[400], rat[401] and human[398] kidneys. We applied this kind of mechanical approach to kidney organoids.

Upon sieving, we manage to obtain a fraction composed of more or less spherical and compact cellular aggregates with a diameter of ~100 µm (Fig. 48A). When plated, epithelial cells migrated out spreading around these aggregates within 1 day (Fig. 48B), in a very similar way compared to kidney-derived sieved glomeruli[402].

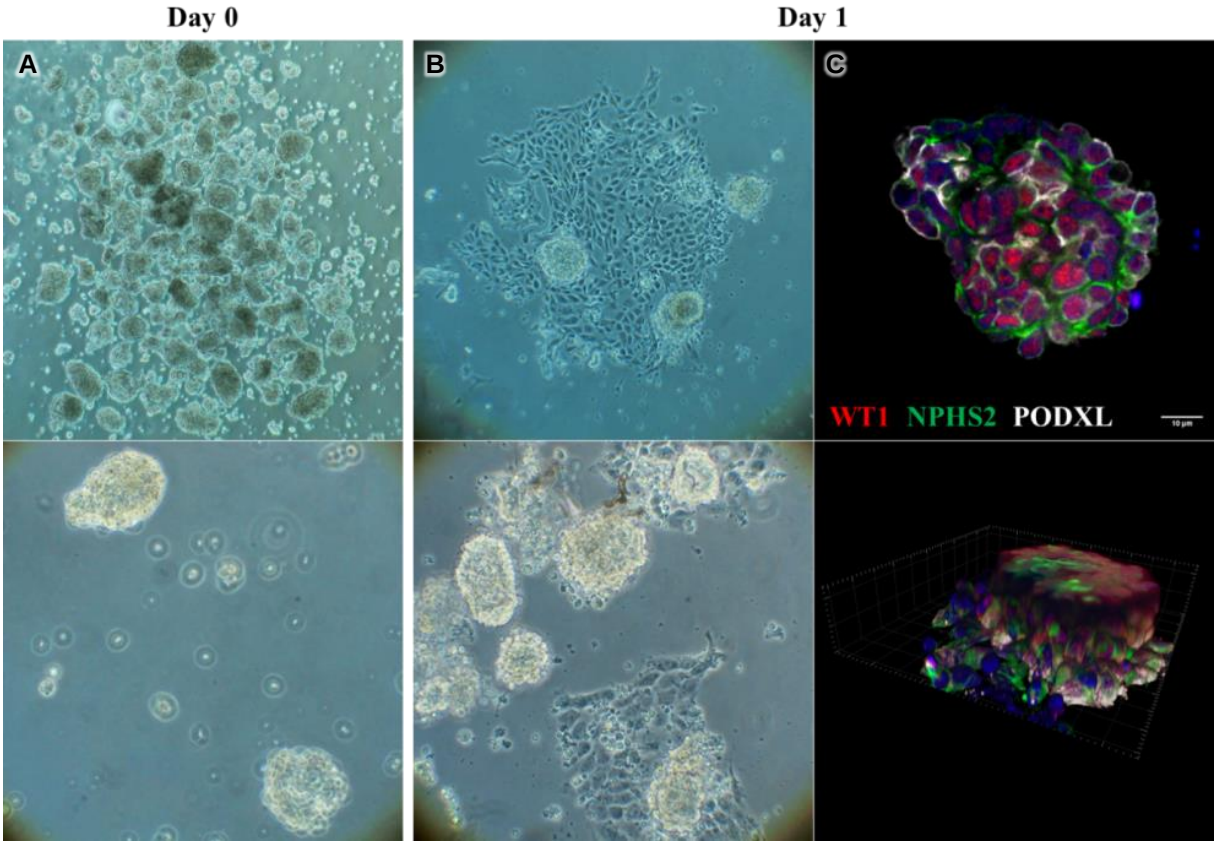

Figure 48: Glomerular sieving. **A)** Sieved spherical aggregates. (5X magnification, upper panel; 20X magnification, lower panel). **B)** Cultured aggregates 1 day after sieving. (5X magnification, upper panel. 20X magnification, lower panel). Cell aggregates had attached to the surface and cell had started to migrate and spread around. **C)** Immunofluorescence staining for WT1 (red), podocin (NPHS2, green) and podocalyxin (PODXL, white) 1 day after sieving. The cell aggregate expresses podocyte markers connoting it as a glomerulus. Transversal optical section (upper panel) and 3D reconstitution (lower panel).

IF staining revealed that only a fraction of these aggregates actually expressed WT1, podocin and podocalyxin markers with appropriate localization (Fig. 48C), confirming we succeeded in isolating glomeruli from kidney organoids. Glomerular epithelial cells migrating out of them progressively showed a decreased expression of podocyte markers in a way that was proportional to their distance from the glomerulus (data not shown). Even though this podocyte dedifferentiation in culture has been extensively observed for primary cultures[287,402], it has never been reported for kidney organoid-derived podocytes so far. Only more recently, a similar loss of identity within 2 days has been published for kidney organoid-isolated glomeruli-derived podocytes[279]. Anyhow, not all the aggregates isolated from organoids turned out to be glomeruli, some of them being LTL^+ portions of proximal tubules (data not shown). The presence or absence of a Bowman's capsule-like structure, as well as the size and shape of glomeruli within each kidney organoids largely disfavor this sieving approach, which would require more homogeneous biomechanical properties of glomeruli to robustly

discriminate them from all the other components. In addition, glomerular sieving requires substantial manual handling, which is hard to standardize. Given a specific filter size, the pressure and type of movements applied by the experimenter influence the result, drastically reducing the reproducibility of the procedure. For the reasons mentioned above, we considered the mechanical sieving technique not suitable to reproducibly isolate glomerular podocytes with an acceptable degree of purity.

B) Podocyte fluorescence-activated cell sorting (FACS)

Another strategy we considered was to isolate podocytes by FACS. This technique implied the setting up of two major axes, namely dissociation and detection conditions.

- Good **dissociation** at the single cell level is an absolute prerequisite for FACS. At the same time, the dissociation phase should be as delicate as possible towards the cells in order to minimize cell death, but also cell stress that may perturbs their transcriptome. The optimal balance between efficient single cell separation and gentle manipulation was a tricky compromise to found.

- The choice of the appropriate **markers** to specifically identify the podocyte population among the various cell types that compose kidney organoids is critical for their successful isolation. Setting up of staining conditions and suitable **gating** strategy are then required to optimize the procedure.

B.a) Kidney organoid dissociation

Since kidney organoids are compacted structures made of densely packed epithelial cells, enzymatic treatment associated with mechanical proceeding is necessary to dissociate them. First tests of dissociation were performed using **accutase**, an enzymatic mixture with proteolytic and collagenolytic activity. Accutase is widely used in stem cell research and flow cytometry applications as a gentler substitute for trypsin. However, the use of accutase alone turned off to be quite inefficient since most cells still formed aggregates upon treatment. We then compared accutase to **trypsin**, since the latter has also been used to dissociate kidney organoids[278]. No substantial improvement was achieved, unless we prolonged the treatment at the detriment of cell viability. The compactness of kidney organoids prompted us to test a two-steps enzymatic dissociation using **collagenase IV** before accutase, in combination with **DNase I** to digest DNA leaked from damaged cells. In the meanwhile, we also considered a cold protease method to reduce gene expression artefacts[403], using the **psychrophilic protease from *Bacillus licheniformis*** that is active at 6°C or colder. However, cold dissociation inevitably presented extensive cell reaggregation, even in the presence of DNase I, leading to massive cells loss during the procedure. Finally, the best option selected, leading to an efficient dissociation of kidney organoids while preventing significant cell mortality, contemplated the use of **collagenase** (A or II), **pancreatin** and **DNase I**.

B.b) Detection conditions

Cell surface markers being more suitable for flow cytometry applications than intracellular ones, we evaluated **nephrin** and **podocalyxin** as the best markers for podocyte FACS-sorting since they had already been used by the group of Dr. R. Nishinakamura to validate podocyte identity in kidney organoids by flow cytometry[278]. Using the same antibodies, we found that nephrin expression was unexpectedly almost undetectable. On the contrary, podocalyxin presented a wide range of expression, with two cell populations, which I called "**Podocalyxin^{high}**" and "**Podocalyxin^{low}**" (Fig. 49A). To better characterize these cell populations, we plated these cells in culture upon FACS. Both populations proliferated, reaching confluence in ~1 week. The vast majority of cells had a classic epithelial phenotype. Among them, sparse huge and flat cells highly resembling mature podocytes where observed in both Podocalyxin^{high} and Podocalyxin^{low}-derived cultures (Fig. 49B). IF revealed only a small fraction of cells retained podocalyxin expression (Fig. 49C), while WT1, nephrin and podocin expression was not detected (data not shown). In line with their proliferative behaviour, most of the cells were positive for the proliferation marker Ki-67 (Fig. 49C). No evident differences were observed between Podocalyxin^{high} and Podocalyxin^{low} cells in terms of morphology, proliferation and podocyte markers expression.

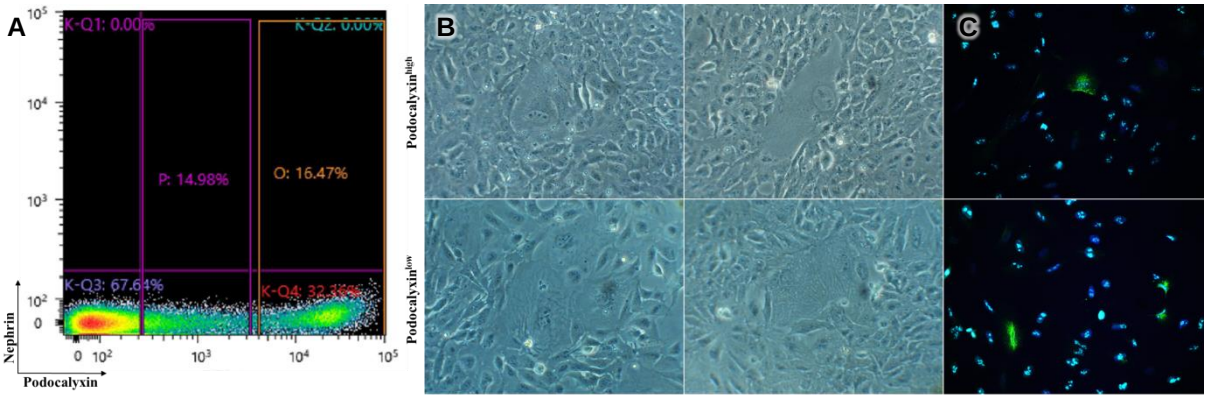

Figure 49: Podocalyxin^{high} and Podocalyxin^{low} cell populations. **A)** Cytofluorimetric profile of kidney organoid dissociated cells stained for nephrin (y axis) and podocalyxin (x axis). About one third of kidney organoid cells display podocalyxin at a high level. In between this Podocalyxin^{high} and the negative population, a fraction of cells are characterized by low podocalyxin expression. **B)** Confluent cultures of Podocalyxin^{high} and Podocalyxin^{low} cell populations after 1 week of culture. Podocyte-like huge and flat cells are visible in both cell populations. **C)** Podocalyxin^{high} and Podocalyxin^{low} immunofluorescence staining for podocalyxin (green) and Ki-67 (cyan). Almost all cells are proliferative, as evidenced by positive Ki-67 staining, but only an exiguous fraction of the express podocalyxin.

We speculated that the features of these cells could be due to either podocyte dedifferentiation or contamination by other cell types or both. To evaluate these aspects, we analyzed Podocalyxin^{high} and Podocalyxin^{low} cells by flow cytometry. We analyzed again nephrin and podocalyxin expression, but also LTL and Thy-1 membrane glycoprotein (CD90), which identify proximal tubular cells and stromal cells, respectively. In accordance with IF staining (Fig. 49C), the number of podocalyxin^{+} cells was drastically low, as well as the intensity of the signal (Fig. 50). Nephrin was not detected.

Interestingly, over 40% of cells were LTL$^+$, a percentage that rose up to ~70% for the Podocalyxin^{low} (Fig. 50). CD90 cells represented a minor fraction in both samples.

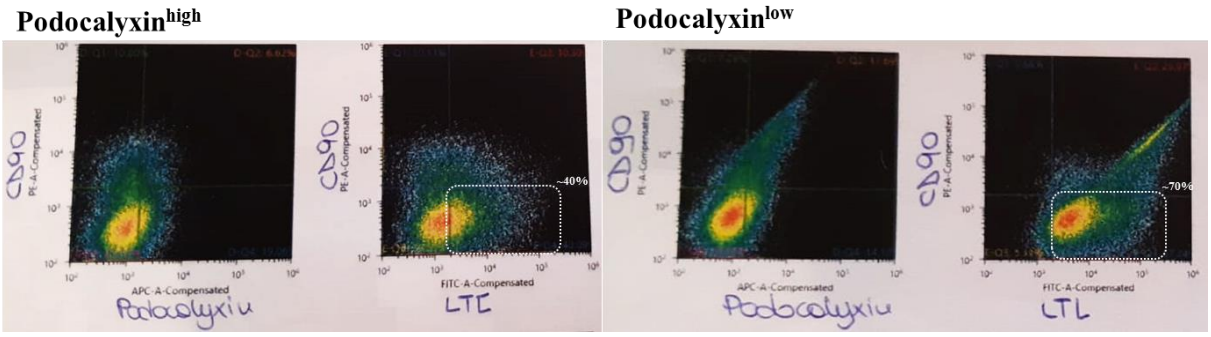

Figure 50: Podocalyxin^{high} and Podocalyxin^{low} cells after 1 week in culture. Cytofluorimetric profile of Podocalyxin^{high} (left panel) and Podocalyxin^{low} (right panel) stained for Thy-1 membrane glycoprotein (CD90, y axis) and podocalyxin (left) or LTL (right) (x axis). A considerable amount of the cells under analysis express LTL, particularly in the Podocalyxin^{low} population.

These observations suggested the presence of a contamination derived from proximal tubular cells, which seemed to be more important in Podocalyxin^{low} than Podocalyxin^{high} cells. Of note, podocalyxin has been shown to be also expressed in proximal tubules[404]. By IF, I evidenced its strong expression in podocytes of kidney organoids, whereas, in most tubules, podocalyxin staining is not detected. However, some portions of proximal tubules display luminal staining of podocalyxin, particularly those closed to the glomeruli (Fig. 44B).

Given all these results, we realized that in the absence of combination with a podocyte reporter, such as the NPHS1^{GFP} line used by the group of Dr. R. Nishinakamura[278], the nephrin$^+$/podocalyxin$^+$ signal is not strong enough to distinguish the putative podocyte population from the nephrin$^-$/podocalyxin$^-$ one. We finally considered including LTL as an exclusion marker in the subsequent FACS experiences. In that way, we would be able to increase the purity of the podocyte population by getting rid of contaminant proximal tubular cells (LTL$^+$/podocalyxin$^+$). Doing so, we finally manage to set up a **three-labels gating strategy** that allowed us to discriminate our cell population of interest (Fig. 51). We first plotted cells on the nephrin and LTL axes, gating the nephrin$^+$/LTL$^-$ cells. This step allowed us to enrich for presumptive podocytes while excluding proximal tubular cells at the same time. Subsequently we plotted this population on the podocalyxin axis to ultimately purify **nephrin$^+$/podocalyxin$^+$/LTL$^-$ cells**.

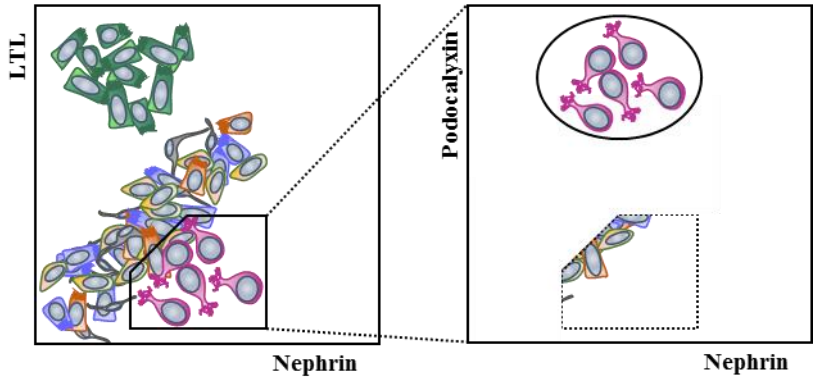

Figure 51: Gating strategy. Schematic representation of the gating strategy applied to isolate the nephrin$^+$/podocalyxin$^+$/LTL$^-$ cell population. First, cells were plotted on LTL and nephrin axes (left panel), and nephrin$^+$/LTL$^-$ cells were selected. These cells were then plotted on podocalyxin and nephrin axes (right panel). Nephrin$^+$/podocalyxin$^+$ cells were gated for sorting.

8. Pilot transcriptomic analysis of nephrin^{+}/podocalyxin^{+}/LTL^{-} cells

Since our main objective was to obtain transcriptomic profiles from kidney organoid-derived podocytes in order to identify relevant dysregulated processes related to the disease, we wondered whether these nephrin^{+}/podocalyxin^{+}/LTL^{-} FACS-sorted cells, theoretically corresponding to podocytes, displayed a genuine "podocyte identity". Secondly, we aimed to verify if our experimental conditions for podocyte isolation were suitable to reach the right amount of cells necessary to obtain RNAs of good quality and in sufficient quantity to a subsequently carry out the transcriptomic analysis.

We therefore performed a **pilot analysis** using a single control, 005#04, and one SRNS^{NPHS2} patient-derived cell line, 007#27. Differentiation has been conducted in parallel. Besides nephrin^{+}/podocalyxin^{+}/LTL^{-} presumptive podocytes, we also collected LTL^{+} proximal tubular cells. We FACS-sorted over 70 000 nephrin^{+}/podocalyxin^{+}/LTL^{-} cells from the 005#04 and 007#27 iPSC-derived organoids, ~200 000 LTL^{+} cells from the 005#04 and ~100 000 LTL^{+} cells from the 007#27 iPSC-derived organoids.

The RNA quality was suboptimal but adequate; all samples having an RNA integrity number (RIN) greater than 7.8. We obtained a limited amount of RNA instead, with only 4 ng available from the podocyte samples. However, thanks to a dedicated kit for cDNA libraries construction starting from small amount of RNA, this condition allowed us to perform whole transcriptome next-generation sequencing (NGS) at the Genomic Platform of the *Imagine Institute*, obtaining ~50 million reads per sample.

A) Podocyte identity

Unsupervised clustering clearly separated the nephrin^{+}/podocalyxin^{+}/LTL^{-} population from the LTL^{+} one (Fig. 52A). Not surprisingly, samples shared more similarity according to the cell type, which shaped their transcriptome more deeply than their genetic background.

Afterwards, I focused on the nephrin^{+}/podocalyxin^{+}/LTL^{-} population. In order to verify if they well correspond to podocytes, I assembled a **consensus list of 124 podocyte-related genes** based on selected publications that report genes expressed in GFP^{+} fraction isolated from NPHS1^{GFP} kidney organoids[278], podocyte cluster of newborn mouse kidney[403], a panel of 100 human glomerular enriched genes[279] and podocyte cluster markers in kidney organoids[405] (Fig. 52B). The greatest majority of the preselected genes - 108/124 (87.1%) - were found to be expressed at a level above the 95th percentile in the control, with 71 of them (68.3%) even over the 99th percentile (Appendix, Table A1). The same enrichment at the top mostly expressed genes in nephrin^{+}/podocalyxin^{+}/LTL^{-} FACS-sorted cells was equally observed when averaging the 005#04 and 007#27 expression levels (data not shown). Very well established podocyte markers such as *NPHS1, NPHS2, PODXL, WT1* and *MAFB* were

comprised among the 50 genes with the highest level of expression (Table 3). All these observation confirmed that the nephrin^{+}/podocalyxin^{+}/LTL^{-} FACS-sorted population is effectively composed by - and will be hereafter referred to as - **podocytes**.

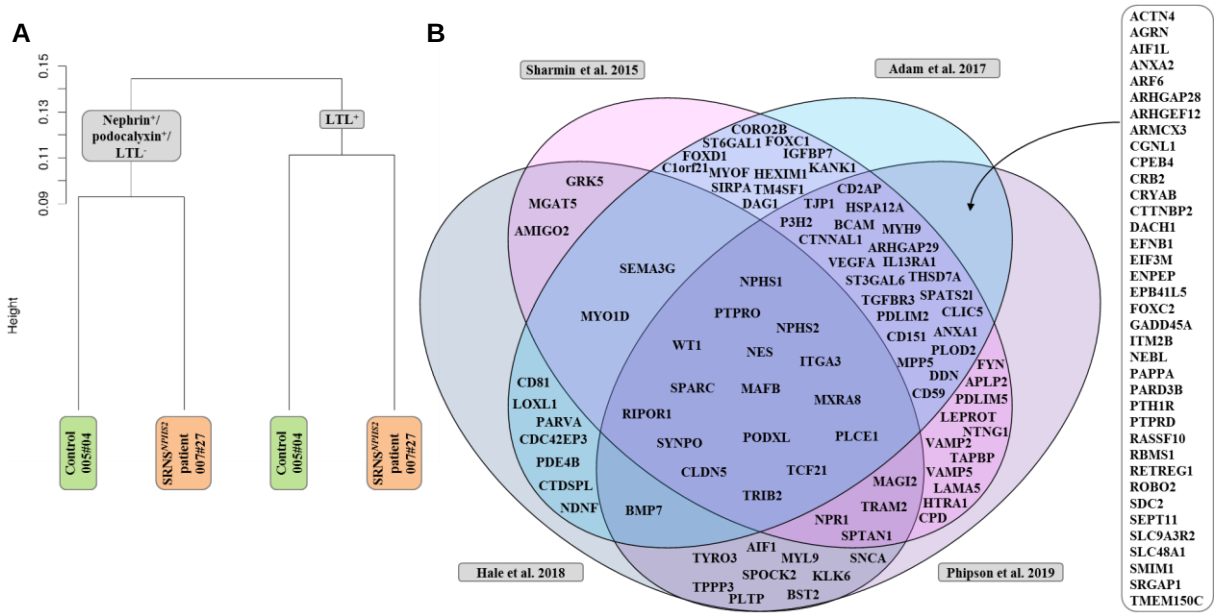

Figure 52: RNA-Seq pilot analysis. **A)** Unsupervised clustering. Control 005#04 (green) and patient 007#27 (orange) kidney organoid-isolated nephrin^{+}/podocalyxin^{+}/LTL^{-} putative podocytes cluster together and apart from the LTL^{+} proximal tubular cells. Clustering has been performed using the average linkage method[406] on DESeq2 normalized P50 gene list. **B)** Venn diagram of podocyte-related genes reported by *Sharmin et al. 2015* [278], *Adam et al. 2017* [403], *Hale et al. 2018* [279] and *Phipson et al. 2019* [405]. A consensus list of 124 podocyte-related genes was established by selecting genes reported by at least 2 of the publications mentioned above.

Table 3: Podocyte-related genes comprised in the top 50 most expressed genes

#	Gene	Name	005#04	007#27
2	*PODXL*	podocalyxin like	71953.54	65642.42
4	*PTPRO*	protein tyrosine phosphatase, receptor type O	31961.41	30391.48
6	*TJP1*	tight junction protein 1	25864.66	26048.66
15	*CLIC5*	chloride intracellular channel 5	16992.16	14602.41
16	*TGFBR3*	transforming growth factor beta receptor 3	16722.83	14745.04
18	*SPARC*	secreted protein acidic and cysteine rich	14631.55	14044.32
19	*PTPRD*	protein tyrosine phosphatase, receptor type D	13886.13	14305.53
20	*MYH9*	myosin heavy chain 9	13683.51	13633.00
22	*MAFB*	MAF bZIP transcription factor B	13482.54	10851.67
25	*VEGFA*	vascular endothelial growth factor A	12848.32	11330.15
26	*THSD7A*	thrombospondin type 1 domain containing 7A	12698.41	8378.00
31	*ROBO2*	roundabout guidance receptor 2	11471.15	8949.35
33	*MAGI2*	membrane associated guanylate kinase, WW and PDZ domain containing 2	11362.43	13137.11
34	***NPHS2***	NPHS2, podocin	11292.42	5890.22
35	*ENPEP*	glutamyl aminopeptidase	10794.93	6822.31
38	*ITM2B*	integral membrane protein 2B	9863.36	7081.04
39	*NPHS1*	NPHS1, nephrin	9318.10	7569.47
41	*SPTAN1*	spectrin alpha, non-erythrocytic 1	9080.88	8780.19
43	*SEPT11*	septin 11	8978.75	7235.28
44	*LAMA5*	laminin subunit alpha 5	8952.39	8089.41
46	*WT1*	Wilms tumor 1	8580.10	7662.35
48	*MPP5*	membrane palmitoylated protein 5	8090.02	7748.59

Table reporting the podocyte-related markers that are comprised among the 50 most expressed genes in the control. The first column (#) indicates the position ranking of genes classed by expression level in the control. The last columns report the DESeq2 normalized gene expression level in control (005#04) and SRNS^{NPHS2} patient (007#27) kidney organoid-isolated podocytes. *NPHS2* is highlighted in bold.

B) Maturation degree

Since all kidney organoid differentiation protocols share the same problem of the lack of maturity, we wondered how to determine the maturation stage of our FACS-sorted podocytes. The expression of "mature" markers of differentiation, especially the presence of nephrin and podocin, which are first expressed *in vivo* at the S-shaped body stage, was already validated at the protein level by IF. Here, their great expression level is a convincing confirmation of the relative maturity of podocytes in kidney organoids.

The GBM is composed of a network of laminin and type IV collagen and its composition evolves during glomerulogenesis. In immature GBM, the network is mainly composed of **laminin α1β1γ1** chains and **type IV collagen α1α2α1** chains. As glomerulogenesis progresses, a switch occurs towards **laminin α5β2γ1** and **type IV collagen α3α4α5** chains. Therefore, the expression of specific isoforms of laminin and collagen is indicative of the GBM maturation and consequently of podocytes. Interestingly, I found that the most expressed isoforms of **laminin** were the **α5, γ1 and β2 chains** in that order, figuring in the top 200 most highly expressed genes (Table 4 and Appendix, Table A2). **Laminin β1** chain was also strongly expressed, while **α1** was detected at a lower extent. On the same principle, **type IV collagen α5** and **α1 and α2 chains** were abundantly expressed, but type IV collagen α3 and α4 chain expression was week (Table 4 and Appendix, Table A2). Abundant mature GBM laminin isoforms co-existing with ones of the immature GBM, as well as a similar pattern of type IV collagen chain expression, have already been reported in glomeruli isolated from kidney organoids[279]. Laminin α1 to α5 switch occurs rapidly *in vivo* at the capillary loop stage, while β1 persists concomitantly with β2 upregulation, before to decline with progressive glomerular maturation[38,407]. Type IV collagen α1α2α1 is found until late capillary loop stage, when α3α4α5 starts to appear[38]. Laminin and type IV collagen expression pattern is therefore consistent with a capillary loop stage of development.

Table 4: Glomerular laminin and collagen IV isoforms

#	Gene	Name	State	005#04	007#27
Laminins					
44	*LAMA5*	laminin subunit alpha 5	Mature	8952.39	8089.41
77	*LAMC1*	laminin subunit gamma 1	Immature/Mature	6136.29	4914.18
155	*LAMB2*	laminin subunit beta 2	Mature	4236.10	3227.47
602	*LAMB1*	laminin subunit beta 1	Immature	1878.77	2936.40
7257	*LAMA1*	laminin subunit alpha 1	Immature	149.91	144.29
Collagens					
200	*COL4A2*	collagen type IV alpha 2 chain	Immature	3601.88	4264.05
529	*COL4A1*	collagen type IV alpha 1 chain	Immature	2050.92	3141.23
722	*COL4A5*	collagen type IV alpha 5 chain	Mature	1692.63	1470.27
6758	*COL4A4*	collagen type IV alpha 4 chain	Mature	172.15	619.46
8921	*COL4A3*	collagen type IV alpha 3 chain	Mature	93.90	305.17

Table reporting the glomerular laminin and collagen IV isoforms. The first column (#) indicates the position ranking of genes classed by expression level in the control. The "state" column classify the laminin and collagen IV isoforms as "immature" or "mature" based on their abundance in the developing or mature GBM, respectively. The last columns report the DESeq2 normalized gene expression level in control (005#04) and SRNS^{NPHS2} patient (007#27) kidney organoid-isolated podocytes.

I also took advantage of a piece of evidence coming from single-cell (sc) transcriptomic analysis of kidney organoids addressing to maturity "quantification"[375]. Conversely to differentiation-related genes, developmental markers such as *OSR1* and *POU3F* were almost undetectable. Finally, I checked the expression of transcription factors identified in adult human podocytes[375]. Albeit only a small fraction of them (18.4%) has been reported to be expressed by podocytes in organoids differentiated either with the Takasato's or with the Morizane's protocol, I found 24/38 (63.2%) transcription factors exceeding the 95th percentile, 9 of which (23.7%) above the 99th one, such as *TULP4*, *DACH1* and *BAZ2B* (Appendix, Table A3).

In light of these observations, I was confident enough about the maturity degree achieved, which seemed to be at least comparable to what reported in literature, namely most likely corresponding to a capillary loop stage.

C) Preliminary comparison of patient *versus* control podocytes

Once the podocyte identity of nephrin^{+}/podocalyxin^{+}/LTL^{-} FACS-sorted cells has been demonstrated and their maturity evaluated as adequate to perform relevant molecular analysis in a podocyte-specific pathological context, I performed a **preliminary analysis comparing patient *versus* control podocyte transcriptomic profiles**, even though no replicates could be made for this pilot experiment with a 1 *versus* 1 analysis preventing the possibility of any statistical analysis.

The SRNS^{NPHS2} 007 patient iPSC line harbors a homozygous mutation in the *NPHS2* gene leading to the p.R138Q substitution in the podocin. I thus firstly checked the relative **expression of *NPHS2***. I found it was **reduced by half** in the patient compared to the control (Table 3). This observation was the opposite of what has been reported in podocin R140Q mouse models[183,408]. Likewise, **candidate gene investigation** based on data obtained from Nphs2$^{R140Q/R140Q}$ and Nphs2$^{-/-}$ mice[183] failed to evidence a good correlation between the expression patterns of mutant/wild-type mice and patient/control podocytes (Table 5).

Table 5: Candidate gene expression in Nphs2 mouse models and SRNS^{NPHS2} 007#27 podocytes

		Nphs2$^{R140Q/R140Q}$		Nphs2$^{-/-}$		007#27
Gene	**Name**	**P4**	**P12**	**P5**	**P12**	
Nphs1	Nephrin	0.80±0.19 ↓	0.87±0.20 ↓	1.94±0.84 ↑	0.58±0.20* ↓	0,81 ↓
Cd2ap	CD2-associated protein	1.83±0.43* ↑	1.52±0.19 ↑	1.38±0.17 ↑	1.05±0.15	1,44 ↑
Trpc6	Transient receptor potential channel 6	Undetectable	0.92±0.33	1.06±0.53	0.48±0.11 ↓↓	1,31 ↑
Plce1	Phospholipase Cε-1	1.31±0.24 ↑	0.91±0.20	1.96±0.81 ↑	0.45±0.21* ↓↓	0,84 ↓
Wt1	Wilms' tumor homolog	1.43±0.43 ↑	1.01±0.38	1.09±0.21	0.79±0.20 ↓	1,00
Lmx1b	Lmx1b transcription factor	1.09±0.38	0.64±0.37 ↓	0.93±0.22	0.72±0.28 ↓	0,83 ↓
Tcf21	Transcription factor 21	1.37±0.36 ↑	1.47±0.30 ↑	0.78±0.21 ↓	0.81±0.27 ↓	1,00
Mafb	MAF bZIP transcription factor B	1.84±0.43 ↑	2.29±0.90* ↑↑	1.05±0.33	0.83±0.29 ↓	0,80 ↓
Zhx1	Zinc fingers and homeoboxes 1	1.80±0.32 ↑	1.56±0.50 ↑	0.80±0.13 ↓	0.67±0.13* ↓	0,88 ↓
Zhx2	Zinc Zinc fingers and homeoboxes 2	1.50±0.40 ↑	1.86±0.70* ↑	1.14±0.24 ↑	0.77±0.31 ↓	0,82 ↓

(Continued)

Table 5 | *Continued*

Zhx3	Zinc fingers and homeoboxes 3	1.82±0.49 ↑	1.29±0.36 ↑	1.01±0.40	0.99±0.46	1,04
Vegfa	Vascular endothelial growth factor-A	1.50±0.25 ↑	0.59±0.09 ↓	0.83±0.17 ↓	0.59±0.18 ↓	0,88 ↓
Serpine1	Plasminogen activator inhibitor-1	5.43±1.98* ↑↑	7.98±2.62* ↑↑	4.26±0.77* ↑↑	4.28±1.62 ↑↑	18,63 ↑↑
Tgfb1	Transforming growth factor-β	1.44±0.26 ↑	2.07±0.60* ↑↑	1.27±0.28	0.90±0.14	0,70 ↓

Table reporting candidate gene fold change expression in $Nphs2^{R140Q/R140Q}$ and $Nphs2^{-/-}$ mouse models and in $SRNS^{NPHS2}$ 007#27 patient kidney organoid-isolated podocytes. $Nphs2^{R140Q/R140Q}$ and $Nphs2^{-/-}$ mean expression level (± SD) compared to wild-type mice have been taken from *Philippe et al. 2008* [183] (P, postnatal day). The last column (007#27) reports the fold change expression in the $SRNS^{NPHS2}$ patient compared to control. Up- and down-regulated genes are indicated with red and green arrows respectively (2 arrows indicate a fold change expression >2).

Gene ontology (GO) analysis was performed on genes with a fold change above 2, excluding the ones having a low difference between the samples to reduce the effect of the background. Upregulated genes in $SRNS^{NPHS2}$ 007#27 patient podocytes were found enriched in antiviral immunity, protein folding or degradation, cell adhesion and nucleic acid binding or transcriptional regulation categories. Downregulated genes were indeed related to cell adhesion and cell junction roles.

The comparison of patient and control-derived podocytes was poorly conclusive, the presence of a single podocyte sample for each category being the major limitation. Anyhow, the identification of pathological mechanisms was beyond the scope of this pilot analysis, which had a positive outcome concerning the most important points of podocyte identity and maturity. The results obtained were globally encouraging, which led us conclude we could apply the same experimental procedures to a larger number of samples to perform proper comparisons.

9. Vascularization Attempts

In order to reproduce more faithfully the features of the GFB, one of its basic components, endothelial cells, being absent in kidney organoids, we sought to vascularize them. Integration of a proper capillary component in our system would have allowed us to dispose of a more relevant model to study **structural and functional alterations** related to NS. It would have also been favorable to push **podocyte maturation** further.

At the time we considered to perform vascularization attempts, the only work presenting vascularized kidney organoids - and glomeruli - was published by Dr. R. Nishinakamura's laboratory[10,278]. They performed *in vivo* transplantation of spinal cord-induced nephron progenitor aggregates under the renal capsule of immunodeficient mice. I proposed instead to perform ***in ovo* transplantation** of kidney organoids **on the chick embryo chorioallantoic membrane** (CAM) (Fig. 53 and 54). I considered this approach as an option after having assisted to a talk given by Pr. M. Little at the ISSCR 2017 Annual Meeting in Boston, in which she presented preliminary unpublished results.

I set up collaboration with Pr. S. Saule (Unit Director of the UMR3347/U1020 "Signalizations, Radiobiology and Cancer" at the *Curie Institute*) and I was trained to the *in ovo* transplantation technique by Dr. E. Indersie (PostDoctoral Researcher in the Dr. O. Ayrault's team "Signalization, development and cerebral tumors" at the *Curie Institute*). Our first concern was the detection of organoids after deposition on the CAM, given their small size. According to Dr. E. Indersie's experience, we decided to use sterile plastic rings to confine the zone where the organoid was deposed (Fig. 53B). We transplanted differentiated kidney organoids at D23 and D30.

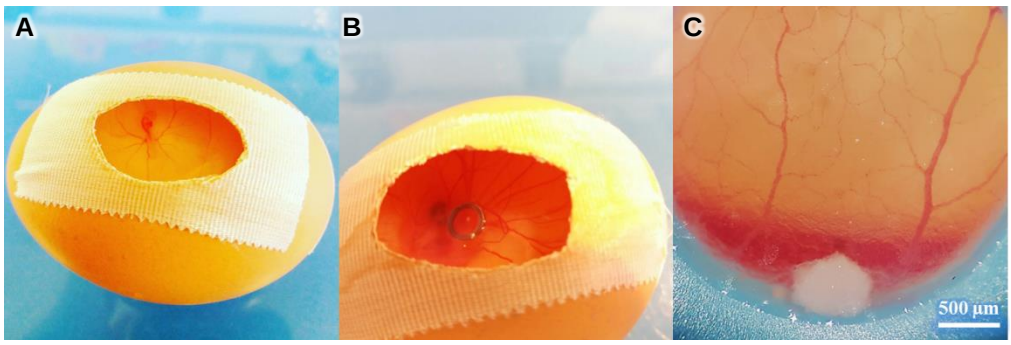

Figure 53: Kidney organoid *in ovo* transplantation. **A)** E3 chick embryo. A window has been opened on the top of the egg before the CAM developed and attached to the shell. At that time the embryo is distinguishable and it is possible to perceive heart beating. **B)** Deposition of a kidney organoid on the CAM at E6 on a zone delineated by a sterile plastic ring. The kidney organoid is visible as a white spot at the center of the plastic ring. **C)** Kidney organoid stuck on the plastic ring upon transplantation. During the follow-up, transplanted kidney organoids slides on the side and acquired white spongy appearance.

Almost all the transplanted organoids slid to one side and settled on the plastic ring. They had white spongy appearance (Fig. 53C). In some cases the CAM dehydrated at the ring level, which resulted in deformation and keratinization of the zone. None of the transplanted organoids survived the procedure. We excluded the use of the plastic ring for the following experiments since they were neither suitable for maintaining CAM integrity, nor to facilitate organoids hanging on the membrane.

While the first experience was performed at the *Curie Institute*, we equipped our laboratory for the following ones. I encountered problems of **chick embryos mortality** at first, that I solved by both adjusting the temperature and humidity of the egg incubator and by progressively improving my handling skills. I tested several conditions, including the variation of organoids number from 1 to 10 per egg, the age of the organoids (D21 *versus* D30), the inclusion in Geltrex matrix at a 2:3 or 3:4 ratio with BDM, the addition of VEGF 10 ng/ml or FGF2 10 ng/ml pro-angiogenetic factors, the scratching of the membrane before transplantation and the dissociation or withdrawal of clusters of D9 NPCs.

Altogether, I employed a total of 180 fertilized chick eggs, 110 of them (61.1%) received the renal explant between embryonic developmental day 6 to 8 (E6 to E8). 73 chick embryos (66.4% of the transplanted) survived until the end of the procedure at E14. Among them, I obtained **one single potential vascularized organoid** (Fig. 54).

The condition that worked consisted in the deposition of 10 D21 kidney organoids embedded into Geltrex matrix on the CAM at E7. Particularly, these organoids were obtained from the SRNS^{NPHS2} 007#27 patient iPSC line.

Until 2 days post-transplantation (E8 and E9), distinct organoid masses were still discernible on the CAM. At E10, **infiltration of host blood vessels** into a fused lacteal structure was appreciable. Vasculature further maturated the following days, forming small spots that could have been attributable to presumptive glomerular tufts (E11 and E13). Unexpectedly, the structure had a more disorganized appearance by the day of sample collection, at E14 (Fig. 54A). This vascularized graft was collected for further histological analysis (Fig. 54B).

Histological observation revealed the presence of identifiable renal structures on the CAM, comprising both **tubules** and **podocytes** (Fig. 54C). Under TEM, podocyte-like cells were recognized to wrap around chick blood vessels (of note, chick erythrocytes are nucleated cells), extending cellular processes reminiscent of FPs (Fig. 54D).

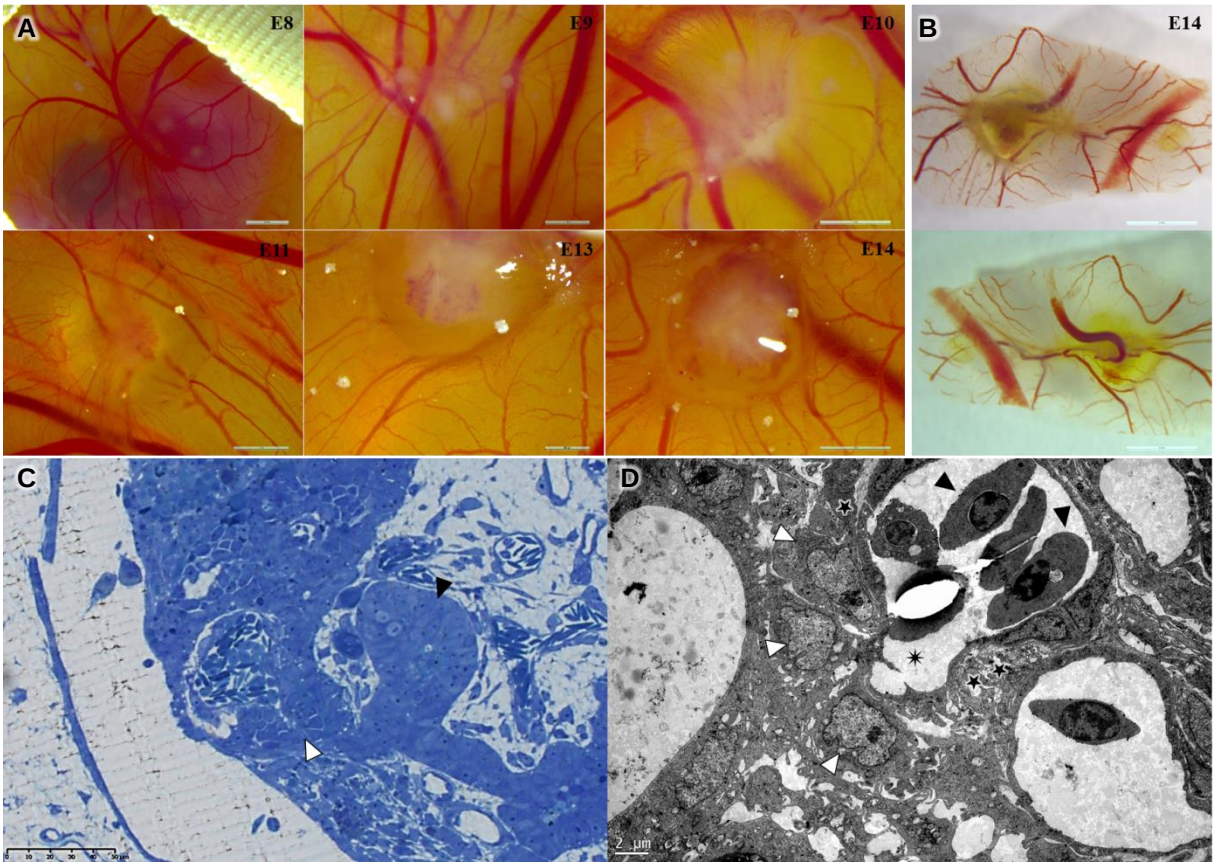

Figure 54: Kidney organoid vascularized on the chick embryo CAM. **A)** Follow-up of the graft from E8 to E14. Starting from E10 it is possible to appreciate invasion of host vessels into the graft. The previously separated kidney organoids partially fused. Between E11 and 13, the vasculature seems to arrange into a branching organization, ending in small spherical structures at the tips; a framework that has disappeared by E14. **B)** Kidney organoid transplant gathered from the CAM. Front (upper panel) and back (lower panel) sides. **C)** Semi-thin section of the graft stained with Toluidine blue. Podocytes (white arrow). Tubules (black arrow). **D)** Kidney organoid graft under transmission electron microscopy. Podocyte-like cells (white arrows), cellular processes (stars), blood vessel lumen (asterisk), chick erythrocytes (black arrows).

Seeking for the optimal conditions to robustly vascularize kidney organoids on the chick embryo CAM turned out to be sensibly time-consuming. A variety of parameters still required proper-setting up, including the choice of the most suitable differentiation stage of organoids and several technical aspects of manipulation during the graft.

Meanwhile, other research groups have succeeded in vascularizing kidney organoids by transplanting either NPCs sub-cutaneously[278,382], or fully differentiated kidney organoids under the renal capsule[280] in immunocompromised mice. We thus hesitated between an intermediate step of progenitors, or organoids that have completed their differentiation, since both conditions have been shown to work; at least in mouse. Secondly, we wondered about eventual species barrier that would disfavor human organoids survival in an avian environment.

Only more recently, kidney organoid vascularization on the chick embryo CAM has been published by Dr. N. Montserrat's laboratory[376], demonstrating the suitability of this highly accessible and fascinating tool for sustaining organoid biology.

RESULTS

Part 2: Disease modeling

In this part of my PhD thesis dissertation, I will report the work I performed aimed to unravel new pathological mechanisms underlying hereditary renal and nephro-cerebral diseases.

I will deal with:

- **Steroid-resistant nephrotic syndrome**

Here I present work related to the phenotypic characterization of SRNS^{NPHS2} patient-derived kidney organoids. The results are presented in the form of article (**Article 2**, in preparation), although some of the analysis is still in progress and unfortunately incomplete at the time of writing my thesis manuscript. Consequently, a brief discussion was added at the end of the article. A more exhaustive discussion will be proposed in the general "Discussion" section. I will also provide supplementary results that are complementary to the article

- **Galloway-Mowat syndrome**

Here I report phenotypic characterization of GAMOS^{GON7} and GAMOS^{OSGEP} patient-derived kidney organoids and late cortical progenitor cells, modeling both the renal and neurological aspects of the disease.

Early-onset SRNS
Podocin p.R138Q

1. Introduction to Article 2

The objective of my PhD has been to unravel new actors and molecular networks driving podocyte differentiation and/or maintenance, and to identify new pathophysiological mechanisms leading to hereditary SRNS.

The work I have done on 007 SRNS^{NPHS2} patient-derived kidney organoids is presented as an article that has to be further completed before submission (**Article 2**). As a reminder, the 007 iPSC line is derived from a patient with early-onset SRNS and bearing a mutation in the *NPHS2* gene that leads to podocin p.R138Q substitution (Results, Part 1, Table 2). The *NPHS2* gene has a particular significance for Pr. C. Antignac's laboratory, since it has been identified by the group[60], and the p.R138Q is the most common pathogenic mutation associated to SRNS in Europe. At the time I started kidney organoid differentiation, only a few studies on tubular disorders using kidney organoids[7] were published. Since this particular mutation leads to an early and severe kidney phenotype, we first started with this patient iPSC line to confirm the relevance of using kidney organoids to model glomerular diseases, and to gain more insights into the pathology.

I demonstrated, by differentiating 007 SRNS^{NPHS2} iPSCs into kidney organoids that these latter display lower expression level and altered subcellular localization of p.R138Q podocin, with diffuse perinuclear staining. Upon CRISPR/Cas9-mediated correction of patient iPSCs, we succeeded in rescuing the proper podocin localization and expression level.

Moreover, I investigated the transcriptomic profile of FACS-sorted podocytes to gain insights into the molecular mechanisms underlying the disease. Unexpectedly, RNA-Seq data from these cells suggest implication of an interferon-like response activation in p.R138Q patient podocytes, although further analyses are required to discriminate between a mutation effect or the influence of the patient genetic background.

Article 2

CRISPR/Cas9-mediated rescue of the mutant p.R138Q podocin mislocalization in steroid-resistant nephrotic syndrome patient-derived kidney organoids

Giulia Menara, Bruno Estèbe, Aurélien Juven, Mikaëlle Bocel, Nathalie Lefort, Céline Banal, Nicolas Goudin, Alain Schmitt, Christine Bole, Nicolas Cagnard, Corinne Antignac & Géraldine Mollet

(in preparation)

Original article

CRISPR/Cas9-mediated rescue of the mutant p.R138Q podocin mislocalization in steroid-resistant nephrotic syndrome patient-derived kidney organoids

Giulia Menara[1], Bruno Estèbe[1], Aurélien Juven[1], Mikaëlle Bocel[1], Nathalie Lefort[1,2], Céline Banal[1,2], Nicolas Goudin[3], Alain Schmitt[4], Christine Bole[5], Nicolas Cagnard[6], Corinne Antignac[1,7], Géraldine Mollet[1]*

[1] Université de Paris, *Imagine Institute*, Laboratory of Hereditary Kidney Diseases, Inserm UMR 1163, Paris, France
[2] iPS cells Platform, *Imagine Institute*, Inserm UMR 1163, Paris, France
[3] Imaging Platform, *Imagine Institute*, Inserm UMR 1163, Paris, France
[4] Electron microscopy Platform, *Cochin Institute*, Paris, France
[5] Genomics Platform, *Imagine Institute*, Inserm UMR 1163, Paris, France
[6] Bioinformatic Platform, *Imagine Institute*, Inserm UMR 1163, Paris, France
[7] Département de Génétique, *Assistance Publique - Hôpitaux de Paris, Hôpital Necker-Enfants Malades*, Paris, France

*Corresponding author
geraldine.mollet@inserm.fr

Abstract

Hereditary steroid-resistant nephrotic syndrome (SRNS) is a mainly autosomal recessive glomerulopathy characterized by a massive leakage of protein in the urine. Podocyte damage is a hallmark event in SRNS pathogenesis, leading to structural alterations of the glomerular filtration barrier. We have obtained patient cells harboring a homozygous missense mutation in the *NPHS2* gene encoding podocin, which is responsible for the p.R138Q substitution. This is the most frequent mutation leading to early-onset SRNS that rapidly progress to end-stage kidney disease. Here we present work comparing patient *versus* healthy control kidney organoids differentiated from induced pluripotent stem cells (iPSCs). Mutant organoids display lower expression level and altered subcellular localization of p.R138Q podocin, with a diffuse perinuclear staining indicative of endoplasmic reticulum retention. We have succeeded in rescuing this phenotype and observed proper podocin re-localization upon CRISPR/Cas9-mediated correction of patient-derived iPSCs. We finally investigated the transcriptomic profile of podocytes isolated from organoids in order to gain insights into the molecular mechanisms underlying the disease. Unexpectedly, RNA-Seq data analysis suggests implication of an interferon-like response activation in patient podocytes.

Introduction

Nephrotic syndrome is due to structural alterations of the glomerular filtration barrier (GFB), which constitutes the filtration apparatus of kidneys. The GFB is a three-layered structure composed by a fenestrated endothelium, the glomerular basement membrane and the podocyte. Podocytes are highly specialized epithelial cells enwrapping glomerular capillaries with their interdigitated cellular processes, called foot processes (FPs). A specialized inter-cellular junction, the slit diaphragm (SD), bridges adjacent FPs, acting as a molecular mesh that prevents urinary excretion of high molecular weight plasma proteins. Any injury occurring at the podocyte level induces FP effacement and loss of the SD, leading to structural alterations of the GFB and consequently to urinary protein leakage, which is the main feature of NS. Genetic studies of hereditary NS led to the identification of almost 50 genes that, if mutated, are responsible for monogenic forms (Preston et al. 2019). Among them, *NPHS1* and *NPHS2* (Boute et al. 2000; Kestilä et al. 1998), the major genes involved in steroid-resistant NS (SRNS), encode nephrin and podocin, respectively, which are essential component of the SD.

Over the past years, *in vitro* studies of hereditary NS using human and mouse podocyte cell lines have greatly advanced our knowledge of podocyte biology. However, these models have limitations, particularly the absence of a three-dimensional structure required to fully recapitulate the complex organization of the GFB, making glomerular

disorders currently challenging to model. The advent of induced pluripotent stem cells (iPSCs) has opened up new avenues for *in vitro* disease modeling. Indeed, their pluripotent ability, coupled with indefinite self-renewal capacity, allow to dispose of a powerful tool almost limitless in availability and conceivable applications. Since iPSCs can be directly derived from easily accessible patient cells, this technique allows modeling of kidney disease with cells with the patient's own genetic background. Several groups had recently succeed in recreating *in vitro* appropriate conditions leading iPSCs to undertake a renal fate (Morizane et al. 2015; Taguchi et al. 2014; Takasato et al. 2015). Differentiation is directed by applying specific stimuli that are spatiotemporally integrated by cells, thus recapitulating the sequential stages of embryonic kidney development. Kidney organoids have recently emerged as powerful tools in modeling renal diseases. Since they contain almost all the different segments of the nephron, from the glomerulus to the proximal and distal tubules, organoids were first used to model tubular diseases such as autosomal dominant polycystic kidney disease (ADPKD) (Freedman et al. 2015; Cruz et al. 2017), which is the most common hereditary kidney disease, characterized by formation of cysts in tubules (Torres, Harris, and Pirson 2007), or to model nephronophthisis (Forbes et al. 2018), a rare renal ciliopathy. With regards to SRNS, two groups recently used kidney organoids to model SRNS linked to *NPHS1* mutations. The first group highlighted a defective translocation to the cell surface of mutant nephrin in kidney organoids differentiated from patient-derived iPSCs bearing a homozygous missense mutation in *NPHS1*. Mutant podocytes failed to form "pre-SD domains", or proper SDs upon *in vivo* vascularization (Tanigawa et al. 2018). Similarly, organoid-derived glomeruli, obtained from a compound heterozygous patient with *NPHS1* mutations and congenital NS, display hypertrophic podocytes with markedly reduced proteins levels of both nephrin and podocin (Hale et al. 2018).

Here, we have obtained patient-derived iPSCs harboring homozygous c.413G>A missense mutation in the *NPHS2* gene leading to arginine to glutamine amino acid substitution at position 138 of podocin (p.R138Q), which is the most frequent mutation leading to early-onset SRNS (Boute et al. 2000; Hinkes et al. 2007). In this study, we describe the generation and characterization of kidney organoids differentiated from the p.R138Q patient iPSC line and from the p.R138Q-corrected patient iPSC line upon CRISPR/Cas9 gene editing. We show that p.R138Q podocin is expressed at a lower level and displayed an altered subcellular localization in patient-derived kidney organoids, characterized by a perinuclear staining pattern. Conversely, gene correction by CRISPR/Cas9 rescued these defects. Finally, to get further insight into the potential dysregulated molecular pathways that could contribute or accompany the development of the disease linked to this particular mutation, we performed transcriptomic analysis on podocytes isolated from the p.R138Q patient-derived kidney organoids and observed an unexpected activation of an interferon-like response transcriptomic signature in these patient podocytes.

Results

p.R138Q podocin-mutated iPSCs differentiation into kidney organoids

Peripheral blood mononuclear cells (PBMCs) were obtained from a patient affected with SRNS and harboring the homozygous p.R138Q mutation and from three healthy individuals. After PBMCs reprogramming by non-integrative Sendai viral transduction (Menara et al. 2020), two independent iPSC clones were selected for the patient (007#27 and 007#34) and one clone for each control (005#04, 009#02 and 013#19). These iPSC lines were differentiated into kidney organoids adapting an already published protocol (Morizane and Bonventre 2017) (**Fig. 1A**).

Differentiations, performed on patient- and healthy control-derived iPS cell lines, displayed similar progression throughout the protocol steps (**Fig. S1**). Particularly, the pivotal emergence of nephron progenitor cells (NPCs) was evidenced by morphological changes occurring in the culture around differentiation day 9 (D9), when clusters of epithelial structures tended to emerge, most probably corresponding to pretubular aggregates or very early renal vesicles (Morizane and Bonventre 2017) (**Fig. 1B**). We further validated the identity of these progenitors by performing immunofluorescence staining for SIX2, PAX2 and LHX1, and showed prominent expression of SIX2, the major regulator of multipotent NPC population (Kobayashi et al. 2008), mainly staining nuclei which are disposed in a circular manner (**Fig. 1C**). Some of the cells within or in the proximity of these structures also co-expressed PAX2 and LHX1 (**Fig. 1C**), confirming the nephrogenic potential of induced cells at this stage.

Upon 21 days, elaborated three-dimensional structures emerged in the culture (**Fig. 1D**). Tufts of tangled epithelial architectures indicated the end of differentiation with successful obtaining of kidney organoids. Immunofluorescence staining on these organoids revealed the ordered structural development of $WT1^+$ glomeruli, LTL^+ proximal and $ECAD^+$ distal tubules (**Fig. 1E**). We observed an extensive variability in the differentiation efficiency of the various cell lines as reported in the literature (Freedman 2015). As expected, the p.R138Q mutation did not impair the ability of patient-derived iPSCs to differentiate into kidney organoids. Conversely, the p.R138Q-mutated clones, in particular the 007#27 clone, displayed a very efficient rate of differentiation, consistently producing numerous organoids in most of the experiments carried out. Glomerular-like structures in control and patient-derived organoids stained positive for several podocyte-specific markers such as podocin, WT1, podocalyxin, synaptopodin (**Fig. 2C**) and nephrin (**Fig. 6**).

Altered subcellular localization of p.R138Q podocin in mutant glomeruli

Patient and control kidney organoids display several glomerular-like structures containing a central cluster of cells, occasionally surrounded by a Bowman's capsule-like

structure connected to tubular structures (**Fig. 2A**). Podocyte-like cells in these glomeruli are organized in clusters of polarized octopus-shaped cells extending cellular protrusions, resembling primary and secondary processes, at their basal side towards the center of the glomeruli (**Fig. 2B**). Intercellular junctions were found to connect these basal projections (**Fig. 2C**), but establishment of proper FPs connected by reliable SD is absent in kidney organoids. Whether organoids derived from patient or control iPSCs, the general structure of the glomerulus and cell morphology, as well as podocyte process ultrastructure were not disrupted by the expression of the p.R138Q mutation (**Fig. 2**).

We thus investigated podocin expression at the protein level by immunofluorescence. While the expression of wild-type and p.R138Q mutant podocin was found to be podocyte-specific and concomitant with the presence of the other typical podocyte markers (**Fig. 3D**), we observed a fainter podocin immunostaining in p.R138Q mutant glomeruli compared to controls (**Fig. 3**). This reduced amount of mutant podocin protein is consistent with our previous results reporting massive proteasomal degradation of the p.R138Q podocin (Serrano-Perez et al. 2018). In addition, we noticed that subcellular localization of p.R138Q mutant podocin appeared to be altered with the mutant form showing wide perinuclear localization, conversely to the wild-type podocin that is found to be basally located in podocytes (**Fig. 3**).

Since impairment of the p.R138Q mutant podocin to reach the plasma membrane has already been evidenced in patient biopsies (Zhang et al. 2004) and p.R140Q (the murine p.R138Q equivalent) knock-in mouse models (Philippe et al. 2008), this diffuse perinuclear staining observed in mutant organoids could be indicative of endoplasmic reticulum (ER) retention. Moreover, functional studies using overexpression of the p.R138Q (or mouse p.R140Q) podocin in cellular systems have shown the mutated protein to be retained in the ER (Huber et al. 2003; Nishibori et al. 2004; Ohashi et al. 2003; Roselli et al. 2004). We thus proceeded further to investigate this localization by performing co-immunostaining of podocin with ER markers. We used calreticulin (CALR, **Fig. 4A**), calnexin (CANX, **Fig. 4B**) and the protein disulfide isomerase (PDI, **Fig. 4A**). We observed a certain proportion of podocin to be located into the ER both evidenced by its partial co-localization with the ER markers (**Fig. 4**). Not surprisingly, a fraction of podocin was detected in the ER of control glomeruli (**Fig. 4**, left panels), since podocin has been shown to follow the classical pathway of exocytosis (Roselli et al. 2004), but the vast majority of the protein is abundantly located at the basal plasma membrane. As the p.R138Q podocin is unable to accomplish the whole exocytic pathway, the proportion of the ER located podocin on the total amount of expressed protein would reasonably be higher for the mutant compared to the wild-type form. In an attempt to quantify the relative amount of podocin located into the ER, we applied an imaging analysis based on interactive machine learning (Berg et al. 2019). Upon binary segmentation of the podocin and calreticulin stainings (**Fig. 5A** and **B**), we calculated the Manders' overlap coefficient (Manders et al. 1993) to get the proportion of podocin co-localizing with

calreticulin. The latter was, as expected, significantly higher in p.R138Q glomeruli (~82% in average) compared to control conditions (~57% in average) (**Fig. 5C**). Conversely, the fraction of ER occupied by podocin is slightly higher in controls (~35% *versus* ~24% in average), possibly reflecting the higher stability of the wild-type form (Serrano-Perez et al. 2018) (**Fig. S2**). These results showed that, despite a global reduction of its protein level, the p.R138Q podocin is mainly located in the perinuclear region of the podocyte cell body, corresponding partially to the ER compartment, while it is virtually absent in the basal compartment, in line with its ER retention.

Finally, since it has been shown in co-transfected HEK293 cells that the p.R138Q mutation results in alteration of wild-type nephrin trafficking, without disrupting the interaction between both proteins (Huber et al. 2003; Nishibori et al. 2004), we wondered whether the subcellular localization of nephrin would be impacted by that of podocin p.R138Q in patient-derived kidney organoids. Indeed, nephrin subcellular localization has been shown to be altered in kidney biopsies from patient carrying mutations in *NPHS2* (Zhang et al. 2004) and in R140Q knock-in mouse models (Philippe et al. 2008). Using two different anti-nephrin antibodies, targeting either the intracellular or the extracellular domain (kindly provided by the Tryggvason's laboratory), nephrin was found to localize in the central part of the glomerulus, where podocyte basal protrusions extend, in both control and p.R138Q patient-derived kidney organoids (**Fig. 6** and **Fig. S3**). In our hands, nephrin expression and localization seem to be unaffected by the podocin status, since there was no obvious difference between control and p.R138Q mutated organoids.

Rescue of podocin mislocalization in CRISPR/Cas9-corrected patient organoids

We next proceed with the correction of the p.R138Q mutation in 007#27 patient iPSC line using CRISPR/Cas9 gene editing to revert the observed phenotype. In our CRISPR/Cas9 strategy to obtain knock-in (KI) iPSC clones, we used a single-stranded donor oligonucleotide (ssoDN) carrying the wild-type c.413 G nucleotide and an additional nucleotide substitution, not predicted to be pathogenic nor to modify or create splicing sites, but introduced to increase KI efficiency and to facilitate iPSC clone screening (**Fig. 7A** and **Fig. S4**). This nucleotide change disrupts both the PAM motif, to avoid re-cutting upon homologous recombination, and the recognition site of the BseNI restriction enzyme. We thus successfully obtained gene-corrected isogenic iPSC clones with the p.R138Q mutation at the heterozygous state, as well as CRISPR/Cas9 internal isogenic controls, meaning that these clones were subjected to the same genome editing procedure but without having undergone any modifications. All gene-edited isogenic iPSC clones were verified by Sanger sequencing for the absence of CRISPR off-target indels in the twenty most likely off-target sites (**Table S1**). We then differentiated these gene-edited isogenic iPSC clones to obtain kidney organoids. All of them gave rise to organoids similarly to the other iPSC clones. We then investigated

podocin expression pattern in the corrected iPSC clones compared to the internal isogenic control and to the unedited 007 patient iPSC clones. As expected, internal unmodified controls displayed the same mislocalization phenotype previously described for organoids carrying the podocin p.R138Q mutation (**Fig. 7B**). Conversely, in the gene-corrected organoids, podocin correctly re-localized at the basal membrane of podocytes (**Fig. 7C**) thereby confirming the correction of the mutation at the protein level.

p.R138Q podocytes transcriptional profile

Although a recent study allowed a better understanding of the defective trafficking and degradation mechanisms of the p.R138Q mutant podocin (Serrano-Perez et al. 2018), little is known about possible alterations in molecular pathways. Since the podocin p.R138Q mutation is responsible for early manifestation of SRNS, we reasoned that iPSC-derived kidney organoids, which correspond to an embryonic nephrogenic state (Takasato et al. 2015), could recapitulate the initial molecular events whose dysregulation underlies the establishment of the disease. In order to unveil such processes, we set up a fluorescence-activated cell sorting (FACS) protocol to isolate a pure population of nephrin^{+}/podocalyxin^{+}/LTL^{-} podocyte-like cells from dissociated kidney organoids. We performed two independent differentiation experiments for the p.R138Q 007#27 iPSC clone and four independent differentiation experiments for two control iPSC clones, the 005#04 line collected in triplicates, and the 013#19 line. We thus investigated the transcriptomic profile of patient and control-derived podocytes by RNA-Seq.

Unsupervised clustering did not separate podocin p.R138Q from control samples (**Fig. 8A**), underlying a greater variability from one differentiation to another rather than an effect of the causative mutation and even of the genetic background. Anyway, all the nephrin^{+}/podocalyxin^{+}/LTL^{-} cells strongly expressed podocyte-related markers. Specific genes such as *WT1*, *MAFB*, *NPHS1* and *PODXL* were found to be in the top 50 most highly expressed genes (**Table S2**), confirming the podocyte identity of these sorted cells. Unexpectedly, a strong immunity signature was significantly present in p.R138Q mutant podocytes. Indeed, upregulated genes (**Table S3** and **Fig. 8B**) were enriched for "type I interferon signaling pathway", "antigen processing and presentation […] via MHC class I" and "defense response to virus" gene ontology (GO) categories (Thomas et al. 2003) (**Fig. S5**). The interferon signaling (**Fig. 8C**), and within it the response to interferon α and β (type I) in particular, displayed a positive z-score upon ingenuity pathway analysis, indicating an activation of the pathway (**Fig. 8D**). Significantly downregulated genes (**Table S4**) were not enriched for any biological process, molecular function or cellular component GO categories. While the results of RNA-Seq data strongly suggest the activation of interferon type I-like response activation, validation of this signature is pending.

Discussion

In this study, we intended to develop iPSC-derived kidney organoid culture to obtain a meaningful "SRNS in a dish" model, compared to already existing cellular models such as immortalized human and mouse podocyte cell lines that have reached theirs limits. Improving *in vitro* podocyte models becomes necessary to better understand the pathological mechanisms that underlay podocyte dysfunction in patients with mutations in known NS genes or in new candidate genes to prove their pathogenicity.

Here, we generated iPSCs from a SRNS patient carrying the most frequent mutation leading to early-onset SRNS, that is, the mutation in the *NPHS2* gene leading to the p.R138Q substitution in podocin. We successfully differentiated kidney organoids that recapitulate the organization of *in vivo* nephrons. While in conditionally immortalized podocyte cell lines the expression of SD proteins that characterize mature podocytes, such as nephrin and podocin, is extremely variable, even sometimes absent (Chittiprol et al. 2011), we could robustly maintain it in the kidney organoid system. Remarkably, we were able to evidence a defect in endogenous p.R138Q podocin mutant amount and subcellular localization. We did not evidenced any difference in nephrin expression instead, which seemed to be unaffected by the podocin status.

Current literature is essentially in agreement with the fact that p.R138Q podocin is retained into the ER (Huber et al. 2003; Nishibori et al. 2004; Ohashi et al. 2003; Roselli et al. 2004) to be afterwards degraded by the proteasome (Serrano-Perez et al. 2018). Here we show that the p.R138Q podocin is mainly located in the perinuclear region of the podocyte cell body, which includes the ER compartment. We thus confirmed its impairment in reaching the basal membrane domain, by observing for the first time the expression pattern of the human p.R138Q podocin at the homozygous state in a physiologically relevant context. Upon CRISPR/Cas9-mediated correction of patient iPSCs, we succeeded in re-establishing proper podocin localization and expression level.

Finally, we performed RNA-Seq analysis on podocytes isolated from the p.R138Q kidney organoids to identify molecular pathways potentially deregulated that could participate or accompany the development of the disease in this specific condition. Unexpectedly, we identified the activation of an IFN-like response in p.R138Q patient podocytes. Although a similar antiviral IFN-like signature was already been evinced by an independent preliminary experience we previously performed (data not shown), proper validation of the RNA-Seq results is still pending. Thus, we can not conclude for the moment about a potential IFN implication in SRNS pathogenesis.

Materials and Methods

iPSC culture

Control and patient-derived IMAGINi007 (Menara et al. 2020) iPSC lines reprogrammed from PBMCs at the iPS Platform of the Imagine Institute were cultured in mTeSR1 or mTeSR Plus (05825, StemCell Technologies) medium on Vitronectin XF or Matrigel hESC-Qualified Matrix, LDEV-free (354277, Corning) - coated 35 mm dishes. Medium was changed every day or occasionally it was supplemented with 10 ng/ml StemBeads FGF2 (SB501, StemCulture) when 1 to 2 days of medium change were skipped. iPSCs colonies morphology was daily monitored under the Stereo Dynascopic Microscope and cleaning up was performed manually using needles or tips to ensure maintenance of an undifferentiated state. iPSCs were passaged with a frequency of about one week by mechanical cutting of colonies followed by clumps detaching and transfer into another culture dish.

Kidney organoids differentiation

The procedure for kidney organoids differentiation from iPSCs was performed according to a published protocol (adapted from Morizane et al. 2015). Inductive treatment was directly performed on iPSC colonies obtained by mechanical clumps passing. 14 mm Ø coverslips were eventually deposed at the bottom of wells for some applications. Differentiation was started by switching to Basic Differentiation Medium (BDM), consisting by Advanced RPMI 1640 (12633020, Thermo Fisher Scientific) medium with 1X GlutaMAX supplement (35050061, Thermo Fisher Scientific), which was supplemented with 8 µM CHIR 99021 (1386, Axon Medchem) and 5 ng/ml Noggin (120-10C, PeproTech) for 4 days to induce the late primitive streak. 10 ng/ml Activin A (120-14E, PeproTech) was used for the following 3 days to lead differentiation towards the posterior intermediate mesoderm. Medium was then supplemented with 10 ng/ml FGF9 (273-F9-025, R&D Systems) from day 7 to day 14, combined with a 1 to 2 days pulse of 3 µM CHIR 99021 from day 8 or 9, depending on observation of cell morphology. From the induced metanephric mesenchyme, pretubular aggregates and subsequently renal vesicles raised. Kidney organoids development occurred spontaneously during the following week, without addition of any other factor. All along differentiation medium was changed every 2 or 3 days.

Immunofluorescence (IF)

Samples were fixed in PFA 4% at room temperature for 30 min - 1 h and subsequently blocked and permeabilized in BSA 2%/Triton X-100 0,1% for 1 h at room temperature. BSA 2%/Triton X-100 0,1% was equally used for primary and secondary antibodies dilutions. Primary antibodies, including rabbit anti-SIX2 1:200 (11562-1-AP, Proteintech), goat anti-PAX2 1:100 (AF3364, R&D Systems), mouse anti-LHX1 1:50 (4F2-c, Developmental Studies Hybridoma Bank), rat anti-E-cadherin 1:400 (13-1900, Thermo Fisher Scientific), mouse anti-WT1 1:100 (sc-7385, Santa Cruz Biotechnology), rabbit anti-podocin 1:200 (AP-P35, C. Antignac's laboratory production), goat anti-podocalyxin 1:500 (AF1658, R&D Systems), goat anti-synaptopodin 1:50 (sc-21537, Santa Cruz Biotechnology), guinea pig anti-nephrin 1:100 (GP-N2, ProGen), mouse anti-nephrin 1:100 (48E11, kindly provided by Tryggvason's laboratory), mouse anti-calreticulin 1:200 (ALX-804-014-R100, Enzo Life Sciences), mouse anti-calnexin 1:400 (sc-23954, Santa Cruz Biotechnology), mouse anti-PDI 1:200 and (ADI-SPA-891, Enzo Life Sciences), were incubated overnight at 4°C, with the exception of the anti-nephrin antibody, which required a 1 h incubation at 37°C. Fluorescein-labeled *Lotus Tetragonolobus* lectin (LTL) (FL-1321, Vector Laboratories) was used at 1:200 together with primary antibodies. Fluorescently labeled donkey Alexa Fluor 488, 555 and 647 secondary antibodies (Life Technologies) diluted 1:200 were incubated at room temperature for 2 h in appropriate combinations. Nuclei were stained with DAPI (sc-3598, Santa Cruz Biotechnology) 3 µg/ml together with secondary antibodies. Coverslips were then mounted on slides using Mowiol 4-88 (81381, Sigma-Aldrich) mounting medium. Samples were observed and imaged on a Spinning Disk Confocal Microscope (Zeiss). Images visualization and analysis has been performed on ImageJ and/or ZEN (blue edition) (Zeiss) software.

Imaging and co-localization analysis

Glomeruli were manually encircled based on PODXL IF staining using the "Poligon selections" function on ImageJ, to next apply "Edit; Clear Outside" command. Images were loaded on the ilastik software to perform a "Pixel Classification" analysis, treating each channel individually. The software was trained to discriminate the staining of interest on a subset of representative images, and Single Segmentations were exported. Single Segmentations were converted into binary images, and Manders' coefficients were obtained using the JACoP plugin on ImageJ, performing the "M1 and M2 coefficients analysis". Unpaired two-tailed t-test has been applied to compare Manders' coefficients using the GraphPad Prism 8 software.

Transmission electron microscopy (TEM)

Samples were fixed in 2,5% Glutheraldeyhde at room temperature for 30 min - 1 h and kept in the fixative at 4°C until processing at the Electron Microscopy Platform of the Cochin Institut. Samples were post-fixed with 0.1 M Osmium Tetroxyde at 4°C for 1 h and washed three times in H2O. Uranyl Acetate staining was performed previous to a dehydration step, carried out in successive baths of 70%, 90% and 100% Ethanol. Samples were then immersed in two Propylene Oxide baths and then in a 1:1 Prepolymer/Propylene Oxide mixture. They were finally included in gelatin capsules in pure Prepolymer, which were made polymerize for at least 24 h in an oven at 60°C. Sections of 90 nm were obtained through a Reichert Ultracut S Ultramicrotome (Leica). Samples were observed and imaged on a JEM-1011 Transmission Electron Microscope (JEOL).

RT-qPCR

RNA was extracted using the RNeasy Mini Kit (74104, Qiagen) according to manufacturer's instructions. Random Hexamer Primers (SO142, Thermo Fisher scientific) and dNTPs were mixed to 0,5 - 1 µg of total RNA for RT. After a denaturation step at 65°C for 5 min, 5X First-Strand Buffer, DTT, SuperScript II Reverse Transcriptase (180640, Thermo Fisher scientific) and RiboLock RNase Inhibitor (EO0381, Thermo Fisher scientific) were added to samples. RT reaction consisted in incubations at 25°C for 10 min and at 42°C for 50, followed by enzyme heat inactivation at 70°C for 15 min. cDNA was stored at -20°C until performing qPCR. qPCR was performed using Power SYBR Green PCR Master Mix (4367659, Thermo Fisher scientific) and the following specific primers:

Gene	Forward primer	Reverse primer
OCT4	5'-CGACCATCTGCCGCTTTG-3'	5'-GGTTGCCTCTCACTCGGTTCT-3'
SOX2	5'-GACCAGCTCGCAGACCTACAT-3'	5'-GACTTGACCACCGAACCCAT-3'
T	5'-AGGTACCCAACCCTGAGGA-3'	5'-GCAGGTGAGTTGTCAGAATAGGT-3'
TBX6	5'-GTGTCTTTCCATCGTGTCAAGC-3'	5'-TATGCGGGGTTGGTACTTGTG-3'
WT1	5'-CACAGCACAGGGTACGAGAG-3'	5'-CAAGAGTCGGGGCTACTCCA-3'
HOXD11	5'-AGAAGAGCAGCAGCGCAGT-3'	5'-CAGTTCGCGGATCTGGTACTT-3'
SIX2	5'-GCCGAGGCCAAGGAAAGGGAGAA-3'	5'-AGCAGTGCGGGGCTGGATGA -3'
PAX2	5'-CGCCTCCAATGACCCA-3'	5'-GCCCTCAGACACATCTTCATC-3'
GAPDH	5'- CATGAGAAGTATGACAACAGC-3'	5'- AGTCCTTCCACGATACCAAAGT-3'

qPCR reaction has been performed running samples in triplicates on a Stratagene Mx3000P System (Agilent Technologies) and data were analyzed using the MxPro qPCR software (Agilent Technologies). Gene of interest was normalized to *GAPDH* expression.

CRISPR/Cas9 gene editing

iPSCs were supplied with 10 µM Y-27632 (1683 AxonMed) at least 2 h before nucleofection. Cells were dissociated with TrypLE Select Enzyme (12563-011, Thermo Fisher scientific) and 800 000 cells/nucleofection were pelleted by centrifugation. Pellets were resuspended in 30 µl of P3 Primary Cell Nucleofector Solution supplied with Supplement 1 of the P3 Primary Cell 4D-Nucleofector X Kit S (V4XP-3032, Lonza). 25% of P3 cellular solution was kept as non-transfected control. Pre-constituted crRNA:tracrRNA/CAS9 RNP complex (300 pmol gRNA and 150 pmol Cas9) and 300 pmol ssODN were mixed to the remaining 75% P3 cellular solution. The mix (22 µl) was transferred into a 20 µl Nucleocuvette and nucleofected on a 4D-Nucleofector System with Core (AAF-1002B, Lonza) and X Units (AAF-1002X, Lonza) using the CA-137 program. After 2-5 min incubation at RT, cells were resuspended into mTeSR Plus medium supplemented with 1:10 CloneR (05888, StemCell Technologies) and plated at 100 000 cells/cm2 on Matrigel-coated supports. After 1 day, cell medium was supplemented with 10 µM Y-27632 at least 2h before to be dissociated with TrypLE Select Enzyme. Cells with the highest GFP+ signal were sorted on a SH800S Cell Sorter (Sony Biotechnology) and plated at a density of 25 cells/cm2 on CellAdhere Laminin-521 (77003, StemCell Technologies) -coated culture dishes in mTeSR Plus medium supplemented with 1:10 CloneR. Fresh medium was added or replaced every 2 to 3 days, switching to unsupplemented mTeSR1 Plus medium starting from day 7 post-plating. Clone piking was performed around day 14. For each clone, half colony was pursued in culture and half was used for screening. DNA for screening was extracted using the QuickExtract DNA Extraction Solution (QE09050, Biosearch Technologies). The *NPHS2* exon 3 region was amplified by PCR using the forward 5'-TCAAAATTCTGTCTATGGGT-3' and reverse 5'-CATTTAATCTGAGGTCCATA-3' primers (Eurogentec) and the amplicon was digested using the BseNI restriction enzyme (R0527, New England Biolabs). According to the digestion profile, selected clones underwent Sanger sequencing to confirm the type of genomic modification. The 12 exonic and 8 intronic most probable off-target sites according to CRISPOR (Concordet and Maximilian 2018) CFD score were checked by PCR and Sanger sequencing to validate the absence of off-target genome editing at these sites.

Kidney organoid dissociation

Manually collected D21 kidney organoids were incubated into 2,5 mg/ml Collagenase II (17101-015, Life Technologies) / 10 mg/ml Pancreatin (P1625, Sigma-Aldrich) / 150 U/ml DNase I (18047019, Thermo Fisher scientific) mix for 10 to 15 min at 37°C, encouraging dissociation by pipetting every 2 to 4 min. A second enzymatic dissociation step was performed in the first series by incubation in Accutase (07920, StemCell Technologies) / 150 U/ml DNase I mix for 10 at 37°C, encouraging dissociation by pipetting every 2 min.

Podocytes FACS-sorting

Cell suspensions obtained upon kidney organoid dissociation were incubated in Fc blocking reagent (Miltenyi Biotec, 130-059-901) diluted 1:5 into FACS buffer (PBS / 2,5% FBS / 2,5 mM EDTA). Samples were subsequently stained with mouse anti-nephrin (48E11, kindly provided by Tryggvason's laboratory), goat anti-podocalyxin (R&D Systems, AF1658) and fluorescein-labeled *Lotus tetragonolobus* lectin (LTL) (Vector Laboratories, FL-1321) diluted 1:50 into FACS Buffer, and incubated on ice for 20 min. Followed incubation with fluorescently labeled donkey Alexa Fluor anti-mouse 555 and anti-goat 647 secondary antibodies (Life Technologies) diluted 1:200 on ice for 20 min. Cells were resuspended in FACS buffer and filtered by passing them through a 35 µm Cell Strainer Snap Cap (Corning, 352235). 5 µl/10^6 cells of 7-AAD (BD Biosciences, 559925) was added to samples and incubated for 10 min in order to exclude non-viable cells. Nephrin$^+$/podocalyxin$^+$/LTL$^-$ cells were FACS-sorted on a BD FACSAria II (BD Biosciences, 643179) flow cytometer at the Cell Sorting Facility of the SFR-Necker and directly collected into RLT lysis buffer (from RNeasy Micro Kit, Qiagen, 74004) supplied with 1% β-Mercaptoethanol. FACS-sorted cells were frozen and stored at -80°C until RNA extraction.

RNA-Seq

RNA was extracted from FACS sorted cells using the RNeasy Micro Kit (Qiagen, 74004), by thawing FACS-sorted lysed cells and proceeding according to manufacturer's instructions. RNA quantity and quality was assessed by automated electrophoresis using the TapeStation system (Agilent Technologies). RNA-Seq libraries were prepared starting from 4 ng of total RNA using the Ovation SoLoRNA-Seq System kit (0500-32, Nugen) according to manufacturer's instructions. Briefly, after DNase treatment and random primer annealing, the first cDNA strand was synthetized from total RNA. Second cDNA strand was produced and then ligated to Illumina compatible adaptors containing both sample index and a Unique Molecular Index (UMI). The cDNA produced was PCR amplified after an initial test to evaluate the suitable number of PCR cycles to apply to each sample. cDNA corresponding to ribosomal RNA were selectively fragmented using the AnyDeplete technology (formerly known as InDA-C). Few PCR cycles were performed to finalize the RNAseq library preparation. An equimolar pool of the final indexed RNA-Seq libraries was prepared and sequenced on an NovaSeq6000 (Illumina) producing paired-end reads of 100 bases + 100 bases. A total of ~50 millions of passing filter paired-end reads was produced per library.

RNA-Seq and analysis

FASTQ files were mapped to the ENSEMBL GRCh38/hg38 reference human genome using Hisat2 and counted by featureCounts from the Subread R package. Read count normalizations and groups comparisons were performed by three independent and complementary statistical methods: DESeq2, edgeR and LimmaVoom. Flags were computed from counts normalized to the mean coverage. All normalized counts <20 were considered as background (flag 0) and ≥20 as signal (flag=1). Cluster analysis was performed on DESeq2 P50 lists, regrouping the genes showing flag=1 for at least half of the compared samples, by hierarchical clustering using the Spearman correlation similarity measure and ward linkage algorithm. Samples were compared using the DESeq2 statistical method, applying the Bonferroni and Benjamin-Hochberg (BH) corrections for multiple hypothesis testing. Statistically significant upregulated and downregulated gene lists (BH-corrected p-value<0.05) were subjected to GO enrichment analysis for biological process on geneontology.org. Functional analyses were carried out using Ingenuity Pathway Analysis (IPA, Qiagen) on >2 fold change expression filtered results of the three statistical methods.

References

Berg, Stuart et al. 2019. “Ilastik: Interactive Machine Learning for (Bio)Image Analysis.” *Nature Methods*.

Boute, Nicolas et al. 2000. “NPHS2, Encoding the Glomerular Protein Podocin, Is Mutated in Autosomal Recessive Steroid-Resistant Nephrotic Syndrome.” *Nature Genetics*.

Chittiprol, Seetharamaiah et al. 2011. “Marker Expression, Behaviors, and Responses Vary in Different Lines of Conditionally Immortalized Cultured Podocytes.” *American Journal of Physiology - Renal Physiology*.

Concordet, Jean-Paul, and Haeussler Maximilian. 2018. “CRISPOR: Intuitive Guide Selection for CRISPR/Cas9 Genome Editing Experiments and Screens.” *Nucleic Acids Research*.

Cruz, Nelly M. et al. 2017. “Organoid Cystogenesis Reveals a Critical Role of Microenvironment in Human Polycystic Kidney Disease.” *Nature Materials*.

Forbes, Thomas A. et al. 2018. “Patient-IPSC-Derived Kidney Organoids Show Functional Validation of a Ciliopathic Renal Phenotype and Reveal Underlying Pathogenetic Mechanisms.” *American Journal of Human Genetics*.

Freedman, Benjamin S. 2015. “Modeling Kidney Disease with IPS Cells.” *Biomarker Insights*.

Freedman, Benjamin S. 2015. “Modelling Kidney Disease with CRISPR-Mutant Kidney Organoids Derived from Human Pluripotent Epiblast Spheroids.” *Nature Communications*.

Hale, Lorna J. et al. 2018. “3D Organoid-Derived Human Glomeruli for Personalised Podocyte Disease Modelling and Drug Screening.” *Nature Communications*.

Hinkes, Bernward G. et al. 2007. “Nephrotic Syndrome in the First Year of Life: Two Thirds of Cases Are Caused by Mutations in 4 Genes (NPHS1, NPHS2, WT1, and LAMB2).” *Pediatrics*.

Huber, Tobias B. et al. 2003. “Molecular Basis of the Functional Podocin-Nephrin Complex: Mutations in the NPHS2 Gene Disrupt Nephrin Targeting to Lipid Raft Microdomains.” *Human Molecular Genetics*.

Kestilä, Marjo et al. 1998. “Positionally Cloned Gene for a Novel Glomerular Protein - Nephrin - Is Mutated in Congenital Nephrotic Syndrome.” *Molecular Cell*.

Kobayashi, Akio et al. 2008. “Six2 Defines and Regulates a Multipotent Self-Renewing Nephron Progenitor Population throughout Mammalian Kidney Development.” *Cell Stem Cell*.

Manders, Erik MM, Verbeek FJ, and Aten JA. 1993. “Measurement of Co-Localization of Objects in Dual-Colour Confocal Images.” *Journal of Microscopy*.

Menara, Giulia, Lefort N, Antignac C, and Mollet G. 2020. “Generation of an Induced Pluripotent Stem Cell (IPSC) Line (IMAGINi007) from a Patient with Steroid-Resistant Nephrotic Syndrome Carrying the Homozygous p.R138Q Mutation in the Podocin-Encoding NPHS2 Gene.” *Stem Cell Research*.

Morizane, Ryuji et al. 2015. “Nephron Organoids Derived from Human Pluripotent Stem Cells Model Kidney Development and Injury.” *Nature Biotechnology*.

Morizane, Ryuji, and Bonventre JV. 2017. “Generation of Nephron Progenitor Cells and Kidney Organoids from Human Pluripotent Stem Cells.” *Nature Protocols*.

Nishibori, Yukino et al. 2004. “Disease-Causing Missense Mutations in NPHS2 Gene Alter Normal Nephrin Trafficking to the Plasma Membrane.” *Kidney International*.

Ohashi, Teiko et al. 2003. “Intracellular Mislocalization of Mutant Podocin and Correction by Chemical Chaperones.” *Histochemistry and Cell Biology*.

Philippe, A. et al. 2008. “A Missense Mutation in Podocin Leads to Early and Severe Renal Disease in Mice.” *Kidney International*.

Preston, Rebecca, Stuart HM and Lennon R. 2019. “Genetic Testing in Steroid-Resistant Nephrotic Syndrome: Why, Who, When and How?” *Pediatric Nephrology*.

Roselli, Séverine et al. 2004. “Plasma Membrane Targeting of Podocin through the Classical Exocytic Pathway: Effect of NPHS2 Mutations.” *Traffic*.

Serrano-Perez, Maria-Carmen et al. 2018. “Endoplasmic Reticulum-Retained Podocin Mutants Are Massively Degraded by the Proteasome.” *Journal of Biological Chemistry*.

Taguchi, Atsuhiro et al. 2014. “Redefining the in Vivo Origin of Metanephric Nephron Progenitors Enables Generation of Complex Kidney Structures from Pluripotent Stem Cells.” *Cell Stem Cell*.

Takasato, Minoru et al. 2015. “Kidney Organoids from Human IPS Cells Contain Multiple Lineages and Model Human Nephrogenesis.” *Nature*.

Tanigawa, Shunsuke et al. 2018. “Organoids from Nephrotic Disease-Derived IPSCs Identify Impaired NEPHRIN Localization and Slit Diaphragm Formation in Kidney Podocytes.” *Stem Cell Reports*.

Thomas, Paul D. et al. 2003. “PANTHER: A Library of Protein Families and Subfamilies Indexed by Function.” *Genome Research*.

Torres, Vicente E., Harris PC and Pirson Y. 2007. “Autosomal Dominant Polycystic Kidney Disease.” *Lancet*.

Zhang, Shao-Yu et al. 2004. “In Vivo Expression of Podocyte Slit Diaphragm-Associated Proteins in Nephrotic Patients with NPHS2 Mutation.” *Kidney International*.

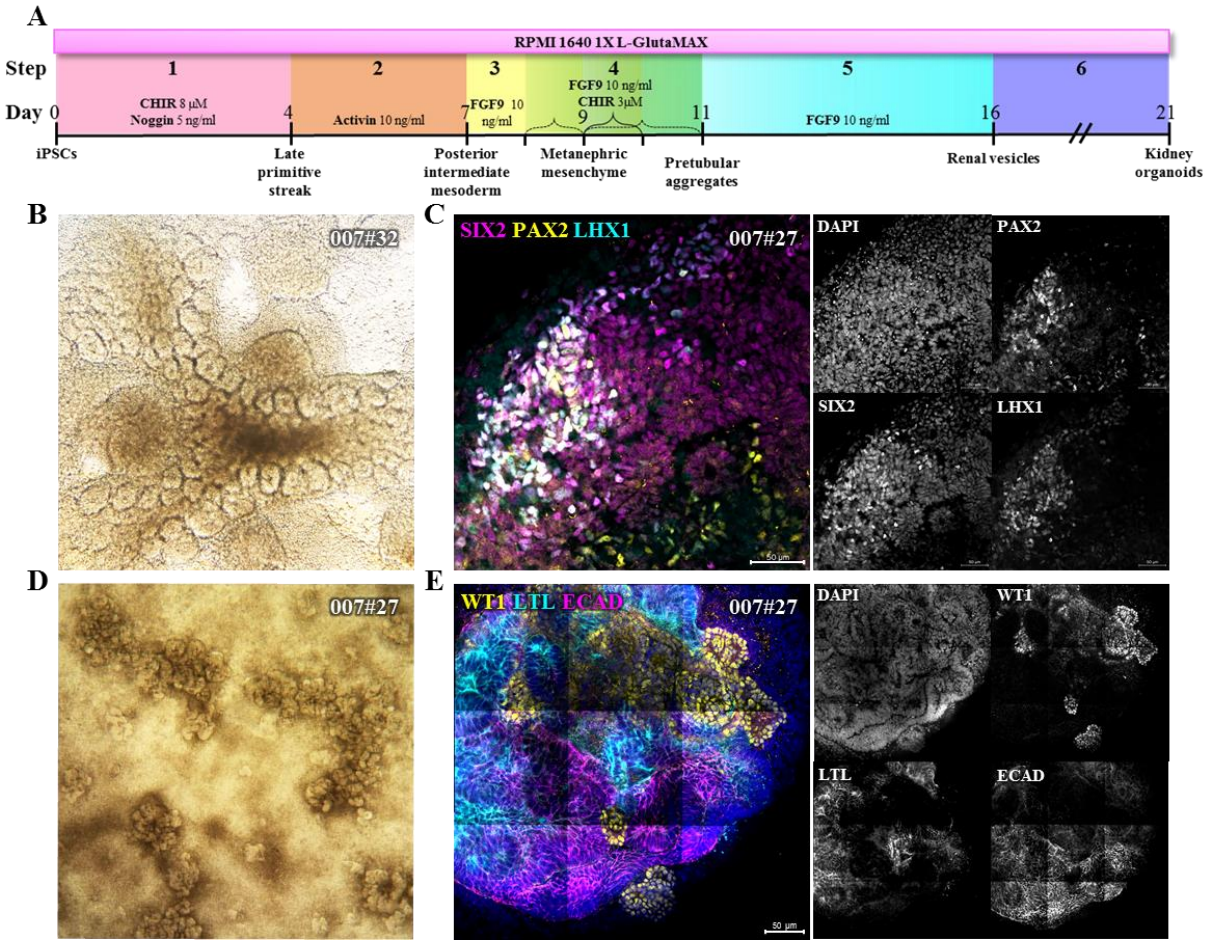

Figure 1. Kidney organoids differentiation. **A)** Schematic representation of the 21 days lasting differentiation protocol applied to induce nephron progenitor cells (B and C) and kidney organoids (D and E) from iPSCs. Differentiation protocol consists of six successive steps to reproduce the sequential stages of embryonic kidney development, as described elsewhere (Morizane and Bonventre 2017). Timing of "Step 4" is adjusted according to cell morphology (dashed braces correspond to adjustments compared to the canonical protocol, filled brace). **B)** p.R138Q D9 NPCs on light microscopy (20X magnification). Differentiating cells undergo epithelialization and around D9 they display a characteristic honeycomb morphology with radial cells departing from a central lumen **C)** Immunostaining for NPC markers SIX2 (magenta), PAX2 (yellow) and LHX1 (cyan) on D9 NPCs (20X magnification). NPCs are arranged in a circular disposition of $SIX2^{+}$ nuclei, displaying a certain extension of PAX2 and/or LHX1 co-expression. **D)** p.R138Q D21 kidney organoids on light microscopy (10X magnification). Distinct 3D structures adherent to the support emerge from the differentiating culture. **E)** Immunostaining for specific markers of nephron portions on p.R138Q D21 kidney organoids (20X magnification, Tile reconstruction). D21 kidney organoids are stained for WT1 (yellow, glomeruli), LTL (cyan, proximal tubules) and ECAD (magenta, distal tubules), highlighting glomeruli, proximal tubules and distal tubules, respectively.

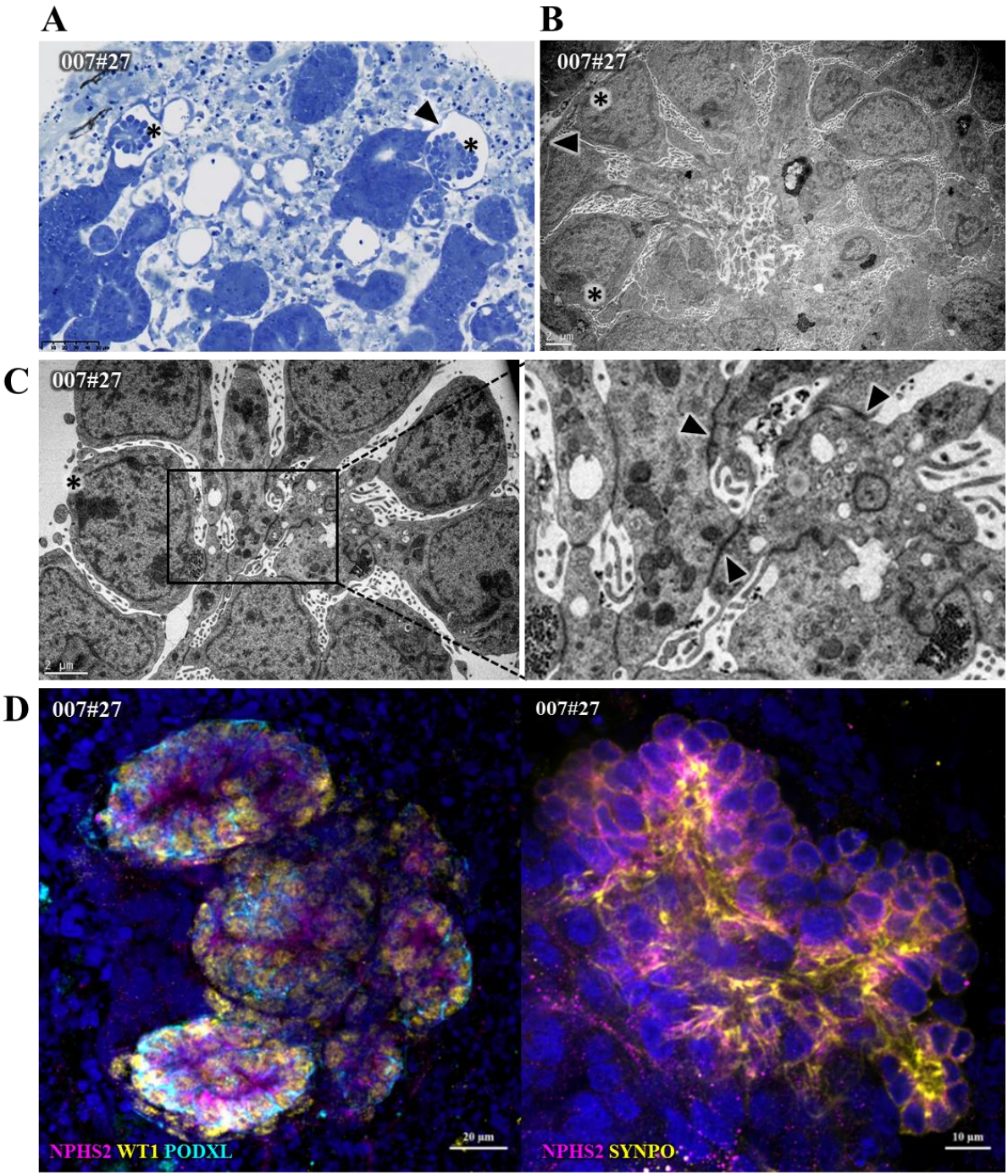

Figure 2. p.R138Q kidney organoids glomerular features. **A)** Semi-thin section of a D21 p.R138Q patient kidney organoid stained with Toluidine blue. Over the strongly blue-stained tubular structures, glomeruli containing podocyte-like cells (asterisks) are easily distinguishable, with parietal-like cells (black arrow) lining a capsule. **B)** Transmission electron microscopy of a D21 p.R138Q patient glomerulus. Podocytes (asterisks) enclosed into a capsule (black arrow) extend interconnected cellular protrusions towards the center of the glomerulus. **C)** Transmission electron microscopy of D21 p.R138Q patient podocytes (asterisks). Podocyte basal processes are connected by intercellular junctions (black arrows) **D)** Immunostaining for podocyte markers on D21 p.R138Q patient glomeruli. Patient iPSC-derived glomerular podocytes express all the examined podocyte markers. Left panel: podocin (NPHS2, magenta), WT1 (yellow) and podocalyxin (PODXL, cyan) (40X magnification). Right panel: podocin (NPHS2, magenta) and synaptopodin (SYNPO, yellow) (63X magnification).

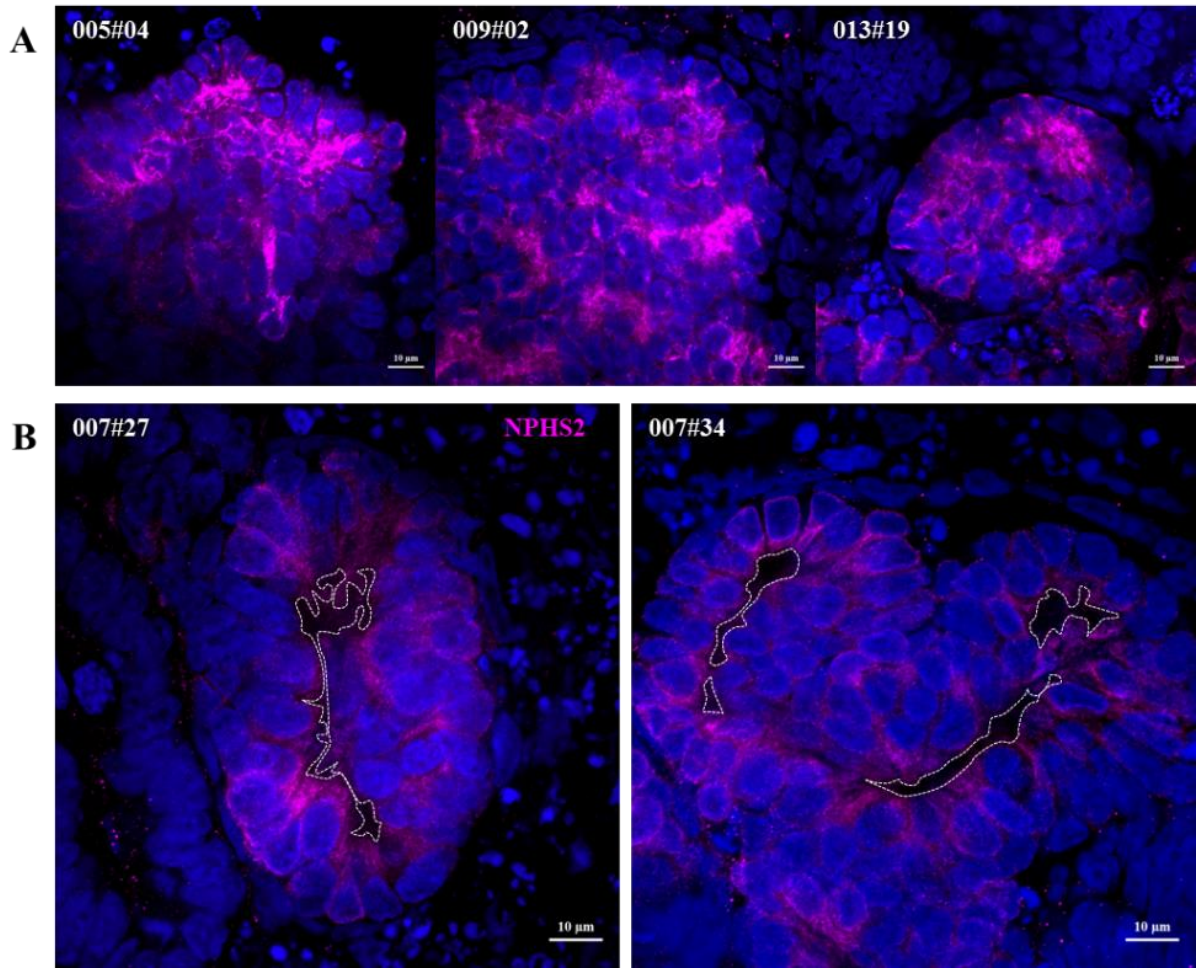

Figure 3. Podocin expression in kidney organoid glomeruli. Immunostaining for podocin (NPHS2, magenta) on **A)** control organoids and **B)** p.R138Q mutated kidney organoids (63X magnification). Lack of podocin staining at the basal side of p.R138Q podocytes is evidenced by a dashed line.

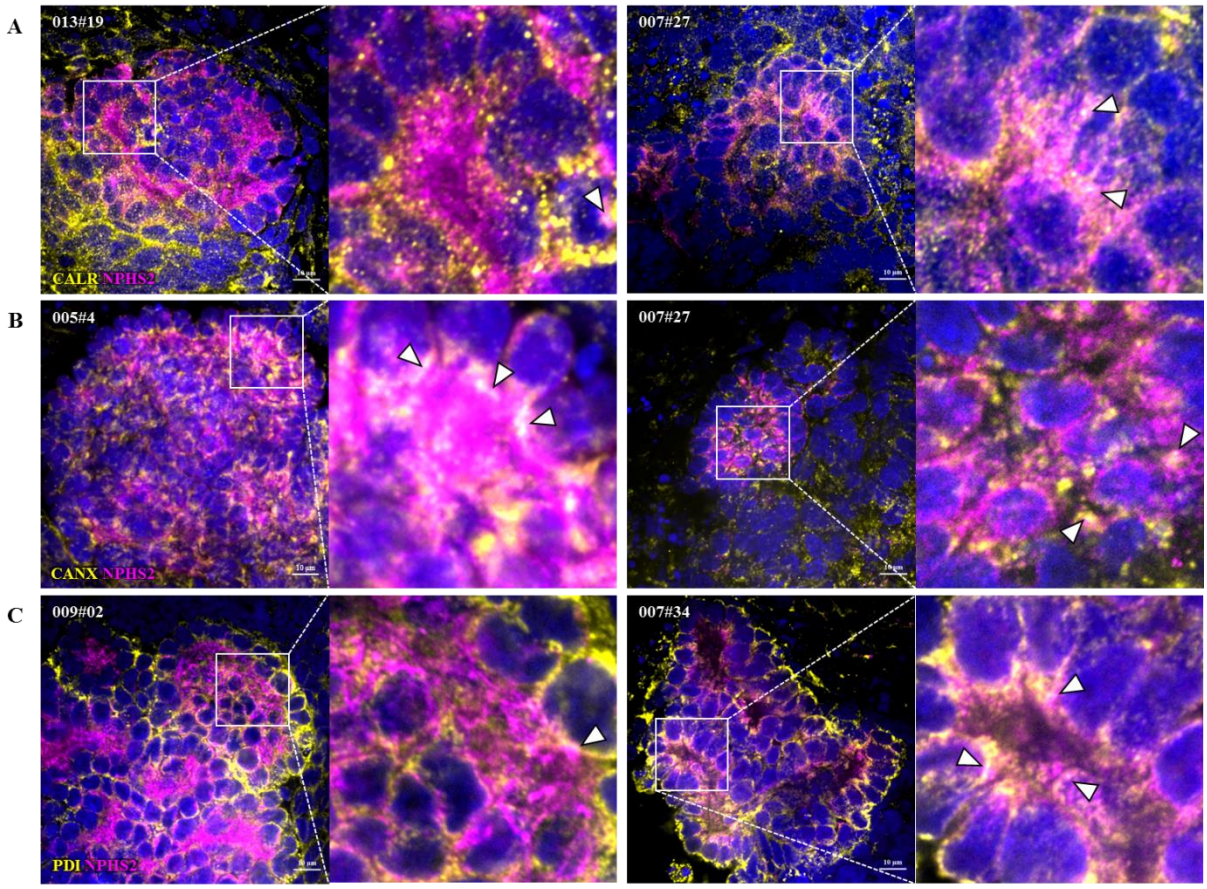

Figure 4. Co-localization of podocin and ER markers. Immunostaining for podocin (NPHS2, magenta) and the ER markers **A)** calreticulin (CALR), **B)** calnexin (CANX) or **C)** protein disulfide isomerase (PDI) (yellow) on control (left panels) and p.R138Q patient (right panels) glomeruli. Co-localization of podocin with ER markers is highlighted with white arrows (63X magnification).

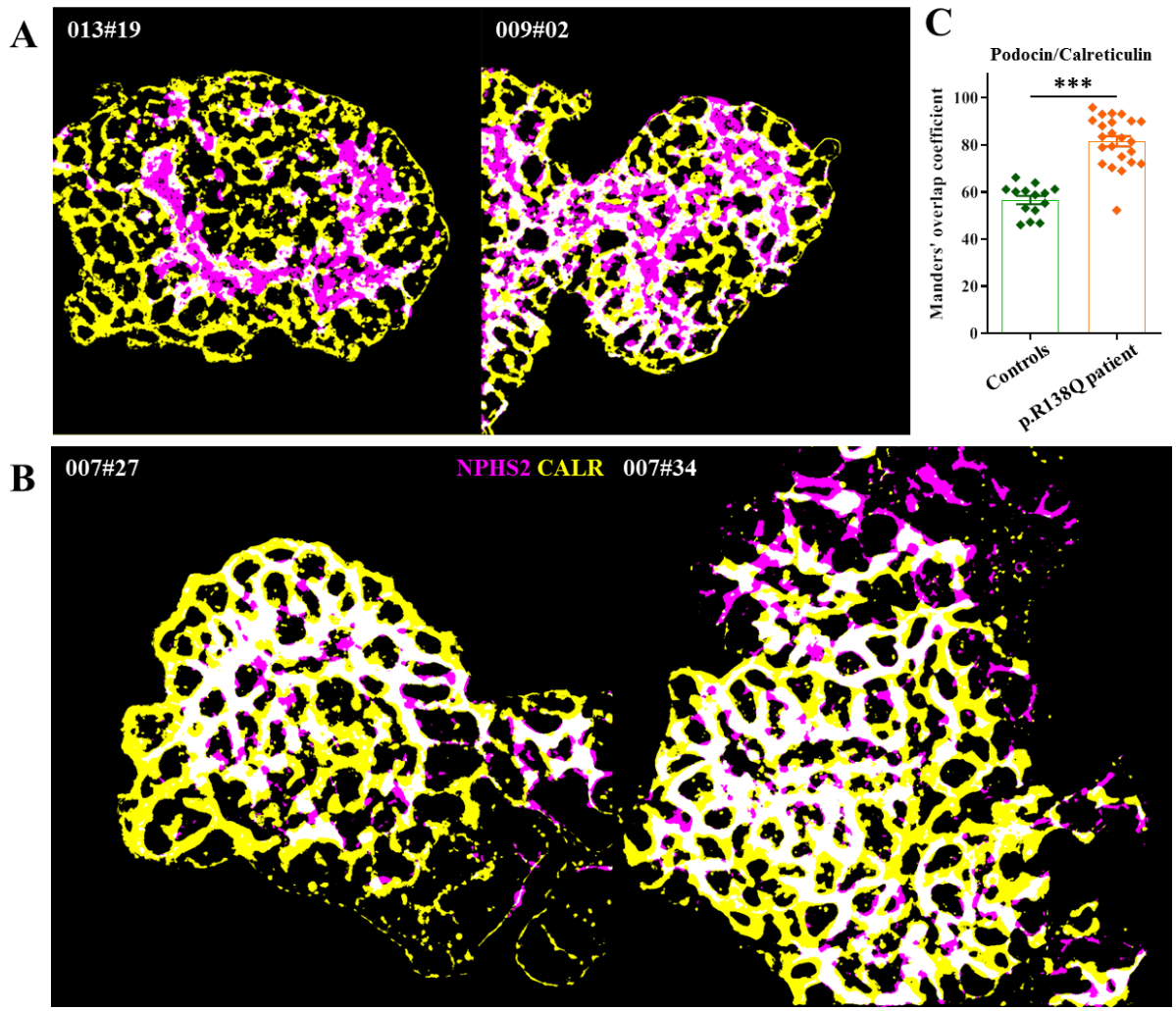

Figure 5. Co-localization analysis of podocin and calreticulin. Superposition of binary segmentations performed on podocin (NPHS2, magenta) and calreticulin (CALR, yellow) stainings on glomeruli from **A)** control and **B)** p.R138Q patient kidney organoids. Co-localization is evidenced in white. **C)** Manders' overlap coefficient of podocin on calreticulin. p.R138Q patient glomeruli display a 24.98% ± 3.133 increase of podocin/calreticulin Manders' overlap coefficient compared to controls (mean ± SEM. Controls, n=14; p.R138Q, n=23). Unpaired two-tailed t-test has been applied (***, p-value<0.0001).

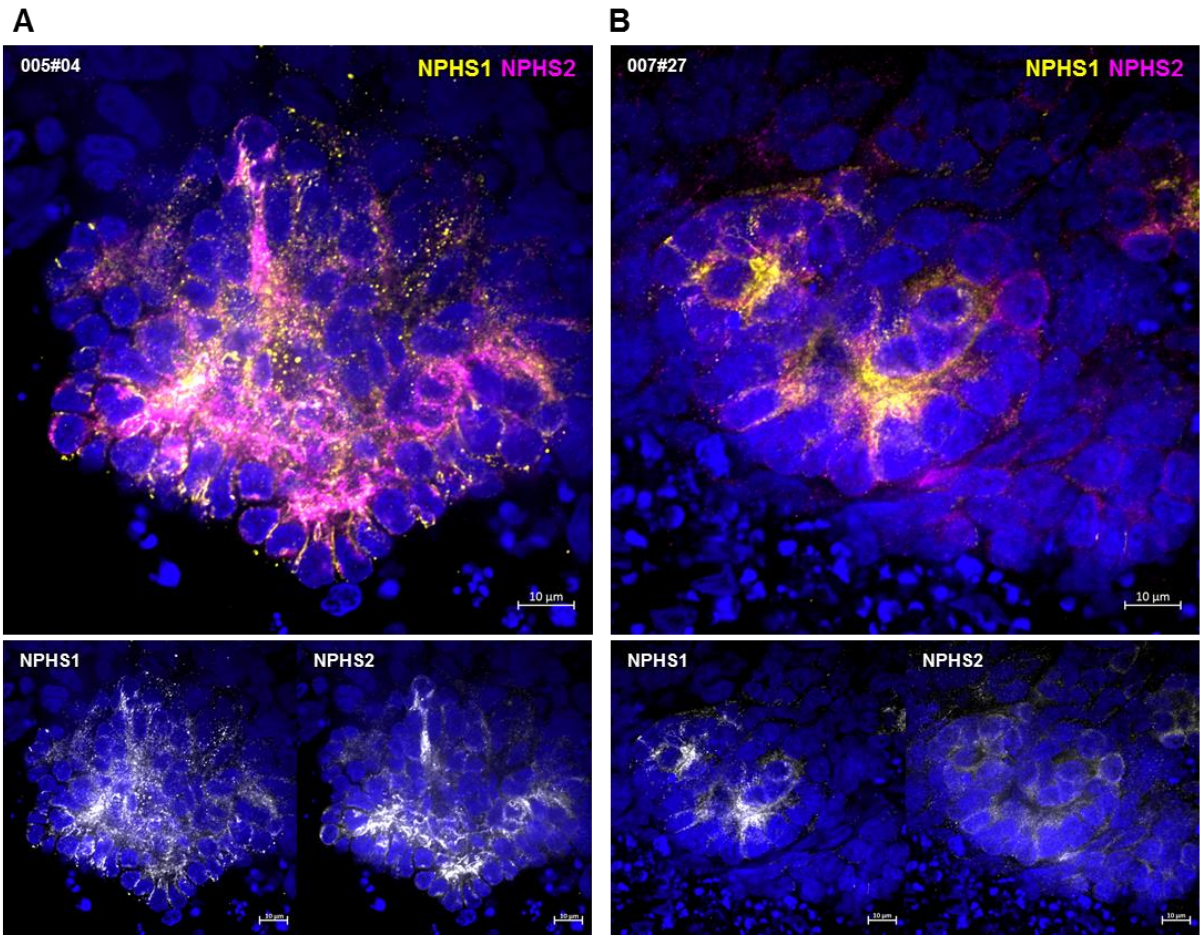

Figure 6. Nephrin and p.R138Q podocin expression in kidney organoid glomeruli. Immunostaining for nephrin (NPHS1, yellow) and podocin (NPHS2, magenta) on glomeruli from **A)** control and **B)** p.R138Q patient kidney organoids. Nephrin and podocin co-localize at the basal processes of podocytes in control kidney organoids. In p.R138Q patient glomeruli, nephrin is also basally located, in the central part of the glomerulus, while podocine does not reach the basal podocyte processes (63X magnification). Anti-nephrin antibody targeting the intracellular domain.

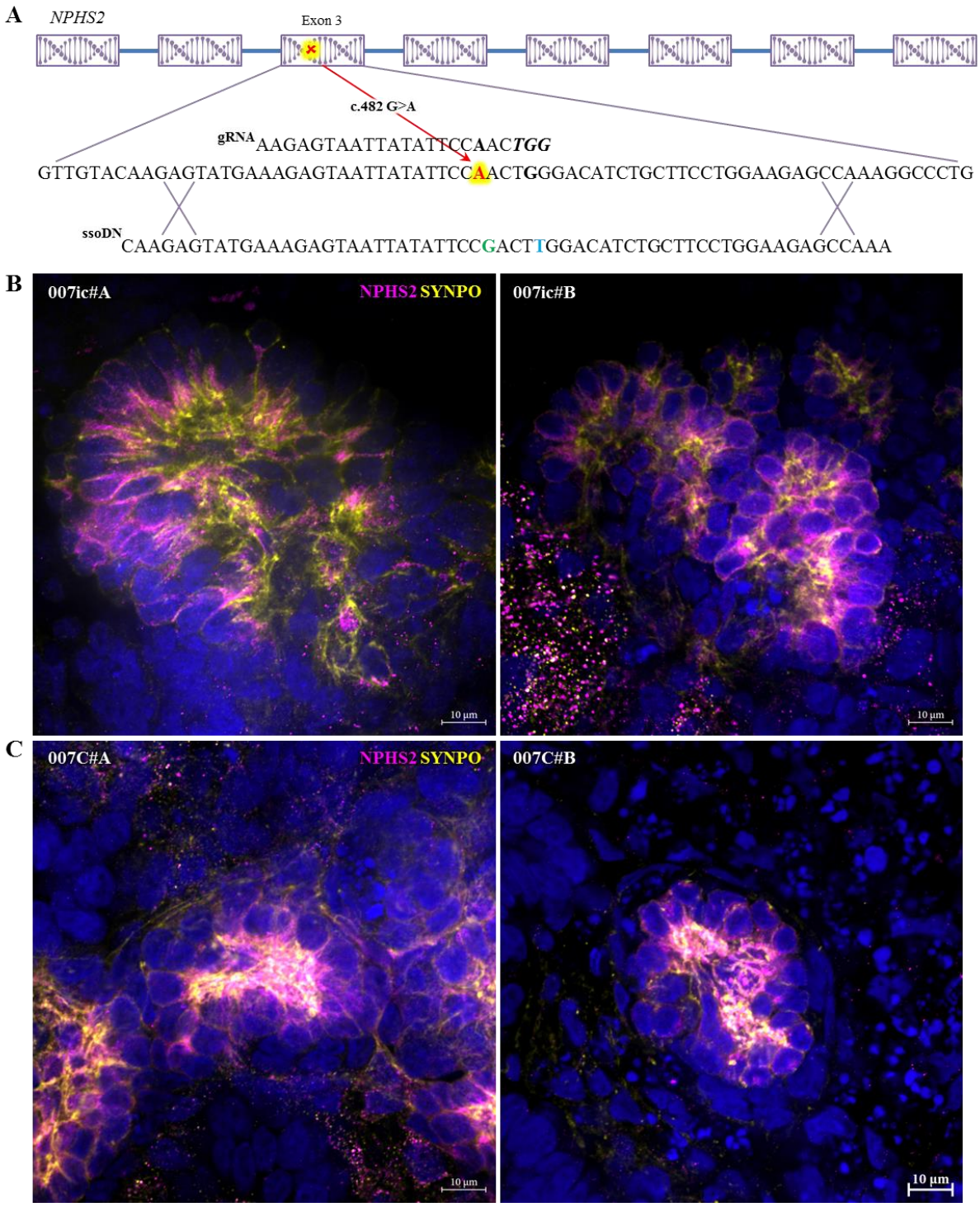

Figure 7. CRISPR/Cas9-mediated correction of patient mutation. **A)** Schematic representation of the CRISPR/Cas9 gene editing strategy. The Cas9 is directed towards the target exon 3 of the *NPHS2* gene by the designed guide RNA (gRNA; PAM motif in bold italic). An exogenous donor single-stranded oligo deoxynucleotide oligo DNA (ssoDN) is provided as a template for homologous recombination. The ssoDN contains the wild-type nucleotide (G, in green) to correct the patient c.482 G>A mutation (in red, highlighted in yellow) on *NPHS2* exon 3. An additional silent substitution of a G towards a T (in blue) has been inserted in the ssoDN to increase the knock-in efficiency and for screening facilitation purpose. **B and C)** Immunostaining for podocin (NPHS2, magenta) and synaptopodin (SYNPO, yellow) on glomeruli from (B) internal controls (ic=internal control) and (C) CRISPR/Cas9 corrected (C=CRISPR/Cas9 corrected) clones. In the CRISPR/Cas9-corrected 007#CA and #CB clones the basal expression of podocin, co-localizing with synaptopodin, is reestablished (63X magnification).

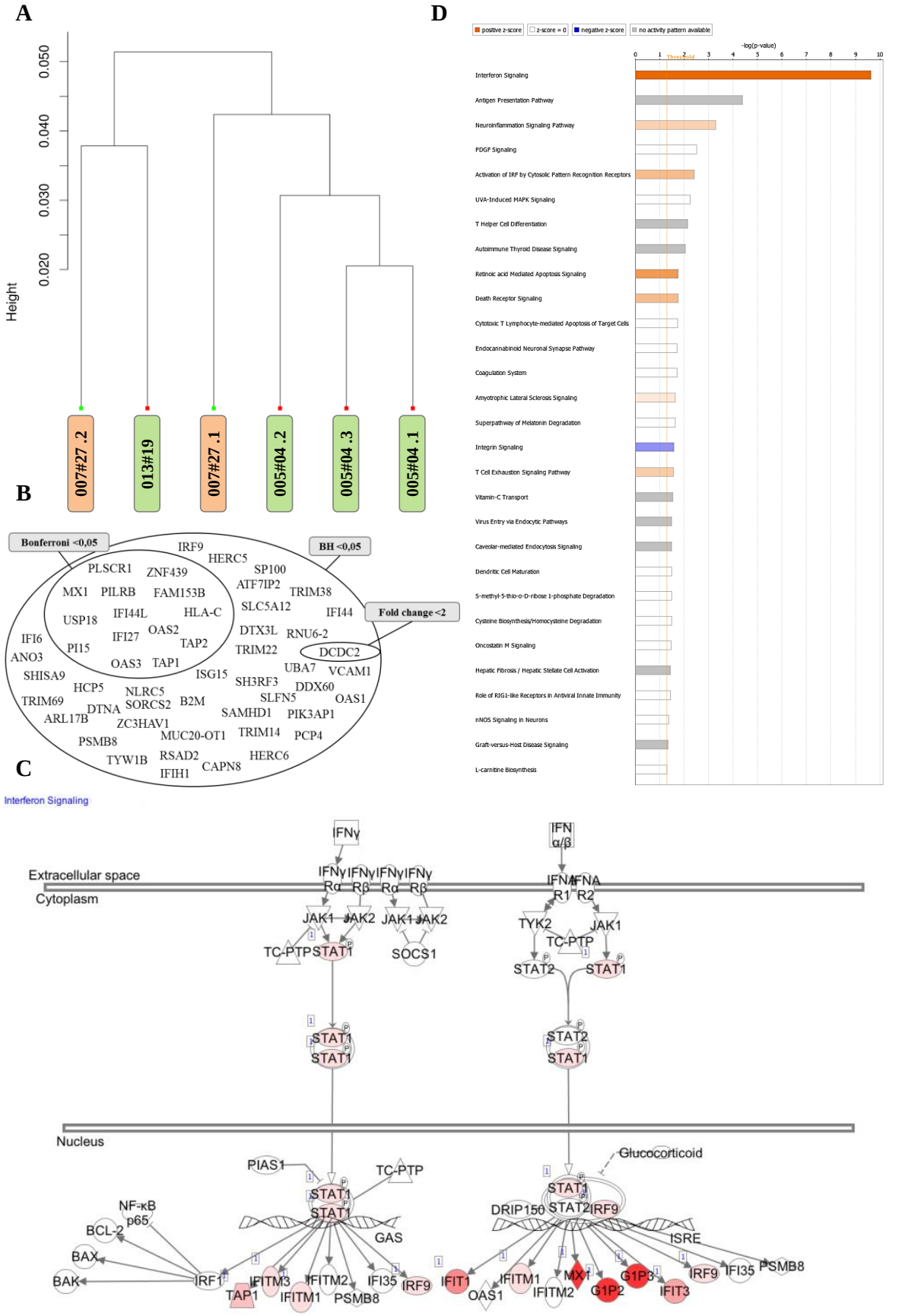

Figure 8. Transcriptomic profiling of podocytes isolated from kidney organoids. **A)** Unsupervised clustering by average of control (green) and p.R138Q patient (orange) podocyte samples. **B)** Venn diagram of significantly upregulated genes upon Bonferroni and Benjamin-Hochberg correction for multiple hypothesis testing. They all present a fold change>2, except DCDC2. **C)** Interferon signaling pathway. Relative gene expression is represented on a green to red color scale. **D)** Ingenuity Canonical Pathway analysis. Z-score is represented on a blue to orange color scale, where blue refers to the inhibition and orange to the activation of the pathway.

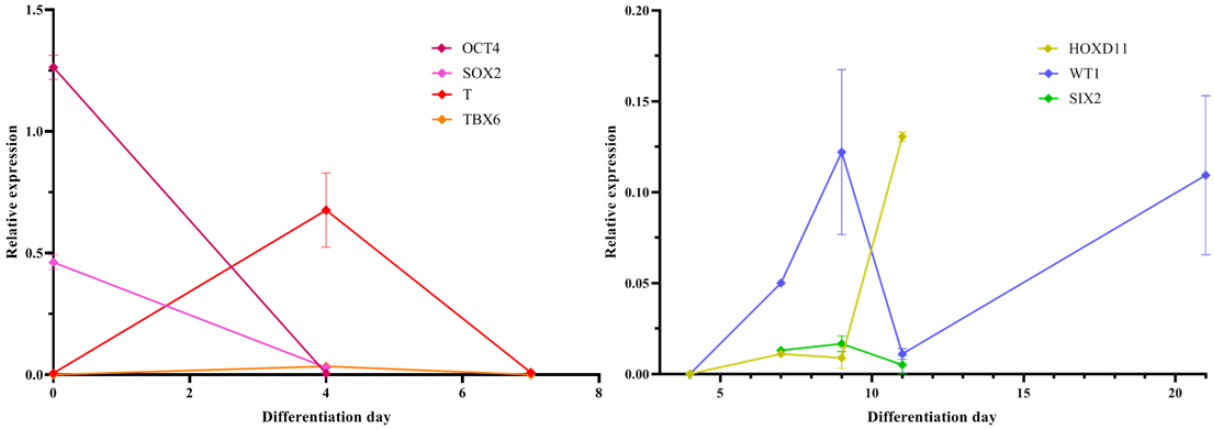

Supplementary figure 1. RT-qPCR time course for differentiation markers. RT-qPCR time course for *OCT4*, *SOX2*, *T* and *TBX6* from day 0 to day 7 (left panel) and for *HOXD11*, *WT1* and *SIX2* from day 7 to day 21 (right panel). The expression of the pluripotency markers *OCT4* and *SOX2* drastically dropped down upon iPSC induction, and it was virtually absent at D4. The expression of *T* picked at that time, accompanied by limited upregulation of *TBX6*. *HOXD11*, *WT1* and *SIX2* from day 7 to day 21. The expression of *SIX2* and *WT1* picked at D9, when NPCs are supposed to arise. After rapid extinction, *WT1* expression was detected again at D21, *videlicet* in kidney organoids. HOWD11 expression increased later than expected.

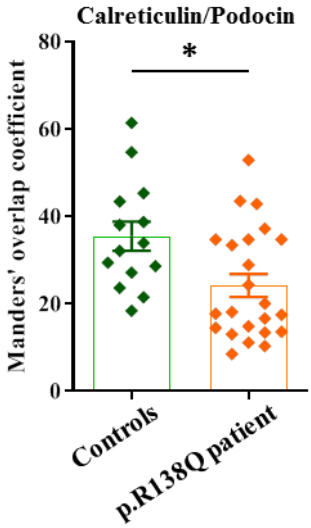

Supplementary figure 2. Manders' overlap coefficient of calreticulin on podocin. p.R138Q patient glomeruli display a 11.25% ± 4.253 decrease of calreticulin/podocin Manders' overlap coefficient compared to controls (mean ± SEM. Controls, n=14; p.R138Q, n=23). Unpaired two-tailed t-test has been applied (*, p-value=0.0121).

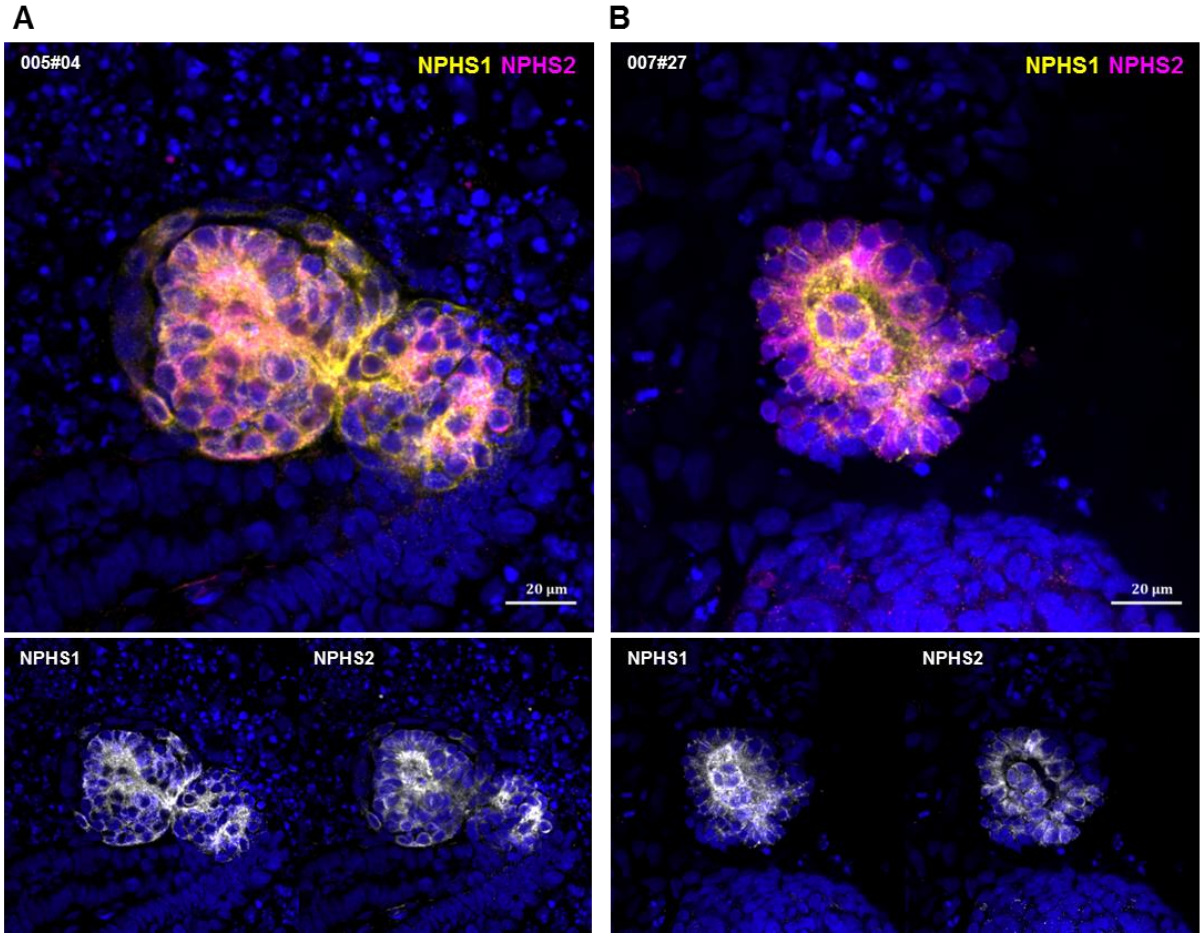

Supplementary figure 3. Nephrin and p.R138Q podocin expression in kidney organoid glomeruli. Immunostaining for nephrin (NPHS1, yellow) and podocin (NPHS2, magenta) on glomeruli from **A)** control and **B)** p.R138Q patient kidney organoids. Analogously to previous results using the anti-nephrin antibody that targets the intracellular domain, nephrin displays a similar basal expression in both control and p.R138Q podocytes (63X magnification). Anti-nephrin antibody targeting the extracellular domain.

A

TCAAAATTCTGTCTATGGGTTCAAAAATTAACATGGTTAATATACTTTTTCATTTCTGAAATTTTACACTTACTA
AATATAGATTTTGGAAACTTAAGTATTAATAGAAATTTTTTCCTGGTTCTCAAAACAAAAAATTTCTGATATCT
AGGATCATTCTTATGCCAAGGCCTTTTGAAGACTTTTTCTTTCTGGGAGTGATTTGAAAGGATTAAATTTCTCT
TTAGGTTGTACAAGAGTATGAAAGAGTAATTATATTCCAACTGGGACATCTGCTTCCTGGAAGAGCCAAAGG
CCCTGGTAAAAAAACACTCTTTTTTTTCTAAACACCTCTCTCCTGACTTGCCAATTTCTTCAACCCATGCAGATT
TGTAATATGGACCTCAGATTAAATG

TCAAAATTCTGTCTATGGGTTCAAAAATTAACATGGTTAATATACTTTTTCATTTCTGAAATTTTACACTTACTA
AATATAGATTTTGGAAACTTAAGTATTAATAGAAATTTTTTCCTGGTTCTCAAAACAAAAAATTTCTGATATCT
AGGATCATTCTTATGCCAAGGCCTTTTGAAGACTTTTTCTTTCTGGGAGTGATTTGAAAGGATTAAATTTCTCT
TTAGGTTGTACAAGAGTATGAAAGAGTAATTATATTCCGACTGGTACATCTGCTTCCTGGAAGAGCCAAAGGC
CCTGGTAAAAAAACACTCTTTTTTTTCTAAACACCTCTCTCCTGACTTGCCAATTTCTTCAACCCATGCAGATTT
GTAATATGGACCTCAGATTAAATG

B

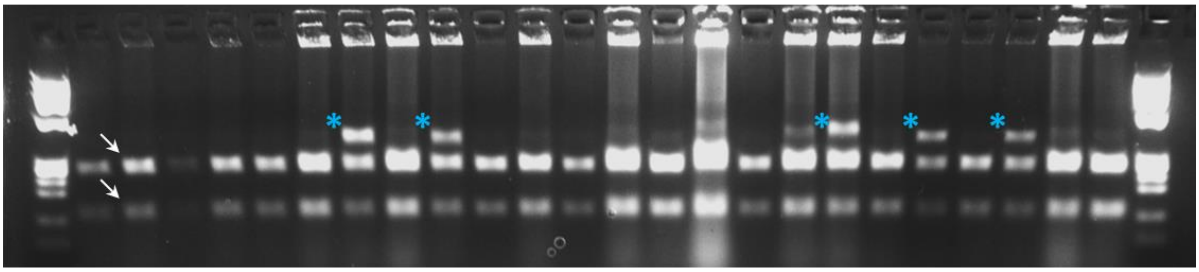

C

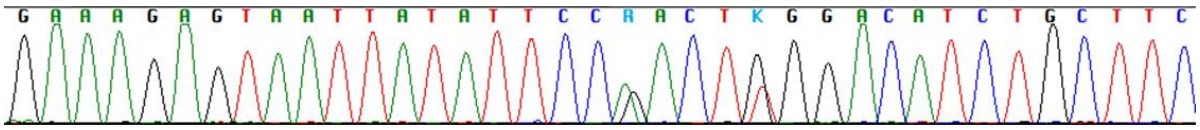

Supplementary figure 4. CRISPR/Cas9 gene editing strategy. **A)** Unmodified (upper panel) or gene edited (lower panel) p.R138Q patient amplicon sequences of the exon 3 region. Primers are underlined. Patient c.482 G>A mutation (red, highlighted in yellow) is corrected with the wild-type base (G, green). An additional c.488 G>T silent substitution (blue) is also introduced. This variant disrupts both the PAM motif (circled in purple) and the ACTGG(1/-1)^ recognition site of the BseNI restriction enzyme (underlined in red). **B)** Screening of CRISPR/Cas9-obtained clones by BseNI enzymatic digestion. Unmodified clones display the 2 expected bands (arrows). Presumptive heterozygous KI clones display an additional band (blue asterisk) corresponding to the undigested amplicon. **C)** Representative example of Sanger sequencing validation of a presumptive CRISPR/Cas9-mediated KI clone. The chromatogram confirms the presence of both c.482 G>A and c.488 G>T substitutions at the heterozygous state.

	Homo sapiens (REF)	upload_1 (▼Hierarchy NEW! ⑦)					
GO biological process complete	#	#	expected	Fold Enrichment	+/-	raw P value	FDR
cytosol to endoplasmic reticulum transport	3	2	.01	> 100	+	6.43E-05	1.42E-02
ISG15-protein conjugation	6	3	.02	> 100	+	1.33E-06	4.79E-04
vesicle fusion with endoplasmic reticulum-Golgi intermediate compartment (ERGIC) membrane	6	2	.02	> 100	+	1.79E-04	3.60E-02
regulation of ribonuclease activity	9	3	.02	> 100	+	3.45E-06	1.08E-03
└regulation of nuclease activity	22	3	.06	53.02	+	3.53E-05	8.13E-03
antigen processing and presentation of endogenous peptide antigen via MHC class I	21	5	.05	92.57	+	5.80E-09	2.71E-06
└antigen processing and presentation of endogenous peptide antigen	21	5	.05	92.57	+	5.80E-09	2.80E-06
└antigen processing and presentation of peptide antigen	194	6	.50	12.03	+	1.21E-05	3.14E-03
└antigen processing and presentation	222	6	.57	10.51	+	2.53E-05	6.09E-03
└immune system process	2806	32	7.22	4.43	+	4.52E-15	5.14E-12
└antigen processing and presentation of endogenous antigen	28	5	.07	69.43	+	2.06E-08	9.12E-06
└antigen processing and presentation of peptide antigen via MHC class I	103	6	.26	22.65	+	3.54E-07	1.34E-04
type I interferon signaling pathway	67	13	.17	75.44	+	1.21E-20	4.82E-17
└cytokine-mediated signaling pathway	692	17	1.78	9.55	+	1.13E-12	7.46E-10
└cellular response to cytokine stimulus	1027	17	2.64	6.44	+	4.84E-10	2.48E-07
└response to cytokine	1118	18	2.88	6.26	+	2.01E-10	1.06E-07
└response to organic substance	3019	19	7.76	2.45	+	1.15E-04	2.46E-02
└response to stimulus	8495	37	21.85	1.69	+	3.90E-05	8.85E-03
└cellular response to organic substance	2391	18	6.15	2.93	+	1.76E-05	4.38E-03
└cellular response to chemical stimulus	2926	18	7.53	2.39	+	2.50E-04	4.98E-02
└cell surface receptor signaling pathway	2417	19	6.22	3.06	+	4.95E-06	1.40E-03
└signal transduction	5061	26	13.02	2.00	+	1.60E-04	3.26E-02
└cellular response to type I interferon	67	13	.17	75.44	+	1.21E-20	3.86E-17
└response to type I interferon	72	13	.19	70.20	+	2.82E-20	6.40E-17
└innate immune response	766	24	1.97	12.18	+	2.09E-20	5.55E-17
└defense response to other organism	952	26	2.45	10.62	+	8.65E-21	4.58E-17
└defense response	1342	28	3.45	8.11	+	1.66E-19	2.64E-16
└response to stress	3580	28	9.21	3.04	+	5.83E-09	2.65E-06
└response to other organism	1327	28	3.41	8.20	+	1.24E-19	2.46E-16
└response to external biotic stimulus	1329	28	3.42	8.19	+	1.29E-19	2.28E-16
└response to external stimulus	2443	29	6.28	4.62	+	7.85E-14	7.34E-11
└response to biotic stimulus	1353	28	3.48	8.05	+	2.05E-19	2.96E-16
└multi-organism process	2832	30	7.28	4.12	+	4.35E-13	3.14E-10
└immune response	1868	28	4.80	5.83	+	8.14E-16	9.96E-13
interferon-gamma-mediated signaling pathway	72	10	.19	54.00	+	9.50E-15	1.01E-11
└cellular response to interferon-gamma	164	10	.42	23.71	+	2.01E-11	1.18E-08
└response to interferon-gamma	186	10	.48	20.90	+	6.52E-11	3.70E-08
negative regulation of viral genome replication	63	8	.16	49.37	+	1.03E-11	6.27E-09
└negative regulation of viral life cycle	86	8	.22	36.17	+	1.03E-10	5.63E-08
└negative regulation of viral process	104	10	.27	37.39	+	2.84E-13	2.15E-10
└negative regulation of multi-organism process	227	13	.58	22.27	+	2.91E-14	2.89E-11
└regulation of multi-organism process	779	21	2.00	10.48	+	1.85E-16	2.45E-13
└regulation of viral process	207	12	.53	22.54	+	2.78E-13	2.21E-10
└regulation of symbiosis, encompassing mutualism through parasitism	225	12	.58	20.74	+	7.09E-13	4.90E-10
└regulation of viral life cycle	146	10	.38	26.63	+	6.76E-12	4.30E-09
└regulation of viral genome replication	98	10	.25	39.67	+	1.64E-13	1.37E-10
negative regulation of type I interferon production	45	5	.12	43.20	+	1.78E-07	7.09E-05
└regulation of type I interferon production	129	7	.33	21.10	+	5.53E-08	2.38E-05
└regulation of cytokine production	711	10	1.83	5.47	+	1.28E-05	3.28E-03
defense response to virus	200	19	.51	36.94	+	1.28E-24	2.03E-20
└response to virus	287	20	.74	27.10	+	2.09E-23	1.66E-19
└immune effector process	1079	21	2.78	7.57	+	9.98E-14	8.82E-11
regulation of type I interferon-mediated signaling pathway	35	3	.09	33.33	+	1.26E-04	2.64E-02
└regulation of innate immune response	453	10	1.17	8.58	+	2.42E-07	9.39E-05
└regulation of immune response	1139	14	2.93	4.78	+	8.35E-07	3.09E-04
└regulation of immune system process	1667	18	4.29	4.20	+	9.87E-08	4.02E-05
└regulation of response to biotic stimulus	527	13	1.36	9.59	+	7.65E-10	3.80E-07
└regulation of response to external stimulus	1091	13	2.81	4.63	+	3.14E-06	9.99E-04
└regulation of defense response	769	13	1.98	6.57	+	6.30E-08	2.63E-05
└regulation of response to stress	1508	15	3.88	3.87	+	4.25E-06	1.25E-03
antigen processing and presentation of exogenous peptide antigen via MHC class I, TAP-dependent	76	5	.20	25.58	+	2.03E-06	7.02E-04
└antigen processing and presentation of exogenous peptide antigen via MHC class I	80	5	.21	24.30	+	2.58E-06	8.37E-04
└antigen processing and presentation of exogenous peptide antigen	176	5	.45	11.05	+	1.00E-04	2.18E-02
└antigen processing and presentation of exogenous antigen	183	5	.47	10.62	+	1.19E-04	2.53E-02
regulation of defense response to virus	77	5	.20	25.25	+	2.16E-06	7.30E-04
└regulation of immune effector process	467	8	1.20	6.66	+	2.65E-05	6.29E-03
positive regulation of innate immune response	336	8	.86	9.26	+	2.54E-06	8.40E-04
└positive regulation of defense response	463	8	1.19	6.72	+	2.50E-05	6.11E-03
└positive regulation of multi-organism process	500	9	1.29	7.00	+	5.32E-06	1.48E-03
└positive regulation of response to biotic stimulus	358	8	.92	8.69	+	4.01E-06	1.23E-03
└positive regulation of response to external stimulus	596	8	1.53	5.22	+	1.43E-04	2.94E-02
└positive regulation of immune response	847	10	2.18	4.59	+	5.58E-05	1.25E-02
└positive regulation of immune system process	1150	12	2.96	4.06	+	3.00E-05	7.01E-03
protein polyubiquitination	300	7	.77	9.07	+	1.29E-05	3.26E-03
└protein ubiquitination	698	10	1.80	5.57	+	1.09E-05	2.89E-03
└protein modification by small protein conjugation	777	11	2.00	5.50	+	4.15E-06	1.24E-03
└protein modification by small protein conjugation or removal	987	12	2.54	4.73	+	6.61E-06	1.81E-03
viral process	702	11	1.81	6.09	+	1.58E-06	5.59E-04
└symbiotic process	783	11	2.01	5.46	+	4.46E-06	1.29E-03
└interspecies interaction between organisms	855	11	2.20	5.00	+	1.01E-05	2.73E-03

Supplementary figure 5. Gene ontology analysis of upregulated genes. Table of significantly enriched GO categories for the significantly upregulated genes (BH-corrected p-value<0.05) in p.R138Q patient podocytes compared to controls.

Name	CFD score (CRISPOR)
exon:CMTM6/CMTM7	0,02
exon:CSGALNACT2	0,09
exon:CT60	0,14
exon:FBXO7	0,00
exon:FOXP1	0,06
exon:FRY	0,08
exon:NRIP1/AF127577.10	0,17
exon:NUP205	0,00
exon:RP11-74K11.1	0,02
exon:SLC1A3	0,23
exon:SULT1C2	0,51
exon:VPRBP	0,03
intron:NAP1L4	0,55
intron:GABRG2	0,37
intron:KDM4C	0,35
intron:DLC1	0,32
intron:CPPED1	0,30
intron:SYNJ1	0,26
intron:PKD2	0,24
intron:EPHB1	0,23

Supplementary table 1. Off-target sites screened. Table reporting the 12 exonic and 8 intronic most probable off-target sites according to CRISPOR CFD score that were checked by PCR and Sanger sequencing to validate the absence of off-target genome editing at these sites

	Gene	Name	005#04.1	005#04.2	005#04.3	013#19	007#27.1	007#27.2
1	*MALAT1*	metastasis associated lung adenocarcinoma transcript 1	196355,90	118136,70	157754,70	92247,27	139164,90	123294,70
2	*PODXL*	podocalyxin like	62537,17	49153,70	55114,83	98491,58	26078,82	82668,15
3	*CCN2*	cellular communication network factor 2	38617,74	30698,49	38610,67	26717,76	29567,82	18899,38
4	*EEF1A1*	eukaryotic translation elongation factor 1 alpha 1	32606,41	32912,98	31207,01	31678,13	30185,44	20078,51
5	*PTPRO*	protein tyrosine phosphatase receptor type O	29287,83	19850,90	28797,36	45909,17	8613,15	41643,61
6	*FREM2*	FRAS1 related extracellular matrix 2	27038,77	24227,64	27546,44	43386,09	14178,60	37394,07
7	*SPARC*	secreted protein acidic and cysteine rich	23696,97	21763,31	25733,72	32008,88	19721,40	23212,06
8	*TJP1*	tight junction protein 1	21546,92	19237,66	22799,99	33868,54	8136,40	29453,41
9	*HIPK2*	homeodomain interacting protein kinase 2	19795,35	24035,72	21528,01	27773,88	16406,76	24623,04
10	*FAT1*	FAT atypical cadherin 1	21963,73	18692,56	21657,05	29645,94	14133,29	27568,79
11	*FRAS1*	Fraser extracellular matrix complex subunit 1	24602,71	20221,12	22449,74	23301,54	20416,84	22463,37
12	*SLC16A1*	solute carrier family 16 member 1	24566,04	19805,48	25386,97	20023,54	27199,79	16669,08
13	*NOTCH2*	notch receptor 2	20748,75	20386,92	18589,02	24740,85	18455,63	16937,48
14	*ACTG1*	actin gamma 1	14788,76	25936,77	19246,52	20393,38	9562,73	10451,83
15	*DDX17*	DEAD-box helicase 17	22294,98	16255,48	19595,02	21793,61	15929,01	22024,62
16	*ACTB*	actin beta	12974,85	24212,88	19391,36	17003,85	10128,14	9300,95
17	*HSP90B1*	heat shock protein 90 beta family member 1	22110,41	13426,62	18374,83	18631,89	18420,17	15907,09
18	*MAFB*	MAF bZIP transcription factor B	17080,59	14302,19	15178,63	23350,16	10974,28	17942,11
19	*CLIC5*	chloride intracellular channel 5	13983,26	10571,63	13236,86	25188,85	5244,33	20010,37
20	*H19*	H19 imprinted maternally expressed transcript	12166,90	22080,16	18211,55	10078,97	7495,14	6639,38
21	*MAGI2-AS3*	MAGI2 antisense RNA 3	13868,36	9518,90	15695,68	23347,30	5678,73	22228,21
22	*TGFBR3*	transforming growth factor beta receptor 3	11888,21	9487,10	12855,01	27736,71	4080,02	18024,37
23	*AKAP12*	A-kinase anchoring protein 12	14435,51	15909,11	20041,84	10065,63	17081,51	11024,36
24	*SRRM2*	serine/arginine repetitive matrix 2	13400,21	19452,30	14442,13	12829,86	12275,52	12493,50
25	*MYH9*	myosin heavy chain 9	13110,52	14160,24	15226,92	17313,64	9779,44	16305,95
26	*PTPRD*	protein tyrosine phosphatase receptor type D	13801,13	13082,52	14617,70	17002,90	8745,15	15974,39
27	*CANX*	calnexin	15297,24	12133,13	14568,54	14837,27	12540,49	11693,28
28	*KIRREL1*	kirre like nephrin family adhesion molecule 1	12814,72	14454,37	12433,65	16906,63	9058,39	17908,87
29	*AHNAK*	AHNAK nucleoprotein	11467,74	14986,98	14609,80	13182,54	9730,18	13485,67
30	*EIF4G2*	eukaryotic translation initiation factor 4 gamma 2	13259,65	11218,94	14475,49	11776,59	13560,00	9487,91
31	*PEG10*	paternally expressed 10	11994,55	11925,31	9959,91	15795,22	6734,69	13712,52
32	*DSC2*	desmocollin 2	11961,55	9492,78	13961,08	11149,40	11589,93	10244,09
33	*SEPTIN11*	septin 11	9222,35	7546,30	10434,82	18676,69	4356,81	10795,01
34	*NPNT*	nephronectin	8933,88	7239,68	10835,11	18143,86	2294,15	14516,89

35	*SERINC5*	serine incorporator 5	11011,81	10893,01	10759,62	11952,93	7705,94	13246,35
36	*SPTAN1*	spectrin alpha, non-erythrocytic 1	9959,40	9571,13	11757,71	12251,28	8487,07	10318,04
37	*EEF2*	eukaryotic translation elongation factor 2	9193,01	12851,98	9836,13	11625,04	7107,03	6798,92
38	*UNC5C*	unc-5 netrin receptor C	11937,10	7966,48	8677,39	13393,19	9638,58	13724,98
39	*VIM*	vimentin	6945,18	11329,10	10797,36	12782,20	6252,02	7792,75
40	*PRRC2C*	proline rich coiled-coil 2C	9234,57	10309,30	10617,41	11110,32	9383,45	9193,75
41	*NORAD*	non-coding RNA activated by DNA damage	9362,91	8621,74	11050,18	12086,38	7617,28	8926,18
42	*PLOD2*	procollagen-lysine,2-oxoglutarate 5-dioxygenase 2	10311,43	8915,87	9330,50	12512,45	8791,44	10206,69
43	*ROBO2*	roundabout guidance receptor 2	9314,02	6735,45	10516,46	14495,07	3636,75	12873,25
44	*LAMC1*	laminin subunit gamma 1	10744,13	8621,74	10349,67	11291,42	6911,01	10883,93
45	*NPHS1*	NPHS1 adhesion molecule, nephrin	10365,21	9534,79	8786,25	12313,23	6320,97	10656,24
46	*VEGFA*	vascular endothelial growth factor A	10003,41	10019,71	8319,24	12196,95	4102,67	9802,02
47	*CPXM1*	carboxypeptidase X, M14 family member 1	5328,06	8309,44	5806,00	20828,03	5458,08	16521,17
48	*YWHAZ*	tyrosine 3-monooxygenase/tryptophan 5-monooxygenase activation protein zeta	9204,01	9545,02	10809,65	10479,31	9145,07	7778,63
49	*HNRNPA2B1*	heterogeneous nuclear ribonucleoprotein A2/B1	12413,81	7513,36	10573,52	8720,68	11482,56	8689,36
50	*WT1*	WT1 transcription factor	9718,61	8718,27	8293,78	12269,39	6698,24	10373,72

Supplementary table 2. Top 50 most expressed genes in FACS-sorted podocytes. DESeq2 normalized expression of the top 50 most expressed genes in nephrin^{+}/podocalyxin^{+}/LTL^{-} FACS-sorted cells. Genes are classed by control average expression.

Gene	p-val	p-BH	p-Bonf	007#27.1	007#27.2	Mean R138Q	005#04.1	005#04.2	005#04.3	013#19	Mean ctrl	Ratio	Delta
ZNF439	3,90E-23	1,14E-18	2,28E-18	218,68	147,08	182,879	11,00	6,81	8,78	11,44	9,507795	19,23	173,37
AC112206.2	1,06E-17	1,23E-13	6,16E-13	146,77	133,78	140,2775	17,11	9,09	8,78	11,44	11,6035	12,09	128,67
H4C6	1,62E-17	1,58E-13	9,47E-13	485,62	70,63	278,1272	2,44	1,14	0,88	0,00	1,114524	249,55	277,01
FAM153B	2,81E-17	2,34E-13	1,64E-12	131,99	255,11	193,5499	2,44	2,27	14,05	2,86	5,4052	35,81	188,14
ZNF717	1,82E-15	1,18E-11	1,06E-10	79,79	126,31	103,047	1,22	3,41	0,00	0,95	1,395601	73,84	101,65
GTF2H2B	1,72E-14	1,00E-10	1,00E-09	139,88	116,33	128,1048	8,56	11,36	16,68	17,16	13,43718	9,53	114,67
PKIB	1,32E-12	6,99E-09	7,69E-08	503,35	265,91	384,6304	72,12	43,15	54,43	24,78	48,61978	7,91	336,01
AC020951.1	1,37E-11	6,68E-08	8,01E-07	59,10	56,51	57,80375	2,44	1,14	1,76	0,95	1,572278	36,76	56,23
AL353684.1	1,13E-09	5,09E-06	6,61E-05	99,49	108,02	103,7568	22,00	4,54	4,39	8,58	9,877999	10,50	93,88
PI4KAP1	1,32E-09	5,52E-06	7,72E-05	183,22	156,22	169,7187	39,11	52,24	30,72	40,03	40,52779	4,19	129,19
MTND4P12	1,87E-09	6,80E-06	1,09E-04	1180,07	757,01	968,5391	171,12	340,69	211,56	168,71	223,0215	4,34	745,52
AC005537.2	2,06E-08	6,32E-05	1,20E-03	30,54	49,86	40,19688	2,44	2,27	0,88	1,91	1,875025	21,44	38,32
AC112206.4	7,50E-08	2,19E-04	4,38E-03	48,27	42,38	45,32288	6,11	5,68	4,39	3,81	4,997912	9,07	40,32
HLA-C	8,98E-08	2,49E-04	5,23E-03	293,54	1476,62	885,0791	138,12	186,24	113,24	142,98	145,1459	6,10	739,93
PILRB	1,30E-07	3,44E-04	7,57E-03	125,10	131,29	128,1957	41,56	42,02	32,48	28,60	36,16313	3,54	92,03
AC022905.1	1,61E-07	4,08E-04	9,38E-03	36,45	68,14	52,29256	6,11	3,41	7,02	7,63	6,041654	8,66	46,25
PI15	4,26E-07	9,94E-04	2,49E-02	96,53	129,63	113,0817	36,67	12,49	18,43	8,58	19,04364	5,94	94,04
AC106798.1	4,61E-07	1,03E-03	2,69E-02	91,61	68,14	79,87356	15,89	4,54	4,39	18,11	10,73307	7,44	69,14
LINC01362	5,45E-07	1,18E-03	3,17E-02	42,36	55,67	49,01546	8,56	5,68	7,90	1,91	6,010311	8,16	43,01
TAP1	7,00E-07	1,41E-03	4,08E-02	21,67	289,17	155,4226	20,78	7,95	11,41	11,44	12,8947	12,05	142,53
AP000350.6	8,28E-07	1,61E-03	4,83E-02	117,22	110,52	113,8685	4,89	18,17	8,78	33,36	16,2998	6,99	97,57
MX1	8,60E-07	1,62E-03	5,01E-02	23,64	4759,74	2391,693	14,67	6,81	11,41	10,49	10,84461	220,54	2380,85
IFI44L	1,49E-06	2,71E-03	8,68E-02	3,94	16772,12	8388,028	8,56	1,14	4,39	13,34	6,856394	1223,39	8381,17
B2M	1,62E-06	2,87E-03	9,47E-02	639,29	4129,88	2384,582	502,37	469,02	426,63	351,73	437,4351	5,45	1947,15
AC103810.2	2,24E-06	3,63E-03	1,31E-01	58,12	63,15	60,63507	17,11	12,49	5,27	10,49	11,3391	5,35	49,30
ZNF486	2,84E-06	4,48E-03	1,66E-01	259,06	122,15	190,6078	9,78	10,22	10,53	59,10	22,40766	8,51	168,20
SAMHD1	3,37E-06	5,01E-03	1,97E-01	229,51	714,63	472,0699	135,68	121,51	130,80	130,59	129,6433	3,64	342,43
PSMB8	3,44E-06	5,01E-03	2,00E-01	11,82	154,56	83,18958	8,56	6,81	6,14	6,67	7,046783	11,81	76,14
SORCS2	4,18E-06	5,80E-03	2,44E-01	389,09	245,96	317,5268	78,23	144,23	59,69	55,28	84,35778	3,76	233,17
RNU6-2	5,75E-06	7,79E-03	3,35E-01	33,49	36,56	35,02675	3,67	0,00	5,27	4,77	3,424966	10,23	31,60
MUC20-OT1	7,86E-06	1,02E-02	4,59E-01	586,10	853,40	719,7466	152,79	170,35	138,70	363,16	206,2489	3,49	513,50
OAS3	7,91E-06	1,02E-02	4,61E-01	8,87	2497,04	1252,951	8,56	3,41	6,14	0,95	4,76528	262,93	1248,19
AL445490.1	8,82E-06	1,11E-02	5,14E-01	0,00	112,18	56,08986	0,00	1,14	0,00	0,95	0,522205	107,41	55,57
SLC5A12	9,82E-06	1,19E-02	5,72E-01	258,08	392,21	325,1465	147,90	88,58	119,39	132,49	122,0894	2,66	203,06
AC131649.2	1,05E-05	1,25E-02	6,14E-01	94,56	52,35	73,45699	26,89	12,49	10,53	10,49	15,10048	4,86	58,36
ZC3HAV1	1,29E-05	1,51E-02	7,53E-01	383,18	1584,64	983,9107	262,80	225,99	265,98	284,05	259,7053	3,79	724,21
DDX60	1,35E-05	1,55E-02	7,90E-01	93,58	4016,03	2054,806	34,22	39,75	57,06	48,61	44,91091	45,75	2009,90
AL162388.1	1,44E-05	1,61E-02	8,39E-01	43,34	45,70	44,52221	12,22	5,68	3,51	9,53	7,736121	5,76	36,79
Z99129.3	1,56E-05	1,72E-02	9,12E-01	52,21	37,39	44,80007	11,00	5,68	7,90	10,49	8,766131	5,11	36,03
AC093866.1	1,61E-05	1,74E-02	9,39E-01	660,96	317,43	489,193	207,79	114,70	97,44	50,52	117,6127	4,16	371,58
SLFN5	2,08E-05	2,09E-02	1,00E+00	142,83	798,55	470,6918	123,45	97,66	110,61	94,37	106,5226	4,42	364,17
OAS1	2,22E-05	2,15E-02	1,00E+00	4,93	1933,65	969,2857	1,22	0,00	3,51	2,86	1,898301	510,61	967,39
IFIH1	2,34E-05	2,24E-02	1,00E+00	10,84	1189,94	600,3857	6,11	6,81	10,53	6,67	7,532919	79,70	592,85
OAS2	2,45E-05	2,27E-02	1,00E+00	0,99	2369,90	1185,443	0,00	1,14	1,76	1,91	1,199418	988,35	1184,24
ZNF737	2,71E-05	2,47E-02	1,00E+00	450,16	265,08	357,6189	171,12	76,09	84,27	130,59	115,5174	3,10	242,10
ABCA9	3,01E-05	2,70E-02	1,00E+00	204,89	68,97	136,9286	6,11	9,09	6,14	45,75	16,77358	8,16	120,16
CAPN8	3,31E-05	2,88E-02	1,00E+00	138,89	108,02	123,4575	45,23	31,80	36,87	57,19	42,77086	2,89	80,69
PCP4	3,77E-05	3,16E-02	1,00E+00	226,56	171,18	198,8681	66,00	101,07	83,39	66,72	79,2984	2,51	119,57
AL512283.1	3,83E-05	3,16E-02	1,00E+00	30,54	19,94	25,23959	4,89	0,00	0,88	0,00	1,441771	17,51	23,80
TRIM38	3,85E-05	3,16E-02	1,00E+00	230,50	157,05	193,775	75,78	77,22	71,98	92,46	79,36197	2,44	114,41
SH3RF3	4,90E-05	3,91E-02	1,00E+00	264,97	117,17	191,0701	77,01	60,19	66,72	54,33	64,56032	2,96	126,51
AP000350.2	5,73E-05	4,25E-02	1,00E+00	55,16	50,69	52,92531	0,00	3,41	2,63	16,20	5,561136	9,52	47,36
TSPEAR-AS2	5,75E-05	4,25E-02	1,00E+00	40,39	47,36	43,87562	14,67	10,22	4,39	6,67	8,987482	4,88	34,89
IFI6	5,75E-05	4,25E-02	1,00E+00	21,67	4960,84	2491,254	35,45	19,31	22,82	41,94	29,87917	83,38	2461,38
LINC01415	5,77E-05	4,25E-02	1,00E+00	52,21	97,22	74,71466	28,11	9,09	13,17	3,81	13,54463	5,52	61,17
VCAM1	5,85E-05	4,25E-02	1,00E+00	524,04	102,21	313,1236	59,89	107,89	45,65	66,72	70,03724	4,47	243,09
SP100	5,90E-05	4,25E-02	1,00E+00	31,52	1214,87	623,193	7,33	12,49	25,46	16,20	15,3718	40,54	607,82
HERC5	6,27E-05	4,46E-02	1,00E+00	21,67	818,50	420,0837	9,78	10,22	16,68	12,39	12,26737	34,24	407,82
IRF9	7,00E-05	4,87E-02	1,00E+00	33,49	265,91	149,6994	28,11	32,93	24,58	27,64	28,31708	5,29	121,38
UBA7	7,01E-05	4,87E-02	1,00E+00	13,79	237,65	125,7227	9,78	22,71	11,41	19,06	15,74168	7,99	109,98

Supplementary table 3. Significantly upregulated genes in p.R138Q patient podocytes compared to controls. DESeq2 normalized expression of significantly upregulated genes (BH-corrected p-value<0.05) in p.R138Q patient podocytes compared to controls.

Gene	p-val	p-BH	p-Bonf	007#27.1	007#27.2	Mean R138Q	005#04.1	005#04.2	005#04.3	013#19	Mean ctrl	Ratio	Delta	Flags_g1
SQOR	3,68E-31	2,15E-26	2,15E-26	27,58	35,73	31,65616	444,92	408,83	399,41	323,13	394,0736	0,08	362,42	2
PLCG2	1,20E-22	2,33E-18	6,99E-18	91,61	78,11	84,85933	970,52	585,99	680,32	1171,46	852,0723	0,10	767,21	2
NLRP2	2,00E-18	2,92E-14	1,17E-13	1,97	2,49	2,23147	211,46	119,24	212,44	290,72	208,4647	0,01	206,23	0
EPAS1	3,24E-17	2,36E-13	1,89E-12	39,40	33,24	36,31993	194,35	304,35	312,51	237,34	262,1375	0,14	225,82	2
LINC01291	1,47E-09	5,72E-06	8,58E-05	0,00	0,00	0	84,34	72,68	79,88	95,32	83,0554	0,00	83,06	0
BX322639.1	2,88E-09	9,89E-06	1,68E-04	0,00	0,00	0	62,34	77,22	85,15	75,30	75,00316	0,00	75,00	0
LMOD1	6,34E-09	2,05E-05	3,70E-04	46,30	51,52	48,90813	128,34	210,09	255,45	281,19	218,7686	0,22	169,86	2
ZSCAN1	3,20E-07	7,78E-04	1,87E-02	0,00	5,82	2,90836	64,78	57,92	41,26	23,83	46,94695	0,06	44,04	0
EIF3C	5,79E-07	1,21E-03	3,37E-02	57,13	69,80	63,4664	195,57	423,59	277,40	157,28	263,4583	0,24	199,99	2
SYT11	1,68E-06	2,87E-03	9,77E-02	43,34	103,04	73,19037	220,02	285,04	228,24	238,30	242,8984	0,30	169,71	2
TCEAL2	2,12E-06	3,52E-03	1,23E-01	109,34	181,98	145,6597	475,48	281,64	554,79	606,23	479,5334	0,30	333,87	2
SEMA5A	3,32E-06	5,01E-03	1,94E-01	240,35	302,47	271,4093	562,26	782,45	1118,36	637,68	775,1894	0,35	503,78	2
LINC02303	4,08E-06	5,80E-03	2,38E-01	13,79	4,15	8,972653	116,12	39,75	68,47	37,17	65,37805	0,14	56,41	0
FRRS1L	8,97E-06	1,11E-02	5,23E-01	17,73	14,13	15,92843	53,78	63,60	78,13	49,57	61,26754	0,26	45,34	0
AL591846.2	1,68E-05	1,78E-02	9,78E-01	8,87	10,80	9,833907	66,00	30,66	43,01	49,57	47,31162	0,21	37,48	0
ADM	1,74E-05	1,81E-02	1,00E+00	137,91	207,74	172,8226	517,04	399,74	374,84	366,02	414,41	0,42	241,59	2
CHCHD2	2,03E-05	2,08E-02	1,00E+00	87,67	184,47	136,0708	426,59	540,56	473,15	255,45	423,9389	0,32	287,87	2
UGT2B7	2,14E-05	2,11E-02	1,00E+00	0,00	0,83	0,415480	39,11	35,20	35,11	31,46	35,22179	0,01	34,81	0
LRRC3B	2,38E-05	2,24E-02	1,00E+00	18,72	48,20	33,45571	150,34	67,00	153,62	156,32	131,8225	0,25	98,37	1
CHST9	3,11E-05	2,74E-02	1,00E+00	71,91	55,67	63,791	205,35	115,83	250,18	166,81	184,5433	0,35	120,75	2
C1DP1	3,45E-05	2,95E-02	1,00E+00	4,93	1,66	3,29353	26,89	23,85	32,48	21,92	26,28558	0,13	22,99	0
TAS2R64P	4,30E-05	3,48E-02	1,00E+00	1,97	0,83	1,400516	31,78	26,12	23,70	12,33	23,49817	0,06	22,10	0
PARM1	5,01E-05	3,95E-02	1,00E+00	39,40	100,55	69,97385	144,23	232,81	223,85	338,38	234,8166	0,30	164,84	2
LPAR1	5,49E-05	4,25E-02	1,00E+00	75,85	48,20	62,02174	174,79	224,86	170,30	115,34	171,3204	0,36	109,30	2
CSRP1	8,96E-05	6,00E-02	1,00E+00	238,38	221,04	229,7071	387,47	596,21	523,19	430,84	484,4275	0,47	254,72	2
IQSEC3	1,03E-04	6,67E-02	1,00E+00	16,75	9,14	12,94303	33,00	57,92	37,75	237,34	91,5024	0,14	78,56	0
KLHDC7A	1,06E-04	6,77E-02	1,00E+00	11,82	1,66	6,741176	45,23	77,22	71,98	12,33	51,70564	0,13	44,96	0
HSPB8	1,32E-04	8,00E-02	1,00E+00	99,49	137,94	118,7141	193,13	365,67	319,53	267,84	286,5441	0,41	167,83	2
AL356489.2	1,38E-04	8,23E-02	1,00E+00	3,94	3,32	3,631993	48,89	32,93	46,53	5,72	33,51756	0,11	29,89	0
PUF60	1,45E-04	8,37E-02	1,00E+00	451,15	454,54	452,841	734,61	1253,74	943,67	852,15	946,0425	0,48	493,20	2
ZNF155	2,19E-04	1,15E-01	1,00E+00	29,55	18,28	23,91611	70,89	73,82	75,49	51,47	67,91903	0,35	44,00	2
ACTG1	2,24E-04	1,16E-01	1,00E+00	9562,73	10451,83	10007,28	14788,76	25936,77	19246,52	20393,38	20091,36	0,50	10084,08	2
WASH2P	2,59E-04	1,27E-01	1,00E+00	42,36	76,45	59,40247	138,12	115,83	150,99	185,87	147,7036	0,40	88,30	2
MRI1	2,61E-04	1,27E-01	1,00E+00	69,94	78,11	74,02393	155,23	179,43	172,06	128,68	158,8499	0,47	84,83	2
TRPM5	2,72E-04	1,31E-01	1,00E+00	30,54	22,44	26,48603	55,00	145,36	57,06	98,18	88,90065	0,30	62,41	2
PSPHP1	2,79E-04	1,32E-01	1,00E+00	0,99	0,83	0,907998	44,00	34,07	38,62	0,00	29,17426	0,03	28,27	0
AF127577.4	2,83E-04	1,32E-01	1,00E+00	148,74	231,01	189,8738	471,81	387,25	542,50	309,78	427,8377	0,44	237,96	2
NACA3P	3,08E-04	1,39E-01	1,00E+00	6,90	9,97	8,433391	24,45	23,85	41,26	71,49	40,26041	0,21	31,83	0
MT1X	3,28E-04	1,44E-01	1,00E+00	22,66	26,59	24,62329	46,45	68,14	88,66	73,40	69,16061	0,36	44,54	2
WASH6P	3,36E-04	1,44E-01	1,00E+00	12,81	9,14	10,97302	62,34	34,07	25,46	49,57	42,85744	0,26	31,88	0
CKB	4,57E-04	1,85E-01	1,00E+00	338,85	306,62	322,7384	490,15	976,65	571,47	776,85	703,7773	0,46	381,04	2
RAMP2-AS1	4,70E-04	1,88E-01	1,00E+00	7,88	15,79	11,83427	44,00	51,10	35,99	33,36	41,11487	0,29	29,28	0
SYPL2	5,31E-04	2,01E-01	1,00E+00	38,42	19,94	29,17973	78,23	122,65	76,37	58,14	83,84811	0,35	54,67	2
NEDD9	5,42E-04	2,03E-01	1,00E+00	575,26	919,87	747,5673	1300,54	1244,66	1674,91	1830,11	1512,555	0,49	764,99	2
DTX4	5,42E-04	2,03E-01	1,00E+00	531,92	769,47	650,6946	1037,74	1260,56	1380,83	1181,95	1215,27	0,54	564,58	2
H19	5,96E-04	2,20E-01	1,00E+00	7495,14	6639,38	7067,258	12166,90	22080,16	18211,55	10078,97	15634,39	0,45	8567,14	2
HERC2P2	8,00E-04	2,73E-01	1,00E+00	791,97	795,23	793,5992	2070,60	2098,65	1588,00	996,08	1688,333	0,47	894,73	2
PDGFD	8,24E-04	2,79E-01	1,00E+00	860,92	773,62	817,273	2461,74	2060,04	3064,52	861,68	2111,995	0,39	1294,72	2
PDGFRA	9,46E-04	3,10E-01	1,00E+00	93,58	52,35	72,96447	267,69	112,43	158,89	194,45	183,363	0,40	110,40	2
ZNF185	9,51E-04	3,10E-01	1,00E+00	674,75	912,40	793,5723	1334,77	1281,00	1372,06	1462,19	1362,5	0,58	568,93	2

Supplementary table 4. Top 50 most significantly downregulated genes in p.R138Q patient podocytes compared to controls. DESeq2 normalized expression of downregulated genes in p.R138Q patient podocytes compared to controls. Genes are classed by p-value.

2. Complementary results

A) Proteasome inhibition

In a podocyte cell line stably expressing p.R138Q podocin, it has been shown that proteasome plays a predominant role in massive degradation of p.R138Q mutant podocin and that its inhibition promotes a partial re-addressing of mutant podocin to podocyte plasma membrane protrusions, namely filopodia[184]. We therefore sought to determine whether it was the case also in kidney organoids by performing an overnight treatment of D21 SRNS*NPHS2* 007#27 patient kidney organoids with different doses (0.1, 0.5 or 1.0 µM) of bortezomib, a reversible proteasome inhibitor. Immunofluorescence staining with podocin and nephrin did not show any obvious change, neither in podocin expression level nor in its localization, in the bortezomib treated organoids compared to those exposed to the vehicle (DMSO) (Fig. 55).

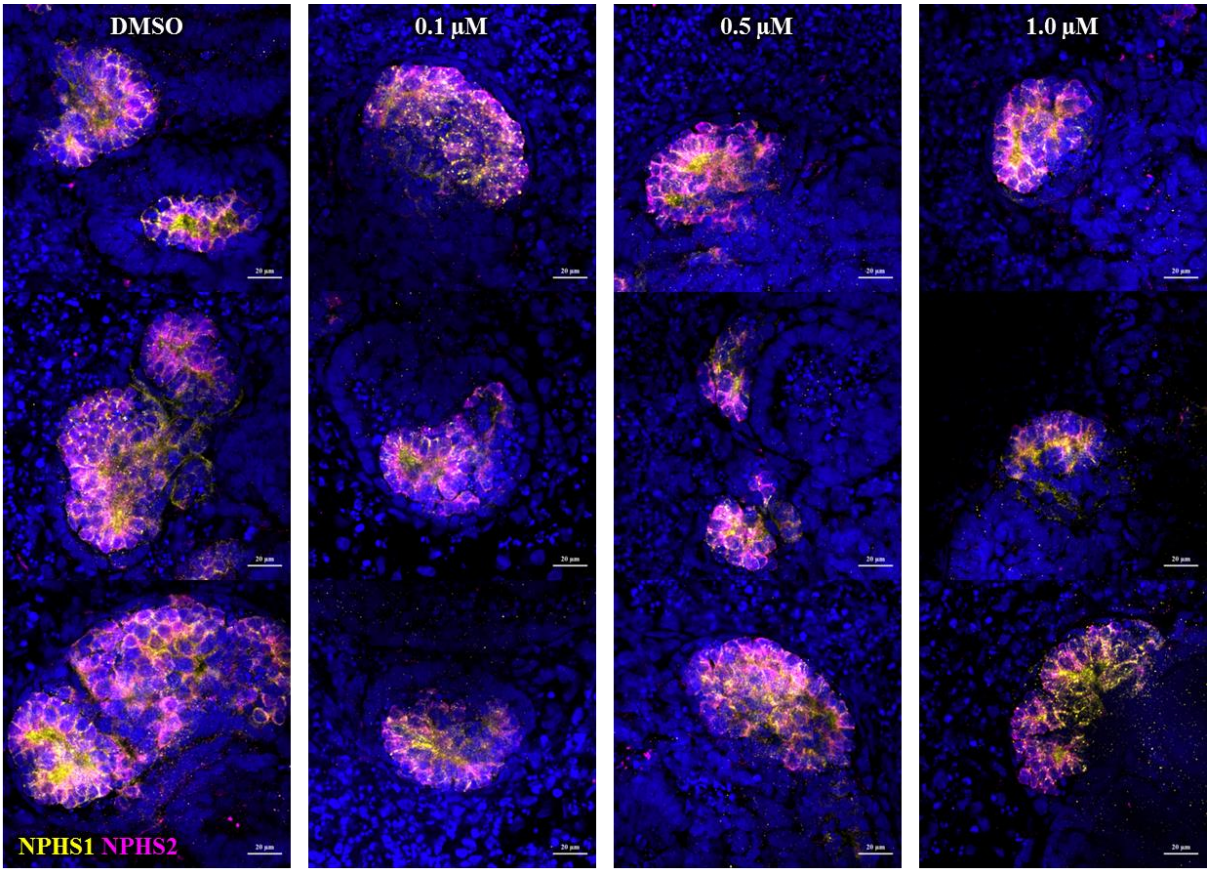

Figure 55: Proteasome inhibition. Immunofluorescence staining on D21 kidney organoids for nephrin (NPHS1, yellow) and podocin (NPHS2, magenta) upon overnight bortezomib treatment. Representative images of untreated (DMSO) and 0.1, 0.5 or 1.0 µM bortezomib-treated glomeruli are reported in different columns. Nephrin and podocin staining are substantially equivalent in kidney organoid glomeruli exposed to the vehicle or treated with the proteasome inhibitor bortezomib.

No difference was analogously evidenced by extending treatment duration to 20 or 24 hours, a condition that conversely seemed to deteriorate the status of organoids and increase cell death (data not shown). These results suggest that, in the kidney organoid system, bortezomib does neither impact p.R138Q podocin expression level, nor its localization to the plasma membrane following proteasome inhibition.

B) *NPHS2* expression

Since it has been demonstrated that mutant *Nphs2* transcript is upregulated in both knock-in *Nphs2*$^{R140Q/R140Q}$ and conditionally inducible hemizygous *Nphs2*$^{R140Q/-}$ mouse models[183,408], I checked the expression level of *NPHS2* in the transcriptome of the SRNS^{NPHS2} 007#27 patient podocytes compared to control. Despite a non-statistically significant difference, I observed a ~60% decrease of the mutant transcript expression level in SRNS^{NPHS2} 007#27 podocytes compared to controls. A similar trend was also present in the pilot RNA-Seq experiment, displaying a 2-fold reduction in *NPHS2* expression. However, there is little evidence regarding the expression of human mutant *NPHS2* transcripts in the literature. For instance, no transcript changes have been highlighted in a compound heterozygous p.R138Q/p.V180M podocin patient by *in situ* hybridization[179].

C) Validation of the interferon-like response activation

Despite unexpected, the IFN signature was not only outstanding from the "official" podocyte transcriptomic profiling, but also detectable in the RNA-Seq pilot analysis, in which the presence of an antiviral response had already been highlighted by GO analysis performed on differentially expressed genes. The comparison of only one patient *versus* one control sample imposed at that time to adopt semi-subjective criteria in defining the gene sets, while preventing from the possibility to apply any statistics. However, in light of this second RNA-Seq analysis, the credibility of the antiviral/IFN response called upon reconsideration.

When comparing the upregulated genes in SRNS^{NPHS2} 007#27 patient podocytes in both RNA-Seq experiments, their high level of correspondence was striking. The most (significantly) upregulated genes included of note *OAS1*, *2* and *3*, *IFI27*, *44* and *44L*, *MX1*, *HLA-C* and many other IFN-stimulated genes. The persistence of the immunity signature in independent experiments strongly supports its reliability, especially if considering the great variability in differentiation of iPSCs into organoids and the influence of the dissociation and sorting processes on the transcriptome. Nevertheless, the relevance of a hypothetical model of pathogenesis that implies this kind of immunity mechanism raises innumerous legitimate questions.

On the basis of these considerations, I estimated to investigate the IFN I-like response activation as a candidate pathological mechanism, aware that proper validation is certainly needed. Beyond a definitive confirmation of the hypothetical activation of this pathway in 007#27 podocytes, our major concern is to determine whether this activation is clone-, line- or mutation-dependent.

If assuming the IFN signature to be truthful for the 007#27 podocytes - the probability of its detection as a mere coincidence or due to an artifact in three independently differentiated and collected samples analyzed in two separated RNA-Seq experiments being extremely weak - the facts remains that it could be due to the line/clone intrinsic properties.

CRISPR/Cas9 corrected 007#27 clones we generated represent the ideal control to prove the involvement of this mutation in the activation of the INF response. Shutdown of the response in corrected podocytes would prove the causality of the mutation, while its persistence would refer to an effect of the genetic background instead.

Therefore, I have planned to perform a **subsequent RNA-Seq analysis** using new batches of podocytes isolated from kidney organoids. Samples collection for this purpose has been scheduled for July 2020. The project will include several SRNS^{NPHS2} 007 patient clones (007#27, 007#32, 007#34), 007#27 CRISPR/Cas9 corrected clones (007C#A, 007C#B, 007C#C...), internal unmodified CRISPR/Cas9 controls (007ic#A, 007ic#B) and healthy controls (005#04, 013#19).

Meanwhile, having no samples left to validate this results by RT-qPCR, I took advantage of **immortalized podocyte cell lines** established from a patient bearing the p.R138Q mutation at the homozygous state (named LP) and from a healthy control (named LY) (both kindly provided by Pr. M. Saleem, Bristol, UK). I investigated the **expression of IFN-stimulated genes**, *MX1*, *IFIT1*, *IRF9* and *OAS2* by RT-qPCR. Under permissive conditions, at 33°C, the expression of all of these genes was slightly higher in the control LY cell line compared to the p.R138Q patient LP one. Upon differentiation, which was performed by switching the culture at 37°C for 14 days[289], this difference was attenuated or even inverted in "differentiated" podocytes (Fig. 56).

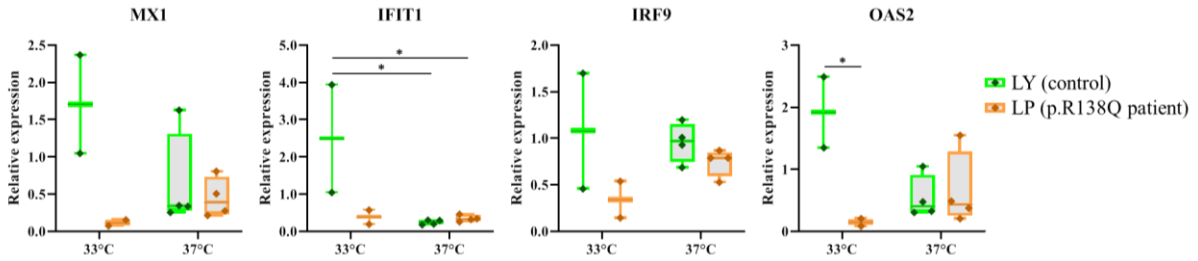

Figure 56: RT-qPCR for IFN-stimulated genes in immortalized podocyte cell lines. Relative expression of *MX1*, *IFIT1*, *IRF9* and *OAS2* in control LY (green) and p.R138Q patient LP (orange) immortalized podocyte cell lines grown under permissive conditions (33°C) or "differentiated" (37°C). Undifferentiated podocytes grown at 33°C display a similar expression profile for the IFN-stimulated genes under investigation, with higher expression in control LY podocytes compared to the p.138Q patient LP ones. The expression level of these genes is comparable between "differentiated" (37°C) control LY and p.138Q patient LP podocytes instead. Statistical significance has been reached for *IFIT1*, whose expression in control LY podocytes is significantly higher under permissive conditions (33°C) compared to both LY and LP "differentiated" podocytes (37°C), and for *OAS2*, for which the significant difference between undifferentiated (33°C) control LY and p.138Q patient LP podocytes disappears upon differentiation (37°C). Relative expression has been calculated using the $2^{-\Delta\Delta Ct}$ method normalizing on *HPRT* expression. Two-way ANOVA with Turkey's multiple comparison correction has been applied (*, p-value<0.05).

Anyhow, this weak tendency did not denote a veritable activation of the IFN response pathway in these differentiated podocytes. Furthermore, when checking the expression of ***NPHS2*** by RT-qPCR, the **transcript** was **not detectable** in the differentiated podocytes (data not shown). Podocyte maturation was thus only partial, since cell morphology clearly evolved into a typical large arborized aspect, with expression of synaptopodin detected by IF (data not shown), but no expression of *NPHS2* at the mRNA level.

Lack of expression of the causative gene clearly questions the relevance of this system. To overcome this problem, I sought to employ **transduced immortalized podocytes** that **overexpress** the **wild-type podocin** or mutant forms of podocin, **p.R138Q** or **p.A284V**, the latter leading to a mutant protein localized in vesicles instead of being ER-retained as observed for p.R138Q, suggesting a different pathological mechanism[409]. Nevertheless, all the transduced podocytes, whatever the construct they expressed, displayed an upregulation of the tested markers compared to non-transfected podocytes (NT) (Fig. 57). The effect was generally more important in differentiated podocytes compared to those in an undifferentiated state at 33°C. Most probably, lentiviral transduction activates *per se* the innate immune response. For these reasons, I did not take these results into account, since overexpression likely introduced a considerable bias.

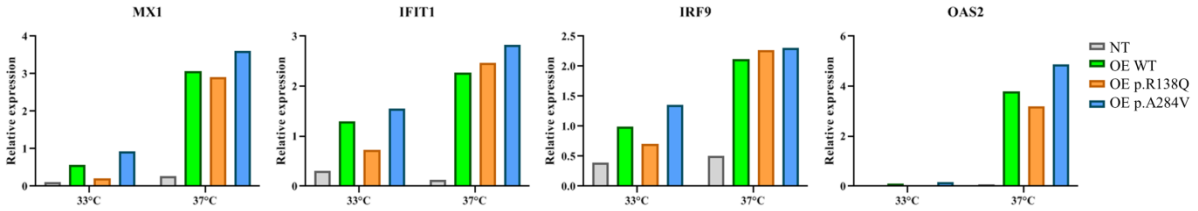

Figure 57: RT-qPCR for IFN-stimulated genes in immortalized podocyte cell lines overexpressing podocin constructs. Relative expression of *MX1*, *IFIT1*, *IRF9* and *OAS2* in non-transduced (grey) or transduced immortalized podocyte cell lines overexpressing the wild-type (green), p.R138Q (orange) or p.A284V (blue) podocin constructs, grown under permissive conditions (33°C) or differentiated (37°C). The expression level of the IFN-stimulated genes under investigation is higher in transduced podocytes regardless the podocin construct. This is particularly true for "differentiated" podocytes (37°C). Relative expression has been calculated using the $2^{-\Delta\Delta Ct}$ method normalizing on *HPRT* expression.

Finally, I sought to verify whether strong IFN-stimulated genes expression was already associated with the SRNS^{NPHS2} 007 patient line - or more specifically with the 007#27 clone - in iPSCs or at early differentiation stages, corresponding to the emergence of NPCs. I thus performed RT-qPCR on iPSCs and NPCs at D8, 9 and10, using the 009#02 and 013#19 as controls and 2 independent clones of the SRNS^{NPHS2} line, the 007#27 and #34. I added IFN-stimulated (IFN+) and untreated (IFN-) fibroblast samples as controls. *IFIT1* and *OAS2* expression were neither detected in control 013#19 nor in SRNS^{NPHS2} 007#34 cells, at any time point (Fig. 58).

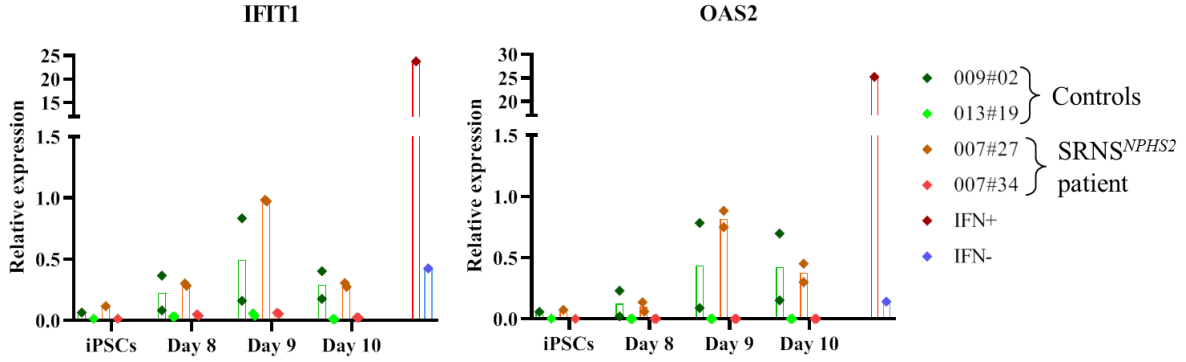

Figure 58: RT-qPCR for IFN-stimulated genes in iPSCs and NPCs. Relative expression of *IFIT1* and *OAS2* in control 009#02 and 013#19 (green) and SRNS^{NPHS2} 007#27 and 007#34 patient (orange) iPSCs and nephron progenitor-like cells at D8,9 and 10, and in IFN-stimulated (IFN+, red) or untreated (IFN-, blue) fibroblasts. The control 009#02 and the SRNS^{NPHS2} 007#27 patient lines have similar expression profiles for *IFIT1* and *OAS2*. However their expression is far lower than IFN-stimulated cells. Relative expression has been calculated using the $2^{-\Delta\Delta Ct}$ method normalizing on *HPRT* expression.

Weak expression of both *IFIT1* and *OAS2* was observed in control 009#02 and SRNS^{NPHS2} 007#27 cells instead, "peaking" at D9 (Fig. 58). Nevertheless, the expression level was one order of magnitude lower with respect to IFN-stimulated fibroblasts, and comparable to the untreated ones, suggesting it would be likely represent a "basal" state. Both in the pilot and in the following RNA-Seq experiments, IFN-stimulated genes displayed considerable expression level in SRNS^{NPHS2} patient podocytes, having a fold-change of hundreds or even thousand times compared to control, in which they constitute the background transcriptional noise. Despite this result does not validate the IFN signature identified by RNA-Seq, it prompts to exclude its presence in SRNS^{NPHS2} 007 patient cells in steady-state (iPSCs) and at early developmental stages (NPCs). According to these data, the IFN-like response activation would not be exclusively SRNS^{NPHS2} 007#27 patient line/clone-dependent, rather it may manifest in this line/clone in specific conditions, as in the context of differentiated podocytes, increasing the likelihood of its implication in the disease.

If the new RNA-Seq data analysis confirms the implication of the INF-like response, complementary analysis on animal models, such as in the Nphs2$^{R140Q/R140Q}$ mouse model[183], or ideally investigation on patient biopsies would finally help to elucidate the effective implication of an IFN-like response in the pathogenesis of podocin p.R138Q-related SRNS.

D) Functional protein association network analysis

With the aim of highlighting potential implication of up- or down-regulation of genes in the context of NS, I performed a **functional protein association network analysis**. For that, I selected all the significant differentially expressed genes (BH-corrected p-value<0.05), and seek for interactions with genes associated with NS (Introduction, Chapter 2, Table 1)

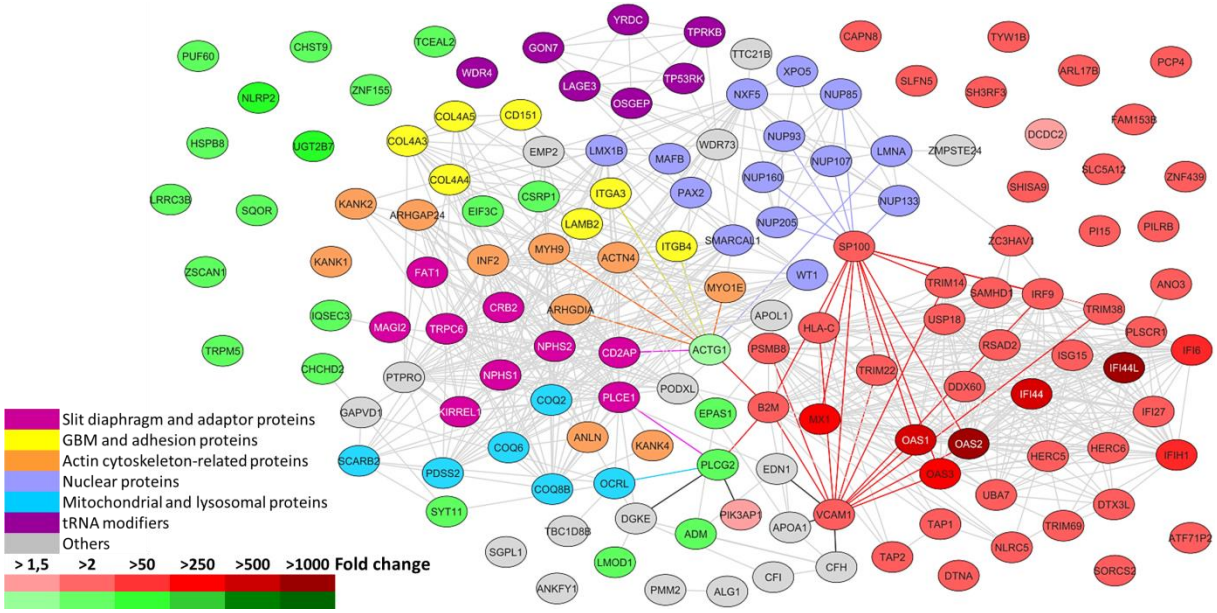

Figure 59: Functional protein association network. Network of functional protein association between significant differentially expressed genes (BH-corrected p-value<0.05) and genes associated with NS. Up- and down regulated gene fold change in R138Q podocytes is expressed on a red or green scale, respectively. The various categories of NS-related genes are reported with different colors. Relevant interactions are highlighted in colors.

using the STRING database[410]. About half of the downregulated and one third of the up-regulated genes did not display functional association with any other queries (Fig. 59).

Not surprisingly, the **INF signature** was evidenced by the densely interconnected cluster of proteins already mentioned, comprised in the "type I interferon signaling pathway", "antigen processing and presentation […] via MHC class I" and "defense response to virus" gene ontology (GO) categories (Fig. 59). This compact immunity interactome displayed few connections with the NS network, principally passing through the proteins encoded by *SP100* and *VCAM1* (Fig. 59). Significantly down-regulated genes do not display functional interaction among their protein products, which may explain the absence of GO enrichment for any category. Part of them is uniformly incorporated within the NS network, among which *PLCG2* and *ACTG1* are the major nodes.

D.a) Nuclear autoantigen Sp-100 (*SP100*) and nuclear bodies (NBs)

The nuclear autoantigen Sp-100, encoded by the *SP100* gene, is a constitutive component of the **nuclear bodies** (NB), also known as promyelocytic leukemia NBs, given by their principal constituent protein, PML. NBs are dynamic sub-nuclear organelles involved in several biological processes, including regulation of transcription and translation, senescence, apoptosis and antiviral defence[411]. They normally range from 2 to 30 distinct spots per cell with a size of 0.2 to 1 µm, depending on the cell type, cell cycle phase and developmental stage[412]. Interestingly, NBs are stress-responsive structures, whose size and number increase in response to several kinds of stimuli. In the context of the antiviral immunity, they are **induced by IFN** and they associate with the transcriptionally active **MHC class I *locus***. In addition, PML NBs have also been related to the **unfolded protein response**, but mainly nuclear unfolded proteins have been shown to elicit this response at present[413–416].

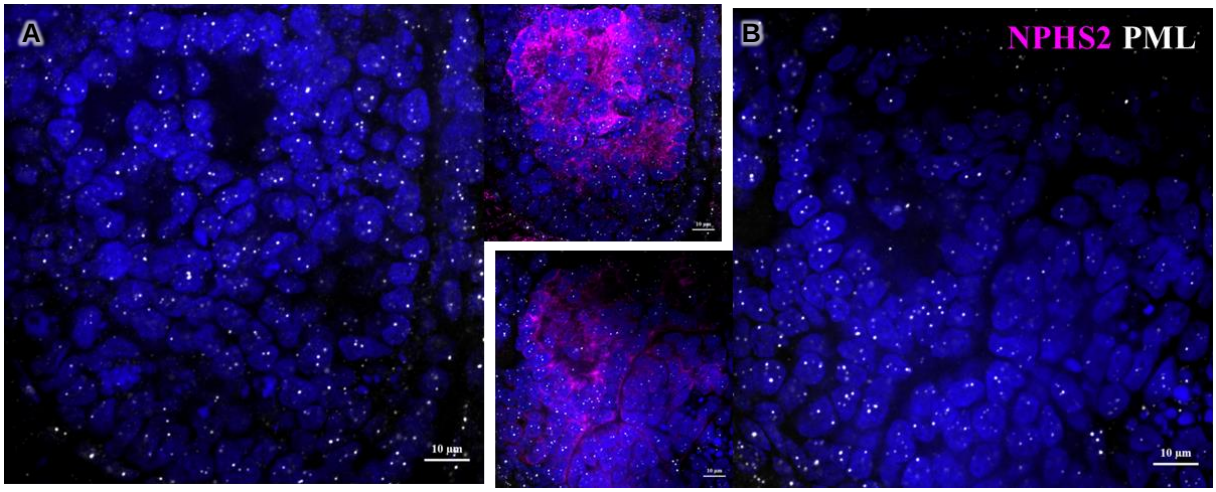

Figure 60: Nuclear bodies. Immunofluorescence staining for podocin (NPHS2, magenta) and promyelocytic leukemia (PML, grey) on **A)** control and **B)** SNRS^{NPHS2} patient D21 kidney organoids. Middle panels: double staining. External panels: single PML staining. The size and number of NBs per nucleus, as defined by PML staining, are not noticeably different between control and SNRS^{NPHS2} patient glomeruli in kidney organoids.

Anyway, despite the fact that both *PML* and *SP100* are induced by IFN at the transcriptional level, *SP100* 40 fold expression increase was not accompanied by a significant change in *PML* expression in R138Q podocytes compared to controls, according to the RNA-Seq data. Consistently with that, no obvious change in NB pattern was observed by IF in R138Q and control kidney organoid glomeruli stained for PML (Fig. 60).

D.b) Vascular cell adhesion protein 1 (*VCAM1*)

The vascular cell adhesion protein 1 is an adhesion molecule of the Ig superfamily which plays a pathogenic role in several inflammatory renal injuries[417]. Although circulating VCAM-1 is as a biomarker for primary FSGS, its increase has prevalently been ascribed to **endothelial dysfunction** occurring in NS[418,419]. Indeed, *VCAM1* expression marks endothelial activation by pro-inflammatory cytokines, mediating leukocyte adhesion and signal transduction. Nevertheless, besides its predominant role in inflamed endothelium, *VCAM1* is expressed in other cell types, including professional antigen presenting cells such as macrophages and dendritic cells[420,421]. *VCAM1* expression has been reported to be stimulated by TNFα in human conditionally immortalized podocytes[422,423], and to be also upregulated by TNFα in mouse primary podocytes[422], but its role in pathogenic conditions remains elusive.

D.c) Phospholipase C γ2 (*PLCG2*) and PI3K adapter protein 1 (*PIK3AP1*)

The phospholipase C is a family of phosphodiesterases responsible for the production of the second messengers inositol 1,4,5-trisphosphate (IP_3) and diacylglycerol (DAG) through the hydrolysis of phosphatidylinositol 4,5-bisphosphate (PIP_2) located at the inner leaflet of the plasma membrane. PIP_2 is also the substrate of the phosphoinositide 3-kinase, which mediates PIP_2 phosphorylation to generate phosphatidylinositol 3,4,5-trisphosphate (PIP_3), and whose regulator *PIK3AP1* is upregulated in turn. Interestingly, both *PLCG2* and *PIK3AP* have been implicated in the regulation of the immune response[424,425], advocating again immune properties of the podocyte.

D.d) Actin γ1 (*ACTG1*) and actin-related proteins

Actin γ1, encoded by the *ACTG1* gene, is a cytoplasmic actin comprised among the top 50 most abundantly expressed genes in control kidney organoid podocytes (Appendix, Table A5), and its expression is reduced by half in R138Q podocytes (Article 2, Table S4). Right below the threshold of significance settled for the analysis (p-value$<3\times10^{-4}$ for down regulated genes), *ACTB*, encoding actin β, displayed a similar 2 fold reduction (p-value 1.27×10^{-3}). Despite no NS-associated gene reached statistical significance after correction for multiple test hypotheses, several genes encoding protein related to the actin cytoskeleton, cell adhesion or polarity, namely *CRB2*, *CD151*, *ARGHDIA* and *KANK*, displayed a 35.5 ± 0.77 % expression decrease in R138Q podocytes compared to controls (mean ± SEM; p-value<0.05. Appendix, Table A4), likely disturbing the actin cytoskeleton dynamics.

Galloway-Mowat Syndrome
KEOPS complex

In the present study, we disposed of iPSC lines derived from 3 patients affected with GAMOS, 2 of which bearing mutations in the *GON7* gene, and the other in *OSGEP*. We differentiated GAMOS^{GON7} and GAMOS^{OSGEP} iPSCs towards disease-relevant cell/tissue types, namely kidney organoids and late CPCs. We employed these patient-derived iPSC derivatives to assess the impact of GAMOS mutations on the biology of podocytes and neurons, in an attempt to highlight common and/or specific pathophysiological mechanisms of these cell types.

1. Characterization of GAMOS kidney organoids

Kidney organoids were differentiated from the iPSC lines GAMOS^{GON7} IMAGINE 006 and GAMOS^{OSGEP} IMAGINE 008. Both lines similarly generated organoids, suggesting the absence of major developmental defects in nephron morphogenesis. As it could be expected, these lines and relative clones displayed variable responsiveness to induction between them and compared to healthy controls. Diversity in differentiation efficiency and on organoids morphology reflected that variability. Anyhow, all the main features of kidney organoids were maintained in patient derivatives: both GAMOS^{GON7} and GAMOS^{OSGEP} organoids displayed a general architecture analogous to healthy controls, with structured nephron segments (Fig. 61A). Glomeruli were composed by clusters of podocytes expressing all their specific markers (Fig. 61B), with no evident differences pointing out.

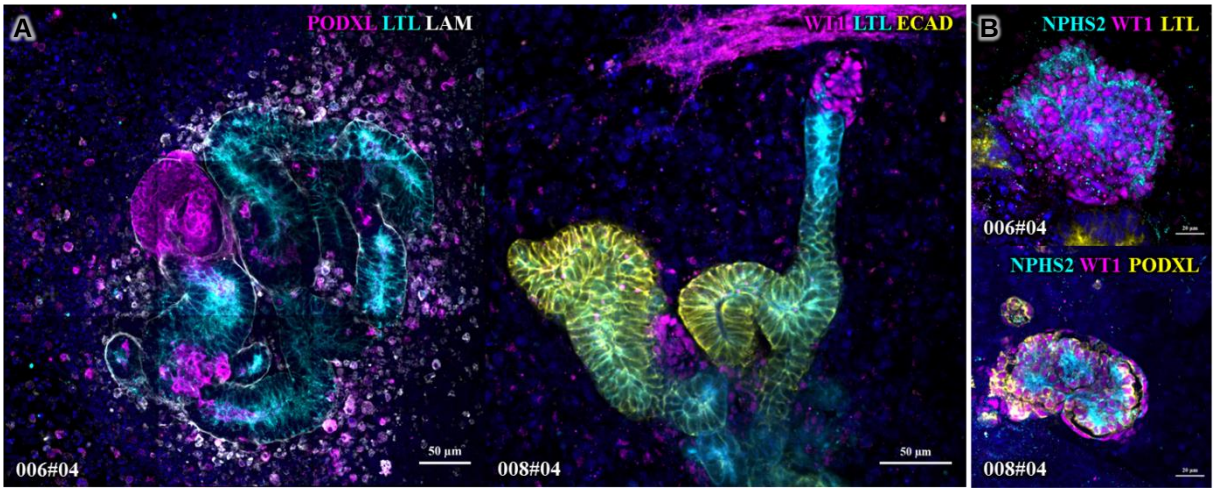

Figure 61: Characterization of GAMOS patient kidney organoids by IF. Immunofluorescence staining on GAMOS patient D21 kidney organoids. **A)** Left panel: GAMOS^{GON7} 006#04 patient kidney organoid stained for podocalyxin (PODXL, magenta), LTL (cyan) and laminin (LAM, grey). Right panel: GAMOS^{OSGEP} 008#04 patient kidney organoid stained for WT1 (magenta), LTL (cyan) and E-cadherin (ECAD, yellow). **B)** Immunofluorescence staining on D21 GAMOS patient glomeruli. Upper panel: GAMOS^{GON7} 006#04 patient glomerulus stained for podocin (NPHS2, cyan), WT1 (magenta), and podocalyxin (PODXL, yellow). Lower panel: GAMOS^{OSGEP} 008#04 patient glomerulus stained with podocin (NPHS2, cyan), WT1 (magenta), and LTL (yellow). GAMOS patient kidney organoids and glomeruli present as normal.

Podocyte ultrastructure was analyzed at a finer level by TEM in order to unveil potential cellular and/or subcellular alterations. While GAMOS^{GON7} kidney organoids presented with octopus-shaped podocytes nicely organized in glomerular structures, glomeruli in GAMOS^{OSGEP} organoids contained holes filled with apoptotic bodies in between podocytes (Fig. 62). In order to determine whether apoptosis could be a "disease-phenotype" for GAMOS^{OSGEP} podocytes, further investigations were pursued.

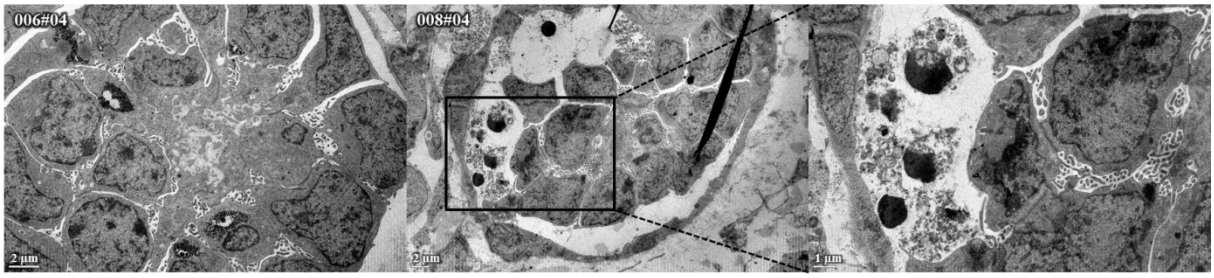

Figure 62: Characterization of GAMOS patient kidney organoids by TEM. D21 GAMOS^{GON7} 006#04 (left panel) and GAMOS^{OSGEP} 008#04 (middle panel) patient glomerular podocytes under TEM. GAMOS^{GON7} patient podocytes nicely organize into compacted glomeruli. GAMOS^{OSGEP} glomeruli present with intercellular holes filled with apoptotic bodies. Right panel: zoom on apoptotic bodies.

I performed IF for the active-cleaved form of caspase 3, highlighting extensive apoptosis in GAMOS^{OSGEP} 008 patient glomeruli, which was instead only sporadically observed in controls, as well as in GAMOS^{GON7} glomeruli (Fig. 63).

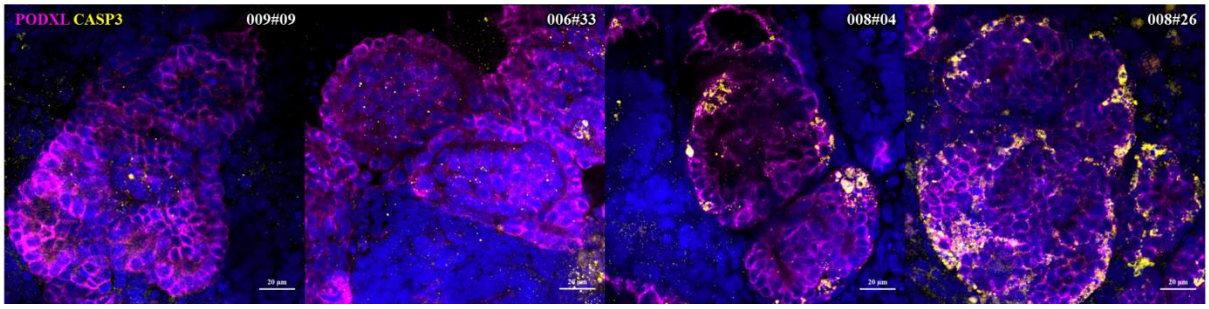

Figure 63: Apoptosis in GAMOS^{OSGEP} patient kidney organoid glomeruli. Immunofluorescence staining for podocalyxin (PODXL, magenta) and active-cleaved caspase 3 (CASP3, yellow) on D21 control 009#09, GAMOS^{GON7} 006#33 and GAMOS^{OSGEP} 008#04 and 008#26 patient glomeruli (panels from left to right). Patches of active-cleaved caspase 3 staining denote substantial apoptotic cell death in GAMOS^{OSGEP} patient glomeruli.

These observations in GAMOS^{OSGEP} patient-derived glomeruli are consistent with our previous published data showing increased apoptosis in immortalized podocyte cell lines and in zebrafish brain following *OSGEP* knock-down or knock-out, respectively[145].

2. Late cortical progenitor cells (CPCs)

iPSCs can be differentiated into several region-specific neuronal and glial subtypes[426], such as cortical and dopaminergic neurons, or astrocytes, oligodendrocytes and microglia. As long as microcephaly disorders are often underlined by a reduced amount of neural progenitor cells, we sought to employ a stable population of self-renewing cortical progenitor cells. We choose to apply the Boissart's 2013 protocol[314] (Fig. 64), which was mastered by the iPSC Platform and by other research groups within the *Imagine Institute*.

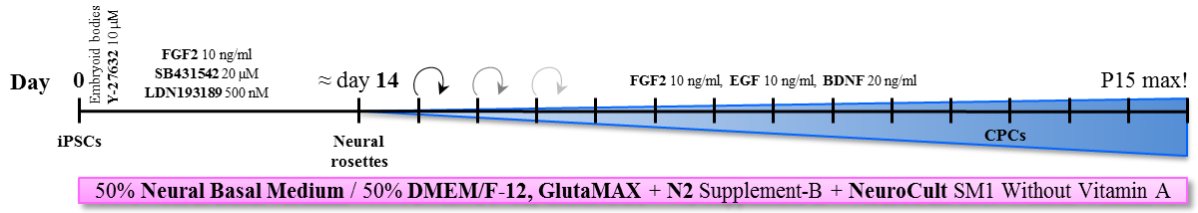

Figure 64: Late cortical progenitor cell differentiation protocol. Schematic representation of the differentiation protocol applied to induce late CPCs from iPSCs. Differentiation protocol consists of an embryoid body generation step, followed by neuroectodermal induction. Neural rosettes emerging in culture around day 14 are manually collected, and split by trypsination (curved arrows) from the following passage onwards, maintaining cells in pro-proliferative conditions for a maximum of 15 passages (P15) as described elsewhere[314].

Actually, the GAMOS-related project of my PhD is inscribed into the "*Microcephaly cross-lab*" program of the *Imagine Institute*, gathering the research and clinical teams of Pr. N. Bahi-Buisson, Dr. A. Pierani, Pr. C. Antignac, Dr. V. Cantagrel, Dr. E. Kabashi, Dr. JP. de Villartay and the iPSC Platform. This inter-disciplinary environment has been favorable for discussion and sharing of information between groups with different domains of expertise.

Functional studies on CPCs may uncover defective mechanisms leading to brain anomalies found in GAMOS patients. We therefore employed CPCs to investigate fundamental cellular processes, such as proliferation and apoptosis, which have already been shown to be perturbed in other cellular systems[145,147].

A) Late CPC induction and quality control

Late CPCs were differentiated from the IMAGINE GAMOS^{GON7} 006 and IMAGINE GAMOS^{OSGEP} 008 patient iPSC lines. Control 004#17 and 005#04 and patient 006#04 and 008#04 CPC lines were generated at the iPSC Platform of the *Imagine Institute*. I performed the induction of the control 009#09 and GAMOS^{GON7} 006#33 and GAMOS^{OSGEP} 008#26 patient cell lines. At that time, M. Boisson, M2 intern, joined our laboratory and work with me on the modeling of neural aspects of GAMOS using late CPCs. I trained her to the induction and culture of CPCs (Fig. 64). We next expanded the CPC line numbers by addition of a second GAMOS^{GON7} CPC line, the 023#11. When necessary, we re-induced some of the clones to always dispose of fresh and good-quality CPCs, below passage 15.

To assess the quality of induced CPC line, we privileged the analysis of the HNK1 and P75 markers by flow cytometry, an approach that is routinely used by the iPSC Platform of the *Imagine Institute* as well as by other research groups working on CPCs inside and outside the *Institute*. Ideally, CPCs should be >95% **HNK1^{+}/P75^{-}**. We considered a threshold of 80-85% as acceptable to validate a CPC line. I validated that way the control 009#09, GAMOS^{GON7} 006#33 and GAMOS^{OSGEP} 008#26 patient CPC lines (Fig. 65A). In addition, I checked the expression of the neuroectodermal intermediate filament **nestin** and the radial glia marker **SOX2** by IF in control 009#09 CPCs as a complementary method (Fig. 65B). All the CPCs that have been used for the following experiments equally underwent analogous validation (data not shown).

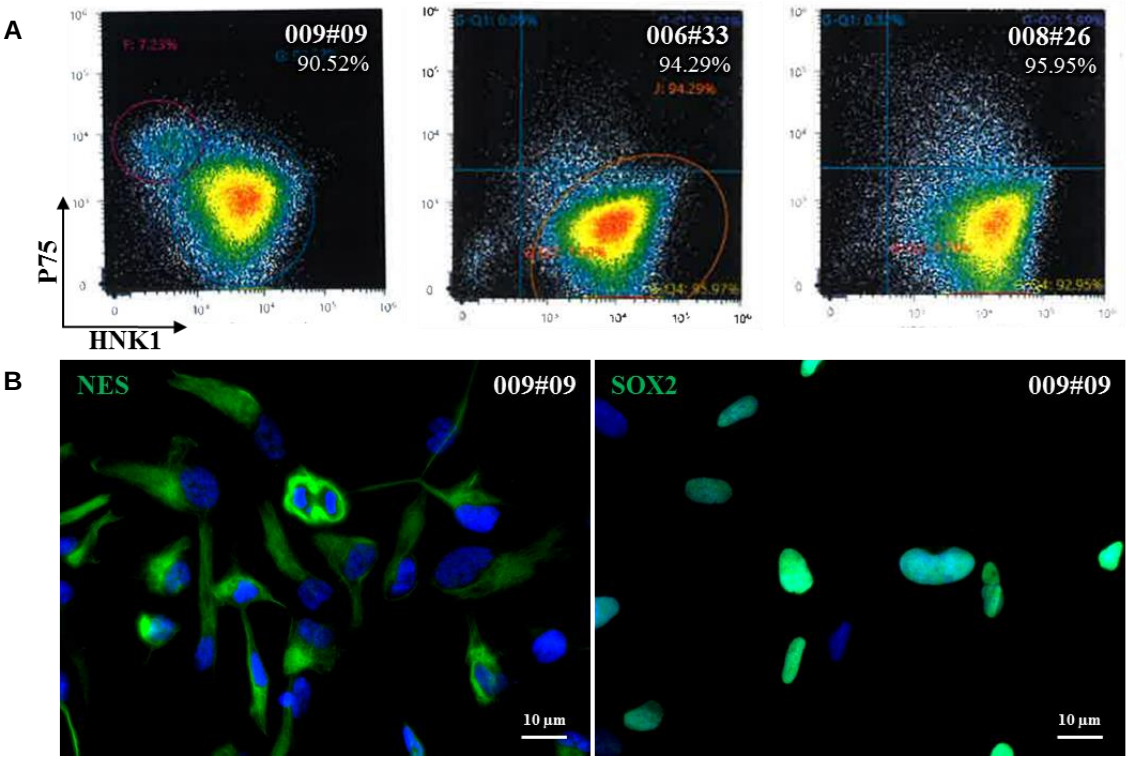

Figure 65: Late cortical progenitor cell quality control. **A)** Cytofluorimetric profiles of CPCs stained for P75 (y axis) and HNK1 (x axis). The percentage of $HNK1^{+}/P75^{-}$ cells is reported. The control 009#09, $GAMOS^{GON7}$ 006#33 and $GAMOS^{OSGEP}$ 008#26 patient CPC lines all pass the quality control, displaying a percentage of $HNK1^{+}/P75^{-}$cells >90%. **B)** Immunofluorescence staining for nestin (NES, green; left panel) and SOX2 (green; right panel) on control 009#09 CPCs. The great majority of CPCs displayed cytoplasmic fiber-like nestin and nuclear SOX2 stainings, consistent with their intermediate filament and transcription factor roles, respectively, and with the neural cellular lineage.

B) Proliferation

B.a) MTT assay

I first employed the MTT assay, a colorimetric analysis based on the reduction of the yellow tetrazole 3-(4,5-dimethylthiazol-2-yl)-2,5-diphenyltetrazolium bromide (MTT) into the violet formazan by NAD(P)H-dependent cellular oxidoreductase enzymes[427]. Variation in the medium color reflects cell metabolic activity, so absorbance measurement provides indirect quantification of cell number. I performed two independent experiments with 3 different initial cell seeding concentrations (5, 4 and 3 $\times 10^4$ cells/cm^2), but I did not observe the establishment of a typical growth curve of cell proliferation upon 4 days of follow-up (Fig. 66). Fluctuating absorbance measurements that do not fit with a logistic growth model may be due attributable to various parameters, including technical or biological factors. One possible explanation might rely on the high proliferation rate of LCPCs, which is likely sustained by a strong metabolic activity that would be over the detection limit/sensibility of the technique. Alternatively, we simply fail in finding the optimal experimental conditions to perform this kind of assay. Whatever the explanation, we decided to move towards a different approach to evaluate proliferation, as described below.

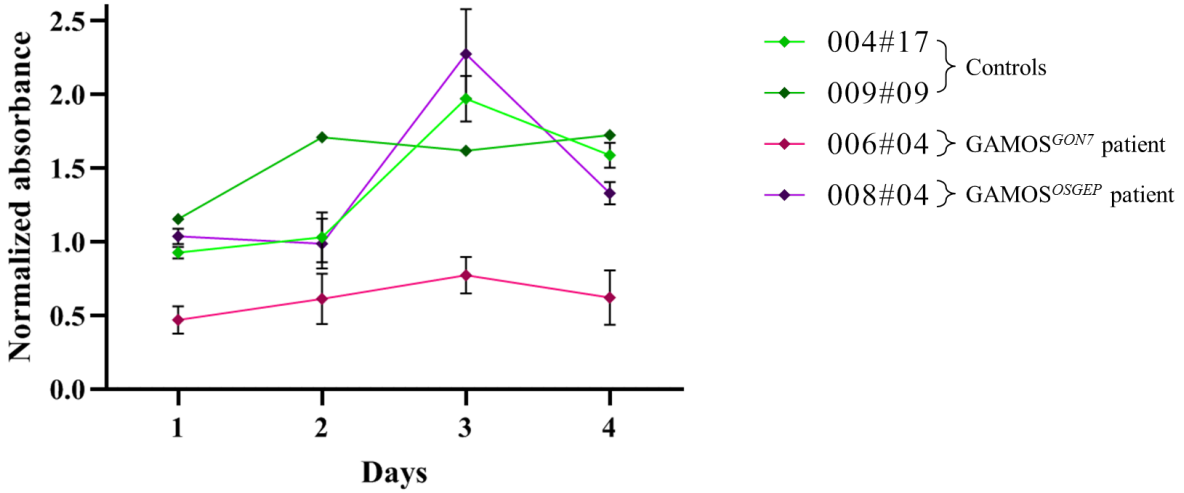

Figure 66: Late cortical progenitor cell MTT proliferation assay. Time course quantification of late CPC absorbance between day 1 and day 4. The absorbance measurements do not fit with a typical grown curve. Mean ± SEM (n=2).

B.b) IncuCyte

The IncuCyte system performs automated image acquisition over time, allowing following and analyzing changes of defined parameters that happen in cell culture in real-time. Seven independent experiments have been conducted in total, using the control 004#04, 005#04 and 009#09, GAMOS^{GON7} 006#04, 006#33 and 023#11 and GAMOS^{OSGEP} 008#04 and 008#26 patient CPC lines in different series. We evaluated cell proliferation by measuring the phase object confluence - meaning the percentage of the image area occupied by objects (Fig. 67) - over time, obtaining growth curves.

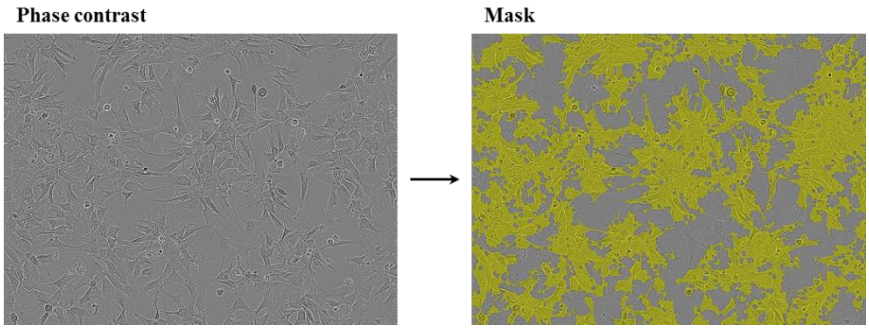

Figure 67: Late cortical progenitor cell IncuCyte phase contrast mask. Representative image of an IncuCyte phase contrast picture of CPCs and of the mask (yellow) generated with the IncuCyte analysis software.

Great extent of variability has been observed even among **controls** (Fig. 68A). In particular, the 004#17 CPCs displayed abnormal aggregation into apoptotic spherical structures labelled with the apoptosis marker Annexin V (Fig. 68B). Medium supplementation with laminin did not improve cell deficiency, which tended to reach a peak of 60-80% confluence before to inevitably decline (Fig. 68A). We thus excluded this 004#17 line from the comparative analysis. The 009#09 CPC line displayed the most robust and consistent proliferation behavior, even though 2 out of the 7 replicates showed a slightly slower progress (Fig. 68A, dark green, n=6 and 7). The 005#04 CPC line proliferated at a lower rate compared to the 009#09 one, and had a lower constancy. Of the triplicates we carried out, one shaved a cellular confluence close to 0% (Fig. 68A, light green, n=6), most indubitably due to technical problems. This replicate was not taken into account.

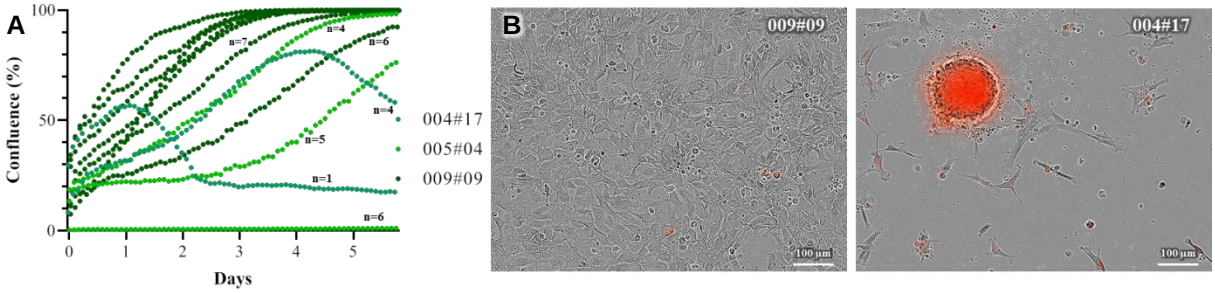

Figure 68: Control late cortical progenitor cell IncuCyte proliferation assay. **A)** Growth curves of control CPC lines. Distinct experiment series are indicated as n=1 to 7. **B)** Representative images of 009#09 (left panel) and 004#17 (right panel) control CPC lines stained for Annexin V 3 days after seeding. Phase contrast and red fluorescence channel.

When taking into account only the exploitable experiments, we observed a substantially similar proliferative behavior of GAMOS^{GON7} CPCs compared to controls (Fig. 69). Curiously, the GAMOS^{OSGEP} 008#04 and 008#26 clones, issued from the same cell line - and thus related to the same patient - proliferated in a remarkably different way. In particular, 008#04 CPCs systematically failed to reach confluence in all the experiments. Rather, they growth until an average 60-70% cell confluence before to decline (Fig. 69).

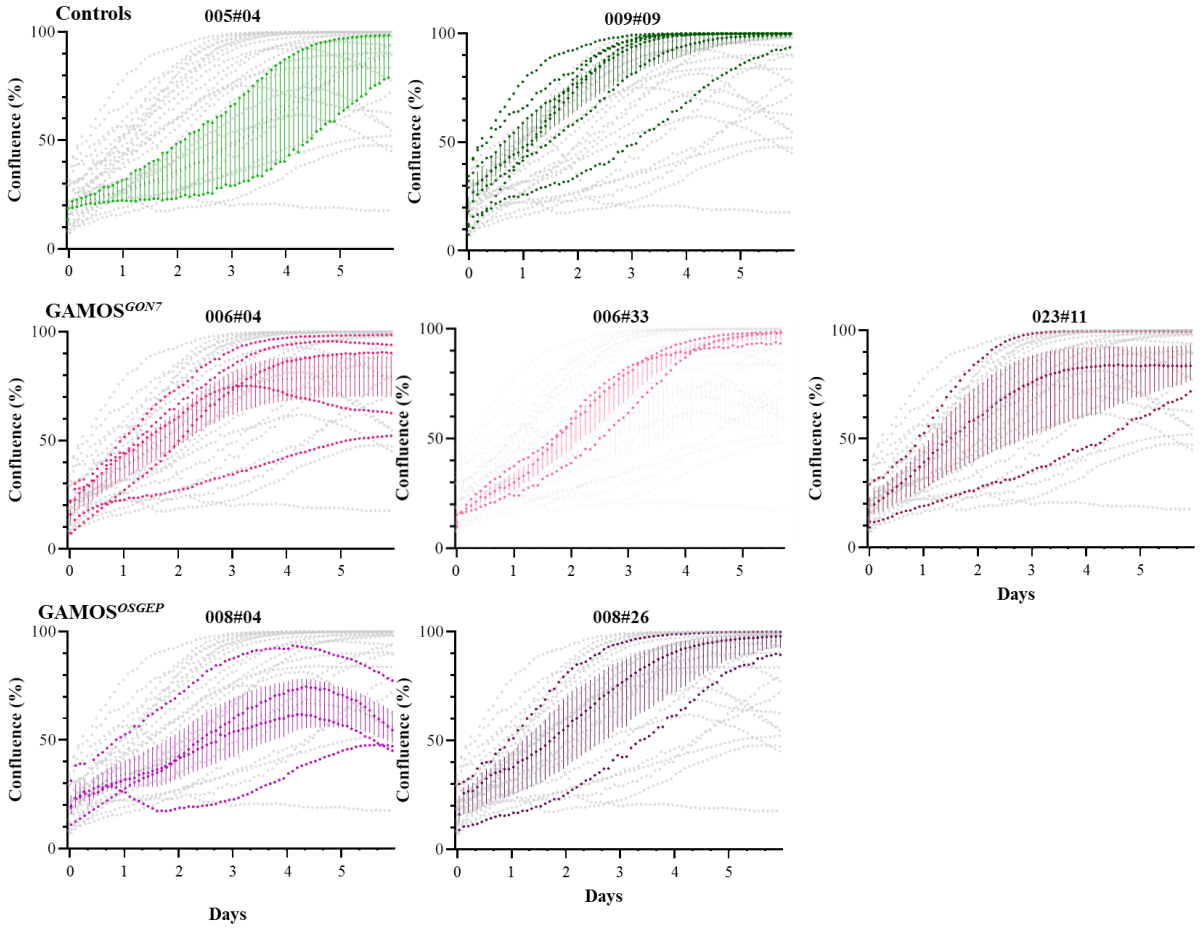

Figure 69: Late cortical progenitor cell IncuCyte proliferation assay. Growth curves of all control and GAMOS patient-derived CPC lines. Upper panels: control 005#04 (n=2) and 009#09 (n=7) CPC lines. Middle panels: GAMOS^{GON7} 006#04 (n=5), 006#33 (n=3) and 023#11(n=3) patient CPC lines. Lower panel: GAMOS^{OSGEP} 008#04 (n=4) and 008#26 (n=3) patient CPC lines. Individual values and mean ± SEM.

We estimated the proliferation rate by calculating the slope of the curves at the log phase, meaning the period during which cells exponentially grow and that can be approximated as linear (Table 6).

Table 6: Slope of late cortical progenitor cell growth curves at the log phase

		Controls		GAMOS^{GON7}			GAMOS^{OSGEP}	
		005#04	009#09	006#04	006#33	023#11	008#04	008#26
Proliferation assay	1		2.86	1.92			1.45	
	2		1.60	1.66			0.86	
	3		2.33	1.56			1.10	
	4	1.43	2.79	1.85			1.33	
	5	1.66	1.73		1.59	2.54		2,10
	6	-	1.02		1.76	0.74		1,11
	7		1.49	0.52	1.61	1.52		1,38

Table reporting the slope of growth curves at the log phase for the control 005#04 and 009#09, GAMOS^{GON7} 006#04, 006#33 and 023#11 GAMOS^{OSGEP} and 008#04 and 008#26 patient CPC lines.

The growth curve slops were not significantly different among the CPC lines (Fig. 70A) suggesting the absence of a major proliferation defect, even though a weak tendency for a decreased proliferation rate of GAMOS^{GON7} and - slightly more pronounced - GAMOS^{OSGEP} CPCs was observed when grouping the results according to the respective mutation (Fig. 70B).

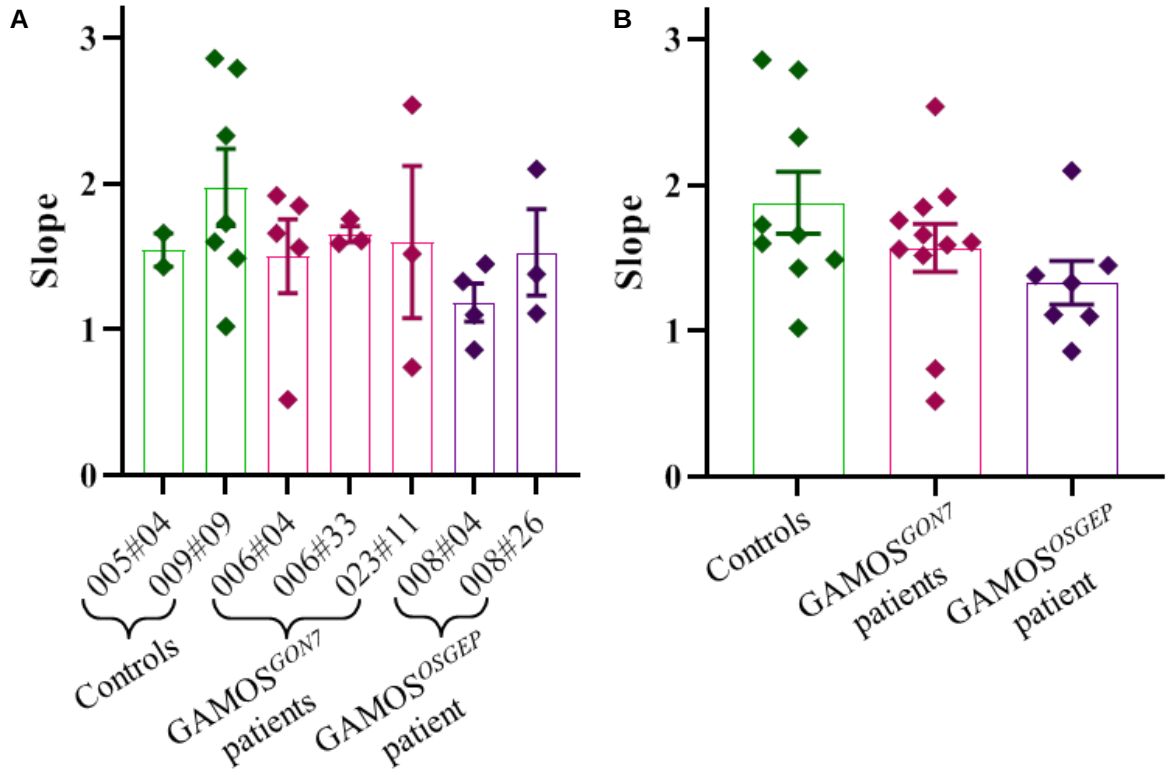

Figure 70: Slope of late cortical progenitor cell growth curves at the log phase. Mean slope of CPC growth curve ± SEM for **A)** independent CPC lines/clones and **B)** grouped CPC lines/clones according to the respective mutation. One-way ANOVA with Turkey's multiple comparison correction has been applied.

C) Apoptosis

We analogously took advantage of the IncuCyte system to evaluate apoptosis in CPCs. This technique allows performing fluorescence labeling of viable cells, which can be followed-up over time. We performed 4 independent experiences using florescence-labeled Annexin V. Over the apoptotic-related signal measurement, which was determined as a percentage of fluorescent object confluence, we also extracted the cell confluence information from images. In order to rapport the absolute apoptotic dimension to the effective cell number, we normalized the Annexin V signal on the relative cell confluence.

We observed increased apoptosis in both GAMOS^{GON7} and GAMOS^{OSGEP} patient-derived CPC lines compared to control, which was particular significant in the first day of culture (Fig. 71).

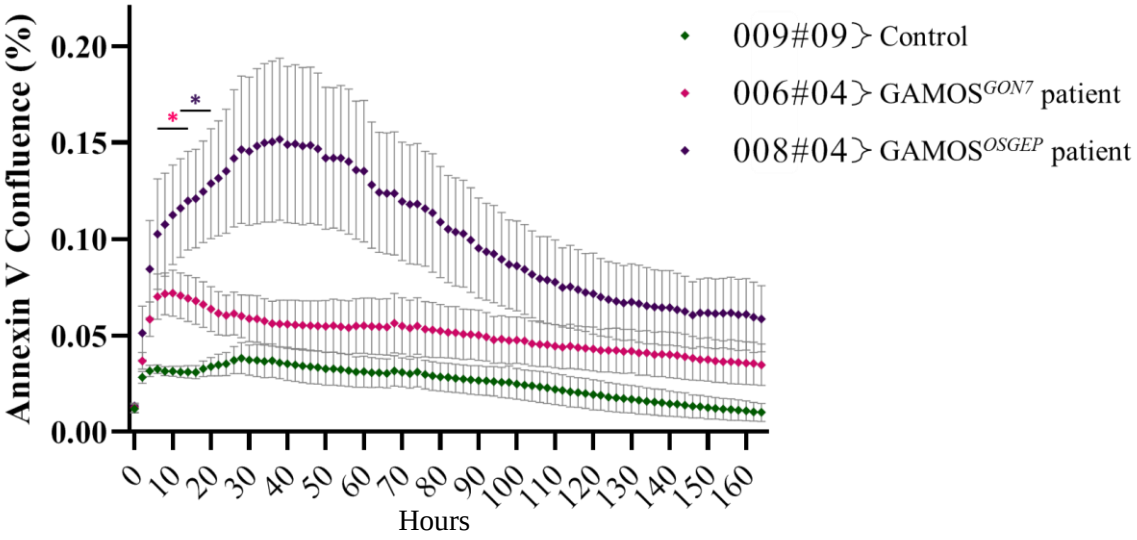

Figure 71: Late cortical progenitor cell IncuCyte apoptosis assay. Time course of CPC Annexin V fluorescence object confluence normalized on cell confluence. The apoptotic curve was significantly higher for the GAMOS^{OSGEP} 008#04 patient CPCs. An increase in the apoptotic rate was instead more moderate for the GAMOS^{GON7} 006#04 patient CPCs. Mean ± SEM. 2-wayANOVA has been applied (n=4; *, p-value>0.05; pink asterisk, GAMOS^{GON7} 006#04 patient *versus* control 009#09; purple asterisk, GAMOS^{OSGEP} 008#04 patient *versus* control 009#09).

These data reinforce the implication of apoptotic cell death as a common mechanism involved in GAMOS pathogenesis, particularly related to *OSGEP* mutations. Apoptosis has indeed already been shown in *OSGEP* knock-down immortalized podocyte cell lines[145], and observed in glomeruli of GAMOS^{OSGEP} patient kidney organoids, as reported above. Here we expanded previous work by demonstrating significant increase of apoptosis in an additional and pathophysiologically relevant cell system, that is, GAMOS patient-derived CPCs.

D) t^{6}A measurement

Since the canonical function of the KEOPS complex is to mediate the post-translational t^{6}A modification on ANN-decoding tRNAs, we measured t^{6}A levels in CPCs by mass spectrometry (Fig. 72). Preliminary analyses have been performed using 2 samples for each CPC line, hampering for the moment the possibility of drawing pertinent conclusions.

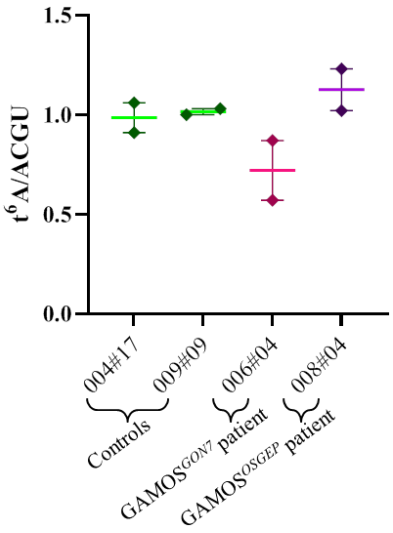

Figure 72: Late cortical progenitor cell t^6A quantification. t^6A amount normalized for the 4 canonical ribonuclesides (adenosine, cytidine, guanosine and uridine).

E) Protein synthesis

Finally, on account of the t^6A contribution in ensuring accurate and efficient translation, *de novo* protein synthesis would be likely affected by mutations in KEOPS components. Despite defective protein synthesis has been evidenced in knock-down of KEOPS subunits in immortalized podocyte cell lines[145,147] I did not observe any translational impairment in GAMOS^{GON7} 006#04 and GAMOS^{OSGEP} 008#04 patient CPCs compared to 2 independent control lines (Fig. 73) in preliminary experiments using HPG incorporation measurement, an alkyne-containing methionine analog. Three other HPG experiments have been conducted in triplicates by an independent experimenter in the laboratory, using 2 controls (005#05 and 009#09), 3 GAMOS^{GON7} (006#04, 006#33 and 023#11) and 2 GAMOS^{OSGEP} 008#04 and 008#26) patient CPC lines (data not shown). We denoted great variability in the data that prevent us to evidence any protein synthesis defects. We do think that we faced a technical issue, rather this technique may be not appropriate for protein synthesis measurement in CPCs.

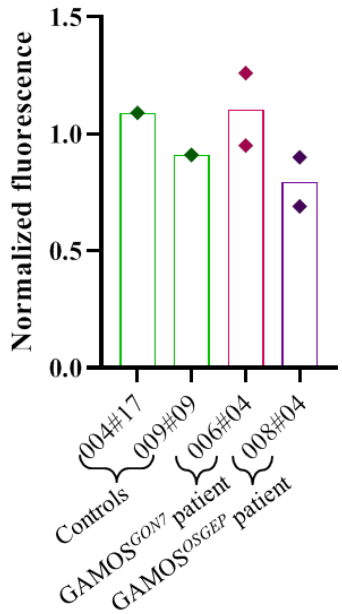

Figure 73: Late cortical progenitor cell HPG protein synthesis assay. Normalized fluorescence intensity (485/535 nm) reflecting HPG incorporation in 1 hour.

DISCUSSION

Setting-up of the necessary tools
iPSCs and kidney organoids

1. iPSCs in disease modeling

The first aim of my PhD thesis has been to develop new *in vitro* tools to obtain meaningful **"genetic disease in a dish" models**. Pr. C. Antignac's research group has focusing its efforts in identifying new genes and deciphering the pathological mechanisms underlying the establishment of hereditary glomerular disorders over the past years. Currently existing cellular models, such as immortalized human and mouse podocyte cell lines, are reaching theirs limits. In particular, the absence of a 3D structure fully recapitulating the complex organization of the GFB makes glomerular disorders challenging to model. Moreover, in conditionally immortalized podocyte cell lines the expression of SD proteins that characterize mature podocytes, such as nephrin and podocin, is extremely variable, even sometimes absent[290], as I denoted when checking the expression of *NPHS2* in LY and LP podocyte cell lines. Animal models unquestionably helped to dissect the molecular actors of glomerular permeability maintenance, but species-specific differences might be responsible for the impossibility of recapitulating the human disease phenotype. In addition, according to the "3R principle", *R*eplacement of animal beings with non-sentient material is ethically advisable when possible. Improving *in vitro* podocyte models becomes necessary to better understand the pathological mechanisms that underlay podocyte dysfunction in patients with mutations in known NS genes or in new candidate genes to prove their pathogenicity. In this context, the advent of iPSCs has opened up new avenues for *in vitro* disease modeling. Since iPSCs can be directly derived from easily accessible patient cells, this technique allows personalized disease modeling with cells with the patient's own genetic background. Alternatively, gene editing can be applied to introduce the putative causative mutation into a control line, when patient cells are not available.

For my thesis, I had the chance to dispose of several patient derived iPSC lines. We published the generation of the SRNS^{NPHS2} IMAGINi007 patient iPSC line as "Lab Resource: Single Cell Line article" in *Stem Cell Research* (**Article 1**)[391], which I signed in first author. This iPSC line represented a valuable tool for the laboratory, allowing to gain insights into the pathological mechanisms that lead to hereditary **SRNS**, as presented in "Results, Part 2".

More recently, the laboratory has turned its attention towards the **GAMOS syndrome**, associating SRNS with microcephaly and additional CNS disorders, for which they have greatly contributed in identifying causative mutations in several genes[145,147,162]. However, the cellular and molecular mechanisms underlying this disease are still poorly understood.

GAMOS raises the fascinating question of deciphering the molecular pathways that could be common to the development and functioning of the glomerulus and the nervous system, in agreement with numerous publications showing that podocytes and neurons share a large number of molecular processes essential to the brain and kidney. During my PhD, I employed 3 GAMOS patient-derived iPSC lines, bearing mutations in genes coding the GON7 (IMAGINE 006 and 023) and OSGEP (IMAGINE 008) subunits of the KEOPS complex. In my thesis, I took advantage of GAMOS^{GON7} and GAMOS^{OSGEP} iPSC lines to model both renal and neural aspects of GAMOS, by differentiating them into disease-relevant derivatives, namely kidney organoids and late CPCs, as presented in "Results, Part 2". As we did for the IMAGINi007 iPSC line (**Article 1**)[391], the GAMOS^{GON7} and GAMOS^{OSGEP}, as well as the 007 CRISPR/Cas9 gene edited iPSC line, in which we corrected the p.R138Q mutation in one allele, can be the object of future publications for the laboratory.

2. Variability in iPSCs and their derivatives

Variability associated with iPSC, and therefore with all the derivatives differentiated from them, is one of the major issues the iPSC community is struggling with. Indeed, iPSC may already present a **variable phenotype** when cultured at their pluripotent state, like for instance a different propensity for spontaneously differentiating, diverse proliferating rate or particular sensibility to handling and culture conditions. When applying a specific inductive protocol aimed to generate a cell type/tissue of interest, iPSCs may display **inconsistent differentiation potential**. Variable responsiveness to the treatment may impact the efficiency of differentiation, but also the characteristics of the final derivatives. Hence, several degrees of more or less predictable and controllable variability may be present at different levels.

A) Genetic variation

The first level of variation directly derives from the genetic landscape that is associated with the individual from which the iPSC line has been derived, human genomes differing for millions of SNPs one from each other. While the possibility of disposing of a personalized experimental system, for example deriving patient-specific iPSCs, represents one of the major advantages of this model, it is also responsible for the great heterogeneity existing among the different iPSC lines derived from distinct individuals. Indeed, the **genetic background** has been shown to highly contribute to the iPSC phenotypic variability, at a rate that has been estimated at 5 to 46%[428]. Many experimental models, both *in vitro* and *in vivo*, rely on a relative homogeneous background, performing for instance overexpression or knockdown of a gene of interest in established cell lines, or using defined strains of animals. To provide an example related to the kidney field, the C57BL/6 mouse strain, widely used for transgenesis, appears to be relatively resistant to the development of glomerulosclerosis, proteinuria and hypertension[429], illustrating the impact of the genetic background in defining specific susceptibilities or resistances.

Moreover, since independent clones are derived for each iPSC line, somatic mosaicism may account for additional - even though minor - variation. In fact, each iPSC clone is generated from a single source cell, which has doubtlessly accumulated **somatic mutations**. While these "germinal" variants already distinguish different iPSC clones, **spontaneous mutations** tend to further accumulate in culture, making clones to drift over time. Some genomic rearrangement are positively selected in iPSCs, the chromosomal 12 and sub-chromosomal 20q11.2 duplications being the most recurrent aneuploidies[430]. Aware of this **genomic instability**, we systematically checked the quality of our iPSCs by performing a karyotype analysis every 10-15 passages. This allowed us to ensure the absence of major rearrangements, such as chromosomal abnormalities. Point mutation and small anomaly identification would require more powerful techniques, such as whole genome - or exon - sequencing. However, the depth of quality controls should be adapted to the downstream application. We and others consider **karyotyping** as adequate and sufficient to validate iPSC clones for disease modeling purpose. A whole genome approach would be crucial instead for assessing the quality of iPSCs in the perspective of using them in therapy for instance.

In order to limit the effect of this variation, **matched control iPSC lines** for ethnicity, gender and age should be preferred. When possible, iPSC lines can be derived from a healthy relative of the patient, ideally a sibling or one of the parents. While for a dominant genetic disease a healthy relative may represent a good control, in recessive disorders it is important to consider that a mutation in the gene of interest can be present in one of the alleles. Unless derived from a healthy individual, the corresponding line might - or not - present different susceptibility than a "real" control, but at the same time it could balance the risk of being confounded by a different genetic background.

As it was the case for countless other domains, the **CRISPR/Cas9** technology has also revolutionized the iPSC-based disease modeling field. It allowed indeed to overcome the issue of inter-line/clone variability by generating **isogenic iPSC clones** that only differ for the desired editing. By applying the CRISPR/Cas9 system to iPSCs, it is possible to correct patient mutations, in order to assess their causality with respect to a given phenotype. *Vice versa*, a specific mutation can be introduced in a control iPSC line. This can be particularly important in the case of limited access to patient cells. To provide an example of the actual potential of the CRISPR/Cas9-mediated genome editing - which refers to kidney organoids - *PKD1*$^{-/-}$ and *PKD2*$^{-/-}$ knock-out PSC lines have been successfully employed to model polycystic kidney disease (PKD)[283,378]. However, when PKD patient-derived iPSCs have been investigated, they "*exhibited dramatic line-to-line variability in their ability to form organoids, regardless of PKD genotype and organoid differentiation protocol. The morphology of tubular structures also varied noticeable between different lines. As such differences reflected a degree of heterogeneity that would confound analysis of PKD-specific effects* [the authors] *focused* [their] *studies on CRISPR-mutant hPSCs* "[283].

B) Epigenetic variation

While most of the iPSC variability is due genetic background, as discussed above, the reprogramming history of a given iPSC line/clone may lead to incomplete and/or aberrant, or simply "different" epigenetic reprogramming. iPSCs may retain some extent of the donor cell **epigenetic memory**, which would bias their propensity of differentiation towards the cell lineage they are derived from[431].

The most common cell sources for reprogramming currently used are fibroblasts and PBMCs, due to their accessibility and establishment of standardized reprogramming protocols. Skin-derived fibroblasts are globally employed to generate iPSCs by the research groups working on kidney organoids worldwide. We disposed instead of PBMCs that were reprogrammed to iPSCs. Anyway this different source wouldn't have any reason to impact kidney organoid differentiation more than fibroblast-derived iPSCs. On the contrary, the PBMC lineage is developmentally closest to the kidney, since both have mesodermal origin. In addition, PBMCs have the advantage to be less exposed to UV-mediated mutagenesis, which accounts for most of the heterogeneity in fibroblast-derived iPSCs mutation rate[432].

C) Kidney organoid differentiation variability

The protocols to generate kidney organoids from iPSCs are generally complex multi-step procedures during which a multitude of different parameters contribute to determine both the efficiency of generation and the features of kidney organoids.

The notorious **iPSC line-to-line** and **clone-to-clone variation** represents thus only the first determinant of differentiation variability. Responsiveness to the kidney organoid inductive protocol might significantly vary among each iPSC clone, even for clones belonging to a same iPSC line, due to their intrinsic properties[378]. Anyhow, these inter-clonal differences contribute to a lesser extent to kidney organoid variability than the experiment-to-experiment variation, as evidenced by scRNA-Seq analysis[405]. Indeed, organoids differentiated in the same experimental batch have been shown to share bigger similarities among them compared to organoids obtained in independent experiments, even if the same protocol was applied for the same iPSC clones[405].

We should initially consider that iPSCs - constituting the basis for differentiation - are an entity in continuous evolution. Depending on the **passage number** or the **different vial** in use, their characteristics might thus not be the same. In order to minimize this effect, we generally employed iPSCs at low passage number (<35), and at similar passage numbers when working with multiple iPSC lines/clones at the same time. Secondly, the iPSC quality and density at the beginning of differentiation is crucial to determine its favorable outcome[280,295]. **iPSC optimal density** must be as high as necessary to allow intercellular contacts and maximize the organoid yield, but at the same time low enough to leave enough space for expansion and morphological changes happening during organoid development.

If at the beginning of my PhD I applied the Morizane's protocol[330] without any variation, which implied enzymatic dissociation and single cell seeding at a defined density, I subsequently moved to an alternative approach. Most of the organoids that I presented in this PhD thesis dissertation have been obtained by directly applying the inductive protocol on iPSC colonies issued from manual clump passaging. This method allowed greatly reducing the cell stress associated with enzymatic dissociation, simplifying at the same time the step of preparation of the iPSC culture for differentiation. Enzymatic dissociation is indeed trickier to perform, and it might easily end up in the failure of the differentiation experiment. However, if rigorously mastered, it allows increasing standardization and homogeneity of kidney organoid generation. This is still a subject of debate in the laboratory, in a continuous effort to improve the efficiency of differentiation and the kidney organoid yield. Dissociating and counting a defined cell number is indeed doubtlessly more objective than visually estimating adequate confluence. This instance let me introduce another point of discussion, which is the subjective **experimenter-associated variation**. At every intervention in person, the different handling, technical gestures or sensibility in decision making, for example when adjusting the "Step 4" according to cell morphology, may contribute to increase variability. If this issue can be present within a same research group, for experimenter formed in the same way, who usually work together exchanging opinions and comparing results, it is even more true between different laboratories. This notion of **inter-laboratory** source of **variation** has already been raised by comparing the proportion of specific cell types obtained by independent group that applied the same differentiation protocol, using scRNA-Seq[433]. Finally, an additional level of unpredictability is banally introduced from the **reagents**, since different batches may vary one from each other, or molecule stability decline over time.

The cumulative effect of the fluctuations in all these parameters, most of them being hardly controllable, is at the basis of the great variability in differentiation efficiency of iPSCs towards kidney organoids. If it has been demonstrated that organoids generated within a same batch are the most similar, particularly with respect to maturation state and nephron patterning and cell proportions[405], each single organoid actually represents a unique stochastically self-organized entity, individually shaped by the directed differentiation process in a singular way.

C.a) Dealing with kidney organoid differentiation variability

To handle this variability, the research groups having set up the differentiation procedures to generate kidney organoids from PSCs worldwide and/or working on this system to gain insights into the human kidney development and disease, rest on the use of **specific markers** that refers to defined developmental stages. I took advantage of these markers, in particular the ones employed in the Morizane's protocol[330], in order to orient and validate the transposition of the latter in our laboratory.

Nevertheless, verification of these specific markers by IF and/or RT-qPCR was laborious, time-consuming and sometimes poorly conclusive, since the timing of expression and regional definition of several markers is still under debate, and differences do exist between model animals in which they have been characterized and human development. In any case, this kind of approach was not appropriate for performing a routine verification of ongoing kidney organoid productions.

We empirically noticed a general correlation between the presence of D9 **renal rosettes**, most probably corresponding to pretubular aggregates or very early renal vesicles[392], and the D21 kidney organoids development. I characterized renal rosettes by means of different techniques, globally agreeing with the fact they would be a morphological readout of the presence of NPCs in the differentiating culture. Therefore, we mainly performed **morphological observation** along the differentiation process, as it turned out to be more convenient and straightforward. Secondly, we estimated the **final yield in kidney organoid** by taking into account both organoid obtaining and their number per surface unit, to adjust the protocol steps a posteriori. Following this optimized procedure allowed us to maximize the differentiation yield, while having at the same time enough differentiated kidney organoids for experimental purpose.

Generation of **lineage-specific reporter cell lines** is a valid alternative to directly monitor the emergence and the relative amount of cell entities of interest. Specifically, the NPC stage can be observed by employing *SIX2* reporters[276,277], and development of the podocyte lineage using *NPHS1*[276,278], *MAFB*[279] or other reporter iPSC lines for podocyte-specific markers. The establishment of reporter iPSC lines would be an important investment for the laboratory. The consistent advantages of disposing of reporter lines would compensate on the long time the technical challenge of inserting big constructs into the iPSC genome.

D) Podocyte variability

Apparently, the variability issue regarding kidney organoids is particularly prominent for podocytes. Indeed, the majority of the most variable genes identified by bulk RNA-Seq have been shown to be restricted to the podocyte cluster when performing scRNA-Seq[405]. This is in part related to the variable **proportion** of the cell types of the nephron segments and to the relative amount of off-target cells, but also to the **maturation** degree achieved.

D.a) Podocyte proportion

The highly variable relative amount of podocytes in the kidney organoid culture greatly hampered the possibility to perform appropriate “bulk” analysis. While IF and TEM procedures were most suitable to characterize kidney organoid podocytes, any procedure disrupting the structural architecture, thus averaging the podocyte contribution with all the various kidney organoid culture components, would have introduced substantial biases.

D.a;i) FACS strategy for podocyte isolation

In order to get rid from the bias introduced by the variable podocyte proportion in kidney organoids, we established a **FACS strategy** allowing the **isolation** of a pure population of **podocytes**. A similar kind of approach, which allows an enrichment of the epithelial $EPCAM^+$ fraction by magnetic-activated cell sorting (MACS) to reduce the transcriptional "noise"[284], was similarly considered by an independent group confronted with comparable problem. Others managed to enrich for the podocyte fraction through glomerular sieving[279], a procedure that was not easy to execute and not reproducible in our hands.

We based our strategy on work coming from Dr. R. Nishinakamura's laboratory, who applied cytofluorimetric analysis in order to validate their *NPHS1*^{GFP} reporter iPSC line, and concluded that "*the monoclonal antibody against the extracellular domain of nephrin, in combination with the anti-podocalyxin antibody, was useful for sorting developing podocytes* "[278]. By following this strategy, we were initially unable to detect the presumptive podocyte population by cytofluorimetry, as defined by the staining for nephrin and podocalyxin (by using exactly the same antibodies as reported by Dr. R. Nishinakamura's group[278]). We realized soon that, unless nephrin and podocalyxin staining has been claimed to be convenient for podocyte sorting, this staining has never been reported alone, but always in combination with the GFP fluorescence[278]. In the absence of a reporter gene, the $nephrin^+$/$podocalyxin^+$ signal was not strong enough to distinguish the putative podocyte population from the $nephrin^-$/$podocalyxin^-$ one.

In the first FACS experiment attempts, we faced to an unexpected cytofluorimetric profile in which nephrin staining was not detected, while podocalyxin defined 2 cell populations that I called $Podocalyxin^{high}$ and $Podocalyxin^{low}$. In order to determine their attributes, we collected, cultured and subjected these cells to a subsequent cytofluorimetric assay. A significant proportion of LTL^+ cells suggested the presence of a contamination derived from proximal tubular cells, which appeared to be greater in $Podocalyxin^{low}$ than $Podocalyxin^{high}$ cells. Since podocalyxin is predominantly expressed by podocyte-like cells in kidney organoids, one could imagine that most of the FACS-sorted $podocalyxin^+$ "podocytes" would have lost their identity after one week of culture, acquiring a cobblestone appearance reminiscent of the primary podocytes in culture[287,402]. In this perspective, a lower proliferative rate of "podocytes" compared to the eventual contaminant cell types would explain their rarity after one week of culture. We could imagine a similar course for $Podocalyxin^{high}$ and $Podocalyxin^{low}$ cells, with the only difference that the $Podocalyxin^{low}$ ones would have been more enriched in tubular cells since the beginning. We could not directly verify a possible podocyte dedifferentiation, but the massive loss of podocalyxin expression is a strong clue in favour of it.

Despite its prominent and high expression in podocytes, podocalyxin is also considered as a marker for proximal tubular cells[404], and I evidenced by IF on kidney organoids that some portions of LTL^+ proximal tubules display luminal staining of podocalyxin, particularly those closed to the glomeruli.

Hence, these independent approaches both converged in highlighting the lack of podocalyxin absolute specificity for podocytes. For this reason, we decided to introduce the LTL marker in the following FACS experiments to exclude proximal tubular cells, part of them being $podocalyxin^+/LTL^+$. So, our final **three-labels gating strategy** consisted in selecting $nephrin^+/LTL^-$ cells, getting rid of contaminant proximal tubular cells, to subsequently gate $nephrin^+$/ $podocalyxin^+$.

Whatever the proportion of podocytes in the kidney organoid culture, FACS of **$nephrin^+/podocalyxin^+/LTL^-$ cells**, which I demonstrated to represent *bona fide* podocytes by analysing their transcriptomic profile in "Results, Part 1", allows isolation of a homogeneous podocyte population. In my thesis we applied this technique to perform RNA-Seq analysis, comparing patient and control kidney organoid-derived podocytes.

D.a;ii) Avenues to improve podocyte isolation

Although we managed to perform 2 independent RNA-Seq analyses this way, improvement of the technique would be highly desirable for further experiments, since sample collection turned out to be a heavy procedure. We have identified several avenues that could improve our podocyte isolation procedure for downstream application.

First of all, a considerable **amount of** good quality starting **organoids**, ideally over 100 for each sample, is required to obtain sufficient podocytes to perform RNA-Seq. Optimization and scaling-up of the differentiation procedure would be favourable to maximize the collection yield. Podocytes represent indeed only a minor fraction of the organoid culture, of ~5% in average.

Moreover their tight cohesion may be responsible for the loss of part of them, due to the resistance of podocyte clusters to enzymatic dissociation[279]. Therefore, the **dissociation** procedure should be revised too, in order to ensure enhanced single-cell separation, particularly concerning podocytes, while maintaining a low mortality rate. We have already progressed in this direction, by finding that a collagenase/pancreatin/DNase I mix is valuable for kidney organoid dissociation. However, we have planned to test Liberase-mediated dissociation, a cold-active protease which has already been applied for kidney organoid dissociation[434,435]. This mild dissociation method might preserve good viability and have a lower impact on the transcriptome.

In addition, we are looking at how we could increase the **signal of nephrin**, which is particularly weak. There are no commercially available fluorescence-coupled primary antibodies against the extracellular domain of nephrin - at least at my knowledge. We already tested biotinylation of the primary antibody in combination with anti-biotin fluorescence-conjugated secondary antibody, without gaining in signal intensity. We are considering changing the secondary antibody for a brighter fluorochrome. More willingly, the establishment of a **podocyte-reporter iPSC line** would represent an important perspective for the laboratory. The use of a fluorescent reporter for podocyte FACS-isolation would allow to skip the staining step, greatly simplifying the procedure and reducing the stress the cells are subjected to.

Lastly, we wondered about the limited **amount of RNA** obtained, which was slightly lower than 0.2 pg/sorted cell. Low total RNA yield has already been reported for podocytes isolated from mouse kidneys[436], raising the possibility that podocyte might actually be a cell type poor in RNA. Yet, the total RNA contained by each mammalian cell has been estimated to range from 1 up to 50 pg[437]. Partial loss could have happened because of the degradation during sample treatment and/or could be due sub-efficient extraction. In fact, sorted cells have been directly collected into RLT lysis buffer of the extraction kit. This decision have been taken based on preliminary experiments in which cells were pelleted and frozen before to be lysed, for which the RNA yield was even lower. Collection in RLT lysis buffer appeared to be an acceptable compromise, although it implied to increase the lysis volume, in order to minimize the contribution of the drop liquid associated with each sorted cell. This adjustment could have been responsible for the decrease in the efficiency of RNA extraction. In addition, specific kits adapted to a small quantity of cells and having characteristics more suited to this particular application could be also be envisaged for the future.

If at least part of these aspects will be improved in the future, FACS-sorting could enlarge the spectrum of the possible techniques that could be applicable to kidney organoids in an unbiased way. These include widely current molecular biology and biochemistry methods, such as RT-qPCR or western blot, but also proteomics, metabolomics, transcriptome profiling, ChIP sequencing and so on.

D.b) Podocyte maturity

Maturation of iPSC derivative is a global concern in the field, since embryonic rather than adult cells and tissues are most often produced; iPSC-derived cardiac myocytes[438] and pancreatic β cells[439] have immature features, just to mention few examples.

While bulk RNA-Seq analyses ascribed kidney organoid similarity to embryonic kidney around the 1st [329] or 2nd [376] gestation trimester, glomeruli-focused investigations are in agreement with the fact that kidney organoid podocytes would correspond to a **capillary loop stage**[279,377].

In line with what reported by independent research groups, I observed basally located intercellular junctions and evidenced by IF the expression of SD-related markers, such as nephrin and podocin, at the basal membrane domain. Ultrastructural investigation by TEM showed apical prominent nuclei, and microvilli at the podocyte apico-lateral surface, filling the intercellular space, consistently with the proposed capillary loop stage[377]. In addition, I highlighted the presence of primary cilia in kidney organoid podocytes by ARL13B IF, a structure that has been shown to disappear along with glomerular maturation[160,440].

Podocyte transcriptomic profiling evidenced abundant laminin α5, γ1 and β2 isoform expression, which are the principal laminin chains composing the mature GBM. Type IV collagen α1 and α2 isoforms, constituting the prevalent collagen chains of the immature GBM, were the most abundantly expressed by kidney organoid podocytes, but the α5 chain, whose expression begins from the capillary loop stage *in vivo*, was also detected at a high level. Type IV collagen α3 and α4 chain expression was weak instead. Very similar expression profile of laminin and type IV collagen isoforms has also been reported in kidney organoid-isolated glomeruli[279], denoting partial switch toward mature GFB components. Finally, I detected the expression of several transcription factors that have been reported for adult human podocytes by scRNA-Seq[375]. In light of these observations, I was confident enough about the degree of maturity achieved, which seemed to be at least comparable to what reported in literature.

3. Kidney organoid vascularization

As long as the kidney organoid field was rapidly progressing in parallel of the advancement of my PhD project, we soon realized the urgency of vascularizing glomeruli to faithfully **recapitulate the structural architecture of the GFB**. Indeed, typical hallmarks of NS pathogenesis, namely FP effacement and loss of the SD, would have otherwise been impossible to model. Even in SRNS^{NPHS2} patient kidney organoids, in which I evidenced a cellular phenotype that was restored upon CRISPR/Cas9-mediated correction of the mutation in iPSCs (**Article 2**), the global organization and subcellular ultrastructure of glomerular podocytes was not altered in avascular organoids. Over the possibility to extend our current knowledge on the pathogenesis of SRNS, the podocin p.R138Q mutation was initially chosen as "positive control" to some extent, given the severity and early manifestation of the related disease, and also the "familiarity" of the laboratory with the *NPHS2* gene and this particular mutation.

The only example of **structural alteration of "*pre-SD domains*"** has been reported by Dr. R. Nishinakamura's group in kidney organoids derived from a patient bearing mutations in the ***NPHS1*** gene[381]. However this kind of domain, correlating with the "*nephrin^{+} rod-like structures on the lateral side of most podocytes*" evidenced by IF, was not present - or extremely rarely detectable - in kidney organoids generated with the Morizane's protocol[330],

and possibly specifically related to the Taguchi's one[10]. Anyway, the authors showed that vascularization strongly improved the potential of characterizing FP and SD alterations, since they observed "*well-developed FPs above the basement membrane*", and highlighted "*impaired SD formation*" in patient-derived vascularized kidney organoids[381].

Nevertheless, there was no applicable procedure I could directly transpose to my work that was published at that time. The Taguchi's protocol[10] was substantially different from the Morizane's one[330,392] I was applying, so I had few reliable landmarks to try to reproduce kidney organoid glomeruli vascularization by transplantation under the renal capsule of immunodeficient mice, since they used spinal cord-induced nephron progenitor aggregates to this purpose[278].

After having assisted to a talk given by Pr. M. Little at the ISSCR 2017 Annual Meeting in Boston, in which she presented preliminary unpublished results showing ***in ovo* transplantation** of kidney organoids on the **chick embryo chorioallantoic membrane** (CAM), I proposed to apply this technique for vascularization in our laboratory. This original method is in fact extremely easy to access, fast to use and cost-effective. Compared to mice, the chick embryo was noticeable more advantageous for the scaling up of the procedures, permitting to increase both the number of samples - and conditions - for each experiment and their frequency. The low rate of "success", having obtained only ~1% potential vascularization, and in addition displaying a disorganized structure with no recognizable glomeruli, prompted us to abandon the chick embryo CAM experiments, in a context in which several groups were performing ***in vivo* transplantation in immunodeficient mice**, either under the renal capsule[278,280,285] or subcutaneously[382].

Only more recently, kidney organoid vascularization has been achieved on the chick embryo CAM[376]. In light of this result, and since kidney organoid vascularization remains a compelling perspective for our laboratory, I would propose to attempt again the vascularization on the chick embryo CAM rather than proceeding with transplantation in mice. Indeed, kidney organoids vascularized on the CAM have demonstrated to possess absolutely comparable features with respect to the ones grown in mice. Of note, the displayed podocytes nicely aligned on a basement membrane, at the opposite side of endothelial cells, with regularly interspaced FPs bridged by a SD[376].

The chick embryo manipulation does not require surgery, the handling being **simple to perform** compared to chirurgical intervention in mice. Moreover experiments can be carried out at the bench, only needing an egg incubator, without the necessity to depend on an animal facility. Kidney organoid vascularization takes place in **only 5 days** on the CAM, while in mouse the implant is generally maintained for 2-4 weeks[278,280,285] under the renal capsule, and up to 12 weeks subcutaneously[382].

During this time, the follow-up of the graft is straightly **accessible for observation and imaging** *in ovo*, while in mice invasive intravital microscopy[280], eventually coupled with the use of specific iPSC reporter lines, is the only way to directly observe its development. Indirect follow-up of the graft evolution is otherwise possible by palpation[382] or by IVIS bio-luminescence analysis of firefly luciferase expressing organoids[285,382]. In addition, the chick CAM system is highly **accessible for experimentation** purpose, as blood vessels are easy to detect for injection of several substances, including for instance fluorescent low or high molecular weight dextrans to evaluate the filtration capacity, or drugs for potential therapeutic treatment screening. Finally, the chick embryo is extremely convenient in terms of **cost** (about 1€/egg) and **space** (several dozens of eggs/incubator).

By retrospectively looking at the experiments I performed and at the data subsequently published[376], if I had to re-start the vascularization experiments on the chick embryo CAM, I would choose to **pool several fully differentiated kidney organoids**, since the Morizane's organoids are smaller than the ones used by Dr. N. Montserrat's group[376], which applied a protocol similar to the Takasato's one[329], and also to increase the probability of survival of the graft. I would mostly attempt to **improve the step of transplantation** of the organoids on the CAM, using Geltrex or Matrigel matrix to stick the graft on the membrane, since many organoids did not "attach" and sometimes slide and get lost, and I would more firmly depose them on a scratched zone of the CAM, more amenable to integrate the graft. Finally, I would leave vascularizing organoids develop for a limited period of time. Indeed, in the only experiment that partially worked on my hands, I - deceitfully - observed a rapid but substantial change in the aspect of the graft. If perfusion of the organoid(s) was observable as early as E10, from E11 to E13 I observed branching organization of vessels, which ended in small spherical structures at the tips. By E14, at the time of collection, this configuration had unfortunately disappeared. I wonder if these dots more intensely red would have related to glomerular capillary tufts, that would have be "destroyed" due to an excessive biomechanical force applied.

4. Kidney organoid-isolated podocyte RNA-Seq

When exploring the transcriptomic landscape of kidney organoid isolated podocytes by RNA-Seq, we drawn wealth of information going far beyond our primary scope, which aimed to identify dysregulates molecular pathway in patient podocytes compared to controls.

We initially employed RNA-Seq data to validate the podocyte identity of the nephrin^{+}/podocalyxin^{+}/LTL^{-} FACS-isolated cells, and to assess their maturation degree. Nevertheless, RNA-Seq is a powerful technique producing tremendous amount of data that are unbiased from prior knowledge. Thus, "collateral" results can be source of expansion of our knowledge of several aspects of podocyte biology, and open new roads for future investigation.

A) New candidate genes for nephrotic syndrome

Genetic and functional studies conducted in the past years have unveiled the central role of the podocyte in the pathogenesis of NS, with all the monogenic forms of the disease being caused by mutations in genes that are relevantly expressed in the podocyte. The probability of identifying a causative mutation largely depends on the age of onset of NS, familial history, association with extra-renal manifestations and type of histological lesions[88]. Still, part of NS genetic cause remains unexplained, in particular for juvenile, adolescent and adult forms[441].

Here we performed 2 independent RNA-Seq analyses on podocytes isolated from kidney organoids. We observed a very good correlation between the different experiments and among the various podocyte samples. As expected, most of the genes associated with NS (Introduction, Chapter 2, Table 1) were found to be highly expressed in kidney organoid-isolated podocytes. Indeed, 42/72 (58.3%) of NS-related genes had an expression level exceeding the 90th percentile, with 15 of them (20.8%) even over the 99th percentile (Appendix, Table A4). If most of the genes already known to be associated with NS are highly expressed in kidney organoid podocytes, we could in turn speculate that genes with a high expression level might include new **candidate genes involved in NS**.

I will provide thereafter few examples of possibly interesting new candidate genes, chosen among the top 20 most abundantly expressed genes in control kidney organoid podocytes (Appendix, Table A5).

A.a) *MALAT1*

MALAT1 stands out from the podocyte transcriptome as the most abundantly expressed gene, with an expression level of almost one order of magnitude superior to the following ones. It codes for a broadly expressed long non-coding RNA (lncRNA)[442,443] that is the precursor of two transcripts, a longer nuclear-retained MALAT1 lncRNA and a shorter MALAT1-associated small cytoplasmic RNA (mascRNA) with a highly conserved tRNA-like structure[444].

RNA processing is an emerging mechanism in the pathogenesis of NS, particularly for the syndromic forms like GAMOS. Several genes already associated with in NS are implicated in tRNA modification (*LAGE3*, *OSGEP*, *TP53RK*, *TPRKB*, *WDR4*, *GON7*, *YRDC*) or encode mitochondrial tRNAs (*MTTL1*). Others mediate RNA nuclear-cytoplasmic transport (*NXF5*, *NUP93*, *NUP205*, *NUP107*, *NUP133*, *NUP85*, *NUP160*).

Recently, the work of Pr. C. Antignac group has focused on the pathogenesis of GAMOS. Our published data demonstrated that mutations in all the components of the t^6A modification on ANN-decoding tRNAs cause GAMOS. Current projects ongoing in the laboratory have unveiled interaction of WDR73 with the integrator complex (Dr. F. Tilley,

under revision), having a role in snRNA and non-polyadenylated RNAs processing. In addition, we identified mutations in *TSEN54*, encoding a subunit of the tRNA-splicing endonuclease (TSEN) complex (F. Miscia, unpublished), which is involved in tRNA maturation by intron removal.

Very interestingly, MALAT1 processing relies on the tRNA maturation machinery, being the substrate of the RNase P and RNase Z and CCA-adding enzyme[444], which act upstream the TSEN complex - and then the KEOPS complex for the ANN-decoding subset of tRNAs - in canonical tRNAs biogenesis[445]. Moreover, MALAT1 undergoes post-transcriptional N6-methyladenosine (m^6A) modification[446] that facilitates the interaction with heterogeneous nuclear ribonucleoproteins C[447], which contribute to several aspects of RNA metabolism including stability, splicing, export and translation regulation[448].

Significant MALAT1 expression increase in kidneys from streptozotocin induced diabetic mice[449] and renal function improvement related to MALAT1 downregulation after bariatric surgery in diabetic rats[450] are additional clue in favor of its relevance in the renal pathological context.

The ensemble of these arguments makes *MALAT1* a promising candidate gene that might contribute to NS pathogenesis, eventually in a syndromic form with extra-renal - most likely neural - manifestations.

A.b) *FREM2*

FREM2, encoding an ECM component, is also comprised among the most highly expressed genes in kidney organoid podocytes. *FREM2* mutations are already known to cause the Fraser syndrome[451], displaying congenital abnormalities of the kidney and urinary tract (CAKUT). Actually, FREM2 is expressed in developing kidney and highly abundant in glomerular, tubular and urothelial cells[452], thus explaining the broad CAKUT phenotype rather than a simple glomerular defect associated with this gene.

A.c) *TJP1*

Another example gathering from the same approach consists in the *TJP1* gene, coding for the tight junction protein ZO-1. ZO-1 is concentrated in the SD domain within podocyte FPs, establishing determinant interactions for its structural integrity. Despite the pivotal role of ZO-1 in maintaining the organization of podocyte architecture, no mutations have been described in NS patients at present. Anyhow, apical displacement of tight junctions have been highlighted in proteinuric glomerular disease rat models[453], and podocyte-specific conditional deletion of *Tjp1* lead to glomerulosclerosis in mice[454]. Moreover, *Tjp1*/*TJP1*expression is reduced in diabetes animal models and diabetic human kidney[455–457], suggesting that *TJP1* may be involved in establishment and/or aggravation of NS.

B) Additional applications

Here I presented possible applications of the data obtained from kidney organoid podocyte transcriptomic profiling, in validating the podocyte identity and evaluating the maturation degree of nephrin^{+}/podocalyxin^{+}/LTL^{-} FACS-isolated cells (Results, Part 1) and I provided few aforementioned examples that show that genes with a high level of expression may represent pertinent new candidates in NS pathogenesis.

Nevertheless, the potential of the RNA-Seq data is certainly unexhausted, and it will be possible to carry out many other analyses to address new raising questions. It will be possible for instance to perform **deeper characterization of podocytes**, by exploring more specific cellular mechanisms and gene networks. In addition, we dispose of a ready-to-use catalogue of the genes expressed in kidney organoid podocytes. It would be useful to **check if specific genes of interest are expressed**, which would be for instance a determinant criterion to evaluate whether starting a project on kidney organoids for these particular genes.

5. Conclusion

During my PhD thesis I opened the way to iPSC-based renal disease modeling by establishing the protocol for kidney organoid differentiation in my host laboratory. This new approach allowed us to highlight cellular phenotypes associated to the pathogenesis of hereditary kidney diseases. We had the chance to explore the molecular landscape of podocytes in a patient-specific context. Although some limitations still persist, in particular the absence of endothelial cells to fully recapitulate a functional GFB, and the technique can be further improved, iPSCs currently represent a complementary system that has been adopted by the laboratory for other research subjects, such as cystinosis or nephronophthisis.

Early-onset SRNS
Podocin p.R138Q

1. Endogenous podocin expression in kidney organoid podocytes
A) p.R138Q podocin decreased expression and mislocalization

Currently existing *in vitro* models for glomerular disorders, such as immortalized human and mouse podocyte cell lines, have greatly advanced our knowledge of podocyte biology, but they are reaching theirs limits. In particular, 2D podocyte culture fails to recapitulate the complex organization of the GFB, while being responsible for the difficulty of maintaining podocyte-related features at the same time. Actually, podocytes display a propensity for losing their identity and dedifferentiating in culture, a phenomenon that I observed when plating mechanically sieved glomeruli. In conditionally immortalized podocyte cell lines, the expression of SD proteins that characterize mature podocytes, such as nephrin and podocin, is extremely variable, even sometimes absent[290]. I was confronted to the lack of *NPHS2* expression at the transcriptional level when using the human conditionally immortalized LY and LP podocyte cell lines. Kidney organoid podocytes are characterized by **robust** and **reproducible expression** of **podocyte-specific markers** instead, including SD-related proteins that are otherwise challenging to detect. Most probably, the 3D organoid architecture provides a favorable environment for podocyte preservation.

Remarkably, we had the chance of observing for the first time the expression pattern of the **endogenous human p.R138Q podocin at the homozygous state** in a physiologically relevant context. We were able that way to evidence a defect in p.R138Q mutant podocin amount and subcellular localization in SRNS^{NPHS2} 007 patient kidney organoid podocytes. Upon CRISPR/Cas9-mediated correction of the mutation in patient iPSCs, we succeeded in re-establishing proper podocin expression level and localization at the basal membrane domain in kidney organoid podocytes.

B) p.R138Q podocin ER retention and proteasomal degradation

Current literature is essentially in agreement with the fact that the p.R138Q podocin is retained into the ER[67,181,182,458] to be afterwards degraded by the proteasome[184], based on functional studies performed by overexpressing wild-type and mutant podocin in cellular systems. However, while mutant podocin has already been shown to be retained into the podocyte cell body *in vivo* in patient biopsies[179] and in the Nphs2$^{R140Q/R140Q}$ (the murine p.R138Q equivalent) knock-in mouse model[183], its precise subcellular localization has never been investigated.

In this study we observed reduced amount of mutant podocin protein, which is consistent with our previous results reporting massive **proteasomal degradation** of the

p.R138Q podocin[184]. Moreover, its wide perinuclear localization could be in agreement with its ER retention. Nevertheless, we did not observe perfect co-localization of p.R138Q podocin with ER markers as it has been shown in cell lines. This could be an artifact due to ER compartment overload upon podocin overexpression. The endogenous level of p.R138Q podocin is likely to be contained by the ER quality control system, which would prevent its accumulation by massively addressing it to the proteasome in the cytosol or eventually to ER-associated degradation[184]. We found that both wild-type and mutant podocin were partially located in the ER, but the relative amount of ER localization was higher for the p.R138Q podocin with respect to the wild-type form. What would be principally responsible for the differential proportion of ER-located protein resides on the scarcity of p.R138Q at the basal domain, where wild-type podocin is predominant instead. Conversely, the fraction of ER occupied by podocin is slightly higher in controls, possibly reflecting the higher stability of the wild-type form[184]. We thus confirmed the impairment of the p.R138Q podocin in reaching the podocyte basal plasma membrane domain. We found indeed that the p.R138Q podocin is mainly located in the **perinuclear region** of the podocyte cell body, corresponding partially to the ER compartment, while it is virtually absent in the basal compartment.

Although several piece of evidence supports ER retention and proteasomal degradation of the p.R138Q podocin, the mutant protein expression level and localization were not impacted when we treated kidney organoids with the proteasome inhibitor bortezomib. It is possible that the complexity of the 3D organoid architecture impairs efficient penetration and/or modifies the response kinetics to the drug compared to a cell monolayer. Alternatively, the contribution of the proteasome might be more modest in degrading the endogenous p.R138Q podocin compared to a cellular system in which it is overexpressed. It should also be considered that the *NPHS2* expression seems to be decreased by half, according to both RNA-Seq experiments. Therefore, endogenous p.R138Q podocin accumulation would be far less pronounced than the overexpressed one[184], since it is presumptively expressed at a significantly lower level. In kidney organoid glomeruli, we did not detect p.R138Q podocin accumulation by IF - which is a poorly quantitative technique by the way - upon bortezomib treatment. Anyhow, some clues from the transcriptomic analysis of kidney organoid-isolated podocytes are in agreement with the proteasomal - particularly with the immunoproteasomal - p.R138Q podocin degradation hypothesis. Indeed, specific subunits of the **immunoproteasome** (*PSMB8* and *PSMB9*) have been found upregulated in 007#27 patient podocytes. Of note, bortezomib targets both the constitutive and the immunoproteasome indiscriminately[459]. It would be intriguing to investigate the effects of immunoproteasome-selective inhibitors on p.R138Q podocin stability in overexpressing cell systems.

C) p.R138Q podocin impact on nephrin expression pattern

It has been shown by co-expression of p.R138Q podocin and nephrin in cellular models that the p.R138Q mutation results in alteration of nephrin trafficking, without disrupting the interaction between both proteins[67,181]. In addition, nephrin distribution is disrupted *in vivo* in patient kidney tissue[179] and in Nphs2$^{R140Q/R140Q}$ knock-in mice[183]. Nephrin was indeed found not only along the glomerular basement membrane, where it displayed a granular and discontinuous distribution, but also in the podocyte body.

In the present study, we did not evidence noticeable nephrin perturbation in SRNS^{NPHS2} patient kidney organoids by IF, using two different antibodies. In addition, we managed to isolate podocytes from control and SRNS^{NPHS2} patient kidney organoids by FACS in a comparable way, using a strategy that is highly dependent on the nephrin staining. Nephrin dysregulation might be dependent on aggravation of the syndrome during the progression of the disease, and thus not be recapitulated at the embryonic-like stage to which kidney organoids correspond.

Podocin is a raft-associated protein localized at specific lipid enriched micro-domains at the slit membrane[63]. It has been proposed to have a role in nephrin recruitment at lipid raft domains, thus enhancing its downstream signaling[67]. p.R138Q podocin is not targeted to lipid rafts and consequently would fail to recruit nephrin there[67]. We cannot conclude about eventual impairment of nephrin recruitment at lipid rafts by p.R138Q podocin in SRNS^{NPHS2} kidney organoids. Indeed nephrin presence at the basal membrane does not exclude its absence from lipid rafts, if the latter are present in kidney organoids. Lipid rafts have not been described in kidney organoids so far. One may speculate the "*rod-like structures on the lateral side of most podocytes*" observed by Dr. S. Tanigawa and colleagues and referred to as "*pre-SD domains*"[381] may include lipid raft patches. However these kinds of pre-SD domains seem to have been observed only when applying the Taguchi's protocol[10] and they are probably absent in other conditions.

2. Interferon-like signature

A) Intrinsic clone or line properties possibly determining the IFN signature

RNA-Seq performed on podocytes isolated from SRNS^{NHPS2} kidney organoids revealed the activation of an **antiviral IFN-like immune response** in p.R138Q podocytes. This finding was unexpected for a SRNS patient. While the role of the immune system in certain forms of idiopathic NS (INS) is far more than hypothetical[70,71], resistance to immunosuppressors and absence of post-transplantation recurrence would strongly exclude the p.R138Q podocin-related NS from the immune classification. Nevertheless, the antiviral IFN-like signature has been evidenced by two independent RNA-Seq experiments. The persistence of this immunity response strongly supports its reliability, especially if considering the great variability in differentiation of iPSCs into organoids and the influence of

the dissociation and sorting processes on the transcriptome. However, it must be considered that both RNA-Seq experiments have been conducted using **only one clone**, the 007#27, of the SRNS^{NPHS2} IMAGINi007 iPSC line derived from **a single patient**. Therefore, we can not rule out the possibility that this result is related to particular iPSC clone (#27) or patient line (007) intrinsic characteristics.

The intrinsic line/clone properties could be explained by particular circumstances to which the reprogrammed PBMCs, from which the 007 iPSC line was derived, have already been exposed or which have occurred in the early stages of the establishment of the iPSC line/clone. Some possibilities include **viral infection** of the source PBMCs or of the iPSC culture. Patient serology, a prerequisite requested by the iPSC Platform of the *Imagine Institute* to perform reprogramming, excluded infection from current pathogens, such as HIV, HBV and HCV. Reprogramming and culture were then performed in standard sterile conditions. Albeit these precautions do not exclude cell infection, screening for any viral contamination was not applicable. Likewise, it should be considered that **reprogramming** is *per se* a viral transduction. However, the ΔF Sendai virus is neither supposed to integrate into the host genome[266], nor to be capable of propagation. The absence of Sendai viral genome is also verified by the iPSC Platform of the *Imagine Institute* as a routine quality control. If the reprogramming process, to which of note all the iPSC lines have been subjected in the same way, would have provoked a hypothetical antiviral sensitization, this would imply the activation of rare and complex mechanisms, at the epigenetic level for example.

Another possibility would be a **genetic predisposition** of the patient to inflammatory processes, deriving from instance from a combination of variants in modifier genes that would favor IFN-response activation. The presence of additional mutations leading to a "type I interferonopathy"[460] properly speaking is absolutely improbable, since the patient did not present other symptoms unrelated to typical SRNS manifestations, and underwent beneficial kidney transplantation. An unsolved but intriguing question remains, concerning the possibility the immunosuppressive treatment the patient have been subjected to tolerate the graft would have somehow impacted PBMCs and the iPSCs generated from them.

Weak evidence disfavors the presence of an IFN-like response dependency on the SRNS^{NPHS2} 007(#27) patient clone/line. Actually, *IFIT1* and *OAS2* IFN-stimulated genes have not been found substantially expressed in iPSCs and NPCs, neither in controls nor in patient clones (007#27 and 007#24). We can speculate the viral immune signature may manifest in this patient line/clones in specific conditions, as in the context of differentiated podocytes, increasing the likelihood of its implication in the disease-related mechanism. It would be interesting to evaluate if the SRNS^{NPHS2} 007(#27) patient clone/line presents increased immunity sensitiveness, by treating iPSCs with IFN and comparing the response of patient and control iPSC lines.

The **CRISPR/Cas9 corrected 007#27 isogenic clones** we generated represent the ideal tool to discriminate between the influence of the clone/line or a mutation-related effect. The results of the transcriptomic profile of the corrected clones are the most awaited, since confirmation of the signature in patient podocytes and shutdown of the response in CRISPR/Cas9 corrected clones would allow us to infer the IFN signature to the p.R138Q mutation. Complementary analysis could be also carried out on SRNS^{NPHS2} patient and CRISPR/Cas9 corrected kidney organoids, validating the results by IF for relevant markers, such as nuclear *versus* absent/low phospho-STAT1 and phospho-STAT2 or presence *versus* absence/decrease of IFN-stimulated genes (MX1, OAS2, IRF9...). Moreover, if the new RNA-Seq data analysis confirms the implication of the INF-like response, it would be interesting to explore whether the Nphs2$^{R140Q/R140Q}$ mouse model[183] recapitulates a similar mechanism, or ideally to investigate patient biopsies to finally relate the IFN-like response to the pathogenesis of podocin p.R138Q-related SRNS.

B) Possible explanation of an eventual IFN-related pathological mechanism

If assuming a causative link between the p.R138Q podocin mutation and the activation of the immune response, it remains to unveil the underlying mechanism.

"**Antiviral innate immunity**", a GO term enriched for genes upregulated in SRNS^{NPHS2} 007#27 patient podocytes, has already been shown to disturb podocyte biology, in particular upon activation of the **double stranded (ds)RNA sensing pathway**[461]. Actually, all the principal sensors of dsRNA, either cytoplasmic (*OAS1-2-3*, *IFIH1*, *DDX60*) or, to a lesser extent, lysosomal (*TLR3*) are significantly upregulated in SRNS^{NPHS2} patient podocytes.

Endogenous immuno-stimulatory self RNAs[462] and viral-independent IFN response activation have already been implicated in human diseases. In the **Aicardi-Goutières syndrome**, *ADAR* mutations are associated with a type I IFN signature[463], likely due to the absence of RNA editing that marks it as "self". A type I IFN signature has been equally evidenced in **tricohepatoenteric syndrome** caused by mutations in the *SKIV2L* gene, affecting RNA homeostasis[464]. Interestingly, the authors propose that episodic activation of the unfolded protein response (UPR) could provide a source of immunogenic self RNAs able to activate dsRNA sensors through IRE-1-dependent RNA decay (RIDD)[465]. This model might fit with a hypothetical mechanism by which the misfolded p.R138Q podocin would directly activate the ER luminal domain of IRE-1[466]. While a proper UPR is not activated according to the transcriptomic data, at least at the moment in which the analysis has been performed, RIDD RNA products would have triggered the dsRNA sensing pathway, culminating in the type I IFN response activation. Also, patients affected with **combined oxidative phosphorylation deficiency** with mutations in the *PNPT1* gene accumulate mitochondrial dsRNA escaping into the cytoplasm, together with upregulation of IFN-stimulated genes and other indicators of immune activation[467]. Here, the authors pulled-down

and sequenced dsRNA using a widely-used monoclonal antibody specific for dsRNA, a technique that can be considered to identify the main hypothetical p.R138Q-related dsRNAs.

Whether the mechanism proposed above represents the trigger of a downstream pathogenic cascade, it is itself responsible for podocyte dysfunction or neither of them, an alternative or additional mechanism would rely on podocyte antigen-presenting capacity[468]. Indeed, we found a GO enrichment for the "**antigen presentation**" category in genes upregulated in SRNS^{NPHS2} 007#27 patient podocytes. IPA showed upregulation of the **MHC class I pathway** in spite of the class II. All the basic components of this path, namely the MHC class I C-α and β2-microglobulin chains (*HLA-C* and *B2M*), the transporter associated with antigen processing (*TAP1* and *TAP2*) and, very interestingly, specific subunits of the immunoproteasome (*PSMB8* and *PSMB9*) were significantly upregulated in SRNS^{NPHS2} patient podocytes. We can thus suppose that generation of immunogenic peptides, most probably derived from the misfolded p.R138Q podocin, is pretty plausible. Actually, the entire machinery implicated in their eventual presentation to **cytotoxic CD8$^+$ T lymphocytes** is set up.

Involvement of T cells has been proposed in various types of kidney disease, including **INS**[71]. Double-edged, it is also an evidence supporting responsiveness to immunosuppressors, which is unquestionably not the case for p.R138Q podocin-related SRNS. If looking at specific sub-cellular type, CD8$^+$ cells have been shown to be more abundant in PBMCs of SRNS patients with marked proteinuria, while helper CD4$^+$ T lymphocytes are generally decreased in SS and SRNS patients, leading the authors suggest the lower the CD4$^+$ count and the higher the CD8$^+$ count, the greater would be steroid unresponsiveness[469]. In agreement with that, *in vivo* depletion of CD8$^+$ T cells has been demonstrated to protect mice with **adriamycin-induced nephropathy** from renal functional impair[470]. Of note, this mouse model is considered an excellent model of human non immunological FSGS[471]. The immunosuppressive treatments for INS target the B lymphocytes (Rituximab) or T lymphocytes, but with preferential helper CD4$^+$ T cell targeting (Corticosteroids, Cyclosporine A, Tacrolimus). Again, in the adriamycin-induced nephropathy mouse model, CD4$^+$ T cells depletion aggravated the histologic and functional damage, which was accompanied by increased interstitial infiltration of macrophages and CD8$^+$ cells[472]. A possible mechanism that may escape immunosuppressive therapy would thus rely on recognition of immunogenic p.R138Q podocin-derived peptides, presented by podocytes through the MHC class I complex, to CD8$^+$ T lymphocytes. CD8$^+$ cell-mediated cytotoxicity would induce apoptosis of the target podocyte. Moreover, it would be compatible with absence of post-transplantation recurrence, since generation of immunogenic peptides would be intrinsically related to the p.R138Q mutation.

Through the **functional interaction network analysis**, I aimed to feature some clues that may relate the gene expression dysregulation observed in SRNS^{NPHS2} 007#27 patient podocytes with key proteins of this highly specialized renal cell type. The RNA-Seq results were thus integrated with the current genetic information about NS, in order to evidence molecular components through which the downstream effect of the p.R138Q mutation might converge to disturb podocyte biology.

Once again, the main cues gathering from the analysis were globally related to the immune system. ***SP100*** nicely correlated several aspects of the proposed pathological mechanism at issue, ascribing them to **nuclear bodies** (NB). These include induction by the IFN signaling pathway, transcriptional activation of the MHC I *locus* and unfolded protein response[411,412,473]. Indeed, *SP100* expression is **induced by IFN**[474]. However, the expression of Sp-100's constitutive partner, PLM, remained invariable at both transcript and protein levels. Most of the reports on NBs presuppose multiprotein complex formation with invariable PML/Sp-100 core. Furthermore, these studies predominantly concentrate on PML, which is considered as the archetype of NBs. Therefore, it is difficult to make the distinction between ordinary NBs and possibly independent functions ascribed to Sp-100 only. PML has been shown to organize the chromatin architecture of the MHC class I *locus*[475], activating the expression of class I *HLAs*, *TAP1*, *TAP2*, *PSMB8* and *PSMB9*[476], thus enhancing **antigen presentation** trough the **MHC class I**[477]. Despite these observations strikingly fit with the observed upregulation of the same pathway in R138Q podocytes, contradictory data discredit the involvement of PML in the regulation of the MHC class I expression[478]. It is tempting to speculate that this specific function would be attributable to Sp-100 only, and that PML would indirectly promote the expression of MHC class I-related genes through Sp-100 activation, but without being necessary to achieve this function.

Over the proposed nuclear role in regulation of transcription, a significant fraction of Sp-100 is also found - sometime even predominantly - in the **cytoplasm** in steady-state cells, although the nuclear/cytoplasmic proportion changes in favor of the nuclear location upon IFN stimulation[479]. Cytoplasmic translocation of NB components has been demonstrated in lymphocytic choriomeningitis virus[480], HIV-1[481] or respiratory syncytial virus[482] infected cells, where NBs have been propose to limit viral replication. Given the connection described between NBs and the **unfolded protein response** and **protein degradation** pathways[411], we can imagine that a similar mechanism could take place in the cytoplasm, a compartment in which NB roles are emerging[483,484]. The misfolded p.R138Q podocin protein might activate *SP100* expression by mimicking the features of a viral antigen. Sp-100 would thus contribute to the degradation of the mutant p.R138Q podocin in a similar way to what happens during a viral infection. In order to assess that, it would be opportune to attest if the *SP100* upregulation in SRNS^{NPHS2} 007#27 patient podocytes correlates with an increase and/or a modification in the corresponding protein expression pattern.

The **phospholipase C ε1** is relevant for podocyte function, and it has been linked to the pathogenesis of NS with variable response to therapy[53]. More recently, mutations in *PLCG2*, encoding the **phospholipase C γ2** isozyme, has been proposed to **associate with SSNS**[485,486]. Remarkably, expression quantitative trait loci (eQTL) analysis of NS patients highlighted a highly significant *PLCG2* genetic regulation in the glomerulus[487], suggesting it may modulate NS. Nevertheless, its role in podocyte physiology and pathology has not been elucidated. Hypermorphic gain of function mutations that lead to constitutive PLCG2 activation have been described not only for variants associated with **SSNS**[486], but also in patients with **dominantly inherited autoinflammatory disease with immunodeficiency**[488] or with **cold urticaria, immunodeficiency and autoimmunity**[489], and in mice with **autoimmune and inflammatory disease** displaying **glomerulonephritis**[490]. Loss of function or hypomorphic *PLCG2* mutations have not been described instead[491]. We can hypothesize that downregulation of *PLCG2* might perturb the Ca^{2+} mobilization and have repercussions on the actin cytoskeleton dynamics[492]. Interestingly, this analysis evidenced a possible mechanism underlying actin cytoskeleton dysregulation. Indeed, SRNS^{NPHS2} 007#27 patient podocytes would possibly present a shift from PIP_2 hydrolysis into IP_3 and DAG, which induces an increase in intracellular Ca^{2+} flux and downstream ERK signaling activation, towards PIP_2 phosphorylation, with consequent production of PIP_3 and AKT/mTOR pathway activation. However it is difficult to predict the biological outcome based on the *PLCG2* and *PIK3AP* mRNA expression level only, since the signaling pathways mentioned above are highly dynamically regulated by post-transcriptional events such as phosphorylation and dephosphorylation. The fact remains that several actin-related components, including *ACTG1*, *ACTB*, *CRB2*, *CD151*, *ARGHDIA* and *KANK*, are downregulated in R138Q podocytes. The transcriptional concurrent deregulation of actin and actin-related genes is likely to negatively impact the podocyte biology, whose complex cytoarchitecture is sustained by an actin-based cytoskeleton.

Galloway-Mowat Syndrome
KEOPS complex

The majority of the genes encoding KEOPS subunits are considered to be "essential" genes[230,231], hampering the maintenance of podocyte cell lines in long term cultures and preventing us from performing many other studies[145,147]. In addition, inactivation of KEOPS genes results in an early lethality in mouse and zebrafish models[145]. In order to establish pertinent animal models, a project aimed to generate and characterize mouse strains carrying mutations identified in patients for the *OSGEP* or *LAGE3* genes - introduced by CRISPR/Cas9 - has been recently carried out in the laboratory by J. Patat. Unfortunately, these mice lack renal or cerebral/cerebellar phenotype, only displaying a reduced body size when mutated for *LAGE3*.

Here, we have chosen to use iPSCs as an *in vitro* model since they offer the possibility to model both renal and neural aspects of GAMOS by using patient-derived iPSCs, differentiated towards the specific lineages relevant to GAMOS pathogenesis. This will give us the opportunity to investigate various cellular processes in the own patient background, in which the endogenous mutated proteins are expressed.

Therefore, iPSC-derived kidney organoids and late cortical progenitor cells (CPC) have been employed in this work to assess the impact of GAMOS mutations, in particular *GON7* and *OSGEP* mutations, on the biology of podocytes and neurons, analyzing several cellular and molecular aspects that have been already associated with GAMOS pathogenesis in other systems[145,147] and attempting to highlight common and/or specific pathological mechanisms in these cell types.

1. GAMOS iPSC derivatives phenotypic characterization
A) Apoptosis increase in GAMOS pathogenesis

Increased apoptosis has already been proposed to be "*integral in the pathogenesis of GAMOS in individuals with mutations in genes encoding KEOPS subunits*"[145]. This hypothesis stems from previous published work of the laboratory and collaborators that demonstrated a high apoptotic rate in immortalized podocyte cell lines knocked-down for the genes encoding KEOPS subunits[145,147]. Indeed, this may reflect podocyte depletion that has been described to play a major role in the development of glomerulosclerosis[493]. In addition, while the microcephalic phenotype is generally attributed to neural progenitor pool exhaustion, most frequently due to decreased proliferation and/or premature neuronal differentiation[494], microcephaly in GAMOS patients has been proposed to be "*probably due to increased apoptosis of neuronal progenitor cells*"[145]. However this aspect has been never investigated so far in a neuronal cellular system.

Here we investigated apoptosis rate in renal and neural lineages expressing the endogenous mutated KEOPS subunits. Very interestingly, I observed by TEM on GAMOS^{OSGEP} kidney organoid glomeruli, holes filled with apoptotic bodies in between podocytes, and also patches of cells that are positively labelled for the active-cleaved form of caspase 3 by IF, whereas it was only sporadically in controls. Moreover, we highlighted a considerable increase in apoptosis in GAMOS^{OSGEP} and - to a lesser extent - in GAMOS^{GON7} patient CPC lines, which was particular significant in the first day of culture.

Altogether, in this study both renal and neural systems have pointed to an increase in apoptosis, especially for GAMOS^{OSGEP} derivatives. These findings further corroborate previous work of the laboratory[145,147], suggesting the implication of a pathological mechanisms relying on apoptotic cell death, which seems to be common to both podocytes and neural progenitors. While it was possible to quantify the apoptosis rate in late CPCs by Annexin V labeling thanks to the IncuCyte system, IF staining for the active-cleaved form of caspase 3 provided essentially qualitative evaluation of apoptosis in kidney organoids. Annexin V cytofluorimetric analysis could represent a complementary quantitative technique to evaluate the amplitude of apoptosis in podocytes. This kind of analysis would require improvement of the kidney organoid dissociation and podocyte FACS-sorting, as previously mentioned. Nevertheless, we should be aware of the fact that apoptotic podocytes may have a decreased cell-surface expression of nephrin, due to its endocytic internalization[495]. Considering that the nephrin signal is already weak in normal conditions, apoptotic Annexin V^{+} podocytes might thus be missed in this kind of analysis.

B) Investigation of other GAMOS-related phenotypes

Kidney organoids differentiated from GAMOS^{GON7} and GAMOS^{OSGEP} patient iPSCs did not denote any major developmental defects in nephron morphogenesis or structural anomalies in the general organoid architecture and cellular organization, as evidenced by IF and TEM - except for the aspects secondary to apoptosis.

In late CPCs, over the significant increased apoptosis highlighted in GAMOS^{OSGEP} and GAMOS^{GON7} patient CPCs, we only denoted a weak tendency for a decreased proliferation rate of GAMOS^{GON7} and - slightly more pronounced - GAMOS^{OSGEP} CPCs. This may likely correlate with the higher apoptotic rate evidenced for these CPC lines.

In addition, since the canonical function of the KEOPS complex is to mediate the post-translational t^{6}A modification on ANN-decoding tRNAs, thus ensuring accurate and efficient translation, we sought to determine the amount of the t^{6}A modification on tRNAs and evaluate the impact of mutant KEOPS components in *de novo* protein synthesis in GAMOS^{GON7} and GAMOS^{OSGEP} patient CPCs. However, preliminary analysis of t^{6}A quantification by mass spectrometry and HPG protein synthesis assay are poorly conclusive and further experiments need to be performed to draw any conclusions.

We faced many technical issues as well as a high variation between the different experiments that we carried out during the characterization of these CPC lines. The great degree of variability manifested by late CPCs differentiated from iPSCs, either between clones from the same line or between different lines, among controls or derived from different patients bearing the same mutation, has certainly contributed in confounding the analysis of mutation-dependent effects, preventing us from deciphering cellular and molecular mechanisms underlining GAMOS pathogenesis. Further investigation and refining of suitable experimental techniques for CPCs are needed to better understand the cellular and molecular dysregulated mechanisms associated with mutant KEOPS complex subunits.

2. RNA processing and the tRNA hypothesis

Since the beginning of genetic studies on GAMOS, with the discovery of causative mutations in *WDR73*[162], the implication of RNA processing disturbance rather than the initially proposed microtubule-associated defect is profiling as the common denominator in GAMOS pathogenesis. In particular **tRNA modifiers**, including all the actors of the t^6A biosynthesis, YRDC and the KEOPS complex subunits LAGE3, OSGEP, TP53RK, TPRKB and GON7[145,147], as well as WDR4[196] mediating the m^7G modification, have been subsequently been implicated in GAMOS. Ongoing work in the laboratory is aimed to characterize the implication of the of the TSEN complex, specifically of its TSEN54 subunit, in GAMOS, since *TSEN54* mutations have been recently identified in patients (F. Miscia, unpublished). Very interestingly, the TSEN complex intervenes in the **splicing of tRNAs**, further supporting the hypothesis that correct tRNA processing would be particularly crucial for podocyte and neuron functioning. In addition, Dr. F. Tilley's work (under revision) has demonstrated interaction of WDR73 with the integrator complex, suggesting a role for this protein in snRNA and non-polyadenylated RNA processing. To complete the panel and exhaustively consider the genetic information about GAMOS, nucleoporins implication might be explained by their requirement for proper nucleo-cytoplasmic transport of RNAs. Of note, shuttling from these intracellular compartments is fundamental for tRNA maturation[496].

Whether the global GAMOS phenotype actually derives from defects in RNA biology remains to be formally proven, even though several lines of evidence point in that direction. Secondly, one may wonder if the disease specifically relies on tRNA defects, or if it encompasses dysregulation of several classes of RNA. Even though WDR73 and the integrator complex have not been implicated if tRNA processing, this does not exclude they could. To explore this perspective, it would be interesting to pull down the protein of interest, WDR73, INT9 and/or INT11, and verify the eventual binding of tRNA by ribonucleoprotein immunoprecipitation followed by RT-qPCR or sequencing[497], or *vice versa* to analyze tRNA interactome(s), assessing if the aforementioned proteins interact with specific tRNA(s)[498].

3. t^6A deficiency impact on podocytes and neurons

The KEOPS complex was originally described as a chromatin associated complex involved in telomere maintenance[220], regulation of transcription[227], chromosome segregation and genomic stability[233], before to be ascribed to the t^6A modification of ANN-decoding tRNAs[215,217,234]. However, effective involvement of the KEOPS complex in these "genomic" phenomena may be secondary to pleiotropic effects of translation perturbation, unless they are specie-specific in *Saccharomyces cerevisiae* and/or other lower eukaryotes. It should be also considered the fact that highly evolutionary conservation of KEOPS components are incoherent with a primary function restricted to eukaryotic exclusive mechanisms such as telomeres, chromatin state and chromosomal segregation. Its ancestral biochemical function, universally conserved in all the domains of life[217], would thus correspond to tRNA modification. No difference in telomeres length have indeed been observed patient leukocytes bearing mutations in *OSGEP*, *TP53RK*[145], *YRDC* or *GON7*[147].

In any case, the questioning about the specific renal and neural susceptibility to deficient t^6A modification on tRNA remains largely unsolved. It must be considered that, with the only exception of GON7, the co-existence of 2 null mutations has never been reported in patients for any component of the t^6A biosynthetic pathway. Indeed, an amorphic allele is always accompanied by a hypomorphic one, suggesting the complete absence of the t^6A modification on ANN-decoding RNAs is incompatible with life. Only for the GON7 subunit, which has been hypothesized to have a regulatory role in the stability of the complex[147], 2 nonsense mutations can be tolerated.

A decrease in t^6A-modified tRNAs would greatly impact **protein translation efficiency and fidelity**. Leaky scanning bypass of start AUG codons produces N-terminal truncated proteins in the best cases, or aberrant peptides from most common out-of-frame misinitiation. Increased frameshift rate during elongation is equally responsible for misfolded protein production. In addition, protein co-translational folding can be perturbed by the modification of ribosomal speed. As a consequence, unfolded and misfolded proteins accumulate and form insoluble protein aggregates[208]. Post-mitotic cells, such as podocytes and neurons, could be more sensitive to this accumulation, being less efficient in degrading them and since aggregates would not dilute by cell division. Alternatively - or in addition - we can imagine that the podocyte and neural proteome should be particularly enriched in ANN-encoded amino acids, or that key proteins expressed in these cell types would be encoded by mRNAs particularly abundant in ANN-type codons, or containing long stretches of them. Bioinformatics analysis of the proteome should be conducted in order to inspect this hypothesis and maybe identify crucial clues to decipher GAMOS pathogenesis.

Secondly, the cell type specific **tRNAome** might also be considered. Indeed, each codon can be read by different tRNA isodecoders, meaning distinct tRNA species carrying the same amino acid but with sequence variation in the tRNA body. The human genome contain over 270 isodecoder genes[499], which present specific expression patterns and variable abundance[500]. This let speculate that tRNA isodecoders have biologically non-redundant roles. Moreover, the **tRNA epitranscriptome** is composed by a heterogeneous population of tRNAs displaying various modification patterns. Hence, cells expressing distinct tRNA isodecoders or presenting specific patterns of tRNA modifications might respond differently to the translational stress induced by the decrease in the t^6A modification.

4. Perspectives

We recently managed to obtain the transcriptomic profiles of both GAMOS^{GON7} and GAMOS^{OSGEP} patient-derived kidney organoid-isolated podocytes and late CPCs by RNA-Seq. The analysis of these data, comparing patients *versus* controls for each cell type and integrating the results of podocyte and CPC experiments, will be highly informative to highlight common and/or specific pathological mechanisms of these cell types.

Still, establishment of a robust procedure for kidney organoid podocyte isolation is most awaited, as discussed above. This would allow performing “bulk” molecular analyses, such as RT-qPCR or western blot, on a pure podocyte population. In the specific case of GAMOS, kidney organoid isolated podocytes can be used to measure the t^6A level or to perform ribosome profiling for instance, to evaluate the effect of mutations on protein translation.

Finally, we have not fully exploited all the possibilities of iPSC and an open perspective is represented by the possibility to generate brain organoids from GAMOS^{GON7} and GAMOS^{OSGEP} patient-derived iPSCs, a model system that would be most powerful to highlight mechanisms leading to microcephaly[327].

MATERIALS AND METHODS

iPSC reprogramming

Patient-derived peripheral blood mononuclear cells (PBMCs) were reprogrammed to iPSCs at the *iPSCs Platform* of the *Imagine Institute* using the **CytoTune-iPS 2.0 Sendai Reprogramming kit** (A16517, Thermo Fisher scientific). PBMCs were cultured in **StemPro-34 SFM** medium (10639011, Thermo Fisher scientific) supplemented with 20 ng/ml **IL-3** (AF-200-03, PeproTech), 20 ng/ml **IL-6** (AF-200-06, PeproTech), 100 ng/ml **SCF** (AF-300-07, PeproTech) and 100 ng/ml **Flt3-Ligand** (AF-300-19, PeproTech) for 4 days before transduction. 250˙000 cells were transduced overnight with **KOS**, **hc-Myc** and **hKlf4** reprogramming vectors at a 5-5-3 MOI. 3 days after transduction, cells were plated on **Vitronectin XF**- (07180, StemCell Technologies) coated culture dishes in complete **StemPro-34 SFM** medium at first, and in **StemPro-34 SFM** medium without any cytokine from the following day. Transition to **ReproTeSR** medium (05920, StemCell Technologies) was performed starting from day 7 at 1:1 ratio, and then replaced with entire **ReproTeSR** medium until emergence of iPSCs colonies, appearing after 2 - 3 weeks. iPSCs colonies were manually picked under a **Lynx Stereo Dynascopic Microscope** (Vision Engineering) and transferred onto fresh **Vitronectin XF**-coated culture dishes for expansion in **mTeSR1** medium (85850, StemCell Technologies).

iPSC quality controls

iPSCs clones were expanded for at least 10 passages before further characterization and quality controls, performed at the iPSC Platform of the *Imagine Institute*. Quality controls included:

- Mycoplasma test: Mycoplasma contamination was checked every month using a **MycoAlert PLUS Mycoplasma Detection kit** (LT07-710, Lonza) according to manufacturer's instructions.
- Alkaline phosphatase activity: alkaline phosphatase staining was performed according to manufacturer’s instructions.
- Karyotype: molecular karyotype was performed using an **Infinium Core-24 v1.2 kit** (20024566, Illumina) containing 300,000 SNPs. Data were analyzed with **BeadStudio/ GenomeStudio software** (Illumina).
- Identity match: matching the iPSCs genotype with that of parental PBMCs for 8 informative SNPs confirmed the origin of iPSCs.
- Surface antigen and transcription factor: the expression of pluripotent stem cell markers was assessed by immunofluorescence staining for **OCT4** and **SOX2** and by cytofluorimetric assay of **TRA-1-81** and **SSEA-4**.

- *In vitro* trilineage differentiation by embryoid body (EB) formation: 25 to 30 iPSCs colonies were manually cut into small clumps, collected and transferred into low attachment dishes. EBs were cultured in suspension for 7 to 9 days with DMEM/F-12 medium supplemented with 20% **pluriQ Serum Replacement** (GSM-6101, GlobalStem), 1% Non-essential amino acids, 1% Penicillin-streptomycin and 0.2% β-mercaptoethanol (31350010, ThermoFisher Scientific). EBs were then collected for RNA analyses or transferred onto gelatin-coating dishes for 1 week and stained using antibodies specific for early differentiation for each germ layer. EBs were cultured at 37°C in a humidified atmosphere containing 5% CO2 with the culture medium refreshed every other day. Trilineage potential evaluation was performed using the TaqMan hPSC Scorecard assay according to the manufacturer's and by immunofluorescence staining for ectodermal **TUJ1**, mesodermal **α-SMA** and endodermal **α-FP** markers.

iPSC culture

iPSCs were cultured in **mTeSR1** or **mTeSR Plus** (85850 or 05825, StemCell Technologies) medium on **Vitronectin XF (**07180, StemCell Technologies) -coated **35** or **60 mm dishes**. Medium was changed every day or occasionally it was supplemented with 10 ng/ml **StemBeads FGF2** (SB501, StemCulture) when 1 to 2 days of medium change were skipped. iPSCs colonies morphology was daily monitored under a **Lynx Stereo Dynascopic Microscope** (Vision Engineering) and cleaning up was performed manually using needles or tips to ensure maintenance of an undifferentiated state. Phase contrast microscopy was occasionally employed to observe cells. iPSCs were passaged with a frequency of about one week by mechanical cutting of colonies followed by clumps detaching and transfer into another culture dish.

Culture medium/matrix tests were performed with **ReproFF2** (RCHEMD006, ReproCELL) medium, **Geltrex** LDEV-Free hESC-qualified reduced growth factor basement membrane matrix (A1413302, Gibco by Life Technologies) and **Matrigel** LDEV-free hESC-qualified matrix, (354277, Corning).

CRISPR/Cas9-mediated genome editing

iPSCs were supplied with 10 µM **Y-27632** (1683, AxonMed) at least 2 h before nucleofection. Cells were dissociated with **TrypLE Select Enzyme** (12563-011, Thermo Fisher scientific) and 800 000 cells/nucleofection were pelleted by centrifugation. Pellets were resuspended in 30 µl of **P3 Primary Cell Nucleofector Solution** supplied with **Supplement 1** of the **P3 Primary Cell 4D-Nucleofector X kit S** (V4XP-3032, Lonza). 25% of P3 cellular solution was kept as non-transfected control. Pre-constituted **crRNA:tracrRNA/CAS9 RNP complex** (300 pmol gRNA and 150 pmol Cas9) and 300 pmol **ssODN** were mixed to the remaining 75% P3 cellular solution. The mix (22 µl) was

transferred into a 20 µl Nucleocuvette and nucleofected on a **4D-Nucleofector System** with **Core** (AAF-1002B, Lonza) and **X Unit**s (AAF-1002X, Lonza) using the CA-137 program. After 2-5 min incubation at room temperature, cells were resuspended into mTeSR Plus medium supplemented with 1:10 **CloneR** (05888, StemCell Technologies) and plated at 100 000 cells/cm^2 on Matrigel-coated supports. After 1 day, cell medium was supplemented with 10 µM **Y-27632** at least 2h before to be dissociated with **TrypLE Select Enzyme**. Cells with the highest GFP$^+$ signal were sorted on a **SH800S Cell Sorter** (Sony Biotechnology) and plated at a density of 25 cells/cm^2 on **CellAdhere Laminin-521** (77003, StemCell Technologies) -coated culture dishes in mTeSR Plus medium supplemented with 1:10 **CloneR**. Fresh medium was added or replaced every 2 to 3 days, switching to unsupplemented mTeSR1 Plus medium starting from day 7 post-plating. Clone piking was performed around day 14. For each clone, half colony was pursued in culture and half was used for screening. DNA for screening was extracted using the **QuickExtract DNA Extraction Solution** (QE09050, Biosearch Technologies). The *NPHS2* exon 3 region was amplified by PCR using the forward 5'-TCAAAATTCTGTCTATGGGT-3' and reverse 5'-CATTTAATCTGAGGTCCATA-3' primers (Eurogentec) and the amplicon was digested using the BseNI restriction enzyme (R0527, New England Biolabs). According to the digestion profile, selected clones underwent Sanger sequencing to confirm the type of genomic modification. The 12 exonic and 8 intronic most probable off-target sites according to CRISPOR CFD score were checked by PCR and Sanger sequencing to validate the absence of off-target genome editing at these sites.

Kidney organoid differentiation

The procedure for kidney organoid differentiation from iPSCs was performed according to a published protocol (adapted from *Morizane et al. 2015*). It was performed on iPSC colonies about one week after mechanical clumps passing. Alternatively, iPSCs were detached using **Accutase** (07920, StemCell Technologies) and seeded at a density of 1,5×10^4 cells/cm^2 on **Vitronectin XF**-coated supports. Cells were cultured for about 3 days with daily changing of **mTeSR1** medium supplemented with 10 µM **Y-27632** (72304, StemCell Technologies or 1683, AxonMed) for the first day, until they reach an appropriate confluence of about 50% to start differentiation. **14 mm Ø coverslips** were eventually deposed at the bottom of wells for some applications. Differentiation was started by switching to **Basic Differentiation Medium** (BDM), consisting by **Advanced RPMI 1640** (12633020, Thermo Fisher scientific) medium with **1X GlutaMAX supplement** (35050061, Thermo Fisher scientific), which was supplemented with 8 µM **CHIR 99021** (1386, Axon Medchem) and 5 ng/ml **Noggin** (120-10C, PeproTech) for 4 days to induce the late primitive streak. 10 ng/ml **Activin A** (120-14E, PeproTech) was used for the following 3 days to lead differentiation towards the posterior intermediate mesoderm. Medium was then supplemented with 10 ng/ml

FGF9 (273-F9-025, R&D Systems) from day 7 to day 14, combined with a 1 to 2 days pulse of 3 µM CHIR 99021 from day 8 or 9, depending on observation of cell morphology. From the induced metanephric mesenchyme, pretubular aggregates and subsequently renal vesicles raised. Kidney organoids development occurred spontaneously during the following week, without addition of any other factor. All along differentiation medium was changed every 2 or 3 days.

Kidney organoid *in ovo* transplantation

Fertilized **chicken eggs** (*Gallus gallus domesticus*, Earl Les Bruyeres, Dangers, France) at the segmentation stage, namely embryonic developmental day 0 (E0), were incubated laying on a side at 37° C in a 70% humidity atmosphere. At E2 or E3, a window was opened on the top of the shell after incision of the air chamber. The window was sealed with **silk-like surgical tape** (1538P-1SD, Durapore). Kidney organoids or nephron progenitor cells at D9 were deposed on the chorioallantoic membrane between E6 and E8. Several conditions have been tested, including the variation of organoids number from 1 to 10 per egg or differentiation stage (D21 versus D30), the positioning of a **plastic ring** surrounding the zone of the graft, the inclusion in **Geltrex** matrix at a 2:3 or 3:4 ratio with **BDM**, the adding of **VEGF** 10 ng/ml or **FGF2** 10 ng/ml pro-angiogenetic factors, the scratching of the membrane previous to transplantation and the dissociation or withdrawal of whole clusters of D9 nephron progenitor cells. Follow-up was performed under a **stereomicroscope**. All embryos were sacrificed at E14 maximum by *in ovo* **PFA 4%** fixation at room temperature for 30 min. The grafts were collected by cutting the CAM out of the rest of the embryo.

Immunofluorescence (IF)

D21 kidney organoids at were fixed in **4% PFA** at room temperature for 30 min - 1 h. Samples were subsequently blocked and permeabilized in **2% BSA/0,1% Triton X-100** for 1 h at room temperature. **2% BSA/0,1% Triton X-100** was equally used for primary and secondary antibodies dilutions. Primary antibodies, including rabbit anti-**T** 1:50 (sc-20109, Santa Cruz Biotechnology), goat anti-**TBX6** 1:200 (AF4744-SP, R&D Systems), mouse anti-**WT1** 1:100 (sc-7385, Santa Cruz Biotechnology), rabbit anti-**SIX2** 1:200 (11562-1-AP, Proteintech), goat anti-**PAX2** 1:100 (AF3364, R&D Systems), mouse anti-**LHX1** 1:50 (4F2-c, Developmental Studies Hybridoma Bank), rabbit anti-**podocin** 1:200 (AP-P35, C. Antignac's laboratory production or P0372 Sigma-Aldrich), goat anti-**podocalyxin** 1:500 (AF1658, R&D Systems), goat anti-**synaptopodin** 1:50 (sc-21537, Santa Cruz Biotechnology) or mouse anti-**synaptopodin** 1:50 (65194, Progen), guinea pig anti-**nephrin** 1:100 (GP-N2, ProGen), mouse anti-**nephrin** 1:100 (48E11, kindly provided by Tryggvason's laboratory), mouse anti-**LRP2** 1:3000 (ab184676, abcam), rat anti-**E-cadherin** 1:400 (13-1900, Thermo Fisher Scientific), rabbit anti-**ARL13B** (17711-1-AP, Proteintech), rabbit anti-**Ki-67** (ab16667, abcam), rabbit

anti-**laminin** 1:500 (L9393, Sigma-Aldrich), mouse anti-**calreticulin** 1:200 (ALX-804-014-R100, Enzo Life Sciences), mouse anti-**calnexin** 1:400 (sc-23954, Santa Cruz Biotechnology), mouse anti-**PDI** 1:200 (ADI-SPA-891, Enzo Life Sciences), rabbit anti-**cleaved caspase 3 Asp175** 1:400 (9664, Cell Signaling Tecnhnology) and mouse anti-**PML** 1:100 (sc-966, Santa Cruz Biotechnology), were incubated overnight at 4°C, with the exception of the anti-nephrin antibody, which required a 1 h incubation at 37°C. Fluorescein-labeled ***Lotus tetragonolobus*** **Lectin** (FL-1321, Vector Laboratories) was used at 1:200 together with primary antibodies. Fluorescently labeled **donkey Alexa Fluor 488**, **555** and **647** secondary antibodies (Life Technologies) diluted 1:200 were incubated at room temperature for 2 h in appropriate combinations. Nuclei were stained with 3 µg/ml **DAPI** (sc-3598, Santa Cruz Biotechnology) for 15 min and coverslips were then mounted on slides using **Mowiol 4-88** (81381, Sigma-Aldrich) mounting medium. Samples were observed and imaged on a **Spinning Disk Confocal Microscope** (Zeiss). Images visualization and analysis has been performed on ImageJ and/or ZEN (blue edition) (Zeiss) software.

Co-localization analysis

Glomeruli were manually encircled based on PODXL IF staining using the "**Poligon selections**" function on **ImageJ**, to next apply "**Edit; Clear Outside**" command. Images were loaded on the **ilastik** software to perform a "**Pixel Classification**" analysis, treating each channel individually. The software was trained to discriminate the staining of interest on a subset of representative images, and **Single Segmentations** were exported. Single Segmentations were converted into **Binary images**, and Manders' coefficients were obtained using the **JACoP** plugin on ImageJ, performing the "**M1 and M2 coefficients analysis**". **Unpaired two-tailed t-test** has been applied to compare Manders' coefficients using the **GraphPad Prism 8** software.

Transmission electron microscopy (TEM)

Samples were fixed in **2,5% Glutheraldeyhde** at room temperature for 30 min - 1 h and kept in the fixative at 4°C until processing at the Electron Microscopy Platform of the *Cochin Institut*. Samples were post-fixed with **0.1 M Osmium Tetroxyde** at 4°C for 1 h and washed three times in **H_2O**. **Uranyl Acetate** staining was performed previous to a dehydration step, carried out in successive baths of **70%**, **90%** and **100% Ethanol**. Samples were then immersed in two **Propylene Oxide** baths and then in a **1:1 Prepolymer/Propylene Oxide** mixture. They were finally included in **gelatin capsules** in pure **Prepolymer**, which were made polymerize for at least 24 h in an oven at 60°C. Sections of **90 nm** were obtained through a **Reichert Ultracut S Ultramicrotome** (Leica). Samples were observed and imaged on a **JEM-1011 Transmission Electron Microscope** (JEOL).

Reverse transcription and quantitative PCR (RT-qPCR)

RNA was extracted using the **RNeasy Mini 74104 kit** (Qiagen) according to manufacturer's instructions. **Random Hexamer Primers** (SO142, Thermo Fisher scientific) and **dNTPs** were mixed to **0,5 - 1 µg** of **total RNA** for RT. After a denaturation step at 65°C for 5 min, **5X First-Strand buffer**, **DTT**, **SuperScript II Reverse Transcriptase** (180640, Thermo Fisher scientific) and **RiboLock RNase Inhibitor** (EO0381, Thermo Fisher scientific) were added to samples. RT reaction consisted in incubations at 25°C for 10 min and at 42°C for 50, followed by enzyme heat inactivation at 70°C for 15 min. cDNA was stored at -20°C until performing qPCR. qPCR was performed using Power SYBR Green PCR Master Mix (4367659, Thermo Fisher scientific) and the following specific primers:

Gene	Forward primer	Reverse primer
OCT4	5'-CGACCATCTGCCGCTTTG-3'	5'-GGTTGCCTCTCACTCGGTTCT-3'
SOX2	5'-GACCAGCTCGCAGACCTACAT-3'	5'-GACTTGACCACCGAACCCAT-3'
T	5'-AGGTACCCAACCCTGAGGA-3'	5'-GCAGGTGAGTTGTCAGAATAGGT-3'
TBX6	5'-GTGTCTTTCCATCGTGTCAAGC-3'	5'-TATGCGGGGTTGGTACTTGTG-3'
WT1	5'-CACAGCACAGGGTACGAGAG-3'	5'-CAAGAGTCGGGGCTACTCCA-3'
HOXD11	5'-AGAAGAGCAGCAGCGCAGT-3'	5'-CAGTTCGCGGATCTGGTACTT-3'
SIX2	5'-GCCGAGGCCAAGGAAAGGGAGAA-3'	5'-AGCAGTGCGGGGCTGGATGA -3'
PAX2	5'-CGCCTCCAATGACCCA-3'	5'-GCCCTCAGACACATCTTCATC-3'
NPHS2	5'-GGCTGAAGCGCAAAGACAAG-3'	5'-GCAGCCTTTTCCGCTTCTG-3'
IFIT1	5'-TGGACAAGGTGGAGAACATTT-3'	5'-CCATCCTTCCTCACAGTCTATTT-3'
MX1	5'-CAGTTACCAGGACTACGAGATTG-3'	5'-TGACTGATTCCCATTCCTTCC-3'
IRF9	5'-GCCACAGGAAGTTACAGACA-3'	5'-CCCGTTGTAGATGAAGGTGAG-3'
OAS2	5'-CCAGGAGAAGCTGTGTATCTATTG-3'	5'-ATTACTGGCCTCGCTGATTG-3'
HPRT	5'- TCTTTGCTGACCTGCTGGATT-3'	5'- GTTGAGAGATCATCTCCACCAATTACT-3'
GAPDH	5'- CATGAGAAGTATGACAACAGC-3'	5'- AGTCCTTCCACGATACCAAAGT-3'

qPCR reaction has been performed running samples in triplicates on a Stratagene Mx3000P System (Agilent Technologies) and data were analyzed using the MxPro qPCR software (Agilent Technologies).

Glomerular sieving

Manually collected D21 kidney organoids were washed in PBS, encouraging initial dissociation by pipetting. Organoid/cell solution was placed onto a **40 µm Strainer** hydrated with PBS, allowing single-cells to flow through by gravity to be discarded. The remaining aggregates were transferred onto a **100 µm Strainer** and gently pressed with rotatory movements using a **sterile syringe plunger**. The sieved fraction was collected and cultured in **BDM** supplemented with **10% FBS**. Analysis was performed 24 h after seeding.

Kidney organoid dissociation

Several dissociations strategies have been tested to get individual cells from kidney organoids. These included the use of different combinations of enzymatic reagents, including 0,25% trypsin/EDTA, accutase, *Bacillus Licheniformis* psychrophilic protease diluted 1:50 or 1:20 into PBS with 5 mM $CaCl_2$ in combination with DNase I, Collagenases (IV, A and II), Pancreatin and optimization of the incubation times.

The best selected option contemplated incubation of manually collected D21 kidney organoids into 2,5 mg/ml **Collagenase /** 10 mg/ml **Pancreatin** (P1625, Sigma-Aldrich) **/** 150 U/ml **DNase I** (18047019, Thermo Fisher scientific) mix for 10 to 15 min at 37°C, encouraging dissociation by pipetting every 2 to 4 min. Collagenase A (10103586001, Sigma Aldrich) was chosen for the first series of samples for RNA-Seq, while Collagenase II (17101-015, Life Technologies) was instead used for the second one. A second enzymatic dissociation step was performed in the first series by incubation in **Accutase** (07920, StemCell Technologies) **/** 150 U/ml **DNase I** mix for 10 at 37°C, encouraging dissociation by pipetting every 2 min. This step turn out to be not necessary and removed when preparing the second collection of RNA-Seq-dedicated samples.

Podocytes FACS-sorting

Cell suspensions obtained upon kidney organoid dissociation was incubated in **Fc blocking reagent** (Miltenyi Biotec, 130-059-901) diluted **1:5** into **FACS buffer** (PBS / 2.5% FBS / 2.5 mM EDTA) on ice for 10 min. Samples were subsequently stained with mouse anti-human **nephrin** (48E11, kindly provided by Tryggvason's laboratory), goat anti-human **podocalyxin** (R&D Systems, AF1658) and fluorescein-labeled ***Lotus tetragonolobus*** **Lectin** (LTL) (Vector Laboratories, FL-1321) diluted 1:50 into **FACS buffer**, and incubated on ice for 20 min. Followed incubation with fluorescently labeled **donkey Alexa Fluor anti-mouse 555** and **anti-goat 647** secondary antibodies (Life Technologies) diluted 1:200 on ice for 20 min. Cells were resuspended in **FACS buffer** and filtered by passing them through a **35 µm Cell Strainer Snap Cap** (Corning, 352235). 5 µl/10^6 cells of **7-AAD** (BD Biosciences, 559925) was added to samples and incubated for 10 min in order to exclude non-viable cells. **Nephrin$^+$/Podocalyxin$^+$/LTL$^-$ cells** were FACS-sorted on a **BD FACSAria II** (BD Biosciences, 643179) flow cytometer at the *Cell Sorting Facility* of the *SFR Necker* and directly collected into **RLT lysis buffer** (from RNeasy Micro kit**,** Qiagen, 74004) supplied with 1% β-Mercaptoethanol. FACS-sorted cells were frozen and stored at -80°C until RNA extraction.

RNA sequencing (RNA-Seq)

RNA was extracted from FACS sorted cells using the **RNeasy Micro kit** (74004, Qiagen), by thawing FACS-sorted lysed cells and proceeding according to manufacturer's instructions. RNA quantity and quality was assessed by automated electrophoresis using the **TapeStation** system (Agilent Technologies). RNA-Seq libraries were prepared starting from 3-4 ng of total RNA using the **Ovation SoLoRNA-Seq System kit** (0500-32, Nugen) according to manufacturer's instructions. Briefly, after **DNase** treatment and **random primer** annealing, the first cDNA strand was synthetized from total RNA. Second cDNA strand was produced and then ligated to Illumina compatible adaptors containing both sample index and a

Unique Molecular Index (UMI). The cDNA produced was PCR amplified after an initial test to evaluate the suitable number of PCR cycles to apply to each sample. cDNA corresponding to ribosomal RNA were selectively fragmented using the **AnyDeplete** technology. Few PCR cycles were performed to finalize the RNAseq library preparation. An equimolar pool of the final indexed RNA-Seq libraries was prepared and sequenced on an **HiSeq2500** (paired-end reads of 130 bases + 130 bases; Illumina) for the "pilot RNA-Seq" (NGS2018_2231 project) or on a **NovaSeq6000** (paired-end reads of 100 bases + 100 bases; Illumina) for the second RNA-Seq (NGS2019_2748 project) (podocytes). A total of ~50 millions of passing filter paired-end reads was produced per library.

RNA-Seq analysis

FASTQ files were mapped to the ENSEMBL GRCh38/hg38 reference human genome using **Hisat2** and counted by **featureCounts** from the **Subread R package**. Read count normalizations and groups comparisons were performed by three independent and complementary statistical methods: **DESeq2**, **edgeR** and **LimmaVoom**. Flags were computed from counts normalized to the mean coverage. All normalized counts <20 were considered as background (flag 0) and ≥20 as signal (flag=1). Cluster analysis was performed on DESeq2 P50 lists, regrouping the genes showing flag=1 for at least half of the compared samples, by hierarchical clustering using the **Spearman's correlation similarity** measure and **Ward's linkage** algorithm. Samples were compared using the DESeq2 statistical method, applying the Bonferroni and Benjamin-Hochberg corrections for multiple hypothesis testing. Statistically significant upregulated and downregulated gene lists (BH-corrected p-value<0.05) were subjected to **GO enrichment analysis** for biological process on geneontology.org. Functional analyses were carried out using **Ingenuity Pathway Analysis** (IPA, Qiagen) on >2 fold change expression filtered results of the three statistical methods. For the functional interaction network analysis, statistically significant upregulated (BH-corrected p-value<0.05) and downregulated gene lists (uncorrected p-value<3×10^{-4}) were uploaded on the **STRING database** together with the genes associated with NS (Introduction, Chapter 2, Table 1), searching for multiple proteins. The simple tabular text output was exported and the network was imported on the **Cytoscape** software for visualization and layout designing.

Late cortical progenitor cell (CPC) induction

Late CPCs were derived from iPSCs according to a published protocol (adapted from *Boissart et al. 2013*). mTeSR medium was replaced with **N2B27 medium**, consisting of a 1:1 **Neurobasal** and **DMEM/F-12, GlutaMAX** media mix containing 1:50 **NeuroCult SM1 Without Vitamin A** (05731, StemCell Technologies) and 1:100 **N2 Supplement-B** (07156, StemCell Technologies), supplemented with 10 ng/ml **FGF2** (100-18B, PeproTech), 500 nM **LDN** (72146, StemCell Technologies), 20 µM **SB431542** (72232, StemCell Technologies)

and 10 µM **Y-27632**. iPSCs colonies were mechanically cut, followed by clumps detaching and transfer on a non-adherent support. Clumps were left floating for 6 h in order to form embryoid body like 3D structures, which were subsequently transferred onto a **Poly-L-Ornithine** (P4957, Sigma-Aldrich)**/Laminin** (23017-015, Thermo Fisher scientific**)** -coated culture dish. Neural rosettes appearing approximatively 12-14 days of culture in N2B27 medium supplemented with **FGF2** (10 ng/ml), **LDN** (500 nM) and **SB431542** (20 µM) were manually collected and transferred to a **Poly-L-Ornithine/Laminin**-coated culture dish in N2B27 medium supplemented with 10 ng/ml **FGF2**, 10 ng/ml **EGF** (AF-100-15, PeproTech) and 20 ng/ml **BDNF** (450-02, PeproTech). NPCs were maintained in these culture conditions and split by trypsinization when reaching confluence for up to 15 passages.

Late CPC quality controls

Cell suspensions obtained upon CPC trypsination was incubated in **Fc blocking reagent** (Miltenyi Biotec, 130-059-901) diluted **1:5** into **FACS buffer** (PBS / 2.5% FBS / 2.5 mM EDTA) on ice for 15 min. Samples were subsequently stained with anti-human **CD57-FITC** (HNK1; 130-122, Miltenyi Biotec) and **CD271(LNGFR)-PE** (P75; 130-113, Miltenyi Biotec) fluorescently-conjugated antibodies diluted 1:10 into FACS buffer, and incubated on ice for 30 min. Cells were resuspended in **FACS buffer** at a concentration of 5×10^6 cells/ml and filtered by passing them through a **35 µm Cell Strainer Snap Cap** (Corning, 352235). 5 µl/10^6 cells of **7-AAD** (BD Biosciences, 559925) was added to samples and incubated for 10 min in order to exclude non-viable cells. Cells were then acquired on a **SH800S Cell Sorter** (Sony Biotechnology) flow cytometer at the *Cell Sorting Facility* of the *SFR Necker*. Cells passed the quality control check if the population of $HNK1^+/P75^-$ cells was greater than 80%.

MTT proliferation assay

MTT proliferation assay has been performed using the **CellTiter 96 AQueous Nonradioactive Cell Proliferation Assay kit** (MTS) (G5421, Promega). Late CPCs were seeded in triplicates into **Poly-L-Ornithine/Laminin**-coated 96 well plates at a density of 3, 4 or 5×10^4 cells/cm^2. Cell proliferation was assessed starting from the following day by adding 20 µl of **MTS/PSM solution** at a 1:20 ration to 100 µl cell culture medium, and incubating cells for 2 hours. Absorbance measurement was performed on day 1, 2, 3 and 4 on a **TriStar multimode reader** (LB941, Berthold Technologies) using a 560 measurement filter and subtracting the blank background absorbance.

IncuCyte proliferation assay

Late CPCs were seeded in quadruplicates into **Poly-L-Ornithine/Laminin**-coated 24 well plates at a density of 5×10^4 cells/cm^2. Plates were incubated into an **IncuCyte S3 Live-Cell Analysis System** (4647, Sartorius). Follow-up was performed for ~6 days, taking 16

phase contrast images/well every 2 h using a 20X objective. **Object Mask** based on phase contrast was generated using the **IncuCyte analysis software**. Cell proliferation was evaluated by measuring the **Phase Object Confluence (%)** over time, obtaining growth curves. The **log phase** was identified by using the coefficient of correlation (R^2) as an indicator of the linearity of the curve, choosing the time window in which R^2 was closer to 1. Cell proliferation rate was estimated by calculating the **slope** of the curves at the log phase.

IncuCyte apoptosis assay

Late CPCs were seeded in triplicates into **Poly-L-Ornithine/Laminin**-coated 96 well plates at a density of 5×10^4 cells/cm^2. Cell medium was supplemented with 1:200 IncuCyte Annexin V Red Reagent for apoptosis (4641, Sartorius). Plates were incubated into an **IncuCyte S3 Live-Cell Analysis System** (4647, Sartorius). Follow-up was performed for ~6 days, taking 9 phase contrast and red fluorescence images/well every 2 h using a 20X objective. **Object Masks** based on phase contrast and red fluorescence were generated using the **IncuCyte analysis software**. Cell apoptosis was evaluated by measuring the **Red Object Confluence (%)** over time normalized on the matched **Phase Object Confluence (%)**.

t^6A measurement

Total RNA was isolated with **Invitrogen TRIzol** reagent (15596018, Thermo Fisher scientific) according to the manufacturer's directions. After size-based fractionation, tRNA fractions were hydrolyzed to be analyzed by **liquid chromatography-tandem mass spectrometry** (LC-MS/MS). MS signals for t^6A were first normalized to the peak area of the [^{15}N]2-deoxyadenosine internal standard control, and then normalized for the 4 canonical ribonuclesides (adenosine, cytidine, guanosine and uridine).

HPG protein synthesis assay

HPG protein synthesis assay has been performed using the **Click-iT HPG Alexa Fluor 488 Protein Synthesis Assay kit** (C10428, Life Technologies). Late CPCs were seeded in triplicates into **Poly-L-Ornithine/Laminin**-coated **96 well SensoPlates** (655892, Greiner Bio-One) at a density of 1×10^5 cells/cm^2. The following day, were incubated in **L-methionine-free medium** supplemented with 1:1000 **Click-iT HPG** for 2h, before to be fixed and permeabilized according to manufacturer's instructions. Cells were subsequently incubated in **Click-iT reaction cocktail** at room temperature for 30 min in the dark, and then rinsed with **Click-iT reaction rinse buffer**. Nuclei were stained by incubating cells in **HCS NuclearMask Blue Stain** diluted 1:2000 into **PBS** at room temperature for 30 min in the dark. Samples were scanned into PBS on a **TriStar multimode reader** (LB941, Berthold Technologies). HPG 432 nm fluorescence intensity was normalized to nuclear 533 nm signal.

BIBLIOGRAPHY

1. Amerman, E. C. Human Anatomy & Physiology. in (ed. Pearson) (2019).
2. Bertram, J. F., Douglas-Denton, R. N., Diouf, B., Hughson, M. D. & Hoy, W. E. Human nephron number: implications for health and disease. in *Pediatric Nephrology* (2011). doi:10.1007/s00467-011-1843-8.
3. Barlow, P., Owen, D. A. & Graham, C. DNA synthesis in the preimplantation mouse embryo. *J. Embryol. Exp. Morphol.* (1972).
4. Dyce, J., George, M., Goodall, H. & Fleming, T. P. Do trophectoderm and inner cell mass cells in the mouse blastocyst maintain discrete lineages. *Development* (1987).
5. Fleming, T. P. A quantitative analysis of cell allocation to trophectoderm and inner cell mass in the mouse blastocyst. *Dev. Biol.* (1987) doi:10.1016/0012-1606(87)90055-8.
6. Chapter 28- Fertilization to Implantation. *BIO 202 Human Anatomy & Physiology II* https://www.youtube.com/watch?v=VikPwLnkpxU%0A (2016).
7. Mammalian Reproduction. *SlidePlayer* https://slideplayer.com/slide/5131980/.
8. Gilbert, S. F. Developmental Biology, 10th Edition. in (ed. Associates, S. (MA): S.) (2000).
9. Mugford, J. W., Sipilä, P., Kobayashi, A., Behringer, R. R. & McMahon, A. P. Hoxd11 specifies a program of metanephric kidney development within the intermediate mesoderm of the mouse embryo. *Dev. Biol.* (2008) doi:10.1016/j.ydbio.2008.03.044.
10. Taguchi, A. *et al.* Redefining the in vivo origin of metanephric nephron progenitors enables generation of complex kidney structures from pluripotent stem cells. *Cell Stem Cell* (2014) doi:10.1016/j.stem.2013.11.010.
11. Grobstein, C. Inductive epithelio-mesenchymal interaction in cultured organ rudiments of the mouse. *Science (80-.).* (1953) doi:10.1126/science.118.3054.52.
12. Costantini, F. & Kopan, R. Patterning a complex organ: Branching morphogenesis and nephron segmentation in kidney development. *Developmental Cell* (2010) doi:10.1016/j.devcel.2010.04.008.
13. Herzlinger, D., Koseki, C., Mikawa, T. & Al-Awqati, Q. Metanephric mesenchyme contains multipotent stem cells whose fate is restricted after induction. *Development* (1992).
14. Little, M. H., Combes, A. N. & Takasato, M. Understanding kidney morphogenesis to guide renal tissue regeneration. *Nat. Rev. Nephrol.* (2016) doi:10.1038/nrneph.2016.126.
15. Carroll, T. J., Park, J. S., Hayashi, S., Majumdar, A. & McMahon, A. P. Wnt9b plays a central role in the regulation of mesenchymal to epithelial transitions underlying organogenesis of the mammalian urogenital system. *Dev. Cell* (2005) doi:10.1016/j.devcel.2005.05.016.
16. Barak, H. *et al.* FGF9 and FGF20 Maintain the Stemness of Nephron Progenitors in Mice and Man. *Dev. Cell* (2012) doi:10.1016/j.devcel.2012.04.018.
17. Stark, K., Vainio, S., Vassileva, G. & McMahon, A. P. Epithelial transformation of metanephric mesenchyme in the developing kidney regulated by Wnt-4. *Nature* (1994) doi:10.1038/372679a0.
18. Kispert, A., Vainio, S. & McMahon, A. P. Wnt-4 is a mesenchymal signal for epithelial transformation of metanephric mesenchyme in the developing kidney. *Development* (1998).
19. Müller, U. *et al.* Integrin α8β1 is critically important for epithelial-mesenchymal interactions during kidney morphogenesis. *Cell* (1997) doi:10.1016/S0092-8674(00)81903-0.
20. Georgas, K. *et al.* Analysis of early nephron patterning reveals a role for distal RV proliferation in fusion to the ureteric tip via a cap mesenchyme-derived connecting segment. *Dev. Biol.* (2009) doi:10.1016/j.ydbio.2009.05.578.
21. Uhlenhaut, N. H. & Treier, M. Transcriptional regulators in kidney disease: gatekeepers of renal homeostasis. *Trends in Genetics* (2008) doi:10.1016/j.tig.2008.05.001.
22. Woolf, A. S., Winyard, P. J. D., Hermanns, M. H. & Welham, S. J. M. Maldevelopment of the Human Kidney and Lower Urinary Tract. An Overview. in *The Kidney: From Normal Development to Congenital Disease* (2003). doi:10.1016/B978-012722441-1/50023-3.
23. Hinchliffe, S. A., Sargent, P. H., Howard, C. V., Chan, Y. F. & Van Velzen, D. Human intrauterine renal growth expressed in absolute number of glomeruli assessed by the disector method and cavalieri principle. *Lab. Investig.* (1991).
24. Scott, R. P. & Quaggin, S. E. The cell biology of renal filtration. *Journal of Cell Biology* (2015) doi:10.1083/jcb.201410017.
25. Satchell, S. C. & Braet, F. Glomerular endothelial cell fenestrations: An integral component of the glomerular filtration barrier. *American Journal of Physiology - Renal Physiology* (2009) doi:10.1152/ajprenal.90601.2008.
26. Dean, D. F. & Molitoris, B. A. The Physiology of the Glomerulus. in *Critical Care Nephrology: Third Edition* (2019). doi:10.1016/B978-0-323-44942-

7.00007-8.

27. Miner, J. H. The glomerular basement membrane. *Experimental Cell Research* (2012) doi:10.1016/j.yexcr.2012.02.031.

28. Tojo, A. & Kinugasa, S. Mechanisms of glomerular albumin filtration and tubular reabsorption. *International Journal of Nephrology* (2012) doi:10.1155/2012/481520.

29. Singh, A. *et al.* Glomerular endothelial glycocalyx constitutes a barrier to protein permeability. *J. Am. Soc. Nephrol.* (2007) doi:10.1681/ASN.2007010119.

30. Kanwar, Y. S. & Farquhar, M. G. Presence of heparan sulfate in the glomerular basement membrane. *Proc. Natl. Acad. Sci. U. S. A.* (1979) doi:10.1073/pnas.76.3.1303.

31. Kerjaschki, D., Sharkey, D. J. & Farquhar, M. G. Identification and characterization of podocalyxin - The major sialoprotein of the renal glomerular epithelial cell. *J. Cell Biol.* (1984) doi:10.1083/jcb.98.4.1591.

32. Harvey, S. J. *et al.* Disruption of glomerular basement membrane charge through podocyte-specific mutation of agrin does not alter glomerular permselectivity. *Am. J. Pathol.* (2007) doi:10.2353/ajpath.2007.061116.

33. Welsh, G. I. & Saleem, M. A. The podocyte cytoskeleton-key to a functioning glomerulus in health and disease. *Nature Reviews Nephrology* (2012) doi:10.1038/nrneph.2011.151.

34. Pavenstädt, H., Kriz, W. & Kretzler, M. Cell biology of the glomerular podocyte. *Physiological Reviews* (2003) doi:10.1152/physrev.00020.2002.

35. Schell, C., Wanner, N. & Huber, T. B. Glomerular development - Shaping the multi-cellular filtration unit. *Seminars in Cell and Developmental Biology* (2014) doi:10.1016/j.semcdb.2014.07.016.

36. Quaggin, S. E. & Kreidberg, J. A. Development of the renal glomerulus: Good neighbors and good fences. *Development* (2008) doi:10.1242/dev.001081.

37. Miner, J. H. *et al.* The laminin α chains: Expression, developmental transitions, and chromosomal locations of α1-5, identification of heterotrimeric laminins 8- 11, and cloning of a novel α3 isoform. *Journal of Cell Biology* (1997) doi:10.1083/jcb.137.3.685.

38. Abrahamson, D. R., St. John, P. L., Stroganova, L., Zelenchuk, A. & Steenhard, B. M. Laminin and type IV collagen isoform substitutions occur in temporally and spatially Distinct patterns in developing kidney glomerular basement membranes. *J. Histochem. Cytochem.* (2013) doi:10.1369/0022155413501677.

39. Durbeej, M. *et al.* Expression of laminin α1, α5 and β2 chains during embryogenesis of the kidney and vasculature. *Matrix Biol.* (1996) doi:10.1016/S0945-053X(96)90159-6.

40. Miner, J. H. Developmental biology of glomerular basement membrane components. *Current Opinion in Nephrology and Hypertension* (1998) doi:10.1097/00041552-199801000-00003.

41. Fukasawa, H., Bornheimer, S., Kudlicka, K. & Farquhar, M. G. Slit diaphragms contain tight junction proteins. *J. Am. Soc. Nephrol.* (2009) doi:10.1681/ASN.2008101117.

42. Reiser, J., Kriz, W., Kretzler, M. & Mundel, P. The glomerular slit diaphragm is a modified adherens junction. *J. Am. Soc. Nephrol.* (2000).

43. Weide, T. & Huber, T. B. Signaling at the slit: Podocytes chat by synaptic transmission. *Journal of the American Society of Nephrology* (2009) doi:10.1681/ASN.2009070691.

44. Rodewald, R. & Karnovsky, M. J. Porous substructure of the glomerular slit diaphragm in the rat and mouse. *J. Cell Biol.* (1974) doi:10.1083/jcb.60.2.423.

45. Wartiovaara, J. *et al.* Nephrin strands contribute to a porous slit diaphragm scaffold as revealed by electron tomography. *J. Clin. Invest.* (2004) doi:10.1172/JCI22562.

46. Grahammer, F. *et al.* A flexible, multilayered protein scaffold maintains the slit in between glomerular podocytes. *JCI Insight* (2016) doi:10.1172/jci.insight.86177.

47. Tryggvason, K. Unraveling the mechanisms of glomerular ultrafiltration: Nephrin, a key component of the slit diaphragm. *J. Am. Soc. Nephrol.* (1999).

48. Kestilä, M. *et al.* Positionally cloned gene for a novel glomerular protein - Nephrin - Is mutated in congenital nephrotic syndrome. *Mol. Cell* (1998) doi:10.1016/S1097-2765(00)80057-X.

49. Donoviel, D. B. *et al.* Proteinuria and Perinatal Lethality in Mice Lacking NEPH1, a Novel Protein with Homology to NEPHRIN. *Mol. Cell. Biol.* (2001) doi:10.1128/mcb.21.14.4829-4836.2001.

50. Gerke, P., Huber, T. B., Sellin, L., Benzing, T. & Walz, G. Homodimerization and heterodimerization of the glomerular podocyte proteins nephrin and NEPH1. *J. Am. Soc. Nephrol.* (2003) doi:10.1097/01.ASN.0000057853.05686.89.

51. Shih, N. Y. *et al.* Congenital nephrotic syndrome in mice lacking CD2-associated protein. *Science (80-.).* (1999) doi:10.1126/science.286.5438.312.

52. Reiser, J. *et al.* TRPC6 is a glomerular slit diaphragm-associated channel required for normal renal function. *Nat. Genet.* (2005) doi:10.1038/ng1592.

53. Hinkes, B. *et al.* Positional cloning uncovers mutations

in PLCE1 responsible for a nephrotic syndrome variant that may be reversible. *Nat. Genet.* (2006) doi:10.1038/ng1918.

54. Inoue, T. *et al.* FAT is a component of glomerular slit diaphragms. *Kidney Int.* (2001) doi:10.1046/j.1523-1755.2001.0590031003.x.

55. Bierzynska, A. *et al.* MAGI2 mutations cause congenital nephrotic syndrome. *J. Am. Soc. Nephrol.* (2017) doi:10.1681/ASN.2016040387.

56. Grahammer, F., Schell, C. & Huber, T. B. The podocyte slit diaphragm - From a thin grey line to a complex signalling hub. *Nature Reviews Nephrology* (2013) doi:10.1038/nrneph.2013.169.

57. Huber, T. B., Köttgen, M., Schilling, B., Walz, G. & Benzing, T. Interaction with Podocin Facilitates Nephrin Signaling. *J. Biol. Chem.* (2001) doi:10.1074/jbc.C100452200.

58. Patrakka, J. & Tryggvason, K. Nephrin - a unique structural and signaling protein of the kidney filter. *Trends in Molecular Medicine* (2007) doi:10.1016/j.molmed.2007.06.006.

59. Fuchshuber, A. *et al.* Mapping a gene (SRN1) to chromosome 1q25-q31 in idiopathic nephrotic syndrome confirms a distinct entity of autosomal recessive nephrosis. *Hum. Mol. Genet.* (1995) doi:10.1093/hmg/4.11.2155.

60. Boute, N. *et al.* NPHS2, encoding the glomerular protein podocin, is mutated in autosomal recessive steroid-resistant nephrotic syndrome. *Nat. Genet.* (2000) doi:10.1038/74166.

61. Roselli, S. *et al.* Podocin localizes in the kidney to the slit diaphragm area. *Am. J. Pathol.* (2002) doi:10.1016/S0002-9440(10)64357-X.

62. Lindström, N. O. *et al.* Conserved and divergent molecular and anatomic features of human and mouse nephron patterning. *J. Am. Soc. Nephrol.* (2018) doi:10.1681/ASN.2017091036.

63. Schwarz, K. *et al.* Podocin, a raft-associated component of the glomerular slit diaphragm, interacts with CD2AP and nephrin. *J. Clin. Invest.* (2001) doi:10.1172/JCI200112849.

64. Novus Biologicals. Podocin/NPHS2 Antibody. https://www.novusbio.com/products/podocin-nphs2-antibody_nbp2-33570.

65. Huber, T. B. *et al.* Podocin and MEC-2 bind cholesterol to regulate the activity of associated ion channels. *Proc. Natl. Acad. Sci. U. S. A.* (2006) doi:10.1073/pnas.0607465103.

66. Roselli, S., Moutkine, I., Gribouval, O., Benmerah, A. & Antignac, C. Plasma membrane targeting of podocin through the classical exocytic pathway: Effect of NPHS2 mutations. *Traffic* (2004) doi:10.1046/j.1600-0854.2003.00148.x.

67. Huber, T. B. *et al.* Molecular basis of the functional podocin-nephrin complex: Mutations in the NPHS2 gene disrupt nephrin targeting to lipid raft microdomains. *Hum. Mol. Genet.* (2003) doi:10.1093/hmg/ddg360.

68. Downie, M. L., Gallibois, C., Parekh, R. S. & Noone, D. G. Nephrotic syndrome in infants and children: Pathophysiology and management. *Paediatr. Int. Child Health* (2017) doi:10.1080/20469047.2017.1374003.

69. Benoit, G., MacHuca, E. & Antignac, C. Hereditary nephrotic syndrome: A systematic approach for genetic testing and a review of associated podocyte gene mutations. *Pediatric Nephrology* (2010) doi:10.1007/s00467-010-1495-0.

70. De Fátima Pereira, W. *et al.* The role of the immune system in idiopathic nephrotic syndrome: A review of clinical and experimental studies. *Inflammation Research* (2014) doi:10.1007/s00011-013-0672-6.

71. Colucci, M., Corpetti, G., Emma, F. & Vivarelli, M. Immunology of idiopathic nephrotic syndrome. *Pediatric Nephrology* (2018) doi:10.1007/s00467-017-3677-5.

72. Shalhoub, R. J. Pathogenesis of lipoid nephrosis: a disorder of T-cell function. *Lancet* (1974) doi:10.1016/S0140-6736(74)91880-7.

73. Tejani, A. *et al.* Cyclosporine A induced remission of relapsing nephrotic syndrome in children. *Kidney Int.* (1988) doi:10.1038/ki.1988.59.

74. Yokoyama, H. *et al.* Immunodynamics of minimal change nephrotic syndrome in adults T and B lymphocyte subsets and serum immunoglobulin levels. *Clin. Exp. Immunol.* (1985).

75. Benz, K., Dötsch, J., Rascher, W. & Stachel, D. Change of the course of steroid-dependent nephrotic syndrome after rituximab therapy. *Pediatr. Nephrol.* (2004) doi:10.1007/s00467-004-1434-z.

76. Rangan, G. K., Pippin, J. W. & Couser, W. G. C5b-9 regulates peritubular myofibroblast accumulation in experimental focal segmental glomerulosclerosis. *Kidney Int.* (2004) doi:10.1111/j.1523-1755.2004.00957.x.

77. He, C., Imai, M., Song, H., Quigg, R. J. & Tomlinson, S. Complement inhibitors targeted to the proximal tubule prevent injury in experimental nephrotic syndrome and demonstrate a key role for C5b-9. *J. Immunol.* (2005) doi:10.4049/jimmunol.174.9.5750.

78. McCarthy, E. T., Sharma, M. & Savin, V. J. Circulating permeability factors in idiopathic nephrotic syndrome and focal segmental glomerulosclerosis. *Clinical Journal of the American Society of*

Nephrology (2010) doi:10.2215/CJN.03800609.

79. Kang, H. G., Ha, I. S. & Cheong, H. Il. Recurrence and treatment after renal transplantation in children with FSGS. *BioMed Research International* (2016) doi:10.1155/2016/6832971.

80. Artero, M. L., Sharma, R., Savin, V. J. & Vincenti, F. Plasmapheresis reduces proteinuria and serum capacity to injure glomeruli in patients with recurrent focal glomerulosclerosis. *Am. J. Kidney Dis.* (1994) doi:10.1016/S0272-6386(12)80381-7.

81. Kemper, M. J., Wolf, G. & Müller-Wiefel, D. E. Transmission of glomerular permeability factor from a mother to her child. *New England Journal of Medicine* (2001) doi:10.1056/NEJM200102013440517.

82. Gallon, L., Leventhal, J., Skaro, A., Kanwar, Y. & Alvarado, A. Resolution of recurrent focal segmental glomerulosclerosis after retransplantation. *The New England journal of medicine* (2012) doi:10.1056/NEJMc1202500.

83. Zimmerman, S. W. & Mann, S. Increased urinary protein excretion in the rat produced by serum from a patient with recurrent focal glomerular sclerosis after renal transplantation. *Clin. Nephrol.* (1984).

84. Rastogi, V., Doshi, S. & Kaleem, A. Minimal Change Disease Associated with High-dose Aspirin. *Cureus* (2018) doi:10.7759/cureus.3408.

85. Breitbarth A, A. N. Focal segmental glomerulosclerosis (FSGS), collapsing variant. *PathologyOutlines.com* http://www.pathologyoutlines.com/topic/kidneyfsgscollapsing.html (2020).

86. Said, S. M. *et al.* Myeloproliferative neoplasms cause glomerulopathy. *Kidney Int.* (2011) doi:10.1038/ki.2011.147.

87. Lefevre, G. M., Patel, S. R., Kim, D., Tessarollo, L. & Dressler, G. R. Altering a histone H3K4 methylation pathway in glomerular podocytes promotes a chronic disease phenotype. *PLoS Genet.* (2010) doi:10.1371/journal.pgen.1001142.

88. Dogra, S. & Kaskel, F. Steroid-resistant nephrotic syndrome: a persistent challenge for pediatric nephrology. *Pediatr. Nephrol.* (2017) doi:10.1007/s00467-016-3459-5.

89. Hinkes, B. G. *et al.* Nephrotic syndrome in the first year of life: two thirds of cases are caused by mutations in 4 genes (NPHS1, NPHS2, WT1, and LAMB2). *Pediatrics* (2007) doi:10.1542/peds.2006-2164.

90. Wiggins, R. C. The spectrum of podocytopathies: A unifying view of glomerular diseases. *Kidney International* (2007) doi:10.1038/sj.ki.5002222.

91. Ichikawa, I., Ma, J., Motojima, M. & Matsusaka, T. Podocyte damage damages podocytes: Autonomous vicious cycle that drives local spread of glomerular sclerosis. *Current Opinion in Nephrology and Hypertension* (2005) doi:10.1097/01.mnh.0000165884.85803.e1.

92. Matsusaka, T. *et al.* Podocyte injury damages other podocytes. *J. Am. Soc. Nephrol.* (2011) doi:10.1681/ASN.2010090963.

93. Machuca, E., Benoit, G. & Antignac, C. Genetics of nephrotic syndrome: Connecting molecular genetics to podocyte physiology. *Hum. Mol. Genet.* (2009) doi:10.1093/hmg/ddp328.

94. Preston, R., Stuart, H. M. & Lennon, R. Genetic testing in steroid-resistant nephrotic syndrome: why, who, when and how? *Pediatric Nephrology* (2019) doi:10.1007/s00467-017-3838-6.

95. Boyer, O. *et al.* LMX1B mutations cause hereditary FSGS without extrarenal involvement. *J. Am. Soc. Nephrol.* (2013) doi:10.1681/ASN.2013020171.

96. Kim, J. H. *et al.* CD2-associated protein haploinsufficiency is linked to glomerular disease susceptibility. *Science (80-.).* (2003) doi:10.1126/science.1081068.

97. Winn, M. P. *et al.* Medicine: A mutation in the TRPC6 cation channel causes familial focal segmental glomerulosclerosis. *Science (80-.).* (2005) doi:10.1126/science.1106215.

98. Ebarasi, L. *et al.* Defects of CRB2 cause steroid-resistant nephrotic syndrome. *Am. J. Hum. Genet.* (2015) doi:10.1016/j.ajhg.2014.11.014.

99. Gee, H. Y. *et al.* FAT1 mutations cause a glomerulotubular nephropathy. *Nat. Commun.* (2016) doi:10.1038/ncomms10822.

100. Lahrouchi, N. *et al.* Homozygous frameshift mutations in FAT1 cause a syndrome characterized by colobomatous-microphthalmia, ptosis, nephropathy and syndactyly. *Nat. Commun.* (2019) doi:10.1038/s41467-019-08547-w.

101. Solanki, A. K. *et al.* Mutations in KIRREL1, a slit diaphragm component, cause steroid-resistant nephrotic syndrome. *Kidney Int.* (2019) doi:10.1016/j.kint.2019.06.016.

102. Barker, D. F. *et al.* Identification of mutations in the COL4A5 collagen gene in Alport syndrome. *Science (80-.).* (1990) doi:10.1126/science.2349482.

103. Mochizuki, T. *et al.* Identification of mutations in the α3(IV) and α4(IV) collagen genes in autosomal recessive Alport syndrome. *Nat. Genet.* (1994) doi:10.1038/ng0994-77.

104. Jefferson, J. A. *et al.* Autosomal dominant Alport

syndrome linked to the type IV collage α3 and α4 genes (COL4A3 and COL4A4). *Nephrol. Dial. Transplant.* (1997) doi:10.1093/ndt/12.8.1595.

105. Lemmink, H. H. *et al.* Mutations in the type IV collagen α3 (COL4A3) gene in autosomal recessive alport syndrome. *Hum. Mol. Genet.* (1994) doi:10.1093/hmg/3.8.1269.

106. Badenas, C. *et al*. Mutations in the COL4A4 and COL4A3 genes cause familial benign hematuria. *J. Am. Soc. Nephrol.* (2002).

107. Kambham, N. *et al.* Congenital focal segmental glomerulosclerosis associated with β4 integrin mutation and epidermolysis bullosa. *Am. J. Kidney Dis.* (2000) doi:10.1053/ajkd.2000.8293.

108. Crew, V. K. *et al.* CD151, the first member of the tetraspanin (TM4) superfamily detected on erythrocytes, is essential for the correct assembly of human basement membranes in kidney and skin. *Blood* (2004) doi:10.1182/blood-2004-04-1512.

109. Zenker, M. *et al.* Congenital nephrosis, mesangial sclerosis, and distinct eye abnormalities with microcoria: An autosomal recessive syndrome. *Am. J. Med. Genet.* (2004) doi:10.1002/ajmg.a.30310.

110. Hasselbacher, K. *et al.* Recessive missense mutations in LAMB2 expand the clinical spectrum of LAMB2-associated disorders. *Kidney Int.* (2006) doi:10.1038/sj.ki.5001679.

111. Has, C. *et al.* Integrin α3 mutations with kidney, lung, and skin disease. *N. Engl. J. Med.* (2012) doi:10.1056/NEJMoa1110813.

112. Kaplan, J. M. *et al.* Mutations in ACTN4, encoding α-actinin-4, cause familial focal segmental glomerulosclerosis. *Nat. Genet.* (2000) doi:10.1038/73456.

113. Seri, M. *et al.* Mutations in MYH9 result in the May-Hegglin anomaly, and Fechtner and Sebastian syndromes. *Nat. Genet.* (2000) doi:10.1038/79063.

114. Brown, E. J. *et al.* Mutations in the formin gene INF2 cause focal segmental glomerulosclerosis. *Nat. Genet.* (2010) doi:10.1038/ng.505.

115. Boyer, O. *et al.* INF2 mutations in Charcot-Marie-Tooth disease with glomerulopathy. *N. Engl. J. Med.* (2011) doi:10.1056/NEJMoa1109122.

116. Mele, C. *et al.* MYO1E mutations and childhood familial focal segmental glomerulosclerosis. *N. Engl. J. Med.* (2011) doi:10.1056/NEJMoa1101273.

117. Akilesh, S. *et al.* Arhgap24 inactivates Rac1 in mouse podocytes, and a mutant form is associated with familial focal segmental glomerulosclerosis. *J. Clin. Invest.* (2011) doi:10.1172/JCI46458.

118. Gupta, I. R. *et al.* ARHGDIA: A novel gene implicated in nephrotic syndrome. *J. Med. Genet.* (2013) doi:10.1136/jmedgenet-2012-101442.

119. Gee, H. Y. *et al.* ARHGDIA mutations cause nephrotic syndrome via defective RHO GTPase signaling. *J. Clin. Invest.* (2013) doi:10.1172/JCI69134.

120. Gbadegesin, R. A. *et al.* Mutations in the gene that encodes the F-Actin binding protein anillin cause FSGS. *J. Am. Soc. Nephrol.* (2014) doi:10.1681/ASN.2013090976.

121. Gee, H. Y. *et al.* KANK deficiency leads to podocyte dysfunction and nephrotic syndrome. *J. Clin. Invest.* (2015) doi:10.1172/JCI79504.

122. Pelletier, J. *et al.* Germline mutations in the Wilms' tumor suppressor gene are associated with abnormal urogenital development in denys-drash syndrome. *Cell* (1991) doi:10.1016/0092-8674(91)90194-4.

123. Barbaux, S. *et al.* Donor splice-site mutations in WT1 are responsible for Frasier syndrome. *Nat. Genet.* (1997) doi:10.1038/ng1297-467.

124. Jeanpierre, C. *et al.* Identification of constitutional WT1 mutations, in patients with isolated diffuse mesangial sclerosis, and analysis of genotype/phenotype correlations by use of a computerized mutation database. *Am. J. Hum. Genet.* (1998) doi:10.1086/301806.

125. Dreyer, S. D. *et al.* Mutations in LMX1B cause abnormal skeletal patterning and renal dysplasia in nail patella syndrome. *Nat. Genet.* (1998) doi:10.1038/ng0598-47.

126. Boerkoel, C. F. *et al.* Mutant chromatin remodeling protein SMARCAL1 causes Schimke immuno-osseous dysplasia. *Nat. Genet.* (2002) doi:10.1038/ng821.

127. Javor, E. D. *et al*. Proteinuric nephropathy in acquired and congenital generalized lipodystrophy: Baseline characteristics and course during recombinant leptin therapy. *J. Clin. Endocrinol. Metab.* (2004) doi:10.1210/jc.2003-032140.

128. Thong, K. M. *et al.* Cosegregation of focal segmental glomerulosclerosis in a family with familial partial lipodystrophy due to a mutation in LMNA. *Nephron - Clin. Pract.* (2013) doi:10.1159/000354716.

129. Zankl, A. *et al.* Multicentric carpotarsal osteolysis is caused by mutations clustering in the amino-terminal transcriptional activation domain of MAFB. *Am. J. Hum. Genet.* (2012) doi:10.1016/j.ajhg.2012.01.003.

130. Sato, Y. *et al.* A mutation in transcription factor MAFB causes Focal Segmental Glomerulosclerosis with Duane Retraction Syndrome. *Kidney Int.* (2018) doi:10.1016/j.kint.2018.02.025.

131. Esposito, T. *et al.* Unique X-linked familial FSGS with co-segregating heart block disorder is associated with a

mutation in the NXF5 gene. *Hum. Mol. Genet.* (2013) doi:10.1093/hmg/ddt215.

132. Amiel, J. *et al.* PAX2 mutations in renal-coloboma syndrome: Mutational hotspot and germline mosaicism. *Eur. J. Hum. Genet.* (2000) doi:10.1038/sj.ejhg.5200539.

133. Barua, M. *et al.* Mutations in PAX2 associate with adult-onset FSGS. *J. Am. Soc. Nephrol.* (2014) doi:10.1681/ASN.2013070686.

134. Braun, D. A. *et al.* Mutations in nuclear pore genes NUP93, NUP205 and XPO5 cause steroid-resistant nephrotic syndrome. *Nat. Genet.* (2016) doi:10.1038/ng.3512.

135. Rosti, R. O. *et al.* Homozygous mutation in NUP107 leads to microcephaly with steroid-resistant nephrotic condition similar to Galloway-Mowat syndrome. *J. Med. Genet.* (2017) doi:10.1136/jmedgenet-2016-104237.

136. Fujita, A. *et al.* Homozygous splicing mutation in NUP133 causes Galloway–Mowat syndrome. *Ann. Neurol.* (2018) doi:10.1002/ana.25370.

137. Braun, D. A. *et al.* Mutations in multiple components of the nuclear pore complex cause nephrotic syndrome. *J. Clin. Invest.* (2018) doi:10.1172/JCI98688.

138. Kurogouchi, F. *et al.* A case of mitochondrial cytopathy with a typical point mutation for MELAS, presenting with severe focal-segmental glomerulosclerosis as main clinical manifestation. *Am. J. Nephrol.* (1998) doi:10.1159/000013406.

139. López, L. C. *et al.* Leigh syndrome with nephropathy and CoQ10 deficiency due to decaprenyl diphosphote synthase subunit 2 (PDSS2) mutations. *Am. J. Hum. Genet.* (2006) doi:10.1086/510023.

140. Quinzii, C. *et al.* A mutation in para-hydroxybenzoate-polyprenyl transferase (COQ2) causes primary coenzyme Q10 deficiency. *Am. J. Hum. Genet.* (2006) doi:10.1086/500092.

141. Heeringa, S. F. *et al.* COQ6 mutations in human patients produce nephrotic syndrome with sensorineural deafness. *J. Clin. Invest.* (2011) doi:10.1172/JCI45693.

142. Ashraf, S. *et al.* ADCK4 mutations promote steroid-Resistant nephrotic syndrome through CoQ10 biosynthesis disruption. *J. Clin. Invest.* (2013) doi:10.1172/JCI69000.

143. Berkovic, S. F. *et al.* Array-Based Gene Discovery with Three Unrelated Subjects Shows SCARB2/LIMP-2 Deficiency Causes Myoclonus Epilepsy and Glomerulosclerosis. *Am. J. Hum. Genet.* (2008) doi:10.1016/j.ajhg.2007.12.019.

144. Hoopes, R. R. *et al.* Dent disease with mutations in OCRL1. *Am. J. Hum. Genet.* (2005) doi:10.1086/427887.

145. Braun, D. A. *et al.* Mutations in KEOPS-complex genes cause nephritic syndrome with primary microcephaly. *Nat. Genet.* (2017) doi:10.1038/ng.3933.

146. Trimouille, A. *et al.* Further delineation of the phenotype caused by biallelic variants in the WDR4 gene. *Clin. Genet.* (2018) doi:10.1111/cge.13074.

147. Arrondel, C. *et al.* Defects in t6A tRNA modification due to GON7 and YRDC mutations lead to Galloway-Mowat syndrome. *Nat. Commun.* (2019) doi:10.1038/s41467-019-11951-x.

148. Vogt, B. A., Wyatt, R. J., Burke, B. A., Simonton, S. C. & Kashtan, C. E. Inherited factor H deficiency and collagen type III glomerulopathy. *Pediatr. Nephrol.* (1995) doi:10.1007/BF00858956.

149. Sethi, S., Fervenza, F. C., Zhang, Y. & Smith, R. J. H. Secondary focal and segmental glomerulosclerosis associated with single-nucleotide polymorphisms in the genes encoding complement factor H and C3. *Am. J. Kidney Dis.* (2012) doi:10.1053/j.ajkd.2012.04.011.

150. Matthijs, G. *et al.* Mutations in PMM2, a phosphomannomutase gene on chromosome 16p13, in carbohydrate-deficient glycoprotein type 1 syndrome (Jaeken syndrome). *Nat. Genet.* (1997) doi:10.1038/ng0597-88.

151. Sadallah, S., Gudat, F., Laissue, J. A., Spath, P. J. & Schifferli, J. A. Glomerulonephritis in a patient with complement factor I deficiency. *Am. J. Kidney Dis.* (1999) doi:10.1016/S0272-6386(99)70155-1.

152. Schwarz, M. *et al.* Deficiency of GDP-Man:GlcNAc2-PP-Dolichol Mannosyltransferase Causes Congenital Disorder of Glycosylation Type Ik. *Am. J. Hum. Genet.* (2004) doi:10.1086/382492.

153. Agarwal, A. K. *et al.* Focal segmental glomerulosclerosis in patients with mandibuloacral dysplasia owing to ZMPSTE24 deficiency. *J. Investig. Med.* (2006) doi:10.2310/6650.2006.05068.

154. Genovese, G. *et al.* Association of trypanolytic ApoL1 variants with kidney disease in African Americans. *Science (80-.).* (2010) doi:10.1126/science.1193032.

155. Santucci, L. *et al.* Protein-protein interaction heterogeneity of plasma apolipoprotein A1 in nephrotic syndrome. *Mol. Biosyst.* (2011) doi:10.1039/c0mb00127a.

156. Ozaltin, F. *et al.* Disruption of PTPRO causes childhood-onset nephrotic syndrome. *Am. J. Hum. Genet.* (2011) doi:10.1016/j.ajhg.2011.05.026.

157. Lemaire, M. *et al.* Recessive mutations in DGKE

cause atypical hemolytic-uremic syndrome. *Nat. Genet.* (2013) doi:10.1038/ng.2590.

158. Ozaltin, F. *et al.* DGKE variants cause a glomerular microangiopathy that mimics membranoproliferative GN. *J. Am. Soc. Nephrol.* (2013) doi:10.1681/ASN.2012090903.

159. Gee, H. Y. *et al.* Mutations in EMP2 cause childhood-onset Nephrotic syndrome. *Am. J. Hum. Genet.* (2014) doi:10.1016/j.ajhg.2014.04.010.

160. Cong, E. H. *et al.* A homozygous missense mutation in the ciliary gene TTC21B causes familial FSGS. *J. Am. Soc. Nephrol.* (2014) doi:10.1681/ASN.2013101126.

161. Yang, F. *et al.* Association of endothelin-1 gene polymorphisms with the clinical phenotype in primary nephrotic syndrome of children. *Life Sci.* (2014) doi:10.1016/j.lfs.2014.04.010.

162. Colin, E. *et al.* Loss-of-function mutations in WDR73 Are responsible for microcephaly and steroid-resistant nephrotic syndrome: Galloway-mowat syndrome. *Am. J. Hum. Genet.* (2014) doi:10.1016/j.ajhg.2014.10.011.

163. Kang, H. G. *et al.* Loss of podocalyxin causes a novel syndromic type of congenital nephrotic syndrome. *Exp. Mol. Med.* (2017) doi:10.1038/emm.2017.227.

164. Lin, F. J. *et al.* First identification of PODXL nonsense mutations in autosomal dominant focal segmental glomerulosclerosis. *Clin. Sci.* (2019) doi:10.1042/CS20180676.

165. Lovric, S. *et al.* Mutations in sphingosine-1-phosphate lyase cause nephrosis with ichthyosis and adrenal insufficiency. *J. Clin. Invest.* (2017) doi:10.1172/JCI89626.

166. Hermle, T. *et al.* GAPVD1 and ANKFY1 mutations implicate RAB5 regulation in nephrotic syndrome. *J. Am. Soc. Nephrol.* (2018) doi:10.1681/ASN.2017121312.

167. Dorval, G. *et al.* TBC1D8B Loss-of-Function Mutations Lead to X-Linked Nephrotic Syndrome via Defective Trafficking Pathways. *Am. J. Hum. Genet.* (2019) doi:10.1016/j.ajhg.2018.12.016.

168. Ruf, R. G. *et al.* Patients with Mutations in NPHS2 (Podocin) Do Not Respond to Standard Steroid Treatment of Nephrotic Syndrome. *J. Am. Soc. Nephrol.* (2004) doi:10.1097/01.ASN.0000113552.59155.72.

169. Weber, S. *et al.* NPHS2 mutation analysis shows genetic heterogeneity of steroid-resistant nephrotic syndrome and low post-transplant recurrence. *Kidney Int.* (2004) doi:10.1111/j.1523-1755.2004.00776.x.

170. Hildebrandt, F. & Heeringa, S. F. Specific podocin mutations determine age of onset of nephrotic syndrome all the way into adult life. *Kidney International* (2009) doi:10.1038/ki.2008.693.

171. Bierzynska, A. *et al.* Genomic and clinical profiling of a national nephrotic syndrome cohort advocates a precision medicine approach to disease management. *Kidney Int.* (2017) doi:10.1016/j.kint.2016.10.013.

172. Ardiles, L. G., Carrasco, A. E., Carpio, J. D. & Mezzano, S. A. Late onset of familial nephrotic syndrome associated with a compound heterozygous mutation of the podocin-encoding gene. *Nephrology* (2005) doi:10.1111/j.1440-1797.2005.00481.x.

173. Monteiro, E. J. B., Pereira, A. C., Pereira, A. B., Krieger, J. E. & Mastroianni-Kirsztajn, G. NPHS2 mutations in adult patients with primary focal segmental glomerulosclerosis. *J. Nephrol.* (2006).

174. Tsukaguchi, H. *et al.* NPHS2 mutations in late-onset focal segmental glomerulosclerosis: R229Q is a common disease-associated allele. *J. Clin. Invest.* (2002) doi:10.1172/jci16242.

175. He, N. *et al.* Recessive NPHS2 (Podocin) mutations are rare in adult-onset idiopathic focal segmental glomerulosclerosis. *Clin. J. Am. Soc. Nephrol.* (2007) doi:10.2215/CJN.02690806.

176. McKenzie, L. M. *et al.* NPHS2 variation in sporadic focal segmental glomerulosclerosis. *J. Am. Soc. Nephrol.* (2007) doi:10.1681/ASN.2007030319.

177. Machuca, E. *et al.* Clinical and epidemiological assessment of steroid-resistant nephrotic syndrome associated with the NPHS2 R229Q variant. *Kidney Int.* (2009) doi:10.1038/ki.2008.650.

178. Stenson, P. D. *et al.* Human Gene Mutation Database (HGMD®): 2003 Update. *Human Mutation* (2003) doi:10.1002/humu.10212.

179. Zhang, S.-Y. *et al.* In vivo expression of podocyte slit diaphragm-associated proteins in nephrotic patients with NPHS2 mutation. *Kidney Int.* (2004) doi:10.1111/j.1523-1755.2004.00840.x.

180. Hinkes, B. *et al.* Specific Podocin Mutations Correlate with Age of Onset in Steroid-Resistant Nephrotic Syndrome. *J. Am. Soc. Nephrol.* (2008) doi:10.1681/ASN.2007040452.

181. Nishibori, Y. *et al.* Disease-causing missense mutations in NPHS2 gene alter normal nephrin trafficking to the plasma membrane. *Kidney Int.* (2004) doi:10.1111/j.1523-1755.2004.00898.x.

182. Ohashi, T., Uchida, K., Uchida, S., Sasaki, S. & Nihei, H. Intracellular mislocalization of mutant podocin and correction by chemical chaperones. *Histochem. Cell Biol.* (2003) doi:10.1007/s00418-003-0511-x.

183. Philippe, A. *et al.* A missense mutation in podocin leads to early and severe renal disease in mice. *Kidney Int.* (2008) doi:10.1038/ki.2008.27.

184. Serrano-Perez, M.-C. *et al.* Endoplasmic reticulum-retained podocin mutants are massively degraded by the proteasome. *J. Biol. Chem.* (2018) doi:10.1074/jbc.RA117.001159.

185. Kadurin, I., Hubert, S. & Gründer, S. A single conserved proline residue determines the membrane topology of stomatin. *Biochem. J.* (2009) doi:10.1042/BJ20081662.

186. Galloway, W. H. & Mowat, A. P. Congenital microcephaly with hiatus hernia and nephrotic syndrome in two sibs. *J. Med. Genet.* (1968) doi:10.1136/jmg.5.4.319.

187. Francis, F. *et al.* Human disorders of cortical development: From past to present. *European Journal of Neuroscience* (2006) doi:10.1111/j.1460-9568.2006.04649.x.

188. Microcephaly Then and Now. *Prezi.com* https://prezi.com/iwv4kvehmhbv/microcephaly-then-and-now/ (2014).

189. Pang, T., Atefy, R. & Sheen, V. Malformations of cortical development. *Neurologist* (2008) doi:10.1097/NRL.0b013e31816606b9.

190. Rosti, R. O. *et al.* Extending the mutation spectrum for Galloway-Mowat syndrome to include homozygous missense mutations in the WDR73 gene. *Am. J. Med. Genet. Part A* (2016) doi:10.1002/ajmg.a.37533.

191. Ben-Omran, T. *et al.* Nonsense mutation in the WDR73 gene is associated with Galloway-Mowat syndrome. *J. Med. Genet.* (2015) doi:10.1136/jmedgenet-2014-102707.

192. Vodopiutz, J. *et al.* WDR73 mutations cause infantile neurodegeneration and variable glomerular kidney disease. *Hum. Mutat.* (2015) doi:10.1002/humu.22828.

193. Jinks, R. N. *et al.* Recessive nephrocerebellar syndrome on the Galloway-Mowat syndrome spectrum is caused by homozygous protein-truncating mutations of WDR73. *Brain* (2015) doi:10.1093/brain/awv153.

194. Jiang, C. *et al.* WDR73 missense mutation causes infantile onset intellectual disability and cerebellar hypoplasia in a consanguineous family. *Clin. Chim. Acta* (2017) doi:10.1016/j.cca.2016.10.029.

195. El Younsi, M. *et al.* WDR73-related galloway mowat syndrome with collapsing glomerulopathy. *Eur. J. Med. Genet.* (2019) doi:10.1016/j.ejmg.2018.10.002.

196. Braun, D. A. *et al.* Mutations in WDR4 as a new cause of Galloway–Mowat syndrome. *Am. J. Med. Genet. Part A* (2018) doi:10.1002/ajmg.a.40489.

197. Hezwani, M. & Fahrenkrog, B. The functional versatility of the nuclear pore complex proteins. *Seminars in Cell and Developmental Biology* (2017) doi:10.1016/j.semcdb.2017.05.004.

198. Miyake, N. *et al.* Biallelic Mutations in Nuclear Pore Complex Subunit NUP107 Cause Early-Childhood-Onset Steroid-Resistant Nephrotic Syndrome. *Am. J. Hum. Genet.* (2015) doi:10.1016/j.ajhg.2015.08.013.

199. Park, E. *et al.* NUP107 mutations in children with steroid-resistant nephrotic Syndrome. *Nephrol. Dial. Transplant.* (2017) doi:10.1093/ndt/gfw103.

200. Ziehler, W. A., Day, J. J., Fierke, C. A. & Engelke, D. R. Effects of 5' leader and 3' trailer structures on pre-tRNA processing by nuclear RNase P. *Biochemistry* (2000) doi:10.1021/bi000603n.

201. Hou, Y. M. CCA addition to tRNA: Implications for tRNA quality control. *IUBMB Life* (2010) doi:10.1002/iub.301.

202. Abelson, J., Trotta, C. R. & Li, H. tRNA splicing. *Journal of Biological Chemistry* (1998) doi:10.1074/jbc.273.21.12685.

203. El Yacoubi, B., Bailly, M. & de Crécy-Lagard, V. Biosynthesis and Function of Posttranscriptional Modifications of Transfer RNAs. *Annu. Rev. Genet.* (2012) doi:10.1146/annurev-genet-110711-155641.

204. Kirchner, S. & Ignatova, Z. Emerging roles of tRNA in adaptive translation, signalling dynamics and disease. *Nature Reviews Genetics* (2015) doi:10.1038/nrg3861.

205. Tuorto, F. & Lyko, F. Genome recoding by tRNA modifications. *Open Biology* (2016) doi:10.1098/rsob.160287.

206. Lyons, S. M., Fay, M. M. & Ivanov, P. The role of RNA modifications in the regulation of tRNA cleavage. *FEBS Letters* (2018) doi:10.1002/1873-3468.13205.

207. Phizicky, E. M. & Hopper, A. K. tRNA biology charges to the front. *Genes and Development* (2010) doi:10.1101/gad.1956510.

208. Thiaville, P. C. *et al.* Global translational impacts of the loss of the tRNA modification t6A in yeast. *Microb. Cell* (2016) doi:10.15698/mic2016.01.473.

209. Torres, A. G., Batlle, E. & Ribas de Pouplana, L. Role of tRNA modifications in human diseases. *Trends in Molecular Medicine* (2014) doi:10.1016/j.molmed.2014.01.008.

210. Kellner, S. *et al.* Profiling of RNA modifications by multiplexed stable isotope labelling. *Chem. Commun.* (2014) doi:10.1039/c3cc49114e.

211. Su, D. *et al.* Quantitative analysis of tRNA modifications by HPLC-coupled mass spectrometry. *Nat. Protoc.* (2014) doi:10.1038/nmeth.2836.Independent.

212. Grosjean, H. *et al.* Predicting the Minimal Translation Apparatus: Lessons from the Reductive Evolution of Mollicutes. *PLoS Genet.* (2014)

doi:10.1371/journal.pgen.1004363.

213. Murphy, F. V., Ramakrishnan, V., Malkiewicz, A. & Agris, P. F. The role of modifications in codon discrimination by tRNALysUUU. *Nat. Struct. Mol. Biol.* (2004) doi:10.1038/nsmb861.

214. Dube, S. K., Marcker, K. A., Clark, B. F. C. & Cory, S. Nucleotide sequence of N-formyl-methionyl-transfer RNA. *Nature* (1968) doi:10.1038/218232a0.

215. El Yacoubi, B. *et al.* A role for the universal Kae1/Qri7/YgjD (COG0533) family in tRNA modification. *EMBO J.* (2011) doi:10.1038/emboj.2010.363.

216. Lin, C. A., Ellis, S. R. & True, H. L. The Sua5 Protein Is Essential for Normal Translational Regulation in Yeast. *Mol. Cell. Biol.* (2010) doi:10.1128/mcb.00754-09.

217. Daugeron, M. C. *et al.* Gcn4 misregulation reveals a direct role for the evolutionary conserved EKC/KEOPS in the t 6A modification of tRNAs. *Nucleic Acids Res.* (2011) doi:10.1093/nar/gkr178.

218. Lauhon, C. T. Mechanism of N6-threonylcarbamoyladenonsine (t6A) biosynthesis: Isolation and characterization of the intermediate threonylcarbamoyl-AMP. *Biochemistry* (2012) doi:10.1021/bi301233d.

219. Perrochia, L., Guetta, D., Hecker, A., Forterre, P. & Basta, T. Functional assignment of KEOPS/EKC complex subunits in the biosynthesis of the universal t6A tRNA modification. *Nucleic Acids Res.* (2013) doi:10.1093/nar/gkt720.

220. Downey, M. *et al.* A Genome-Wide Screen Identifies the Evolutionarily Conserved KEOPS Complex as a Telomere Regulator. *Cell* (2006) doi:10.1016/j.cell.2005.12.044.

221. Mao, D. Y. L. *et al.* Atomic Structure of the KEOPS Complex: An Ancient Protein Kinase-Containing Molecular Machine. *Mol. Cell* (2008) doi:10.1016/j.molcel.2008.10.002.

222. Costessi, A. *et al.* The human EKC/KEOPS complex is recruited to cullin2 ubiquitin ligases by the human tumour antigen PRAME. *PLoS One* (2012) doi:10.1371/journal.pone.0042822.

223. Zhang, W. *et al.* Crystal structures of the Gon7/Pcc1 and Bud32/Cgi121 complexes provide a model for the complete yeast KEOPS complex. *Nucleic Acids Res.* (2015) doi:10.1093/nar/gkv155.

224. Drew, K., Müller, C. L., Bonneau, R. & Marcotte, E. M. Identifying direct contacts between protein complex subunits from their conditional dependence in proteomics datasets. *PLoS Comput. Biol.* (2017) doi:10.1371/journal.pcbi.1005625.

225. Miyoshi, A. *et al.* Identification of CGI-121, a novel PRPK (p53-related protein kinase)-binding protein. *Biochem. Biophys. Res. Commun.* (2003) doi:10.1016/S0006-291X(03)00333-4.

226. Lopreiato, R. *et al.* Analysis of the interaction between piD261/Bud32, an evolutionary conserved protein kinase of Saccharomyces cerevisiae, and the Grx4 glutaredoxin. *Biochem. J.* (2004) doi:10.1042/BJ20030638.

227. Kisseleva-Romanova, E. *et al.* Yeast homolog of a cancer-testis antigen defines a new transcription complex. *EMBO J.* (2006) doi:10.1038/sj.emboj.7601235.

228. Seki, Y. *et al.* Sequencing analysis of a putative human O-sialoglycoprotein endopeptidase gene (OSGEP) and analysis of a bidirectional promoter between the OSGEP and APEX genes. *Gene* (2002) doi:10.1016/S0378-1119(02)00429-8.

229. Hecker, A. *et al.* An archaeal orthologue of the universal protein Kae1 is an iron metalloprotein which exhibits atypical DNA-binding properties and apurinic-endonuclease activity in vitro. *Nucleic Acids Res.* (2007) doi:10.1093/nar/gkm554.

230. Arigoni, F. *et al.* A genome-based approach for the identification of essential bacterial genes. *Nat. Biotechnol.* (1998) doi:10.1038/nbt0998-851.

231. Galperin, M. Y. & Koonin, E. V. 'Conserved hypothetical' proteins: Prioritization of targets for experimental study. *Nucleic Acids Research* (2004) doi:10.1093/nar/gkh885.

232. Blomen, V. A. *et al.* Gene essentiality and synthetic lethality in haploid human cells. *Science (80-.).* (2015) doi:10.1126/science.aac7557.

233. Ben-Aroya, S. *et al.* Toward a Comprehensive Temperature-Sensitive Mutant Repository of the Essential Genes of Saccharomyces cerevisiae. *Mol. Cell* (2008) doi:10.1016/j.molcel.2008.02.021.

234. Srinivasan, M. *et al.* The highly conserved KEOPS/EKC complex is essential for a universal tRNA modification, t6A. *EMBO J.* (2011) doi:10.1038/emboj.2010.343.

235. Nobel Media AB. The 2012 Nobel Prize in Physiology or Medicine - Press Release. *Nobelprize.org* (2012).

236. Evans, M. J. & Kaufman, M. H. Establishment in culture of pluripotential cells from mouse embryos. *Nature* (1981) doi:10.1038/292154a0.

237. Martin, G. R. Isolation of a pluripotent cell line from early mouse embryos cultured in medium conditioned by teratocarcinoma stem cells. *Proc. Natl. Acad. Sci. U. S. A.* (1981) doi:10.1073/pnas.78.12.7634.

238. Thomson, J. A. Embryonic stem cell lines derived

from human blastocysts. *Science (80-.).* (1998) doi:10.1126/science.282.5391.1145.

239. EuroStemCells. iPS cells and reprogramming: turn any cell of the body into a stem cell. https://www.eurostemcell.org/ips-cells-and-reprogramming-turn-any-cell-body-stem-cell.

240. The Nobel Prize. The Nobel Prize in Physiology or Medicine 2012.

241. Takahashi, K. & Yamanaka, S. Induction of pluripotent ptem cells from mouse embryonic and adult fibroblast cultures by defined factors. *Cell* (2006) doi:10.1016/j.cell.2006.07.024.

242. Takahashi, K. *et al.* Induction of Pluripotent Stem Cells from Adult Human Fibroblasts by Defined Factors. *Cell* (2007) doi:10.1016/j.cell.2007.11.019.

243. Yu, J. *et al.* Induced pluripotent stem cell lines derived from human somatic cells. *Science (80-.).* (2007) doi:10.1126/science.1151526.

244. Aasen, T. *et al.* Efficient and rapid generation of induced pluripotent stem cells from human keratinocytes. *Nat. Biotechnol.* (2008) doi:10.1038/nbt.1503.

245. Kim, J. B. *et al.* Pluripotent stem cells induced from adult neural stem cells by reprogramming with two factors. *Nature* (2008) doi:10.1038/nature07061.

246. Nishishit, N., Takenaka, C., Fusaki, N. & Kawamata, S. Generation of human induced pluripotent stem cells from cord blood cells. in *Induced Stem Cells* (2011). doi:10.1089/scd.2011.0078.

247. Hanna, J. *et al.* Direct Reprogramming of Terminally Differentiated Mature B Lymphocytes to Pluripotency. *Cell* (2008) doi:10.1016/j.cell.2008.03.028.

248. Eminli, S. *et al.* Differentiation stage determines potential of hematopoietic cells for reprogramming into induced pluripotent stem cells. *Nat. Genet.* (2009) doi:10.1038/ng.428.

249. Aoi, T. *et al.* Generation of pluripotent stem cells from adult mouse liver and stomach cells. *Science (80-.).* (2008) doi:10.1126/science.1154884.

250. Stadtfeld, M., Brennand, K. & Hochedlinger, K. Reprogramming of Pancreatic β Cells into Induced Pluripotent Stem Cells. *Curr. Biol.* (2008) doi:10.1016/j.cub.2008.05.010.

251. Wernig, M. *et al.* A drug-inducible transgenic system for direct reprogramming of multiple somatic cell types. *Nat. Biotechnol.* (2008) doi:10.1038/nbt1483.

252. Zhang, X. B. Cellular Reprogramming of Human Peripheral Blood Cells. *Genomics, Proteomics and Bioinformatics* (2013) doi:10.1016/j.gpb.2013.09.001.

253. Carotta, S. *et al.* Directed differentiation and mass cultivation of pure erythroid progenitors from mouse embryonic stem cells. *Blood* (2004) doi:10.1182/blood-2004-02-0570.

254. Meng, X. *et al.* Efficient reprogramming of human cord blood CD34+ cells into induced pluripotent stem cells with OCT4 and SOX2 alone. *Mol. Ther.* (2012) doi:10.1038/mt.2011.258.

255. Soldner, F. *et al.* Parkinson's Disease Patient-Derived Induced Pluripotent Stem Cells Free of Viral Reprogramming Factors. *Cell* (2009) doi:10.1016/j.cell.2009.02.013.

256. Woltjen, K. *et al.* PiggyBac transposition reprograms fibroblasts to induced pluripotent stem cells. *Nature* (2009) doi:10.1038/nature07863.

257. Stadtfeld, M., Nagaya, M., Utikal, J., Weir, G. & Hochedlinger, K. Induced pluripotent stem cells generated without viral integration. *Science (80-.).* (2008) doi:10.1126/science.1162494.

258. Okita, K., Nakagawa, M., Hyenjong, H., Ichisaka, T. & Yamanaka, S. Generation of mouse induced pluripotent stem cells without viral vectors. *Science (80-.).* (2008) doi:10.1126/science.1164270.

259. Junying, Y. *et al.* Human induced pluripotent stem cells free of vector and transgene sequences. *Science (80-.).* (2009) doi:10.1126/science.1172482.

260. Fusaki, N., Ban, H., Nishiyama, A., Saeki, K. & Hasegawa, M. Efficient induction of transgene-free human pluripotent stem cells using a vector based on Sendai virus, an RNA virus that does not integrate into the host genome. *Proc. Japan Acad. Ser. B Phys. Biol. Sci.* (2009) doi:10.2183/pjab.85.348.

261. Jia, F. *et al.* A nonviral minicircle vector for deriving human iPS cells. *Nat. Methods* (2010) doi:10.1038/nmeth.1426.

262. Warren, L. *et al.* Highly efficient reprogramming to pluripotency and directed differentiation of human cells with synthetic modified mRNA. *Cell Stem Cell* (2010) doi:10.1016/j.stem.2010.08.012.

263. Zhou, H. *et al.* Generation of Induced Pluripotent Stem Cells Using Recombinant Proteins. *Cell Stem Cell* (2009) doi:10.1016/j.stem.2009.04.005.

264. Hou, P. *et al.* Pluripotent stem cells induced from mouse somatic cells by small-molecule compounds. *Science (80-.).* (2013) doi:10.1126/science.1239278.

265. Faísca, P. & Desmecht, D. Sendai virus, the mouse parainfluenza type 1: A longstanding pathogen that remains up-to-date. *Res. Vet. Sci.* (2007) doi:10.1016/j.rvsc.2006.03.009.

266. Bitzer, M., Armeanu, S., Lauer, U. M. & Neubert, W. J. Sendai virus vectors as an emerging negative-strand RNA viral vector system. *Journal of Gene Medicine*

(2003) doi:10.1002/jgm.426.

267. Jinek, M. *et al.* A programmable dual-RNA-guided DNA endonuclease in adaptive bacterial immunity. *Science (80-.).* (2012) doi:10.1126/science.1225829.

268. Deltcheva, E. *et al.* CRISPR RNA maturation by trans-encoded small RNA and host factor RNase III. *Nature* (2011) doi:10.1038/nature09886.

269. Cong, L. *et al.* Multiplex genome engineering using CRISPR/Cas systems. *Science (80-.).* (2013) doi:10.1126/science.1231143.

270. Max-Planck-Gesellschaft. Arbeitsweise von CRISPR-Cas9. https://www.mpg.de/11032932/crispr-cas9-mechanismus.

271. Choulika, A., Perrin, A., Dujon, B. & Nicolas, J. F. Induction of homologous recombination in mammalian chromosomes by using the I-SceI system of Saccharomyces cerevisiae. *Mol. Cell. Biol.* (1995) doi:10.1128/mcb.15.4.1968.

272. Capecchi, M. R. Altering the genome by homologous recombination. *Science (80-.).* (1989) doi:10.1126/science.2660260.

273. Gibson, G. J. & Yang, M. What rheumatologists need to know about CRISPR/Cas9. *Nature Reviews Rheumatology* (2017) doi:10.1038/nrrheum.2017.6.

274. Hockemeyer, D. & Jaenisch, R. Induced pluripotent stem cells meet genome editing. *Cell Stem Cell* (2016) doi:10.1016/j.stem.2016.04.013.

275. Howden, S. E. *et al.* Simultaneous Reprogramming and Gene Correction of Patient Fibroblasts. *Stem Cell Reports* (2015) doi:10.1016/j.stemcr.2015.10.009.

276. Boreström, C. *et al.* A CRISP(e)R view on kidney organoids allows generation of an induced pluripotent stem cell–derived kidney model for drug discovery. *Kidney Int.* (2018) doi:10.1016/j.kint.2018.05.003.

277. Howden, S. E., Vanslambrouck, J. M., Wilson, S. B., Tan, K. S. & Little, M. H. Reporter-based fate mapping in human kidney organoids confirms nephron lineage relationships and reveals synchronous nephron formation. *EMBO Rep.* (2019) doi:10.15252/embr.201847483.

278. Sharmin, S. *et al.* Human induced pluripotent stem cell-derived podocytes mature into vascularized glomeruli upon experimental transplantation. *J. Am. Soc. Nephrol.* (2015) doi:10.1681/ASN.2015010096.

279. Hale, L. J. *et al.* 3D organoid-derived human glomeruli for personalised podocyte disease modelling and drug screening. *Nat. Commun.* (2018) doi:10.1038/s41467-018-07594-z.

280. van den Berg, C. W. *et al.* Renal subcapsular transplantation of PSC-derived kidney organoids induces neo-vasculogenesis and significant glomerular and tubular maturation in vivo. *Stem Cell Reports* (2018) doi:10.1016/j.stemcr.2018.01.041.

281. Soldner, F. *et al.* Generation of isogenic pluripotent stem cells differing exclusively at two early onset parkinson point mutations. *Cell* (2011) doi:10.1016/j.cell.2011.06.019.

282. Freedman, B. S. *et al.* Modelling kidney disease with CRISPR-mutant kidney organoids derived from human pluripotent epiblast spheroids. *Nat. Commun.* (2015) doi:10.1038/ncomms9715.

283. Cruz, N. M. *et al.* Organoid cystogenesis reveals a critical role of microenvironment in human polycystic kidney disease. *Nature Materials* (2017) doi:10.1038/NMAT4994.

284. Forbes, T. A. *et al.* Patient-iPSC-Derived Kidney Organoids Show Functional Validation of a Ciliopathic Renal Phenotype and Reveal Underlying Pathogenetic Mechanisms. *Am. J. Hum. Genet.* (2018) doi:10.1016/j.ajhg.2018.03.014.

285. Low, J. H. *et al.* Generation of Human PSC-Derived Kidney Organoids with Patterned Nephron Segments and a De Novo Vascular Network. *Cell Stem Cell* (2019) doi:10.1016/j.stem.2019.06.009.

286. Epomedicine. Germ Layers Derivatives - Mnemonics. (2017).

287. Shankland, S. J., Pippin, J. W., Reiser, J. & Mundel, P. Podocytes in culture: Past, present, and future. *Kidney International* (2007) doi:10.1038/sj.ki.5002291.

288. Mundel, P., Reiser, J. & Kriz, W. Induction of differentiation in cultured rat and human podocytes. *J. Am. Soc. Nephrol.* (1997).

289. Saleem, M. A. *et al.* A conditionally immortalized human podocyte cell line demonstrating nephrin and podocin expression. *J. Am. Soc. Nephrol.* (2002).

290. Chittiprol, S., Chen, P., Petrovic-Djergovic, D., Eichler, T. & Ransom, R. F. Marker expression, behaviors, and responses vary in different lines of conditionally immortalized cultured podocytes. *Am. J. Physiol. - Ren. Physiol.* (2011) doi:10.1152/ajprenal.00234.2011.

291. Song, B. *et al.* The Directed Differentiation of human iPS cells into kidney podocytes. *PLoS One* (2012) doi:10.1371/journal.pone.0046453.

292. Ciampi, O. *et al.* Generation of functional podocytes from human induced pluripotent stem cells. *Stem Cell Res.* (2016) doi:10.1016/j.scr.2016.06.001.

293. Musah, S. *et al.* Mature induced-pluripotent-stem-cell-derived human podocytes reconstitute kidney glomerular-capillary-wall function on a chip. *Nat. Biomed. Eng.* (2017) doi:10.1038/s41551-017-0069.

294. Qian, T. *et al.* Directed Differentiation of Human

Pluripotent Stem Cells to Podocytes under Defined Conditions. *Sci. Rep.* (2019) doi:10.1038/s41598-019-39504-8.

295. Rauch, C. *et al.* Differentiation of human iPSCs into functional podocytes. *PLoS One* (2018) doi:10.1371/journal.pone.0203869.

296. Musah, S., Dimitrakakis, N., Camacho, D. M., Church, G. M. & Ingber, D. E. Directed differentiation of human induced pluripotent stem cells into mature kidney podocytes and establishment of a Glomerulus Chip. *Nat. Protoc.* (2018) doi:10.1038/s41596-018-0007-8.

297. Yoshimura, Y. *et al.* Manipulation of nephron-patterning signals enables selective induction of podocytes from human pluripotent stem cells. *J. Am. Soc. Nephrol.* (2019) doi:10.1681/ASN.2018070747.

298. Min, S. Y., Ha, D. S. & Ha, T. S. Puromycin aminonucleoside triggers apoptosis in podocytes by inducing endoplasmic reticulum stress. *Kidney Res. Clin. Pract.* (2018) doi:10.23876/j.krcp.2018.37.3.210.

299. Hariharan, K. *et al.* Parallel generation of easily selectable multiple nephronal cell types from human pluripotent stem cells. *Cell. Mol. Life Sci.* (2019) doi:10.1007/s00018-018-2929-2.

300. Chambers, S. M. *et al.* Highly efficient neural conversion of human ES and iPS cells by dual inhibition of SMAD signaling. *Nat. Biotechnol.* (2009) doi:10.1038/nbt.1529.

301. Xu, R. H. *et al.* NANOG is a direct target of TGFβ/Activin-mediated SMAD signaling in human ESCs. *Cell Stem Cell* (2008) doi:10.1016/j.stem.2008.07.001.

302. Vallier, L. *et al.* Activin/Nodal signalling maintains pluripotency by controlling Nanog expression. *Development* (2009) doi:10.1242/dev.033951.

303. Hemmati-Brivanlou, A. & Melton, D. A. A truncated activin receptor inhibits mesoderm induction and formation of axial structures in Xenopus embryos. *Nature* (1992) doi:10.1038/359609a0.

304. Xu, R. H. *et al.* BMP4 initiates human embryonic stem cell differentiation to trophoblast. *Nat. Biotechnol.* (2002) doi:10.1038/nbt761.

305. Gammill, L. S. & Bronner-Fraser, M. Neural crest specification: Migrating into genomics. *Nat. Rev. Neurosci.* (2003) doi:10.1038/nrn1219.

306. StudyBlue.com. Human Brain, Memory and Learning. https://www.studyblue.com/#flashcard/view/2583723.

307. Tropepe, V. *et al.* Direct neural fate specification from embryonic stem cells: A primitive mammalian neural stem cell stage acquired through a default mechanism. *Neuron* (2001) doi:10.1016/S0896-6273(01)00263-X.

308. Muñoz-Sanjuán, I. & Brivanlou, A. H. Neural induction, the default model and embryonic stem cells. *Nat. Rev. Neurosci.* (2002) doi:10.1038/nrn786.

309. Zhang, S. C., Wernig, M., Duncan, I. D., Brüstle, O. & Thomson, J. A. In vitro differentiation of transplantable neural precursors from human embryonic stem cells. *Nat. Biotechnol.* (2001) doi:10.1038/nbt1201-1129.

310. Yoo, Y. D., Huang, C. T., Zhang, X., Lavaute, T. M. & Zhang, S. C. Fibroblast growth factor regulates human neuroectoderm specification through ERK1/2-PARP-1 pathway. *Stem Cells* (2011) doi:10.1002/stem.758.

311. Elkabetz, Y. *et al.* Human ES cell-derived neural rosettes reveal a functionally distinct early neural stem cell stage. *Genes Dev.* (2008) doi:10.1101/gad.1616208.

312. Conti, L. *et al.* Niche-independent symmetrical self-renewal of a mammalian tissue stem cell. *PLoS Biol.* (2005) doi:10.1371/journal.pbio.0030283.

313. Tabar, V. *et al.* Migration and differentiation of neural precursors derived from human embryonic stem cells in the rat brain. *Nat. Biotechnol.* (2005) doi:10.1038/nbt1088.

314. Boissart, C. *et al.* Differentiation from human pluripotent stem cells of cortical neurons of the superficial layers amenable to psychiatric disease modeling and high-throughput drug screening. *Transl. Psychiatry* (2013) doi:10.1038/tp.2013.71.

315. Lancaster, M. A. & Knoblich, J. A. Organogenesisin a dish: Modeling development and disease using organoid technologies. *Science* (2014) doi:10.1126/science.1247125.

316. Sasai, Y. Next-generation regenerative medicine: Organogenesis from stem cells in 3D culture. *Cell Stem Cell* (2013) doi:10.1016/j.stem.2013.04.009.

317. Townes, P. L. & Holtfreter, J. Directed movements and selective adhesion of embryonic amphibian cells. *J. Exp. Zool.* (1955) doi:10.1002/jez.1401280105.

318. Li, M. & Izpisua Belmonte, J. C. Organoids - Preclinical models of human disease. *New England Journal of Medicine* (2019) doi:10.1056/NEJMra1806175.

319. Sato, T. *et al.* Single Lgr5 stem cells build crypt-villus structures in vitro without a mesenchymal niche. *Nature* (2009) doi:10.1038/nature07935.

320. Sato, T. *et al.* Long-term expansion of epithelial organoids from human colon, adenoma, adenocarcinoma, and Barrett's epithelium. *Gastroenterology* (2011) doi:10.1053/j.gastro.2011.07.050.

321. Barker, N. *et al.* Lgr5+ve Stem Cells Drive Self-

Renewal in the Stomach and Build Long-Lived Gastric Units In Vitro. *Cell Stem Cell* (2010) doi:10.1016/j.stem.2009.11.013.

322. Huch, M. *et al.* Unlimited in vitro expansion of adult bi-potent pancreas progenitors through the Lgr5/R-spondin axis. *EMBO J.* (2013) doi:10.1038/emboj.2013.204.

323. Huch, M. *et al.* In vitro expansion of single Lgr5 + liver stem cells induced by Wnt-driven regeneration. *Nature* (2013) doi:10.1038/nature11826.

324. Hisha, H. *et al.* Establishment of a novel lingual organoid culture system: Generation of organoids having mature keratinized epithelium from adult epithelial stem cells. *Sci. Rep.* (2013) doi:10.1038/srep03224.

325. Spence, J. R. *et al.* Directed differentiation of human pluripotent stem cells into intestinal tissue in vitro. *Nature* (2011) doi:10.1038/nature09691.

326. Eiraku, M. *et al.* Self-organizing optic-cup morphogenesis in three-dimensional culture. *Nature* (2011) doi:10.1038/nature09941.

327. Lancaster, M. A. *et al.* Cerebral organoids model human brain development and microcephaly. *Nature* (2013) doi:10.1038/nature12517.

328. Takebe, T. *et al.* Vascularized and functional human liver from an iPSC-derived organ bud transplant. *Nature* (2013) doi:10.1038/nature12271.

329. Takasato, M. *et al.* Kidney organoids from human iPS cells contain multiple lineages and model human nephrogenesis. *Nature* (2015) doi:10.1038/nature15695.

330. Morizane, R. *et al.* Nephron organoids derived from human pluripotent stem cells model kidney development and injury. *Nat. Biotechnol.* (2015) doi:10.1038/nbt.3392.

331. Lancaster, M. A. & Knoblich, J. A. Generation of cerebral organoids from human pluripotent stem cells. *Nat. Protoc.* (2014) doi:10.1038/nprot.2014.158.

332. Qian, X. *et al.* Brain-Region-Specific Organoids Using Mini-bioreactors for Modeling ZIKV Exposure. *Cell* (2016) doi:10.1016/j.cell.2016.04.032.

333. Qian, X., Song, H. & Ming, G. L. Brain organoids: Advances, applications and challenges. *Development (Cambridge)* (2019) doi:10.1242/dev.166074.

334. Quadrato, G. *et al.* Cell diversity and network dynamics in photosensitive human brain organoids. *Nature* (2017) doi:10.1038/nature22047.

335. Mariani, J. *et al.* Modeling human cortical development in vitro using induced pluripotent stem cells. *Proc. Natl. Acad. Sci. U. S. A.* (2012) doi:10.1073/pnas.1202944109.

336. Jo, J. *et al.* Midbrain-like Organoids from Human Pluripotent Stem Cells Contain Functional Dopaminergic and Neuromelanin-Producing Neurons. *Cell Stem Cell* (2016) doi:10.1016/j.stem.2016.07.005.

337. Monzel, A. S. *et al.* Derivation of Human Midbrain-Specific Organoids from Neuroepithelial Stem Cells. *Stem Cell Reports* (2017) doi:10.1016/j.stemcr.2017.03.010.

338. Muguruma, K., Nishiyama, A., Kawakami, H., Hashimoto, K. & Sasai, Y. Self-organization of polarized cerebellar tissue in 3D culture of human pluripotent stem cells. *Cell Rep.* (2015) doi:10.1016/j.celrep.2014.12.051.

339. Sakaguchi, H. *et al.* Generation of functional hippocampal neurons from self-organizing human embryonic stem cell-derived dorsomedial telencephalic tissue. *Nat. Commun.* (2015) doi:10.1038/ncomms9896.

340. Ozone, C. *et al.* Functional anterior pituitary generated in self-organizing culture of human embryonic stem cells. *Nat. Commun.* (2016) doi:10.1038/ncomms10351.

341. Bagley, J. A., Reumann, D., Bian, S., Lévi-Strauss, J. & Knoblich, J. A. Fused cerebral organoids model interactions between brain regions. *Nat. Methods* (2017) doi:10.1038/nmeth.4304.

342. Birey, F. *et al.* Assembly of functionally integrated human forebrain spheroids. *Nature* (2017) doi:10.1038/nature22330.

343. Xiang, Y. *et al.* Fusion of Regionally Specified hPSC-Derived Organoids Models Human Brain Development and Interneuron Migration. *Cell Stem Cell* (2017) doi:10.1016/j.stem.2017.07.007.

344. Varki, A., Geschwind, D. H. & Eichler, E. E. Human uniqueness: Genome interactions with environment, behaviour and culture. *Nature Reviews Genetics* (2008) doi:10.1038/nrg2428.

345. Rakic, P. Evolution of the neocortex: A perspective from developmental biology. *Nature Reviews Neuroscience* (2009) doi:10.1038/nrn2719.

346. Eiraku, M. *et al.* Self-organized formation of polarized cortical tissues from ESCs and its active manipulation by extrinsic signals. *Cell Stem Cell* (2008) doi:10.1016/j.stem.2008.09.002.

347. Kadoshima, T. *et al.* Self-organization of axial polarity, inside-out layer pattern, and species-specific progenitor dynamics in human ES cell-derived neocortex. *Proc. Natl. Acad. Sci. U. S. A.* (2013) doi:10.1073/pnas.1315710110.

348. Florio, M. & Huttner, W. B. Neural progenitors, neurogenesis and the evolution of the neocortex. *Development (Cambridge)* (2014)

doi:10.1242/dev.090571.

349. Hansen, D. V., Lui, J. H., Parker, P. R. L. & Kriegstein, A. R. Neurogenic radial glia in the outer subventricular zone of human neocortex. *Nature* (2010) doi:10.1038/nature08845.

350. Camp, J. G. *et al.* Human cerebral organoids recapitulate gene expression programs of fetal neocortex development. *Proc. Natl. Acad. Sci. U. S. A.* (2015) doi:10.1073/pnas.1520760112.

351. Jeong, H. & Tiwari, V. K. Exploring the complexity of cortical development using single-cell transcriptomics. *Frontiers in Neuroscience* (2018) doi:10.3389/fnins.2018.00031.

352. Di Lullo, E. & Kriegstein, A. R. The use of brain organoids to investigate neural development and disease. *Nature Reviews Neuroscience* (2017) doi:10.1038/nrn.2017.107.

353. Li, R. *et al.* Recapitulating cortical development with organoid culture in vitro and modeling abnormal spindle-like (ASPM related primary) microcephaly disease. *Protein Cell* (2017) doi:10.1007/s13238-017-0479-2.

354. Gabriel, E. *et al.* CPAP promotes timely cilium disassembly to maintain neural progenitor pool . *EMBO J.* (2016) doi:10.15252/embj.201593679.

355. Iefremova, V. *et al.* An Organoid-Based Model of Cortical Development Identifies Non-Cell-Autonomous Defects in Wnt Signaling Contributing to Miller-Dieker Syndrome. *Cell Rep.* (2017) doi:10.1016/j.celrep.2017.03.047.

356. Bershteyn, M. *et al.* Human iPSC-Derived Cerebral Organoids Model Cellular Features of Lissencephaly and Reveal Prolonged Mitosis of Outer Radial Glia. *Cell Stem Cell* (2017) doi:10.1016/j.stem.2016.12.007.

357. Bershteyn, M. *et al.* Cell-autonomous correction of ring chromosomes in human induced pluripotent stem cells. *Nature* (2014) doi:10.1038/nature12923.

358. Koning, M., van den Berg, C. W. & Rabelink, T. J. Stem cell-derived kidney organoids: engineering the vasculature. *Cellular and Molecular Life Sciences* (2019) doi:10.1007/s00018-019-03401-0.

359. Takasato, M. *et al.* Directing human embryonic stem cell differentiation towards a renal lineage generates a self-organizing kidney. *Nat. Cell Biol.* (2014) doi:10.1038/ncb2894.

360. Taguchi, A. & Nishinakamura, R. Higher-order kidney organogenesis from pluripotent stem cells. *Cell Stem Cell* (2017) doi:10.1016/j.stem.2017.10.011.

361. Gadue, P., Huber, T. L., Paddison, P. J. & Keller, G. M. Wnt and TGF-β signaling are required for the induction of an in vitro model of primitive streak formation using embryonic stem cells. *Proc. Natl. Acad. Sci. U. S. A.* (2006) doi:10.1073/pnas.0603916103.

362. Tam, P. P. L. & Loebel, D. A. F. Gene function in mouse embryogenesis: Get set for gastrulation. *Nature Reviews Genetics* (2007) doi:10.1038/nrg2084.

363. Kubo, A. *et al.* Development of definitive endoderm from embryonic stem cells in culture. *Development* (2004) doi:10.1242/dev.01044.

364. D'Amour, K. A. *et al.* Efficient differentiation of human embryonic stem cells to definitive endoderm. *Nat. Biotechnol.* (2005) doi:10.1038/nbt1163.

365. Sumi, T., Tsuneyoshi, N., Nakatsuji, N. & Suemori, H. Defining early lineage specification of human embryonic stem cells by the orchestrated balance canonical Wnt/β-catenin, activin/Nodal and BMP signaling. *Development* (2008) doi:10.1242/dev.021121.

366. Lam, A. Q. *et al.* Rapid and efficient differentiation of human pluripotent stem cells into intermediate mesoderm that forms tubules expressing kidney proximal tubular markers. *J. Am. Soc. Nephrol.* (2014) doi:10.1681/ASN.2013080831.

367. Pourquié, O. *et al.* Lateral and axial signals involved in avian somite patterning: A role for BMP4. *Cell* (1996) doi:10.1016/S0092-8674(00)81291-X.

368. Vigneau, C. *et al.* Mouse embryonic stem cell-derived embryoid bodies generate progenitors that integrate long term into renal proximal tubules in vivo. *J. Am. Soc. Nephrol.* (2007) doi:10.1681/ASN.2006101078.

369. Lindström, N. O. *et al.* Integrated β-catenin, BMP, PTEN, and notch signalling patterns the nephron. *Elife* (2015) doi:10.7554/eLife.04000.001.

370. Xia, Y. *et al.* Directed Differentiation of Human Pluripotent Cells to Ureteric Bud Kidney Progenitor-Like Cells. *Nat. Cell Biol.* (2013) doi:10.1038/ncb2872.

371. Mae, S. I. *et al.* Generation of branching ureteric bud tissues from human pluripotent stem cells. *Biochem. Biophys. Res. Commun.* (2018) doi:10.1016/j.bbrc.2017.11.105.

372. Quaggin, S. E. Kindling the Kidney. *N. Engl. J. Med.* (2016) doi:10.1056/NEJMcibr1514351.

373. Harder, J. L. *et al.* Organoid single cell profiling identifies a transcriptional signature of glomerular disease. *JCI Insight* (2019) doi:10.1172/jci.insight.122697.

374. Little, M. H., Kumar, S. V. & Forbes, T. Recapitulating kidney development: Progress and challenges. *Seminars in Cell and Developmental Biology* (2019) doi:10.1016/j.semcdb.2018.08.015.

375. Wu, H. *et al*. Comparative analysis and refinement of human PSC-derived kidney organoid differentiation with single-cell transcriptomics. *Cell Stem Cell* (2018) doi:10.1016/j.stem.2018.10.010.

376. Garreta, E. *et al.* Fine tuning the extracellular environment accelerates the derivation of kidney organoids from human pluripotent stem cells. *Nat. Mater.* (2019) doi:10.1038/s41563-019-0287-6.

377. Kim, Y. K. *et al.* Gene-edited human kidney organoids reveal mechanisms of disease in podocyte development. *Stem Cells* (2017) doi:10.1002/stem.2707.

378. Czerniecki, S. M. *et al*. High-throughput screening enhances kidney organoid differentiation from human pluripotent stem cells and enables automated multidimensional phenotyping. *Cell Stem Cell* (2018) doi:10.1016/j.stem.2018.04.022.

379. Lancaster, M. A. Brain organoids get vascularized. *Nature Biotechnology* (2018) doi:10.1038/nbt.4133.

380. Homan, K. A. *et al*. Flow-enhanced vascularization and maturation of kidney organoids in vitro. *Nat. Methods* (2019) doi:10.1038/s41592-019-0325-y.

381. Tanigawa, S. *et al*. Organoids from nephrotic disease-derived iPSCs identify impaired NEPHRIN localization and slit diaphragm formation in kidney podocytes. *Stem Cell Reports* (2018) doi:10.1016/j.stemcr.2018.08.003.

382. Bantounas, I. *et al.* Generation of functioning nephrons by implanting human Pluripotent stem cell-derived kidney progenitors. *Stem Cell Reports* (2018) doi:10.1016/j.stemcr.2018.01.008.

383. Alieva, M., Ritsma, L., Giedt, R. J., Weissleder, R. & Van Rheenen, J. Imaging windows for long-term intravital imaging: General overview and technical insights. *IntraVital* (2014) doi:10.4161/intv.29917.

384. Zarychta-Wiśniewska, W. *et al.* In vivo imaging system for explants analysis—A new approach for assessment of cell transplantation effects in large animal models. *PLoS One* (2017) doi:10.1371/journal.pone.0184588.

385. OpenStax.org. Biology 2e. https://openstax.org/books/biology-2e/pages/29-4-reptiles.

386. Dbios.org. Chick embryo development laminated poster educational wall charts.

387. Nowak-Sliwinska, P., Segura, T. & Iruela-Arispe, M. L. The chicken chorioallantoic membrane model in biology, medicine and bioengineering. *Angiogenesis* (2014) doi:10.1007/s10456-014-9440-7.

388. Ribatti, D. The chick embryo chorioallantoic membrane (CAM). A multifaceted experimental model. *Mechanisms of Development* (2016) doi:10.1016/j.mod.2016.05.003.

389. Torres, V. E., Harris, P. C. & Pirson, Y. Autosomal dominant polycystic kidney disease. *Lancet* (2007) doi:10.1016/S0140-6736(07)60601-1.

390. Hildebrandt, F. & Zhou, W. Nephronophthisis-associated ciliopathies. *Journal of the American Society of Nephrology* (2007) doi:10.1681/ASN.2006121344.

391. Menara, G., Lefort, N., Antignac, C. & Mollet, G. Generation of an induced pluripotent stem cell (iPSC) line (IMAGINi007) from a patient with steroid-resistant nephrotic syndrome carrying the homozygous p.R138Q mutation in the podocin-encoding NPHS2 gene. *Stem Cell Res.* **46:101878**, (2020).

392. Morizane, R. & Bonventre, J. V. Generation of nephron progenitor cells and kidney organoids from human pluripotent stem cells. *Nat. Protoc.* (2017) doi:10.1038/nprot.2016.170.

393. Braam, S. R. *et al.* Recombinant vitronectin is a functionally defined substrate that supports human embryonic stem cell self-renewal via αVβ5 integrin. *Stem Cells* (2008) doi:10.1634/stemcells.2008-0291.

394. Kaku, Y. *et al*. PAX2 is dispensable for in vitro nephron formation from human induced pluripotent stem cells. *Sci. Rep.* (2017) doi:10.1038/s41598-017-04813-3.

395. Morizane, R., Miyoshi, T. & Bonventre, J. V. Concise review: kidney generation with human pluripotent stem cells. *Stem Cells* (2017) doi:10.1002/stem.2699.

396. Perez-Gomez, M. V, Sanchez-Niño, M. D. & Ortiz, A. Megalin/lipoprotein receptor-related protein 2 autoimmunity and kidney disease. *Clin. Kidney J.* (2020) doi:10.1093/ckj/sfz171.

397. Guo, J. *et al.* WT1 is a key regulator of podocyte function: reduced expression levels cause crescentic glomerulonephritis and mesangial sclerosis. *Hum. Mol. Genet.* (2002) doi:10.1093/hmg/11.6.651.

398. Nagi, A. H. & Kirkwood, W. A quick method for the isolation of glomeruli from human kidney. *J. Clin. Pathol.* (1972) doi:10.1136/jcp.25.4.361.

399. Kabgani, N. *et al.* Primary cultures of glomerular parietal epithelial cells or podocytes with proven origin. *PLoS One* (2012) doi:10.1371/journal.pone.0034907.

400. Wang, H. *et al.* A simple and highly purified method for isolation of glomeruli from the mouse kidney. *Am. J. Physiol. Renal Physiol.* (2019) doi:10.1152/ajprenal.00293.2019.

401. Rush, B. M., Small, S. A., Stolz, D. B. & Tan, R. J. An efficient sieving method to isolate intact glomeruli

from adult rat kidney. *J. Vis. Exp.* (2018) doi:10.3791/58162.

402. Ni, L., Saleem, M. & Mathieson, P. W. Podocyte culture: Tricks of the trade. *Nephrology* (2012) doi:10.1111/j.1440-1797.2012.01619.x.

403. Adam, M., Potter, A. S. & Potter, S. S. Psychrophilic proteases dramatically reduce single-cell RNA-seq artifacts: A molecular atlas of kidney development. *Dev.* (2017) doi:10.1242/dev.151142.

404. Cheng, H. Y. *et al.* Molecular identification of canine podocalyxin-like protein 1 as a renal tubulogenic regulator. *J. Am. Soc. Nephrol.* (2005) doi:10.1681/ASN.2004121145.

405. Phipson, B. *et al.* Evaluation of variability in human kidney organoids. *Nat. Methods* (2019) doi:10.1038/s41592-018-0253-2.

406. Eisen, M. B., Spellman, P. T., Brown, P. O. & Botstein, D. Cluster analysis and display of genome-wide expression patterns. *Proc. Natl. Acad. Sci. U. S. A.* (1998) doi:10.1073/pnas.95.25.14863.

407. St John, P. L. & Abrahamson, D. R. Glomerular endothelial cells and podocytes jointly synthesize laminin-1 and -11 chains. *Kidney Int.* (2001) doi:10.1046/j.1523-1755.2001.0600031037.x.

408. Tabatabaeifar, M. *et al.* An inducible mouse model of podocin-mutation-related nephrotic syndrome. *PLoS One* (2017) doi:10.1371/journal.pone.0186574.

409. Tory, K. *et al.* Mutation-dependent recessive inheritance of NPHS2-associated steroid-resistant nephrotic syndrome. *Nat. Genet.* (2014) doi:10.1038/ng.2898.

410. Szklarczyk, D. *et al.* STRING v11: Protein-protein association networks with increased coverage, supporting functional discovery in genome-wide experimental datasets. *Nucleic Acids Res.* (2019) doi:10.1093/nar/gky1131.

411. Everett, R. D. & Chelbi-Alix, M. K. PML and PML nuclear bodies: Implications in antiviral defence. *Biochimie* (2007) doi:10.1016/j.biochi.2007.01.004.

412. Bernardi, R. & Pandolfi, P. P. Structure, dynamics and functions of promyelocytic leukaemia nuclear bodies. *Nature Reviews Molecular Cell Biology* (2007) doi:10.1038/nrm2277.

413. Lafarga, M. *et al.* Clastosome: A subtype of nuclear body enriched in 19S and 20S proteasomes, ubiquitin, and protein substrates of proteasome. *Mol. Biol. Cell* (2002) doi:10.1091/mbc.E02-03-0122.

414. Kumada, S. *et al.* Promyelocytic leukemia protein is redistributed during the formation of intranuclear inclusions independent of polyglutamine expansion: An immunohistochemical study on marinesco bodies. *J. Neuropathol. Exp. Neurol.* (2002) doi:10.1093/jnen/61.11.984.

415. Dovey, C. L., Varadaraj, A., Wyllie, A. H. & Rich, T. Stress responses of PML nuclear domains are ablated by ataxin-I and other nucleoprotein inclusions. *J. Pathol.* (2004) doi:10.1002/path.1604.

416. Fu, L. *et al.* Nuclear aggresomes form by fusion of PML-associated aggregates. *Mol. Biol. Cell* (2005) doi:10.1091/mbc.E05-01-0019.

417. Dal Canton, A. Adhesion molecules in renal disease. *Kidney Int.* (1995) doi:10.1038/ki.1995.466.

418. Zhang, Q. *et al.* Biomarkers of endothelial dysfunction in patients with primary focal segmental glomerulosclerosis. *Nephrology* (2012) doi:10.1111/j.1440-1797.2012.01575.x.

419. Roca, N. *et al.* Relationship between soluble urokinase-type plasminogen activator receptor and serum biomarkers of endothelial activation in patients with idiopathic nephrotic syndrome. *Clin. Kidney J.* (2020) doi:10.1093/ckj/sfz173.

420. Ulyanova, T. *et al.* VCAM-1 expression in adult hematopoietic and nonhematopoietic cells is controlled by tissue-inductive signals and reflects their developmental origin. *Blood* (2005) doi:10.1182/blood-2004-09-3417.

421. Kong, D. H., Kim, Y. K., Kim, M. R., Jang, J. H. & Lee, S. Emerging roles of vascular cell adhesion molecule-1 (VCAM-1) in immunological disorders and cancer. *International Journal of Molecular Sciences* (2018) doi:10.3390/ijms19041057.

422. Visweswaran, G. R. R. *et al.* Targeting rapamycin to podocytes using a vascular cell adhesion molecule-1 (VCAM-1)-harnessed SAINT-based lipid carrier system. *PLoS One* (2015) doi:10.1371/journal.pone.0138870.

423. Wright, R. D. & Beresford, M. W. Podocytes contribute, and respond, to the inflammatory environment in lupus nephritis. *Am. J. Physiol. - Ren. Physiol.* (2018) doi:10.1152/ajprenal.00512.2017.

424. Gresset, A., Sondek, J. & Harden, T. K. The phospholipase C isozymes and their regulation. *Subcell. Biochem.* (2015) doi:10.1007/978-94-007-3012-0_3.

425. Troutman, T. D. *et al.* Role for B-cell adapter for PI3K (BCAP) as a signaling adapter linking Toll-like receptors (TLRs) to serine/threonine kinases PI3K/Akt. *Proc. Natl. Acad. Sci. U. S. A.* (2012) doi:10.1073/pnas.1118579109.

426. McKinney, C. E. Using induced pluripotent stem cells derived neurons to model brain diseases. *Neural Regeneration Research* (2017) doi:10.4103/1673-5374.211180.

427. Stockert, J. C., Horobin, R. W., Colombo, L. L. & Blázquez-Castro, A. Tetrazolium salts and formazan products in cell biology: viability assessment, fluorescence imaging, and labeling perspectives. *Acta Histochemica* (2018) doi:10.1016/j.acthis.2018.02.005.

428. Kilpinen, H. *et al.* Common genetic variation drives molecular heterogeneity in human iPSCs. *Nature* (2017) doi:10.1038/nature22403.

429. Rabe, M. & Schaefer, F. Non-transgenic mouse models of kidney disease. *Nephron* (2016) doi:10.1159/000445171.

430. Laurent, L. C. *et al.* Dynamic changes in the copy number of pluripotency and cell proliferation genes in human ESCs and iPSCs during reprogramming and time in culture. *Cell Stem Cell* (2011) doi:10.1016/j.stem.2010.12.003.

431. Kim, K. *et al.* Donor cell type can influence the epigenome and differentiation potential of human induced pluripotent stem cells. *Nat. Biotechnol.* (2011) doi:10.1038/nbt.2052.

432. D'Antonio, M. *et al.* Insights into the mutational burden of human induced pluripotent stem cells from an integrative multi-omics approach. *Cell Rep.* (2018) doi:10.1016/j.celrep.2018.06.091.

433. Combes, A. N., Zappia, L., Er, P. X., Oshlack, A. & Little, M. H. Single-cell analysis reveals congruence between kidney organoids and human fetal kidney. *Genome Med.* (2019) doi:10.1186/s13073-019-0615-0.

434. Higgins, J. W. *et al.* Bioprinted pluripotent stem cell-derived kidney organoids provide opportunities for high content screening. *bioRxiv* (2018) doi:10.1101/505396.

435. Kumar, S. V. *et al.* Kidney micro-organoids in suspension culture as a scalable source of human pluripotent stem cell-derived kidney cells. *Dev.* (2019) doi:10.1242/dev.172361.

436. Bukosza, E. N. *et al.* Podocyte RNA sequencing reveals Wnt- And ECM-associated genes as central in FSGS. *PLoS One* (2020) doi:10.1371/journal.pone.0231898.

437. Livesey, F. J. Strategies for microarray analysis of limiting amounts of RNA. *Briefings Funct. Genomics Proteomics* (2003) doi:10.1093/bfgp/2.1.31.

438. Machiraju, P. & Greenway, S. C. Current methods for the maturation of induced pluripotent stem cellderived cardiomyocytes. *World Journal of Stem Cells* (2019) doi:10.4252/wjsc.v11.i1.33.

439. Hrvatin, S. *et al.* Differentiated human stem cells resemble fetal, not adult, β cells. *Proc. Natl. Acad. Sci. U. S. A.* (2014) doi:10.1073/pnas.1400709111.

440. Ichimura, K., Kurihara, H. & Sakai, T. Primary cilia disappear in rat podocytes during glomerular development. *Cell Tissue Res.* (2010) doi:10.1007/s00441-010-0983-7.

441. Santín, S. *et al.* Clinical utility of genetic testing in children and adults with steroid-resistant nephrotic syndrome. *Clin. J. Am. Soc. Nephrol.* (2011) doi:10.2215/CJN.05260610.

442. Ji, P. *et al.* MALAT-1, a novel noncoding RNA, and thymosin β4 predict metastasis and survival in early-stage non-small cell lung cancer. *Oncogene* (2003) doi:10.1038/sj.onc.1206928.

443. Amodio, N. *et al.* MALAT1: A druggable long non-coding RNA for targeted anti-cancer approaches. *Journal of Hematology and Oncology* (2018) doi:10.1186/s13045-018-0606-4.

444. Wilusz, J. E., Freier, S. M. & Spector, D. L. 3′ end processing of a long nuclear-retained noncoding RNA yields a tRNA-like cytoplasmic RNA. *Cell* (2008) doi:10.1016/j.cell.2008.10.012.

445. Hayne, C. K., Schmidt, C. A., Haque, M. I., Matera, A. G. & Stanley, R. E. Reconstitution of the human tRNA splicing endonuclease complex: insight into the regulation of pre-tRNA cleavage. *Nucleic Acids Res.* (2020) doi:10.1093/nar/gkaa438.

446. Brown, J. A., Kinzig, C. G., Degregorio, S. J. & Steitz, J. A. Methyltransferase-like protein 16 binds the 3'-terminal triple helix of MALAT1 long noncoding RNA. *Proc. Natl. Acad. Sci. U. S. A.* (2016) doi:10.1073/pnas.1614759113.

447. Liu, N. *et al.* N6 -methyladenosine-dependent RNA structural switches regulate RNA-protein interactions. *Nature* (2015) doi:10.1038/nature14234.

448. Geuens, T., Bouhy, D. & Timmerman, V. The hnRNP family: insights into their role in health and disease. *Human Genetics* (2016) doi:10.1007/s00439-016-1683-5.

449. Puthanveetil, P., Chen, S., Feng, B., Gautam, A. & Chakrabarti, S. Long non-coding RNA MALAT1 regulates hyperglycaemia induced inflammatory process in the endothelial cells. *J. Cell. Mol. Med.* (2015) doi:10.1111/jcmm.12576.

450. Wu, D. *et al.* Downregulation of lncRNA MALAT1 contributes to renal functional improvement after duodenal-jejunal bypass in a diabetic rat model. *J. Physiol. Biochem.* (2018) doi:10.1007/s13105-018-0636-y.

451. Jadeja, S. *et al.* Identification of a new gene mutated in Fraser syndrome and mouse myelencephalic blebs. *Nat. Genet.* (2005) doi:10.1038/ng1549.

452. Uhlén, M. *et al.* Tissue-based map of the human proteome. *Science (80-.).* (2015) doi:10.1126/science.1260419.

453. Kim, B. S. *et al.* Impact of cyclosporin on podocyte ZO-1 expression in puromycin aminonucleoside nephrosis rats. *Yonsei Med. J.* (2005) doi:10.3349/ymj.2005.46.1.141.

454. Itoh, M. *et al.* The structural and functional organization of the podocyte filtration slits is regulated by Tjp1/ZO-1. *PLoS One* (2014) doi:10.1371/journal.pone.0106621.

455. Kurihara, H., Anderson, J. M., Kerjaschki, D. & Farquhar, M. G. The altered glomerular filtration slits seen in puromycin aminonucleoside nephrosis and protamine sulfate-treated rats contain the tight junction protein ZO-1. *Am. J. Pathol.* (1992).

456. Rincon-Choles, H. *et al.* ZO-1 expression and phosphorylation in diabetic nephropathy. *Diabetes* (2006) doi:10.2337/diabetes.55.04.06.db05-0355.

457. Li, Y. *et al.* Epithelial-to-mesenchymal transition is a potential pathway leading to podocyte dysfunction and proteinuria. *Am. J. Pathol.* (2008) doi:10.2353/ajpath.2008.070057.

458. Roselli, S. *et al.* Early Glomerular filtration defect and severe renal disease in podocin-deficient mice. *Mol. Cell. Biol.* (2004) doi:10.1128/mcb.24.2.550-560.2004.

459. Ettari, R. *et al.* Immunoproteasome-selective and non-selective inhibitors: A promising approach for the treatment of multiple myeloma. *Pharmacology and Therapeutics* (2018) doi:10.1016/j.pharmthera.2017.09.001.

460. Rodero, M. P. & Crow, Y. J. Type I interferon-mediated monogenic autoinflammation: The type i interferonopathies, a conceptual overview. *J. Exp. Med.* (2016) doi:10.1084/jem.20161596.

461. Yamashita, M. *et al.* Antiviral innate immunity disturbs podocyte cell function. *J. Innate Immun.* (2013) doi:10.1159/000345255.

462. Streicher, F. & Jouvenet, N. Stimulation of Innate Immunity by Host and Viral RNAs. *Trends in Immunology* (2019) doi:10.1016/j.it.2019.10.009.

463. Rice, G. I. *et al.* Mutations in ADAR1 cause Aicardi-Goutières syndrome associated with a type i interferon signature. *Nat. Genet.* (2012) doi:10.1038/ng.2414.

464. Eckard, S. C. *et al.* The SKIV2L RNA exosome limits activation of the RIG-I-like receptors. *Nat. Immunol.* (2014) doi:10.1038/ni.2948.

465. Hollien, J. & Weissman, J. S. Decay of endoplasmic reticulum-localized mRNAs during the unfolded protein response. *Science (80-.).* (2006) doi:10.1126/science.1129631.

466. Gardner, B. M. & Walter, P. Unfolded proteins are Ire1-activating ligands that directly induce the unfolded protein response. *Science (80-.).* (2011) doi:10.1126/science.1209126.

467. Dhir, A. *et al.* Mitochondrial double-stranded RNA triggers antiviral signalling in humans. *Nature* (2018) doi:10.1038/s41586-018-0363-0.

468. Goldwich, A. *et al.* Podocytes are nonhematopoietic professional antigen-presenting cells. *J. Am. Soc. Nephrol.* (2013) doi:10.1681/ASN.2012020133.

469. Lama, G. *et al.* T-lymphocyte populations and cytokines in childhood nephrotic syndrome. *Am. J. Kidney Dis.* (2002) doi:10.1053/ajkd.2002.32769.

470. Wang, Y., Wang, Y. P., Tay, Y. C. & Harris, D. C. H. Role of CD8+ cells in the progression of murine adriamycin nephropathy. *Kidney Int.* (2001) doi:10.1046/j.1523-1755.2001.059003941.x.

471. Okuda, S. *et al.* Adriamycin-induced nephropathy as a model of chronic progressive glomerular disease. *Kidney Int.* (1986) doi:10.1038/ki.1986.28.

472. Wang, Y. *et al.* Depletion of CD4+ T cells aggravates glomerular and interstitial injury in murine adriamycin nephropathy. *Kidney Int.* (2001) doi:10.1046/j.1523-1755.2001.059003975.x.

473. Hsu, K. S. & Kao, H. Y. PML: Regulation and multifaceted function beyond tumor suppression. *Cell and Bioscience* (2018) doi:10.1186/s13578-018-0204-8.

474. Grötzinger, T., Sternsdorf, T., Jensen, K. & Will, H. Interferon-modulated expression of genes encoding the nuclear-dot-associated proteins Sp100 and promyelocytic leukemia protein (PML). *Eur. J. Biochem.* (1996) doi:10.1111/j.1432-1033.1996.0554z.x.

475. Kumar P, P. *et al.* Functional interaction between PML and SATB1 regulates chromatin-loop architecture and transcription of the MHC class I locus. **9**, 45–56 (2007).

476. Zheng, P. *et al.* Proto-oncogene PML controls genes devoted to MHC class I antigen presentation. *Nature* (1998) doi:10.1038/24628.

477. Chang, S. K. *et al.* Proto-oncogene PML enhances antigen presentation by MHC class I molecules in human lung cancer cells. *Mol. Cells* (2002).

478. Bruno, S. B. *et al.* The PML gene is not involved in the regulation of MHC class I expression in human cell lines. *Blood* **101**, 3514–3519 (2003).

479. Sternsdorf, T., Jensen, K. & Will, H. Evidence for covalent modification of the nuclear dot-associated proteins PML and Sp100 by PIC1/SUMO-1. *J. Cell Biol.* (1997) doi:10.1083/jcb.139.7.1621.

480. Borden, K. L. B., Campbell Dwyer, E. J. & Salvato, M. S. An Arenavirus RING (Zinc-Binding) Protein Binds the Oncoprotein Promyelocyte Leukemia

Protein (PML) and Relocates PML Nuclear Bodies to the Cytoplasm. *J. Virol.* (1998) doi:10.1128/jvi.72.1.758-766.1998.

481. Turelli, P. *et al.* Cytoplasmic recruitment of INI1 and PML on incoming HIV preintegration complexes. *Mol. Cell* (2001) doi:10.1016/s1097-2765(01)00255-6.

482. Brasier, A. R. *et al.* Nuclear heat shock response and novel nuclear domain 10 reorganization in respiratory syncytial virus-infected A549 Cells identified by high-Resolution two-dimensional gel electrophoresis. *J. Virol.* (2004) doi:10.1128/jvi.78.21.11461-11476.2004.

483. Carracedo, A., Ito, K. & Pandolfi, P. P. The nuclear bodies inside out: PML conquers the cytoplasm. *Current Opinion in Cell Biology* (2011) doi:10.1016/j.ceb.2011.03.011.

484. Jin, G., Wang, Y. J. & Lin, H. K. Emerging cellular functions of cytoplasmic PML. *Frontiers in Oncology* (2013) doi:10.3389/fonc.2013.00147.

485. Gbadegesin, R. A. *et al.* HLA-DQA1 and PLCG2 are candidate risk loci for childhood-onset steroid-sensitive nephrotic syndrome. *J. Am. Soc. Nephrol.* (2015) doi:10.1681/ASN.2014030247.

486. Parker, L. *et al.* Phospholipase C-gamma 2 activity in familial steroid-sensitive nephrotic syndrome. *Pediatr. Res.* (2019) doi:10.1038/s41390-018-0259-6.

487. Gillies, C. E. *et al.* An eQTL landscape of kidney tissue in human nephrotic syndrome. *Am. J. Hum. Genet.* (2018) doi:10.1016/j.ajhg.2018.07.004.

488. Zhou, Q. *et al.* A hypermorphic missense mutation in PLCG2, encoding phospholipase Cγ2, causes a dominantly inherited autoinflammatory disease with immunodeficiency. *Am. J. Hum. Genet.* (2012) doi:10.1016/j.ajhg.2012.08.006.

489. Ombrello, M. J. *et al.* Cold urticaria, immunodeficiency, and autoimmunity related to PLCG2 deletions. *N. Engl. J. Med.* (2012) doi:10.1056/NEJMoa1102140.

490. Yu, P. *et al.* Autoimmunity and inflammation due to a gain-of-function mutation in phospholipase Cγ2 that specifically increases external Ca2+ entry. *Immunity* (2005) doi:10.1016/j.immuni.2005.01.018.

491. Koss, H., Bunney, T. D., Behjati, S. & Katan, M. Dysfunction of phospholipase Cγ in immune disorders and cancer. *Trends in Biochemical Sciences* (2014) doi:10.1016/j.tibs.2014.09.004.

492. Greka, A. & Mundel, P. Calcium Regulates Podocyte Actin Dynamics. *Semin. Nephrol.* (2012) doi:10.1016/j.semnephrol.2012.06.003.

493. Wharram, B. L. *et al.* Podocyte depletion causes glomerulosclerosis: Diphtheria toxin-induced podocyte depletion in rats expressing human diphtheria toxin receptor transgene. *J. Am. Soc. Nephrol.* (2005) doi:10.1681/ASN.2005010055.

494. Pirozzi, F., Nelson, B. & Mirzaa, G. From microcephaly to megalencephaly: determinants of brain size. *Dialogues Clin. Neurosci.* (2018) doi:10.31887/dcns.2018.20.4/gmirzaa.

495. Qin, X. S. *et al.* Phosphorylation of nephrin triggers its internalization by raft-mediated endocytosis. *J. Am. Soc. Nephrol.* (2009) doi:10.1681/ASN.2009010011.

496. Chatterjee, K., Nostramo, R. T., Wan, Y. & Hopper, A. K. tRNA dynamics between the nucleus, cytoplasm and mitochondrial surface: Location, location, location. *Biochimica et Biophysica Acta - Gene Regulatory Mechanisms* (2018) doi:10.1016/j.bbagrm.2017.11.007.

497. Niranjanakumari, S., Lasda, E., Brazas, R. & Garcia-Blanco, M. A. Reversible cross-linking combined with immunoprecipitation to study RNA-protein interactions in vivo. *Methods* (2002) doi:10.1016/S1046-2023(02)00021-X.

498. Jazurek, M., Ciesiolka, A., Starega-Roslan, J., Bilinska, K. & Krzyzosiak, W. J. Identifying proteins that bind to specific RNAs - Focus on simple repeat expansion diseases. *Nucleic Acids Research* (2016) doi:10.1093/nar/gkw803.

499. Geslain, R. & Pan, T. Functional analysis of human tRNA isodecoders. *J. Mol. Biol.* (2010) doi:10.1016/j.jmb.2009.12.018.

500. Goodenbour, J. M. & Pan, T. Diversity of tRNA genes in eukaryotes. *Nucleic Acids Res.* (2006) doi:10.1093/nar/gkl725.

APPENDIX

Table A1: Podocyte-related markers expression

	Gene	Name	005#04	007#27
2	*PODXL*	podocalyxin like	71953.54	65642.42
4	*PTPRO*	protein tyrosine phosphatase, receptor type O	31961.41	30391.48
6	*TJP1*	tight junction protein 1	25864.66	26048.66
15	*CLIC5*	chloride intracellular channel 5	16992.16	14602.41
16	*TGFBR3*	transforming growth factor beta receptor 3	16722.83	14745.04
18	*SPARC*	secreted protein acidic and cysteine rich	14631.55	14044.32
19	*PTPRD*	protein tyrosine phosphatase, receptor type D	13886.13	14305.53
20	*MYH9*	myosin heavy chain 9	13683.51	13633.00
22	*MAFB*	MAF bZIP transcription factor B	13482.54	10851.67
25	*VEGFA*	vascular endothelial growth factor A	12848.32	11330.15
26	*THSD7A*	thrombospondin type 1 domain containing 7A	12698.41	8378.00
31	*ROBO2*	roundabout guidance receptor 2	11471.15	8949.35
33	*MAGI2*	membrane associated guanylate kinase, WW and PDZ domain containing 2	11362.43	13137.11
34	***NPHS2***	NPHS2, podocin	11292.42	5890.22
35	*ENPEP*	glutamyl aminopeptidase	10794.93	6822.31
38	*ITM2B*	integral membrane protein 2B	9863.36	7081.04
39	*NPHS1*	NPHS1, nephrin	9318.10	7569.47
41	*SPTAN1*	spectrin alpha, non-erythrocytic 1	9080.88	8780.19
43	*SEPT11*	septin 11	8978.75	7235.28
44	*LAMA5*	laminin subunit alpha 5	8952.39	8089.41
46	*WT1*	Wilms tumor 1	8580.10	7662.35
48	*MPP5*	membrane palmitoylated protein 5	8090.02	7748.59
57	*SYNPO*	synaptopodin	7013.49	6985.67
59	*ARHGAP28*	Rho GTPase activating protein 28	6788.63	7387.03
60	*NTNG1*	netrin G1	6711.20	4050.10
63	*NES*	nestin	6685.67	5731.83
66	*TRIB2*	tribbles pseudokinase 2	6650.25	5149.69
72	*CGNL1*	cingulin like 1	6376.80	6326.41
73	*P3H2*	prolyl 3-hydroxylase 2	6310.08	5694.52
82	*TCF21*	transcription factor 21	6011.09	2782.16
88	*BCAM*	basal cell adhesion molecule (Lutheran blood group)	5956.73	5600.81
97	*ARHGEF12*	Rho guanine nucleotide exchange factor 12	5695.63	7149.86
103	*APLP2*	amyloid beta precursor like protein 2	5501.24	5479.74
108	*SRGAP1*	SLIT-ROBO Rho GTPase activating protein 1	5343.10	6332.22
110	*RBMS1*	RNA binding motif single stranded interacting protein 1	5321.69	6092.56
111	*NEBL*	nebulette	5305.21	5420.03
115	*EPB41L5*	erythrocyte membrane protein band 4.1 like 5	5101.77	5312.23
117	*PDLIM5*	PDZ and LIM domain 5	5015.28	4444.82
118	*PLOD2*	procollagen-lysine,2-oxoglutarate 5-dioxygenase 2	5000.46	4728.43
124	*PLCE1*	phospholipase C epsilon 1	4848.90	5738.47
127	*PARD3B*	par-3 family cell polarity regulator beta	4825.02	5123.99
133	*ARHGAP29*	Rho GTPase activating protein 29	4721.24	5543.59
136	*EIF3M*	eukaryotic translation initiation factor 3 subunit M	4685.82	3521.03
142	*AGRN*	agrin	4582.04	3861.86
154	*SPOCK2*	SPARC (osteonectin), cwcv and kazal like domains proteoglycan 2	4260.81	3357.67
156	*DACH1*	dachshund family transcription factor 1	4225.39	4458.09
195	*SDC2*	syndecan 2	3670.24	2337.68
199	*CPD*	carboxypeptidase D	3620.82	3496.98
231	*MXRA8*	matrix remodeling associated 8	3335.01	2553.29
237	*ACTN4*	actinin alpha 4	3270.77	2574.02
257	*CPEB4*	cytoplasmic polyadenylation element binding protein 4	3111.80	3374.25
263	*FOXC1*	forkhead box C1	3096.15	3337.76
235	*MGAT5*	alpha-1,6-mannosylglycoprotein 6-beta-N-acetylglucosaminyltransferase	3302.06	2851.82
283	*TYRO3*	TYRO3 protein tyrosine kinase	2969.30	2315.29
300	*ST3GAL6*	ST3 beta-galactoside alpha-2,3-sialyltransferase 6	2894.35	2716.65
322	*GADD45A*	growth arrest and DNA damage inducible alpha	2811.16	1922.22
333	*ITGA3*	integrin subunit alpha 3	2747.74	2683.48
339	*DDN*	dendrin	2709.85	1730.66
354	*SPATS2L*	spermatogenesis associated serine rich 2 like	2611.83	3055.82
362	*CD2AP*	CD2 associated protein	2577.24	2287.92
375	*FYN*	FYN proto-oncogene, Src family tyrosine kinase	2503.11	2384.12
384	*EFNB1*	ephrin B1	2460.28	1850.08

(Continued)

Table A1 | *Continued*

415	*CTTNBP2*	cortactin binding protein 2	2367.21	2864.26
438	*DAG1*	dystroglycan 1	2290.61	2002.66
465	*TRAM2*	translocation associated membrane protein 2	2211.53	2326.90
481	*PTH1R*	parathyroid hormone 1 receptor	2174.47	1613.74
510	*ANXA2*	annexin A2	2106.11	1625.35
522	*AIF1L*	allograft inflammatory factor 1 like	2070.69	2489.43
531	*LEPROT*	leptin receptor overlapping transcript	2043.51	2058.22
553	*HTRA1*	HtrA serine peptidase 1	1968.55	1376.57
574	*PAPPA*	pappalysin 1	1925.72	2764.75
99th percentile			1905.89	
595	*BMP7*	bone morphogenetic protein 7	1886.19	1622.86
597	*FOXC2*	forkhead box C2	1886.19	2067.34
730	*CORO2B*	coronin 2B	1682.74	1477.74
740	*PLTP*	phospholipid transfer protein	1662.15	1350.03
785	*ANXA1*	annexin A1	1592.14	2486.12
973	*TAPBP*	TAP binding protein	1367.28	1333.45
987	*TMEM150C*	transmembrane protein 150C	1354.93	1149.35
1029	*IL13RA1*	interleukin 13 receptor subunit alpha 1	1321.16	1050.67
1044	*CDC42EP3*	CDC42 effector protein 3	1304.68	1293.64
1051	*ST6GAL1*	ST6 beta-galactoside alpha-2,6-sialyltransferase 1	1299.74	951.99
1067	*HSPA12A*	heat shock protein family A (Hsp70) member 12A	1284.09	1410.57
1123	*ARMCX3*	armadillo repeat containing X-linked 3	1240.44	1097.94
1154	*CRB2*	crumbs 2, cell polarity complex component	1212.43	988.48
1159	*NPR1*	natriuretic peptide receptor 1	1209.14	911.35
1218	*PARVA*	parvin alpha	1168.78	1087.16
1248	*CD59*	CD59 molecule (CD59 blood group)	1147.36	951.99
1253	*IGFBP7*	insulin like growth factor binding protein 7	1143.24	1329.30
1283	*RIPOR1*	RHO family interacting cell polarization regulator 1	1120.18	1257.98
1286	*MYOF*	myoferlin	1118.53	1206.57
1355	*SLC48A1*	solute carrier family 48 member 1	1064.17	973.55
1421	*CTNNAL1*	catenin alpha like 1	1023.81	993.45
1438	*KANK1*	KN motif and ankyrin repeat domains 1	1014.75	908.87
1456	*ARF6*	ADP ribosylation factor 6	998.28	856.62
1527	*MYL9*	myosin light chain 9	962.04	852.48
1628	*SEMA3G*	semaphorin 3G	911.79	670.87
1773	*CD81*	CD81 molecule	850.02	719.80
1847	*HEXIM1*	hexamethylene bisacetamide inducible 1	817.07	714.82
1853	*BST2*	bone marrow stromal cell antigen 2	814.60	1109.55
1864	*C1orf21*	chromosome 1 open reading frame 21	808.84	899.75
1920	*SLC9A3R2*	SLC9A3 regulator 2	788.25	582.97
2144	*RETREG1*	reticulophagy regulator 1	714.94	589.60
2319	*RASSF10*	Ras association domain family member 10	663.87	444.48
2370	*VAMP2*	vesicle associated membrane protein 2	650.69	519.94
2448	*AMIGO2*	adhesion molecule with Ig like domain 2	633.40	544.82
2454	*MYO1D*	myosin ID	633.40	623.60
2604	*TPPP3*	tubulin polymerization promoting protein family member 3	596.33	558.92
2671	*CTDSPL*	CTD small phosphatase like	581.51	831.75
95th percentile			530,44	
3006	*PDLIM2*	PDZ and LIM domain 2	512.32	658.43
3090	*NDNF*	neuron derived neurotrophic factor	497.49	434.53
3099	*CD151*	CD151 molecule (Raph blood group)	495.85	393.90
3197	*TM4SF1*	transmembrane 4 L six family member 1	478.55	840.04
3303	*FOXD1*	forkhead box D1	463.72	270.34
3857	*SNCA*	synuclein alpha	387.95	338.34
4267	*LOXL1*	lysyl oxidase like 1	340.17	422.92
4539	*GRK5*	G protein-coupled receptor kinase 5	314.64	349.12
4652	*SIRPA*	signal regulatory protein alpha	304.76	554.77
5148	*KLK6*	kallikrein related peptidase 6	266.04	185.75
5566	*CLDN5*	claudin 5	238.86	179.95
5696	*VAMP5*	vesicle associated membrane protein 5	228.98	112.78
6666	*AIF1*	allograft inflammatory factor 1	176.26	140.14
12511	*SMIM1*	small integral membrane protein 1 (Vel blood group)	30.48	12.44
15014	*CRYAB*	crystallin alpha B	14.83	17.41
27267	*PDE4B*	phosphodiesterase 4B	0.82	4.15

Table reporting the 124 consensus podocyte-related markers expression. The first column (#) indicates the position ranking of genes classed by expression level in the control. The last columns report the DESeq2 normalized gene expression level in control (005#04) and SRNS^{NPHS2} patient (007#27) kidney organoid-isolated podocytes. (Pilot RNA-Seq analysis).

Table A2: Laminin and collagen IV isoforms expression

	Gene	Name	State	005#04	007#27
Laminins					
44	***LAMA5***	laminin subunit alpha 5	Mature	8952.39	8089.41
77	***LAMC1***	laminin subunit gamma 1	Immature/ Mature	6136.29	4914.18
155	***LAMB2***	laminin subunit beta 2	Mature	4236.10	3227.47
602	***LAMB1***	laminin subunit beta 1	Immature	1878.77	2936.40
4936	*LAMC3*	laminin subunit gamma 3		280.05	193.22
5044	*LAMA4*	laminin subunit alpha 4		272.63	326.73
7257	***LAMA1***	laminin subunit alpha 1	Immature	149.91	144.29
7985	*LAMA2*	laminin subunit alpha 2		121.90	51.41
13034	*LAMB4*	laminin subunit beta 4		25.53	47.27
15313	*LAMB3*	laminin subunit beta 3		14.00	8.29
21612	*LAMA3*	laminin subunit alpha 3		3.29	2.49
26661	*LAMC2*	laminin subunit gamma 2		0.82	1.66
Collagens					
40	*COL1A2*	collagen type I alpha 2 chain		9200.31	3004.40
169	*COL3A1*	collagen type III alpha 1 chain		3995.59	3794.69
200	***COL4A2***	collagen type IV alpha 2 chain	Immature	3601.88	4264.05
306	*COL1A1*	collagen type I alpha 1 chain		2882.82	2083.10
529	***COL4A1***	collagen type IV alpha 1 chain	Immature	2050.92	3141.23
722	***COL4A5***	collagen type IV alpha 5 chain	Mature	1692.63	1470.27
1190	*COL18A1*	collagen type XVIII alpha 1 chain		1183.60	1053.99
1230	*COL6A1*	collagen type VI alpha 1 chain		1160.54	885.65
2088	*COL27A1*	collagen type XXVII alpha 1 chain		731.41	679.99
2595	*COL6A2*	collagen type VI alpha 2 chain		598.80	571.36
2756	*COL4A3BP*	collagen type IV alpha 3 binding protein		565.86	524.92
3499	*COL2A1*	collagen type II alpha 1 chain		432.42	316.78
3556	*COL5A2*	collagen type V alpha 2 chain		424.19	744.67
4402	*COL6A3*	collagen type VI alpha 3 chain		327.82	201.51
5157	*COL7A1*	collagen type VII alpha 1 chain		265.22	168.34
6755	*COL4A6*	collagen type IV alpha 6 chain		172.97	185.75
6758	***COL4A4***	collagen type IV alpha 4 chain	Mature	172.15	619.46
7072	*COL13A1*	collagen type XIII alpha 1 chain		158.14	71.32
7103	*COL5A1*	collagen type V alpha 1 chain		156.50	150.10
7321	*COL12A1*	collagen type XII alpha 1 chain		147.44	219.75
7827	*COL6A6*	collagen type VI alpha 6 chain		127.67	63.85
8921	***COL4A3***	collagen type IV alpha 3 chain	Mature	93.90	305.17
9453	*COL28A1*	collagen type XXVIII alpha 1 chain		80.72	48.93
10442	*COL10A1*	collagen type X alpha 1 chain		58.48	76.29
10847	*COL25A1*	collagen type XXV alpha 1 chain		51.07	58.05
12060	*COL14A1*	collagen type XIV alpha 1 chain		34.59	25.71
12111	*COL16A1*	collagen type XVI alpha 1 chain		33.77	79.61
12184	*COL11A1*	collagen type XI alpha 1 chain		32.95	35.66
12860	*COL26A1*	collagen type XXVI alpha 1 chain		27.18	30.68
13149	*COL9A3*	collagen type IX alpha 3 chain		24.71	9.12
13427	*COL22A1*	collagen type XXII alpha 1 chain		23.06	5.80
13785	*COL17A1*	collagen type XVII alpha 1 chain		20.59	13.27
14793	*COL9A2*	collagen type IX alpha 2 chain		15.65	4.98
14794	*COL23A1*	collagen type XXIII alpha 1 chain		15.65	14.10
15795	*COL8A2*	collagen type VIII alpha 2 chain		12.35	7.46
16341	*COL9A1*	collagen type IX alpha 1 chain		10.71	24.88
16420	*COL11A2*	collagen type XI alpha 2 chain		10.71	17.41
19188	*COL5A3*	collagen type V alpha 3 chain		5.77	4.15
20788	*COL24A1*	collagen type XXIV alpha 1 chain		4.12	9.95
21675	*COL21A1*	collagen type XXI alpha 1 chain		3.29	8.29
22836	*COL19A1*	collagen type XIX alpha 1 chain		2.47	0.83
22949	*COL8A1*	collagen type VIII alpha 1 chain		2.47	11.61

(Continued)

Table A2 | *Continued*

24458	*COL20A1*	collagen type XX alpha 1 chain	1.65	6.63
24941	*COL15A1*	collagen type XV alpha 1 chain	1.65	0.83
31929	*COL6A5*	collagen type VI alpha 5 chain	0.00	0.00

Table reporting the glomerular laminin and collagen IV isoforms. The first column (#) indicates the position ranking of genes classed by expression level in the control. The "state" column classify the laminin and collagen IV isoforms as "immature" or "mature" based on their abundance in the developing or mature GBM, respectively. The last columns report the DESeq2 normalized gene expression level in control (005#04) and SRNS^{NPHS2} patient (007#27) kidney organoid-isolated podocytes. (Pilot RNA-Seq analysis).

Table A3: Adult human podocyte transcription factors

	Gene	Name	005#04	007#27	Takasato	Morizane
22	*MAFB*	MAF bZIP transcription factor B	13482.54	10851.67	1	1
46	*WT1*	Wilms tumor 1	8580.10	7662.35	1	1
123	*TULP4*	tubby like protein 4	4864.55	4135.51	1	1
156	*DACH1*	dachshund family transcription factor 1	4225.39	4458.09	0	1
321	*BAZ2B*	bromodomain adjacent to zinc finger domain 2B	2813.63	2863.43	0	0
324	*RERE*	arginine-glutamic acid dipeptide repeats	2796.34	2977.04	0	0
334	*ZEB2*	zinc finger E-box binding homeobox 2	2746.92	2318.61	0	0
349	*ARID1B*	AT-rich interaction domain 1B	2646.43	2330.22	0	0
418	*SMAD2*	SMAD family member 2	2359.79	2347.63	0	0
99th percentile			1905.89			
643	*TCF7L2*	transcription factor 7 like 2	1817.00	1477.74	1	0
925	*JARID2*	jumonji and AT-rich interaction domain containing 2	1415.88	1212.38	0	0
928	*LMX1B*	LIM homeobox transcription factor 1 beta	1410.11	1172.57	0	0
1160	*BACH1*	BTB domain and CNC homolog 1	1208.31	1175.06	1	0
1189	*ZNF521*	zinc finger protein 521	1186.07	1074.72	0	0
1194	*DACH2*	dachshund family transcription factor 2	1181.96	853.31	0	1
1237	*SMAD6*	SMAD family member 6	1157.25	1408.91	0	1
1272	*ZBTB7C*	zinc finger and BTB domain containing 7C	1127.59	1043.21	1	1
1353	*TEAD1*	TEA domain transcription factor 1	1065.82	1046.52	0	0
1601	*CERS6*	ceramide synthase 6	929.09	699.06	0	0
1713	*HMGN3*	high mobility group nucleosomal binding domain 3	869.79	738.87	1	0
1783	*TCF7L1*	transcription factor 7 like 1	845.90	752.97	0	0
1910	*NFIC*	nuclear factor I C	791.54	888.14	0	0
2119	*NFATC3*	nuclear factor of activated T cells 3	723.18	567.21	0	0
2215	*ZBTB1*	zinc finger and BTB domain containing 1	695.17	846.67	0	0
95th percentile			530,44			
3118	*CASZ1*	castor zinc finger 1	491.73	509.99	0	0
3307	*SOX6*	SRY-box 6	462.90	551.46	0	0
3433	*ELF1*	E74 like ETS transcription factor 1	441.48	491.75	0	0
3529	*ZNF124*	zinc finger protein 124	428.30	223.07	0	0
4225	*TSHZ2*	teashirt zinc finger homeobox 2	345.11	235.51	0	0
5239	*SMAD1*	SMAD family member 1	261.10	208.97	0	0
5447	*KLF7*	Kruppel like factor 7	246.28	366.53	0	0
5527	*ETV6*	ETS variant 6	241.33	249.61	0	0
6253	*ZNF846*	zinc finger protein 846	197.68	167.51	0	0
6334	*PRDM5*	PR/SET domain 5	193.56	218.92	0	0
7143	*ZNF250*	zinc finger protein 250	154.85	133.51	0	0
8236	*IKZF2*	IKAROS family zinc finger 2	112.84	148.44	0	0
10919	*HIVEP3*	human immunodeficiency virus type I enhancer binding protein 3	49.42	68.00	0	0
11910	*TSHZ3*	teashirt zinc finger homeobox 3	36.24	29.85	0	0

Table reporting adult human podocyte transcription factor expression. The first column (#) indicates the position ranking of genes classed by expression level in the control. DESeq2 normalized gene expression level in control (005#04) and SRNS^{NPHS2} patient (007#27) kidney organoid-isolated podocytes is reported in the respective columns. The last columns report the identification (1) or absence (0) of expression of the relative genes detected by Wu and colleagues[1] in kidney organoid podocyte cluster applying the Takasato's or the Morizane's protocol. (Pilot RNA-Seq analysis).

Table A4: Nephrotic syndrome-related gene expression

Gene	Gene	p-val	p-BH	p-Bonf	007#27.1	007#27.2	Mean R138Q	005#04.1	005#04.2	005#04.3	013#19	Mean ctrl	Ratio	Delta
podocalyxin	PODXL	5,00E-01	1,00E+00	1,00E+00	26078,82	82668,15	54373,49	62537,17	49153,70	55114,83	98491,58	66324,32	0,82	11950,83
protein tyros	PTPRO	5,41E-01	1,00E+00	1,00E+00	8613,15	41643,61	25128,38	29287,83	19850,90	28797,36	45909,17	30961,32	0,81	5832,94
FAT atypical	FAT1	6,60E-01	1,00E+00	1,00E+00	14133,29	27568,79	20851,04	21963,73	18692,56	21657,05	29645,94	22989,82	0,91	2138,78
MAF bZIP tra	MAFB	3,68E-01	1,00E+00	1,00E+00	10974,28	17942,11	14458,2	17080,59	14302,19	15178,63	23350,16	17477,89	0,83	3019,69
myosin heav	MYH9	4,74E-01	1,00E+00	1,00E+00	9779,44	16305,95	13042,69	13110,52	14160,24	15226,92	17313,64	14952,83	0,87	1910,14
kirre like ne	KIRREL1	8,21E-01	1,00E+00	1,00E+00	9058,39	17908,87	13483,63	12814,72	14454,37	12433,65	16906,63	14152,34	0,95	668,71
NPHS1 adhe	NPHS1	3,39E-01	1,00E+00	1,00E+00	6320,97	10656,24	8488,609	10365,21	9534,79	8786,25	12313,23	10249,87	0,83	1761,26
WT1 transcri	WT1	4,95E-01	1,00E+00	1,00E+00	6698,24	10373,72	8535,98	9718,61	8718,27	8293,78	12269,39	9750,012	0,88	1214,03
NPHS2 stom	NPHS2	2,83E-01	1,00E+00	1,00E+00	1211,59	7604,96	4408,274	7267,87	4611,82	5978,93	18855,89	9178,627	0,48	4770,35
membrane a	MAGI2	5,05E-01	1,00E+00	1,00E+00	2570,94	8816,50	5693,72	7152,97	5011,56	6208,05	9345,97	6929,637	0,82	1235,92
scavenger re	SCARB2	5,84E-01	1,00E+00	1,00E+00	3586,52	6031,95	4809,23	4048,30	3266,09	4355,81	5464,61	4283,701	1,12	525,53
laminin subu	LAMB2	3,05E-01	1,00E+00	1,00E+00	2116,84	4251,20	3184,019	3324,69	4694,72	3212,87	4911,76	4036,01	0,79	851,99
phospholipa	PLCE1	7,56E-01	1,00E+00	1,00E+00	697,41	5068,03	2882,718	3053,34	2075,94	2857,35	6017,45	3501,02	0,82	618,30
actinin alpha	ACTN4	6,68E-02	1,00E+00	1,00E+00	1227,36	2952,40	2089,879	2580,30	3681,73	3080,32	3683,10	3256,364	0,64	1166,49
integrin subu	ITGA3	3,04E-01	1,00E+00	1,00E+00	1520,90	3183,41	2352,153	2263,72	3216,12	2838,92	3614,48	2983,308	0,79	631,16
												99th percentile		
CD2 associat	CD2AP	8,74E-01	1,00E+00	1,00E+00	1438,15	2853,52	2145,836	1992,37	1404,78	1774,10	3810,83	2245,521	0,96	99,69
exportin 5 [S	XPO5	7,58E-01	1,00E+00	1,00E+00	1656,83	1324,55	1490,691	1509,56	1861,31	1746,01	1195,29	1578,042	0,94	87,35
collagen type	COL4A5	9,08E-01	1,00E+00	1,00E+00	1209,62	2025,88	1617,753	1487,55	1193,55	1488,81	2137,99	1576,977	1,03	40,78
GTPase activ	GAPVD1	7,15E-01	1,00E+00	1,00E+00	1333,74	1716,77	1525,252	1479,00	1235,57	1430,87	1597,54	1435,744	1,06	89,51
crumbs cell p	CRB2	4,30E-02	1,00E+00	1,00E+00	889,49	1636,99	1263,24	1625,68	2655,12	1680,18	2008,36	1992,331	0,63	729,09
KN motif and	KANK1	2,24E-01	1,00E+00	1,00E+00	911,16	1302,12	1106,637	1501,00	1213,99	1277,25	1492,69	1371,232	0,81	264,60
LIM homeob	LMX1B	1,61E-01	1,00E+00	1,00E+00	580,19	1246,44	913,3137	1031,63	1442,26	911,19	1915,90	1325,245	0,69	411,93
nucleoporin	NUP205	8,18E-01	1,00E+00	1,00E+00	1638,11	879,16	1258,636	1370,21	1437,71	1519,53	967,48	1323,735	0,95	65,10
sphingosine-	SGPL1	7,04E-01	1,00E+00	1,00E+00	1235,24	1204,06	1219,649	1359,21	1261,69	1267,59	1263,92	1288,104	0,95	68,46
inverted for	INF2	2,64E-01	1,00E+00	1,00E+00	544,72	1148,39	846,5564	633,16	1357,08	897,15	1817,72	1176,278	0,72	329,72
complement	CFH	6,64E-01	1,00E+00	1,00E+00	135,93	1499,05	817,4943	495,04	705,23	1364,16	1954,98	1129,85	0,72	312,36
lamin A/C [S	LMNA	6,35E-02	1,00E+00	1,00E+00	781,13	821,82	801,4769	958,29	1393,43	1053,40	1023,72	1107,21	0,72	305,73
CD151 molec	CD151	2,80E-02	1,00E+00	1,00E+00	659,97	788,58	724,278	898,40	1316,20	947,18	1148,59	1077,593	0,67	353,32
nucleoporin	NUP133	9,35E-01	1,00E+00	1,00E+00	999,81	883,31	941,5614	1025,52	793,81	1046,38	950,32	954,0082	0,99	12,45
myosin IE [S	MYO1E	5,48E-01	1,00E+00	1,00E+00	459,03	1143,40	801,2145	660,05	774,50	860,28	1515,56	952,5982	0,84	151,38
ankyrin repe	ANKFY1	3,57E-01	1,00E+00	1,00E+00	899,34	1307,93	1103,635	950,96	891,47	887,49	1034,21	941,0321	1,17	162,60
Rho GTPase	ARHGAP24	5,88E-01	1,00E+00	1,00E+00	945,63	738,72	842,1793	909,40	981,19	1193,86	671,04	938,8715	0,90	96,69
nucleoporin	NUP160	7,37E-01	1,00E+00	1,00E+00	1251,00	687,20	969,1001	880,07	860,81	1083,25	789,24	903,3402	1,07	-65,76
												95th percentile		
tetratricopep	TTC21B	4,87E-01	1,00E+00	1,00E+00	789,01	696,35	742,6795	756,61	591,67	721,58	568,10	659,4888	1,13	83,19
nucleoporin	NUP107	4,93E-01	1,00E+00	1,00E+00	974,20	535,97	755,0851	697,94	578,04	711,92	637,68	656,3957	1,15	-98,69
OCRL inosito	OCRL	6,11E-01	1,00E+00	1,00E+00	515,17	599,12	557,1483	592,82	570,09	578,49	676,76	604,5411	0,92	47,39
paired box 2	PAX2	5,49E-01	1,00E+00	1,00E+00	987,99	432,93	710,4608	574,49	893,75	556,55	385,09	602,4663	1,18	107,99
zinc metallo	ZMPSTE24	3,47E-01	1,00E+00	1,00E+00	581,17	388,06	484,6149	585,49	484,92	676,81	570,00	579,3046	0,84	94,69
anillin actin	ANLN	3,91E-01	1,00E+00	1,00E+00	1098,32	346,51	722,4128	673,49	479,24	752,30	296,44	550,3692	1,31	172,04
Rho GDP dis	ARHGDIA	3,34E-02	1,00E+00	1,00E+00	341,81	358,14	349,9758	411,92	567,82	502,12	537,60	504,8635	0,69	154,89
KN motif and	KANK2	1,02E-02	1,00E+00	1,00E+00	225,57	299,98	262,775	347,14	440,63	410,83	597,65	449,0591	0,59	186,28
SWI/SNF rel	SMARCAL1	8,90E-01	1,00E+00	1,00E+00	265,96	442,90	354,4309	358,14	317,98	306,36	397,48	344,9894	1,03	9,44
												90th percentile		
nucleoporin	NUP93	9,95E-01	1,00E+00	1,00E+00	415,69	216,05	315,8675	271,35	366,81	362,55	259,27	314,9938	1,00	0,87
TP53 regulat	TP53RK	1,22E-01	1,00E+00	1,00E+00	287,63	152,90	220,2636	301,91	331,61	378,35	242,11	313,493	0,70	93,23
nucleoporin	NUP85	7,31E-01	1,00E+00	1,00E+00	301,42	293,33	297,3751	279,91	305,49	286,17	251,64	280,8025	1,06	16,57
O-sialoglyco	OSGEP	6,52E-01	1,00E+00	1,00E+00	259,06	167,85	213,4593	259,13	225,99	251,06	198,26	233,6112	0,91	20,15
phosphomar	PMM2	6,43E-01	1,00E+00	1,00E+00	233,45	128,80	181,1262	162,57	261,20	271,25	125,82	205,2087	0,88	24,08
epithelial m	EMP2	9,05E-01	1,00E+00	1,00E+00	270,88	128,80	199,8419	188,24	221,45	237,89	125,82	193,3496	1,03	6,49
decaprenyl c	PDSS2	4,74E-01	1,00E+00	1,00E+00	240,35	201,09	220,7206	193,13	164,67	213,31	201,12	193,057	1,14	-27,66
coenzyme Q	COQ8B	5,74E-01	1,00E+00	1,00E+00	90,62	220,20	155,414	151,57	235,08	148,35	189,68	181,1702	0,86	25,76
WD repeat d	WDR73	8,80E-01	1,00E+00	1,00E+00	149,73	181,98	165,8529	202,90	149,90	147,48	144,88	161,292	1,03	4,56
TP53RK bind	TPRKB	6,19E-01	1,00E+00	1,00E+00	163,52	110,52	137,0169	141,79	96,53	146,60	102,94	121,9649	1,12	15,05
diacylglycer	DGKE	3,19E-01	1,00E+00	1,00E+00	109,34	186,97	148,1526	113,68	105,61	163,28	68,63	112,7989	1,31	35,35
coenzyme Q	COQ2	7,10E-02	1,00E+00	1,00E+00	72,89	54,84	63,86803	112,45	69,27	113,24	100,08	98,76287	0,65	34,89
WD repeat d	WDR4	4,76E-01	1,00E+00	1,00E+00	104,41	52,35	78,38217	81,89	129,46	100,07	69,58	95,25323	0,82	16,87
coenzyme Q	COQ6	1,33E-01	1,00E+00	1,00E+00	75,85	54,84	65,34559	112,45	86,31	100,07	74,35	93,29563	0,70	27,95
ALG1 chitobi	ALG1	1,38E-01	1,00E+00	1,00E+00	64,03	61,49	62,75922	67,23	102,21	82,52	103,90	88,96197	0,71	26,20
yrdC N6-thre	YRDC	9,84E-01	1,00E+00	1,00E+00	113,28	60,66	86,96963	74,56	102,21	87,78	83,88	87,10797	1,00	0,14
transient rec	TRPC6	1,60E-01	1,00E+00	1,00E+00	186,17	56,51	121,3386	64,78	54,51	83,39	102,94	76,40781	1,59	44,93
GON7 subun	GON7	9,48E-01	1,00E+00	1,00E+00	68,95	53,18	61,067	50,11	43,15	86,03	67,68	61,7432	0,99	0,68
TBC1 domair	TBC1D8B	5,59E-01	1,00E+00	1,00E+00	34,48	35,73	35,10379	36,67	19,31	30,72	30,50	29,30032	1,20	5,80
collagen type	COL4A4	5,46E-03	9,19E-01	1,00E+00	14,78	189,46	102,1173	19,56	23,85	22,82	40,03	26,56569	3,84	75,55
complement	CFI	2,39E-02	1,00E+00	1,00E+00	39,40	78,11	58,75588	37,89	32,93	12,29	21,92	26,25951	2,24	32,50
L antigen fan	LAGE3	2,09E-01	1,00E+00	1,00E+00	11,82	13,30	12,5579	15,89	23,85	16,68	25,74	20,53831	0,61	7,98
integrin subu	ITGB4	1,90E-01	1,00E+00	1,00E+00	5,91	8,31	7,109912	11,00	18,17	9,66	15,25	13,51953	0,53	6,41
collagen type	COL4A3	1,32E-03	3,74E-01	1,00E+00	17,73	91,41	54,56817	9,78	7,95	13,17	19,06	12,48979	4,37	42,08
apolipoprote	APOA1	4,93E-01	1,00E+00	1,00E+00	24,63	6,65	15,63679	6,11	6,81	9,66	20,02	10,64961	1,47	4,99
KN motif and	KANK4	7,39E-01	1,00E+00	1,00E+00	8,87	7,48	8,171985	4,89	4,54	2,63	14,30	6,590765	1,24	1,58
apolipoprote	APOL1	3,06E-04	1,39E-01	1,00E+00	6,90	116,33	61,61489	3,67	11,36	8,78	0,95	6,188705	9,96	55,43
endothelin 1	EDN1	5,18E-01	1,00E+00	1,00E+00	13,79	4,99	9,388133	7,33	4,54	11,41	0,00	5,822066	1,61	3,57
nuclear RNA	NXF5	9,66E-01	1,00E+00	1,00E+00	1,97	4,15	3,062438	1,22	2,27	4,39	3,81	2,923873	1,05	0,14
mitochondri	MT-TL1	1,00E+00	1,00E+00	1,00E+00	0,00	0,00	0	0,00	0,00	0,00	0,00	0	1,00	0,00

Table reporting the expression of the genes associated with nephrotic syndrome. DESeq2 normalized gene expression level in controls (005#04 and 013#19) and SRNS^{NPHS2} patient (007#27) kidney organoid-isolated podocytes is reported in the respective columns. Genes are classed by average expression level in the controls. (Second RNA-Seq analysis).

Table A5: Most abundantly expressed genes in control kidney organoid podocytes

		A		B					
Gene	**Name**	**005#04**	**#**	**005#04.1**	**005#04.2**	**005#04.3**	**013#19**	**Average**	**#**
MALAT1	metastasis associated lung adenocarcinoma transcript 1	203703,4	1	196355,9	118136,7	157754,7	92247,3	141123,7	1
PODXL	podocalyxin like	71953,5	2	62537,2	49153,7	55114,8	98491,6	66324,3	2
PTPRO	protein tyrosine phosphatase receptor type O	31961,4	4	29287,8	19850,9	28797,4	45909,2	30961,3	5
FREM2	FRAS1 related extracellular matrix 2	22494,2	7	27038,8	24227,6	27546,4	43386,1	30549,7	6
TJP1	tight junction protein 1	25864,7	6	21546,9	19237,7	22800,0	33868,5	24363,3	8
EEF1A1	eukaryotic translation elongation factor 1 alpha 1	18366,9	12	32606,4	32913,0	31207,0	31678,1	32101,1	4
FAT1	FAT atypical cadherin 1	20542,2	8	21963,7	18692,6	21657,1	29645,9	22989,8	10
DDX17	DEAD-box helicase 17	27116,6	5	22295,0	16255,5	19595,0	21793,6	19984,8	15
HIPK2	homeodomain interacting protein kinase 2	18917,9	11	19795,4	24035,7	21528,0	27773,9	23283,2	9
SPARC	secreted protein acidic and cysteine rich	14631,5	18	23697,0	21763,3	25733,7	32008,9	25800,7	7
FRAS1	Fraser extracellular matrix complex subunit 1	16143,0	17	24602,7	20221,1	22449,7	23301,5	22643,8	11
HSP90B1	heat shock protein 90 beta family member 1	18157,6	13	22110,4	13426,6	18374,8	18631,9	18135,9	17
MAGI2-AS3	MAGI2 antisense RNA 3	19340,4	9	13868,4	9518,9	15695,7	23347,3	15607,6	21
CLIC5	chloride intracellular channel 5	16992,2	15	13983,3	10571,6	13236,9	25188,9	15745,2	19
SRRM2	serine/arginine repetitive matrix 2	17789,5	14	13400,2	19452,3	14442,1	12829,9	15031,1	24
TGFBR3	transforming growth factor beta receptor 3	16722,8	16	11888,2	9487,1	12855,0	27736,7	15491,8	22
ACTB	actin beta	12898,6	23	12974,9	24212,9	19391,4	17003,9	18395,7	16
MAFB	MAF bZIP transcription factor B	13482,5	22	17080,6	14302,2	15178,6	23350,2	17477,9	18
H19	H19 imprinted maternally expressed transcript	13577,3	21	12166,9	22080,2	18211,6	10079,0	15634,4	20
MYH9	myosin heavy chain 9	13683,5	20	13110,5	14160,2	15226,9	17313,6	14952,8	25
PTPRD	protein tyrosine phosphatase receptor type D	13886,1	19	13801,1	13082,5	14617,7	17002,9	14626,1	26
NOTCH2	notch receptor 2	10460,5	37	20748,8	20386,9	18589,0	24740,9	21116,4	13
AHNAK	AHNAK nucleoprotein	12119,4	28	11467,7	14987,0	14609,8	13182,5	13561,8	29
KIRREL1	kirre like nephrin family adhesion molecule 1	11820,4	29	12814,7	14454,4	12433,7	16906,6	14152,3	28
ACTG1	actin gamma 1	8628,7	45	14788,8	25936,8	19246,5	20393,4	20091,4	14
CANX	calnexin	11462,9	32	15297,2	12133,1	14568,5	14837,3	14209,0	27
NPNT	nephronectin	10544,5	36	8933,9	7239,7	10835,1	18143,9	11288,1	34
VEGFA	vascular endothelial growth factor A	12848,3	25	10003,4	10019,7	8319,2	12197,0	10134,8	46
ROBO2	roundabout guidance receptor 2	11471,2	31	9314,0	6735,5	10516,5	14495,1	10265,3	43
SPTAN1	spectrin alpha, non-erythrocytic 1	9080,9	41	9959,4	9571,1	11757,7	12251,3	10884,9	36
PRRC2C	proline rich coiled-coil 2C	9032,3	42	9234,6	10309,3	10617,4	11110,3	10317,9	40
NPHS1	NPHS1 adhesion molecule, nephrin	9318,1	39	10365,2	9534,8	8786,2	12313,2	10249,9	45
WT1	WT1 transcription factor	8580,1	46	9718,6	8718,3	8293,8	12269,4	9750,0	50
HNRNPA2B1	heterogeneous nuclear ribonucleoprotein A2/B1	7950,8	50	12413,8	7513,4	10573,5	8720,7	9805,3	49

Table reporting the most abundantly expressed genes in control kidney organoid podocytes. DESeq2 normalized gene expression level in controls (005#04 and 013#19) from the pilot (A columns) and second (B columns) is reported in the respective columns. The # columns indicate the position ranking of genes classed by expression level in the control (A) or by average expression level in controls (B).

Article 3

Defects in t6A tRNA modification due to *GON7* and *YRDC* mutations lead to Galloway-Mowat syndrome

Christelle Arrondel, Sophia Missoury, Rozemarijn Snoek, Julie Patat, **Giulia Menara**, Bruno Collinet, Dominique Liger, Dominique Durand, Olivier Gribouval, Olivia Boyer, Laurine Buscara, Gaëlle Martin, Eduardo Machuca, Fabien Nevo, Ewen Lescop, Daniela A. Braun, Anne-Claire Boschat , Sylvia Sanquer, Ida Chiara Guerrera, Patrick Revy, Mélanie Parisot, Cécile Masson, Nathalie Boddaert, Marina Charbit, Stéphane Decramer, Robert Novo, Marie-Alice Macher, Bruno Ranchin, Justine Bacchetta, Audrey Laurent, Sophie Collardeau-Frachon, Albertien M. van Eerde, Friedhelm Hildebrandt, Daniella Magen, Corinne Antignac, Herman van Tilbeurgh & Géraldine Mollet

Nature Communications *10, (2019) 3967*

Original article

nature COMMUNICATIONS

ARTICLE

https://doi.org/10.1038/s41467-019-11951-x OPEN

Defects in t^6A tRNA modification due to *GON7* and *YRDC* mutations lead to Galloway-Mowat syndrome

Christelle Arrondel et al.#

N^6-threonyl-carbamoylation of adenosine 37 of ANN-type tRNAs (t^6A) is a universal modification essential for translational accuracy and efficiency. The t^6A pathway uses two sequentially acting enzymes, YRDC and OSGEP, the latter being a subunit of the multiprotein KEOPS complex. We recently identified mutations in genes encoding four out of the five KEOPS subunits in children with Galloway-Mowat syndrome (GAMOS), a clinically heterogeneous autosomal recessive disease characterized by early-onset steroid-resistant nephrotic syndrome and microcephaly. Here we show that mutations in *YRDC* cause an extremely severe form of GAMOS whereas mutations in *GON7*, encoding the fifth KEOPS subunit, lead to a milder form of the disease. The crystal structure of the GON7/LAGE3/OSGEP subcomplex shows that the intrinsically disordered GON7 protein becomes partially structured upon binding to LAGE3. The structure and cellular characterization of GON7 suggest its involvement in the cellular stability and quaternary arrangement of the KEOPS complex.

Correspondence and requests for materials should be addressed to H.T. (email: herman.van-tilbeurgh@i2bc.paris-saclay.fr) or to G.M. (email: geraldine.mollet@inserm.fr). #A full list of authors and their affiliations appears at the end of the paper.

Transfer RNAs (tRNA) are subject to multiple post-transcriptional modifications that are important for the stabilization of their ternary structure and the precision of the decoding process[1]. The majority of the complex modifications are concentrated in the anticodon region of the tRNAs and are crucial for accuracy of protein synthesis. The threonylcarbamoylation of the N^6 nitrogen of the adenosine at position 37 (t^6A) of most ANN-accepting tRNAs represents one of the very few nucleotide modifications that exists in every domain of life[2,3]. The t^6A biosynthesis pathway consists of two steps: firstly, the YRDC enzyme (Sua5 in yeast) synthesizes an unstable threonylcarbamoyl-AMP intermediate (TC-AMP) and in a second step, the KEOPS protein complex transfers the TC-moiety from TC-AMP onto the tRNA substrate[4]. Enzymes that synthesize TC-AMP exist in two versions depending on the organism: a short form which only has the YrdC domain (such as human YRDC) and a long form which has an extra Sua5 domain (yeast SUA5 for instance). The eukaryotic KEOPS complex contains five subunits GON7/LAGE3/OSGEP/TP53RK/TPRKB that are arranged linearly in that order[5–8]. OSGEP is the catalytic subunit that carries out the TC-transfer reaction and its orthologs are present in virtually all sequenced genomes[9]. The other subunits are essential for the t^6A modification of tRNA, but their precise roles are as yet unknown, especially that of GON7, an intrinsically disordered protein (IDP), which was only recently identified in humans[5,7]. Fungal Gon7 was shown to be an IDP that adopts a well-defined structure covering 50% of its sequence upon complex formation with Pcc1 (LAGE3 homolog)[8]. In humans, GON7 was recently shown to be also structurally disordered in absence of the other KEOPS complex subunits. GON7 was proposed to be a very remote homolog of the yeast Gon7 protein although its structure upon complex formation remains unknown[5,7].

tRNA modifications have been demonstrated to play a role in the development of the brain and nervous system, and an increasing number of defects in these modifications are now being linked to various human neurodevelopmental disorders[10]. We recently identified autosomal recessive mutations in genes encoding four of the five subunits of human KEOPS complex, namely *LAGE3*, *OSGEP*, *TP53RK,* and *TPRKB* in patients with Galloway-Mowat syndrome (GAMOS, OMIM#251300). GAMOS is a rare neuro-renal disorder characterized by the co-occurrence of steroid-resistant nephrotic syndrome (SRNS) with microcephaly and neurological impairment[11]. GAMOS is clinically heterogeneous, reflecting a genetic heterogeneity. Indeed, disease-causing mutations have been identified in eight genes to date: four in KEOPS genes and four in other unrelated genes, *WDR73*, *WDR4*, *NUP133*, and *NUP107* (refs. [12–17]). SRNS is typically detected in the first months of life and most often rapidly progresses to end-stage renal disease (ESRD) within a few months; however, there are rarer cases with preserved renal function in adulthood[18]. Kidney lesions range from minimal change disease, to focal segmental glomerulosclerosis (FSGS) that might be of the collapsing type, or diffuse mesangial sclerosis (DMS). Cerebral imaging findings include cerebral and cerebellar atrophy, and gyration and/or myelination defects. These anomalies are associated with neurological deficits such as psychomotor impairment, hypotonia, seizures, and more rarely sensorineural blindness and deafness. Affected children may also present with facial and/or skeletal dysmorphic features. The prognosis of GAMOS is poor, and most affected children die before 6 years of age.

Here we present 14 GAMOS-affected individuals from seven families, with mutations in *GON7* (alias *C14orf142*) and *YRDC*, both genes encoding proteins involved in the biosynthesis of the t^6A modification. These data, together with our previous work, show that mutations in genes encoding all the proteins involved in the two chemical steps of t^6A lead to GAMOS. Furthermore, we determine the crystal structure of the GON7/LAGE3/OSGEP KEOPS subcomplex showing that GON7 becomes structured upon binding to LAGE3. The structure also explains our observations that GON7 stabilizes the remainder of the KEOPS complex and directs its quaternary organization.

Results

Identification of *GON7* and *YRDC* mutations in GAMOS patients. Through whole-exome sequencing in individuals with GAMOS, we identified mutations in the *GON7* gene in 11 affected individuals from 5 unrelated families and in the *YRDC* gene in 3 affected individuals from 2 unrelated families (Fig. 1a–d and Supplementary Table 1). Four of the families with *GON7* mutations (Families A to D) carried the same homozygous nonsense mutation (c.21 C>A, p.Tyr7*) which causes a stop codon at position 7 of the protein. These families, all originating from the same region of Algeria, shared a common haplotype at the *GON7* locus indicating a founder effect (Supplementary Table 2). The affected individual of the fifth family (Family E) carried a different mutation involving the same residue at position 7 and leading to a frameshift (c.19dup, p.Tyr7Leufs*16). Both *GON7* mutations are predicted to lead to the absence of protein expression and, as expected, no protein was detected in cells available from the affected individuals from family A, B, and C (Supplementary Fig. 1a, c). Two compound heterozygous *YRDC* mutations were identified in Family F: a missense mutation (c.251 C>T, p.Ala84Val) and a 4-base pair deletion leading to a frameshift (c.721_724del, p.Val241Ilefs*72). In Family G, we identified a homozygous in-frame deletion of Leucine 265 (c.794_796 del, p.Leu265del). For both families, western blot and qPCR analysis on cell extracts from affected children showed the presence of YRDC transcripts and proteins (Supplementary Fig. 1b, d). To make a prediction of the effect of the *YRDC* mutations on the protein, we created a three-dimensional (3D) structural model of human YRDC using the structure of the YRDC domain of the archaeal Sua5 (PDB 4E1B, 20% sequence identity[19]) and mapped these mutations onto this in silico model (Fig. 1e). Structures of YRDC domains are very well conserved and sequence alignment shows that the human YRDC only has minor insertions/deletions compared to Sua5 (Supplementary Fig. 2). The replacement of Ala84, located in a hydrophobic region between a β-sheet and a connecting α-helix, by the larger amino acid valine might perturb optimal packing and destabilize the structure of the protein. The YRDC Leu265del mutation affects a highly conserved amino acid and creates a deletion in a C-terminal peptide that hangs over the active site and could have a role in enzyme activity.

Early-onset proteinuria was observed in all affected children, with first detection ranging from between birth and 5 years. All but three children reached ESRD between 1.5 months and 6 years of age. All individuals carrying *YRDC* mutations presented with congenital or infantile SRNS detected from between birth and 4 months of age and died early, whereas most of the individuals carrying *GON7* mutations were alive at last follow-up, with either a functioning graft or with normal renal function despite a mild to heavy proteinuria (Supplementary Table 1). Kidney biopsies, when available, typically displayed FSGS (Families A, C, and E) or DMS (Families B, F, and G) (Fig. 2a–d). In addition to developmental delay, primary microcephaly was present in the two affected children of one family with *YRDC* mutations, whereas the affected child in the second *YRDC* family and all *GON7*-mutated individuals presented with post-natal microcephaly. Brain magnetic resonance imaging revealed a spectrum of cerebellar and cortical hypoplasia or atrophy with thin corpus callosum and ventricular dilation, myelination delay, and in one case a simplified gyral pattern (Individual G.II-2) (Fig. 2e–n,

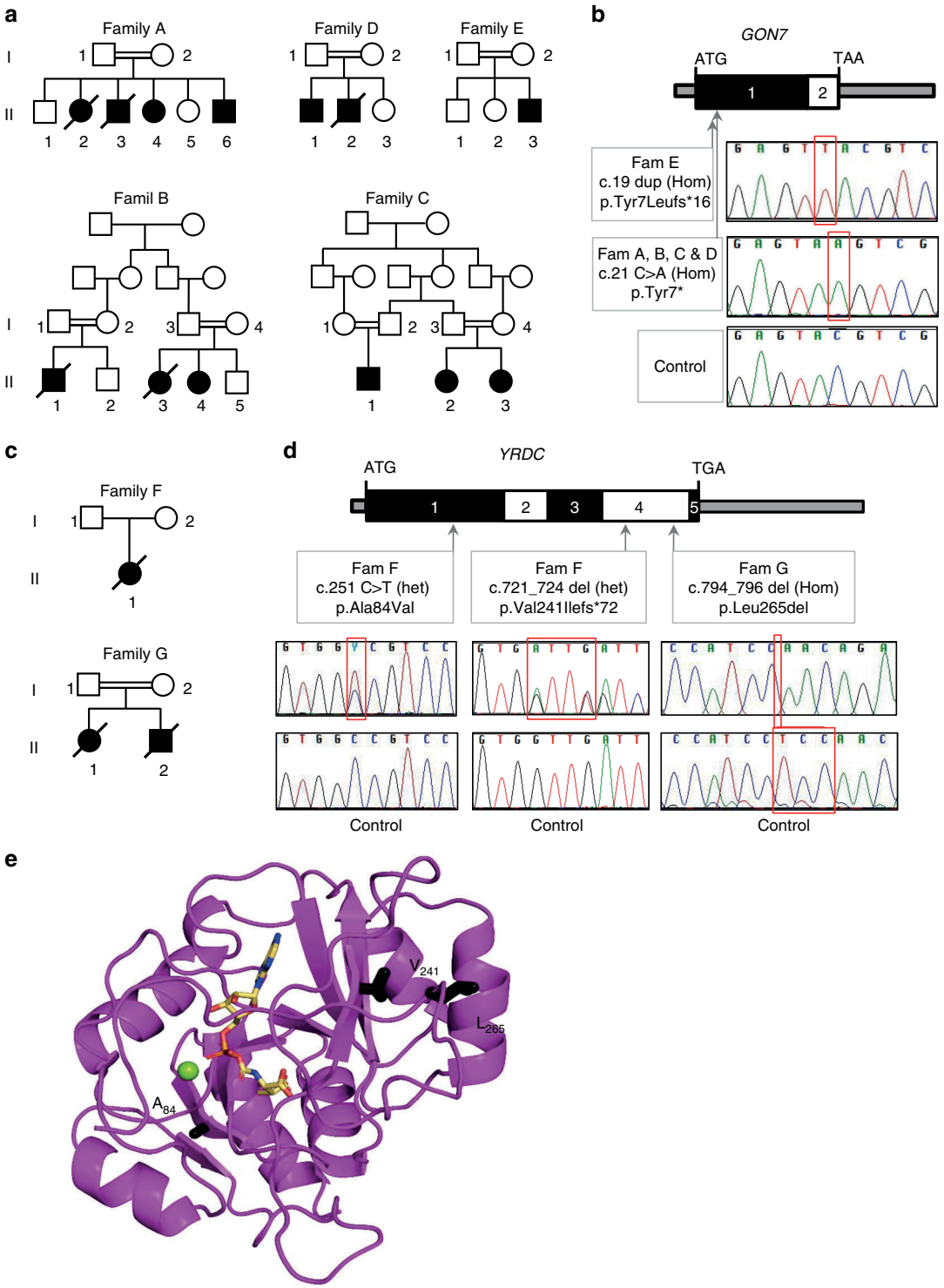

Fig. 1 Identification of mutations in *GON7* and *YRDC* in patients with Galloway-Mowat syndrome. **a**, **c** Pedigrees of families with mutations in *GON7* (**a**) and in *YRDC* (**c**). Affected individuals are in black. **b**, **d** Organization of exons of human *GON7* and *YRDC* cDNAs. Positions of start and stop codons are indicated. Arrows indicate positions of the identified mutations. Lower panels show the sequencing traces for affected individuals with identified mutated nucleotide indicated with a red square (Hom: homozygous; het, heterozygous). **e** Representation of a 3D model of human YRDC, bound to the reaction product threonylcarbamoyl-adenylate, in sticks. The model was constructed using the crystal structure of *Sulfolobus tokodaii* Sua5 (PDB code 4E1B). The side chains of the three mutated residues are in black sticks. The green sphere represents an Mg^{2+} ion

Supplementary Fig. 3). Extra-renal features included facial dysmorphy, arachnodactyly, hiatal hernia with gastro-esophageal reflux, congenital hypothyroidism (solely in the *YRDC* cases), and myoclonia. This clinical picture is highly reminiscent of that observed in GAMOS-affected individuals with mutations in *LAGE3*, *OSGEP*, *TP53RK*, and *TPRKB*[13]. However, individuals with *GON7* mutations presented with milder neurological and renal manifestations, always with post-natal microcephaly and no gyration defects, later onset of proteinuria (median age 18 months vs. 1) and slower progression to ESRD

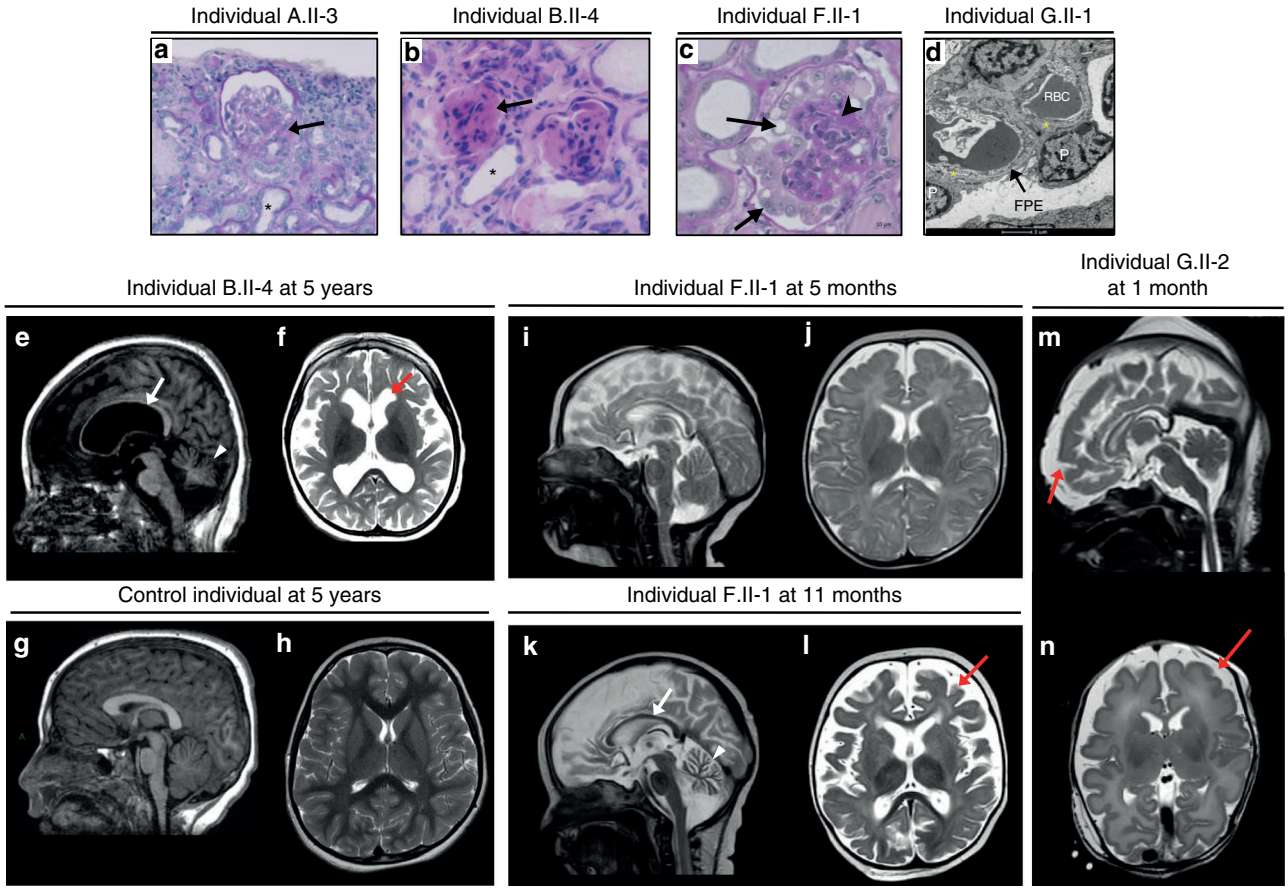

Fig. 2 Kidney pathology analysis and neuroimaging. Light and transmission electron microscopy (TEM) of kidney sections of patients with *GON7* (**a**, **b**) or *YRDC* mutations (**c**, **d**). **a** Individual A.II-3 displays a retracted glomerulus with a focal segmental glomerulosclerosis lesion at the vascular pole (black arrow) and tubular dilations (black star) (PAS; ×200 magnification). **b** Individual B.II-4 displays diffuse mesangial sclerosis with tiny, retracted and sclerosed glomeruli (black arrow) with dilated tubes surrounded by flat epithelial cells (black star) and interstitial fibrosis (H&E; ×400 magnification). **c** Individual F.II-1 displays a marked glomerular tuft collapsing (arrowhead) surrounded by a layer of enlarged and vacuolized podocytes (black arrows) (PAS stain; ×400 magnification, scale bar, 10 µm). **d** TEM of individual G.II-1 shows diffuse foot process effacement (FPE; black arrow), a classical hallmark of nephrotic syndrome, along a glomerular basement membrane (GBM) with abnormal folded and laminated segments (yellow stars), alternating with others with normal appearance. P podocyte, RBC red blood cell. Scale bar, 2 µm. Brain MRI of patients with *GON7* (**e**, **f**) and *YRDC* mutations (**i**–**n**). **e**, **f** Brain MRI abnormalities in individual B.II-4 at 5 years. Sagittal T1-weighted image (**e**) shows important cortical subtentorial atrophy as well as corpus callosal (arrow) and cerebellar atrophy (arrowhead). The axial T2-weighted image (**f**) shows abnormal myelination and ventricular dilatation (red arrow). **g**, **h** Brain MRI of a 5-year old control showing sagittal T1 (**g**) and axial T2 (**h**) weighted images. **i**–**l** Brain MRI abnormalities in individual F.II-1 at 5 months (**i**, **j**) and 11 months (**k**, **l**). Sagittal T2-weighted image shows normal pattern at 5 months (**i**) evolving to a progressive major cerebellar (arrowhead) and cortical atrophy with a very thin corpus callosum (arrow) at 11 months (**k**). The axial T2-weighted image is normal at 5 months (**j**) but shows a very marked abnormality of myelination and cortical atrophy (red arrow) at 11 months (**l**). **m**, **n** Brain MRI abnormalities in individual G.II-2 at 1 month. Sagittal T2 (**m**) and axial T2 (**n**) weighted images show gyral anomalies with marked frontal gyral simplification (red arrow) and myelination delay

(median age 49 months in 8/11 children vs. 5 months in 3/3 children), and a longer survival compared to the *YRDC* cases.

Impact of *YRDC* and *GON7* mutations on t^{6}A biosynthesis. To assess the pathogenicity of *YRDC* mutations, we first used a yeast heterologous expression and complementation assay as previously performed for *OSGEP* mutations identified in GAMOS individuals[13]. Indeed, the deletion of *SUA5*, the *YRDC* ortholog in *S. cerevisiae* leads to a very severe growth defect, similarly to the deletion of each of the genes encoding the five KEOPS subunits[3,6,20,21]. We therefore heterologously expressed the human YRDC cDNAs encoding wild-type (WT) and mutant proteins in the *Δsua5* strain to evaluate their ability to rescue the slow growth phenotype. Since the catalytic activity of YRDC does not require protein partners, the WT YRDC protein efficiently complemented the *Δsua5* growth defect (Fig. 3a). Although a somewhat similar complementation was observed for the p.Ala84Val and p.Leu265del mutants, the p.Val241Ilefs*72 mutant was notably unable to improve the poor growth of the *Δsua5* strain (Fig. 3a). All YRDC proteins were efficiently expressed in *Δsua5* strain, except the p.Val241Ilefs*72 mutant that was barely detectable by western blot, suggesting that it is likely being degraded by an intracellular proteolytic machinery (Fig. 3b). Using mass spectrometry, we then analyzed the t^{6}A content of these transformed *Δsua5* yeast strains. As expected, since Sua5 is the only enzyme in yeast that generates TC-AMP, the *Δsua5* mutant was unable to synthetize t^{6}A, whereas the WT YRDC expressing strain exhibited t^{6}A levels comparable with those measured for WT Sua5 (Fig. 3c). The p.Ala84Val and p.Leu265del mutants showed a slight, but significant decrease in t^{6}A levels. In contrast, like in the *Δsua5* strain, no trace of t^{6}A modification could be detected in the p.Val241Ilefs*72 mutant (Fig. 3c). In line with the results of the growth complementation assay, there was a

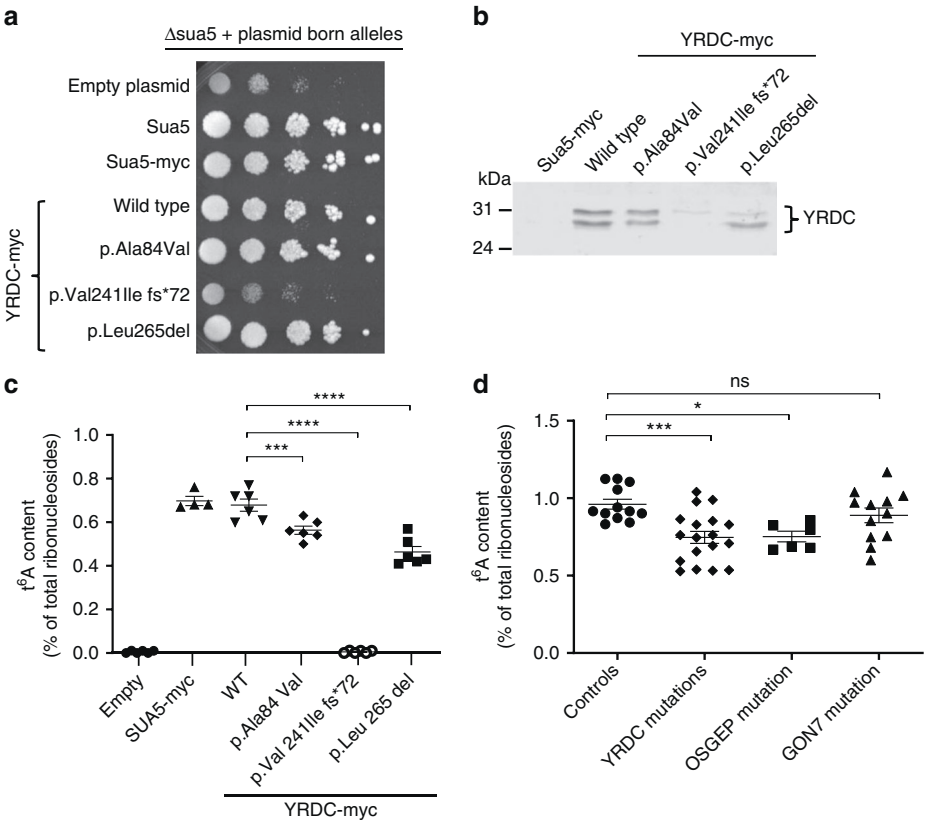

Fig. 3 Effects of *YRDC* and *GON7* mutations on t^6A biosynthesis. **a** Evaluation of fitness of *Δsua5* yeast strains expressing human YRDC variants (spots are from 10-fold serial dilutions of cell suspensions at $OD_{600nm} = 0.5$, and three independent clones were evaluated) and **b** western blot analysis on total protein extracts from *Δsua5* yeast cells expressing human *YRDC* variants using anti-hYRDC antibody. **c**, **d** Mass spectrometry (LC-MS/MS) quantification of t^6A modification in total tRNAs extracted from *Δsua5* yeast cells expressing human YRDC variants (**c**) (mean ± s.e.m. of two independent LC-MS/MS experiments (technical replicates), each measuring samples from three independent yeast transformants; one-way ANOVA (F (5,28) = 269.4, $p < 0.0001$), Dunnett's multiple comparisons test, $^{***}p = 0.0008$, $^{****}p < 0.0001$) and from cultured primary skin fibroblasts from controls (two unaffected individuals) and affected individuals with either the p.Tyr7* *GON7* mutation (two individuals), or the *YRDC* mutations (three individuals) or with the p.Arg352Gln *OSGEP* mutation in the homozygous state (individual «CP» described in Braun et al.[13]) (**d**) (mean ± s.e.m. of two independent LC-MS/MS experiments (technical replicates), each measuring samples from three independent cell culture experiments; one-way ANOVA (F (3,44) = 6.446, $p < 0.001$), Dunnett's multiple comparisons test, n.s. = 0.4894, $^{*}p = 0.0169$, $^{***}p = 0.008$). Source data are provided as a Source Data file

direct correlation between cell fitness and t^6A content. This allowed us to classify *YRDC* mutations into hypomorphic (encoding p.Ala84Val and p.Leu265del) and amorphic (encoding p.Val241Ilefs*72) alleles, as has been previously shown for *OSGEP* mutations[13]. A similar approach could not be applied for *GON7* mutations since GON7 failed to complement the growth defect of the *Δgon7* yeast strain (see ref. [7] and our data). We therefore measured the t^6A content in fibroblasts from two individuals with the p.Tyr7* *GON7* mutation, three individuals with *YRDC* mutations and one individual with the p.Arg325Gln *OSGEP* mutation. The t^6A levels were significantly decreased in both *YRDC*- and *OSGEP*-mutated fibroblasts, and to a lesser extent in *GON7*-mutated fibroblasts (Fig. 3d) confirming the impact of these mutations on t^6A biosynthesis in affected individuals. In addition, we demonstrated that, similarly to individuals with *OSGEP* or *TP53RK* mutations[13], telomere length was not affected in individuals with *YRDC* and *GON7* mutations (Supplementary Fig. 4). This confirms that contrary to what has been demonstrated in yeast, human YRDC, and KEOPS complex are not involved in telomere maintenance in human cells[22–24].

In vitro characterization of WT and mutants YRDC. To compare the stability and structure of the WT YRDC with those of the p.Ala84Val and p.Leu265del mutants, we expressed and purified these proteins in an *E. coli* expression system (Supplementary Table 3). The three proteins could be purified but we noticed that both mutants were less stable and less soluble compared to the WT (Supplementary Methods). To probe the proper folding of the YRDC WT and mutants, we collect 1D ^{1}H-NMR spectra (Supplementary Fig. 5a). All the spectra displayed well-dispersed signals for amide protons as well as several signals at chemical shifts lower than 0.8 ppm that are typical of methyl groups in the hydrophobic core of proteins, suggesting the WT and mutants were well folded. To compare their enzymatic properties, we measured their TC-AMP synthesizing activities in vitro by quantifying the pyrophosphate reaction product. The p.Ala84Val and p.Leu265del mutants have lost about 75% and 30% of their activities respectively compared to WT (Supplementary Fig. 5b). The activities of these mutants are compatible with their hypomorphic nature, as suggested by the results of the yeast *Δsua5* complementation experiments (Fig. 3a).

Proliferation, apoptosis, and protein synthesis defects. We have previously shown that transient gene expression knockdown (KD) of human KEOPS components *OSGEP*, *TP53RK*, and *TPRKB* leads to perturbations of various cellular processes including proliferation and apoptosis[13]. Similarly here, we transiently depleted the expression of *GON7* and *YRDC*, as well as *LAGE3* and *OSGEP* as

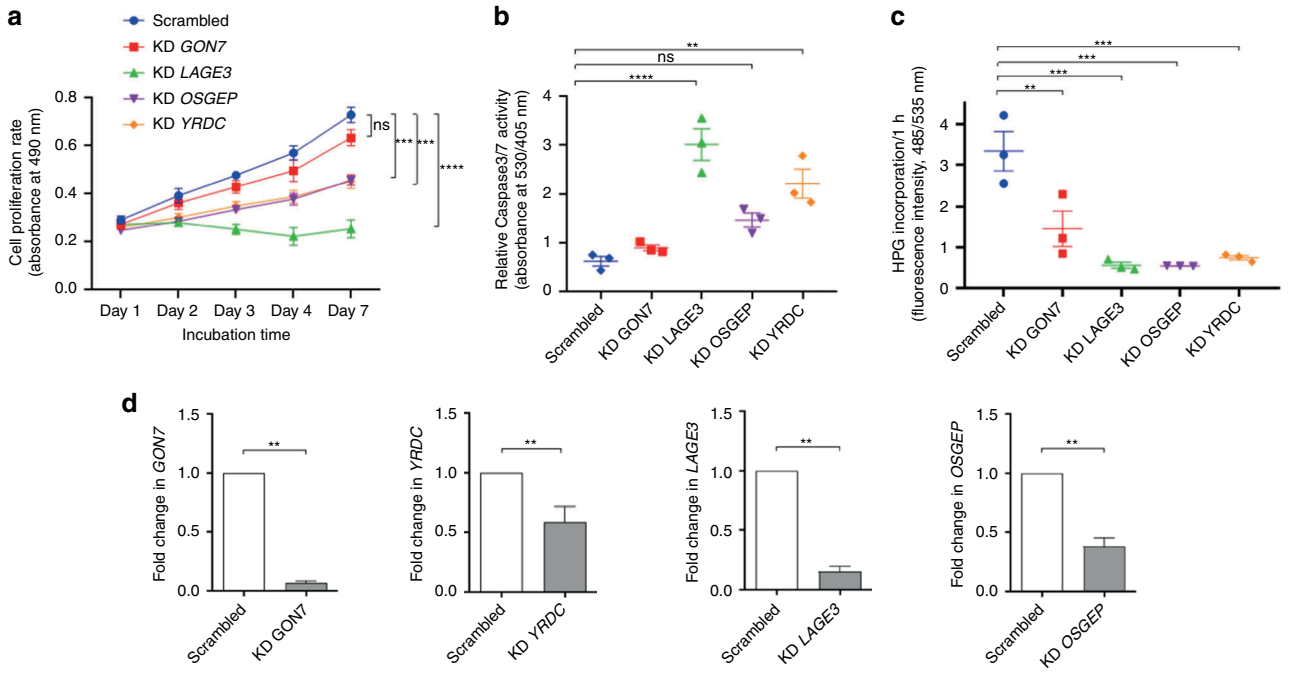

Fig. 4 Proliferation, apoptosis, and protein synthesis defects upon *GON7* and *YRDC* knockdown. Transient knockdown (KD) of *GON7*, *LAGE3*, *YRDC*, and *OSGEP* was performed by lentiviral transduction of shRNA in immortalized human podocyte cell lines with a scrambled (non-targeting) shRNA as control. **a** Cell proliferation was assessed using a colorimetric MTT assay over 7 days, measuring absorbance at 490 nm at days 1, 2, 3, 4, and 7 (mean ± s.e.m. of $n = 5$ experiments, with each experiment performed in triplicate; two-way ANOVA ($p < 0.0001$), Dunnett's multiple comparisons test, n.s. = 0.2031, ***$p < 0.0007$, ****$p < 0.0001$). **b** Cell apoptosis was evaluated by quantification of caspase 3/7 activation on the basis of fluorescence intensity (530/405 nm). Absolute values were normalized to DAPI fluorescence intensity as an internal control and compared to non-targeting shRNA-treated control cells (scrambled) (mean ± s.e.m. of $n = 3$ experiments with each experiment performed in triplicate; one-way ANOVA (F (4,10) = 21.42, $p < 0.0001$), Dunnett's multiple comparisons test, n.s. = 0.0556, **$p = 0.0012$, ****$p < 0.0001$). **c** Protein biosynthesis rates were assessed on the basis of incorporation of HPG, an alkyne-containing methionine analog. After 2 h, alkyne-containing proteins were quantified on the basis of fluorescence intensity (485/535 nm). Absolute values were normalized to DAPI fluorescence intensity as an internal control and compared to control cells (mean ± s.e.m. of $n = 3$ experiments, with each experiment performed in triplicate, one-way ANOVA (F (4,10) = 16.36, p= 0.0002), Dunnett's multiple comparisons test, **$p = 0.0035$, ****$p < 0.0003$). **d** Relative expression of *GON7*, *YRDC*, *LAGE3*, and *OSGEP* transcripts were normalized to that of HPRT in KD podocytes compared to non-targeting shRNA control treated cells (mean ± s.e.m. of $n = 5$ experiments, with each experiment being performed in triplicate; two-tailed Mann–Whitney test, **$p < 0.05$). Source data are provided as a Source Data file

positive controls, in an immortalized human podocyte cell line[25]. We then demonstrated using a colorimetric cell proliferation assay that diminished expression of all four of these genes decreased cell proliferation, with the strongest decrease being observed in *LAGE3* KD podocytes (Fig. 4a). Despite efficient *GON7* KD, cells exhibited only a slight decrease in cell proliferation compared to cells treated with the control scrambled shRNA (Fig. 4a, d). The impairment of cell proliferation in *YRDC* and *OSGEP* KD cells was less marked than in *LAGE3* KD cells, which could be explained by a less efficient gene silencing (Fig. 4d). By measuring Caspase-3/7 activity, we next demonstrated that apoptosis was inversely related to proliferation with *LAGE3* KD podocytes displaying the highest rate of apoptosis (Fig. 4b). Since loss of t^6A modification impacts global translation in yeast[26], we also quantified the newly synthetized protein levels, which were decreased in all KD cells (Fig. 4c), even in *GON7* KD podocytes where proliferation and apoptosis rates were not drastically affected (Fig. 4a, b). Altogether, these results reinforce our previous findings for the other KEOPS subunits, OSGEP, TP53RK, and TPRBK, and confirm that mutations which alter t^6A biosynthesis in human cells have an impact on cell survival through decreased proliferation and protein synthesis, ultimately leading to apoptosis.

Structure of the human GON7/LAGE3/OSGEP subcomplex. To better understand the role of human GON7 and how its loss of function could be connected with GAMOS, we set out to determine its structure and to establish how it interacts with the other KEOPS subunits. We had either crystal structures (TPRKB) or good quality 3D models (LAGE3, OSGEP, TP53RK) for all of the KEOPS subunits at our disposal, except for GON7 (ref. [6]). Based on very weak sequence similarity, it was proposed, that GON7 is a remote homolog of yeast Gon7 (ref. [7]). We first investigated the structure of GON7 in solution by collecting a 2D ^{1}H-^{15}N Band-Selective Optimized Flip Angle Short Transient Heteronuclear Multiple-Quantum Correlation (SOFAST-HMQC) NMR spectrum of a ^{15}N-labeled GON7 sample. The poor spectral dispersion in the ^{1}H dimension of the 2D correlation spectrum showed that GON7 lacks well-defined structure, confirming the conclusions of Wan et al.[7]. Adding non-labeled LAGE3 to the sample, caused the shift and/or disappearance for many crosspeaks, suggesting GON7 interacts with LAGE3 (Supplementary Fig. 6a). We further characterized the conformation of GON7 in solution by small-angle X-ray scattering (SAXS) measurements. By representing the scattering data as a dimensionless Kratky plot ($qR_g^2 \times I_q/I_0$ versus qR_g), one can assess qualitative information on the degree of compactness of the scattering object[27]. The plateau observed for GON7 is characteristic of a fully disordered protein, possibly with very short elements of secondary structure (Fig. 5a), confirming our NMR data (Supplementary Fig. 6a). We then purified the recombinant GON7/LAGE3/OSGEP complex and analyzed its behavior in solution by SAXS. Our SAXS data

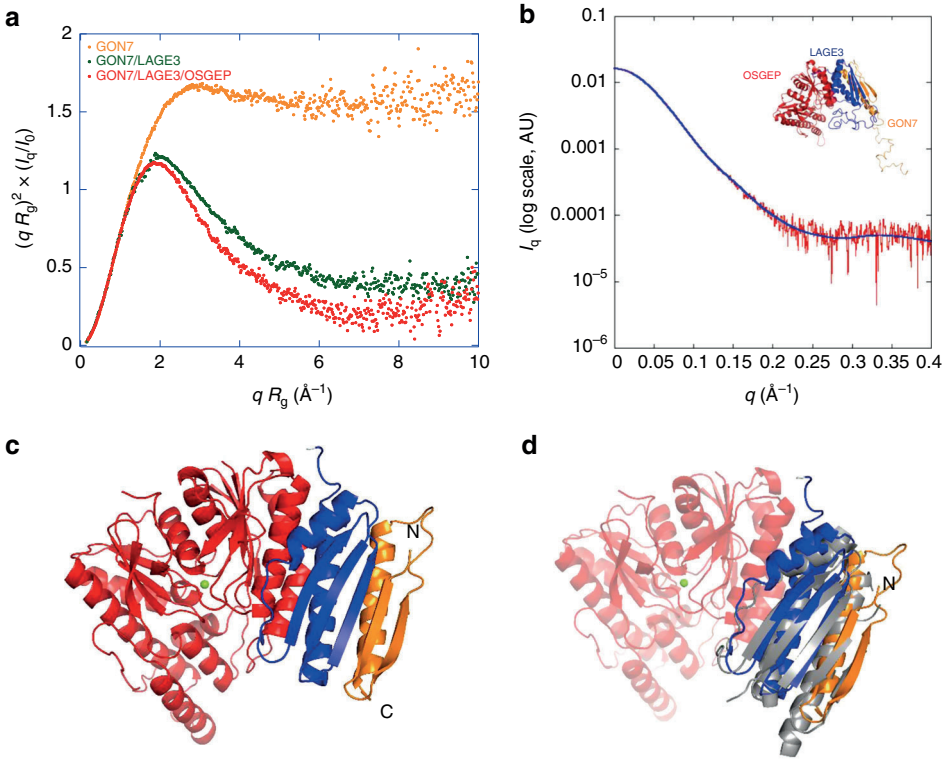

Fig. 5 Structure of the GON7/LAGE3/OSGEP complex. **a** Normalized Kratky plot of intensity scattering of GON7 (orange) and of the GON7/LAGE3 (green) and GON7/LAGE3/OSGEP complexes (red). q: scattering vector, R_g radius of gyration, I_q: scattering intensity, I_0: scattering intensity at zero angle. **b** Experimental x-ray scattering curve of the GON7/LAGE3/OSGEP complex (red). The blue curve represents the calculated scattering curve for the corresponding crystal structure of the complex. This yielded a good fit with the experimental data ($\chi^2 = 0.33$). The inset shows the BUNCH model. **c** Representation of the crystal structure of the GON7/LAGE3/OSGEP complex: GON7 (gold), LAGE3 (blue), OSGEP (red). The N and C-termini of GON7 are labeled. The crystal lacked density for GON7 beyond residue 50. The active site of OSGEP is highlighted by the Mg^{2+} ion (green). **d** Superimposition of the yeast Gon7/Pcc1 complex (gray) onto GON7/LAGE3/OSGEP. GON7/LAGE3/OSGEP (same color code as in panel **c**)

established that the complex has a 1:1:1 stoichiometry in solution (Fig. 5b, Supplementary Table 4). In contrast with GON7, the dimensionless Kratky plot for GON7/LAGE3/OSGEP shows a bell-shaped curve with a maximum for $qR_g \approx 2$ (Fig. 5a). This shape suggests that the complex is mainly compact, but that disordered regions are still present. In addition, the comparison of the distance distribution functions of GON7/LAGE3/OSGEP and GON7 shows that the latter alone is more extended than the complex (Supplementary Fig. 6b). In full agreement, the ^{15}N SOFAST-HMQC NMR spectrum of the complex reveals that about 35 amino-acid residues of GON7 remains flexible and disordered in the complex whereas ~35 crosspeaks vanished upon complex formation. These latter crosspeaks likely correspond to amino-acid residues engaged in the interaction with LAGE3 and thus experiencing extensive line-broadening due to the large molecular size of the complex. We therefore deduced that GON7 is becoming partially ordered upon complex formation with LAGE3/OSGEP and set out to determine its structure by X-ray crystallography. We obtained 1.9 Å resolution diffraction data of the GON7/LAGE3/OSGEP complex (Fig. 5c, d, Supplementary Table 5). The structure could be solved by molecular replacement using our 3D models of OSGEP and LAGE3 (refs. [8,13,23]). LAGE3 contains 60 residues at the N-terminus that are absent in the Pcc1 orthologs from yeast and archaea and that are predicted to be disordered. We did not observe any electron density for this N-terminal peptide, confirming this region indeed lacks a stable structure. We cannot exclude however that partial proteolysis removed this peptide during the long crystallization process. LAGE3 is at the center of the complex, binding on one side to OSGEP and on the other to GON7, which does not directly interact with OSGEP (Fig. 5c). The structures of the LAGE3 and OSGEP subunits are very similar to their archaeal/fungal Pcc1 and Kae1 orthologs respectively. The two helices of LAGE3 associate with the N-terminal helices of OSGEP into a helical bundle. Only 45% of the GON7 sequence adopts a well-defined structure upon binding to LAGE3, confirming our SAXS- and NMR-based conclusions (Fig. 5a, Supplementary Fig. 6a–d). The N-terminal peptide of GON7 forms a β-hairpin between Met1 and Ser20 and the region between Gly25 and Pro50 forms a helix that lies parallel against the β-hairpin (Supplementary Fig. 7). Electron density for GON7 was absent for residues 21 to 24 and for the region beyond position 50. The C-terminal half of GON7 is highly enriched in acidic and sparse in hydrophobic amino acids and predicted to be unfolded. Despite their very weak sequence similarity (19% identity, 34% similarity), the structures of human GON7 and yeast Gon7 are almost identical (RMSD = 1.41 Å for 45 Cα positions; yeast Gon7 PDB entry: 4WXA) (Fig. 5d, Supplementary Fig. 7). The β-hairpin of GON7 aligns with the β-sheet of LAGE3 to form a continuous five stranded anti-parallel sheet. The helix of GON7 packs in an anti-parallel orientation against the C-terminal helix of LAGE3. The complex is stabilized mainly by the hydrophobic packing of side chains emanating from β1 and α1 of GON7 and α2 and β1 of LAGE3. The association mode between GON7 and LAGE3 is very similar to that of the yeast Pcc1/Gon7 complex, illustrated by their superposition (RMSD = 1.4 Å; Fig. 5d). Structure based sequence alignment between human GON7 and yeast Gon7 shows that only 6 out of 45 ordered residues (12%) are conserved (Supplementary Fig. 7). Compared to human GON7, yeast Gon7 is longer by about 20 residues that were disordered in its structure.

The experimental SAXS curve of the GON7/LAGE3/OSGEP complex in solution is in excellent agreement ($\chi^2 = 0.33$) with the scattering curve calculated on the all-atom model built using the program BUNCH from the crystal structure (see Methods) (Fig. 5b). We therefore conclude that, although sharing very low sequence homology, human GON7 and yeast Gon7 are homologs that interact identically with their respective partners (LAGE3, Pcc1) in the human and yeast KEOPS complex.

Role of human GON7 in KEOPS complex stability in vivo. We further explored the deleterious cellular effects of the GAMOS-associated *GON7* mutations. We first confirmed by mass spectrometry analysis that in a human podocyte cell line stably overexpressing either 2HA-tagged GON7 or V5-tagged LAGE3, the four additional KEOPS subunits significantly co-purified with GON7 or LAGE3, respectively, thus confirming that a five-subunit KEOPS complex is present in these renal glomerular cells (Supplementary Fig. 8a). We have previously demonstrated that the majority of GAMOS-associated mutations in genes encoding KEOPS complex components do not affect the intermolecular interactions between the LAGE3/OSGEP/TP53RK/TPRKB subunits[13]. In order to check whether mutations in LAGE3 affected GON7 binding, we co-expressed 2HA-tagged GON7 with WT or mutant V5-tagged LAGE3 in HEK293T cells. Our co-immunoprecipitation experiments demonstrated that the LAGE3 mutations found in GAMOS individuals do not prevent binding to GON7 (Supplementary Fig. 8b). Intriguingly, however, we noticed that co-expression of GON7 with LAGE3 in HEK293T cells led to an increased expression level of GON7, and to a lesser extent of LAGE3, suggesting that the interaction stabilizes both proteins (Fig. 6a). We therefore studied the stability of GON7 and LAGE3 in a time-course experiment using cycloheximide, an inhibitor of protein biosynthesis, in HEK293T cells transiently expressing either 2HA-GON7 or V5-LAGE3 alone or co-expressing both tagged-proteins. When expressed alone, GON7 and LAGE3 protein levels decreased, suggesting both proteins may be unstable in absence of their partner. This is particularly obvious for GON7 whose protein level decreased by half within an hour following cycloheximide addition (Fig. 6b, Supplementary Fig. 9). On the contrary, when co-expressed, we observed an increase of both GON7 and LAGE3 protein levels reflecting an increase in their stability. We wondered whether the absence of GON7 also impacts the stability of the whole KEOPS complex and indeed, we were able to demonstrate that the protein levels of the four KEOPS subunits were decreased in cells of individuals mutated for *GON7*, whereas they were not affected in cells of individuals with *OSGEP* or *WDR73* mutations, the latter being also responsible for a specific subset of GAMOS cases not linked to a t^6A biosynthesis defect[15] (Fig. 6c, Supplementary Fig. 10a). In addition, we demonstrated that this protein level decrease was not due to transcriptional regulation (Supplementary Fig. 10b). Altogether, these results suggest that the absence of GON7 affects KEOPS stability resulting in a decreased expression level of the four other subunits, which might impact t^6A levels.

Discussion

In this study, we identified mutations in two genes encoding proteins involved in t^6A biosynthesis in GAMOS patients: *YRDC* encoding the enzyme that synthesizes the TC-AMP intermediate used by the KEOPS complex and *GON7* encoding the fifth subunit of the KEOPS complex. Functional analysis of these specific mutations has revealed that they directly impact t^6A modification (*YRDC*) and/or affect the stability of the KEOPS complex (*GON7*). These results complement our previous findings and establish that mutations in all the genes involved in this pathway lead to GAMOS.

All individuals bearing *GON7* or *YRDC* mutations present with the clinical features of GAMOS, similarly to the individuals previously reported to have mutations in the genes encoding the four other KEOPS subunits. In addition, we have expanded the GAMOS phenotype spectrum by describing congenital hypothyroidism to be associated with *YRDC* mutations. Although the two *GON7* mutations encode truncated non-functional proteins, we noticed that they unexpectedly result in a less severe clinical outcome compared to that of individuals affected by mutations in other KEOPS subunit genes or in *YRDC*, for which biallelic null mutations were not found. This suggests that the absence of GON7 has less severe consequences for cell life compared to the other components of the t^6A biosynthesis pathway, where four out of six are encoded by genes considered to be essential[28]. This less severe clinical outcome correlates with our data showing that GON7 loss of function and depletion in fibroblasts and podocytes, respectively, have globally a weaker effect on t^6A levels, proliferation, apoptosis, and protein synthesis compared to that of other KEOPS subunits and YRDC mutations or depletion. However, although our data have confirmed that GON7 is a functional homolog of Gon7, the effect of their absence in human and yeast, respectively, is markedly different since in the absence of Gon7, the yeast KEOPS complex has only very low t^6A activity and cell growth is dramatically affected[3]. Altogether, our data in humans suggest that GON7 is not as essential in humans as in yeast for t^6A biosynthesis.

Our biochemical and structural data provide a molecular framework to understand the pathophysiological effects of the GAMOS-associated mutations. The structure of the GON7/LAGE3/OSGEP complex shows that GON7 is bound exclusively to the non-catalytic LAGE3 subunit, distant from the catalytic center of OSGEP. It has been shown in vitro that the intact human KEOPS complex has a 1:1:1:1:1 stoichiometry, in contrast with the complex lacking GON7 which has a 2:2:2:2 stoichiometry[7]. The latter stoichiometry has also been observed for the archaeal KEOPS complex, for which no fifth subunit similar to Gon7 has yet been discovered. The Pcc1 subunit constitutes the dimerization unit of archaeal KEOPS[29] and this is also very likely the case for the LAGE3 subunit of human KEOPS in absence of GON7 (ref. [7]). In line with these results, our structure of the GON7/LAGE3/OSGEP complex shows that GON7 competes with LAGE3 for dimerization, explaining the different stoichiometries of the KEOPS complex observed in the absence or presence of GON7. Indeed, GON7 covers a large hydrophobic surface of LAGE3 (Supplementary Fig. 11), which is very likely occupied by another LAGE3 subunit in the context of a homomeric dimer, as observed in the structure of Pcc1 dimer[29]. The exposure of this hydrophobic surface due to the absence of GON7 in the GAMOS patients may affect the solubility and activity of the KEOPS complex, and indeed, our data from experiments on cell lines further indicate that GON7 contributes to the stability of the KEOPS complex and/or to the maintenance of the correct (catalytically active) quaternary structure as evidenced by the decrease in KEOPS subunits protein levels observed in GON7 patient cells. Taken together, our data demonstrated that GON7 impacts the stability of the KEOPS complex therefore having an effect on its enzymatic activity. This is in line with the in vitro data of Sicheri's group showing that in presence of GON7, KEOPS t^6A activity is potentiated[29] and with our in vivo data showing that t^6A levels in *GON7*-mutated patient fibroblasts are slightly decreased compared to *YRDC*- and *OSGEP*-mutated fibroblasts.

Although human GON7 and yeast Gon7 have low sequence identity, their structures and interactions with LAGE3 and Pcc1,

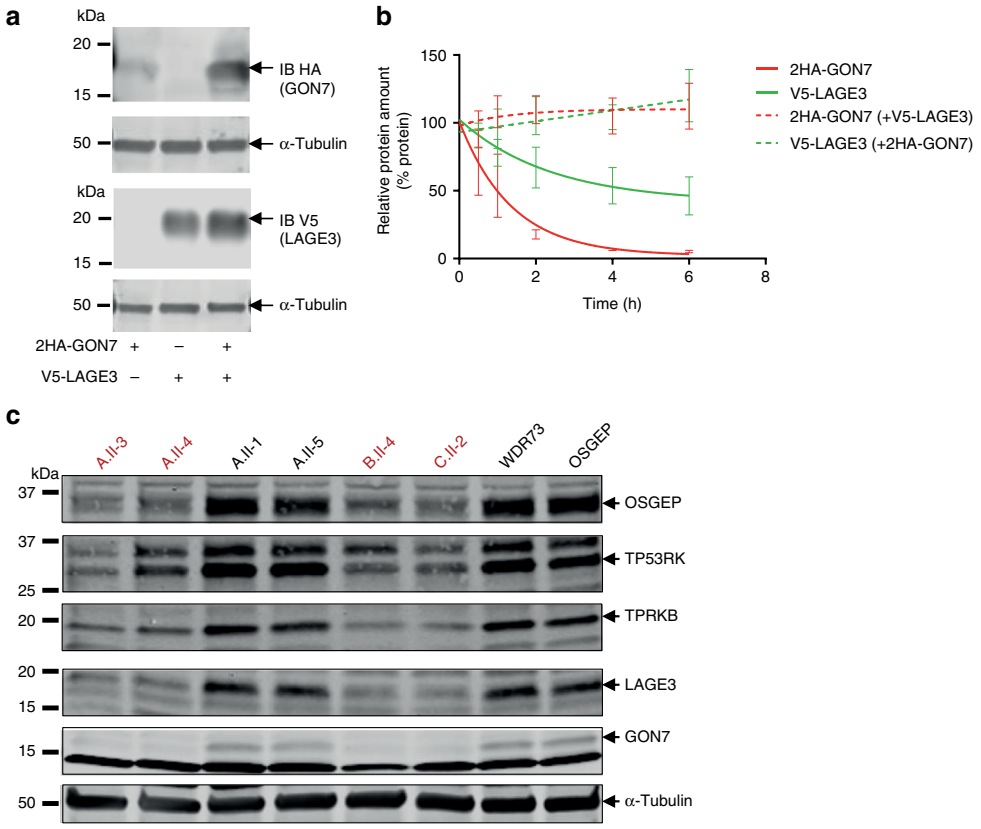

Fig. 6 Role of GON7 on KEOPS complex stability. **a** Immunoblot analysis of HEK293T cell lysates expressing either 2HA-tagged GON7 or V5-tagged LAGE3 alone or co-expressing both proteins. Anti-HA and anti-V5 antibodies were used to assess GON7 and LAGE3 expression, respectively, with α-tubulin used as loading control. **b** Representation of cycloheximide chase experiments by fitting a one-phase exponential decay curve to experimental data (one representative experiment is shown in Supplementary Fig. 9) (mean ± s.e.m. of $n = 3$ experiments). HEK293T cells were transfected with either 2HA-tagged GON7 or V5-tagged LAGE3 alone or with both proteins before being subjected to treatment with 100 µg/ml cycloheximide for the indicated time points in order to assess rates of protein degradation followed by western blotting of the cell lysates for both proteins with anti-HA and anti-V5 antibodies, respectively. GON7 and LAGE3 protein levels were normalized to those of α-tubulin at each time point. **c** Western blot analysis of protein expression level of the five KEOPS subunits in lymphoblastoid cell lines from two unaffected relatives (A.II-1 and A.II-5), four individuals with the *GON7* mutation p.Tyr*7, one individual with the *OSGEP* mutations p.Arg325Gln and p.Arg280His (individual «N2705» described in Braun et al.[13]), and one individual with GAMOS linked to *WDR73* mutations (individual A.II-4 described in Colin et al.[15]). One representative western blot is shown (three independent experiments were performed). α-Tubulin was used as a loading control. Source data are provided as a Source Data file

respectively, are nearly identical. It is therefore surprising that GON7 could not complement the yeast Δ*gon7* deletion mutant[7]. Comparison of the GON7/LAGE3 and Gon7/Pcc1 complexes shows that the hydrophobic character of the residues at the interface is very well conserved (Supplementary Fig. 7). However quite a few amino-acid substitutions between GON7 and Gon7 might create steric clashes that weaken or disrupt the interaction with Pcc1, explaining the lack of complementation. Nevertheless, the exquisite superposition of GON7 and Gon7 qualifies them as orthologs and confirms that GON7 is the functional fifth subunit of the human KEOPS complex. Such discrepancies between the protein sequence and structure conservation between distant species might be relevant in other protein complex, with their characterization helping to identify new candidate genes for human monogenic disorders.

An increasing number of mutations are being identified in genes encoding tRNA-modifying enzymes that are linked to human neurodevelopmental disorders. Very recently, mutations in *WDR4*, initially described to cause a distinct form of microcephalic primordial dwarfism and brain malformations[30,31], have been identified in individuals with GAMOS[14]. WDR4 is a component of the METTL1/WDR4 holoenzyme, an N^7-methylguanosine (m^7G) methyltransferase that is responsible for the highly conserved m^7G modification on a specific subset of tRNAs[32,33]. Interestingly, it has been shown that the absence of m^7G tRNA modification leads to impaired cell proliferation, neural differentiation, and a decrease in global translation with a less efficient translation of mRNAs involved in cell division and brain development, consistent with the microcephaly and brain anomalies found in individuals with *WDR4* mutations[34]. Similarly, as a consequence of the decrease in t^6A levels observed in affected individual's cells, perturbed protein translation could impact the translation of specific mRNA involved in kidney and brain development and/or podocyte/neuron maintenance. It is likely that the requirement for t^6A-modified tRNAs levels is dependent of the cell-type and/or cell cycle as has been previously shown in *D. melanogaster* where highly proliferative cells of the wing imaginal discs are more affected by the absence of t^6A modification than fully differentiated photoreceptors[35]. Neuronal progenitors that have high mitotic activity probably have higher demands for protein translation, making them more vulnerable to any perturbation in the tight regulation of tRNA modifications. Furthermore, another potential regulatory step to spatiotemporally modulate these tRNA modifications and thus protein translation is the tissue- and developmental stage-specific expression of the tRNA-modifying enzymes[36,37]. YRDC and

KEOPS subunits could be differentially expressed between specific cell-types in the brain (neural progenitors) and the kidney (podocytes) and/or during development/differentiation explaining the tissue involvement and the course of the disease as well as its clinical outcome. Further studies on neuronal/renal progenitors and neurons/podocytes differentiated from induced pluripotent stem cells obtained from individuals with mutations in YRDC and KEOPS subunits will probably provide further insights into the pathogenesis of GAMOS.

Together, our data strongly emphasize the importance and relevance of the t^6A biosynthesis pathway in the pathogenesis of GAMOS. Further investigations are needed to fully characterize all the KEOPS mutations at the biochemical, structural, and enzyme activity levels to better understand their impact on KEOPS complex-dependent t^6A biosynthesis activity and how they influence the clinical phenotypes. Genes encoding components of the t^6A biosynthesis pathway have to be added to the growing list of translation-associated proteins whose loss of function are responsible for rare genetic disorders.

Methods

Patients and families. Written informed consent was obtained from participants or their legal guardians, and the study was approved by the Comité de Protection des Personnes "Ile-De-France II." Genomic DNA samples were isolated from peripheral blood leukocytes using standard procedures.

Whole-exome sequencing and mutation calling. We performed whole-exome sequencing using Agilent SureSelect All Exon 51 Mb V5 capture-kit on a HiSeq2500 (Illumina) sequencer (paired-end reads: 2 × 100 bases). Sequences were aligned to the human Genome Reference Consortium Human Build 37 (GRCh37) genome assembly with the Lifescope suite from Life Technologies. Variant calling was made using the Genome Analysis Toolkit pipeline. Then, variants were annotated using a pipeline designed by the Paris Descartes University Bioinformatics platform. We assumed the causal variant: (i) segregates with the disease status, (ii) is novel or has a minor allele frequency <1/1000 in gnomAD, (iii) was not found in >10/2352 projects of our in-house database. Missense variant pathogenicity was evaluated using in silico prediction tools (PolyPhen2, SIFT and Mutation Taster). Sanger sequencing was used to validate the variant identified by exome sequencing and to perform segregation analysis in the families. Sequence were analyzed with the Sequencher software (Gene Codes, Ann Arbor, MI) and positions of mutations were numbered from the A of the ATG-translation initiation codon. For Family G, WES, and SNP-array were performed according to standard diagnostic procedures and WES quality criteria at the UMC Utrecht, the Netherlands. The patient–parent quartet WES with sibling-sharing analysis focused on the regions of homozygosity determined by SNP-array (parents are consanguineous in the eighth degree).

Plasmids, cell culture, establishment of cell lines. The following expression vectors were used in this publication: LentiORF pLEX-MCS (Open Biosystems), pESC-TRP with a c-myc tag (Agilent), and pLKO.1-TRC Cloning vector (# Plasmid 10878, Addgene). The LentiORF pLEX-MCS plasmid was modified by site-directed mutagenesis (QuickChange kit, Agilent) to insert one *Nhe*I restriction site, and either two copies of the Human influenza hemagglutinin (HA) tag or one copy of the V5 epitope tag allowing epitope-tagging at the N-terminal of the encoded protein. Human full-length *GON7, LAGE3*, and *YRDC* cDNA (NM_032490.5, NM_006014.4, and NM_024640.4, respectively) were amplified by PCR from IMAGE cDNA clones (IMAGE 4796574, IMAGE 5485603, IMAGE 5211591, and IMAGE 6147134, respectively), and subcloned into the modified pLEX-MCS plasmid using either *Spe*I and *Xho*I (for *GON7* and *LAGE3*) or *Nhe*I and *Xho*I (for *YRDC*). Human *YRDC* cDNA was also subcloned into the *Bam*HI and *Sal*I sites of pESC-TRP. Site-directed mutagenesis (QuickChange kit, Agilent) was used to generate the mutations used in this study. An adapted cloning protocol was used to obtain the C-terminal extension found for the YRDC p.Val241Ilefs*72 mutant. For gene silencing, the shRNA sequences described in Supplementary Table 6 were cloned into the lentiviral pLKO.1-TRC Cloning Vector using the *Age*I and *Eco*RI restriction sites. This vector contains a cassette conferring puromycin resistance. All constructs were verified by Sanger sequencing.

The human immortalized podocyte cell line (AB8/13) provided by M. Saleem (University of Bristol, UK) was grown at 33 °C with 7% CO_2 in RPMI 1640 medium supplemented with 10% fetal bovine serum, insulin-transferrin-selenium, glutamine, and penicillin and streptomycin (all from Life Technologies), and human primary fibroblasts, obtained from patient skin biopsies, were cultured in OPTIMEM medium supplemented with 10% fetal bovine serum, sodium pyruvate, glutamine, fungizone, and penicillin and streptomycin (all from Life Technologies) at 37 °C with 7% CO_2. Obtention and culture of lymphoblastoid cell lines are detailed in Supplementary Methods. Human podocytes stably overexpressing 2HA-GON7 or V5-LAGE3, or transiently depleted for *GON7*, *LAGE3*, *OSGEP*, or *YRDC* were obtained by transduction with lentiviral particles and subsequent puromycin selection (2 µg/ml). HEK293T cells (ATCC CRL-3216) were transiently transfected using Lipofectamine® 2000 (ThermoFisher Scientific).

Antibodies and chemical compounds. The following antibodies were used in the study: mouse anti-α-tubulin (T5168, used at 1:1000), mouse anti-actin (A5316, used at 1:1000), mouse anti-HA (12CA5, at 1/1000), rabbit anti-GON7 (HPA 051832, used at 1:500), rabbit anti-LAGE3 (HPA 036122, used at 1/500), rabbit anti-TPRKB (HPA035712, used at 1:500), rabbit anti-OSGEP (HPA 039751, used at 1/1000), and mouse anti-GAPDH (MAB374, used at 1/2000) from Sigma-Aldrich; mouse anti-V5 (MCA1360, used at 1/1000) from Bio-Rad; rabbit anti-YRDC (PA5-56366, used at 1:500) from ThermoFisher Scientific; rabbit anti-LAGE3 (NBP2-32715, used at 1:1000) and mouse anti-OSGEP (NBP2-00823, used at 1:500) from Novus Biologicals; rabbit anti-TP53RK (AP17010b, used at 1:500) from Abgent. Secondary antibodies for immunoblotting were sheep: anti-mouse and donkey anti-rabbit HRP-conjugated antibodies (GE Healthcare, UK), and IRDye 800CW Donkey anti-rabbit (926-32213) and IRDye 680RD Donkey anti-mouse (926-68072) antibodies (LI-COR). Cycloheximide (C7698), Nuclease P1 (N8630), phosphodiesterase I from snake venom (P3243), and alkaline phosphatase (P4252) were purchased from Sigma-Aldrich.

Yeast culture and heterologous complementation assay. Yeast cells were grown at 28 °C in standard rich medium YEPD (1% yeast extract, 2% peptone, 2% glucose) or minimal supplemented media (0.67% YNB, 2% carbon source). Cells were transformed using the lithium acetate method[38]. Media were supplemented with 2% agar for solid media. The *S. cerevisiae* W303 derived strain, *Δsua5::KanMX* (YCplac33-*SUA5*)[39], was used as the host for the complementation assay. For each pESC-TRP plasmid derivative to be tested, three independent clones were selected after transformation and grown on GLU-TRP media. Clones were then streaked onto GAL-TRP containing 0.1% 5-fluoroorotic acid (5-FOA) to counter-select the YCplac33-*SUA5* plasmid (containing *URA3*). After two rounds of selection, clones were checked for their acquired Ura- phenotype, their plasmid content was confirmed by sequencing after plasmid rescue before being finally evaluated for fitness by a 10-fold serial dilution spotted onto GAL-TRP minimal supplemented media. Empty pESC-TRP, pESC-TRP-*SUA5,* and pESC-TRP-*SUA5-myc* were used as negative and positive controls, respectively.

Quantitative real-time PCR. Total mRNA from knocked down podocytes, primary skin fibroblasts, and LCLs was isolated using Qiagen Extraction RNeasy® Kit and treated with DNase I. One microgram total RNA was reverse-transcribed using Superscript II, according to the manufacturer's protocol (Life Technologies). The relative expression levels of the mRNA of interest were determined by real-time PCR using Power SYBR Green ROX Mix (ThermoFisher Scientific) with specific primers listed in Supplementary Table 7. Samples were run in triplicate and gene of interest expression was normalized to human hypoxanthine-guanine phosphoribosyl transferase (*Hgprt*). Data were analyzed using the $2^{-\Delta\Delta Ct}$ method.

Quantification of t^6A modification. Yeast tRNAs were extracted and purified from actively growing cells (at OD_{600nm} of approximately 3×10^7 cells/ml) with phenol induced cell permeabilization, LiCl-selective precipitation, and subsequent ion exchange-chromatography purification on an AXR-80 column (Nucleobond, Macherey-Nagel), according to the manufacturer's instructions. For human primary fibroblasts, the two-step protocol that was applied is detailed in Supplementary Methods. Ten micrograms of yeast tRNAs and approximately 1 µg of human fibroblast tRNAs were then enzymatically hydrolyzed into ribonucleosides with nuclease P1, phosphodiesterase, and alkaline phosphatase, deproteonized by filtration, and finally dried under vacuum according to the protocol of Thuring et al.[40]. t^6A ribonucleoside was analyzed using the quantitative LC/MS-MS protocol of Thüring et al.[40]. Quantification of t^6A was performed by integration of the peaks of interest and expressed relative to the total area of the peaks corresponding to the four canonical unmodified ribonucleosides assessed in the same sample for normalization. tRNA extracted from three independent samples were each measured twice (two technical replicates). Detailed information are provided in Supplementary Methods.

Protein extraction and immunoblotting. Proteins from KD podocytes, primary fibroblasts, and LCLs were extracted in lysis buffer containing 150 mM NaCl, 50 mM Tris-HCl pH 7, 0.5% Triton-X100 with Complete™ protease inhibitors (Roche), as in Serrano-Perez et al.[41]. Fifty micrograms of proteins were loaded onto acrylamide gels and blotted onto nitrocellulose membranes (Amersham). The membranes were blocked in 1× Tris-buffered saline, 0.1% Tween 20 (TBST) with 5% bovine serum albumin or in Odyssey (LI-COR Bioscience) blocking buffer. Membranes were then incubated with the indicated primary antibodies, washed, and then incubated with either HRP-conjugated or LI-COR IRDye secondary antibodies. Signals were detected using ECL reagents (Amersham Biosciences) and acquired in a Fusion Fx7 darkroom (Vilber Lourmat) or acquired with Odyssey CLx near-infrared fluorescent imaging system (LI-COR Bioscience). Densitometry

quantification was performed either using Bio-1D software or using *Image studio lite* software (version 5.2). Uncropped and unprocessed blots are provided in the Source Data file.

Immunoprecipitation and cycloheximide chase experiments. For immunoprecipitation, HEK293T cells were transiently transfected with the adequate plasmids (2HA-tagged GON7, V5-tagged-LAGE3 wild-type (WT) and/or mutants) using calcium phosphate. Forty-eight hours post transfection, cells were lysed in 150 mM NaCl, 25 mM Tris-HCl pH 8, 0.5% Triton with protease inhibitors and HA-tagged GON7 was immunoprecipitated using the μMACS^{TM} Epitope Tag Protein Isolation Kit (Miltenyi Biotec). Briefly, fresh lysates (1–1.5 mg of protein) were incubated either with mouse anti-V5 antibodies, followed by a 30-min incubation with magnetic beads coupled to protein A, or directly with magnetic beads coupled to an HA antibody. Immunoprecipitated proteins were isolated using μMACS® Separation Columns in a magnetic μMACS separator and subsequently eluted with 1× Laemmli buffer. Lysates and immunoprecipitated samples were subjected to immunoblot[41]. To assess rates of protein degradation, HEK293T cells transiently expressing either 2HA-GON7 or V5-LAGE3 alone, or co-expressing both proteins were incubated with cycloheximide at a final concentration of 100 μg/ml for the indicated time periods (0.5, 1, 2, 4, and 6 h). Total protein extracts and immunoblotting were performed as described above. Anti-HA and anti-V5 antibodies were used to reveal GON7 and LAGE3, respectively. Relative GON7 and LAGE3 protein amounts were normalized to those of α-tubulin at each time point.

Cell proliferation, apoptosis, and protein synthesis assays. Cell proliferation, apoptosis level, and rates of protein synthesis were assessed in KD podocytes using the CellTiter 96 Aqueous Non-Radioactive Cell Proliferation Assay (MTT) (Promega), the Caspase-3/7 Green detection Reagent (C10423; ThermoFisher Scientific), and the Click-iT HPG Alexa Fluor 488 Protein Synthesis Assays (C10428; ThermoFisher Scientific), respectively, according to the manufacturer's instructions. Detailed information are provided in Supplementary Methods.

Proteomic studies. Human podocyte cell lines stably expressing either 2HA-GON7 or V5-LAGE3 were used to perform proteomic studies. 2HA-GON7 and V5-LAGE3 were immunoprecipitated as described in the section above. Eluates were processed according to Braun et al.[13]. Two groups (control IP versus IP HA or IP V5), each containing three biological replicates, were used for statistical analysis. Only proteins that were identified at least three times out of six were retained. A *t*-test was performed, and the data were represented in a volcano plot (FDR < 0.01, S0 = 2, 250 randomizations).

Telomeric restriction fragment. Measurement of the length of the terminal restriction fragments was performed by Southern blotting according to Touzot et al.[42].

Expression and purification of KEOPS subunits. All structural work was done using the full-length proteins of GON7, LAGE3, and OSGEP.

For NMR experiments, two vectors were ordered from Genscript (Piscataway, USA) for the expression of either unlabeled his-tagged LAGE3 (vector "pET21a-LAGE3_hisTEV_op") or ^{15}N-labeled his-tagged GON7 (vector "pET24d-C14_hisTEV_op") whose sequences are shown in Supplementary Table 8. Expression and purification of LAGE3 and ^{15}N-GON7 and subcomplex LAGE3/^{15}N-GON7 preparation are described in detail in Supplementary Methods.

For SAXS or crystallogenesis experiments, preparation of unlabeled GON7 and GON7/LAGE3/OSGEP subcomplex, and co-expression and purification of the KEOPS subunits are detailed in Supplementary Methods and Supplementary Figs. 12 and 13. Fractions of the heterotrimeric GON7/LAGE3/OSGEP complex eluted from size exclusion chromatography (Supplementary Table 9) were then re-loaded onto NiIDA and washed with lysis buffer A supplemented with increasing concentrations of NaCl (0.2; 0.5; 1, and 2 M) in order to remove traces of contaminants. Bound proteins were eluted using three fractions of 2 ml of buffer A supplemented with 100, 200, and 400 mM imidazole and the three subunits complex was concentrated to 8.3 mg/ml for crystallization trials. A unique crystal was obtained using the sitting-drop vapor diffusion method after more than 6 months incubation at 4 °C. The successful condition was composed of 100 nl of protein solution and 100 nl of 30% PEG 4000, 0.1 M Tris-HCl pH 8.5 and 0.2 M magnesium chloride. The crystal was cryo-protected by quick-soaking in reservoir solution supplemented with 30% glycerol prior to flash freezing in liquid nitrogen.

Modeling and crystal structure determination. Modeling of YRDC: the Phyre2 and I-tasser webservers both proposed high confidence models for YRDC based on the StSua5 crystal structure despite weak sequence identity between the two species. A 3D model of YRDC was built using the MODELLER software[43]. X-ray diffraction data collection was carried out on beamline Proxima1 at the SOLEIL Synchrotron (Saint-Aubin, France) at 100 K. Data were processed, integrated, and scaled with the XDS program package[44]. The crystal belonged to space group $P4_3$. The OSGEP and LAGE3 subunits were positioned by molecular replacement with the programs PHASER[45] and MOLREP, implemented in the CCP4 suite[46] using the structures of MjKae1 (PDB ID: 2VWB) and ScPcc1 (PDB ID: 4WX8) as search models. Residual electron density showed clearly the presence of the GON7 subunit, which was constructed using the program BUCCANEER[46]. The initial structure was refined using the BUSTER program[47] and completed by interactive and manual model building using COOT[48]. The correctness of the assigned GON7 sequence was verified by omit mFo-DFc, 2mFo-DFc, Prime-and-switch electron density maps[49] (Supplementary Fig. 14). One copy of the GON7/LAGE3/OSGEP heterotrimer was present in the asymmetric unit. Data collection and refinement statistics are gathered in Supplementary Table 5. The coordinates have been deposited at the Protein Data Bank (code 6GWJ).

Small-angle X-ray analysis. SAXS experiments were carried out at the SOLEIL synchrotron SWING beamline (Saint-Aubin, France). The sample to detector (Aviex CCD) distance was set to 1500 mm, allowing reliable data collection over the momentum transfer range $0.008\ Å^{-1} < q < 0.5\ Å^{-1}$ with $q = 4\pi\sin\theta/\lambda$, where 2θ is the scattering angle and λ is the wavelength of the X-rays ($\lambda = 1.0$ Å). To isolate the various species in solution, SAXS data were collected on samples eluting from an online size exclusion high-performance liquid chromatography (SEHPLCBio-SEC3Agilent) column and directly connected to the SAXS measuring cell. sixty-five microliters of GON7/LAGE3/OSGEP and GON7 samples concentrated at 1.5 and 6.7 mg/l, respectively, were injected into the column pre-equilibrated with a buffer composed of 20 mM MES pH 6.5, 200 mM NaCl, and 5 mM 2-mercaptoethanol. Flow rate was 300 μl/min, frame duration was 1.0 s, and the dead time between frames was 0.5 s. The protein concentration was estimated by UV absorption measurement at 280 and 295 nm using a spectrometer located immediately upstream of the SAXS measuring cell. A large number of frames were collected before the void volume and averaged to account for buffer scattering. SAXS data were normalized to the intensity of the incident beam and background (i.e. the elution buffer) subtracted using the program FoxTrot[50], the Swing in-house software. The scattered intensities were displayed on an absolute scale using the scattering by water. Identical frames under the main elution peak were selected and averaged for further analysis. Radii of gyration, maximum particle dimensions, and molecular masses were determined using PrimusQT[51] (Supplementary Table 4). The BUNCH program[52] was then used to build atomic models of GON7/LAGE3/OSGEP starting from the crystal structure and by determining the optimal position of the missing regions as to fit the data. In a final step, we substituted the dummy residues of these flexible parts with all-atom descriptions using the programs PD2 and SCWRL4 (ref. [53]). An ultimate adjustment was performed using the program CRYSOL[54]. The modeling was repeated 10 times and the best model was deposited in SASBDB[55] with codes SASDFK8, SASDFM8, and SASDFL8 for GON7, GON7/LAGE3, and GON7/LAGE3/OSGEP, respectively.

Statistical analyses. GraphPad Prism 8.0 software was used for the graphical representation and statistical analysis of cell-based data. Results are presented as mean ± s.e.m. of at least $n = 3$ independent experiments. For statistical analysis, data sets comparing more than three conditions (to a control group) were analyzed with ANOVA followed by Dunnett's multiple comparisons test or by using Kruskal–Wallis test followed by a Dunn's multiple comparisons test. Data sets with only two conditions to compare were analyzed using an unpaired *t*-test or a Mann–Whitney test. $P < 0.05$ was considered statistically significant. A standard confidence interval of 95% was applied in all analyses. Displayed in the figures are the mean values of all technical replicates for each of the independent experiments (displayed as single data points). Black lines indicate the mean values of all independent experiments.

Reporting summary. Further information on research design is available in the Nature Research Reporting Summary linked to this article.

Data availability

The source data underlying Figs. 3c–d, 4 and 6 and Supplementary Figs. 1, 5b, 8b, 9 and 10 are provided as a Source Data file. Patients' consent was not obtained for public deposition of whole-exome sequencing data, but these are available from the corresponding author upon reasonable request. Other data generated during the current study are available from the corresponding authors upon reasonable request. Accession codes for deposited data: crystal structure of GON7/LAGE3/OSGEP (PDB ID: 6GWJ, [https://www.rcsb.org/structure/6GWJ]); SAXS model codes SASDFK8, SASDFM8, and SASDFL8 for GON7, GON7/LAGE3, and GON7/LAGE3/OSGEP, respectively.

Received: 18 March 2019 Accepted: 9 August 2019
Published online: 03 September 2019

References

1. El Yacoubi, B., Bailly, M. & de Crecy-Lagard, V. Biosynthesis and function of posttranscriptional modifications of transfer RNAs. *Annu. Rev. Genet.* **46**, 69–95 (2012).

2. El Yacoubi, B. et al. A role for the universal Kae1/Qri7/YgjD (COG0533) family in tRNA modification. *EMBO J.* **30**, 882–893 (2011).
3. Srinivasan, M. et al. The highly conserved KEOPS/EKC complex is essential for a universal tRNA modification, t6A. *EMBO J.* **30**, 873–881 (2011).
4. Lauhon, C. T. Mechanism of N6-threonylcarbamoyladenonsine (t(6)A) biosynthesis: isolation and characterization of the intermediate threonylcarbamoyl-AMP. *Biochemistry* **51**, 8950–8963 (2012).
5. Costessi, A. et al. The human EKC/KEOPS complex is recruited to Cullin2 ubiquitin ligases by the human tumour antigen PRAME. *PLoS One* **7**, e42822 (2012).
6. Mao, D. Y. et al. Atomic structure of the KEOPS complex: an ancient protein kinase-containing molecular machine. *Mol. Cell* **32**, 259–275 (2008).
7. Wan, L. C. et al. Proteomic analysis of the human KEOPS complex identifies C14ORF142 as a core subunit homologous to yeast Gon7. *Nucleic Acids Res.* **45**, 805–817 (2017).
8. Zhang, W. et al. Crystal structures of the Gon7/Pcc1 and Bud32/Cgi121 complexes provide a model for the complete yeast KEOPS complex. *Nucleic Acids Res.* **43**, 3358–3372 (2015).
9. Thiaville, P. C., Iwata-Reuyl, D. & de Crecy-Lagard, V. Diversity of the biosynthesis pathway for threonylcarbamoyladenosine (t(6)A), a universal modification of tRNA. *RNA Biol.* **11**, 1529–1539 (2014).
10. Ramos, J. & Fu, D. The emerging impact of tRNA modifications in the brain and nervous system. *Biochim. Biophys. Acta Gene Regul. Mech.* **1862**, 412–428 (2019).
11. Galloway, W. H. & Mowat, A. P. Congenital microcephaly with hiatus hernia and nephrotic syndrome in two sibs. *J. Med. Genet.* **5**, 319–321 (1968).
12. Braun, D. A. et al. Mutations in multiple components of the nuclear pore complex cause nephrotic syndrome. *J. Clin. Invest.* **128**, 4313–4328 (2018).
13. Braun, D. A. et al. Mutations in KEOPS-complex genes cause nephrotic syndrome with primary microcephaly. *Nat. Genet.* **49**, 1529–1538 (2017).
14. Braun, D. A. et al. Mutations in WDR4 as a new cause of Galloway-Mowat syndrome. *Am. J. Med. Genet. A* **176**, 2460–2465 (2018).
15. Colin, E. et al. Loss-of-function mutations in WDR73 are responsible for microcephaly and steroid-resistant nephrotic syndrome: Galloway-Mowat syndrome. *Am. J. Hum. Genet.* **95**, 637–648 (2014).
16. Fujita, A. et al. Homozygous splicing mutation in NUP133 causes Galloway-Mowat syndrome. *Ann. Neurol.* **84**, 814–828 (2018).
17. Rosti, R. O. et al. Homozygous mutation in NUP107 leads to microcephaly with steroid-resistant nephrotic condition similar to Galloway-Mowat syndrome. *J. Med. Genet.* **54**, 399–403 (2017).
18. Vodopiutz, J. et al. WDR73 mutations cause infantile neurodegeneration and variable glomerular kidney disease. *Hum. Mutat.* **36**, 1021–1028 (2015).
19. Parthier, C. et al. The O-carbamoyltransferase TobZ catalyzes an ancient enzymatic reaction. *Angew. Chem. Int. Ed. Engl.* **51**, 4046–4052 (2012).
20. El Yacoubi, B. et al. The universal YrdC/Sua5 family is required for the formation of threonylcarbamoyladenosine in tRNA. *Nucleic Acids Res.* **37**, 2894–2909 (2009).
21. Kisseleva-Romanova, E. et al. Yeast homolog of a cancer-testis antigen defines a new transcription complex. *EMBO J.* **25**, 3576–3585 (2006).
22. Downey, M. et al. A genome-wide screen identifies the evolutionarily conserved KEOPS complex as a telomere regulator. *Cell* **124**, 1155–1168 (2006).
23. Hecker, A. et al. Structure of the archaeal Kae1/Bud32 fusion protein MJ1130: a model for the eukaryotic EKC/KEOPS subcomplex. *EMBO J.* **27**, 2340–2351 (2008).
24. Liu, Y. Y. et al. Yeast KEOPS complex regulates telomere length independently of its t(6)A modification function. *J. Genet. Genomics* **45**, 247–257 (2018).
25. Saleem, M. A. et al. A conditionally immortalized human podocyte cell line demonstrating nephrin and podocin expression. *J. Am. Soc. Nephrol.* **13**, 630–638 (2002).
26. Thiaville, P. C. et al. Global translational impacts of the loss of the tRNA modification t(6)A in yeast. *Micro Cell.***3**, 29–45 (2016).
27. Bizien, T. et al. A brief survey of state-of-the-art BioSAXS. *Protein Pept. Lett.* **23**, 217–231 (2016).
28. Blomen, V. A. et al. Gene essentiality and synthetic lethality in haploid human cells. *Science* **350**, 1092–1096 (2015).
29. Wan, L. C. et al. Structural and functional characterization of KEOPS dimerization by Pcc1 and its role in t6A biosynthesis. *Nucleic Acids Res.* **44**, 6971–6980 (2016).
30. Shaheen, R. et al. Mutation in WDR4 impairs tRNA m(7)G46 methylation and causes a distinct form of microcephalic primordial dwarfism. *Genome Biol.* **16**, 210 (2015).
31. Trimouille, A. et al. Further delineation of the phenotype caused by biallelic variants in the WDR4 gene. *Clin. Genet.* **93**, 374–377 (2018).
32. Alexandrov, A., Martzen, M. R. & Phizicky, E. M. Two proteins that form a complex are required for 7-methylguanosine modification of yeast tRNA. *RNA* **8**, 1253–1266 (2002).
33. Leulliot, N. et al. Structure of the yeast tRNA m7G methylation complex. *Structure* **16**, 52–61 (2008).
34. Lin, S. et al. Mettl1/Wdr4-Mediated m(7)G tRNA methylome is required for normal mRNA translation and embryonic stem cell self-renewal and differentiation. *Mol. Cell* **71**, 244–255 e245 (2018).
35. Rojas-Benitez, D., Eggers, C. & Glavic, A. Modulation of the proteostasis machinery to overcome stress caused by diminished levels of t6A-modified tRNAs in Drosophila. *Biomolecules* **7**, https://doi.org/10.3390/biom7010025 (2017).
36. de Crecy-Lagard, V. et al. Matching tRNA modifications in humans to their known and predicted enzymes. *Nucleic Acids Res.* **47**, 2143–2159 (2019).
37. Uhlen, M. et al. Proteomics. Tissue-based map of the human proteome. *Science* **347**, 1260419 (2015).
38. Gietz, R. D. & Schiestl, R. H. High-efficiency yeast transformation using the LiAc/SS carrier DNA/PEG method. *Nat. Protoc.* **2**, 31–34 (2007).
39. Pichard-Kostuch, A. et al. Structure-function analysis of Sua5 protein reveals novel functional motifs required for the biosynthesis of the universal t(6)A tRNA modification. *RNA* **24**, 926–938 (2018).
40. Thuring, K., Schmid, K., Keller, P. & Helm, M. Analysis of RNA modifications by liquid chromatography-tandem mass spectrometry. *Methods* **107**, 48–56 (2016).
41. Serrano-Perez, M. C. et al. Endoplasmic reticulum-retained podocin mutants are massively degraded by the proteasome. *J. Biol. Chem.* **293**, 4122–4133 (2018).
42. Touzot, F. et al. Function of Apollo (SNM1B) at telomere highlighted by a splice variant identified in a patient with Hoyeraal-Hreidarsson syndrome. *Proc. Natl. Acad. Sci. USA* **107**, 10097–10102 (2010).
43. Sali, A., Potterton, L., Yuan, F., van Vlijmen, H. & Karplus, M. Evaluation of comparative protein modeling by MODELLER. *Proteins* **23**, 318–326 (1995).
44. Kabsch, W. Xds. *Acta Crystallogr. D Biol. Crystallogr.* **66**, 125–132 (2010).
45. McCoy, A. J. et al. Phaser crystallographic software. *J. Appl. Crystallogr.* **40**, 658–674 (2007).
46. Winn, M. D. et al. Overview of the CCP4 suite and current developments. *Acta Crystallogr. D Biol. Crystallogr.* **67**, 235–242 (2011).
47. Bricogne G. et al. BUSTER version 2.10.3 (Global Phasing Ltd, Cambridge, UK, 2017).
48. Emsley, P. & Cowtan, K. Coot: model-building tools for molecular graphics. *Acta Crystallogr. D Biol. Crystallogr.* **60**, 2126–2132 (2004).
49. Terwilliger, T. C. Using prime-and-switch phasing to reduce model bias in molecular replacement. *Acta Crystallogr. D Biol. Crystallogr.* **60**, 2144–2149 (2004).
50. David, G. & Perez, J. Combined sampler robot and high-performance liquid chromatography: a fully automated system for biological small-angle X-ray scattering experiments at the Synchrotron SOLEIL SWING beamline. *J. Appl. Cryst.* **42**, 892–900 (2009).
51. Franke, D. et al. ATSAS 2.8: a comprehensive data analysis suite for small-angle scattering from macromolecular solutions. *J. Appl. Crystallogr.* **50**, 1212–1225 (2017).
52. Petoukhov, M. V. & Svergun, D. I. Global rigid body modeling of macromolecular complexes against small-angle scattering data. *Biophys. J.* **89**, 1237–1250 (2005).
53. Krivov, G. G., Shapovalov, M. V. & Dunbrack, R. L. Jr. Improved prediction of protein side-chain conformations with SCWRL4. *Proteins* **77**, 778–795 (2009).
54. Svergun, D., Barberato, C. & Koch, M. H. J. CRYSOL—a program to evaluate X-ray solution scattering of biological macromolecules from atomic coordinates. *J. Appl. Cryst.* **28**, 768–773 (1995).
55. Valentini, E., Kikhney, A. G., Previtali, G., Jeffries, C. M. & Svergun, D. I. SASBDB, a repository for biological small-angle scattering data. *Nucleic Acids Res.* **43**, D357–D363 (2015).

Acknowledgements

We are grateful to the patients and their families for their participation. We thank Dr A. Lahoche, Dr. A. Bennour, Dr. C. Loirat, Dr. K. van Gassen, Dr. M. Lilien, and Dr. M. van der Heide-Jalving who helped in the diagnostic process and the follow-up of our patients. We thank G. Froment, D. Nègre, and C. Costa from the lentivector production facility/SFR BioSciences Gerland-Lyon Sud (UMS3444/US8). We acknowledge the use of the biosources of the Necker Imagine DNA biobank (BB-033-00065) and I. Rouvet from CBC BioTec at the CRB-HCL (Hospices Civils de Lyon). We thank Olivier Namy (I2BC, Gif-sur-Yvette, France) for his helpful advices and expertise during the revision process of this article. This work was supported by the Fondation pour le Recherche Médicale (project DEQ2015031682) (to C. Antignac), the European Union's Seventh Framework Programme (FP7/2012, grant 305608 EURenOmics) (to C. Antignac), the Investments for the Future Program (grant ANR-10-IAHY-01) (to C. Antignac), ANR KeoGamo (ANR-18-CE11-0008-01) (to G. Mollet and H.v.T.). This work was supported by the French Infrastructure for Integrated Structural Biology (FRISBI) (ANR-10-INSB-05–01) (to H.v.T.) and the Dutch Kidney Foundation (grant 15OP14) (to A.M.v.E.). S.M. is supported by a Ph.D. grant of the Fondation pour le Recherche Médicale (FRM). P.R. is a scientist from Centre National de la Recherche Scientifique (CNRS).

Author contributions

R.S., O.G., O.B., E.M., F.N., D.A.B., M.P., C.M., A.M.v.E., F.H., D.M., and C. Antignac performed exome sequencing, bioinformatics analysis of exome sequencing data, whole-exome evaluation, Sanger sequencing, and mutation analysis. R.S., O.B., M.C., S.D, R.N., M.-A.M., B.R., J.B., A.L., D.A.B., A.M.v.E., D.M., F.H., and C. Antignac recruited patients and collected detailed clinical information for the study. N.B. provided MRI from control individuals and critically interpreted MRI images from patients. S.C.-F., R.S., and A.M.v.E. provided and analyzed images of renal histology and electron microscopy. C. Arrondel, J.P., B.C., D.L., G. Martin, E.M., and F.N. performed design of expression vectors used in this study. C. Arrondel generated knockdown cell lines, performed in vitro studies (proliferation, apoptosis, and protein synthesis) in immortalized human podocytes, and performed purification of human tRNAs. C. Arrondel, J.P., G. Menara, L.B., G. Martin, E.M., and F.N. performed cell experiments (co-immunoprecipitation, cycloheximide chase, cell culture), qPCR, and western blot experiments. S.M. performed proteins expression and purifications, cristallogenesis trials, diffraction data collection, 3D structure resolution, SAXS data collection, and analysis. B.C. performed OSGEP/LAGE3/GON7-his expression and purification, and nucleosides preparation from tRNA samples and YRDC WT and mutant enzymatic assay. D.L. performed yeast complementation studies, expression, and purification of yeast tRNAs. D.D. performed SAXS data collection and analysis. E.L. collected and analyzed NMR experiments. A.-C.B. and S.S. performed HPLC MS/MS t^6A modification analysis. G. Mollet, G. Martin, and I.C.G. performed proteomic studies in human podocyte cell lines. P.R. performed telomere restriction-fragment assays. C. Arrondel, S.M., J.P., G. Menara, B.C., D.L., D.D., O.G., O.B., L.B., G. Martin, E.M., F.N., E.L., A.-C.B., S.S., I.C.G., P.R., M.P., C.M., A.M.v.E., D.M., C. Antignac, H.v.T., and G.Mollet contributed to the interpretation of the data. G. Mollet, H.v.T. and C.Antignac conceived and coordinated the study, and wrote the manuscript with the input of B.C., D.L., S.M., and C. Arrondel. All authors critically analyzed and edited the manuscript.

Additional information

Supplementary Information accompanies this paper at https://doi.org/10.1038/s41467-019-11951-x.

Competing interests: F.H. is a cofounder and SAB member of Goldfinch-Bio. The remaining authors declare no competing interests.

Reprints and permission information is available online at http://npg.nature.com/reprintsandpermissions/

Peer review information: *Nature Communications* thanks Piotr Neumann, Kazuhito Tomizawa, and other anonymous reviewer(s) for their contribution to the peer review of this work. Peer reviewer reports are available.

Publisher's note: Springer Nature remains neutral with regard to jurisdictional claims in published maps and institutional affiliations.

Open Access This article is licensed under a Creative Commons Attribution 4.0 International License, which permits use, sharing, adaptation, distribution and reproduction in any medium or format, as long as you give appropriate credit to the original author(s) and the source, provide a link to the Creative Commons license, and indicate if changes were made. The images or other third party material in this article are included in the article's Creative Commons license, unless indicated otherwise in a credit line to the material. If material is not included in the article's Creative Commons license and your intended use is not permitted by statutory regulation or exceeds the permitted use, you will need to obtain permission directly from the copyright holder. To view a copy of this license, visit http://creativecommons.org/licenses/by/4.0/.

© The Author(s) 2019

Christelle Arrondel[1,24], Sophia Missoury[2,24], Rozemarijn Snoek[3,4], Julie Patat[1], Giulia Menara[1], Bruno Collinet[2,5], Dominique Liger[2], Dominique Durand[2], Olivier Gribouval[1], Olivia Boyer[1,6], Laurine Buscara[1], Gaëlle Martin[1], Eduardo Machuca[1], Fabien Nevo[1], Ewen Lescop[7], Daniela A. Braun[8], Anne-Claire Boschat[9], Sylvia Sanquer[10,11], Ida Chiara Guerrera[12], Patrick Revy[13], Mélanie Parisot[14], Cécile Masson[15], Nathalie Boddaert[16], Marina Charbit[6], Stéphane Decramer[17], Robert Novo[18], Marie-Alice Macher[19], Bruno Ranchin[20], Justine Bacchetta[20], Audrey Laurent[20], Sophie Collardeau-Frachon[21], Albertien M. van Eerde[3,4], Friedhelm Hildebrandt[8], Daniella Magen[22], Corinne Antignac[1,23], Herman van Tilbeurgh[2] & Géraldine Mollet[1]

[1]Laboratory of Hereditary Kidney Diseases, INSERM UMR1163, Université de Paris, Imagine Institute, Paris, France. [2]Institute for Integrative Biology of the Cell (I2BC), CEA, CNRS, Université Paris-Sud, Université Paris-Saclay, Gif-sur-Yvette, France. [3]Department of Genetics, University Medical Center Utrecht, Utrecht, The Netherlands. [4]Center for Molecular Medicine, Utrecht University, Utrecht, The Netherlands. [5]Institut de Minéralogie, de Physique des Matériaux et de Cosmochimie, UMR7590 CNRS/Sorbonne-Université, UPMC, Paris, France. [6]Department of Pediatric Nephrology, AP-HP, Necker Hospital, Paris, France. [7]Institut de Chimie des Substances Naturelles, CNRS UPR2301, Université Paris-Sud, Université Paris-Saclay, Gif-sur-Yvette, France. [8]Department of Medicine, Boston Children's Hospital, Harvard Medical School, Boston, MA, USA. [9]Mass Spectrometry Facility, INSERM UMR1163, Imagine Institute, Paris, France. [10]Service de Biochimie métabolomique et protéomique, Hôpital Necker-Enfants Malades, Paris, France. [11]INSERM UMR-S1124, Université de Paris, Paris, France. [12]Proteomics Platform 3P5-Necker, Université de Paris—Structure Fédérative de Recherche Necker, Inserm US24/CNRS, UMS3633 Paris, France. [13]Inserm UMR1163, Laboratory of Genome Dynamics in the Immune System, Labellisé Ligue contre le Cancer, Université de Paris, Imagine Institute, Paris, France. [14]Genomics Core Facility, Structure Fédérative de Recherche Necker, INSERM U1163 and Inserm US24/CNRS UMS3633, Université de Paris, Paris, France. [15]Bioinformatics Platform, INSERM UMR1163, Université de Paris, Imagine Institute, Paris, France. [16]Department of Pediatric Radiology, and Imagine Institute, INSERM UMR 1163 and INSERM U1000, Université de Paris, Hôpital Necker-Enfants Malades, Paris, France. [17]Department of Pediatric Nephrology-Internal Medicine, Purpan Hospital, Toulouse, France. [18]Pediatric Nephrology Unit, University Hospital of Lille, Lille, France. [19]Department of Pediatric Nephrology, AP-HP, Robert Debre Hospital, Paris, France. [20]Service de Néphrologie, Rhumatologie et Dermatologie pédiatriques, Hospices Civils de Lyon, Hôpital Femme-Mère-Enfant, Centre de référence de maladies rénales rares, Université de Lyon, Bron, France. [21]Department of Pathology, Hospices Civils de Lyon-Hôpital Femme-Mère-Enfant, Claude Bernard Lyon 1 University, Bron, France. [22]Pediatric Nephrology Institute-Rambam Health Care Campus-Technion Faculty of Medicine, Haifa, Israel. [23]Department of Genetics, AP-HP, Necker Hospital, Paris, France. [24]These authors contributed equally: Christelle Arrondel, Sophia Missoury.